

Pertanika Journal of

**SCIENCE &**

**TECHNOLOGY**

**JST**

**VOL. 32 (4) JUL. 2024**



**PERTANIKA**  
JOURNALS

A scientific journal published by Universiti Putra Malaysia Press

# PERTANIKA JOURNAL OF SCIENCE & TECHNOLOGY

## About the Journal

### Overview

Pertanika Journal of Science & Technology is an official journal of Universiti Putra Malaysia. It is an open-access online scientific journal. It publishes original scientific outputs. It neither accepts nor commissions third party content.

Recognised internationally as the leading peer-reviewed interdisciplinary journal devoted to the publication of original papers, it serves as a forum for practical approaches to improve quality on issues pertaining to science and engineering and its related fields.

Pertanika Journal of Science & Technology currently publishes 6 issues a year (*January, March, April, July, August, and October*). It is considered for publication of original articles as per its scope. The journal publishes in **English** and it is open for submission by authors from all over the world.

The journal is available world-wide.

### Aims and scope

Pertanika Journal of Science & Technology aims to provide a forum for high quality research related to science and engineering research. Areas relevant to the scope of the journal include: bioinformatics, bioscience, biotechnology and bio-molecular sciences, chemistry, computer science, ecology, engineering, engineering design, environmental control and management, mathematics and statistics, medicine and health sciences, nanotechnology, physics, safety and emergency management, and related fields of study.

### History

Pertanika Journal of Science & Technology was founded in 1993 and focuses on research in science and engineering and its related fields.

### Vision

To publish a journal of international repute.

### Mission

Our goal is to bring the highest quality research to the widest possible audience.

### Quality

We aim for excellence, sustained by a responsible and professional approach to journal publishing. Submissions can expect to receive a decision within 90 days. The elapsed time from submission to publication for the articles averages 180 days. We are working towards decreasing the processing time with the help of our editors and the reviewers.

### Abstracting and indexing of Pertanika

Pertanika Journal of Science & Technology is now over 27 years old; this accumulated knowledge and experience has resulted the journal being abstracted and indexed in SCOPUS (Elsevier), Clarivate Web of Science (ESCI), EBSCO, ASEAN CITATION INDEX, Microsoft Academic, Google Scholar, and MyCite.

### Citing journal articles

The abbreviation for Pertanika Journal of Science & Technology is *Pertanika J. Sci. & Technol.*

### Publication policy

*Pertanika* policy prohibits an author from submitting the same manuscript for concurrent consideration by two or more publications. It prohibits as well publication of any manuscript that has already been published either in whole or substantial part elsewhere. It also does not permit publication of manuscript that has been published in full in proceedings.

### Code of Ethics

The *Pertanika* journals and Universiti Putra Malaysia take seriously the responsibility of all of its journal publications to reflect the highest in publication ethics. Thus, all journals and journal editors are expected to abide by the journal's codes of ethics. Refer to *Pertanika*'s **Code of Ethics** for full details, or visit the journal's web link at [http://www.pertanika.upm.edu.my/code\\_of\\_ethics.php](http://www.pertanika.upm.edu.my/code_of_ethics.php)

### Originality

The author must ensure that when a manuscript is submitted to *Pertanika*, the manuscript must be an original work. The author should check the manuscript for any possible plagiarism using any program such as Turn-It-In or any other software before submitting the manuscripts to the *Pertanika* Editorial Office, Journal Division.

All submitted manuscripts must be in the journal's acceptable similarity index range:  
**≤ 20% – PASS; > 20% – REJECT.**

### International Standard Serial Number (ISSN)

An ISSN is an 8-digit code used to identify periodicals such as journals of all kinds and on all media—print and electronic.

Pertanika Journal of Science & Technology: e-ISSN 2231-8526 (Online).

### Lag time

A decision on acceptance or rejection of a manuscript is reached in 90 days (average). The elapsed time from submission to publication for the articles averages 180 days.

### Authorship

Authors are not permitted to add or remove any names from the authorship provided at the time of initial submission without the consent of the journal's Chief Executive Editor.

### Manuscript preparation

For manuscript preparation, authors may refer to *Pertanika*'s **INSTRUCTION TO AUTHORS**, available on the official website of *Pertanika*.

### Editorial process

Authors who complete any submission are notified with an acknowledgement containing a manuscript ID on receipt of a manuscript, and upon the editorial decision regarding publication.

*Pertanika* follows a **double-blind peer-review** process. Manuscripts deemed suitable for publication are sent to reviewers. Authors are encouraged to suggest names of at least 3 potential reviewers at the time of submission of their manuscripts to *Pertanika*, but the editors will make the final selection and are not, however, bound by these suggestions.

Notification of the editorial decision is usually provided within 90 days from the receipt of manuscript. Publication of solicited manuscripts is not guaranteed. In most cases, manuscripts are accepted conditionally, pending an author's revision of the material.

### The journal's peer review

In the peer-review process, 2 to 3 referees independently evaluate the scientific quality of the submitted manuscripts. At least 2 referee reports are required to help make a decision.

Peer reviewers are experts chosen by journal editors to provide written assessment of the **strengths** and **weaknesses** of written research, with the aim of improving the reporting of research and identifying the most appropriate and highest quality material for the journal.

### Operating and review process

What happens to a manuscript once it is submitted to *Pertanika*? Typically, there are 7 steps to the editorial review process:

1. The journal's Chief Executive Editor and the Editor-in-Chief examine the paper to determine whether it is relevance to journal needs in terms of novelty, impact, design, procedure, language as well as presentation and allow it to proceed to the reviewing process. If not appropriate, the manuscript is rejected outright and the author is informed.
2. The Chief Executive Editor sends the article-identifying information having been removed, to 2 to 3 reviewers. They are specialists in the subject matter of the article. The Chief Executive Editor requests that they complete the review within 3 weeks.

Comments to authors are about the appropriateness and adequacy of the theoretical or conceptual framework, literature review, method, results and discussion, and conclusions. Reviewers often include suggestions for strengthening of the manuscript. Comments to the editor are in the nature of the significance of the work and its potential contribution to the research field.

3. The Editor-in-Chief examines the review reports and decides whether to accept or reject the manuscript, invite the authors to revise and resubmit the manuscript, or seek additional review reports. In rare instances, the manuscript is accepted with almost no revision. Almost without exception, reviewers' comments (to the authors) are forwarded to the authors. If a revision is indicated, the editor provides guidelines for attending to the reviewers' suggestions and perhaps additional advice about revising the manuscript.
4. The authors decide whether and how to address the reviewers' comments and criticisms and the editor's concerns. The authors return a revised version of the paper to the Chief Executive Editor along with specific information describing how they have addressed' the concerns of the reviewers and the editor, usually in a tabular form. The authors may also submit a rebuttal if there is a need especially when the authors disagree with certain comments provided by reviewers.
5. The Chief Executive Editor sends the revised manuscript out for re-review. Typically, at least 1 of the original reviewers will be asked to examine the article.
6. When the reviewers have completed their work, the Editor-in-Chief examines their comments and decides whether the manuscript is ready to be published, needs another round of revisions, or should be rejected. If the decision is to accept, the Chief Executive Editor is notified.
7. The Chief Executive Editor reserves the final right to accept or reject any material for publication, if the processing of a particular manuscript is deemed not to be in compliance with the S.O.P. of *Pertanika*. An acceptance letter is sent to all the authors.

The editorial office ensures that the manuscript adheres to the correct style (in-text citations, the reference list, and tables are typical areas of concern, clarity, and grammar). The authors are asked to respond to any minor queries by the editorial office. Following these corrections, page proofs are mailed to the corresponding authors for their final approval. At this point, **only essential changes are accepted**. Finally, the manuscript appears in the pages of the journal and is posted on-line.

Pertanika Journal of  
**SCIENCE  
& TECHNOLOGY**

**Vol. 32 (4) Jul. 2024**



A scientific journal published by Universiti Putra Malaysia Press



## EDITOR-IN-CHIEF

**Luqman Chuah Abdullah**  
*Chemical Engineering*

## CHIEF EXECUTIVE EDITOR

**Mohd Sapuan Salit**

## UNIVERSITY PUBLICATIONS COMMITTEE

### CHAIRMAN

**Zamberi Sekawi**

### EDITORIAL STAFF

#### Journal Officers:

Ellyianur Puteri Zainal  
Kanagamalar Silvarajoo  
Siti Zuhaila Abd Wahid  
Tee Syin Ying

#### Editorial Assistants:

Ku Ida Mastura Ku Baharom  
Siti Juridah Mat Arip  
Zulinaardawati Kamarudin

#### English Editor:

Norhanizah Ismail

### PRODUCTION STAFF

#### Pre-press Officers:

Nur Farrah Dila Ismail  
Wong Lih Jiun

### WEBMASTER

#### IT Officer:

Illi Najwa Mohamad Sakri

### EDITORIAL OFFICE

#### JOURNAL DIVISION

Putra Science Park  
1<sup>st</sup> Floor, IDEA Tower II  
UPM-IMTDC Technology Centre  
Universiti Putra Malaysia  
43400 Serdang, Selangor Malaysia.

#### General Enquiry

Tel. No: +603 9769 1622 | 1616

#### E-mail:

[executive\\_editor.pertanika@upm.edu.my](mailto:executive_editor.pertanika@upm.edu.my)

URL: [www.journals-jd.upm.edu.my](http://www.journals-jd.upm.edu.my)

### PUBLISHER

#### UPM Press

Universiti Putra Malaysia  
43400 UPM, Serdang, Selangor, Malaysia.  
Tel: +603 9769 8851  
E-mail: [penerbit@putra.upm.edu.my](mailto:penerbit@putra.upm.edu.my)  
URL: <http://penerbit.upm.edu.my>



## ASSOCIATE EDITOR

### 2023-2024

#### Adem Kilicman

Mathematical Sciences  
Universiti Putra Malaysia, Malaysia

#### Miss Laiha Mat Kiah

Security Services Sn: Digital Forensic,  
Steganography, Network Security,  
Information Security, Communication  
Protocols, Security Protocols  
Universiti Malaya, Malaysia

#### Saidur Rahman

Renewable Energy, Nanofluids, Energy  
Efficiency, Heat Transfer, Energy Policy  
Sunway University, Malaysia

## EDITORIAL BOARD

### 2022-2024

#### Abdul Latif Ahmad

Chemical Engineering  
Universiti Sains Malaysia, Malaysia

#### Ho Yuh-Shan

Water research, Chemical Engineering  
and Environmental Studies  
Asia University, Taiwan

#### Mohd Zulkifly Abdullah

Fluid Mechanics, Heat Transfer,  
Computational Fluid Dynamics (CFD)  
Universiti Sains Malaysia, Malaysia

#### Ahmad Zaharin Aris

Hydrochemistry, Environmental  
Chemistry, Environmental Forensics,  
Heavy Metals  
Universiti Putra Malaysia, Malaysia

#### Hsiu-Po Kuo

Chemical Engineering  
National Taiwan University, Taiwan

#### Mohd. Ali Hassan

Bioprocess Engineering, Environmental  
Biotechnology  
Universiti Putra Malaysia, Malaysia

#### Azlina Harun@Kamaruddin

Enzyme Technology, Fermentation  
Technology  
Universiti Sains Malaysia, Malaysia

#### Ivan D. Rukhlenko

Nonlinear Optics, Silicon Photonics,  
Plasmonics and Nanotechnology  
The University of Sydney, Australia

#### Nor Azah Yusof

Biosensors, Chemical Sensor, Functional  
Material  
Universiti Putra Malaysia, Malaysia

#### Bassim H. Hameed

Chemical Engineering: Reaction  
Engineering, Environmental Catalysis &  
Adsorption  
Qatar University, Qatar

#### Lee Keat Teong

Energy Environment, Reaction  
Engineering, Waste Utilization,  
Renewable Energy  
Universiti Sains Malaysia, Malaysia

#### Norbahiah Misran

Communication Engineering  
Universiti Kebangsaan Malaysia,  
Malaysia

#### Biswajeet Pradhan

Digital image processing, Geographical  
Information System (GIS), Remote  
Sensing  
University of Technology Sydney,  
Australia

#### Mohamed Othman

Communication Technology and  
Network, Scientific Computing  
Universiti Putra Malaysia, Malaysia

#### Roslan Abd-Shukur

Physics & Materials Physics,  
Superconducting Materials  
Universiti Kebangsaan Malaysia,  
Malaysia

#### Daud Ahmad Israf Ali

Cell Biology, Biochemical, Pharmacology  
Universiti Putra Malaysia, Malaysia

#### Mohd Shukry Abdul Majid

Polymer Composites, Composite  
Pipes, Natural Fibre Composites,  
Biodegradable Composites, Bio-  
Composites  
Universiti Malaysia Perlis, Malaysia

#### Wing Keong Ng

Aquaculture, Aquatic Animal Nutrition,  
Aqua Feed Technology  
Universiti Sains Malaysia, Malaysia

## INTERNATIONAL ADVISORY BOARD

### 2021-2024

#### CHUNG, Neal Tai-Shung

Polymer Science, Composite and  
Materials Science  
National University of Singapore,  
Singapore

#### Mohamed Pourkashanian

Mechanical Engineering, Energy, CFD  
and Combustion Processes  
Sheffield University, United Kingdom

#### Yulong Ding

Particle Science & Thermal Engineering  
University of Birmingham, United  
Kingdom

#### Hiroshi Uyama

Polymer Chemistry, Organic  
Compounds, Coating, Chemical  
Engineering  
Osaka University, Japan

#### Mohini Sain

Material Science, Biocomposites,  
Biomaterials  
University of Toronto, Canada

## ABSTRACTING AND INDEXING OF PERTANIKA JOURNALS

The journal is indexed in SCOPUS (Elsevier), Clarivate-Emerging Sources Citation Index (ESCI), BIOSIS, National Agricultural Science (NAL), Google Scholar, MyCite, ISC. In addition, Pertanika JSSH is recipient of "CREAM" Award conferred by Ministry of Higher Education (MoHE), Malaysia.

The publisher of Pertanika will not be responsible for the statements made by the authors in any articles published in the journal. Under no circumstances will the publisher of this publication be liable for any loss or damage caused by your reliance on the advice, opinion or information obtained either explicitly or implied through the contents of this publication.

All rights of reproduction are reserved in respect of all papers, articles, illustrations, etc., published in Pertanika. Pertanika provides free access to the full text of research articles for anyone, web-wide. It does not charge either its authors or author-institution for refereeing/publishing outgoing articles or user-institution for accessing incoming articles.

No material published in Pertanika may be reproduced or stored on microfilm or in electronic, optical or magnetic form without the written authorization of the Publisher.

Copyright © 2021 Universiti Putra Malaysia Press. All Rights Reserved.



**Pertanika Journal of Science & Technology**  
**Vol. 32 (4) Jul. 2024**

**Contents**

Foreword	i
<i>Mohd Sapuan Salit</i>	
Evaluation of Glutathione S-transferases Expression as Biomarkers by Heavy Metals in <i>Geloina expansa</i> from Sepang Besar River, Selangor, Malaysia	1439
<i>Sarini Ahmad Wakid, Nor Azwady Abd Aziz, Zazali Alias, Muskhazli Mustafa, Wan Mohd Syazwan and Syaizwan Zahmir Zulkifli</i>	
Blood CO Status Classification Using UV-VIS Spectroscopy and PSO-optimized 1D-CNN Model	1461
<i>Audrey Huong, Kim Gaik Tay, Kok Beng Gan and Xavier Ngu</i>	
Effects of Different Throttle Opening and Air Intake Lengths on the Volumetric Efficiency of SI Engine Using 1D Simulation Method	1481
<i>Mohamad Firzan Ahmad Harazi, Abdul Aziz Hairuddin, Azizan As'arry and Siti Ujila Masuri</i>	
Experiment and Analysis of a Hybrid Composite Post-tension Plate Girder	1501
<i>Sahib Al Mustawfi, Nor Azizi Safiee, Nabilah Abu Bakar, Izian Abd Karim and Noor Azline Mohd Nasir</i>	
Conversion Factor Estimation of Stacked Eucalypt Timber Using Supervised Image Classification with Artificial Neural Networks	1527
<i>Vinicius Andrade de Barros, Carlos Pedro Boechat Soares, Gilson Fernandes da Silva, Gianmarco Goycochea Casas and Helio Garcia Leite</i>	
Low Resource Malay Dialect Automatic Speech Recognition Modeling Using Transfer Learning from a Standard Malay Model	1545
<i>Tien-Ping Tan, Lei Qin, Sarah Flora Samson Juan and Jasmina Yen Min Khaw</i>	
The Green Energy Effect on an HCCI Engine from Used Cooking Oil-based Biodiesel from Malaysia	1565
<i>Muntasser Abdulabbas Mossa, Abdul Aziz Hairuddin, Nuraini Abdul Aziz and Hasyuzariza Muhamad Tobib</i>	

<i>Review Article</i>	
Computer Vision—The Frontier of Modern Environmental Diagnostics: A Review	1591
<i>Anna Sergejevna Olkova and Evgeniya Vladimirovna Tovstik</i>	
A Deep Learning-based Classification Model for Arabic News Tweets Using Bidirectional Long Short-Term Memory Networks	1609
<i>Chin-Teng Lin, Mohammed Thanoon and Sami Karali</i>	
Borderline-DEMNET: A Workflow for Detecting Alzheimer’s and Dementia Stage by Solving Class Imbalance Problem	1629
<i>Neetha Papanna Umalakshmi, Simran Sathyanarayana, Pushpa Chickotlikere Nagappa, Thriveni Javarappa and Venugopal Kuppanna Rajuk</i>	
Novel Reactive Power Control Strategy for Mitigating Voltage Rise in the Malaysian Low Voltage Distribution Network with High PV Penetration	1651
<i>Mustafa Abo Alwez, Jasronita Jasni, Raghad Wahab, Mohd Amran Mohd.Radzi and Norhafiz Azis</i>	
<i>Review Article</i>	
Processing Plants Damage Mechanisms and On-Stream Inspection Using Phased Array Corrosion Mapping—A Systematic Review	1665
<i>Jan Lean Tai, Mohamed Thariq Hameed Sultan and Farah Syazwani Shahar</i>	
Effects of Unavailability of Conventional Energy Units on Power Generation System Adequacy	1687
<i>Athraa Ali Kadhem and Noor Izzri Abdul Wahab</i>	
Single Deformation Occurrence During Testing of Kenaf Composite Through Momentum Trapping Modification on Split Hopkinson Pressure Bar	1707
<i>Muhammad Fauzinizam Razali, Sareh Aiman Hilmi Abu Seman, Mohd Syakirin Rusdi and Siti Nuha Majiddah Abdul Aziz</i>	
Application of Fuzzy Analytic Network Process in Selection of Bio- composite Filament for Fused Deposition Modeling Process	1721
<i>Hazliza Aida Che Hamid, Mastura Mohammad Taha, Syahibudil Ikhwan Abdul Kudus, Noryani Muhammad, Mohd Adrinata Shaharuzaman, Loh Yueh Feng and Ahmad Ilyas Rushdan</i>	
Optimizing Bagged Trees in an Ensemble Classifier for Improved Prediction of Diabetes Prevalence in Women	1753
<i>Jose Candia Jr., Airish Mae Adonis and Jessica Perlas</i>	

Determining Process Variability Using Fuzzy Triangular Distribution in Dynamic Value Stream Mapping <i>Thulasi Manoharan, Faieza Abdul Aziz, Zulkiffle Leman and Siti Azfanizam Ahmad</i>	1765
<i>Review Article</i>	
The Importance of Vegetation Landscape in Firefly Habitats <i>Nurhafizul Abu Seri and Azimah Abd Rahman</i>	1789
Vision-Based Multi-Stages Lane Detection Algorithm <i>Fayez Saeed Faizi and Ahmed Khorsheed Al-sulaifanie</i>	1811
The Macrobenthos Diversity and Dominance in Johor Straits, Malaysia <i>Mohd Sophian Mohd Kasihmuddin and Zaidi Che Cob</i>	1829
Electric Transmission Tower Corrosion Assessment Using Analytic Hierarchy Process and Health Index <i>Aina Shazwana Mohd Izhar, Nor Hazwani Nor Khalid, Fathoni Usman, Mohd Supian Abu Bakar, Nur Fadilah Adriyanshah and Hakim Zahari</i>	1855
Simulating Spanning Tree Protocols in a Cable-based Tsunameter System with an Arbitrary Number of Ocean Bottom Units <i>Mohammad Hamdani, Anak Agung Ngurah Ananda Kusuma, Dedy Irawan, Tahar Agastani and Xerandy</i>	1875
Optimum Parameters for Extraction of Cinnamomum verum Leaves Towards $\alpha$ -Glucosidase Inhibition <i>Leong Yao Shen, Norhayati Muhammad, Hariz Haikal Nasuha, Mohd Fadzelly Abu Bakar, Norazlin Abdullah and Nur Fazira Abdul Rahim</i>	1891
Deflection Performance of Particleboards and Their Potential as Built-in Materials <i>Noor Azrieda Abd. Rashid, Hashim W Samsi, Nur Hanina Izzati Khairol Mokhtar, Yanti Abdul Kadir, Khairul Maseat, Siti Zaliha Ali and Muhammad Taufiq Tajuddin</i>	1905
Energy Audit on Two 22-TPH Coal-fired Boilers of a Pineapple Processing Plant <i>Jay Nelson Corbita, Leonel Pabilona and Eliseo Villanueva</i>	1919



# Foreword

Welcome to the fourth issue of 2024 for the *Pertanika Journal of Science and Technology (PJST)*!

PJST is an open-access journal for studies in Science and Technology published by Universiti Putra Malaysia Press. It is independently owned and managed by the university for the benefit of the world-wide science community.

This issue contains 25 articles; three review articles and the rest are regular articles. The authors of these articles come from different countries namely Australia, Brazil, India, Indonesia, Iraq, Malaysia, Philippines, Russian Federation and the Kingdom of Saudi Arabia .

The article “Borderline-DEMNET: A Workflow for Detecting Alzheimer’s and Dementia Stage by Solving Class Imbalance Problem” by Neetha Papanna Umalakshmi et al. from India presents a new workflow called Borderline-DEMNET. This workflow is designed to classify various stages of Alzheimer’s/dementia with more than three classes and employs Borderline-SMOTE to address the issue of imbalanced datasets. The robustness of the work is checked using the ADNI dataset, and the results are impressive. The proposed workflow achieves an accuracy of 99.17% for the Kaggle dataset and 99.14% for the ADNI dataset, demonstrating the high reliability of the research. The article provides detailed information on this study on page 1629.

Mohd Sophian Mohd Kasihmuddin and Zaidi Che Cob from Universiti Kebangsaan Malaysia studied the diversity and dominance of macrobenthos in Johor Straits, Malaysia. Seven hundred thirty macrobenthic individuals and 46 known taxa were identified in sediments of 13 locations in the strait. Annelids *Prionospio* (n=295), *Minuspio* (n=95) and *Mediomastus* (n=82) were concentrated in the central zone. Molluscs dominated the Merambong Shoals area (*Arcualuta*, n=66), and amphipods dominated waters off Santi River (*Leucothoe*, n=26; *Gammarus*, n=11; *Cymadusa*, n=9). PERMANOVA analyses showed significant differences in benthic taxa composition, while BIOENV analyses highlighted water acidity, chlorophyll-a, silts and total organic carbon. The principal component analysis graph indicated higher organic carbon and silts in the central area, implying favorable conditions for Sedentarian polychaetes to thrive. The east and west ends of the strait exhibited higher readings of water acidity and chlorophyll-a, which may directly contribute to a higher diversity of benthic communities in the areas. Lower oxygen levels in two locations in the central area (J3=2.97 mg/L, J4: 2.63 mg/L) exhibited Sedentaria polychaete-dominated region, but zero benthic organisms in another part of the central area (J5-J9, 2.97–0.99 mg/L). Further details of the article are available on page 1829.

The article titled “Simulating Spanning Tree Protocols in a Cable-Based Tsunameter System with an Arbitrary Number of Ocean Bottom Units” by Mohammad Hamdani and colleagues from Indonesia, presents a scalable simulation framework of the Indonesia cable-based tsunameter (INA-CBT) system. The primary aim of their research is to use Layer 2 open protocols such as

spanning tree protocol (STP) and rapid spanning tree protocol (RSTP) as an early warning system to mitigate the impact of disasters. The practical implications of their work are significant, as the proposed model has been successfully scaled up to ten ocean bottom units (OBUs) with a ring topology. The experimental results show that the convergence time values in failover and failback scenarios are still below the system requirement of INA-CBT. As expected, RSTP shows a faster convergence time than STP, but one should be aware of the possible RSTP downtime fluctuations depending on the number of OBUs deployed. The article provides detailed information on this study on page 1875.

We anticipate that you will find the evidence presented in this issue to be intriguing, thought-provoking and useful in reaching new milestones in your own research. Please recommend the journal to your colleagues and students to make this endeavour meaningful.

All the papers published in this edition underwent Pertanika's stringent peer-review process involving a minimum of two reviewers comprising internal as well as external referees. This was to ensure that the quality of the papers justified the high ranking of the journal, which is renowned as a heavily-cited journal not only by authors and researchers in Malaysia but by those in other countries around the world as well.

We would also like to express our gratitude to all the contributors, namely the authors, reviewers, Editor-in-Chief and Editorial Board Members of PJST, who have made this issue possible.

PJST is currently accepting manuscripts for upcoming issues based on original qualitative or quantitative research that opens new areas of inquiry and investigation.

**Chief Executive Editor**

**Mohd Sapuan Salit**

[executive\\_editor.pertanika@upm.edu.my](mailto:executive_editor.pertanika@upm.edu.my)

## Evaluation of Glutathione S-transferases Expression as Biomarkers by Heavy Metals in *Geloina expansa* from Sepang Besar River, Selangor, Malaysia

Sarini Ahmad Wakid<sup>1,2</sup>, Nor Azwady Abd Aziz<sup>1\*</sup>, Zazali Alias<sup>3</sup>, Muskhazli Mustafa<sup>1</sup>, Wan Mohd Syazwan<sup>1</sup> and Syaizwan Zahmir Zulkifli<sup>1</sup>

<sup>1</sup>Department of Biology, Faculty of Science, Universiti Putra Malaysia, 43400 UPM, Serdang, Selangor, Malaysia

<sup>2</sup>School of Biology, Faculty of Applied Sciences, Universiti Teknologi MARA, Cawangan Negeri Sembilan, Kampus Kuala Pilah, 72000, Kuala Pilah, Negeri Sembilan, Malaysia

<sup>3</sup>Institute of Biological Sciences, Faculty of Science, University of Malaya, 50603, Kuala Lumpur, Malaysia

### ABSTRACT

Glutathione S-transferases (GSTs) are enzymes involved in phase II of detoxification metabolism and could be used as biomarkers for water pollution. This study aims to determine heavy metal concentrations in the soft tissue of the mangrove clam *Geloina expansa*, as well as the expression of GSTs in the species. The acid digestion method was used to digest the samples, followed by a standard USEPA 6010B procedure using inductively coupled plasma optical emission spectrometry (ICP-OES) to measure the heavy metal contents in the samples. GST enzyme activity was measured using 1-chloro-2, 4-dinitrobenzene (CDNB) as substrate. One-way ANOVA was performed to compare the mean values of heavy metal concentration, protein concentration, enzyme activity, and specific activity. There was a significant difference ( $p < 0.05$ ) for Zn, total protein, and specific activity in *G. expansa*, but no significant difference in Pb, Cu and enzyme activity. GST enzyme activities were estimated at  $0.16 \pm 0.01$   $\mu\text{mol}/\text{min}$ , with a protein content of  $1.24 \pm 0.04$  mg. The specific activity for GST was  $0.13 \pm 0.01$   $\mu\text{mol}/\text{min}/\text{mg}$ , calculated as the ratio of enzyme activity to the total protein. GST-specific activity

positively correlates with Pb concentration in the soft tissue of *G. expansa*. Detailed studies on the effects of pollution on the expression of GST need to be further investigated for the future use of this species as an efficient biomarker model.

**Keywords:** Biomarker, bivalves, *Geloina expansa*, glutathione S-transferase, heavy metals, SDG 14

### ARTICLE INFO

#### Article history:

Received: 19 April 2023

Accepted: 02 January 2024

Published: 16 July 2024

DOI: <https://doi.org/10.47836/pjst.32.4.01>

#### E-mail addresses:

sarini@uitm.edu.my (Sarini Ahmad Wakid)

azwady@upm.edu.my (Nor Azwady Abd Aziz)

alias@um.edu.my (Zazali Alias)

muskhazli@upm.edu.my (Muskhazli Mustafa)

mhdasyazwan@upm.edu.my (Wan Mohd Syazwan)

eazwan@gmail.com (Syaizwan Zahmir Zulkifli)

\* Corresponding author

## INTRODUCTION

Pollution is often linked to heavy metals in the environment, which must be monitored. Heavy metal pollution in aquatic environments such as mangroves, rivers, estuaries and coastal wetlands has increased significantly due to human activities (Shukor et al., 2023). Due to the increasing industrialisation and urbanisation of most Malaysian cities, significant amounts of pollution are now entering the rivers, leading to concerns about increasing water pollution (Krishnan et al., 2022). Heavy metals in the coastal areas may originate from various sources, including fossil fuel extraction, combustion, agriculture, refining, chemical production, and intentional and unintentional discharges. Heavy metals also enter coastal waters through natural processes such as rock weathering and river discharges (Krishnakumar et al., 2018). These metals are dangerous because of their high toxicity, longevity, and ability to bioaccumulate in the tissues of living organisms (Sharaf & Shehata, 2015). In ecosystems threatened by global environmental change, bivalves have proven to be important bioindicators, providing valuable insights into biodiversity and the state of ecosystems (Lamine, 2023). Bivalves can adapt to changing environmental conditions and store high levels of heavy metals in their tissue (Yap et al., 2016; Yap et al., 2019). Monitoring heavy metals in aquatic ecosystems aligns with Sustainable Development Goal 14 (SDG 14) and Life Below Water (Secretary-General, 2017).

Bivalves are among the first-choice organisms to serve as bioindicator species for chemical and environmental stresses. Bivalves are benthic sentinel species that reside in numerous ecological compartments and live as filter feeders (Helmholz et al., 2016). Because of the widespread distribution of bivalves and their ability to tolerate a wide range of environmental conditions, resulting in organisms directly taking up and accumulating a wide range of pollutants in water, these organisms are a valuable tool for biomonitoring contaminants (Boillot et al., 2015). Bivalves are often used to assess the toxicity and availability of man-made toxins in the aquatic environment (McCarty et al., 2002). Chemical bioaccumulation and alterations in cellular and molecular responses (biomarkers) can be studied on this species with great success (Regoli et al., 2014).

The mangrove clam, *Geloina expansa*, is a bivalve widely distributed in mangrove forests throughout the Indo-West Pacific region (Poutiers, 1998) and is common in tropical countries such as Malaysia (Ong et al., 2017). As a popular shellfish in Malaysian mangroves, it is a commonly harvested resource (Yahya et al., 2018). *Geloina expansa* Mousson, 1849 of the family Cyrenidae is a typical tropical mangrove clam that lives partially submerged in sediment for most of its life. This clam has two equal-sized shells connected by two adductor muscles and a burrowing foot (Morton, 1976). This species was previously known as *Polymesoda expansa* or *Polymesoda erosa* (Yahya et al., 2020; WoRMS Editorial Board, 2022) and was recently reclassified in the World Register of Marine Species. *Geloina expansa* is economically valuable as an edible mollusc and

is directly consumed by humans as a regular food source (Hamli et al., 2012). *Geloina expansa* is highly tolerant to extreme environmental conditions, surviving in a wide range of salinities and inhabiting muddy, brackish, and near-freshwater areas of mangrove swamps (Morton, 1976).

*Geloina expansa* meets a number of the listed requirements of an excellent biomonitor. This species is a sedentary filter-feeder widely distributed in mangrove areas, accumulates pollutants, and can adapt to stressful conditions and a long-life span. It feeds by filtering much stirred-up material from the waters. This feeding method traps many elements in its body, including various nutrients and potential toxins such as trace metals from the water column and surface sediments. Because of its ability to filter water, this species has often been used as a bioindicator in monitoring heavy metals (Edward et al., 2009). To this date, metal pollution studies of cadmium, nickel, chromium, iron, copper, lead, zinc, and arsenic using *G. expansa* as a bioindicator of environmental pollution have been conducted in several areas in Malaysia (Mohd Hamdan et al., 2020; Marlin et al., 2019; Harsonon et al., 2017; Ong et al., 2017; Ong & Ibrahim, 2017; Dabwan & Taufiq, 2016; Yap et al., 2014; Yap & Chew, 2011; Edward et al., 2009).

As a result of water pollution by metal contaminants and accumulation in the tissues of aquatic animals, there is an excessive formation of hydroxyl radicals and superoxide radicals as reactive oxygen species (ROS), including hydrogen peroxide. Besides the increase of oxidative damage and the lack of cellular antioxidants, the accumulation of radicals also contributes to the disturbance of physiological and biochemical mechanisms (Çomaklı et al., 2015). Oxidative stress induced by the accumulation of heavy metals in bivalve tissues can lead to protein degradation, lipid peroxidation (LPO) and other cellular changes such as DNA damage and inactive enzymes (Regoli, 2000; Xu et al., 1999). Bivalves typically perform defence mechanisms to combat free radical formation and ROS, which include changes in respiratory and metabolic rates, activation of alternative energy production pathways, and activation of antioxidant defence and repair processes (de Almeida et al., 2007).

An organism's metabolism involves several antioxidant defence mechanisms, whether enzymatic or not. The glutathione defence system is one of the most important of these defence mechanisms. Glutathione S-transferase (GST) is one of the enzymatic antioxidants in glutathione metabolism. The GST enzyme plays an important role in the metabolism of xenobiotics. GSTs belong to the phase II detoxification enzymes, which can decrease the cellular toxicity of various endogenous and environmental substances by providing a nucleophilic attack on reduced glutathione (GSH) (Espinoza et al., 2012). GST is a vital phase II biotransformation enzyme, and it catalyses the conjugation of glutathione (GSH) to electrophilic xenobiotics and oxidised components to boost their hydrophilicity and permit the elimination of toxins (Ketterer et al., 1983). GSTs have been well studied in

ecotoxicology because of their essential role in detoxification pathways and oxidative stress response (Hoarau et al., 2006). Nowadays, investigating potential biomarkers using a molecular biology approach has gained popularity as a robust method for monitoring environmental pollution studies.

The present study aims to determine the heavy metal concentrations of copper (Cu), zinc (Zn), cadmium (Cd) and lead (Pb) in the soft tissue of *G. expansa* from Sepang Besar River. The correlation between GST activity and heavy metals was assessed to evaluate the potential of GST as a molecular biomarker for monitoring metal pollution. Because of the broad range of tasks that GST enzymes perform in cells, such as the effects of oxidative stress, GST enzymes were selected as biomarkers in the present study. GST-related studies have been conducted on different species of bivalves, with the same emphasis on identifying bivalve GST for environmental contamination. The scope of this information may contain critical facts for environmental management and further enhance the potential of *G. expansa* as an efficient biomarker.

## MATERIALS AND METHODS

### Study Area

This study was conducted in the Sepang Besar River (SBR) mangrove estuary in Selangor, Peninsular Malaysia (2°35'30" N, 101°43'1" E). The mangrove and estuary ecosystem is a dynamic environment with one of the world's highest biodiversity and productive resources (Bianchi, 2013). SBR funnels into the Strait of Malacca, one of the country's main shipping routes and fishing grounds. Within a five-kilometre radius of the SBR confluence, an extensive mangrove area is located near fishing villages, aquaculture facilities, charcoal power plants, and urban development areas (Ya et al., 2014). Several anthropogenic activities, including agricultural activities such as oil palm plantations and upstream aquaculture, have been identified as potential sources of heavy metal pollution to the SBR. River cruising, fishing, fishing boats, and boat repair using anti-fouling agents also contribute to the heavy metal pollution in the river.

### Sample Collection

Mangrove clam (*G. expansa*) was collected from the SBR's mangrove area at three sampling sites. Site 1 is located at the upper estuary (2°39' 14.8 N, 101°44' 34.1 E), Site 2 is at the middle estuary (2°38' 48.9 N, 101°43' 53.6 E), and Site 3 is located nearest to the river mouth, i.e., down-estuary (2°38' 36.8 N, 101°43' 39.7 E). The site selection is based on preliminary studies and surveys conducted in several areas, from the estuary's upper to the down section. The choice of location depends on the accessibility of the area where a clam can be found and the level of low water at the time of sampling. Field observations show

that this species prefers sites with softer sediments, such as water channels and puddles. The sampling was carried out during the rainy season in December 2021. During the collection of clam samples, a long metal rod was dipped into the mud, and the clam's presence was indicated by a clicking sound when the metal came in contact with the clam surface. The clams were collected and placed in an icebox before being taken to the laboratory for examination. Samples were sealed in polyethene bags, transported to the research facility, and stored at -20°C for further analysis.

### Laboratory Pre-analysis

Glassware and other laboratory equipment were cleaned with 10% nitric acid, rinsed with milli-Q water and dried as a precaution. Clams collected for observations were cleaned with water, and their morphometric measurements (length, height, width) were recorded with a digital calliper. The dimensions of the shells were 63.90 to 108.26 mm in length, 58.87 to 105.79 mm in height, and 35.55 to 64.59 mm in width. The soft tissue was dissected from the shell for each clam sample, weighed, transferred to a glass Petri dish, and oven-dried at 60°C until a constant weight was reached. The wet weight of the tissue samples ranged from 8.51 to 50.7 g, and the dry weight ranged from 0.91 to 7.17 g. The dried samples were then pulverised using a porcelain mortar and pestle.

### Determination of Heavy Metal Concentrations in the Soft Tissue of *G. expansa*

Cu, Zn, Cd, and Pb heavy metals were selected because they are bivalves' most common environmental contaminants (Zarykhta et al., 2019; Ong et al., 2017; Ong & Ibrahim, 2017). Acid digestion for clam soft tissue was performed using the standard USEPA 3050B procedure. First, 1 g of the dry weight of the soft tissue sample was digested with nitric acid (HNO<sub>3</sub>) and hydrogen peroxide (H<sub>2</sub>O<sub>2</sub>) additions. Then, the original digestate was treated with hydrochloric acid (HCL), and the sample was kept under reflux. After filtration of the digestate, the filter paper and residues were rinsed twice, once with hot HCL and once with hot reagent water. Before re-filtering, the filter paper and residue were placed back into the digestion flask and refluxed with more HCL. The filter paper and residues were then returned to the digestion flask and refluxed with more HCL before filtering again. The distilled digestion was made up to a final volume of 100 mL with distilled water. Finally, the soft tissue's heavy metal content (Cu, Zn, Cd, Pb) was measured according to the standard procedure US EPA 6010B using the inductively coupled plasma 5100 optical emission spectrometer (ICP-OES). The analytical procedures for the clams were validated using standard reference material (SRM 2976) mussel tissue by the National Institute of Standards and Technology. The recovery percentage is calculated based on the following formula:

$$\text{Recovery (\%)} = (\text{Measured values}) / (\text{Certified values} \times 100 \%).$$

## Homogenisation and Centrifugation of the Samples

The soft tissue of the clam was homogenised (1:5 w/v) in 25 mM phosphate buffer (pH 7.4), which also contained 1.0 mM ethylenediaminetetraacetic acid or tetrasodium salt (EDTA), 0.1 mM dithiothreitol (DTT), 0.1 mM phenylthiourea (PTU), and 10 mM phenylmethylsulfonyl fluoride (PMSF) using IKA Ultra-Turrax T25 homogeniser. The homogenised sample was centrifuged for one hour at 17500 rpm. The pellet was removed, and the supernatant was collected. All procedures were performed in the protein laboratory using a cool box with ice at 4°C to prevent protein degradation.

## Enzyme Activity and Protein Content

GST (EC 2.5.1.18) activity is measured in the presence of reduced glutathione (GSH) using 1-chloro-2,4-dinitrobenzene (CDNB) as substrate (Habig et al., 1974). The conjugation of glutathione with 1-chloro-2,4-dinitrobenzene (CDNB) resulted in thioether glutathione dinitrobenzene (molecular extinction coefficient of 9.6 mM<sup>-1</sup>cm<sup>-1</sup>). GST enzyme activities were determined at 25°C in a Victor X5 Perkin Elmer microplate reader. The total volume of each assay was 200 µL. The reaction mixture is prepared by mixing 190 µL of 0.1 M sodium phosphate buffer (pH 6.5), 3.34 µL of sample, 3.34 µL of 60 mM GSH, and 3.34 µL of 60 mM CDNB. The change in absorbance at 340 nm was recorded for 10 minutes. The reaction solution without the samples served as a blank. Total enzyme activity was determined as µmol/min at 25°C and specific activity as µmol/min/mg protein. The Bradford protein assay was used with bovine serum albumin as the standard to determine protein concentration (Bradford, 1976).

## Statistical Analysis

Six replicates were performed for the clam samples, and the significance ( $p < 0.05$ ) between sites was determined using one-way Analysis of Variance (ANOVA). A post hoc comparison of means using Tukey's honest significant difference (HSD) was done when there was a significant difference between groups ( $p < 0.05$ ). A correlation analysis was later constructed (Pearson's coefficient,  $p < 0.05$ ). All statistical analyses were performed using SPSS ver. 22.0.

## RESULTS AND DISCUSSION

### Heavy Metals Concentration

Heavy metal concentrations in the soft tissue of *G. expansa* at different sampling sites are shown in Table 1. Cd was not detectable at ICP-OES for all samples. The per cent recovery of SRM 2976 for the heavy metal analyses was acceptable, with a value of 144.28% for Cu, 103.88% for Zn, and 105.045% for Pb. According to Krishnan et al. (2023), the accuracy of

the analytical method was evaluated by a recovery test with the certified reference materials SRM 1566b and SRM 2976, which provided excellent results with values between 92.3% and 141.2%. The results demonstrate the reliability and precision of the analytical method and its ability to accurately determine the heavy metal concentration in the samples. In another study by Ong and Ibrahim, 2017, the heavy metals showed a good percentage recovery of over 90% for the certified reference material used with DOLT-4 dogfish liver as a benchmark, so it can be assumed that the analyses and methods used to determine the metal concentrations are reliable.

Heavy metal analyses of soft tissue samples recorded higher concentrations of Zn and Cu compared to Pb. The highest concentration of Zn was recorded in the soft tissues (mean:  $262.86 \pm 36.64$  mg/kg) at all sites. Cu follows it with  $17.03 \pm 2.89$  mg/kg concentrations, while Pb concentrations were  $0.58 \pm 0.008$  mg/kg (Table 1). Concentrations of individual heavy metals varied significantly at different sites (Table 1). Soft tissues from Site 3 (down-estuary) have significantly greater ( $p < 0.05$ ) Zn concentration ( $328.17 \pm 33.61$  mg/kg) compared to those collected from other sites. In contrast, Cu and Pb in the tissues were considerably similar ( $p > 0.05$ ) between sites.

Table 1  
Concentrations of heavy metals in *G. expansa* tissue from three sites in Sepang Besar River

Site	Heavy metal concentration in tissue (mg/kg of dry weight)		
	Cu	Zn	Pb
1	$21.42 \pm 5.46^a$	$201.42 \pm 31.66^a$	$0.75 \pm 0.17^a$
2	$11.58 \pm 1.32^a$	$259.00 \pm 30.77^{ab}$	$0.50 \pm 0.00^a$
3	$18.08 \pm 2.09^a$	$328.17 \pm 33.61^b$	$0.50 \pm 0.00^a$
All Sites	$17.03 \pm 2.89$	$262.86 \pm 36.64$	$0.58 \pm 0.01$

Note. Site 1 = upper estuary; Site 2 = middle estuary; Site 3 = down-estuary. Concentrations of heavy metals are presented in mean  $\pm$  standard error. Values sharing a similar superscript alphabet (a, b, c) within the same column are not significantly different

In general, metal concentrations in *G. expansa* in the present study are considerably similar to those reported in previous studies. Yap et al. (2014) reported concentrations of Zn at  $365 \pm 0.00$   $\mu\text{g/g}$  and Cu at  $21.0 \pm 0.00$   $\mu\text{g/g}$  in *Polymesoda erosa* collected from different sites in the adjacent Sepang Kecil River. Bivalve species may differ in metal composition due to physicochemical and biotic variables that affect metal bioaccumulation (Rajeshkumar & Li, 2018). The variation in the amount of metal that *G. expansa* accumulated showed its affinity for a particular element. Because of their importance in metabolic processes, Zn and Cu are essential elements, while Pb is non-essential and toxic even in very low concentrations (Hussein & Khaled, 2014). The high metal concentrations in the bivalve indicated high metal bioavailabilities of the metals in the sampling site (Yap & Al-Mutairi, 2022; Yap et al., 2006). Many marine organisms require zinc, which they absorb through

their food and the surrounding aquatic environment, but excessive zinc uptake can have toxic effects (Turkmen et al., 2005). Zn poisoning leads to death, impaired growth and reproductive problems (Sorenson, 1991).

As a filter-feeder, *G. expansa* consumes microscopic algae, bacteria, and detritus. They filter a huge amount of seawater by syphoning it in from the posterior ventral side with the inhalation syphon, filtering it through the gills, and then expelling it through the exhalation syphon (Famme et al., 1986). In this way, their tissues absorb pollutants and food particles from the water. This bivalve absorbs trace elements from the surrounding aquatic environment through the cell membrane and ingests food (Boening, 1999). Compared to the amounts found in the aquatic environment in which they live, bivalves have been reported to accumulate up to 100-100,000 times more trace metals in their tissues (Farrington et al., 2016; Casas et al., 2008). Thus, it is possible to find trace metals and other chemical pollutants in bivalve tissues undetectable in seawater (Farrington et al., 2016).

Cu and Zn are expected due to the intensive aquaculture operations along the SBR. For example, shrimp farming contributes greatly to the Cu content of the river, as this element is required to grow and develop aquaculture species. Cu is added to aquatic feed to increase immunity, antioxidant capacity and growth performance (Yuan et al., 2019; Wang et al., 2009). An earlier study in the SBR found that pig farming was the main cause of heavy metal contamination in the area (Ismail & Ramli, 1997). High concentrations of Zn and Cu are fed to pigs, where they act as growth promoters and are added to pig feed to prevent parasite infestation (Zhang et al., 2017; Zhu et al., 2013; Moral et al., 2008). Pig slurry is likely the cause of Cu and Zn contamination (Marszalek et al., 2019; Jensen et al., 2018; Li et al., 2014). Sediment samples collected in 1996 from the mangroves upstream of the SBR, where pig farm effluents were discharged, revealed high Zn and Cu levels of 210–670 mg/kg and 250–550 mg/kg, respectively (Ismail & Ramli, 1997). After one year, the sediment sample collected in 1997 had a high Cu content, which Hossain et al. (2001) found to be 213–518 mg/kg upstream of the SBR. In 2001, Zn and Cu contents were reported to be 430–602 mg/kg and 400–574 mg/kg, respectively (Saed et al., 2002). Due to the novel Nipah disease (*Japanese encephalitis*) in Bukit Pelanduk, located upstream of the SBR, a ban on pig farming was introduced there in 1998 (Singh, 2014). In 2003, after the ban on pig farming, Zn and Cu concentrations of 375–416 and 5.23–22.73 mg/kg, respectively, were detected in the sediment sample (Yap et al., 2007). Ramsie et al. (2014) also reported Zn and Cu concentrations in sediment samples of 246.38 and 77.17 mg/kg, indicating that anthropogenic pollution sources are decreasing over time and the surrounding mangrove ecosystem is recovering from pollution.

In an exponential decay model, decreasing Zn and Cu levels in surface sediments of the SBR were used to describe the inverse correlation between Zn levels and a ban on pig farming over the years. The exponential regression can simulate a scenario in which

Zn levels in SBR sediment decrease more rapidly before and after a ban on pig farming. According to the model, the ban reduced the “considerable ecological risk” of the SBR estuary to “minimal ecological risk” (Yap & Al-Mutairi, 2022). This model was chosen wisely and is appropriate because background levels of metals in sediments will not be zero in naturally occurring sediments worldwide (Wedepohl, 1995) and monitoring studies using surface sediments from SBR as scientific evidence, especially after the ban on pig farming, as well as a detailed assessment of the reduction of metal elements in the previously polluted river. The importance of monitoring metal elements in sediments is beyond question, as is evident from a number of recent publications on these research monitoring activities (Hossain et al., 2021; Wei et al., 2019). According to model simulations with varying degrees of remediation effectiveness, recovery depends largely on source reduction and how close metal concentrations are to background concentrations in the watershed (Moore & Langner, 2012). The current models for Zn and Cu decay in SBR by Yap and Al-Mutairi (2022) can offer intuition into remediation methods and lower restoration costs.

*Geloina expansa* is capable of accumulating trace elements. The reported Pb concentration in soft tissue at Site 1 is  $0.75 \pm 0.17$  mg/kg, and at Sites 2 and 3, it is  $0.5 \pm 0.00$  mg/kg. Pb levels in SBR reported by Ismail and Ramli (1997) were 3.4–46.5 mg/kg. The research was continued in 1998 by Saed et al. (2002), and the Pb levels were reported from 14.90 to 51.24 mg/kg. No significant difference in Pb levels was observed between 1996 and 2010, possibly because pig effluents did not introduce Pb (Yap & Al-Mutairi, 2022). According to Ramsie et al. (2014), the Pb concentration in SBR sediment was 86.89 mg/kg. The considerable accumulation of Pb in the tissues of bivalves is due to the slow excretion of the amorphous granules and their immobilisation in the shell (Viarengo, 1989). Previous studies have shown that lead accumulation in the bivalve species *Macra corralina* increases oxidative stress in the gills due to lead exposure (Chetoui et al., 2019). Lead is a heavy metal (non-essential) produced in natural and industrial processes such as mining, refining, petroleum combustion, and cement production. According to (Livingstone, 2001), the effects of accumulated metals cannot be determined by quantification alone because this method cannot demonstrate the toxic effects of pollution on aquatic organisms. Instead, biochemical biomarkers are often used in ecotoxicological studies to assess how contaminants affect species (Livingstone, 1993).

### **GST Enzyme Activity and Protein Content**

The results of total activity and protein in *G. expansa* are shown in Table 2. The mean value of total protein content was estimated at  $1.24 \pm 0.04$  mg, whereas the mean value of total activity was  $0.16 \pm 0.01$   $\mu\text{mol}/\text{min}$ . Specific activity for *G. expansa* at Site 1 was slightly higher ( $0.15 \pm 0.01$   $\mu\text{mol}/\text{min}/\text{mg}$ ) compared to their counterpart at Site 2 ( $0.12 \pm 0.01$   $\mu\text{mol}/\text{min}/\text{mg}$ ) and 3 ( $0.12 \pm 0.01$   $\mu\text{mol}/\text{min}/\text{mg}$ ). There was a significant difference

( $p < 0.05$ ) in Zn in soft tissue and specific activity of GST at all sites. However, no significant differences were observed between Cu and Pb in soft tissue and total GST activity.

Specific activity positively correlates with Pb concentration in the soft tissue of *G. expansa* ( $p < 0.05$ ;  $R = 0.509$ ) (Table 3). The accumulation of metal ions promotes the production of reactive radicals in cells, which leads to cell damage (Valko et al., 2005; Leonard et al., 2004). Exposure to Pb increases the formation of ROS, resulting in DNA damage, protein oxidation, and cell membrane damage (Flora et al., 2012; Hsu & Guo, 2002; Ercal et al., 2001; Gurer & Ercal, 2000; Halliwell & Gutteridge, 1989). Organisms must have important antioxidant defence systems such as GST, superoxide dismutase (SOD), and catalase (CAT), the three major enzymatic antioxidants, to protect themselves from oxidative stress. An important metabolic enzyme of phase II, glutathione S-transferase, helps detoxify both xenobiotics and oxidative metabolic end products (Jozefczak et al., 2012; Van der Oost et al., 2003).

The present study shows that Pb of *G. expansa* positively correlated with the specific activity of GST specific activity. GST activity increased significantly, supporting the role of GST in protecting against reactive oxygen radicals and reducing the toxicity of Pb, according to similar research by (Shenai-Tirodkar et al., 2017). Pearson correlation showing a positive relationship between GST and Pb concentration ( $p < 0.001$ ) supports this. In the early stages, Pb causes oxidative stress and activates other antioxidant enzymes such as SOD and CAT. At the same time, GST intervenes in the later stages as compensation for the defence system. Pb is one of the most common metals entering water and sediment and can be taken up by most aquatic organisms, particularly bivalves. Filter-feeder bivalves are considered effective toxin carriers because of their relative insensitivity to toxins compared to other aquatic organisms. Bivalve species have different behavioural and physiological defences against various negative stressors. This fact draws attention to the possible function of GST as a detoxification enzyme. GST significantly supports cellular defence against chemically induced toxicity. However, the GST system in bivalves has yet to be comprehensively described (Martins et al., 2014).

The bioaccumulation of Pb in the bivalves and its possible impact on the bioavailability of other metals could still pose significant environmental risks (Fukunaga & Anderson, 2011). Pb is a non-essential metal, and its environmental presence indicates anthropogenic pollution. Pb is hazardous to aquatic life because it can cause membrane damage and stop vital enzymes from working. GST, as an antioxidant enzyme related to Pb toxicity, has been used to evaluate the toxic effects of Pb in manila clam, *Ruditapes philippinarum* (Aouini et al., 2018). The effectiveness of using biomarkers to evaluate Pb toxicity in marine organisms has been demonstrated (Aouini et al., 2018; Wadige et al., 2014). Pb has the capacity to cause damage to membranes and prevent necessary enzymes from functioning (Krause-Nehring et al., 2012). Pb has a high affinity for the sulfhydryl groups of biologically

significant enzymes such as  $\delta$ -aminolevulinic acid dehydratase (ALAD) involved in heme biosynthesis. Pb toxicity will result in higher production of ROS, including glutathione peroxidase (GPx), SOD, and CAT, which could indirectly lead to LPO of cell membranes and the creation of malondialdehyde (Wadige et al., 2014).

Bivalves that live as filter feeders in the sediment of mangrove areas can accumulate large quantities of heavy metal pollutants in their tissue (Choi et al., 2011). Antioxidant enzymes are activated in aquatic organisms to protect cells from oxidative stress caused by pollutants (Livingstone, 2001). GST, along with other antioxidant molecules such as glutathione reductase (GR), CAT, GPx, and SOD, is one of the most commonly studied biomarkers to assess oxidative damage caused by Zhang et al. (2014) suggested that GST is the first enzyme to be activated to cope with oxidative stress and that the increase in antioxidant enzymes may be due to a compensatory mechanism of ROS increase in cells. Elevated concentrations of contaminants can impair the function of biomarkers, or hazardous intermediates formed during xenobiotic metabolism can cause enzyme inactivation. GST activities in the clam *Ruditapes philippinarum*, as well as other biomarkers of oxidative stress such as CAT, GPx, GR and SOD, show that the effects of the depuration period differ from Pb concentrations. The decrease in some antioxidant activities could be due to the decrease of Pb in tissues, while the increase in antioxidant activities could be due to a delay in defence mechanisms. The study shows that Pb is not eliminated from the tissues, and the clam could increase its antioxidant activities to overcome toxicity as a preventive mechanism (Aouini et al., 2018).

GST detoxification enzymes have been used as biomarkers in biomonitoring aquatic pollution because they are an important component of adaptation mechanisms to chemical stress. There has been prior evidence of a relationship between the expression and activity of specific GST isoforms in bivalves and the presence of xenobiotics (Hoarau et al., 2006; Hoarau et al., 2002). The toxicity and environmental quality assessment fields will benefit from a better understanding of bivalve GSTs. Bivalve species such as *Mytilus trossulus* (Istomina et al., 2020), *M. edulis* (Yang et al., 2004; Fitzpatrick et al., 1995), *M. galloprovincialis* (Azevedo et al., 2015; Martins et al., 2014; Vasconcelos et al., 2007; Kaaya et al., 1999; Fitzpatrick et al., 1995), *Donax trunculus* (Amira et al., 2018), *Perna perna* (Sáenz et al., 2010; Kaaya et al., 1999), *Corbicula fluminea* (Martins et al., 2014; Puerto et al., 2011; Martins et al., 2009; Vidal et al., 2002), *Asaphis dichotoma* (Yang et al., 2002), *Atactodea striata* (Yang et al., 2003), *Mercenaria mercenaria* (Blanchette et al., 2002), *Anodonta cygnea* (Martins et al., 2014), *Ruditapes decussatus* (Hoarau et al., 2002), *Ruditapes philippinarum* (Revathy et al., 2012; Umasuthan et al., 2012) have been studied for their ability to isolate and characterise GSTs.

As with other proteins, a specific circumstance leads to the expression of GSTs. Since the expression of GSTs correlates with the amount of substrate exposed, the accumulation of substrate increases the expression of GSTs to the ideal level. Due to their remarkable

ability to detoxify, bivalves are most likely involved in this process, as shown by the fact that they may survive for an extended period after exposure to pollutants. Heavy metals as environmental pollutants can be detoxified by GSTs found in marine animals (Hoarau et al., 2006; Pérez et al., 2004; Fitzpatrick et al., 1997). GST promotes the conjugation of glutathione with foreign substances and helps eliminate reactive oxygen species from the body. Organic electrophiles can be conjugated by GST to the thiol group of glutathione, forming a hydrophobic molecule that is easily eliminated. (Winterbourn, 2008). Increased enzyme activity indicates that the species resists the toxic environment. In contrast, decreased enzyme activity may indicate a less harmful presence in the immediate environment or possibly due to increasing chronic exposure that overcomes the cells' protective system (Cossu et al., 2000).

Table 2

Total protein, total activity and specific activity of GST obtained from soft tissue of *G. expansa* (mean  $\pm$  standard error)

Site	Total protein (mg)	Total activity ( $\mu\text{mol}/\text{min}$ )	Specific activity ( $\mu\text{mol}/\text{min}/\text{mg}$ )
1	1.17 $\pm$ 0.03 <sup>a</sup>	0.17 $\pm$ 0.01 <sup>a</sup>	0.15 $\pm$ 0.01 <sup>b</sup>
2	1.32 $\pm$ 0.04 <sup>b</sup>	0.16 $\pm$ 0.01 <sup>a</sup>	0.12 $\pm$ 0.01 <sup>a</sup>
3	1.23 $\pm$ 0.03 <sup>ab</sup>	0.15 $\pm$ 0.01 <sup>a</sup>	0.12 $\pm$ 0.01 <sup>a</sup>
All Sites	1.24 $\pm$ 0.04	0.16 $\pm$ 0.01	0.13 $\pm$ 0.01

Note. Values sharing a similar superscript alphabet (a, b, c) within the same column are not significantly different.

Table 3

Pearson correlation matrix among heavy metals and GST biomarker in *G. expansa*

	Cu	Zn	Pb	GST
Cu	1.00			
Zn	0.275	1.00		
Pb	0.327	0.254	1.00	
GST	0.302	-0.227	<b>0.509*</b>	1.00

Note.\*correlation is significant at the 0.05 level (2-tailed)

Bioaccumulation of pollutants in different organisms is widely used in ecotoxicology because it reflects the bioavailability of pollutants in the ecosystem (Phillips & Rainbow, 1994). *G. expansa*, a sedentary bivalve found in the mangroves of the Sepang Besar River, can serve as a model organism for biomonitoring potentially toxic metals. GST as a biomarker from this bivalve has allowed the detection of specific biological responses to certain pollutants, such as heavy metals, in laboratory studies or mixed anthropogenic pollutants in field studies.

Proteomics has been used in environmental toxicology to assess changes in the proteome of organisms exposed to environmental factors such as pollution and climate

change, which needs to be better understood for continued and sustainable growth. Researchers are concerned about the potential adverse effects of anthropogenic, persistent, industrial, and emerging environmental contaminants on humans and wildlife. Proteomics and other OMICS technologies, such as genomics, metabolomics, and transcriptomics, have provided additional tools for developing biomarkers that are indicators of both chemical exposure and subsequent biological impact. Using omics technologies to preferentially identify biomarkers would be repeatable and allow for the fast, sensitive, and quantitative assessment of massive biomonitoring programmes. Proteomics research in bivalves may represent one of the most promising research areas for biomonitoring marine pollution (Campos et al., 2012). Developing proteomics technology for studying protein biomarkers to detect various pollutants in bivalves is one of the most challenging tasks. Pollutants in the environment affect the health of bivalves and cause economic losses in the aquaculture industry. Further research is needed to investigate the underlying mechanisms, biological pathways, and interrelationships of putative biomarkers and to evaluate the robustness of GST as a biomarker using accurate methods and new populations of *G. expansa* under different pollution situations.

## CONCLUSION

*G. expansa*, as a sedentary organism, can accumulate and tolerate high concentrations of metals. GST, as a biochemical biomarker, correlates positively with Pb concentrations in the soft tissues of *G. expansa*. Therefore, the oxidative stress generated in this bivalve is associated with the heavy metal concentration. Future studies should be conducted to quantitatively evaluate the expression of GST by Pb exposure in *G. expansa* and to investigate the effects of acute Pb toxicity on oxidative stress in the species.

## ACKNOWLEDGMENTS

The authors acknowledge the financial support provided by the Southeast Asian Regional Center for Graduate Study and Research in Agriculture (SEARCA). The authors also thank Universiti Putra Malaysia and Universiti Teknologi MARA for providing the laboratory facility to conduct the present study.

## REFERENCES

- Amira, A., Merad, I., Almeida, C. M. R., Guimarães, L., & Soltani, N. (2018). Seasonal variation in biomarker responses of *Donax trunculus* from the Gulf of Annaba (Algeria): Implication of metal accumulation in sediments. *Comptes Rendus - Geoscience*, 350(4), 173-179. <https://doi.org/10.1016/j.crte.2018.02.002>
- Aouini, F., Trombini, C., Volland, M., Elcafsi, M., & Blasco, J. (2018). Assessing lead toxicity in the clam *Ruditapes philippinarum*: Bioaccumulation and biochemical responses. *Ecotoxicology and Environmental Safety*, 158, 193-203. <https://doi.org/10.1016/j.ecoenv.2018.04.033>

- Azevedo, C. C., Guzmán-Guillén, R., Martins, J. C., Osório, H., Vasconcelos, V., da Fonseca, R. R., & Campos, A. (2015). Proteomic profiling of gill GSTs in *Mytilus galloprovincialis* from the North of Portugal and Galicia evidences variations at protein isoform level with a possible relation with water quality. *Marine Environmental Research*, 110, 152-161. <https://doi.org/10.1016/j.marenvres.2015.08.008>
- Bianchi, T. S. (2013). Estuaries: Where the river meets the sea. *Nature Education Knowledge*, 4, 12.
- Blanchette, B. N., & Singh, B. R. (2002). Isolation and characterization of glutathione-S-transferase isozyme Q3 from the northern quahog, *Mercinaria mercinaria*. *Journal of Protein Chemistry*, 21, 151-159. <https://doi.org/10.1023/A:1015368532136>
- Boening, D. W. (1999). An evaluation of bivalves as biomonitors of heavy metals pollution in marine waters. *Environmental Monitoring and Assessment*, 55, 459-470. <https://doi.org/10.1023/A:1005995217901>
- Boillot, C., Martinez Bueno, M. J., Munaron, D., Le Dreau, M., Mathieu, O., David, A., Fenet, H., Casellas, C., & Gomez, E. (2015). *In vivo* exposure of marine mussels to carbamazepine and 10-hydroxy-10,11-dihydro-carbamazepine: Bioconcentration and metabolization. *Science of the Total Environment*, 532, 564-570. <https://doi.org/10.1016/j.scitotenv.2015.05.067>
- Bradford, M. M. (1976). A rapid and sensitive method for quantitation of microgram quantities of protein utilizing the principle of protein-dye binding. *Analytical Biochemistry* 72(1-2), 248-254. [https://doi.org/10.1016/0003-2697\(76\)90527-3](https://doi.org/10.1016/0003-2697(76)90527-3)
- Campos, A., Tedesco, S., Vasconcelos, V., & Cristobal, S. (2012). Proteomic research in bivalves: Towards the identification of molecular markers of aquatic pollution. *Journal of Proteomics*, 75(14), 4346-4359. <https://doi.org/10.1016/j.jprot.2012.04.027>
- Casas, S., Gonzalez, J. L., Andral, B., & Cossa, D. (2008). Relation between metal concentration in water and metal content in marine mussels (*Mytilus galloprovincialis*): Impact of physiology. *Environmental Toxicology and Chemistry*, 27(7), 1543-1552. <https://doi.org/10.1897/07-418.1>
- Chetoui, I., Bejaoui, S., Fouzai, C., Trabelsi, W., Nechi, S., Chelbi, E., Ghalghaf, M., El Cafsi, M., & Soudani, N. (2019). Effect of lead graded doses in *Maetra Corallina* gills: Antioxidants status, cholinergic function and histopathological studies. *Journal of Drug Design and Medicinal Chemistry*, 5(1), Article 1. <https://doi.org/10.11648/j.jddmc.20190501.11>
- Choi, J. Y., Yu, J., Yang, D. B., Ra, K., Kim, K. T., Hong, G. H., & Shin, K. H. (2011). Acetylthiocholine (ATC)-cleaving cholinesterase (ChE) activity as a potential biomarker of pesticide exposure in the Manila clam, *Ruditapes philippinarum*, of Korea. *Marine Environmental Research*, 71(3), 162-168. <https://doi.org/10.1016/j.marenvres.2010.12.007>
- Çomaklı, V., Kuzu, M., & Demirdäg, R. (2015). Characterization and purification of glutathione S-transferase from the liver and gill tissues of Ağrı Balık lake trout *Salmo trutta labrax* and the effects of heavy metal ions on its activity. *Journal of Aquatic Animal Health*, 27(3), 145-151. <https://doi.org/10.1080/08997659.2015.1032441>
- Cossu, C., Doyotte, A., Babut, M., Exinger, A., & Vasseur, P. (2000). Antioxidant biomarkers in freshwater bivalves, *Unio tumidus*, in response to different contamination profiles of aquatic sediments. *Ecotoxicology and Environmental Safety*, 45(2), 106-121. <https://doi.org/10.1006/eesa.1999.1842>

- Dabwan, A. H. A., & Taufiq, M. (2016). Bivalves as bio-indicators for heavy metals detection in Kuala Kemaman, Terengganu, Malaysia. *Indian Journal of Science and Technology*, 9(9), 1-6. <https://doi.org/10.17485/ijst/2016/v9i9/88708>
- de Almeida, E. A., Bainy, A. C. D., de Melo Loureiro, A. P., Martinez, G. R., Miyamoto, S., Onuki, J., Barbosa, L. F., Garcia, C. C. M., Prado, F. M., Ronsein, G. E., Sigolo, C. A., Barbosa, C. B., Martins, A. M. G., de Medeiros, M. H. G., & Di Mascio, P. (2007). Oxidative stress in *Perna perna* and other bivalves as indicators of environmental stress in the Brazilian marine environment: Antioxidants, lipid peroxidation and DNA damage. *Comparative Biochemistry and Physiology: A Molecular and Integrative Physiology*, 146(4), 588-600. <https://doi.org/10.1016/j.cbpa.2006.02.040>
- Edward, F. B., Yap, C. K., Ismail, A., & Tan, S. G. (2009). Interspecific variation of heavy metal concentrations in the different parts of tropical intertidal bivalves. *Water, Air, and Soil Pollution*, 196, 297-309. <https://doi.org/10.1007/s11270-008-9777-x>
- Ercal, N., Gurer-Orhan, H., & Aykin-Burns, N. (2001). Toxic metals and oxidative stress part I: Mechanisms involved in metal-induced oxidative damage. *Current Topics in Medicinal Chemistry*, 1(6), 529-539. <https://doi.org/10.2174/1568026013394831>
- Espinoza, H. M., Williams, C. R., & Gallagher, E. P. (2012). Effect of cadmium on glutathione S-transferase and metallothionein gene expression in coho salmon liver, gill and olfactory tissues. *Aquatic Toxicology*, 110-111, 37-44. <https://doi.org/10.1016/j.aquatox.2011.12.012>
- Famme, P., Riisgård, H., & Jørgensen, C. (1986). On direct measurement of pumping rates in the mussel *Mytilus edulis*. *Marine Biology*, 92, 323-327. <https://doi.org/10.1007/BF00392672>
- Farrington, J. W., Tripp, B. W., Tanabe, S., Subramanian, A., Sericano, J. L., Wade, T. L., Knap, A. H. & Edward, D. (2016). Edward D. Goldberg's proposal of "the mussel watch": Reflections after 40 years. *Marine Pollution Bulletin*, 110(1), 501-510. <https://doi.org/10.1016/j.marpolbul.2016.05.074>
- Fitzpatrick, P. J., Krag, T. O. B., Hojrup, P., & Sheehan, D. (1995). Characterization of a glutathione S-transferase and a related glutathione-binding protein from gill of the blue mussel, *Mytilus edulis*. *Biochemical Journal*, 305(1), 145-150. <https://doi.org/10.1042/bj3050145>
- Fitzpatrick, P. J., O'Halloran, J., Sheehan, D., & Walsh, A. R. (1997). Assessment of a glutathione S-transferase and related proteins in the gill and digestive gland of *Mytilus edulis* (L.), as potential organic pollution biomarkers. *Biomarkers*, 2(1), 51-56. <https://doi.org/10.1080/135475097231977>
- Flora, G., Gupta, D., & Tiwari, A. (2012). Toxicity of lead: A review with recent updates. *Interdisciplinary Toxicology*, 5(2), 47-58. <https://doi.org/10.2478/v10102-012-0009-2>
- Fukunaga, A., & Anderson, M. J. (2011). Bioaccumulation of copper, lead and zinc by the bivalves *Macomona liliana* and *Austrovenus stutchburyi*. *Journal of Experimental Marine Biology and Ecology*, 396(2), 244-252. <https://doi.org/10.1016/j.jembe.2010.10.029>
- Gurer, H., & Ercal, N. (2000). Can antioxidants be beneficial in the treatment of lead poisoning? *Free Radical Biology and Medicine*, 29(10), 927-945. [https://doi.org/10.1016/S0891-5849\(00\)00413-5](https://doi.org/10.1016/S0891-5849(00)00413-5)
- Habig, W. H., Pabst, M. J., & Jakoby, W. B. (1974). Glutathione S transferases. The first enzymatic step in mercapturic acid formation. *Journal of Biological Chemistry*, 249(22), 7130-7139. [https://doi.org/10.1016/S0021-9258\(19\)42083-8](https://doi.org/10.1016/S0021-9258(19)42083-8)

- Halliwell, B., & Gutteridge, J. M. C. (1989). Protection against oxidants in biological systems: the superoxide theory of oxygen toxicity. In B. Halliwell & J. M. C. Gutteridge (Eds.), *Free Radical in Biology and Medicine* (pp. 86-123). Clarendon Press.
- Hamli, H., Idris, M. H., Kamal, A. H. M., & King, W. S. (2012). Diversity of edible mollusc (Gastropoda and Bivalvia) at selected division of Sarawak, Malaysia. *International Journal on Advanced Science, Engineering and Information Technology*, 2(4), 5-7.
- Harsono, N. D. B. D., Ransangan, J., Denil, D. J., & Kar, S. T. (2017). Heavy metals in marsh clam (*Polymesoda expansa*) and green mussel (*Perna viridis*) along the northwest coast of Sabah, Malaysia. *Borneo Journal of Marine Science and Aquaculture*, 1, 25-32. <https://doi.org/10.51200/bjomsa.v1i.987>
- Helmholz, H., Ruhnau, C., Pröfrock, D., Erbslöh, H. B., & Prange, A. (2016). Seasonal and annual variations in physiological and biochemical responses from transplanted marine bioindicator species *Mytilus* spp. during a long term field exposure experiment. *Science of the Total Environment*, 565, 626-636. <https://doi.org/10.1016/j.scitotenv.2016.04.202>
- Hoarau, P., Damiens, G., Roméo, M., Gnassia-Barelli, M., & Bebianno, M. J. (2006). Cloning and expression of a GST-pi gene in *Mytilus galloprovincialis*. Attempt to use the GST-pi transcript as a biomarker of pollution. *Comparative Biochemistry and Physiology Part C: Toxicology and Pharmacology*, 143(2), 196-203. <https://doi.org/10.1016/j.cbpc.2006.02.007>
- Hoarau, P., Garello, G., Gnassia-Barelli, M., Romeo, M., & Girard, J. P. (2002). Purification and partial characterization of seven glutathione S-transferase isoforms from the clam *Ruditapes decussatus*. *European Journal of Biochemistry*, 269(17), 4359-4366. <https://doi.org/10.1046/j.1432-1033.2002.03141.x>
- Hossain, M., Othman, S., Bujang, J. S., & Lim, M. T. (2001). Distribution of copper in the Sepang mangrove reserve forest environment, Malaysia. *Journal of Tropical Forest Science*, 13(1), 130-139.
- Hossain, M. S., Ahmed, M. K., Liyana, E., Hossain, M. S., Jolly, Y. N., Kabir, M. J., Akter, S., & Rahman, M. S. (2021). A case study on metal contamination in water and sediment near a coal thermal power plant on the Eastern Coast of Bangladesh. *Environments*, 8(10), Article 108. <https://doi.org/10.3390/environments8100108>
- Hsu, P. C., & Guo, Y. L. (2002). Antioxidant nutrients and lead toxicity. *Toxicology* 180(1), 33-44. [https://doi.org/10.1016/S0300-483X\(02\)00380-3](https://doi.org/10.1016/S0300-483X(02)00380-3)
- Hussein, A., & Khaled, A. (2014). Determination of metals in tuna species and bivalves from Alexandria, Egypt. *Egyptian Journal of Aquatic Research*, 40(1), 9-17. <https://doi.org/10.1016/j.ejar.2014.02.003>
- Ismail, A., & Ramli, R. (1997). Trace metals in sediments and molluscs from an estuary receiving pig farms effluent. *Environmental Technology*, 18(5) 509-515. <https://doi.org/10.1080/09593331808616566>
- Istomina, A., Mazur, A., Chelomin, V., Kukla, S., Slobodskova, V., Zvyagintsev, A., Kolosova, L., Zhukovskaya, A., & Fedorets, Y. (2020). The different biomarkers in the assessment of the marine environmental quality using the representative species *Mytilus trossulus*. *Water, Air, and Soil Pollution*, 231(8), Article 403. <https://doi.org/10.1007/s11270-020-04782-w>
- Jensen, J., Kyvsgaard, N. C., Battisti, A., & Baptiste, K. E. (2018). Environmental and public health related risk of veterinary zinc in pig production-using Denmark as an example. *Environment International*, 114, 181-190. <https://doi.org/10.1016/j.envint.2018.02.007>

- Jozefczak, M., Remans, T., Vangronsveld, J., & Cuypers, A. (2012). Glutathione is a key player in metal-induced oxidative stress defenses. *International Journal of Molecular Sciences*, *13*(3), 3145-3175. <https://doi.org/10.3390/ijms13033145>
- Kaaya, A., Najimi, S., Ribera, D., Narbonne, J. F., & Moukrim, A. (1999). Characterization of glutathione S-transferases (GST) activities in *Perna perna* and *Mytilus galloprovincialis* used as a biomarker of pollution in the Agadir marine bay (South of Morocco). *Bulletin of Environmental Contamination and Toxicology*, *62*, 623-629.
- Ketterer, B., Coles, B., & Meyer, D. J. (1983). The role of glutathione in detoxication. *Environmental Health Perspectives*, *49*, 59-69. <https://doi.org/10.1289/ehp.834959>
- Krause-Nehring, J., Brey, T., & Thorrold, S. R. (2012). Centennial records of lead contamination in Northern Atlantic bivalves (*Arctica islandica*). *Marine Pollution Bulletin*, *64*(2), 233-240. <https://doi.org/10.1016/j.marpolbul.2011.11.028>
- Krishnakumar, P. K., Qurban, M. A., & Sasikumar, G. (2018). Biomonitoring of trace metals in the coastal waters using bivalve molluscs. In H. E. M. Saleh & E. E. Adham (Eds.), *Trace Elements - Human Health and Environment*. Intech Open. <https://doi.org/10.5772/intechopen.76938>
- Krishnan, K., Saion, E., Halimah, M. K., & Yap, C. K. (2023). Utilizing mollusk soft tissue and shells as biomarkers for monitoring heavy metal pollution in mangrove forests. *MethodsX*, *11*, Article 102281. <https://doi.org/10.1016/j.mex.2023.102281>
- Krishnan, K., Saion, E. B., Yap, C. K., Chong, M. Y., & Nadia, A. S. (2022). Determination of trace elements in sediments samples by using neutron activation analysis. *Journal of Experimental Biology and Agricultural Sciences*, *10*(1), 21-31. [https://doi.org/10.18006/2022.10\(1\).21.31](https://doi.org/10.18006/2022.10(1).21.31)
- Lamine, I., Chahouri, A., Moukrim, A., & Alla, A. A. (2023). The impact of climate change and pollution on trematode-bivalve dynamics. *Marine Environmental Research*, *191*, Article 106130. <https://doi.org/10.1016/j.marenvres.2023.106130>
- Leonard, S. S., Harris, G. K., & Shi, X. (2004). Metal-induced oxidative stress and signal transduction. *Free Radical Biology and Medicine*, *37*(12), 1921-1942. <https://doi.org/10.1016/j.freeradbiomed.2004.09.010>
- Li, Z., Ma, Z., van der Kuijp, T. J., Yuan, Z., & Huang, L. (2014). A review of soil heavy metal pollution from mines in China: Pollution and health risk assessment. *Science of the Total Environment*, *468/469*, 843-853.
- Livingstone, D. R. (1993). Biotechnology and pollution monitoring: use of molecular biomarkers in the aquatic environment. *Journal of Chemical Technology & Biotechnology*, *57*(3), 195-211.
- Livingstone, D. R. (2001). Contaminant-stimulated reactive oxygen species production and oxidative damage in aquatic organisms. *Marine Pollution Bulletin*, *42*(8), 656-666. [https://doi.org/10.1016/S0025-326X\(01\)00060-1](https://doi.org/10.1016/S0025-326X(01)00060-1)
- Martins, J. C., Leão, P. N., & Vasconcelos, V. (2009). Differential protein expression in *Corbicula fluminea* upon exposure to a *Microcystis aeruginosa* toxic strain. *Toxicon*, *53*(4), 409-416. <https://doi.org/10.1016/j.toxicon.2008.12.022>
- Martins, J. C., Campos, A., Osório, H., da Fonseca, R., & Vasconcelos, V. (2014). Proteomic profiling of cytosolic glutathione transferases from three bivalve species: *Corbicula fluminea*, *Mytilus galloprovincialis*

- and *Anodonta cygnea*. *International Journal of Molecular Sciences*, 15(2), 1887-1900. <https://doi.org/10.3390/ijms15021887>
- Mohd Hamdan, D. D., Md. Shah, J., Gumpulan, F., Foo, J., & Awang Lukman, K. (2020). The North Borneo Iranun's community's ethnomedicine knowledge on marsh clam (*Geloina expansa*). *Asian Journal of Ethnobiology*, 3(1), 30-38. <https://doi.org/10.13057/asianjethnobiol/y030105>
- Marszalek, M., Kowalski, Z., & Makara, A. (2019). The possibility of contamination of water-soil environment as a result of the use of pig slurry. *Ecological Chemistry and Engineering S*, 26(2), 313-330. <https://doi.org/10.1515/eces-2019-0022>
- McCarty, L. S., Power, M., & Munkittrick, K. R. (2002). Bioindicators versus biomarkers in ecological risk assessment. *Human and Ecological Risk Assessment: An International Journal*, 8(1), 159-164. <https://doi.org/10.1080/20028091056791>
- Moore, J. N., & Langner, H. W. (2012). Can a river heal itself? Natural attenuation of metal contamination in river sediment. *Environmental Science & Technology*, 46(5), 2616-2623. <https://doi.org/10.1021/es203810j>
- Moral, R., Perez-Murcia, M. D., Perez-Espinosa, A., Moreno-Caselles, J., Paredes, C., & Rufete, B. (2008). Salinity, organic content, micronutrients and heavy metals in pig slurries from South-Eastern Spain. *Waste Management*, 28(2), 367-371. <https://doi.org/10.1016/j.wasman.2007.01.009>
- Morton, B. (1976). The biology and functional morphology of the Southeast Asian mangrove bivalve, *Polymesoda (Geloina) erosa* (Solander, 1786) (Bivalvia: Corbiculidae). *Canadian Journal of Zoology*, 54(4), 482-500. <https://doi.org/10.1139/z76-055>
- Ong, M. C., & Ibrahim, A. (2017). Determination of selected metallic elements in marsh clam, *Polymesoda expansa*, collected from Tanjung Lumpur Mangrove Forest, Kuantan, Pahang. *Borneo Journal of Marine Science and Aquaculture*, 1, 65-70.
- Ong, M. C., Kamaruzaman, M. I., Chuen, Y. J., Yunus, K., & Bidai, J. (2017). Metals contamination using *Polymesoda expansa* (Marsh Clam) as bio-indicator in Kelantan River, Malaysia. *Malaysian Journal of Analytical Sciences*, 21(3), 597-604. <https://doi.org/10.17576/mjas-2017-2103-09>
- Pérez, E., Blasco, J., & Solé, M. (2004). Biomarker responses to pollution in two invertebrate species: *Scrobicularia plana* and *Nereis diversicolor* from the Cádiz bay (SW Spain). *Marine Environmental Research*, 58(2-5), 275-279. <https://doi.org/10.1016/j.marenvres.2004.03.071>
- Phillips, D. J. H., & Rainbow, P. S. (1994). *Biomonitoring of trace aquatic contaminants*. Springer Science & Business Media.
- Poutiers, J. M. (1998). Bivalves: Acephala, Lamellibranchia, Polycypoda. In: K. E. Carpenter & V. H. Niem (Eds.), *Food the Living Marine Resources of the Western Central Pacific, Volume 1, Seaweed, Corals, Bivalves and Gastropods* (pp 123-362). FAO, United Nations.
- Puerto, M., Campos, A., Prieto, A., Cameán, A., Almeida, A. M. de, Coelho, A. V., & Vasconcelos, V. (2011). Differential protein expression in two bivalve species; *Mytilus galloprovincialis* and *Corbicula fluminea*; exposed to *Cylindrospermopsis raciborskii* cells. *Aquatic Toxicology*, 101(1), 109-116. <https://doi.org/10.1016/j.aquatox.2010.09.009>

- Rajeshkumar, S., & Li, X. (2018). Bioaccumulation of heavy metals in fish species from the Meiliang Bay, Taihu Lake, China. *Toxicology Reports*, 5, 288-295. <https://doi.org/10.1016/j.toxrep.2018.01.007>
- Ramsie, S. A., Zulkifli, S.Z., Mohamat-Yusuf, F., & Ismail, A. (2014). Geochemical fractionations of heavy metals in sediments of Sepang Besar, *Acta Biologica Malaysiana*, 3,(1) 1-9.
- Regoli, F. (2000). Total oxyradical scavenging capacity (TOSC) in polluted and translocated mussels: A predictive biomarker of oxidative stress. *Aquatic Toxicology*, 50(4), 351-361. [https://doi.org/10.1016/S0166-445X\(00\)00091-6](https://doi.org/10.1016/S0166-445X(00)00091-6)
- Regoli, F., Pellegrini, D., Cicero, A. M., Nigro, M., Benedetti, M., Gorbi, S., Fattorini, D., D'Errico, G., Di Carlo, M., Nardi, A., Gaion, A., Scuderi, A., Giuliani, S., Romanelli, G., Berto, D., Trabucco, B., Guidi, P., Bernardeschi, M., Scarcelli, V., & Frenzilli, G. (2014). A multidisciplinary weight of evidence approach for environmental risk assessment at the Costa Concordia wreck: Integrative indices from Mussel Watch. *Marine Environmental Research*, 96, 92-104. <https://doi.org/10.1016/j.marenvres.2013.09.016>
- Revathy, K. S., Umasuthan, N., Lee, Y., Choi, C. Y., Whang, I., & Lee, J. (2012). First molluscan theta-class Glutathione S-Transferase: Identification, cloning, characterization and transcriptional analysis post immune challenges. *Comparative Biochemistry and Physiology Part B: Biochemistry and Molecular Biology*, 162(1-3), 10-23. <https://doi.org/10.1016/j.cbpb.2012.02.004>
- Saed, K., Ismail, A., Omar, H., & Kusnan, M. (2002). Accumulation of heavy metals (Zn, Cu, Pb, Cd) in flat-tree oysters *Isognomon alatus* exposed to pig farm effluent. *Toxicological and Environmental Chemistry*, 82(1-2), 45-58. <https://doi.org/10.1080/713746657>
- Sáenz, L. A., Seibert, E. L., Zanette, J., Fiedler, H. D., Curtius, A. J., Ferreira, J. F., Alves de Almeida, E., Marques, M. R. F., & Bainy, A. C. D. (2010). Biochemical biomarkers and metals in *Perna perna* mussels from mariculture zones of Santa Catarina, Brazil. *Ecotoxicology and Environmental Safety*, 73(5), 796-804. <https://doi.org/10.1016/j.ecoenv.2010.02.015>
- Secretary-General, U. (2017). *Progress towards the sustainable development goals: Report of the Secretary-General, UN*. United States of America. <https://policycommons.net/artifacts/127525/progress-towards-the-sustainable-development-goals/182695/> on 01 Apr 2024.
- Sharaf, H. M., & Shehata, A. M. (2015). Heavy metals and hydrocarbon concentrations in water, sediments and tissue of *Cyclope neritea* from two sites in Suez Canal, Egypt and histopathological effects. *Journal of Environmental Health Science and Engineering*, 13, Article 14. <https://doi.org/10.1186/s40201-015-0171-5>
- Shenai-Tirodkar, P. S., Gauns, M. U., Mujawar, M. W. A., & Ansari, Z. A. (2017). Antioxidant responses in gills and digestive gland of oyster *Crassostrea madrasensis* (Preston) under lead exposure. *Ecotoxicology and Environmental Safety*, 142, 87-94. <https://doi.org/10.1016/j.ecoenv.2017.03.056>
- Shukor, N. A., Krishnan, K., Shing, W. L., Ariffin, N., & Yong, W. L. (2023). The pollution characteristics of harmful heavy metal in surface sediment of Sepang River, Malaysia. *Environment and Ecology Research*, 11(4), 579-585. <https://doi.org/10.13189/eer.2023.110406>
- Singh, S. (2014, July 3). Ban on pig farming in Bukit Pelanduk still in force. *The Star*. <https://www.thestar.com.my/news/nation/2014/07/03/1998-ban-on-pig-farming-in-bukit-pelanduk-still-in-force/>
- Sorenson, E. M. (1991). *Metal poisoning in fish*. CRC Press.

- Turkmen, A., Turkmen, M., Tepe, Y., & Akyurt, I. (2005). Heavy metals in three commercially valuable fish species from Iskenderun Bay, Northern East Mediterranean Sea, Turkey. *Food Chemistry*, *91*(1), 167-172. <https://doi.org/10.1016/j.foodchem.2004.08.008>
- Umasuthan, N., Revathy, K. S., Lee, Y., Whang, I., Choi, C. Y., & Lee, J. (2012). A novel molluscan sigma-like glutathione S-transferase from Manila clam, *Ruditapes philippinarum*: Cloning, characterization and transcriptional profiling. *Comparative Biochemistry and Physiology Part C: Toxicology & Pharmacology*, *155*(4), 539-550. <https://doi.org/10.1016/j.cbpc.2012.01.001>
- Valko, M., Morris, H., & Cronin, M. T. (2005). Metals, toxicity and oxidative stress. *Current Medicinal Chemistry*, *12*(10), 1161-1208. <https://doi.org/10.2174/0929867053764635>
- Van der Oost, R., Beyer, J., & Vermeulen, N. P. E. (2003). Fish bioaccumulation and biomarkers in environmental risk assessment: A review. *Environmental Toxicology and Pharmacology*, *13*(2), 57-149. [https://doi.org/10.1016/S1382-6689\(02\)00126-6](https://doi.org/10.1016/S1382-6689(02)00126-6)
- Vasconcelos, V. M., Wiegand, C., & Pflugmacher, S. (2007). Dynamics of glutathione-S-transferases in *Mytilus galloprovincialis* exposed to toxic *Microcystis aeruginosa* cells, extracts and pure toxins. *Toxicon*, *50*(6), 740-745. <https://doi.org/10.1016/j.toxicon.2007.06.010>
- Viarengo, A. (1989). Heavy metals in marine invertebrates: mechanisms of regulation and toxicity at the cellular level. *CRC Critical Reviews in Aquatic Sciences*, *1*, 295-317.
- Vidal, M. L., Rouimi, P., Debrauwer, L., & Narbonne, J. F. (2002). Purification and characterisation of glutathione S-transferases from the freshwater clam *Corbicula fluminea* (Müller). *Comparative Biochemistry and Physiology Part C: Toxicology and Pharmacology*, *131*(4), 477-489. [https://doi.org/10.1016/S1532-0456\(02\)00039-X](https://doi.org/10.1016/S1532-0456(02)00039-X)
- Wadige, C. P. M., Taylor, A. M., Maher, W. A., Ubrihien, R. P., & Krikowa, F. (2014). Effects of lead-spiked sediments on freshwater bivalve, *Hyridella australis*: linking organism metal exposure-dose-response. *Aquatic Toxicology*, *149*, 83-93. <https://doi.org/10.1016/j.aquatox.2014.01.017>
- Wang, W., Mai, K., Zhang, W., Ai, Q., Yao, C., Li, H., & Liufu, Z. (2009). Effects of dietary copper on survival, growth and immune response of juvenile abalone, *Haliotis discus hannai* Ino. *Aquaculture*, *297*(1-4), 122-127. <https://doi.org/10.1016/j.aquaculture.2009.09.006>
- Wedepohl, K. H. (1995). The composition of the continental crust. *Geochimica et Cosmochimica Acta*, *(59)*7, 1217-1232.
- Wei, J., Duan, M., Li, Y., Nwankwegu, A. S., Ji, Y., & Zhang, J. (2019). Concentration and pollution assessment of heavy metals within surface sediments of the Raohe Basin, China. *Scientific Reports*, *9*(1), 1-7. <https://doi.org/10.1038/s41598-019-49724-7>
- Winterbourn, C. C. (2008). Reconciling the chemistry and biology of reactive oxygen species. *Nature Chemical Biology*, *4*(5), 278-286. <https://doi.org/10.1038/nchembio.85>
- WoRMS Editorial Board. (2022). *World Register of Marine Species*. <https://www.marinespecies.org> at VLIZ.
- Xu, L., Zheng, G. J., Lam, P. K. S., & Richardson, B. J. (1999). Relationship between tissue concentrations of polycyclic aromatic hydrocarbons and DNA adducts in green-lipped mussels (*Perna viridis*). *Ecotoxicology*, *8*, 73-82. <https://doi.org/10.1023/A:1008910617843>

- Ya, N. A., Singh, H. R., Ramli, N. H., Makhtar, N., Mohd Rashid, H. N., Dzakaria, N., & Samat, A. (2014). Fish diversity in Sepang Besar estuary - A preliminary analysis. *International Journal of Advances in Agricultural and Environmental Engineering*, 1(2), 229-233.
- Yaakub, N., Rohalin, W. M., & Nordin, R. H. (2019). Bioconcentration of cadmium and nickel in mud clams (*Polymesoda expansa*) at Balok River, Pahang. *Journal of Applied Science and Process Engineering*, 6(2), 362-368. <https://doi.org/10.33736/jaspe.1783.2019>
- Yahya, N., Idris, I., Rosli, N. S., & Bachok, Z. (2018). Population dynamics of mangrove clam, *Geloina expansa* (Mousson, 1849) (Mollusca, Bivalvia) in a Malaysian mangrove system of South China Sea. *Journal of Sustainability Science and Management*, 13(5), 203-216.
- Yahya, N., Idris, I., Rosli, N. S., & Bachok, Z. (2020). Mangrove-associated bivalves in Southeast Asia: A review. *Regional Studies in Marine Science*, 38, Article 101382. <https://doi.org/10.1016/j.rsma.2020.101382>.
- Yang, H. L., Nie, L. J., Zhu, S. G., & Zhou, X. W. (2002). Purification and characterization of a novel glutathione S-transferase from *Asaphis dichotoma*. *Archives of Biochemistry and Biophysics*, 403(2), 202-208. [https://doi.org/10.1016/S0003-9861\(02\)00223-0](https://doi.org/10.1016/S0003-9861(02)00223-0)
- Yang, H. L., Zeng, Q. Y., Li, E. Q., Zhu, S. G., & Zhou, X. W. (2004). Molecular cloning, expression and characterization of glutathione S-transferase from *Mytilus edulis*. *Comparative Biochemistry and Physiology Part B: Biochemistry and Molecular Biology*, 139(2), 175-182. <https://doi.org/10.1016/j.cbpc.2004.06.019>
- Yang, H. L., Zeng, Q. Y., Nie, L. J., Zhu, S. G., & Zhou, X. W. (2003). Purification and characterization of a novel glutathione S-transferase from *Atactodea striata*. *Biochem. Biophysical Research Communications*, 307(3), 626-631. [https://doi.org/10.1016/S0006-291X\(03\)01221-X](https://doi.org/10.1016/S0006-291X(03)01221-X)
- Yap, C. K., Edward, F. B., & Tan, S. G. (2014). Bivalve *Polymesoda erosa*: Its potentials as a biomonitor and food safety concern. *Pertanika Journal of Tropical Agricultural Science*, 37(1), 19-38.
- Yap, C. K., & Chew, W. (2011). A higher metal bioavailability and contamination of trace metals in Pantai Lido than Sungai Semerak: Evidence from trace metal concentrations in *Polymesoda expansa* and surface sediments. *Malaysian Applied Biology*, 40(1), 55-59.
- Yap, C. K., & Al-Mutairi, K. A. (2022). Ecological-health risks of potentially toxic metals in mangrove sediments near estuaries after years of piggery farming bans in Peninsular Malaysia. *Sustainability (Switzerland)*, 14(3), 1525. <https://doi.org/10.3390/su14031525>
- Yap, C. K., Ismail, A., Ching, H. L., & Tan, S. (2007). Interpretation of copper and zinc contamination in the aquatic environment of Peninsular Malaysia with special reference to a polluted river, Sepang River. *Wetland Science*, 5, 311-321.
- Yap, C. K., Cheng, W. H., Karami, A., & Ismail, A. (2016). Health risk assessments of heavy metal exposure via consumption of marine mussels collected from anthropogenic sites. *Science of the Total Environment*, 553, 285-296. <https://doi.org/10.1016/j.scitotenv.2016.02.092>
- Yap, C. K., Chew, W., Cheng, W. H., Okamura, H., Harino, H., Peng, S. H. T., Ismail, M.S., & Seng, C. (2019). Higher bioavailability and contamination by copper in the edible mussels, snails and horseshoe crabs at Kampung Pasir Puteh: Evidence of an industrial effluent receiving site at Pasir Gudang area. *Advancements in Bioequivalence & Bioavailability*, 2(5), 000548. <https://doi.org/10.31031/ABB.2019.02.000548>

- Yap, C. K., Ismail, A., Edward, F. B., Tan, S. G., & Siraj, S. S. (2006). Use of different soft tissues of *Perna viridis* as biomonitors of bioavailability and contamination by heavy metals (Cd, Cu, Fe, Pb, Ni, and Zn) in a semi-enclosed intertidal water, the Johore Straits. *Toxicological and Environmental Chemistry*, 88(4), 683-695. <https://doi.org/10.1080/02772240600874139>
- Yuan, Y., Jin, M., Xiong, J., & Zhou, Q. (2019). Effects of dietary dosage forms of copper supplementation on growth, antioxidant capacity, innate immunity enzyme activities and gene expressions for juvenile *Litopenaeus vannamei*. *Fish and Shellfish Immunology*, 84, 1059-1067. <https://doi.org/10.1016/j.fsi.2018.10.075>
- Zarykhta, V. V., Zhang, Z., Kholodkevich, S. V., Kuznetsova, T. V., Sharov, A. N., Zhang, Y., Sun, K., Lv, M., & Feng, Y. (2019). Comprehensive assessments of ecological states of Songhua River using chemical analysis and bivalves as bioindicators. *Environmental Science and Pollution Research*, 26, 33341-33350. <https://doi.org/10.1007/s11356-019-06349-7>
- Zhang, H., Pan, L., & Tao, Y. (2014). Toxicity assessment of environmental pollutant phenanthrene in clam *Venerupis philippinarum* using oxidative stress biomarkers. *Environmental Toxicology and Pharmacology*, 37(2), 697-704. <https://doi.org/10.1016/j.etap.2014.01.018>
- Zhang, D., Wang, X., & Zhou, Z. (2017). Impacts of small-scale industrialized swine farming on local soil, water and crop qualities in a Hilly Red Soil Region of Subtropical China. *International Journal of Environmental Research and Public Health*, 14(12), Article 1524. <https://doi.org/10.3390/ijerph14121524>
- Zhu, J., Li, R., Zhang, Z., Mao, H., & Fan, Z. (2013). *Heavy metal contents in pig manure and feeds under intensive farming and potential hazard on farmlands in Shaanxi Province, China*. Chinese Society for Agricultural Machinery.

## Blood CO Status Classification Using UV-VIS Spectroscopy and PSO-optimized 1D-CNN Model

Audrey Huong<sup>1\*</sup>, Kim Gaik Tay<sup>1</sup>, Kok Beng Gan<sup>2</sup> and Xavier Ngu<sup>3</sup>

<sup>1</sup>Faculty of Electrical and Electronic Engineering, Universiti Tun Hussein Onn Malaysia, 86400 Batu Pahat, Johor, Malaysia

<sup>2</sup>Faculty of Engineering & Built Environment, Universiti Kebangsaan Malaysia, 43600 Bangi, Selangor Malaysia

<sup>3</sup>Institute of Integrated Engineering, Universiti Tun Hussein Onn Malaysia, 86400 Batu Pahat, Johor, Malaysia

### ABSTRACT

Rapid and effective blood carbon monoxide (CO) assessment is of great importance, especially in estimating CO-related morbidity and instituting effective preventive measures. The conventional detection methods using CO breath analysis lack sensitivity, while collecting biological fluid samples for CO level measurement is prone to external contamination and expensive for frequent use. This study proposes a one-dimensional convolutional neural network (1D-CNN) consisting of three stacked biconvolutional layers for binary classification of blood CO status using the diffuse reflectance spectroscopy technique. Iterative particle swarm optimization (PSO) has efficiently found the best network parameters to learn important features from the reflectance spectroscopy data. The findings showed good testing accuracy, specificity, and precision of 92.9%, 90%, and 89.7%, respectively, and a high sensitivity of 96.3% in determining abnormal blood CO among smokers using the proposed CNN network. Comparisons with eight existing machine learning and deep learning models revealed the proposed method's effectiveness in classifying blood CO status while reducing computing time by 8–13 folds. The findings

of this work provide new insights that are valuable for researchers in neural network design automation, healthcare management, and skin-related research, specifically for application in nondestructive evaluation and clinical decision-making.

### ARTICLE INFO

#### Article history:

Received: 16 May 2023

Accepted: 18 December 2023

Published: 16 July 2024

DOI: <https://doi.org/10.47836/pjst.32.4.02>

#### E-mail addresses:

[audrey@uthm.edu.my](mailto:audrey@uthm.edu.my) (Audrey Huong)

[tay@uthm.edu.my](mailto:tay@uthm.edu.my) (Kim Gaik Tay)

[kbgan@ukm.edu.my](mailto:kbgan@ukm.edu.my) (Kok Beng Gan)

[xavier@uthm.edu.my](mailto:xavier@uthm.edu.my) (Xavier Ngu)

\* Corresponding author

**Keywords:** Carbon monoxide, machine learning, network design, optimization, spectroscopy

## INTRODUCTION

Carbon monoxide (CO) is an odorless and colorless gas formed by the incomplete combustion of carbon-based compounds. Once air containing CO gas is inhaled and absorbed into the bloodstream, it binds preferentially to heme irons, forming carboxyhemoglobin (COHb). This condition leads to decreased oxygen-carrying capacity, depriving other cells of the oxygen supply essential for metabolism. It is the key factor for increased oxidative stress and inflammation in cells, causing defects and damage to highly oxygen-dependent organs, including the heart and brain (Carrola et al., 2023).

Smoking tobacco smoke remains a major source of indoor air pollution (Raju et al., 2020). Cigarette smoke produces a CO concentration of 3–6% (Turino, 1981) in the air. This concentration is 2–3 times higher in bidi and cigar smoke (Datta et al., 2022). Indoor combustion sources, current smoking status, and passive smoking are the major contributory factors to the increased CO levels in the blood. Other high-risk groups include workers with significant occupational risk, such as firefighters or charcoal production workers (Idowu et al., 2023). These adverse effects of CO in blood, known as CO toxicity, are factors that increase morbidity and mortality in immunosuppressed patients.

Smoking status and blood CO level have been mentioned in the literature (Hoeng et al., 2019; Nemmar et al., 2022) as reliable biomarkers for assessing outcome measures and predicting future disease development in patients. High-tech medical imaging modalities, such as magnetic resonance imaging (MRI), computed tomography (CT) scan, and retinal imaging, can provide a comprehensive analysis of CO concentration in the body (Vaghefi et al., 2019). They are not widely used for research due to their high cost, unavailability, and lengthy examination time. Biochemical analysis, blood gas analyzer, and ribonucleic acid (RNA) tubes are alternative methods to confirm smoking status, but these devices are invasive. Direct and noninvasive approaches, such as breath analysis and salivary or urinary cotinine tests (Ramani et al., 2023), are more suitable for outpatient management to assess smoking habits. However, the accuracy of expired gas analysis can be compromised in patients suffering from severe airflow obstruction (Papin et al., 2023), while food consumption pattern (i.e., presence of thiocyanate ions in various vegetables, fruits, and milk), lifestyle, and environmental and physical conditions are among the other factors that have a direct effect on the performance of breath analysis (Sharma et al., 2023 & Shreya et al., 2023). The shorter half-life of expired CO also makes it less reliable than cotinine measurement in urine and saliva (Usmani et al., 2008). Nonetheless, external contamination of body fluid samples is common during sample processing, leading to unreliable results. Besides, these test strips can be expensive if large specimens are needed.

Spectroscopy is a simple and noninvasive technique to obtain optical information about a medium across a broad wavelength range. Knowing the properties of light absorption and scattering of the medium enables backward prediction of a substance's concentration

and physical structure based on the measured light signals without destroying its integrity. This nondestructive feature, cost-effectiveness, and flexibility allow its use in endless possibilities. CO oximeter is a state-of-the-art photoelectric device capable of determining the percentage of CO saturation in blood using the optical spectroscopy method and with a fixed calibration curve. A previous study showed an elevation in the percent COHb, or blood CO level measured using a CO oximeter from 4%–6% in the control group to 8%–25% in smoking or acute CO poisoning patients (Bol et al., 2018; Onodera et al., 2016). However, the system can be unreliable for measurements outside the calibration curve defined using the absorbance ratio of isosbestic points 532 nm and 558 nm (Papin et al., 2023).

### Related Works

Deep learning is an emerging technique in artificial intelligence that allows rapid and fully automated extraction of important features from a dataset for the classification task. Among them, CNN is the most widely used method for vision-related tasks. A standard CNN consists of convolutional, pooling, and fully connected layers to learn a hierarchical representation of features from raw data. Pretrained CNNs, such as AlexNet, Residual Network (ResNet), GoogleNet, and Visual Geometry Group (VGGNet), are widely used to learn a new complex task by fine-tuning the weights of neurons in the model.

Most models contain alternating convolutional and pooling layers to abstract features layer by layer. While these pre-trained models are generally recommended and proven promising for two-dimensional (2D) image processing tasks to 3D object recognitions, 1D-CNN for signal processing problems has received little attention compared to its extended counterparts. Some works in the past demonstrated using 2D convolutional models for the 1D signal classification task with considerable success (Ahmad et al., 2021), whereas others designed their 1D model from scratch. The process can be tedious and laborious as it involves tuning network hyperparameters, such as learnable weights and biases, as well as the layers' arrangement and size.

The research community used manual, automatic, or hybrid methods in designing the CNN model for a specific classification task (Yang et al., 2021). While manual methods include brute force or a grid search approach, an automatic search for the best model design can be carried out more aggressively using optimization techniques. Various types of optimization algorithms are available for this purpose, including randomized adaptive search procedures, such as the Markov decision process and Monte Carlo (MC) search, particle swarm optimization (PSO), genetic algorithm (GA), Bayesian optimization (BO), pattern search method, and gray wolf optimization (GWO). Each technique adopts different strategies to minimize a given function or cost measure and could be preferred over others in specific applications. Among these, BO is the most popular technique for optimizing custom-built CNN. This method works by incrementally building a probabilistic model

during optimization. Previous works (Kolar et al., 2021; Ling et al., 2022; Shi et al., 2021) reported considerably good classification accuracy using the 1D-CNN architecture and training hyperparameters optimized using BO for fault diagnosis and safety analysis.

However, this technique does not scale well to higher dimensions and has high computational complexity. Pattern search is a direction-based method taking trial steps in each direction for each parameter within the range specified. The PSO works by iteratively searching in a region defined by the best success of the neighborhood particles. Meanwhile, GWO is based on the mathematical models of the social behaviors of gray wolves guided by iterative prey encircling and hunting processes. The GA method works by randomly generating different populations of generations and mutations in its search. These optimization techniques have also been applied in a wide area of decision-support systems. Layek et al. (2021) demonstrated using GA and PSO to determine the elasticity constant for application in thyroid cancer detection. In Goel et al. (2021), comparisons have been made to evaluate the performance of these techniques in optimizing the feature extraction and classification components. GA, pattern search, PSO, and GWO were shown to produce comparable results in their optimized models for automatic diagnosis of coronavirus disease (COVID-19).

Another work by Tan et al. (2019) showed superiority in the performance of the model optimized using the PSO method compared to its competing models, namely GA and BO, in the security of unmanned aerial vehicle (UAV) networks. This finding is further supported by a review by Korani and Mouhoub (2021), who summarized the different advantages of PSO compared to other population-based algorithms as an optimization method.

Unlike the machine learning method, the neural network offers the advantages of superior generalization and representation abilities at the cost of higher computational complexity and expensive hardware requirements (Asgharzadeh et al., 2023). Machine learning classifiers, for example, support vector machines (SVM),  $k$ -nearest neighbors (KNN), Naïve-Bayes (NB), and regression methods, require less computational and implementation effort, and they are also highly reputable for solving binary problems. Most machine learning algorithms are simple and easy to use, requiring fewer parameters to tune before training. However, their performance is comparatively inferior, especially when it involves nonlinear solutions or complex decision boundaries. To further enhance the performance of classification, some work in the past preferred using a binary classifier optimized using the optimization methods mentioned above for prediction. Examples of important works in this area are using a hybrid SVM-PSO system to improve landslide susceptibility prediction (Zhao & Zhao, 2021). Thote et al. (2017) used a KNN system optimized using GA to discriminate the different faults in transformer fault diagnosis.

Studies of optical reflectance for the classification of CO in vivo have not received much attention among the research community in the field, which is mainly due to the high sensitivity of the measurement to factors other than COHb, such as diversity in human skin colors, thickness, and time-varying physiological states (Huong et al., 2014). Several

recent studies using the optical method, specifically spectroscopy, in smoking and nicotine-related investigations include a comparison study between a five-wavelength transmissive spectrophotometer and the standard radiography blood analyzer for detecting CO poisoning (Lyon et al., 2022). The study reported high consistency in the performance of the optical spectroscopy technique with the control device. Yi et al. (2023) demonstrated fluorescence spectroscopy for in vitro detection of CO in living tissues. Li et al. (2022) designed a novel optical-acoustic technology using an acoustic resonator to detect acoustic wave signals generated by the human exhaled gas molecules (i.e., CO) absorbing laser energy.

These past studies used calibration curves and fitting models to predict the required value. Additional research using the spectroscopy method combined with the deep learning model for examining tissue COHb would be interesting. This article aims to present an optimized 1D-CNN model for a quick and objective classification of a person's blood CO in skin based on diffuse reflectance spectroscopy. This study chose the PSO method for the optimization problem because of its excellent global convergence speed and effectiveness. The contributions of this work are threefold:

1. Advancement of research in developing the CNN model for blood CO classification by creating a new ultraviolet-visible (UV-VIS) spectroscopy dataset of nonsmoking and smoking subjects.
2. An iterative PSO-based optimization strategy in automatically designing a 1D-CNN model to learn abstract features from the spectroscopy data.
3. An effective detection solution for blood CO status with minimal computing resources.

## **MATERIALS AND METHODS**

### **Participants and Selection Criteria**

There is no public dataset for blood CO detection research using optical spectroscopy. This research built the first smoking-related CO dataset from experiments conducted at the Universiti Tun Hussein Onn Malaysia (UTHM) laboratory between 2015 and 2019. This study was approved by the Ethical Committee of UTHM (approval no. 100-9/39). Figure 1 shows the consort diagram of participant recruitment and analysis. One hundred seven subjects consisting of university students and individuals from the public were randomly approached and invited to participate in the studies; 41 declined. Most cite a lack of time and inconvenient schedules and locations as the main reason for their refusal. The remaining 66 volunteers were required to answer questions about their age and smoking habits, disclose their living and occupational status, health information, and medical history, and repeat prescriptions before the screening. The daily air quality index where the participants lived and worked showed acceptable readings with an average value of 25 ppm during the study period.

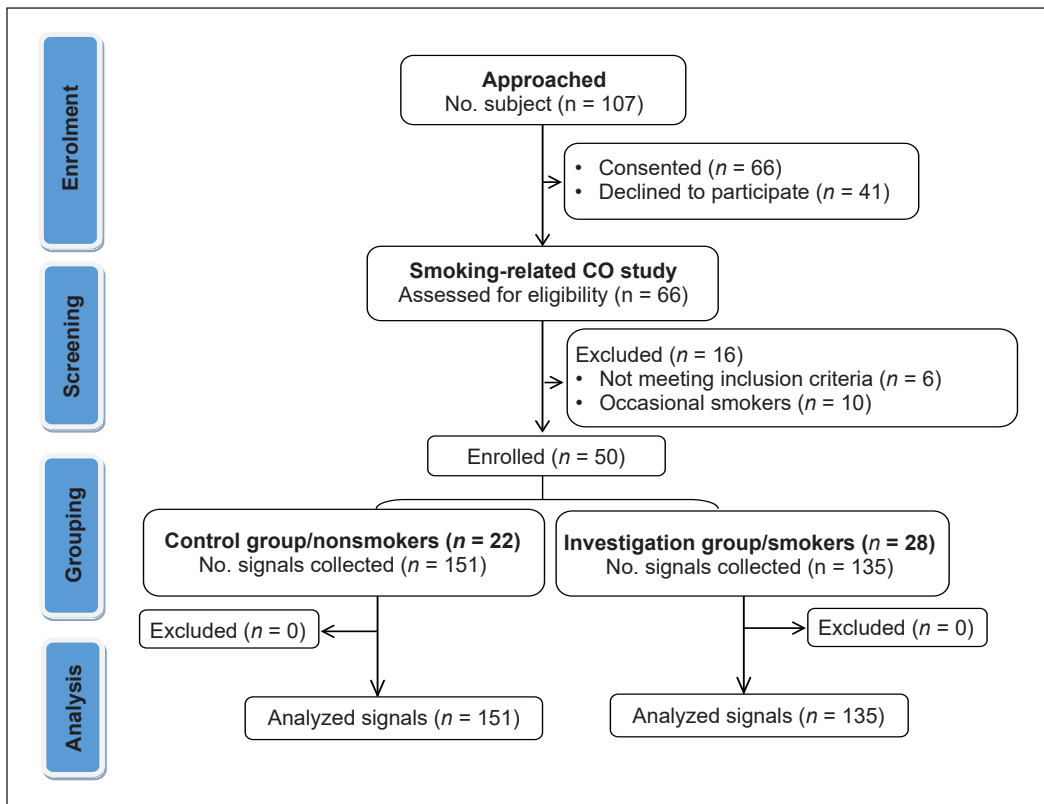


Figure 1. Consort diagram for participant flow

The volunteers were assessed for their eligibility based on inclusion and exclusion criteria. The exclusion criteria included subjects with cardiovascular, endocrine, or respiratory system diseases. Of these respondents, sixteen were excluded because of their inconsistent smoking habits (n = 3), nonsmokers with the possibility of CO exposure in self-report assessment (n = 7), or participants with medical records (n = 6) that could affect the results. Fifty people met the eligibility criteria and were enrolled in the study. These participants are never-smokers with no household cigarette smoke or occupational or indoor combustion exposure (n = 22) or regular smokers (n = 28) aged 18 or older who had smoked at least one cigarette per day for at least two years during the time data was taken. They were aged between 20 and 62 years. They self-declared good general health and were not on long-term medication.

### Experimental System and Data Collection

Information about the sampling and data collection processes and experimental setup used for the measurement of diffuse light reflectance from the skin of control (i.e., nonsmoking) and investigation (smoking) groups were provided in the original studies (Huong & Ngu, 2014, 2015). However, for completeness of this paper, they are summarized here.

Figure 2 shows the schematic experimental setup for skin reflectance spectroscopy. During these experiments, a white light-emitting diode (LED) (Model no. SMD 5730 from Aira Technologies), placed at 80 mm from the skin and 20° from the normal axis, illuminated the selected skin area. The detection system consisted of a UV-VIS spectrometer (model no. USB4000 Ocean Optics, Florida) connected to a bifurcated fiber optic bundle. The fiber tip was placed 35° from the incidence plane and 20–40 mm above the skin. Light reflected from the targeted surface was collected into the optical fiber before being diffracted by the grating (1200 groves/mm) in Figure 2, which spreads the light spectrum (in the wavelength range of 178–898 nm) on a charge-coupled detector (CCD)-array inside the spectrometer. The intensity reading was recorded by a laptop installed with SpectraSuite software for further processing and analysis.

On average, between 4 to 8 spectra were recorded from the index finger of the recruits during the resting state. The studies were carried out in a well-ventilated laboratory with an ambient temperature of  $24 \pm 2^\circ\text{C}$ . A total of 135 and 151 reflectance spectroscopy signals (N) were recorded from 50 subjects: 28 smoking and 22 nonsmoking individuals, respectively. Data analysis using a paired sample t-test performed with SPSS (version 2, IBM Inc.) with a confidence level of 95% showed statistical significance ( $p=0.0171$ ) for inter- and intra-subject variability. Hence, they are treated individually as independent signals for the classification task. These sample sizes are sufficient for clinical research studies, as agree with the minimum sample size requirement of 137 (for smoking) and 101 (nonsmoking group) calculated from the power size formula of Das et al. (2016).

The signals of these volunteers were grouped according to their reported smoking status. These class labels are confirmed with the mean percent carboxyhemoglobin (COHb) values of 3%–7% and 8%–16%, respectively, for smokers and nonsmokers using the MC

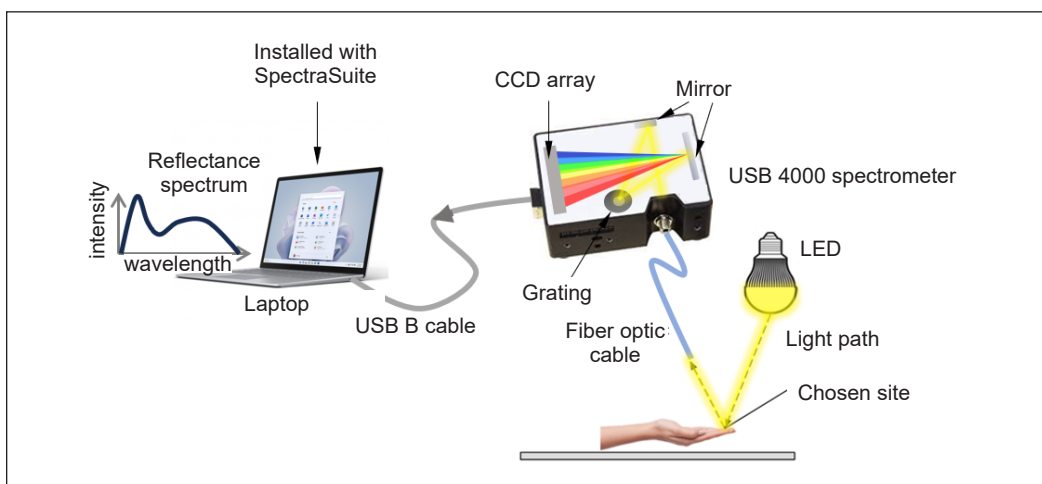


Figure 2. The UV-VIS spectroscopy measurement setup. Diagram also shows the inside of the spectrometer for detection of the reflectance spectrum

approximation (Huong & Ngu, 2014, 2015). Figure 3 shows the participants' stratification based on their smoking status and verification of the class labels.

Based on the original data points of  $1 \times 3648$  from the spectrum in the range of 178 nm to 898 nm (i.e., with spectral resolution of 0.2 nm), a fixed window of length  $1 \times 1415$  was applied to truncate signals in the wavelength range of 420–680 nm in Figure 3, consistent with the output wavelength of the employed LED for the data mining process. Most importantly, there is a considerable variation and strong characteristic absorption peaks for hemoglobin variants in this range, which is suitable for detecting the oxygenation state of hemoglobin using the spectroscopy technique (Nitzan et al., 2020). These data handling processes, from data collection to signal processing and database archiving, are summarized in Figure 3. This study does not consider the feature selection method to preserve all information for investigation. Attempts at enriching the dataset using augmented data by adding and swapping uncertainties (i.e., noises) and the sliding window approach proposed by Ullah et al. (2018) have not yielded improved results. Thus, the original dataset was used and randomly split for training, validation, and testing purposes using a ratio of 60%/20%/20% with a random seed value of 1 for results reproducibility.

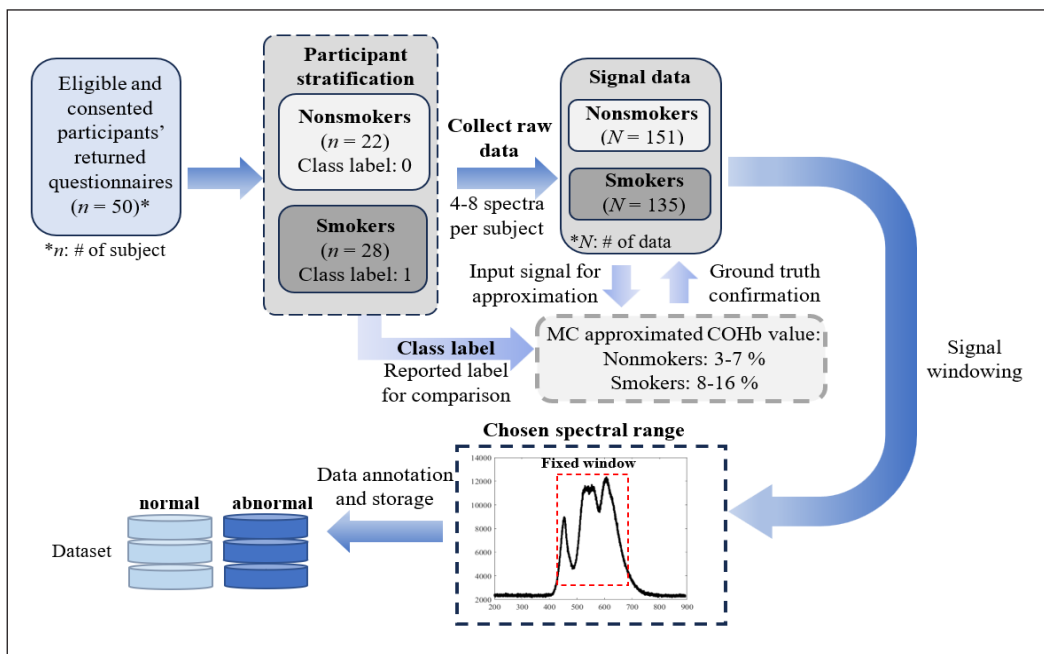


Figure 3. Reflectance spectroscopy data handling process

### Network Architecture Design

The design of an end-to-end 1D CNN used in this research is inspired mainly by the structure and organization of the existing pre-trained networks, consisting of convolutional filters

(CONV), rectified linear unit (ReLU), max pool (POOL), fully connected (FC) layer, and a classifier. Specifically, stacked bi-convolutional and one-pooling layers (i.e., CONV<sub>1</sub>-ReLU<sub>1</sub>-CONV<sub>2</sub>-ReLU<sub>2</sub>-POOL) are adopted as the basic structure of the CNN due to its universality and straightforward design. This architecture of alternating convolutional and pooling layers, like most pre-trained networks such as VGGNet and AlexNet, produces minimal features from the signal. Such an arrangement is referred to as biCONV. Next, two FC layers and a Softmax are followed for probability prediction of the signals for classification. The last layer is the classification output containing abnormal and normal classes.

Several architectures have been attempted in which an additional biCONV block is progressively stacked on top of the preceding layers in each model version to deepen the network. Their classification training and validation accuracies were recorded and compared. The results revealed that the network architecture containing three stacked biCONVs in Figure 4 produced considerably superior classification accuracies (i.e., increased by 5%–10%) than its shallower counterparts and negligible performance differences compared to its deeper counterparts. Therefore, the architecture in Figure 4 is chosen as the final design, and the results from this model are presented in the remainder of this paper.

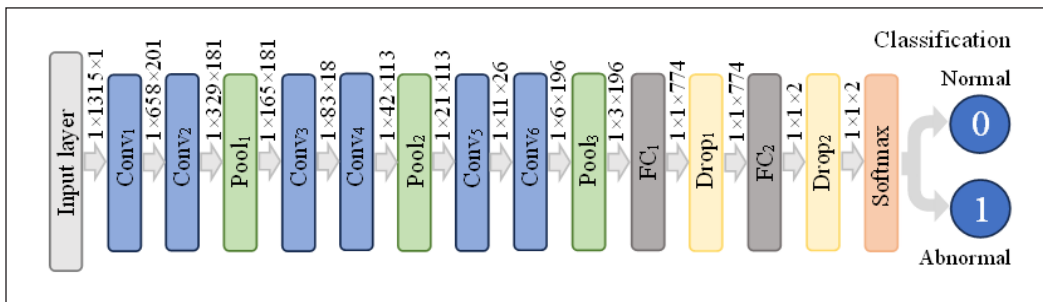


Figure 4. End-to-end 1D-CNN model for blood CO status classification

### Network Parameter Optimization

The most common method for determining network hyperparameters (i.e., CNN kernel size, stride and filter numbers, and training parameters) is a grid search or brute-force method, whose decision is guided based on the classification accuracies of the trained model. The procedure is challenging, expensive, time-consuming, and has a limited coverage area. In this study, parameters of hidden nodes (i.e., input weights and biases) and some of the most important training parameters (i.e., optimizer type, mini-batch size, and initial learning rate) are fine-tuned during the optimization.

This study addressed this challenge by proposing a 16-degree-of-freedom problem to generalize the model for the task. The objective function to be minimized is as Equation 1:

$$f(T_{acc}, V_{acc}, t_s) = ((100 - T_{acc}) + (100 - V_{acc})) \times 1e^3 + \frac{t_s}{1e^3} \tag{1}$$

$T_{acc}$  and  $V_{acc}$  are the training and validation accuracies, respectively, while  $t_s$  is the run time for each search iteration. The iteration terminates prematurely if the validation accuracy fails to improve for ten iterations during the search process. The upper and lower range of variables that directly affect the objective function result is shown in Table 1. Since the neural network was trained from scratch, the learning weights and biases of the neurons were determined based on the kernel size or filter size of the convolutional layers identified through the optimization method.

Figure 5 shows an overview of network development and optimization processes for smoking status classification. After splitting the dataset (collected and annotated in Figure 3) into training, validation, and testing cohorts, the training and validation sets were used to build the classification model and tune the relevant parameters. The PSO method was used for search purposes. The PSO works by iteratively updating the velocity and position of the particles of swarm size 200 by moving each particle based on the best-known previous positions within the boundary limits of the search space specified in Table 1.

Each candidate solution created based on the random number generator was subjected to the search for a maximum of 500 optimization steps, making the search process stochastic, and it was based on the locations of the previous best solutions. This paper implemented the same padding strategy for each layer. It used a pooling size of  $(1 \times 4)$  to overcome the mismatch in the feature map dimensions between the network layers from the chosen parameters. A stride length of  $(1 \times 2)$  was used in all convolutional and pooling layers to ensure consistency in the proposed approach. This program attempted to search for the best solution (i.e., minimize the solution) to the objective function given in Equation 1. The search step for all integer variables was set to 1, and the step change of the initial learning rate was given by  $1e^{-8}$ . Meanwhile, in the efforts to cover the entire search space, this optimization process was repeated 300 times before determining the best solution.

A fixed epoch number was used because the pre-experiment results showed considerably lower significance in its effects on network performance than the mini-batch size and initial learning rate. It could also reduce the complexity of the search and, hence,

Table 1  
*Parameters range in the fine-tuning process*

Description	Parameter	Lower limit	Upper limit
Training hyper-parameter	Optimizer, $Opt$	$\{1 \rightarrow 3; 1: Adam, 2: Sgdm, 3: RMSProp\}$	
	Mini batch size, $\beta$	8	1024
	Initial learning rate, $\chi$	$1e^{-6}$	$1e^{-2}$
Network learnable	Kernel size*	$1 \times 2$	$1 \times 10$
	Filter no.*	$1 \times 2$	$1 \times 256$
	$FC_1$	100	1000

\*For all convolutional blocks ( $Conv_1$ - $Conv_6$ )

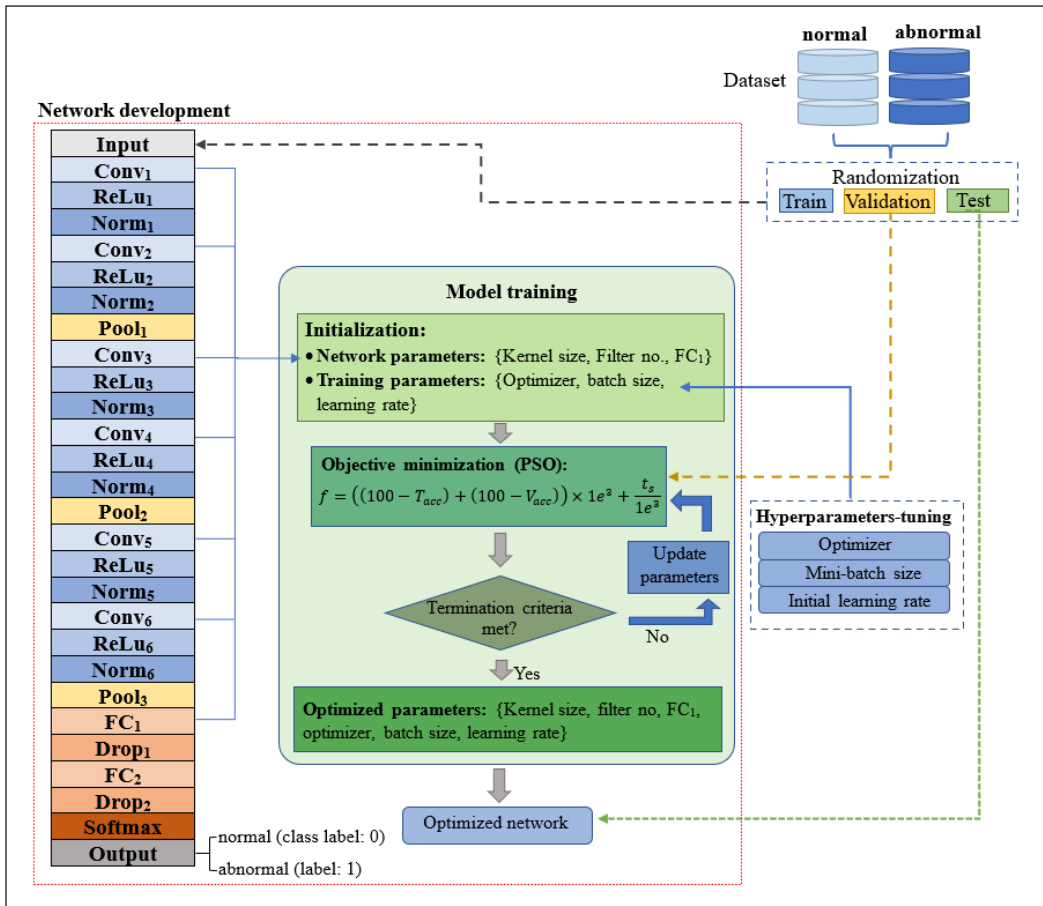


Figure 5. An overview of network development and optimization for smoking status classification

computational resources. Several efforts have been made to improve the generalization of the model, including:

1. incorporating a dropout regularization of factor 0.2 after biCONV and FC layers,
2. using a high epoch number of 500 to increase training time,
3. considering the spectral range that matches the LED output spectrum (i.e., signal windowing shown in Figure 3) to minimize unnecessary features in the analysis and
4. an early stopping function monitors validation accuracy during the training process.

### Evaluation Metrics and Comparisons

Different performance metrics have been used to evaluate the model’s performance for the classification task. Testing data that do not have a role in the training and validation phase was used to test the ability of the trained model to identify the person’s blood CO status. The considered evaluation metrics are accuracy (*Acc*), sensitivity (*Sens*), specificity (*Spec*),

and precision (*Prec*) in Equations 2 to 5, which can be calculated using a confusion matrix. The confusion matrix can be used to detect classification errors with four components: (1) a true negative (*TN*) is when a signal is correctly classified as a normal blood CO (class 0), (2) a true positive (*TP*) correctly classifies the abnormal blood CO case (class 1), (3) a false positive (*FP*) is when a normal blood CO signal is incorrectly classified as abnormal, and (4) a false negative (*FN*) is an error in which an abnormal case is misclassified as normal.

Accuracy (*Acc*) is the proportion of accurate results among the total number of cases examined.

$$Acc = \frac{TP+TN}{TP+TN+FP+FN} \times 100 \% \tag{2}$$

Sensitivity (*Sens*) or recall rate is the probability of a positive abnormal CO result among all abnormal data.

$$Sens = \frac{TP}{TP+FN} \times 100 \% \tag{3}$$

Specificity (*Spec*) is defined as the ability of a test to exclude normal data.

$$Spec = \frac{TN}{TN+FP} \times 100 \% \tag{4}$$

Precision (*Prec*) is the percentage of a correctly classified abnormal case to total positive abnormal results.

$$Prec = \frac{TP}{TP+FP} \times 100 \% \tag{5}$$

This research chose some popular classifiers, namely SVM, KNN, Decision Tree (DT), logical regression (LR), Naïve-Bayes (NB), and some of the popular pre-trained networks (i.e., AlexNet, GoogleNet, and ResNet-18) as the benchmark models for comparison purposes, as summarized in Figure 6. These models were trained and tested using the same spectroscopy dataset for a fair comparison of the results. The threshold *k*-value in the KNN classifier varied manually from 1 to 10; the best result chosen based on the classification accuracy is presented in this work. In the

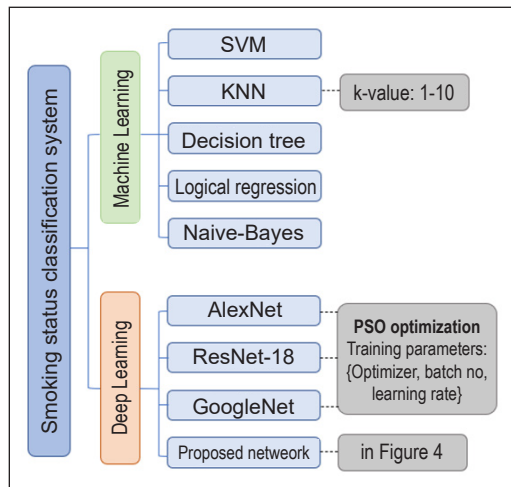


Figure 6. The benchmark methods for comparison with the proposed network

case of pretrained 2D models, the *getframe* function screenshotted each signal's plot before saving it as an image. The image was resized according to the input size allowable for each network. The hyperparameter values, namely optimizer solver, mini-batch size, and initial learning rate, were chosen for training deep models using the PSO method following the minimization process in Figure 5. The weight of all layers was updated during the training process for the spectroscopy dataset.

## RESULTS

This study developed the CNN model from scratch, and the model that yielded the lowest objective function value given in Equation 1 is the best for classifying the blood CO status. This research approached this task by systematically stacking additional biCONVs consecutively to deepen the network. The final design of the 28-layer network shown in Figure 4 gives 841,509 learned parameters to extract features from the spectroscopic data for the smoking classification task. This paper presents the results for 100 sets of training parameters (i.e., optimizer (*Opt*), mini-batch size ( $\beta$ ), and initial learning rate ( $\chi$ )) that produced the lowest  $f$  value, plotted against its  $T_{acc}$  and  $V_{acc}$  in Figure 7. The best training hyperparameter set chosen from this plot is  $Opt = 2$  (i.e., *Sgdm*),  $\beta = 555$ , and  $\chi = 0.0035$ . Since early termination was adopted to speed up the search process, each search iteration time is recorded as ranging between  $t_s = 3$ –50 seconds executed on an NVIDIA Tesla K80 GPU with 12 GB of memory and 13 streaming multiprocessors. Based on the identified hyperparameters, the model training was repeated three times to ensure the reproducibility of the results. Figure 8 shows the best confusion matrix of the proposed 1D CNN system evaluated using the testing set.

The same training and testing procedure was performed on the machine mentioned above for the eight competing models in Figure 6. The mean and standard deviation of

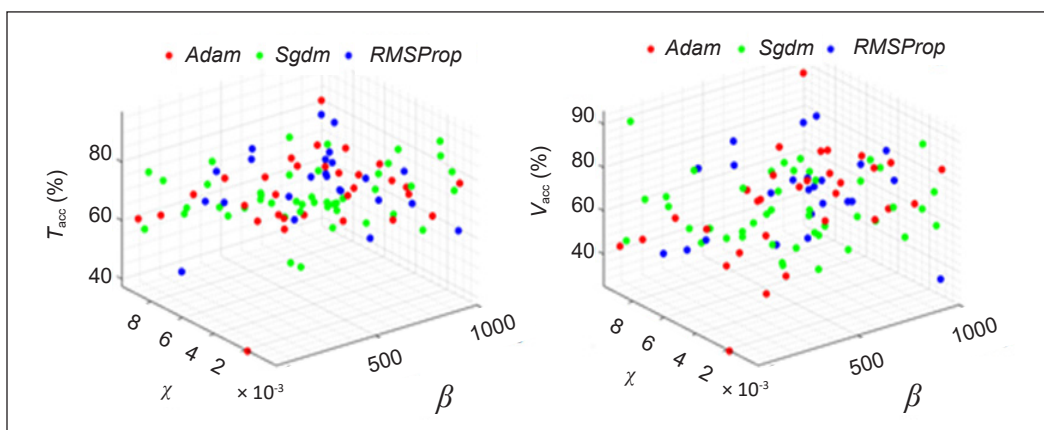


Figure 7. The percent training ( $T_{acc}$ ) and validation accuracies ( $V_{acc}$ ) against 100 best training hyperparameter sets ( $\chi$ : initial learning rate,  $\beta$ : mini-batch size, filled color: optimizer)

the evaluation metrics are shown in Table 2. Also included in this table is the total elapsed time taken to solve the optimal training hyperparameters for the deep learning models (i.e., AlexNet, GoogleNet, ResNet, and the proposed 1D CNN) using the PSO optimization process are shown in Figure 5. The experiments using the KNN method with different  $k$  values in Figure 6 produced the best accuracy result with  $k=7$ . Thus, it is presented in the Table 2.

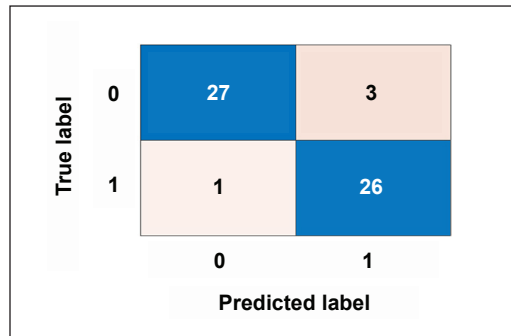


Figure 8. The best confusion matrix of the proposed 1D-CNN model tested on the testing data. Class label 0: normal and 1: abnormal blood CO status

Table 2  
A comparison of blood CO status classification performance between the proposed model and state-of-the-arts

Model	Mean ± SD of evaluated metrics (in %)*				Training time (in s)*	Iterative optimization time (in s)†
	Acc	Sens	Spec	Prec		
SVM	67	100	29.6	61.2	0.52 ± 0.15	-
KNN	82.5	93	70.4	78	0.56 ± 0.36	-
DT	65	67	63	67	0.57 ± 0.39	-
LR	92.9	93	92.5	93	0.76 ± 0.11	-
NB	72	86.7	55.6	68.4	1.4 ± 0.07	-
AlexNet	85.9 ± 1.8	93.3 ± 3.3	77.8 ± 6.4	82.5 ± 3.6	54 ± 37	26,542
GoogleNet	81.3 ± 7	88.9 ± 11	72.8 ± 11	78.8 ± 7	210.5 ± 61	38,982
ResNet-18	88.3 ± 5	92.2 ± 5	83.9 ± 5.6	86.5 ± 4.8	166.4 ± 91	22,495
Proposed model	91.8 ± 1	93.3 ± 3.3	90.1 ± 5.6	91.5 ± 4.3	15.8 ± 8.2	4,750

Note. ACC: accuracy, Sens: Sensitivity, Spec: Specificity, Prec: Precision; \*Mean and standard deviation (SD) results from three runs for optimized model training and testing; †Total time taken in iterative search of optimum training hyperparameters (deep learning models)

## DISCUSSION

This study demonstrated an optimization algorithm to find the appropriate weights and biases, extract important features from the spectroscopy data to classify blood CO and determine the best set of hyperparameters for the improved learning process of the CNN model. This method is used primarily to minimize the problem of classification accuracies and training time. The comparison of different methods in Table 2 shows differences in classification performance depending on the methods. The proposed model achieved a good classification accuracy of 92.9%, confirming the feasibility of the PSO-optimized method for the efficient development of the custom-made 1D-CNN model.

Although classifiers, such as DT, NB, and LR, have a long history of being used for the two-class classification task, the presented results show that the CNN method outperformed

most of these models. The testing accuracy ranged between 85% and 93% using the CNN type of networks compared to 65%–92% using binary classifiers. The spectroscopy data has no visually distinctive features separating normal and abnormal groups. Thus, this may explain why a reasonable decision boundary may not be achieved, rendering most of these linear classifiers fail to differentiate blood CO classes. This problem is not found in the case of pre-trained networks. Even though they were developed for image recognition, they worked acceptably well for the 1D problem, suggesting their sufficiency in extracting important features with deep layers of neurons.

The SVM performs best in many applications through the optimal arrangement of hyperplanes for modeling the decision boundary. However, it fails to detect abnormal blood CO status in smokers with a classification accuracy of 66%. This classifier is overfitting to the nonsmoking class, resulting in perfect precision and specificity rates (i.e., FP rate of 0) but poor sensitivity of 29%. Meanwhile, the KNN method that finds the closest objects in training data to the unknown input produced a reasonably good performance with a classification accuracy of 82% using the k-value of 7, implying that the distance-based strategy works better on small datasets like ours.

An interesting attribute of the proposed model is that it has the least learnable parameters compared to the pre-trained models. Table 2 shows a significant decrease in its optimization and training times by up to 8 and 13 folds, respectively, compared to the deeper models without sacrificing generalization ability. Although some normal data have been misclassified as abnormal, as shown in Figure 8, giving a slightly inferior precision compared to ResNet-18 in Table 2, the designed model eliminates the need for complex architecture and is least likely to suffer from dimensionality problems. The robustness of this model is evident with its superior CO status detection sensitivity of 96.2% in smokers compared to the traditional models in Table 2, suggesting that this shallow and small model can recognize global coarse information with the first two stacked convolutional layers, while final stack layer is sufficient to learn the refining information further.

In addition to optimizing network architecture, this study enhanced the model's generalization through iterative tuning of training hyperparameter sets. Figure 7 shows that Sgdm has a high probability (~50%) of being chosen as the solver, followed by Adam and RMSProp. This outcome is not surprising given the high computing cost of the RMSProp (~1.12 folds longer training time than the others). The experiments found that the most feasible range of initial learning rate is between 0.0043–0.0058 and 522–599 for mini-batch size using the employed spectroscopy dataset. An increase in the initial learning rate produced poor learning efficiency, where the exploding gradients incidence (i.e., training accuracies returned as invalid values) was observed. Meanwhile, the overall lower mean training accuracy of 77.2% compared to 80.98% in validation accuracies implies the possibility of underfitting the network. This issue is understandably due to the small training set. In the earlier experiments, attempts have been made to enlarge the dataset by

incorporating different noise signals into the original data, but no observable changes in the classification performance were noted. This finding can be interpreted as the ability of the proposed model to recognize noise signals (i.e., high frequencies) as unimportant features.

On that note, lower frequency information may be identified as useful features, so extraction of better features through further modifications of the network architecture may be necessary to enhance the performance of the existing model. The final design in Figure 4 is determined after ten tests have been carried out, ranging from one biCONV to five-stack biCONVs, with fully connected layers' dropout rates of 0.2 and 0.5. While the incorporation of dropout 0.2 generally produced better results in terms of classification accuracies than 0.5, the training and validation accuracies remained relatively constant beyond networks comprising three-stack bi-CONVs.

This study is one of the pioneer and preliminary attempts to explore whether the proposed framework and technology can detect blood CO status. Those who chose to participate were self-selected. It limits the generalizability of the study; thus, research needs to be explored in larger samples in the future. Since this is not a strictly controlled experiment, the diet and lifestyles of the participants have not been regulated. Therefore, carefully designed and strict experiment conditions for future investigation are recommended. Studies exploring network capacity for predicting health risks for categories of abnormal CO are also a task for further research.

Classification of blood CO status using light reflectance spectroscopy demonstrated in this study is the first in the field to use optimized deep learning methods. This strategy is an efficient, rapid, and cost-effective approach for the task as compared to conventional breath analysis, which is unreliable in patients with severe airflow obstruction. Unlike the study by Lyon et al. (2023) and Yi et al. (2023) that required daily calibration verification and blood samples to be taken for CO classification using transmissive and fluorescence spectrophotometry systems, the proposed approach performed in-situ and real-time classification based on skin reflectance signals. This system is potentially useful as a tool for pre-hospital triage and evaluation of treatment in CO-poisoning patients.

Future research should include larger data from human subjects of different physical characteristics and health problems to enhance the robustness of the proposed system in assessing a person's CO exposure status and predicting health risks. In terms of classifier design, this study acknowledges the importance of further efforts to improve the developed model for the classification task. A more rigorous design procedure is expected to be further explored to allow more efficient extraction of high-level features for the task.

## CONCLUSION

This paper adopts a PSO-optimized 1D-CNN model for blood CO classification using the optical spectroscopy signal. This work is the first to apply a deep learning approach

combined with spectroscopy to the blood CO abnormality classification task. The proposed optimization framework offers a time and effort-efficient approach to customizing the model. This method achieved comparable performance with most existing pre-trained deeper models while outperforming state-of-the-art binary classifiers. Potential directions for further research include deeper investigations and richer evidence about skin CO differences in a larger population with different physical parameters and clinical presentation to improve study generalization. In addition, there is still room for improving the network structure to extract the target features more accurately.

## ACKNOWLEDGEMENTS

This research is partially funded by the Ministry of Higher Education Malaysia (FRGS/1/2020/TK0/UTHM/02/28).

## REFERENCES

- Ahmad, Z., Tabassum, A., Guan, L., & Khan, N. M. (2021). ECG heartbeat classification using multimodal fusion. In *IEEE Access* (Vol. 9, pp. 100615-100626). IEEE Publishing <https://doi.org/10.1109/ACCESS.2021.3097614>
- Asgharzadeh, H., Ghaffari, A., Masdari, M., & Gharehchopogh, F. S. (2023). Anomaly-based intrusion detection system in the Internet of Things using a convolutional neural network and multi-objective enhanced Capuchin Search Algorithm. *Journal of Parallel and Distributed Computing*, 175, 1-21. <https://doi.org/10.1016/j.jpdc.2022.12.009>
- Bol, O., Koyuncu, S., & Gunay, N. (2018). Prevalence of hidden carbon monoxide poisoning in auto service workers: A prospective cohort study. *Journal of Occupational Medicine and Toxicology*, 13, 13-35. <https://doi.org/10.1186/s12995-018-0214-9>
- Carrola, A., Romão, C. C., & Vieira, H. L. A. (2023). Carboxyhemoglobin (COHb): Unavoidable bystander or protective player? *Antioxidants*, 12(6), Article 1198. <https://doi.org/10.3390/antiox12061198>
- Das, S., Mitra, K., & Mandal, M. (2016). Sample size calculation: Basic principles. *Indian Journal of Anaesthesia*, 60(9), 652-656. <https://doi.org/10.4103/0019-5049.190621>
- Datta, R., Singh, S., Joshi, A., & Marwah, V. (2022). Concept of BIDI years: Relevance to the perioperative period. *Lung India*, 39(4), 337-342. [https://doi.org/10.4103/lungindia.lungindia\\_595\\_21](https://doi.org/10.4103/lungindia.lungindia_595_21)
- Goel, T., Murugan, R., Mirjalili, S., & Chakrabartty, D. K. (2021). OptCoNet: An optimized convolutional neural network for an automatic diagnosis of COVID-19. *Applied Intelligence*, 51, 1351-1366. <https://doi.org/10.1007/s10489-020-01904-z>
- Hoeng, J., Maeder, S., Vanscheeuwijck, P., & Peitsch, M. C. (2019). Assessing the lung cancer risk reduction potential of candidate modified risk tobacco products. *Internal and Emergency Medicine*, 14, 821-834. <https://doi.org/10.1007/s11739-019-02045-z>
- Huong, A., & Ngu, X. (2014). Noninvasive diagnosis of carbon monoxide poisoning using Extended Modified Lambert Beer Model. In *2nd International Conference on Electronic Design (ICED)* (pp. 265-269). IEEE Publishing. <https://doi.org/10.1109/ICED.2014.7015811>.

- Huong, A., & Ngu, X. (2015). *In Situ* monitoring of mean blood oxygen saturation using Extended Modified Lambert Beer model. *Biomedical Engineering: Applications, Basis and Communications*, 27(01), Article 1550004. <https://doi.org/10.4015/S1016237215500040>
- Idowu, O. S., De Azevedo, L. B., Zohoori, F. V., Kanmodi, K., & Pak, T. (2023). Health risks associated with the production and usage of charcoal: A systematic review. *BMJ Open*, 13(7), Article e065914. <https://doi.org/10.1136/bmjopen-2022-065914>
- Kolar, D., Lisjak, D., Pajak, M., & Gudlin, M. (2021). Intelligent fault diagnosis of rotary machinery by convolutional neural network with automatic hyper-parameters tuning using Bayesian Optimization. *Sensors*, 21(7), Article 2411. <https://doi.org/10.3390/s21072411>
- Korani, W., & Mouhoub, M. (2021). Review on nature-inspired algorithms. *Operations Research Forum*, 2, Article 36. <https://doi.org/10.1007/s43069-021-00068-x>
- Layek, K., Basak, B., Samanta, S., Maity, S. P., & Barui, A. (2021). Stiffness prediction on elastography images and neuro-fuzzy based segmentation for thyroid cancer detection. *Applied Optics*, 61(1), 49-59. <https://doi.org/10.1364/ao.445226>
- Li, B., Feng, C., Wu, H., Jia, S., & Dong, L. (2022). Photoacoustic heterodyne breath sensor for real-time measurement of human exhaled carbon monoxide. *Photoacoustics*, 27, Article 100388. <https://doi.org/10.1016/j.pacs.2022.100388>
- Ling, Y., Huang, T., Gao, E., Shan, Q., Hei, D., Zhang, X., Shi, C., & Jia, W. (2022). Improving the estimation accuracy of multi-nuclide source term estimation method for severe nuclear accidents using temporal convolutional network optimized by Bayesian optimization and hyperband. *Journal of Environmental Radioactivity*, 242, Article 106787. <https://doi.org/10.1016/j.jenvrad.2021.106787>
- Lyon, M., Fehlmann, C. A., Augsburger, M., Schaller, T., Zimmermann-Ivol, C., Celi, J., Gartner, B. A., Lorenzon, N., Sarasin, F., & Suppan, L. (2023). Evaluation of a portable blood gas analyzer for prehospital triage in carbon monoxide poisoning: Instrument validation study. *JMIR Formative Research*, 7, Article e48057. <https://doi.org/10.2196/48057>
- Nemmar, A., Al-Salam, S., Beegam, S., Zaaba, N. E., Elzaki, O., Yasin, J., & Ali, B. H. (2022). Waterpipe smoke-induced hypercoagulability and cardiac injury in mice: Influence of cessation of exposure. *Biomedicine & Pharmacotherapy*, 146, Article 112493. <https://doi.org/10.1016/j.biopha.2021.112493>
- Nitzan, M., Nitzan, I., & Arieli, Y. (2020). The various oximetric techniques used for the evaluation of blood oxygenation. *Sensors*, 20(17), Article 4844. <https://doi.org/10.3390/s20174844>
- Onodera, M., Fujino, Y., Kikuchi, S., Sato, M., Mori, K., Beppu, T., & Inoue, Y. (2016). Utility of the measurement of carboxyhemoglobin level at the site of acute carbon monoxide poisoning in rural areas. *Scientifica*, 2016, Article 6192369. <https://doi.org/10.1155/2016/6192369>
- Papin, M., Latour, C., Leclère, B., & Javaudin, F. (2023). Accuracy of pulse CO-oximetry to evaluate blood carboxyhemoglobin level: A systematic review and meta-analysis of diagnostic test accuracy studies. *European journal of emergency medicine: Official Journal of the European Society for Emergency Medicine*, 30(4), 233-243. <https://doi.org/10.1097/MEJ.0000000000001043>
- Raju, S., Siddharthan, T., & McCormack, M. C. (2020). Indoor air pollution and respiratory health. *Clinics in Chest Medicine*, 41(4), 825-843. <https://doi.org/10.1016/j.ccm.2020.08.014>

- Ramani, V. K., Mhaske, M., & Naik, R. (2023). Assessment of carbon monoxide in exhaled breath using the smokerlyzer handheld machine: A cross-sectional study. *Tobacco Use Insights*, *16*, 1-8. <https://doi.org/10.1177/1179173X231184129>
- Sharma, A., Kumar, R., & Varadwaj, P. (2023). Smelling the disease: Diagnostic potential of breath analysis. *Molecular Diagnosis & Therapy*, *27*, 321-347. <https://doi.org/10.1007/s40291-023-00640-7>
- Shi, D., Ye, Y., Gillwald, M., & Hecht, M. (2021). Designing a lightweight 1D convolutional neural network with Bayesian optimization for wheel flat detection using carbody accelerations. *International Journal of Rail Transportation*, *9*(4), 311-341. <https://doi.org/10.1080/23248378.2020.1795942>
- Shreya, S., Annamalai, M., Jirge, V. L., & Sethi, S. (2023). Utility of salivary biomarkers for diagnosis and monitoring the prognosis of nicotine addiction - A systematic review. *Journal of Oral Biology and Craniofacial Research*, *13*(6), 740-750. <https://doi.org/10.1016/j.jobcr.2023.10.003>
- Tan, X., Su, S., Zuo, Z., Guo, X., & Sun, X. (2019). Intrusion detection of UAVs based on the deep belief network optimized by PSO. *Sensors*, *19*(24), Article 5529. <https://doi.org/10.3390/s19245529>
- Thote, P. B., Daigavane, M. B., Daigavane, P., & Gawande, S. P. (2017). An intelligent hybrid approach Using KNN-GA to enhance the performance of digital protection transformer scheme. *Canadian Journal of Electrical and Computer Engineering*, *40*(3), 151-161. <https://doi.org/10.1109/CJECE.2016.2631474>
- Turino, G. M. (1981). Effect of carbon monoxide on the cardiorespiratory system: carbon monoxide toxicity, physiology, and biochemistry. *Circulation*, *63*(1), 253-259.
- Ullah, I., Hussain, M. M., Qazi, E., & Aboalsamh, H. (2018). An automated system for epilepsy detection using EEG brain signals based on deep learning approach. *Expert Systems With Applications*, *107*, 61-71. <https://doi.org/10.1016/j.eswa.2018.04.021>
- Usmani, Z. C., Craig, P., Shipton, D., & Tappin, D. (2008). Comparison of CO breath testing and women's self-reporting of smoking behaviour for identifying smoking during pregnancy. *Substance Abuse Treatment, Prevention, and Policy*, *3*, Article 4. <https://doi.org/10.1186/1747-597X-3-4>
- Vaghefi, E., Yang, S., Hill, S., Humphrey, G., Walker, N., & Squirrell, D. (2019). Detection of smoking status from retinal images: A convolutional neural network study. *Scientific Reports*, *9*, Article 7180. <https://doi.org/10.1038/s41598-019-43670-0>
- Yang, H., Zhang, Y., Yin, C., & Ding, W. (2021). Ultra-lightweight CNN design based on neural architecture search and knowledge distillation: A novel method to build the automatic recognition model of space target ISAR images. *Defence Technology*, *18*(6), 1073-1095. <https://doi.org/10.1016/j.dt.2021.04.014>
- Yi, M., Zhang, N., Liu, X., Liu, J., Zhang, X., Wei, Y., & Shangguan, D. (2023). A mitochondria-targeted fluorescent probe for imaging of endogenous carbon monoxide in living cells. *Spectrochimica Acta. Part A: Molecular and Biomolecular Spectroscopy*, *291*, Article 122377. <https://doi.org/10.1016/j.saa.2023.122377>
- Zhao, S., & Zhao, Z. (2021). A comparative study of landslide susceptibility mapping using SVM and PSO-SVM models based on Grid and Slope Units. *Mathematical Problems in Engineering*, *2021*, Article 8854606. <https://doi.org/10.1155/2021/8854606>



## Effects of Different Throttle Opening and Air Intake Lengths on the Volumetric Efficiency of SI Engine Using 1D Simulation Method

Mohamad Firzan Ahmad Harazi\*, Abdul Aziz Hairuddin, Azizan As'arry and Siti Ujila Masuri

*Department of Mechanical and Manufacturing Engineering, Faculty of Engineering, Universiti Putra Malaysia, 43400 UPM, Serdang, Selangor, Malaysia*

### ABSTRACT

Engine performance is influenced by volumetric efficiency, an engine's ability to put air into its cylinders. It is known for its intake length being tuned based on engine speed due to the air pressure wave behavior. However, the airflow into the intake system is controlled by the throttle opening, so there is a need to study the performance effect of intake length that is tuned based on it. Thus, this current study focuses on the impact of different throttle opening and intake lengths in relation to engine speed on the volumetric efficiency of the Proton CamPro 1.6L SI engine. The simulation runs on different ranges of engine speeds from 1000 rpm to 7000 rpm and different intake lengths with different throttle opening angles. The critical finding of this study revealed that tuning intake length based on throttle opening showed an improvement of 1.3% for volumetric efficiency at the low rpm range. It is by tuning the intake length to 400 mm at a throttle opening of 70° for 1000 rpm and 450 mm intake length with a throttle opening of 50° at 2000 rpm. However, it showed that 90° or wide-open throttle provides the best volumetric efficiency for mid and high-range rpm

for all intake lengths. The highest efficiency achieved is 101% at 4000 rpm with a 500 mm length intake and wide-open throttle. The findings from this study contribute to a good understanding of engine performance through intake length tuned based on throttle opening.

*Keywords:* Engine speed, spark ignition engine, throttle opening, variable intake length, volumetric efficiency

### ARTICLE INFO

#### *Article history:*

Received: 24 May 2023

Accepted: 18 December 2023

Published: 16 July 2024

DOI: <https://doi.org/10.47836/pjst.32.4.03>

#### *E-mail addresses:*

[firzanharazi@gmail.com](mailto:firzanharazi@gmail.com) (Mohamad Firzan Ahmad Harazi)

[ahziz@upm.edu.my](mailto:ahziz@upm.edu.my) (Abdul Aziz Hairuddin)

[zizan@upm.edu.my](mailto:zizan@upm.edu.my) (Azizan As'arry)

[ujila@upm.edu.my](mailto:ujila@upm.edu.my) (Siti Ujila Masuri)

\* Corresponding author

## INTRODUCTION

Two major types of internal combustion engines in the automotive industry include spark ignition (SI) engines and compression ignition (CI) engines. Both types of engines have been subject to study and advancement for their performance and emission improvement. These improvements include the advancements and tuning in injection systems (Channapattana et al., 2023), ignition timing control (Rimkus et al., 2022), intake system tuning (Shin et al., 2022), exhaust system tuning (Allawi et al., 2019) and nanoparticle's additive (Chatur et al., 2023).

One of the important parameters in assessing engine performance is volumetric efficiency (VE), which is used to measure the effectiveness of the engine induction process (Heywood, 2018). On average, SI engines have volumetric efficiency ranging from 80% to 100% across their engine speed range. Thus, various methods and tunings have been studied to maximize the engine's volumetric efficiency. Volumetric efficiency is important for improving engine power output, fuel efficiency, and reduction of emissions. Increasing the volumetric efficiency can lead to significant improvement in combustion efficiency. A study by Talati et al. (2022) showed that they improved volumetric efficiency by using variable intake length, which is tuned based on engine speed. The results showed that the VE could be improved by 6%, which also improves fuel consumption and thermal efficiency by 0.83% and 1.77%, respectively. According to Pahmi et al. (2019), implementing pressure waves during the intake valve opening process increased the volumetric efficiency. This improvement led to an enhanced brake mean effective pressure (BMEP) due to the higher amount of air in the cylinder, producing a greater pressure peak of the mean effective pressure inside the cylinder.

Another experiment was done by Sivashankar et al. (2018), in which they implemented Chrysler's ram theory and Helmholtz resonator theory to determine the optimum length for inertia air charging. The result showed an increase in volumetric efficiency by 6% and a decrease in brake-specific fuel consumption by 11% under full load conditions. Fuel economy and emission can also be improved by volumetric efficiency through downsizing of the engine because improved volumetric efficiency of a smaller engine can provide better or the same power output for the bigger engine but with less volumetric efficiency (Namar et al., 2021). Other than that, a study by Jemni et al. (2013) showed that different intake manifold designs significantly affected both engine performance and emission. It is supported by Raja and Selvam (2022), who researched maximizing the quantity of air in the cylinders by optimizing the intake manifold using CFD. From the result, they observed that flow harnessing in the intake could improve engine torque by 10%, along with an emission reduction.

Among the intake systems used to improve engine VE is variable intake manifold (VIM), which improves engine VE across different engine speeds (Ceviz, 2007). This

technology improves a car's torque and power at different engine speeds through volumetric efficiency (Jagadishsingh et al., 2016). According to Malkhede and Khalane (2015), a constant intake length only provides the best volumetric efficiency at the limited range of engine speed while having an adverse impact on another engine speed. Thus, VIM improves this limitation by having an additional intake length, which provides the best volumetric efficiency at the concerned engine speed. As its name implies, the variable intake manifold has two or more specific stages of intake configuration that vary based on engine speeds (Wan, 2011).

The configuration can be divided into plenum volume and runner intake length (Hartman, 2013). Based on Hosaka & Hamazaki (1991), Honda NSX has implemented a Variable Volume Induction System (VVIS) with a resonance chamber for its intake manifold to increase the torque for a medium speed range. This system has an additional second plenum and is separated from the primary manifold by six butterfly valves that open between 4600 and 4900 rpm by manifold vacuum. It is an example of a variable in the plenum's volume. Another study by Potul et al. (2014) reported that despite its improvement, the intake manifold with a two-stage system requires a very large space as there is a need to accommodate two intake runners for every cylinder. Alves et al. (2018) showed that the intake manifold can be divided into three stages. The first stage is the longer stage in which both valves are closed, forcing the air to travel for the longest way. The second stage is when the lower valve opens and forces the air flow through the intermediate path. The last stage is when the upper valve opens, causing the mixture to flow through the shortest length. However, Potul et al. (2014) argued that the problem with 3-stage VIM is that its entire length of runner is used only for a short range of rpm.

After years of variable intake manifold technology, the continuously variable intake manifold (CVIM) was introduced in 2002, as the BMW V8 became the first standard engine in the world equipped with this technology (Hirschfelder et al., 1990). According to Lenz (1990), it brings the advantage of ideal adaptation of the lengths of intake ports to the desired engine speed, especially at high speed. Through this, they achieved the goal of optimum resonance pipe supercharging across a wide range of engine speeds. Bari & Sawant (2019) found that continuously variable intake manifolds are able to boost volumetric efficiency by an average of 3.2% over the operating speeds of the engine, while a two-variable length intake manifold can boost an average of 1.4% over the operating range.

According to Sawant and Bari (2018), continuous intake tuning can boost the performance of an IC engine by over 4% improvement in volumetric efficiency. It occurs through induction pressure boost by tuning intake systems when the intake valve opens. However, it was found that minimum improvement of volumetric efficiency at high rpm such as 8500rpm. Malkhede and Khalane (2015) supported it, describing that engine with a wide speed range, an idle speed greater than 3000 rpm, and continuously variable intake

runner length can improve volumetric efficiency compared to fixed intake runner length. However, much study is required to improve continuously variable intake manifold because the improved volumetric efficiency is relatively small compared to turbochargers and superchargers. Furthermore, Potul et al. (2014) argued that CVIM has a problem: the entire length of its runners is used only for a short range of rpm. The length cannot continuously decrease as the rpm increases. Thus, the continuously variable intake manifold design should be studied further for improvement.

In driving a car, the main control for its speed is the throttle opening through the throttle pedal. The throttle opening controls the area, allowing air to enter the intake system and the engine cylinder. Although throttle opening is directly proportional to volumetric efficiency (VE) and engine performance, wide-open throttle (WOT) does not exactly cause maximum volumetric efficiency and performance. According to a study by Kardan et al. (2018), the best engine performance was at 75% of the throttle position because a higher load than 75% would result in the choke phenomena at the intake valve. It was found that the engine performance achieves maximum torque, power and thermal efficiency, values which were 4.16Nm, 0.87kW and 18%, respectively. It is supported by a study by Tavakoli et al. (2020), which revealed that the engine was efficiently regulated with the throttle during lower steady-state loads. However, the throttle could not recover the engine characteristics during lower load; thus, its application in the fast transient state is worthless.

A simulation study on the influence of the throttle opening angle on the intake system by Xu and Cho (2017) concludes that the 60° angle of the throttle body had better air velocity distribution and pressure distribution than that of the wide-open throttle and other lower opening angles. In the study, different throttle opening positions of 0°, 30°, 45°, 60° and 90° were compared to find the optimum throttle angle for complete burning and reducing exhaust emission. Complete burning in the engine allows the combustion chamber to be free from unburned fuel, which improves the volumetric efficiency as a larger amount of air-fuel mixture can be drawn into the chamber. It can result in improved overall engine performance. Besides, a real experiment study by Hamada et al. (2023) highlighted that running the SI engine at wide-open throttle conditions resulted in better efficiency, reduced waste heat and reduced environment compared to part throttle conditions. This study evaluated the engine's performance based on thermodynamic analyses performed at different engine speeds from 1500 rpm to 4000 rpm. The improvement in wide-open throttle conditions was due to improved heat quality with combustion and its reduced entropy generation compared to part throttle conditions.

Meanwhile, another study by Talati et al. (2022) showed that an intake manifold with different combinations of opened throttle bodies could further improve volumetric efficiency. From the study, the result indicates that there is an improvement in volumetric efficiency, brake torque, brake specific fuel consumption, brake thermal efficiency and heat

release rate of the engine compared to the stock intake manifold, which was 6.33%, 7.23%, 0.83%, 1.77% and 11.79%, respectively. There is also a study on the effect of unthrottled operation with early intake valve closure on engine performance. The results showed that the gross mechanical efficiency can be improved, but the gross indicated thermal efficiency decreases due to poor combustion. The poor combustion was due to weak turbulence and low gas temperature at the spark timing (Zhou et al., 2020). Another study investigates the differences between gasoline and natural gas for two throttle positions. The study found that gasoline has approximately equal brake power across 1000 to 6000 rpm for 50% throttle compared to 100%. However, brake mean effective pressure (BMEP) for gasoline was better at 50% throttle position compared to 100% throttle position (Aljamali et al., 2014).

The reason why throttle opening has various effects on volumetric efficiency is because intake components in between the throttle body and engine cylinder are also an influential factor. As an example, the intake manifold and intake valve also affect the volumetric efficiency of the engine because the improvement of volumetric efficiency by air intake length tuning is often based on the utilization of compression wave and suction wave effects (Jagadishsingh & Jadhav, 2016; Potul et al., 2014). Through these wave utilization, the volumetric efficiency can be improved by more than 100% (Bari & Sawant, 2019; Ghodke & Bari, 2018; Sawant & Bari, 2017). Therefore, the engine's torque and power can be increased and its curve can be broadened, too.

Based on Mauger (2004), in compression wave, the air flows through the intake manifold runner and past into the cylinder, then strikes the intake valve as it closes. Thus, a high-pressure wave is generated, and it travels back and forth along the closed intake runner length (McKee et al., 2006). When the intake valve opens, a negative pressure wave is produced due to the reduction in cylinder pressure. At the speed of sound, the pressure travels through the columns between the intake valve and the end of the runner. A pressure depression is created when a pressure wave pulse reaches the plenum chamber and decreases gas density at the runner entrance. Through this, the surrounding gas flows immediately into the depression. The incoming gas's inertia causes an effect with a reflected positive pressure wave (Heisler, 1995).

The suction wave is created when the intake valve opens, and the cylinder's vacuum is exposed to the intake manifold. This low-pressure wave travels upstream to airflow and gets reflected from the inlet boundary, which turns to high-pressure waves that travel downstream into the cylinder (Sawant & Bari, 2017). The tuning effect occurs when this wave properly arrives at a time; it increases the local density of intake flow, which helps increase the volumetric efficiency (Tabaczynski, 1982). This effect is termed natural supercharging or acoustic supercharging because if the arrival time is correct with the opening and closing of the intake valve, the region acts like a compressor on a turbocharger or supercharger, which rams air at a pressure above atmospheric (Hamilton et al., 2009).

It is supported by Wang et al. (2021), who studied the impacts of the continuous variable valve lift (CVVL) system and unthrottled load control on the performance of the spark ignition engine. The study found that the intake air mass flow at the intake ports became smoother, plus turbulence flow and its intensity were strengthened when using this method, which is beneficial to accelerating combustion rate and improving combustion efficiency. One of the reasons for the improvement was that the CVVL reduced the reversed mass flow rate by intake flow, which increased engine volumetric efficiency. Second, this unthrottled load control demonstrated the elimination of pressure waves during the intake stroke, increasing the volumetric efficiency. Another study by Bari and Sawant (2019) on the effect of intake runner length and valve timing showed that engine volumetric efficiency can be boosted to 7.78% when using both variations in runner length and valve timing. Meanwhile, the result also showed that the volumetric efficiency can be boosted only to 3.2% when using variations only in runner length. Besides that, a study by Jemni et al. (2021) proved that changing intake length continuously with the rpm can improve an average of 39.7% volumetric efficiency compared to the original engine configuration at 1000 rpm. The study found that using optimal intake length at 500 rpm increases the in-cylinder velocity by about 60%, 58% and 48%. According to these studies, both throttle and intake length showed a relation in pressure wave by intake flow, which affects the volumetric efficiency and engine performance.

Optimal intake runner length can be calculated using either Chrysler Ram theory or Helmholtz Resonator Theory, which was proved by an experimental study by Adithya et al. (2021). Improvement in volumetric efficiency would greatly influence other engine performance characteristics such as brake torque, brake specific fuel consumption (BSFC) and brake thermal efficiency (BTE). Thus, it effectively enhances the spark ignition engine performance under both part and full load conditions (Wasiu et al., 2021). According to these previous studies, both throttle and intake length showed a relation in pressure wave by intake flow, which affects the volumetric efficiency and engine performance.

Numerous engine performance studies have been conducted through experiments and simulations. Both methods have their advantages and disadvantages. As for simulation, the time and cost of developing an efficient engine can be significantly reduced by implementing 1D simulation. Diesel RK, AVL Boost, GT Power, and Lotus Engine Simulation (LES) are among the leading commercial engine simulation packages used in the automotive industry. Researchers used all these as they had the required functionality to predict engine behavior and performance.

Lotus Engine Simulation (LES), which was developed by Lotus Engineering, is also commonly used by researchers and recommended for engine performance improvement. Allawi et al. (2021), who used it for a variable valve timing simulation study, recommended using Lotus software by car manufacturers to improve the engine system performance. Their

study reveals that an overlap case of  $98^\circ$  demonstrates an improvement in brake-specific fuel consumption by 3% and a 6.2% volumetric efficiency. Another study by Magdas et al. (2020) demonstrated how the LES is capable of predicting the interior predestination engine's behavior. Using this software, they approached the 1D simulation possibilities on the variable valve timing system. One of the important results includes adjusting the variable valve opening height up to 15mm to allow an increase in torque by 3Nm and power by 4kW. Based on this, they concluded that simulation using LES provides useful results for further investigation on engine optimization. It is also supported by a study by Nouhov and Chen (2002) that models and simulates the valve timing effect on the 4-stroke spark-ignition engine. They reported that intake valve opening could reduce the backflow during the overlapping periods through the inlet charging effect.

Based on the preceding summarized literature, many studies have been done on the air intake system to improve the spark ignition (SI) engine performance. For simulation software, previous researchers commonly used LES to study the inlet charging effect or the wave pressure phenomenon effect on engine performance which is, closely related to throttle opening and intake runner length as part of the intake system. However, no literature has used LES software to investigate the effects of different throttle openings and air intake lengths on volumetric efficiency in SI engines. Hence, this research aims to investigate the effect of different throttle opening and air intake lengths on the volumetric efficiency of SI engines using the 1D simulation method. This study would help researchers improve the method of tuning both throttle opening and intake length based on engine speed, contributing to better volumetric efficiency and engine performance.

## MATERIALS AND METHODS

### Engine Specifications

This study was done by using Lotus Engine Simulation. The simulation setup for this study is based on the CamPro 1.6 engine from Malaysia automobile manufacturer Proton. Thus, the simulation's engine specification is based on this engine. The intake throttle, intake port, intake plenum, intake port, intake valve, engine cylinder, exhaust valve, and exhaust port are the constant specifications required to execute this simulation. The details of each specification used in the simulation are in Table 1.

Table 1  
*Specifications of the engine*

Components	Specification value
Intake throttle diameter	52 mm
Intake plenum volume	2.5 liters
Intake port throat diameter	28 mm
Intake valve opens	$12^\circ$
Intake valve close	$48^\circ$
Intake valve max lift	8.5 mm
Cylinder bore	76 mm
Cylinder stroke	88 mm
Cylinder con-rod length	180 mm
Cylinder compression ratio	10
Exhaust valve open	$45^\circ$
Exhaust valve close	$20^\circ$
Exhaust valve max lift	8 mm
Exhaust port throat diameter	25 mm

During the simulation, the engine runs through four-stroke cycles: intake, compression, power, and exhaust. There are seven different rpm simulated ranging from 1000 to 7000 rpm. The amount of air that fills the cylinder during each rpm cycle is determined via a fluid flow equation by the 1D simulation. Then, the volumetric efficiency can be determined. For this study, the simulation parameters in the Lotus Engine simulation are set up as shown in Table 2.

Table 2  
*Simulation parameters*

Parameter	Range
Engine speed (rpm)	1000 rpm to 7000 rpm
Intake manifold length (mm)	200 mm to 500 mm
Combustion strategies	Stoichiometric mixture ( $\lambda = 1$ )
52 mm diameter throttle angle (°)	10° to 90°
Spark timing	MBT spark timing

### Configuration of Simulation

The simulation's flow of operations begins with the crank angle in the engine cylinder rotating in the induction cycle, which sucks air from the inlet and moves it via the intake throttle, plenum, runner pipe, intake port, and intake valve before entering the engine cylinder. Next, the compression and power cycle take place based on the crank angle rotation position. The air was consequently forced out of the exhaust exit, followed by the plenum, exhaust port, and exhaust valve. During each rpm cycle, the efficiency of air sucked into the cylinder is calculated based on this process. The flow of operation can be referred to as Figure 1.

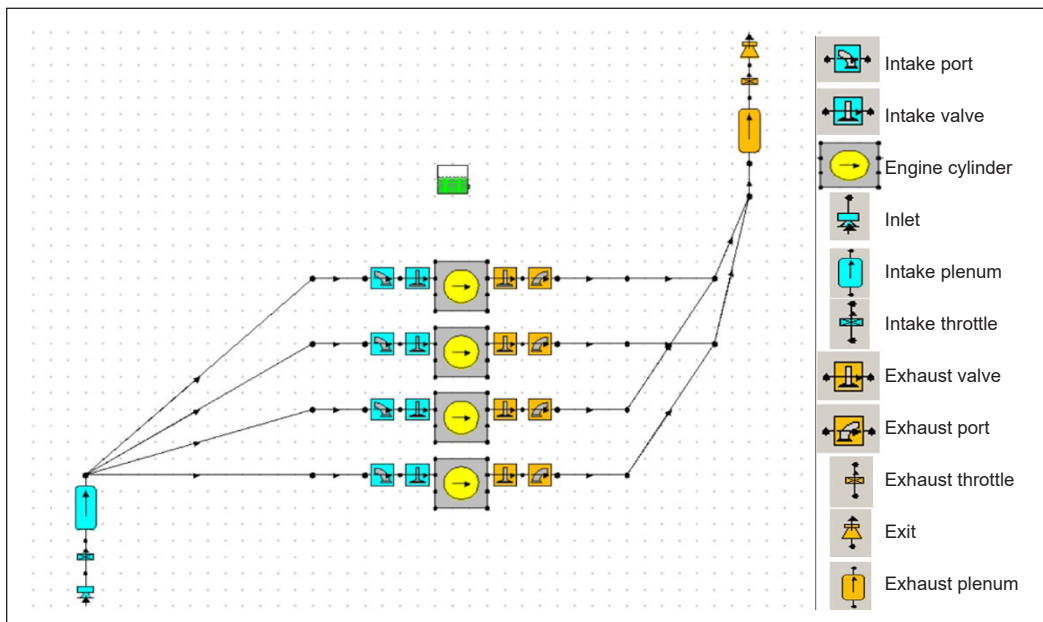


Figure 1. Configuration of simulation in Lotus Engine simulation

## Equations

The wave phenomena inside the engine manifold strongly affect the volumetric efficiency of the engine. This pressure wave traveling inside the runner and plenum of the manifold is calculated by solving conservation equations for mass, momentum, and energy at each time step. The Lotus Engine Simulation Program and study by Winterbone and Yoshitomi (1990) are used for the equation's references.

### *Volumetric Equation*

Based on the ratio of air trapped in a cylinder to the mass of air that might be trapped within the cylinder's swept volume, the 1D simulation solves volumetric efficiency, as shown in Equation 1. Meanwhile, the momentum, continuity and energy equation determine the mass flow rate trapped in the cylinder.

$$\eta = \frac{M_i}{\frac{N}{2} V_s \rho_i} \quad (1)$$

where  $\eta$  = volumetric efficiency;  $M_i$  = mass flow rate;  $\rho_i$  = inlet density;  $V_s$  = piston displacement;  $N$  = engine speed in rev/unit time

### *Momentum Equation*

The momentum equation is also a form of the conservation law, in which the sum of the pressure and shear forces acting on the control volume equals the sum of the momentum change rate in the control volume and the net momentum flux out of it, as in Equation 2.

$$-\frac{\partial(\rho F)}{\partial x} dx + \rho \frac{dF}{dx} dx - \frac{1}{2} \rho u^2 f \pi D dx = \frac{\partial(\rho u F dx)}{\partial t} + \frac{\partial(\rho F u^2)}{\partial x} dx \quad (2)$$

where  $F$  = cross-sectional area;  $\rho$  = density;  $p$  = momentum;  $u$  = initial velocity;  $f$  = friction coefficient;  $D$  = diameter of duct;  $t$  = time

### *Continuity Equation*

According to the continuity equation, the rate at which mass enters a system equals the rate at which mass leaves a system. The gradient of the mass flux, the length of the duct element,  $dx$ , and its cross-sectional area,  $F$ , can all be used to calculate the mass change rate within the control volume (Equation 3).

$$\frac{\partial(\rho F)}{\partial t} + \frac{\partial(\rho u F)}{\partial x} = 0 \quad (3)$$

where  $F$  = cross-sectional area;  $p$  = momentum;  $t$  = time;  $u$  = initial velocity;  $\partial x$  = length of element

### ***Energy Equation***

By applying the first law of thermodynamics to a controlled volume, the energy equation can be derived as Equation 4. The equation had  $e_0$  and  $h_0$  represent the fluid's internal energy and enthalpy of fluid, respectively. This equation can include the radial heat transfer from the gas to the wall or vice versa.

$$\frac{\partial(\rho e_0 F)}{\partial t} + \frac{\partial(\rho u h_0 F)}{\partial x} - q\rho F = 0 \quad (4)$$

where  $F$  = cross-sectional area;  $\rho$  = density;  $e_0$  = internal energy;  $h_0$  = enthalpy;  $t$  = time;  $u$  = initial velocity

## **RESULTS AND DISCUSSION**

This simulation was performed on a 4-cylinder engine with different throttle openings and intake runner lengths-the engine speeds used in the setup range from 1000 to 7000 rpm. The volumetric efficiency maps based on throttle opening and intake runner length are created from the simulation.

### **Validation of the Simulation**

The outcome of this simulation was validated with a study conducted by Mohiuddin and Rahman (2008) that included both experiment and simulation results to ensure the accuracy of this simulation model. Their experimental study was conducted on the same engine type, Proton Campro 1.6, used for this simulation study. The specifications of the engine can be referred to in Table 1. Both experimental results by Mohiuddin and Rahman (2008) and the current simulation result of VE% on the same engine can be compared in Figure 2. It demonstrated a small difference between these VE%, notably between 3000 and 4000 rpm. Overall, the results were close, with an average error of less than 3%. Thus, it can be concluded that the results in Figure 2 prove the validity of this study simulation configuration and the VE% results.

### **Effect of Throttle Angle Opening on Volumetric Efficiency Across a Range of rpm**

The Lotus Engine Simulation was run on a 4-cylinder engine at different intake manifold lengths and throttle angle opening. This setup was repeated at different engine speeds ranging from 1000 to 7000 rpm. The result of volumetric efficiency based on simulation is as in Figure 3. It shows that overall, as the engine rpm increases, the throttle opening angle needs to increase to maintain high volumetric efficiency. However, specifically at 10° to 30°, the volumetric efficiency decreases with the increase in rpm. The graph also showed that when the throttle opens at 40°, the volumetric efficiency increases with rpm

until it peaks at 4000 rpm and starts to fall in efficiency for much higher rpm. Meanwhile, for the range from 50° and above, the volumetric efficiency increases with rpm until it peaks at 5000 rpm and starts to fall in efficiency for much higher rpm. The 3D mapping of volumetric efficiency based on throttle angle and rpm is shown in Figure 3.

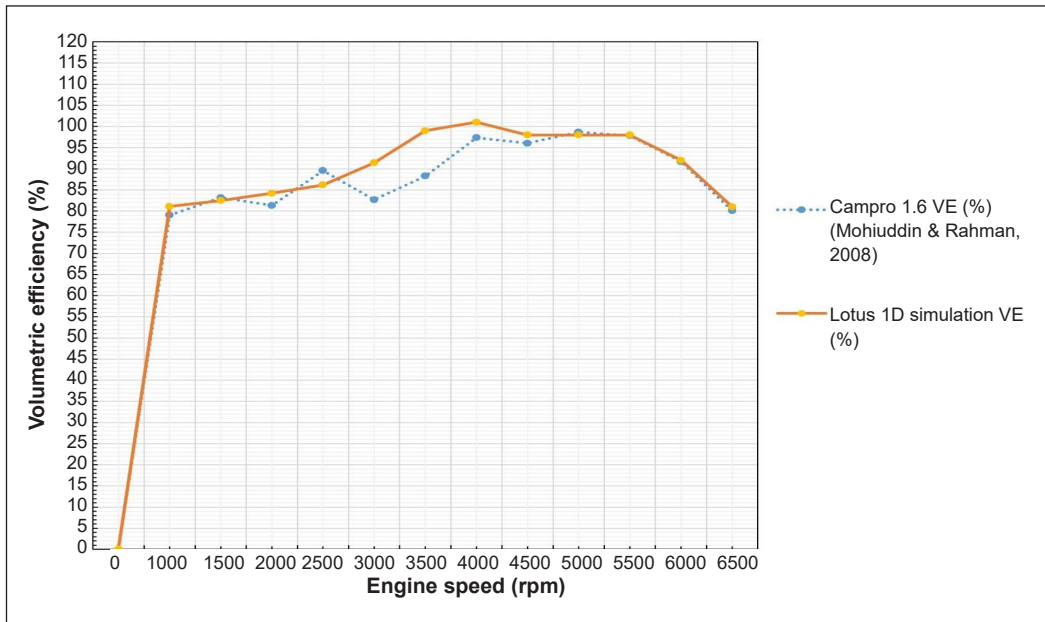


Figure 2. Volumetric efficiency comparison between experimental (Mohiuddin & Rahman, 2008) and Lotus 1D simulation across a range of rpm

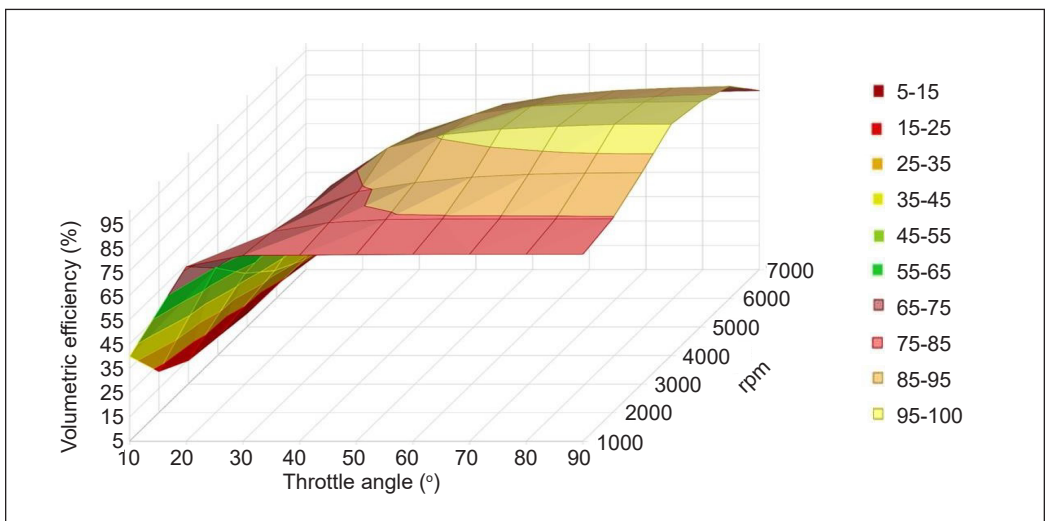


Figure 3. Volumetric efficiency mapping at different throttle angles across a range of rpm

### Effect of Throttle Angle Opening and Variable Intake Runner Length on Volumetric Efficiency Across a Range of rpm

Based on Figure 4, the bigger the throttle opening, the better the volumetric efficiency of the cylinder. A longer intake runner showed better volumetric efficiency, but the differences in each intake runner's length had no major impact on volumetric efficiency. Based on the throttle angle at 30°, the runner length was lower than 350 mm and showed a drop below 80.95% of volumetric efficiency. For runner lengths over 350 mm, the maximum volumetric efficiency achieved is 81.85% at 70° of throttle opening, and the minimum efficiency is 80.95%. It is due to volumetric efficiency in the cylinder being interrelated with the pressure wave. The inlet pressure value during the short period before the intake valve closes almost entirely determined the volumetric efficiency on that rpm (Ohata & Ishida, 1982). The pressure wave at 1000 rpm is not significantly higher than the tuning of runner length and is unable to augment the trapped air mass in the engine cylinder. Mohiuddin and Rahman (2008) agree that the amplitude of the pressure wave nearest to the maximum valve opening is the main concern when tuning the runner length to control arrival time. Overall, a long runner length above 350 mm can achieve high volumetric efficiency earlier than a short runner length below 350 mm.

The preceding fluctuation of the pressure wave can be referred to in Figure 5 for low rpm. The open exhaust valve (EVO) and the closed exhaust valve (EVC) are indicated by yellow lines on both the left and right sides, respectively. Meanwhile, a blue line on both the left and right sides indicates the intake valve opening (IVO), and the intake valve closing (IVC) is indicated by a blue line on both the left and right sides. The inlet pressure value right before the intake valve closes can be determined from the crossing line between the red and blue lines of IVO.

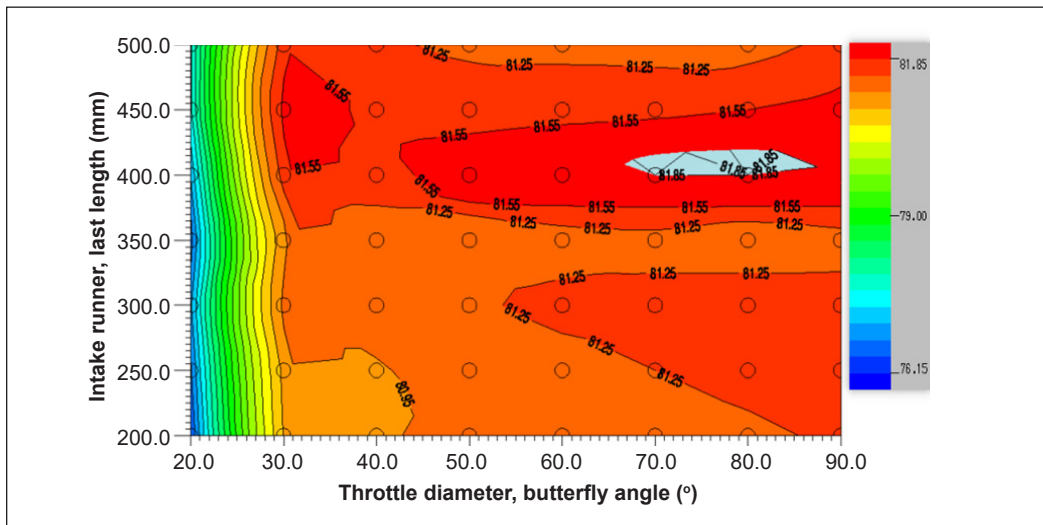


Figure 4. Volumetric efficiency at 1000 rpm

The difference in pressure amplitude for high rpm can be seen in Figure 6, which has 1.70 bar of pressure for maximum amplitude, while Figure 5 shows only 1.06 bar of pressure. The volumetric efficiency can be improved by tuning the runner length so the maximum pressure occurs right before the intake valve opening, as in Figure 6.

Therefore, referring to Figure 7, an intake length above 450 mm is the quickest in terms of achieving high volumetric efficiency of 84% at a 40° throttle opening, while an intake length shorter than 400 mm needs at least 60° of throttle opening to achieve the same volumetric efficiency. The maximum volumetric efficiency is 85.1% at 450 mm of runner length and 50° of throttle opening.

As in Figure 8, an intake length of 500 mm is the quickest in terms of achieving high volumetric efficiency of 91.7% at a 60° throttle opening, while an intake length below 450 mm can only achieve upto 89.4% volumetric efficiency at the same throttle opening. The highest volumetric efficiency is 94% when the intake length is 500 mm and the throttle opening is 90°. This result agreed with a study by Pahmi et al. (2022) that revealed volumetric efficiency was highest at 103% for long-length runners while showing a reduction for shorter-length runners at 2000 rpm and 3000 rpm enginespeeds. However, the study

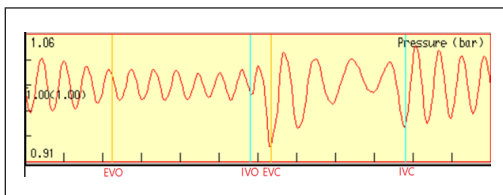


Figure 5. Pressure fluctuation at intake port for full engine cycle at 1000 rpm

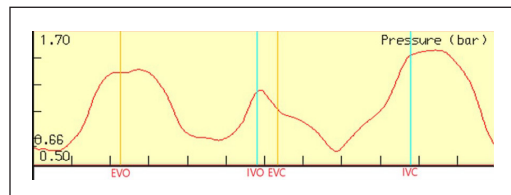


Figure 6. Pressure fluctuation at intake port for full engine cycle at 7000 rpm

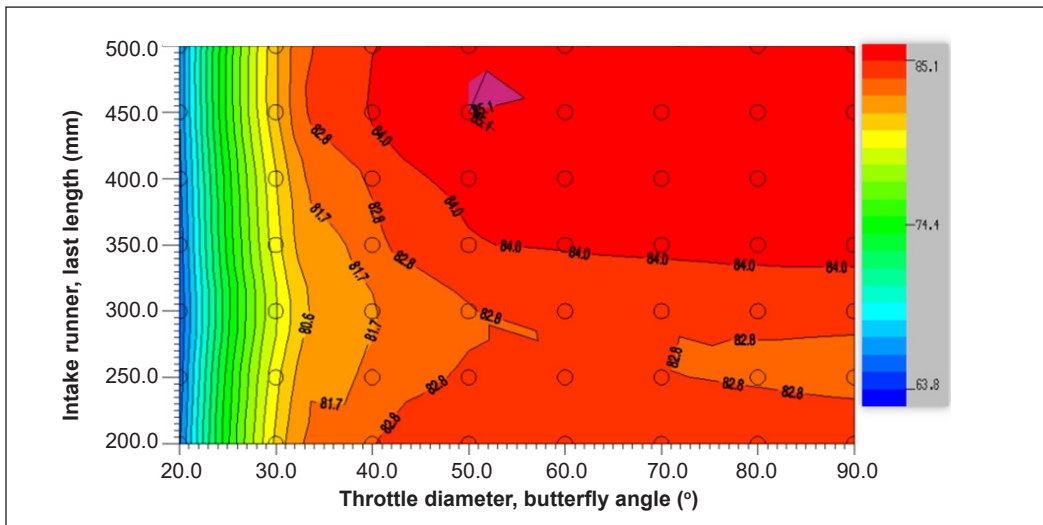


Figure 7. VE (%) of different intake runner lengths across a range of rpm

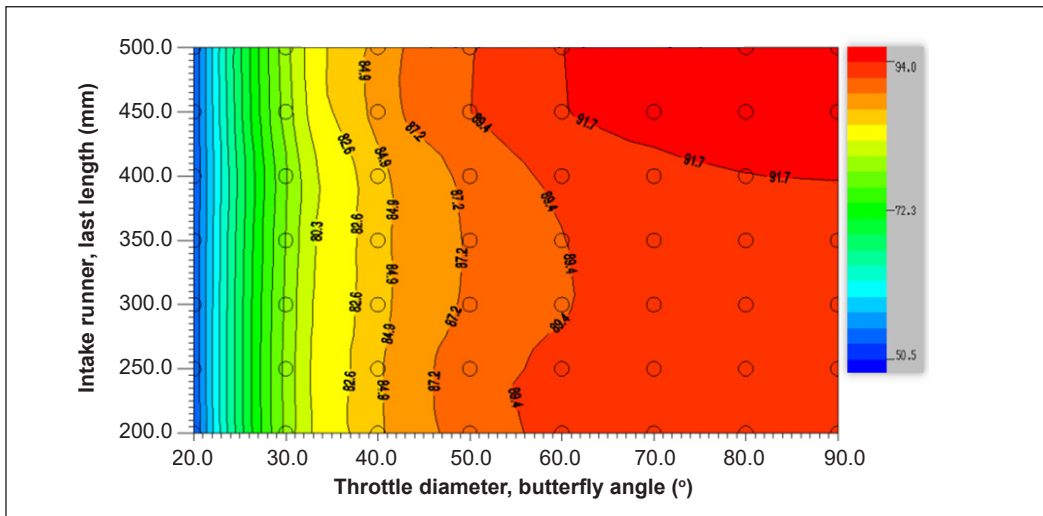


Figure 8. Volumetric efficiency at 3000 rpm

was done on a single-cylinder engine, so the longest length used was 229.7 mm, and the short length runner used was 153.2 mm. This difference in volumetric efficiency is due to the fact that a multiple-cylinder engine would have a reduced mass flow rate during intake stroke when a runner has air back flow that causes another runner to have reverse flow from the suction of the first runner in the same plenum (Ling & Tun, 2006).

As for the 4000 rpm graph in Figure 9, an intake length of 500 mm is the quickest in terms of achieving high volumetric efficiency of 97.8% at 60° throttle opening. In contrast, an intake length below 400 mm needs a bigger degree of throttle opening followed by a decreased intake length to achieve the same volumetric efficiency. The highest achieved volumetric efficiency is 101% at 500 mm of intake length and wide-open throttle.

As for the 5000 rpm graph in Figure 10, an intake length of 450 mm is the quickest in terms of achieving high volumetric efficiency of 94.7% at 60° throttle opening. In contrast, an intake length below 400 mm needs a bigger degree of throttle opening followed by a decrease in intake length to achieve the same high volumetric efficiency. The shortest runner length, 200 mm, needs at least 80° throttle opening to achieve the same volumetric efficiency. The highest volumetric efficiency can be achieved by 98.2% by tuning the intake length to 450 mm and the throttle opening at 90°.

As for the 6000 rpm graph in Figure 11, an intake length below 250 mm is the quickest in achieving a high volumetric efficiency of 90.8% at a 60° throttle opening. In contrast, an intake length above 250 mm needs a bigger degree of throttle opening followed by an increased intake length until 400 mm to achieve the same high volumetric efficiency. The maximum volumetric efficiency achieved for a runner length longer than 400 mm is 87.3%, while the highest volumetric efficiency achieved is 94.3%, and throttle opening is 90°.

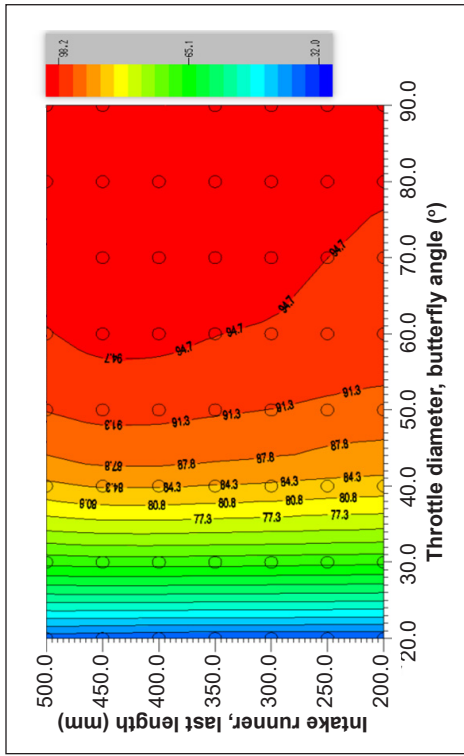


Figure 10. Volumetric efficiency at 5000 rpm

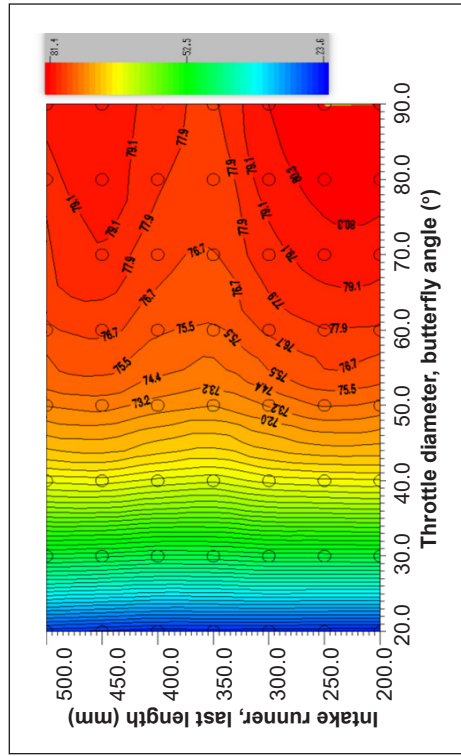


Figure 12. Volumetric efficiency at 7000 rpm

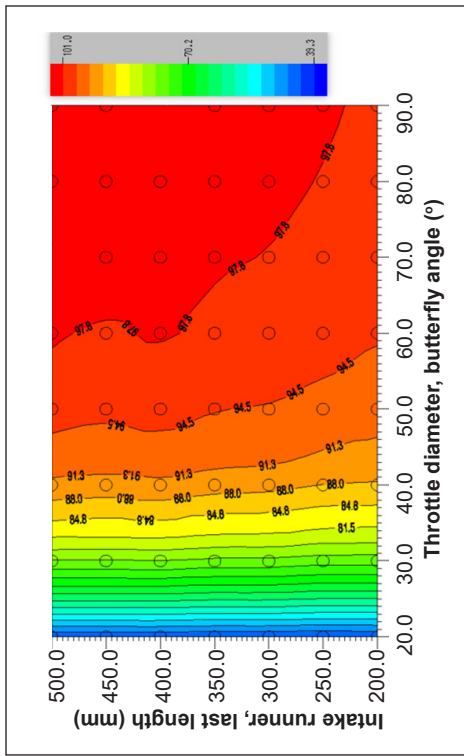


Figure 9. Volumetric efficiency at 4000 rpm

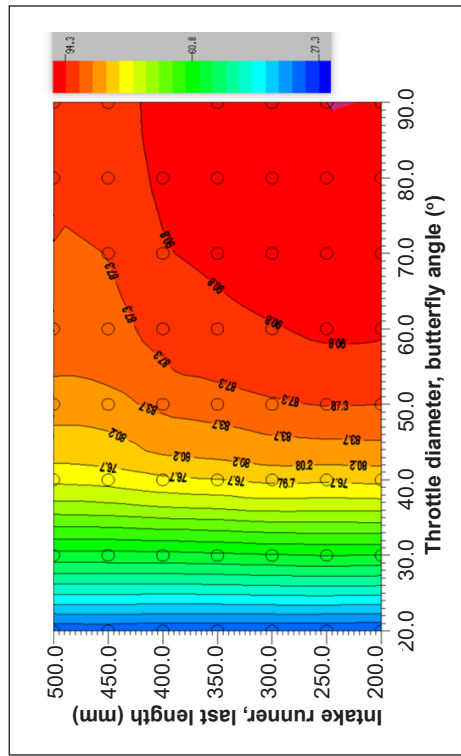


Figure 11. Volumetric efficiency at 6000 rpm

As for the 7000 rpm graph in Figure 12, an intake length of 200 mm is the quickest in achieving a high volumetric efficiency of 80.3% at 80° of throttle opening. A runner length over 300mm can only achieve volumetric efficiency of up to 79.1% compared to 80.3% for short runner length. The highest volumetric efficiency that can be achieved is 81.4% at 200 mm intake length and 90° of throttle opening.

## CONCLUSION

This study conducted a simulation investigation on the effect of different intake runner lengths with different throttle openings on the engine performance characteristics of a 4-cylinder engine. This study was conducted using 1D simulation in Lotus Engine Simulation software. The major findings are presented below:

1. For a lower range of throttle opening (10–30°), the volumetric efficiency decreases with increased rpm.
2. At a 40° throttle opening, the volumetric efficiency increases with the increase of rpm up to 4000 rpm and then drops as rpm goes higher.
3. For a high range of throttle openings (50–90°), the volumetric efficiency increases with the increase of rpm up to 5000 rpm and then drops as rpm goes higher.
4. At 1000 rpm and 2000 rpm, the length of the intake runner does not have any major impact on volumetric efficiency performance, with an improvement of only around 1% due to low-pressure wave amplitude in low rpm engine speed. It was revealed that maximum VE% happens at 70° throttle opening with 400mm intake length and 50° throttle opening with 450mm intake length for these low rpm ranges.
5. At 3000 rpm, an intake length longer than 400mm does have a better effect on volumetric efficiency, around 4%, compared to an intake length shorter than 400mm. Overall, long-length runners need smaller throttle openings to achieve high volumetric efficiency compared to short-length runners.
6. From 4000 rpm until 5000 rpm, the longer length of the intake runner showed major improvement in volumetric efficiency compared to the short length. The highest volumetric efficiency achieved is 101% when the runner length is 500mm at WOT. A long intake length of 400mm and above helps the engine achieve volumetric efficiency of up to 97.8% with a smaller throttle opening of 60°.
7. From 6000 rpm to 7000 rpm, shorter length of intake runner showed major improvement in volumetric efficiency compared to long length runner. The highest volumetric efficiency achieved is 94.3% when runner length is 250mm at WOT. A short intake length of 300mm and below helps the engine achieve volumetric efficiency of up to 90.8% with a smaller throttle opening of 60°.
8. Overall, intake length tuning shows a significant improvement in volumetric efficiency at 60° of throttle opening. Long runner length is best for volumetric

efficiency at low and mid-range rpm (1000–5000 rpm), while short runner length is best for volumetric efficiency at high range rpm (6000–7000 rpm). The WOT of the throttle opening is the best for volumetric efficiency in all rpm ranges of engine speed except at 1000 and 2000 rpm. Both rpm results revealed minor improvement in volumetric efficiency at a low rpm range due to a low inlet pressure wave. Thus, further study is required to determine a possible method for improving the inlet pressure wave.

## ACKNOWLEDGEMENTS

The authors thank Universiti Putra Malaysia for providing research facilities and grant. The study is supported by the GP-IPS research grant from UPM with project code GP-IPS/2021/9706000.

## REFERENCES

- Adithya, K., Ahmed, F., Padmanathan, P., Mohan, C. G., & Prakash, R. (2021). Design optimization of intake manifold of dual fuel engine. *Materials Today: Proceedings*, *45*, 646-651. <https://doi.org/10.1016/j.matpr.2020.02.726>
- Aljamali, S., Mahmood, W., Abdullah, S., & Yusoff, A. (2014). Comparison of performance and emission of a gasoline engine fuelled by gasoline and CNG under various throttle positions. *Journal of Applied Sciences*, *14*(4), 386-390. <https://doi.org/10.3923/jas.2014.386.390>
- Allawi, M. K., Oudah, M. H., & Mejbel, M. K. (2019). Analysis of exhaust manifold of spark-ignition engine by using computational fluid dynamics (CFD). *Journal of Mechanical Engineering Research and Developments*, *42*(5), 211-215.
- Allawi, M., Mejbel, M., & Oudah, M. (2021). Variable Valve Timing (VVT) modelling by Lotus engine simulation software. *International Journal of Automotive and Mechanical Engineering*, *17*, 8397-8410.
- Alves, L. O. F. T., dos Santos, M. G. D., Urquiza, A. B., Guerrero, J. H., de Lira, J. C., & Abramchuk, V. (2018). *Design of a new intake manifold of a single cylinder engine with three stages* [Technical Paper]. SAE International. <https://doi.org/10.4271/2017-36-0172>
- Bari, S., & Sawant, P. (2019). Improvement of performance by 2-step variations of intake runner length and intake valve timing in the induction system of a SI engine. *Energy Procedia*, *160*, 108-115. <http://dx.doi.org/10.1016/j.egypro.2019.02.125>
- Ceviz, M. A. (2007). Intake plenum volume and its influence on the engine performance, cyclic variability and emissions. *Energy Conversion and Management*, *48*(3), 961-966. <https://doi.org/10.1016/j.enconman.2006.08.006>
- Channappattana, S. V., Campli, S., Madhusudhan, A., Notla, S., Arkerimath, R., & Tripathi, M. K. (2023). Energy analysis of DI-CI engine with nickel oxide nanoparticle added azadirachta indica biofuel at different static injection timing based on exergy. *Energy*, *267*, Article 126622. <https://doi.org/10.1016/j.energy.2023.126622>

- Chatur, M. G., Maheshwari, A., & Campli, S. (2023). Investigation of waste cooking oil–diesel blend with copper oxide additives as fuel for diesel engine under variations in compression ratio. *International Journal of Energy and Environmental Engineering*, 14, 791-802. <https://doi.org/10.1007/s40095-022-00549-7>
- Ghodke, S., & Bari, S. (2018). *Effect of integrating variable intake runner diameter and variable intake valve timing on an SI engine's performance*. Transportation Research Board. <https://doi.org/10.4271/2018-01-0380>
- Hamada, K. I., Ibrahim, T. K., Rahim, M. F., Rahman, M. M., & Bakar, R. A. (2023). Throttling effect on the availability and sustainability of a gasoline-fuelled spark ignited multi-cylinder engine. *Engineering Research Express*, 5, Article 045057. <https://doi.org/10.1088/2631-8695/ad0ad3>
- Hamilton, L. J., Cowart, J. S., & Rozich, J. J. (2009, April 20). *The effects of intake geometry on SI engine performance* [Technical Paper]. SAE International. <https://doi.org/10.4271/2009-01-0302>
- Hartman, J. (2013). *How to tune and modify automotive engine management systems* (2nd ed.). Motorbooks International.
- Heisler, H. (1995). *Advanced Engine Technology*. SAE Intl.
- Heywood, J. B. (2018). *Internal combustion engine fundamentals* (2nd ed.). McGraw-Hill Education.
- Hirschfelder, K., Völkl, W., Kühnel, H. U., Sinn, W., & Huck, A. (2002). The first continuously variable intake system in the new eight-cylinder engine from BMW. *MTZ Worldwide*, 63, 2-6. <https://doi.org/10.1007/BF03227525>
- Hosaka, T. & Hamazaki, M. (1991). *Development of the variable valve timing and lift (VTEC) engine for the Honda NSX* [Technical Paper]. SAE International. <https://doi.org/10.4271/910008>
- Jagadishsingh, B., Wankar, A., & Jadhav, N. P. (2016). A review paper on effect of intake manifold geometry on performance of IC engine. *International Journal of Advance Research and Innovative Ideas in Education*, 2(2), 102-106.
- Jagadishsingh, B., & Jadhav, N. (2016). Effect of variable length intake manifold on performance of IC engine. *International Journal of Current Engineering and Technology*, 5, 47-52. <https://doi.org/10.14741/Ijcet/22774106/spl.5.6.2016.9>
- Jemni, M. A., Driss, Z., Kantchev, G., & Abid, M. S. (2013). Intake manifold shape influence on the unsteady in-cylinder flow: Application on LPG bi-fuel engine. In M. Haddar, L. Romdhane, J. Louati & A. B. Amara (Eds.), *Design and Modeling of Mechanical Systems* (pp. 331-338). Springer. [https://doi.org/10.1007/978-3-642-37143-1\\_40](https://doi.org/10.1007/978-3-642-37143-1_40)
- Jemni, M. A., HadjKacem, S., Ammar, M., Saaidia, R., Brayek, M., & Abid, M. S. (2021). Variable intake manifold geometry influence on volumetric efficiency enhancement at gaseous engine starting speeds. *Proceedings of the Institution of Mechanical Engineers, Part E: Journal of Process Mechanical Engineering*, 235(2), 548-559. <https://doi.org/10.1177/0954408920973129>
- Kardan, R., Baharom, M. B., Mohammed, S. E., Aziz, A. R. A., Zainal, A. E. Z., & Firmansyah. (2018). The effect of engine throttle position on the performance characteristics of a crank-rocker engine fitted with a conventional cylinder head. In *6th International Conference on Production, Energy and Reliability 2018: World Engineering Science & Technology Congress (ESTCON)*, (Vol. 2035, No. 1). AIP Publishing. <https://doi.org/10.1063/1.5075549>

- Lenz, H. P. (1992). Basic principles of mixture formation. In *Mixture Formation in Spark-Ignition Engines* (pp. 38-111). Springer. [https://doi.org/10.1007/978-3-7091-6692-5\\_2](https://doi.org/10.1007/978-3-7091-6692-5_2)
- Ling, J. & Tun, L. T. Y. (2006). *CFD analysis of non-symmetrical intake manifold for formula SAE car* [Technical Paper]. SAE International. <https://doi.org/10.4271/2006-01-1976>
- Magdas, V. B., Mastan, D. C., & Burnete, N. (2020). Simulation possibilities of the internal combustion engine management elements using Lotus Engine Simulation software. *IOP Conference Series: Materials Science and Engineering*, 997(1), Article 012121. <https://doi.org/10.1088/1757-899X/997/1/012121>
- Malkhede, D. N., & Khalane, H. (2015). *Maximizing volumetric efficiency of IC engine through intake manifold tuning* [Technical Paper]. SAE International. <https://doi.org/10.4271/2015-01-1738>
- Mauger, T. W. (2004). *Selection of an engine and design of the fuelling system for a Formula SAE car*. [Degree dissertation]. University of Southern Queensland. <https://sear.unisq.edu.au/54/>
- McKee, R. H., McCullough, G., Cunningham, G., Taylor, J. O., McDowell, N., Taylor, J. T., & McCullough, R. (2006). *Experimental optimisation of manifold and camshaft geometries for a restricted 600cc four-cylinder four-stroke engine* [Technical Paper]. SAE International. <https://doi.org/10.4271/2006-32-0070>
- Mohiuddin, A., & Rahman, A. (2008). Investigation and probable solution of low end torque dip problem of Campro 1.6 L engine. *International Journal of Mechanical and Materials Engineering*, 3, 176-186.
- Namar, M. M., Jahanian, O., Shafaghat, R., & Nikzadfar, K. (2021). Engine downsizing; Global approach to reduce emissions: A world-wide review. *HighTech and Innovation Journal*, 2(4), 384-399. <https://doi.org/10.28991/HIJ-2021-02-04-010>
- Nouhov, D. F., & Chen, R. (2002). A simulation study on the effect of inlet valve opening on performance of high speed engines. In *Proceedings of the 17th Internal Combustion Engine Symposium* (pp. 149-152). Society of Automotive Engineers of Japan.
- Ohata, A. & Ishida, Y. (1982). Dynamic inlet pressure and volumetric efficiency of four cycle four cylinder engine [Technical Paper]. SAE International. <https://doi.org/10.4271/820407>
- Pahmi, A., Basri, M. H., Mustafa, M. E., Yaakob, Y., Sharudin, H., Ismail, N. I., & Talib, R. J. (2019). Intake pressure and brake mean effective pressure analysis on various intake manifold design. *Journal of Physics: Conference Series*, 1349(1), Article 012080. <https://doi.org/10.1088/1742-6596/1349/1/012080>
- Pahmi, A., Mustafa, M. E., Basri, M. H., Ismail, N. I., Azmi, H., Sharudin, H., Othman, R., & Mat, S. C. (2022). Effect of intake length on the engine performance of single cylinder engine. *Proceedings of Mechanical Engineering Research Day, 2022*, 129-130.
- Potul, S., Nachnolkar, R., & Bhave, S. (2014). Analysis of change in intake manifold length and development of variable intake system. *International Journal of Scientific & Technology Research*, 3(5), 223-228.
- Raja, K., & Selvam, A. J. (2022). Experimental investigation of four stroke single cylinder SI engine by modified intake manifold by using computational fluid dynamics. *International Journal of Ambient Energy*, 43(1), 229-236. <https://doi.org/10.1080/01430750.2019.1630310>
- Rimkus, A., Vipartas, T., Kriaučiūnas, D., Matijošius, J., & Ragauskas, T. (2022). The effect of intake valve timing on spark-ignition engine performances fueled by natural gas at low power. *Energies*, 15(2), Article 398. <https://doi.org/10.3390/EN15020398>

- Sawant, P., & Bari, S. (2017). Combined effects of variable intake manifold length, variable valve timing and duration on the performance of an internal combustion engine. In *ASME 2017 International Mechanical Engineering Congress and Exposition, Volume 6: Energy* (pp. 1-10). American Society of Mechanical Engineers. <https://doi.org/10.1115/IMECE2017-70470>
- Shin, J., Kim, D., Son, Y., & Park, S. (2022). Effect of intake manifold geometry on cylinder-to-cylinder variation and tumble enhancement in gasoline direct injection engine. *Scientific Reports, 12*, Article 19862. <https://doi.org/10.1038/s41598-022-24079-8>
- Sivashankar, M., Balaji, G., Barathraj, R. K., & Thanigaivelan, V. (2018). Phenomena of brake specific fuel consumption and volumetric efficiency in CI engine by modified intake runner length. *IOP Conference Series: Materials Science and Engineering, 402*, Article 012086. <https://doi.org/10.1088/1757-899X/402/1/012086>
- Tabaczynski, R. J. (1982). *Effects of inlet and exhaust system design on engine performance* [Technical Paper]. SAE International. <https://doi.org/10.4271/821577>
- Talati, H., Aliakbari, K., Ebrahimi-Moghadam, A., Farokhad, H. K., & Nasrabad, A. E. (2022). Optimal design and analysis of a novel variable-length intake manifold on a four-cylinder gasoline engine. *Applied Thermal Engineering, 200*, Article 117631. <https://doi.org/10.1016/j.applthermaleng.2021.117631>
- Tavakoli, S., Schramm, J., & Pedersen, E. (2020, October 14-16). *The effect of air throttle on combustion process and emission formation in marine lean-burn gas engines*. [Paper presentation]. Proceedings of the 5th World Congress on Momentum, Heat and Mass Transfer, Lisbon, Portugal. <https://doi.org/10.11159/CSP20.117>
- Wan, M. (2011). Intake and exhaust. *AutoZine*. [https://www.autozine.org/technical\\_school/engine/Intake\\_exhaust.html](https://www.autozine.org/technical_school/engine/Intake_exhaust.html)
- Wang, J., Duan, X., Wang, W., Guan, J., Li, Y., & Liu, J. (2021). Effects of the continuous variable valve lift system and Miller cycle strategy on the performance behavior of the lean-burn natural gas spark ignition engine. *Fuel, 297*, Article 120762. <https://doi.org/10.1016/j.fuel.2021.120762>
- Wasiu, S., Rosdee, A., Opatola, R. A., Al Haddabi, A., & Khan, A. S. A. (2021). Effects of variable length intake manifold on performance of gasoline engine using GT Power Software. *International Journal of Engineering Research & Technology, 9*(12), 673-678.
- Winterbone, D. E., & Yoshitomi, M. (1990). *The accuracy of calculating wave action in engine intake manifolds* [Technical Paper]. SAE International. <https://doi.org/10.4271/900677>
- Xu, C., & Cho, H. (2017). The analysis of influence of throttle body on engine intake system. *International Journal of Engineering and Technology, 9*(5), 3481-3486. <https://doi.org/10.21817/ijet/2017/v9i5/170905048>
- Zhou, X., Chen, Z., Zou, P., Liu, J., Duan, X., Qin, T., Zhang, S., & Shen, D. (2020). Combustion and energy balance analysis of an unthrottled gasoline engine equipped with innovative variable valvetrain. *Applied Energy, 268*, Article 115051. <https://doi.org/10.1016/j.apenergy.2020.115051>

## Experiment and Analysis of a Hybrid Composite Post-tension Plate Girder

Sahib Al Mustawfi, Nor Azizi Safiee\*, Nabilah Abu Bakar, Izian Abd Karim and Noor Azline Mohd Nasir

*Department of Civil Engineering, Faculty of Engineering, Universiti Putra Malaysia, 43400 UPM, Serdang, Selangor, Malaysia*

### ABSTRACT

Steel plate girders have been employed as structural bridge parts since the 19<sup>th</sup> century. They are typically made up of built-up sections in the shape of I-beams. Web and flange plates withstand shear force and bending moment, respectively. However, plate girders are vulnerable to shear buckling. Shear buckling resistance is increased by adding reinforced vertical stiffeners and, in some cases, longitudinal stiffeners. Nevertheless, these stiffeners are sometimes not enough to prevent extreme shear buckling and only delay the shear buckling of slender web panels. This study investigated a hybrid composite post-tension (HCPT) plate girder by experiment and finite element (FE) analysis. The structural performance of the HCPT plate girder was tested using three specimens: a double-web plate girder, an in-fill concrete double-web plate girder and an in-fill concrete double-web plate girder with prestress. Results showed that the steel web filled with concrete presented preferable strength and behaviour to the hollow steel web because of the concrete in-fill. It had high load capacity, strength and ductility. The concrete in-fill prevented the steel web plate from buckling, and beams generally failed in a ductile manner. Applying prestressing techniques reduced deflection under external loads, increased the load-carrying capacity and enhanced its flexural behaviour by 126% compared to the double web plate girder. The failure mode was changed from web shear

buckling in a double web girder to bending in a hybrid composite plate girder, with an improvement of web shear buckling by 88%. The FE analysis result showed excellent consistency with the experimental result.

### ARTICLE INFO

#### Article history:

Received: 29 May 2023

Accepted: 18 December 2023

Published: 16 July 2024

DOI: <https://doi.org/10.47836/pjst.32.4.04>

#### E-mail addresses:

sahibabah95@yahoo.com; sahibabah85@gmail.com (Sahib Al Mustawfi)

norazizi@upm.edu.my (Nor Azizi Safiee)

nabilah@upm.edu.my (Nabilah Abu Bakar)

nazline@upm.edu.my (Izian Abd Karim)

izian\_abd@upm.edu.my (Noor Azline Mohd Nasir)

\* Corresponding author

**Keywords:** Composite steel concrete prestress girder, finite element analysis, flexural strength, in-fill concrete, tendon, web distortion

## INTRODUCTION

Since the 19<sup>th</sup> century, steel plate girders have been used as structural bridges and large structures to meet the design requirements associated with heavy loads and long spans (Barker & Puckett, 2013; Ismail et al., 2023). The plate girders are typically built-up sections in the form of I-beams made of a combination of steel plates (Aghayere & Vigil, 2020). In addition, plate girders offer not only a larger span but also provide more load capacity. Given its efficient section rigidity, the I-shaped plate girder is commonly utilised as a flexural component (Sim, 2019). Plate girders are primarily designed with very deep and slender webs to minimise the required area for flanges and realise a high strength-to-weight ratio; the web panel resists a significant portion of the shear force in a plate girder, which results in slender web plates that are prone to shear buckling (Ali & Elgammal, 2023; Azmi et al., 2017; Chacón et al., 2011; Ghadami & Broujerdian, 2019; Sim, 2019). To remediate this problem, reinforced vertical and longitudinal stiffeners are added to raise the shear buckling strength and improve moment capacities (Luo et al., 2023). In some cases, stiffeners are not enough to resist high shear and only delay shear buckling of the slender web panels (Al-Azzawi et al., 2020; Azmi et al., 2017; Basher et al., 2011; Frankl, 2017; Yuan et al., 2019).

Incorporating composite-based systems into steel components has been practically idealised by including in-fill concrete. A number of previous researchers used in-fill concrete as an alternative way to improve the buckling issue in slender webs. Cho et al. (2018) investigated the flexural strength of a concrete-filled steel tube composite girder using a simple equation for negative and positive bending moments. The wide flange plates and a thin-walled corrugated steel web produce corrugated steel web girders (Ghanim et al., 2021). The shear buckling performance was investigated by Wang et al. (2018) by using a trapezoidal profile web girder through experimental work and finite element (FE) analysis. The results showed that no global member buckling occurred for flat plate and corrugated web, which was attributed to the flexural stiffness of concrete-filled tubular flanges. The concrete-filled steel tube was examined under shear buckling behaviour by nonlinear FE analysis (FEA). The shear buckling test result indicated enhanced shear buckling resistance compared to the traditional plate girder (Sim, 2019). A simply supported plate girder with a curved concrete-filled tubular flange was investigated analytically and experimentally; the results showed that the rising number of transverse stiffeners enhanced the load-carrying capacity and most minor lateral displacement (Gao et al., 2020).

The growing demand for strengthening bridges and steel structures is due to the increasing load demand during its service life (Kazem et al., 2018). Recent research has focused on prestressed composite girders, active techniques for achieving serviceability because they are efficient for deflection control, strength improvement, and the ability to span longer lengths (Lorenc & Kubica, 2006). External prestressing is frequently used

to strengthen new or present steel plate girder bridges because of its effectiveness and economic feasibility (Ahn et al., 2010). Prestressing techniques have been applied not only to reinforced concrete structures but also to steel plate girders. Amongst the applications in which prestressing techniques were used were in I-shaped cross-sectional steel beams, which were utilised as roof structural elements (Belletti & Gasperi, 2010). Moreover, a steel plate box girder was tested under flexural behaviour and finite element to verify the effectiveness of the prestressing technique; the result showed enhancement proportion by the improvement in the rate of the applied external load (Kambal & Jia, 2018). The request for horizontal members with long spans and floor height reduction has been raised in large-scale architectural buildings (Lee et al., 2015).

Therefore, several attempts have been made to build long-range steel–concrete composite members (Heo et al., 2007). Prestressed composite girders with corrugated webs were examined by experimental work, and the mechanics of horizontal shear transmission between steel girders and concrete were explored; the outcomes demonstrated excellent flexural performance in comparison with that of the non-prestressed specimen (Lee et al., 2015). In addition, prestressed concrete-filled steel tube truss girders were studied by both FEAs and experimental tests; the outcome showed increased flexural strength as the prestress level or shear-span-to-depth ratio rose (Huang et al., 2017). The mechanical properties of the composite box girder with corrugated steel web were analysed through two rounds of tensioning of internal prestressed tendons. An FE model was established based on experimental, theoretical, and numerical results. The findings indicated that the prestress of the concrete floor could be efficiently transferred to the concrete roof during tensioning, while the corrugated steel web mainly transferred the force of the section (Zhang et al., 2023).

This paper presents a study of the efficiency of a newly proposed hybrid composite post-tension (HCPT) plate girder, as shown in Figure 1, which comprises enhanced steel and concrete with prestressing. The arrangement of this plate girder is expected to produce a long span, thereby strengthening the web resistance against shear buckling, reducing the deflection and enhancing the flexural resistance. Combining steel and concrete with prestressing will improve the plate girder's performance. The performance of the HCPT plate girder was assessed using experimental and FEA approaches.

## **MATERIALS AND METHODS**

### **Description of the HCPT Plate Girder System**

The HCPT plate girder was designed based on BS 5950-1:2000 (BS5950, 2008) and BS 8110-1: 1997 (BS8110, 1997). The design was created so the HCPT would fail in the web shear buckling mode. Three specimens were developed to test the performance of the girder and portray the different effects of significant design parameters. The first specimen (FS1)

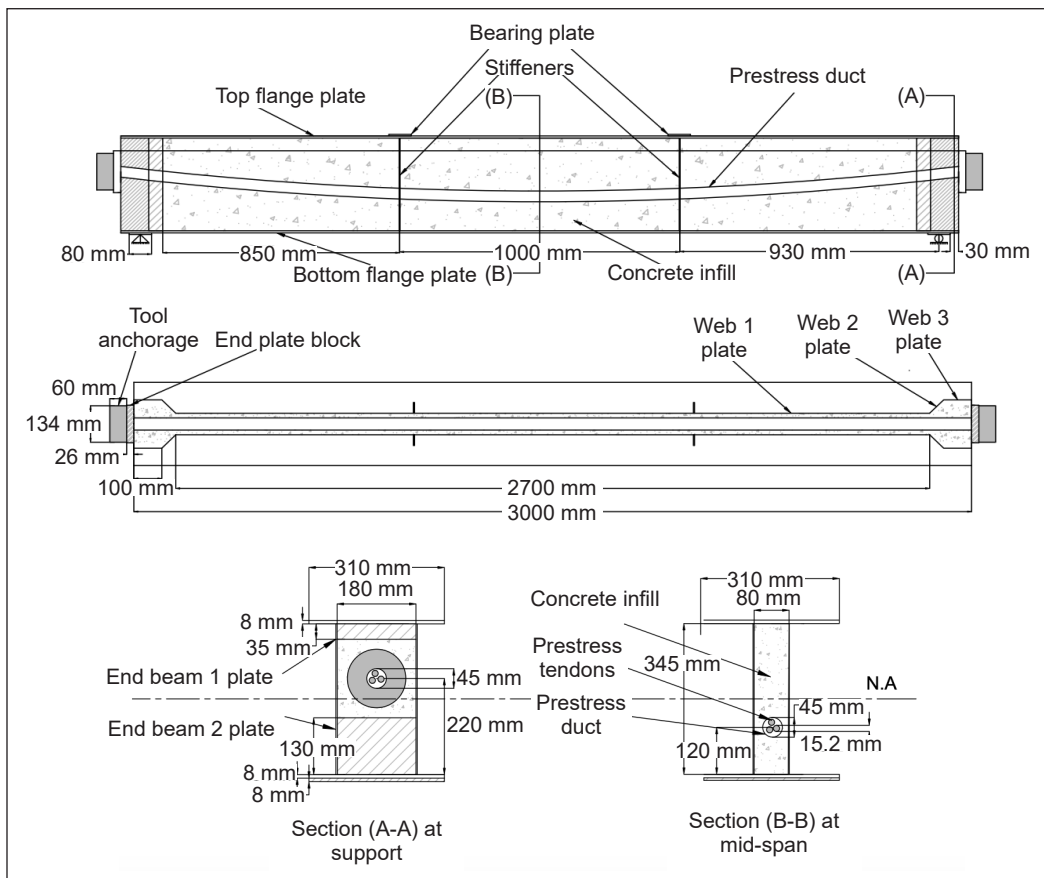


Figure 1. HCPT plate girder

was designed with double webs (the control), the second specimen (FSC2) had concrete in-fill between the double webs, and the third specimen (FSCP3) had concrete in-fill double webs with prestressing steel.

The HCPT plate girders were fabricated using mild steel plates of grade S275. Figure 1 shows the side view, top view and a related cross-section taken at support and mid-span. Flat steel plates with two different thicknesses (2.5 mm for web and stiffener; 8 mm for flange and bearing plate) were used with continuous fillet welds to connect them. The main dimensions remained fixed for all the specimens' girders: span length,  $L = 3000$  mm; web thickness,  $t_w = 2.5$  mm; web depth  $d = 345$  mm; flange width,  $b_f = 310$  mm; flange thickness,  $t_f = 8$  mm; stiffener thickness,  $t_s = 2.5$  mm; web slenderness ratio,  $d/t_w = 138$ ;  $L/d = 8.7$ . Two vertical stiffeners were placed at a point of load application, as illustrated in Figure 2. Grade 40 MPa was used for concrete in-fill. The steel strand comprised three tendons, each having seven wires of 15.24 mm with a 5 m length and a strength of  $f_{pk} = 1860$  MPa (low relaxation).

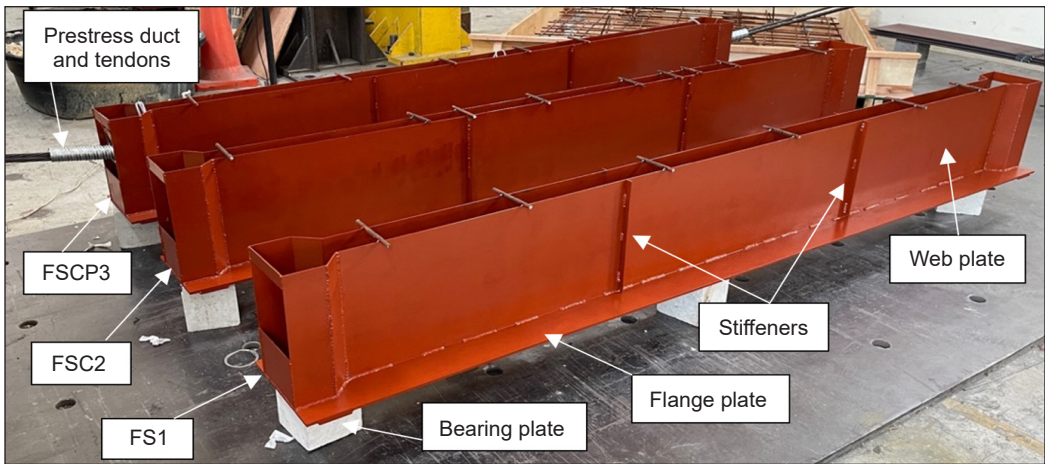


Figure 2. HCPT plate girder specimens before in-fill concrete casting and the top flange

**Experimental Investigation**

In this study, three plate girder specimens were prepared, named FS1, FSC2, and FSCP3. The description of each is presented in Table 1.

**Material Properties**

The characteristics of the main materials, steel and concrete, were evaluated by performing the appropriate test. Steel was tested via a tensile test, and concrete was tested for its mechanical properties.

**Steel Properties**

The basic stress–strain relationship of the steel plate of mild steel plates grade S275 was obtained by performing a tensile test on a coupon sample from the plate girder. A total of six coupons of two thicknesses (2.5 and 8 mm), as shown in Figure 3, were tested in tension. The tests were conducted

in accordance with the provisions of the Standard Test Methods for Tension Testing of Metallic Materials1 E8/E8M – 16a (ASTM, 2016). They were performed on a universal testing machine, INSTRON 3382, with 100 kN maximum capacity. The result of the

Table 1  
Specimen description

Specimen	Description	Cross section
FS1	Double-web plate girder (Control specimen)	
FSC2	In-fill concrete double-web plate girder	
FSCP3	In-fill concrete double-web plate girder with prestress	

stress–strain of the 8- and 2.5-mm plates is shown in Figure 4. Table 2 presents their yield strength, ultimate strength and Young’s modulus.

According to the tensile test results, the observed stresses at the yield point ( $f_y$ ) and ultimate point ( $f_u$ ) exceeded the nominal basic yield stresses ( $f_{yb}$ ) and basic ultimate stresses ( $f_{ub}$ ), which are equal to 275 MPa and 430 MPa, respectively. The nominal basic yield

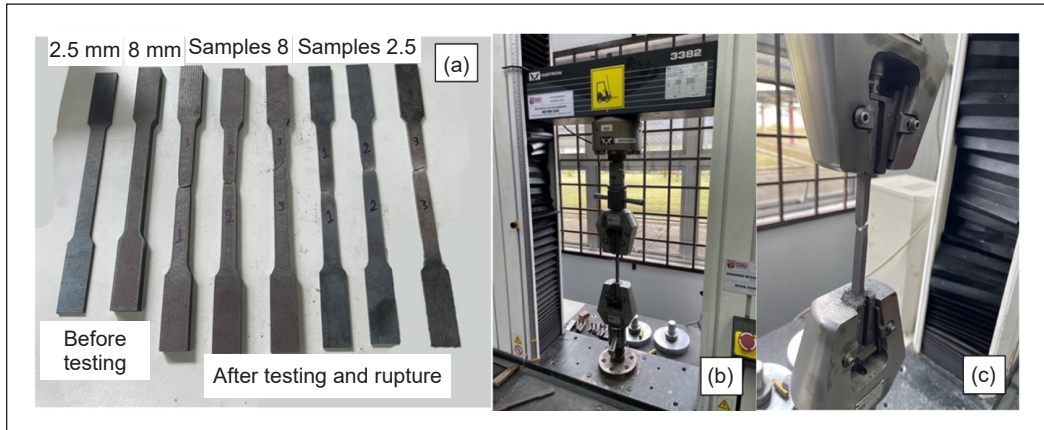


Figure 3. (a) Tension specimens before and after testing and rupture, (b) tensile testing machine and (c) sample after rupture

Table 2  
The tensile test result of the 8 and 2.5 mm-thick steel plates

Plate thickness (mm)	Young’s modulus (MPa)	$f_y$ (MPa)	$f_u$ (MPa)	Elongation (%)	Rupture strength (MPa)
8	205,000	312.3	481.48	33.2	383.7
2.5	210,000	320.6	455.14	28.12	382.2

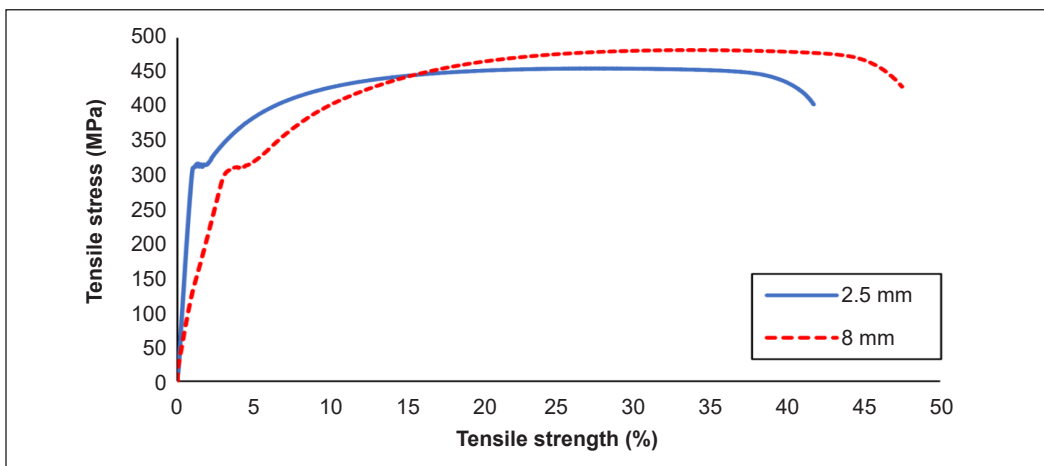


Figure 4. Stress–strain curve for the 8 and 2.5 mm-thick steel plates

and ultimate stresses are average values for relative comparison and reference, but actual material qualities could vary. Material quality, production techniques, and impurities can cause variability. Some samples frequently demonstrate higher strength qualities than the nominal values. The thickness of the specimen used in the tensile test influences the observed stresses; thinner specimens may exhibit higher stresses due to thickness effects. Metals often exhibit plasticity and strain hardening, meaning they can deform and maintain strength after the initial yield point. This behaviour can result in observed ultimate stresses greater than nominal ones. The coupon test samples were cut using a CNC laser, producing a very high amount of heat. This amount would change the steel's properties by tempering it. The 8 mm-thick steel had a lesser yield strength than the 2.5 mm-thick steel because the lower thickness of 2.5 mm steel gained heat faster than the thicker steel of 8 mm. It changed the properties of the 2.5 mm steel, which gained higher yield strength than the 8 mm steel.

The prestressed steel tendons consist of seven high-strength steel strands of  $f_{pk}=1860$  MPa low-relaxation steel with 15.24 mm diameter and 140 mm<sup>2</sup> cross-section. The Young's modulus was 195 GPa, and the tendon was steel grade 270. The nominal weight is 1100 kg/1000m, and the minimum elongation is 3.5 %. The specification details of the prestressing tendon were obtained from the manufacturer of a tendon ( Southern Steel Berhad, 2022), and it complies with the standard (ASTM A416/A416M-16a).

### Concrete Properties

Two different batches of concrete of grade 40 MPa were prepared for each plate girder. The compressive strength was investigated using six concrete cubic specimens with a size of 100 mm × 100 mm × 100 mm at 7 and 28 days, and the splitting tensile strength was examined using three concrete cylinder specimens with 200 mm height and 100 mm diameter at 28 days of curing. The test procedure was in accordance with BS EN 12390-3(2009) (BSI, 2009) for the compressive strength and BS EN 12390-6(2009) (BSI, 2009) for the splitting tensile strength. Table 3 demonstrates the concrete mechanical properties.

Table 3  
*Mechanical properties of concrete*

Mixes	Compressive strength (MPa)		Splitting tensile strength (MPa)
	7 days	28 days	28 days
M1	26.36	41.72	3.24
M2	27.63	38.51	2.56

The two mixes represented the properties of the concrete used as an in-fill to the hollow space between a pair of webs in a double web plate girder specimen. The result was based on two different batches, namely M1 and M2. The difference between these two batches was in the coarse aggregate source.

## Fabrication of Specimens

Each specimen comprised separate structural steel plates, which were welded together to form plate girder. The plate girder was fabricated by assembling the different flange, web and stiffener plates by welding with continuous fillet welds. When welding the thin web plate (2.5 mm), sufficient care was taken to reduce the distortion caused by welding by providing lateral supports at specific intervals to prevent significant initial imperfections of the web, as shown in Figure 5. All specimens were tested by a four-point bending test (i.e., two-point loading at one-third span with simply supported end conditions). A simply supported state was adopted, and the support was placed 30 mm inwards from the ends of the beams at each end, as illustrated in Figure 6.

FSCP3 had steel stirrups for the end block prestress. The steel stirrups with 10 mm diameter, 140 mm length and 50 mm space, as illustrated in Figure 7, are made of steel grade S420. A prestressing company performed the prestress work for the FSCP3 specimen. Three prestressed steel tendons were used, as shown in Figure 8, each consisting of seven high-strength steel strands arranged in a curved profile shape. The steel tendon is placed in



Figure 5. Steel plate assembly process



Figure 6. Support conditions for the HCPT plate girder

the doubled plate girder web duct before concrete casting. The prestress duct used was a 45 mm round duct. In the 78 days following the concrete casting, the tendons were prestressed by a total jacking force from all tendons of 336 kN, with the prestressing force level taken as 50% of the yield strength of the tendon. Two hand tool anchorages, one on each end, with a diameter of 134 mm and a length of 60 mm, were used. The jack was connected to a hydraulic jack, as shown in Figures 9 and 10.

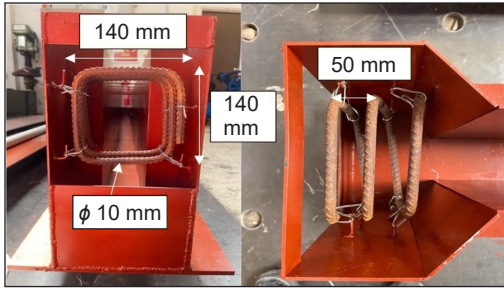


Figure 7. End block steel stirrups for the prestressed specimen (FSCP3)



Figure 8. Prestressed steel tendons are used

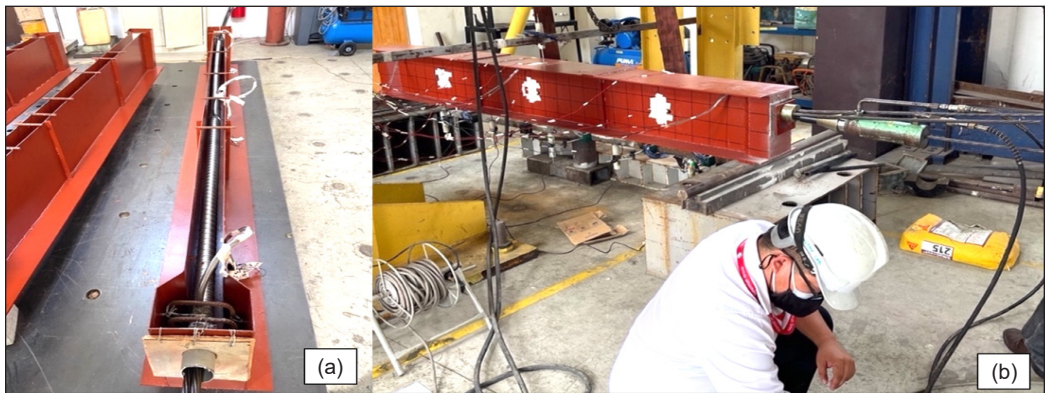


Figure 9. FSCP3 sample: (a) prestressing duct and tendons before concrete casting and (b) prestressing progress by using a prestress jack



Figure 10. (a) Prestress mono jack and (b) hydraulic jack

## Test Setup

Different gauges were used to record the strain, load, displacement and prestress jack force, such as strain gauge, load cell and LVDT, as illustrated in Figure 13. All the data were recorded on a computer using a data acquisition system. A strain gauge of size 5 mm length was used to measure strain in steel components, in plate girder and prestressing tendon, as shown in Figures 11(a) and 11(b). A strain gauge of 30 mm long was used for the concrete; two strain gauges were used for each sample situated on the top surface of the concrete at mid-span, as shown in Figure 11(c). The specimens' vertical deflections were measured using five LVDTs attached to the centre of the bottom flange, as demonstrated in Figure 12. One load cell with a maximum capacity of 1000 kN, located at mid-span, was used. The load was sourced from a hydraulic manual jack. All readings from the strain gauges, load cell and LVDT were recorded at 30 s with 10 kN load-interval increments until failure. For specimen FSCP3, the testing is divided into two steps: first, applying tension to tendons; second, starting the test directly to avoid any losses in prestress tendons.



Figure 11. Strain gauge attached to (a) steel plate girder, (b) prestress tendon and (c) concrete

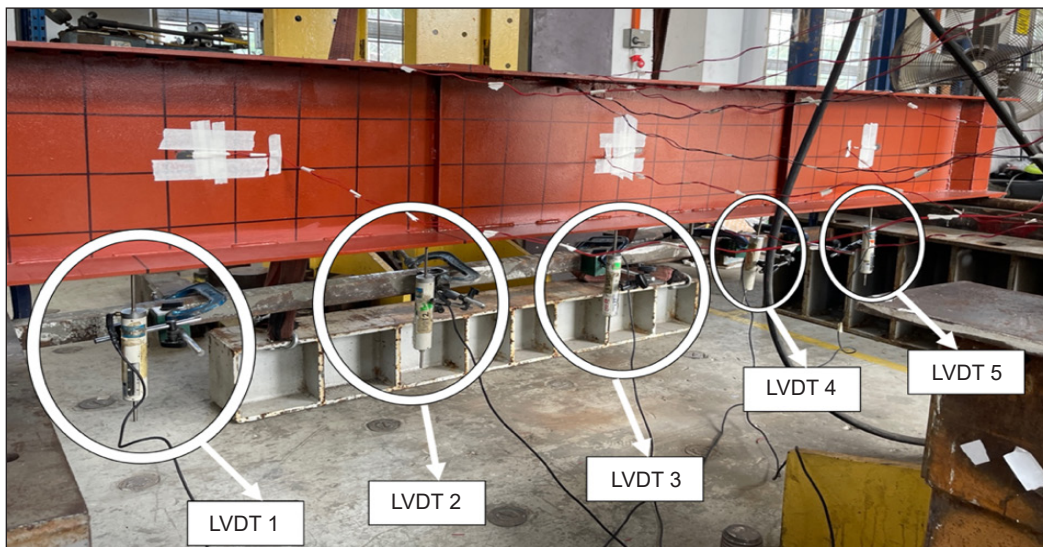


Figure 12. LVDTs affixed in the specimen

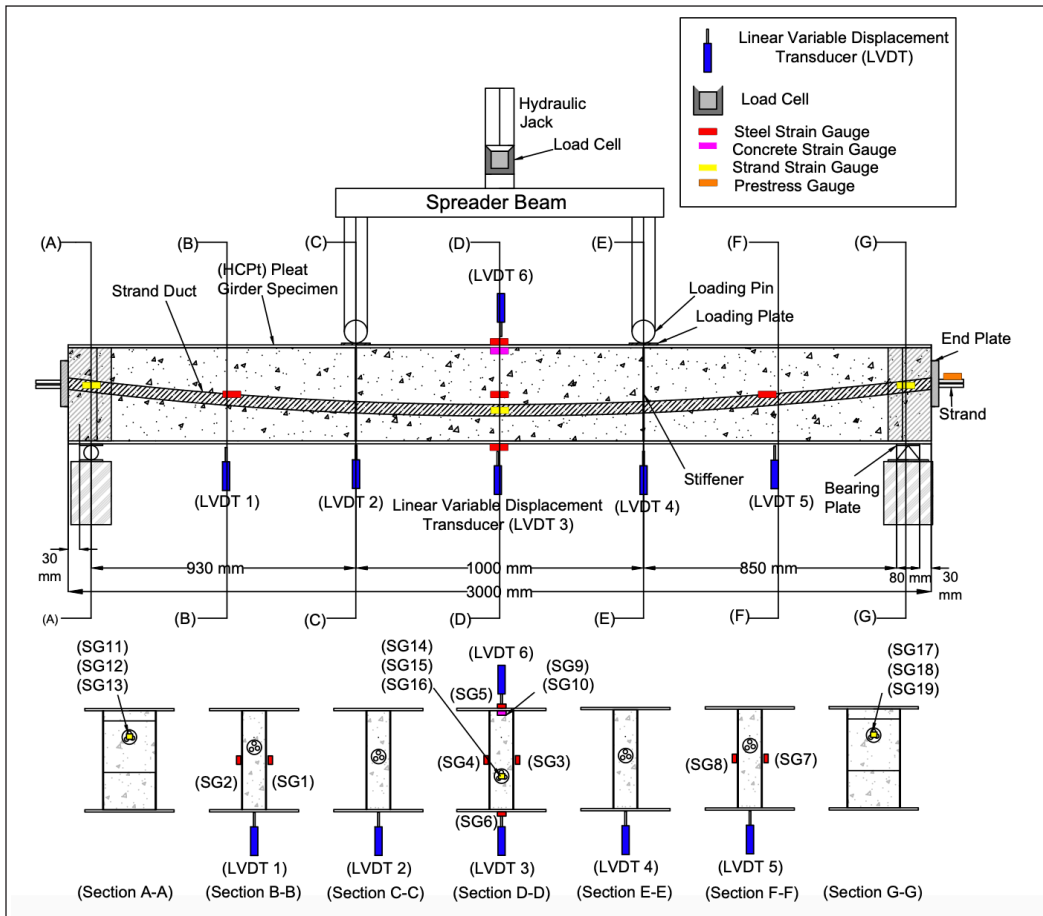


Figure 13. The placement of measurement gauge on plate girder specimen

### FE Modelling

The numerical study used the FE software Abaqus (Manual, A. U., 2020). The experimental results for FS1, FSC2 and FSCP3 were subsequently used to validate the FE models. The selection and type of element used in developing the geometrical model are shown in Table 4 and Figure 14. The overall element mesh size was 40 mm with an aspect ratio of mesh element = 1; the aspect ratio is the ratio between an element’s longest and shortest edge. The command merge in FE Abaqus was used to model the welding effect. The merge command in Abaqus is primarily used to merge nodes close to each other to eliminate redundancy in the model. The material properties of the steel plate of the flange, web, bearing plate, end plate, bar and stirrup are shown in Table 5. The properties of the steel tendon material for the elastic and plastic behaviours are provided in Table 6. For the concrete, with two different batches for the FSC2 model and the FSCP3 model, concrete damage plasticity was used to define the concrete properties. Abaqus’s concrete damage

plasticity model provided a general property for modelling concrete in structure solid type. According to Mander et al. (1988) and GabrielaSanMartín (2008), a concrete material can be characterised by compressive strength  $f_c$ ,  $\epsilon_c$  strain at  $f_c$  and  $\epsilon_u$  ultimate concrete strain capacity. Table 7 provides the details of the concrete properties. The constitutive relation for confined concrete using the concrete damage plasticity model assigned to the concrete material can simulate the confined effect by introducing the dilation angle. The concrete strength will increase when the pressure from the confined increases (Manual, A. S. U. S., 2012).

The FS1 model used a linear buckling step with imperfections to counter some imperfections caused by welding in the specimen. The FSC2 and FSCP3 models are analysed using dynamic and implicit types with a quasi-static application. The interaction between the concrete surface and steel surface and between the concrete surface and tendon surface was modelled using tangential and normal behaviour. A common assumption for

Table 4  
Details for all parts of the plate girder model

Part	Element shape	Element type
Flange, web, and stiffener plate	Shell	S4R
Bearing plate, concrete, end block plate, tendon	Solid	C3D8R
Bar and stirrups	Wire	T3D2

Table 5  
Material properties of the steel plates

Materials	Behaviour	Young's modulus (MPa)	Poisson's ratio	Mass density (tonne/mm)
Steel for bearing plate and end plate	Elastic	200,000	0.3	7.8 E-09
	Elastic	205,000 and 210,000	0.3	7.8 E-09
Steel-S275 for flange, web, and stiffener plates	Plastic	$f_y$ (MPa)		$f_u$ (MPa)
		2.5 mm      8 mm	2.5 mm	8 mm
Reinforcement bar and stirrups	Elastic	200,000	0.3	7.8 E-09
	Plastic	Yield stress		Plastic strain
		420		0

Table 6  
Material properties of the steel tendon

Materials	Behaviour	Young's modulus (MPa)	Poisson's ratio
Steel tendon	Elastic	195,000	0.3
	Plastic	Yield stress	Plastic strain
		1600	0
		1860	0.012

Table 7  
Material properties of the concrete

Materials	Behaviour	Young's modulus (MPa)	Poisson's ratio	Mass density (tonne/mm)
Concrete	Elastic	31521.77898	0.2	2.4 E-09
Batches	Compressive strength ( $f_c$ ) (MPa)	Strain $\epsilon_c$	Strain $\epsilon_u$	Tensile strength ( $f_t$ ) (MPa)
M1	41 MPa	0.0019	0.0055	3.23
M2	38.5 MPa	0.0019	0.0055	2.56
Concrete damage plasticity				
Dilation angle	Eccentricity	$F_{bo}/f_{c0}$	K	Viscosity parameter
42	0.1	1.16	0.667	0.0001

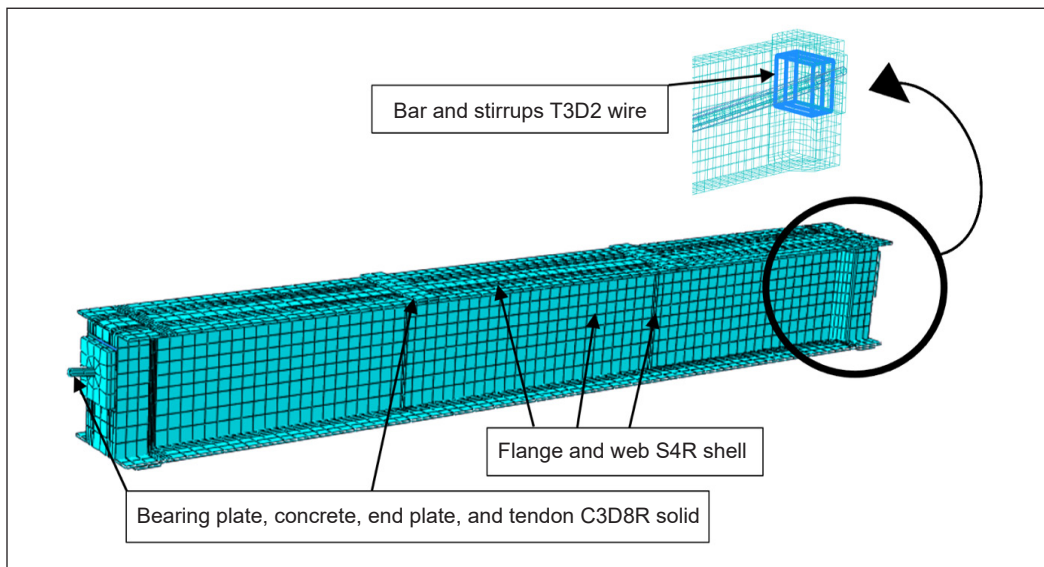


Figure 14. Typical FE mesh for the plate girder model

the coefficient of friction between concrete and steel is often 0.6 to 0.7. The tangential behaviour friction was characterised by a friction coefficient of 0.6, as recommended by Baltay and Gjelsvik (1990), Cho et al. (2018), and Rabbat and Russell (1985). The normal behaviour of pressure overclosure was hard contact, allowing separation. The boundary condition for all models was simply supported. The load for each model was demonstrated by displacement control. The prestress force is simulated by using prestress boundary conditions. The boundary conditions apply forces that simulate the effects of prestressing. The magnitude and direction of the prestress force are specified in terms of the type of applied force (stress) used in the selected region (tendon), and the stress value ( $\sigma_{33} = 800$  MPa) is predefined.

## RESULTS AND DISCUSSION

### Experimental Girder Result

This study tested three hybrid composite plate girder specimens (FS1, FSC2 and FSCP3) under flexural static load until failure. All specimens tested failed due to a combination of bending and shear buckling. The result of load and displacement was taken from the mid-span. The mid-span section was the most critical location in observing the girder behaviour. Figure 15 shows the load–displacement of all specimens. The loading was applied gradually in static by two-point loads. In the first stages of loading, all the girders exhibited positive bending, with only slight deflection seen at the mid-span.

From Figure 15, the first specimen FS1 demonstrated web shear buckling at a load of 288 kN. Moreover, right after that, at an identical magnitude of load, the failure of the specimen occurred. The maximum load corresponds to 5.4 mm displacement when the web buckling happens. At this stage, the FS1 specimen reached the ultimate state. Hence, the shear resistance loss in the web and plate girder collapsed. The second specimen was FSC2; the web shear buckling occurred at a load of 520 kN with 10.5 mm displacement; here, the specimen was able to resist the applied load after the web buckling occurred. Web buckling occurred in a later stage compared to specimen FS1 due to the presence of concrete within the web, which provides more resistance to lateral movement. The load then increased until reaching the maximum of 623.32 kN, corresponding to 18 mm displacement, and reduced afterwards. This phenomenon indicated that the plate girder reached the ultimate load and failed in bending. Compared with FS1, the improvement in maximum load was 116.43%, and the displacement increased by 12.6 mm.

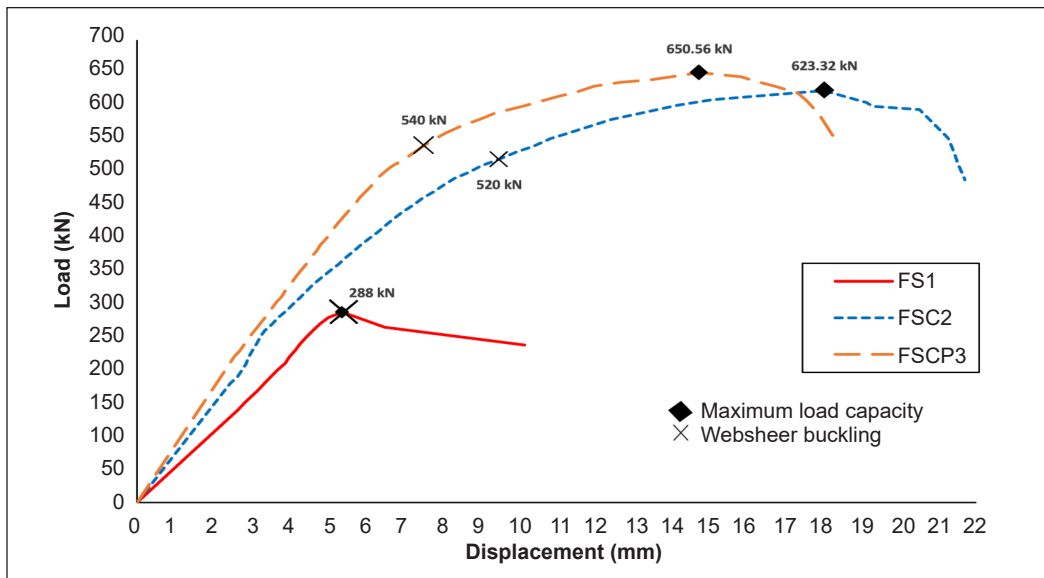


Figure 15. Experimental load–displacement curve for FS1, FSC2 and FSCP3 specimens at mid-span

This enhancement was contributed to by concrete in-fill that produced composite plate girder members that showed improved ductility. The concrete in-fill had a high flexural load capacity, good structural performance, high web buckling resistance strength, stiffness and energy dissipation ability. In this respect, the concrete in-fill was confined by the surrounded steel plate, resulting in a tri-axial state of compression that increased the strength and strain capacity of the concrete; beams generally fail in a very ductile way (Chen & Wang, 2009; Cho et al., 2018; Hu et al., 2003; Kim, 2005; Lu et al., 2009). The effect of the composite plate girder with concrete in-fill was evident at the delaying stage in comparison to FS1 when web shear buckling of the FSC2 specimen occurred at the load of 520 kN, corresponding to 9.5 mm displacement; FSC2 kept resisting until the ultimate load. This result indicated that the improvement in shear buckling resistance compared with FS1 was 80% by delaying the occurrence of web buckling. In particular, when subjected to flexural loading conditions, the crushed in-fill concrete remained confined within the steel, providing energy dissipation with delayed resistance degradation (Cho et al., 2018). Shao and Wang (2017) stated that concrete in-fill enhanced the global stability of the web's flexural strength and local shear buckling.

In the third specimen, FSCP3, the first displacement resulted from the mid-span at the prestress tensioning stage. When tension force was applied to tendons, the upward displacement was  $-0.1$  mm from the experimental work. Web shear buckling occurred at 540 kN with 7.5 mm displacement, and the applied load was sustained until reaching the maximum load of 650.56 kN, equivalent to 14.7 mm displacement before dropped, indicating that the plate girder attained its final state by demonstrated bending failure. In terms of maximum load, FSCP3 improved by 126% and 4.3% compared to FS1 and FSC2, respectively. FSCP3 had the highest stiffness compared with the two other specimens; however, it has less displacement than FSC2. This result was due to the presence of prestress concrete in-filled by producing a prestress composite plate girder. The enhancement of FSCP3 in shear buckling occurrences compared with FS1 was 88%. Unlike the non-prestressed specimen FSC2, the prestressed specimen FSCP3 significantly increased initial stiffness and ultimate strength.

Figure 16 shows the labelling of the plate girder web panel for the schematic referring in the discussion. The FS1 specimen failed by web shear buckling, and the FSC2 and FSCP3 specimens failed by bending. For the FS1 specimen, at loading 288 kN, a diagonal-shaped buckling in the thin web was visible in web plates starting in web panels numbers 3 and 6 at the upper corner of the roller support region, as shown in Figure 17 for the FS1 specimen. At this stage, the FS1 specimen reached the maximum web shear buckling resistance, and the plate girder failed in web shear buckling. A similar observation was obtained at loadings of 520 kN and 540 kN for FSC2 and FSCP3 specimens, respectively. A slight effect from web buckling was exhibited in web panels numbers 1, 3, 4, and 6, with

two parallel diagonal-shaped buckling lines spaced 20 cm apart, as shown in Figure 18. The load continued to increase after the web buckling occurred; the load increased until reaching the maximum load of 623.32 kN for the FSC2 specimen and 650.56 kN for the FSCP3 specimen, which indicated that the plate girder failed in bending.

The FSCP3 model fails at 650.56 kN, and the FSC2 model fails at 623.32 kN, which means an enhancement of 4.4% has been achieved; however, the displacement is decreased

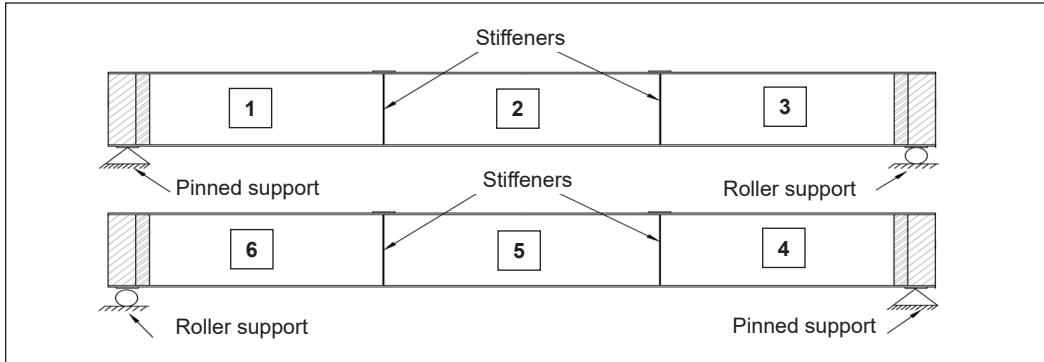


Figure 16. Web panel numbering for double web



Figure 17. Diagonal-shaped buckling at web plates near the roller support for the FS1 specimen

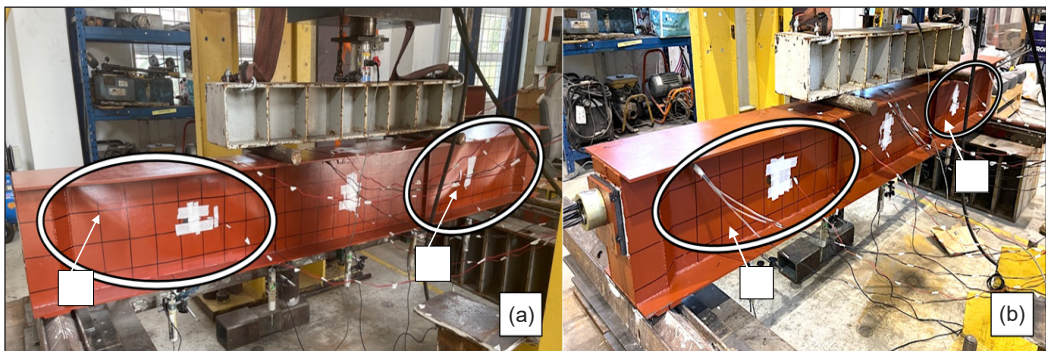


Figure 18. Diagonal-shaped buckling for (a) FSC2 and (b) FSCP3 specimens

by 18% due to the prestress improvement. Prestressing effects impact it; the high initial forces of composite prestressed plate girders incorporate prestressing tendons that introduce high initial compressive forces in the concrete. These forces affect the structural response and lead to a decrease in failure displacement. An investigation has been carried out for various HCPT plate girders FS1, FSC2 and FSCP3 to find out the effect of each part on the HCPT plate girder; the effect percentage had been reviewed for each part, whether it was effective or ineffective.

**Validation of FE Models via Experiment**

FE models were developed using the FEA Abaqus software. The models developed replicated the experimental specimens in terms of their geometric details. The outcomes obtained from the FEA were compared with the experimental results in Table 8 and Figure 19 to validate the accuracy and reliability of the developed FE model.

The FEA results for the FS1 model showed good agreement with similar pattern plotting to experimental results, indicating excellent accuracy. For the FSC2 model, both curves had a good agreement until up to 360 kN and more scatter at load between 360 kN and 603 kN before closely agreeing after load of 604 kN. FE model of FSC2 was stiffer compared to the experimental. The differences in the agreement could be due to the fact that the model consisted of steel and concrete, and concrete is a non-homogeneous material. The FSCP3 model curve was in good agreement with the experimental result. The failure mode for the

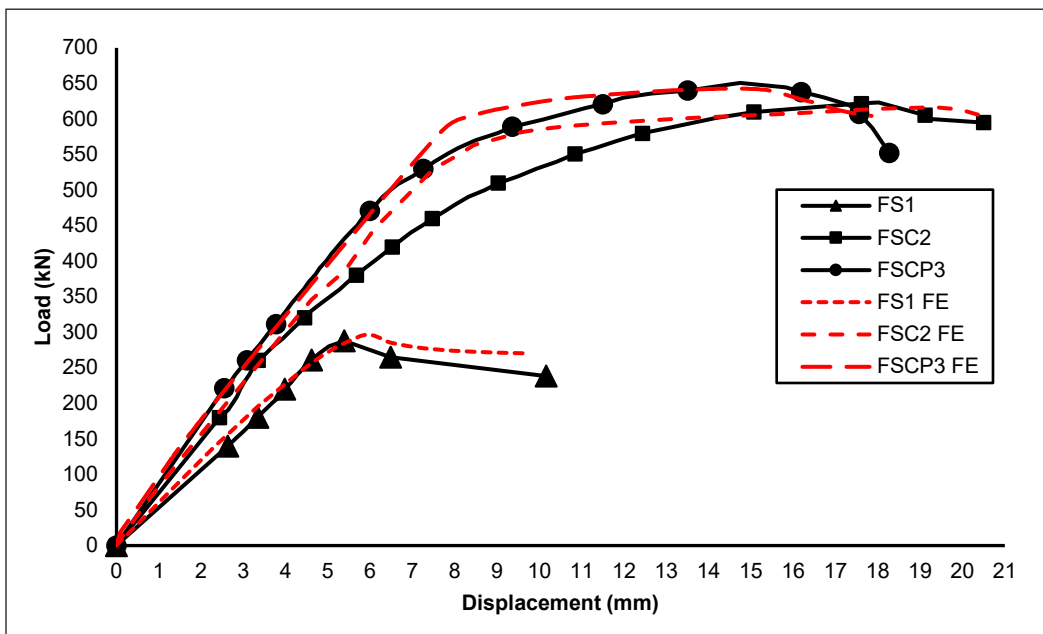


Figure 19. Load-Load-displacement curve for FS1, FSC2 and FSCP3 specimens at mid-span for both FEA and experiment

three FE models was the same as the experimental mode, which portrayed web buckling and bending failure modes. The FE models could predict the load-deflection response and strength of the hybrid composite plate girders with acceptable accuracy and failure mode.

Table 8  
Comparison results obtained by FEA and the experimental

Model	Maximum load capacity		%	Maximum displacement		%
	Experiment	FEA		Experiment	FEA	
FS1	288 kN	297 kN	3%	5.4 mm	5.98 mm	9%
FSC2	623.32 kN	616 kN	1.2%	18 mm	19.1 mm	6%
FSCP3	650.56 kN	642.7 kN	1.2%	14.7 mm	14.6 mm	0.6%

The general failure mode comparison between the FEA and experiment for the FS1 specimen is depicted in Figure 20. Figure 21 compares the FE and experimental failure modes for FS1, which show identical modes in web shear buckling in web panel number 3. The degradation sign shown by web shear buckling occurred at load 288 kN for the experiment. At load 297 kN for FEA, a degradation sign was demonstrated by the web shear buckling line in the diagonal direction observed in web 3 and web 6. The web steel plate panel number 3 did not reach yield in FEA; the strain was 0.0008, and the maximum strain measured by the nearby strain gauge in the experiment was 0.00058, which was less than the yield strain, indicating that the steel was not achieved the yield strain capacity of 0.0015 for S275 when the web buckling occurred. as shown in Figure 21(a), web shear buckling near the roller support. Another sign of degradation was observed in one of the

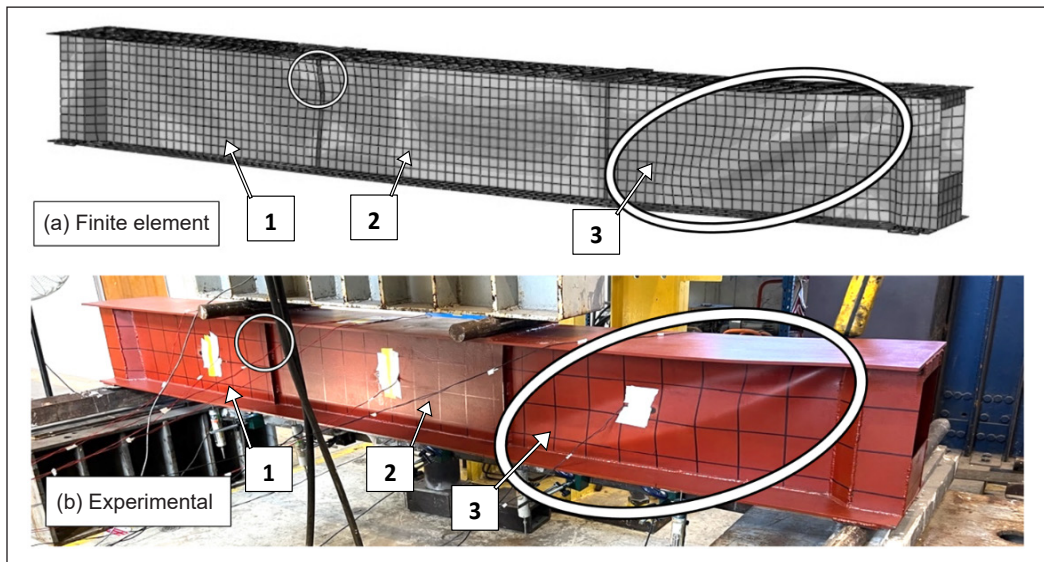


Figure 20. General failure mode for FS1 in Abaqus FE

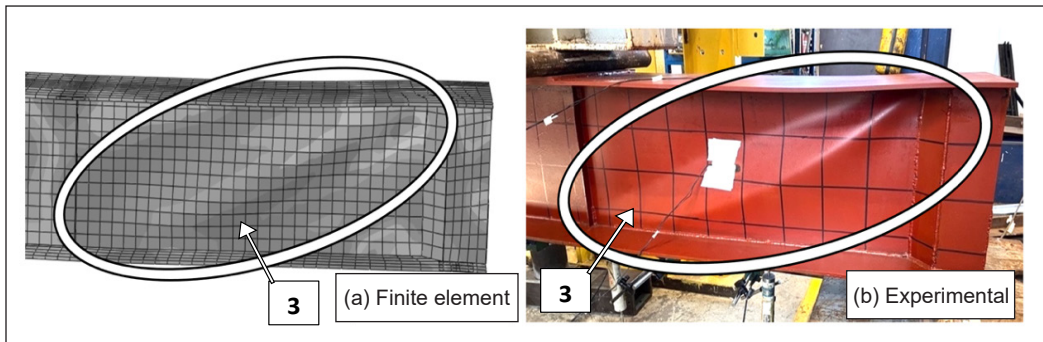


Figure 21. Identical failure mode exhibited in FS1 - web shear buckling near the roller support in both FEA and experimental

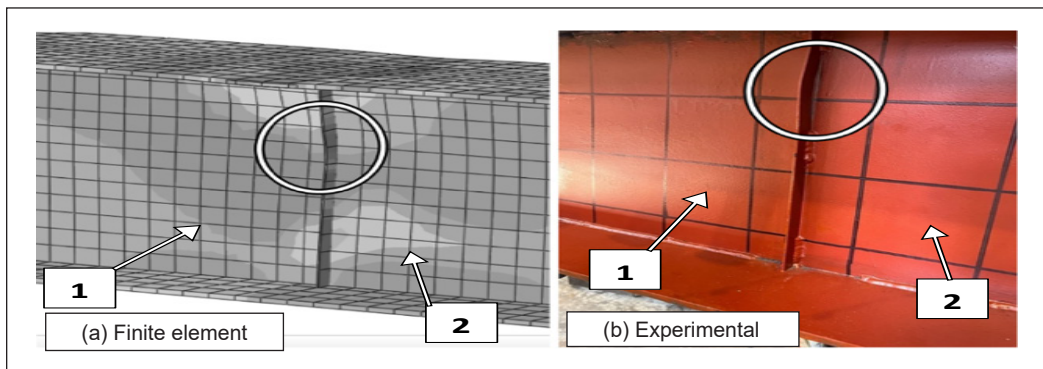


Figure 22. Degradation sign of web stiffeners in (a) FEA and (b) experiment

web stiffeners between panels 1 and 2 on one side only, as shown in Figure 22. The web stiffener buckling was observed to occur in an identical location for the FE and experimental for FS1, where it occurred at stiffeners between panels 1 and 2. The stiffener's failure was local due to the load applied at this point in the advanced stages of loading.

The failure sign in web buckling occurred in FSC2, demonstrated by both FEA and the experiment, as shown in Figure 23. Web shear buckling appeared at panels 1, 3, 4, and 6 of the girders in the experiment and FEA at 520 kN with 9.5 mm displacement and 533 kN with 7.4 mm displacement, respectively. In FEA, however, there are no signs of yielding for both the web and the flange. This discovery is consistent with the experimental results, which show no potential for yield occurring in the web, as seen by the maximum strain recorded at the web plate being 0.00105 for web panel number 3 and the maximum strain recorded at the bottom flange being 0.00105, less than the yield strain of steel, after reaching the ultimate load of 623.32 kN with 18 mm displacement for the experiment and 616 kN with 19.1 mm displacement for the FEA.

For experimental, there is no material yield observed as evidenced by the strain record for the web except the top flange and bottom flange, which reached yield with a recorded

maximum strain of 0.0017; however, in FEA, the web panels numbers 2 and 5 reached yield with a maximum strain of 0.0019, and the top and bottom flanges yielded with maximum strains of 0.0027 and 0.0054, respectively. It can be observed from Figure 19 that the stiffness for the FSC2 model in FEA is higher than the experimental result. It could be attributed to the fact that the material properties utilised in the FEA model are not an exact representation of the actual behaviour of the composite concrete plate girder. As a result, differences in stiffness may occur. Figures 24 and 25 show a close observation of web shear buckling in web panels 1 and 3 for FSC2 by experimental and FEA, which demonstrated the ability of the model to produce similar behaviour of girder as in the experiment.

For the FSCP3 model, in the transfer stage of tendon prestressing, the FE showed 0.14 mm upward deflection, as shown in Figure 26. Web shear buckling occurred in panels 1,

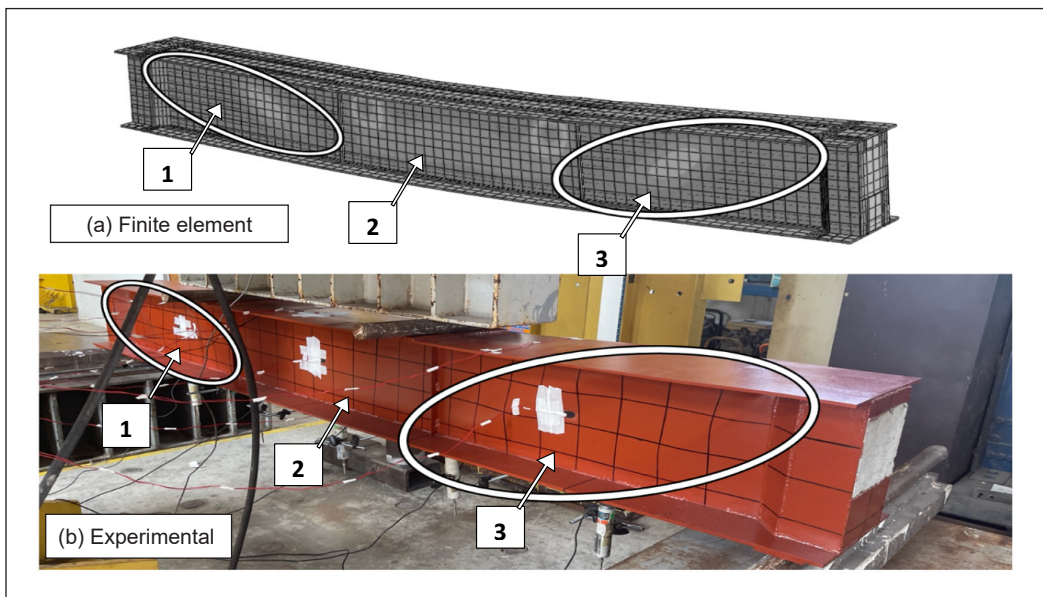


Figure 23. Failure mode for FSC2 in (a) FEA and (b) experiment

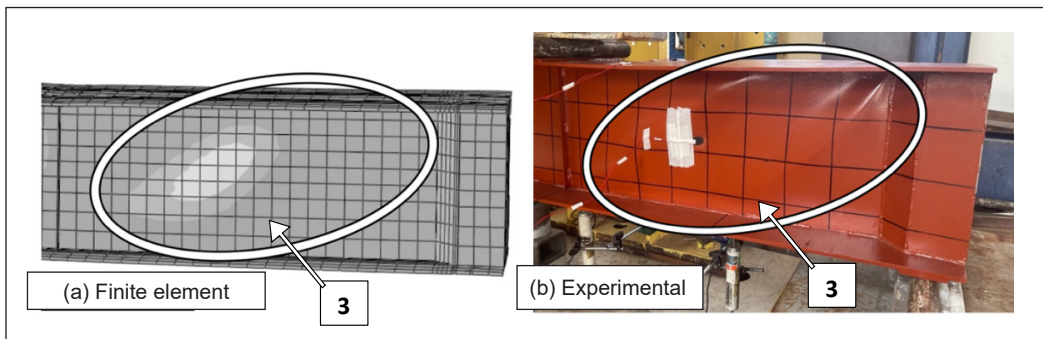


Figure 24. Comparison between the failure mode for FSC2 in web share buckling near the roller support in (a) FEA and (b) experiment

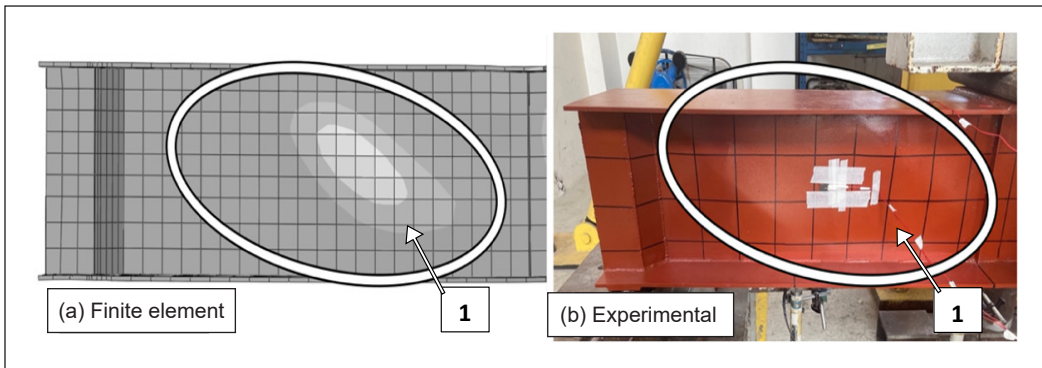


Figure 25. Comparison between the failure mode for FSC2 in web shear buckling near the pinned support in (a) FEA and (b) experiment

3, 4, and 6 of the girders in FEA, which agree well with those observed in an experiment at loads of 540 kN and 564 kN, respectively, as shown in Figures 27 and 28. At this stage, the web was not observed to yield when web buckling occurred in both experimental and FEA, but the bottom flange began to yield when the load reached 588.8 kN with strain recorded at 0.0015 in FEA and 615 kN with strain recorded at 0.00154 in experimental. At the ultimate load, there is no yield recorded in the web plate in both experimental and FEA, except for the top and bottom flanges for both FEA and experimental, where the maximum strain for the top flange was 0.00152 and 0.002 demonstrated by experimental and FEA, respectively. The strain in the bottom flange was 0.0025 and 0.0027 in tension for experimental and FEA, respectively.

The failure modes observed by experimental and FEA are relatively identical to their corresponding experimental counterparts without remarkable differences. The FE models can predict the load-deflection response and strength of the HCpt plate girders with acceptable accuracy by demonstrating similar failure modes. This accuracy in the results enables the Abaqus finite element software to simulate other parameters' effects on the girder's behaviour.

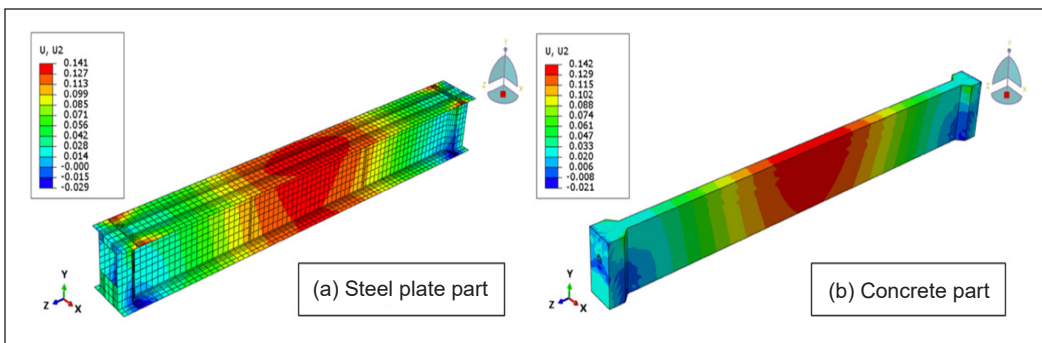


Figure 26. FE model validation for the FSCP3 specimen: (a) steel plate part and (b) concrete part

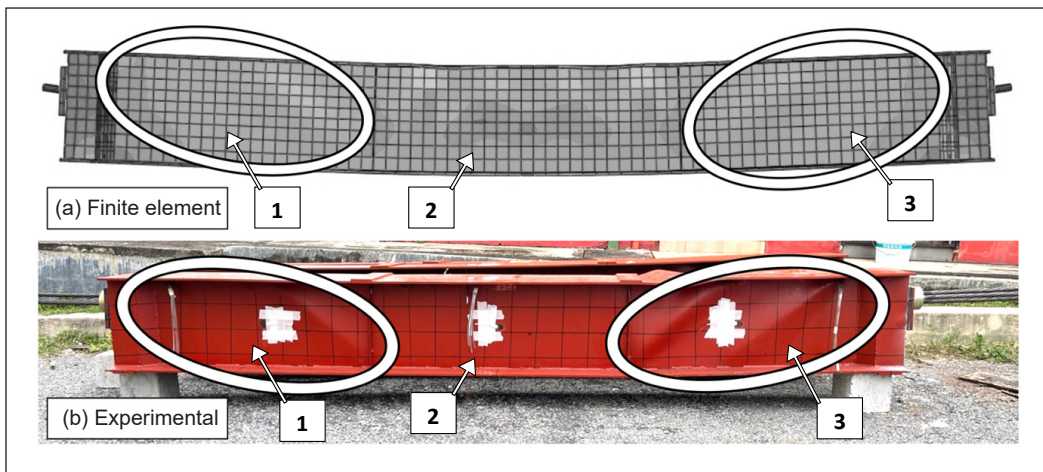


Figure 27. Comparison of the general failure mode for FSCP3 in (a) FEA and (b) experiment

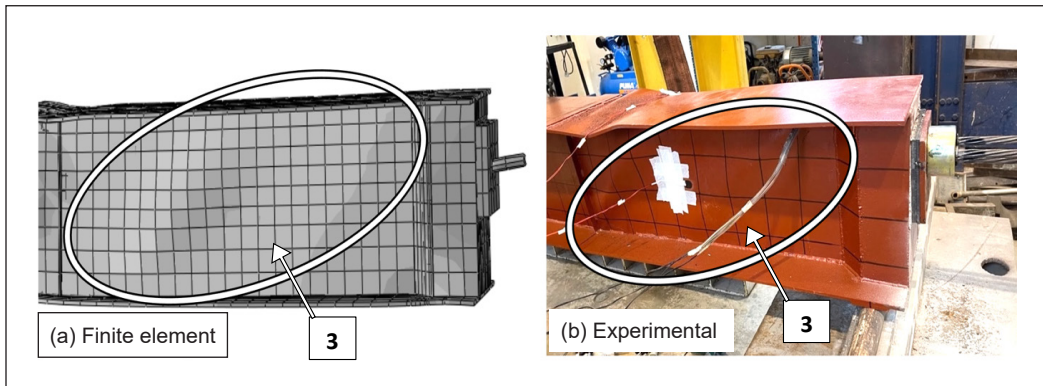


Figure 28. Comparison between the failure mode for FSCP3 in web shear buckling near the roller support in FEA and experiment

## CONCLUSION

The distortion and buckling web, as well as substantial deflection of long-span issues that occurred in traditional plate girder, has been addressed in this study by proposing a hybrid composite plate girder. This structural geometrical modification of the plate has been introduced by establishing the resistance of the web using the double web with in-filled concrete and enhanced with the internal prestressing tendon. The structural behaviour of this renowned plate girder was examined and investigated through experimental and finite element analysis using three specimens: FS1, FSC2 and FSCP3.

For flexural load capacity, in comparison to FS1, FSC2 produced 116.4%, and FSCP3 showed 126% improvement, respectively. In terms of displacement, FSCP3 exhibited a 20% reduction in displacement in comparison to FSC2.

The failure mode for FS1 was web shear buckling; those for FSC2 and FSCP3 were bending. The improvement in web shear buckling resistance produced by FSC2 and FSCP3 was 80% and 88%, respectively, in comparison to FS1.

For the FSC2 and FSCP3 specimens, the concrete in-fill is subjected to confinement effect by tri-axial compression, which is able to reduce the web buckling and improve the strength of the girder. The in-fill concrete was subjected to flexural load, and the concrete remained to provide high ductility and energy dissipation ability, delaying the failure of the girder.

FSCP3 produced the highest stiffness and load capacity compared to FS1 and FSC2, and it had less displacement than FSC2.

The model's FEA result showed excellent agreement with the experimental result. The failure modes simulated by the three models' FE were identical to the experimental work.

## ACKNOWLEDGEMENTS

The authors thank Universiti Putra Malaysia for funding this research using the Geran Inisiatif Putra Siswazah (IPS-UPM) with grant number GP-IPS 2023/9743300.

## REFERENCES

- Aghayere, A. O., & Vigil, J. (2020). *Structural steel design*. Mercury Learning and Information.
- Ahn, J. H., Jung, C. Y., & Kim, S. H. (2010). Evaluation on structural behaviors of prestressed composite beams using external prestressing member. *Structural Engineering and Mechanics*, 34(2), 247-275. <https://doi.org/10.12989/sem.2010.34.2.247>
- Al-Azzawi, Z., Stratford, T., Rotter, M., & Bisby, L. (2020). A new design method for a novel FRP strengthening technique against shear buckling of steel plate girders. *Thin-Walled Structures*, 148, Article 106611. <https://doi.org/10.1016/j.tws.2020.106611>
- Ali, Y., & Elgammal, A. (2023). Compensating steel web-opened beams for the loss in cyclic shear capacity by longitudinal stiffeners. *Delta University Scientific Journal*, 6(1), 123-134. <https://doi.org/10.21608/dusj.2023.291030>
- ASTM. (2016). *E8/E8M-16a: Standard Test Methods for Tension Testing of Metallic Materials*. ASTM International.
- Azmi, M. R., Yatim, M. Y. M., Esa, A., & Badaruzzaman, W. W. (2017). Experimental studies on perforated plate girders with inclined stiffeners. *Thin-Walled Structures*, 117, 247-256. <https://doi.org/10.1016/j.tws.2017.04.021>
- Baltay, P., & Gjelsvik, A. (1990). Coefficient of friction for steel on concrete at high normal stress. *Journal of Materials in Civil Engineering*, 2(1), 46-49. [https://doi.org/10.1061/\(ASCE\)0899-1561\(1990\)2:1\(46\)](https://doi.org/10.1061/(ASCE)0899-1561(1990)2:1(46))
- Barker, R. M., & Puckett, J. A. (2013). *Design of Highway Bridges: An LRFD Approach*. John Wiley & Sons.

- Basher, M., Shanmugam, N. E., & Khalim, A. R. (2011). Horizontally curved composite plate girders with trapezoidally corrugated webs. *Journal of Constructional Steel Research*, 67(6), 947-956. <https://doi.org/10.1016/j.jcsr.2011.01.015>
- Belletti, B., & Gasperi, A. (2010). Behavior of prestressed steel beams. *Journal of Structural Engineering*, 136(9), 1131-1139. [https://doi.org/10.1061/\(ASCE\)ST.1943-541X.0000208](https://doi.org/10.1061/(ASCE)ST.1943-541X.0000208)
- BS5950. (2008). *BS 5950-1: 2000: Structural Use of Steelwork in Building. Part 1. Code of Practice for Design-Rolled and Welded Sections*. British Standard Institution. <https://www.uceb.eu/DATA/CivBook/22.%20BS%205950%20Pt1%202000%20Steelwork%20Design.pdf>
- BS8110. (1997). *Structural Use of Concrete, Part 1. Code of Practice for Design and Construction*. BSI Knowledge. <https://knowledge.bsigroup.com/products/structural-use-of-concrete-code-of-practice-for-design-and-construction?version=standard>
- BSI. (2009). *BS EN 12390-3: 2009: Testing hardened Concrete. Compressive Strength of Test Specimens*. BSI Knowledge. <https://knowledge.bsigroup.com/products/code-of-practice-for-protection-of-below-ground-structures-against-water-from-the-ground?version=standard>
- Chacón, R., Bock, M., & Real, E. (2011). Longitudinally stiffened hybrid steel plate girders subjected to patch loading. *Journal of Constructional Steel Research*, 67(9), 1310-1324. <https://doi.org/10.1016/j.jcsr.2011.03.013>
- Chen, B. C., & Wang, T. L. (2009). Overview of concrete filled steel tube arch bridges in China. *Practice Periodical on Structural Design and Construction*, 14(2), 70-80. [https://doi.org/10.1061/\(ASCE\)1084-0680\(2009\)14:2\(70\)](https://doi.org/10.1061/(ASCE)1084-0680(2009)14:2(70))
- Cho, J., Moon, J., Ko, H. J., & Lee, H. E. (2018). Flexural strength evaluation of concrete-filled steel tube (CFST) composite girder. *Journal of Constructional Steel Research*, 151, 12-24. <https://doi.org/10.1016/j.jcsr.2018.08.038>
- Frankl, B. A. (2017). *Buckling and Shear Capacity of Horizontally Curved Steel Plate Girders*. The University of Nebraska-Lincoln.
- GabrielaSanMartín. (2008). *Technical Note Material Stress-strain Curves-csi*. Computers and Structures, Inc.
- Gao, F., Zuo, G., Deng, L., & Yang, F. (2020). Flexural behaviour of horizontally curved I-girders with round concrete-filled tubular flange. *Journal of Constructional Steel Research*, 170, Article 106090. <https://doi.org/10.1016/j.jcsr.2020.106090>
- Ghadami, A., & Broujerdian, V. (2019). Shear behavior of steel plate girders considering variations in geometrical properties. *Journal of Constructional Steel Research*, 153, 567-577. <https://doi.org/10.1016/j.jcsr.2018.11.009>
- Ghanim, G., Baldawi, W. S., & Ali, A. (2021). A review of composite steel plate girders with corrugated webs. *Engineering and Technology Journal*, 39(12), 1927-1938. <https://doi.org/10.30684/etj.v39i12.2193>
- Heo, B. W., Kwak, M. K., Bae, K. W., & Jeong, S. M. (2007). Flexural capacity of the profiled steel composite beams-deep deck plate. *Journal of Korean Society of Steel Construction*, 19(3), 247-258.

- Hu, H. T., Huang, C. S., Wu, M. H., & Wu, Y. M. (2003). Nonlinear analysis of axially loaded concrete-filled tube columns with confinement effect. *Journal of Structural Engineering*, 129(10), 1322-1329. [https://doi.org/10.1061/\(ASCE\)0733-9445\(2003\)129:10\(1322\)](https://doi.org/10.1061/(ASCE)0733-9445(2003)129:10(1322))
- Huang, W., Lai, Z., Chen, B., & Yao, P. (2017). Experimental behavior and analysis of prestressed concrete-filled steel tube (CFT) truss girders. *Engineering Structures*, 152, 607-618. <https://doi.org/10.1016/j.engstruct.2017.09.035>
- Ismail, M. K., AbdelAleem, B. H., Hassan, A. A., & El-Dakhkhni, W. (2023). Prediction of tapered steel plate girders shear strength using multigene genetic programming. *Engineering Structures*, 295, Article 116806. <https://doi.org/10.1016/j.engstruct.2023.116806>
- Kambal, M. E. M., & Jia, Y. (2018). Theoretical and experimental study on flexural behavior of prestressed steel plate girders. *Journal of Constructional Steel Research*, 142, 5-16. <https://doi.org/10.1016/j.jcsr.2017.12.007>
- Kazem, H., Zhang, Y., Rizkalla, S., Seracino, R., & Kobayashi, A. (2018). CFRP shear strengthening system for steel bridge girders. *Engineering Structures*, 175, 415-424. <https://doi.org/10.1016/j.engstruct.2018.08.038>
- Kim, B. G. (2005). *High Performance Steel Girders with Tubular Flanges*. Lehigh University.
- Lee, D. H., Oh, J. Y., Kang, H., Kim, K. S., Kim, H. J., & Kim, H. Y. (2015). Structural performance of prestressed composite girders with corrugated steel plate webs. *Journal of Constructional Steel Research*, 104, 9-21. <https://doi.org/10.1016/j.jcsr.2014.09.014>
- Lorenc, W., & Kubica, E. (2006). Behavior of composite beams prestressed with external tendons: Experimental study. *Journal of Constructional Steel Research*, 62(12), 1353-1366. <https://doi.org/10.1016/j.jcsr.2006.01.007>
- Lu, H., Han, L. H., & Zhao, X. L. (2009). Analytical behavior of circular concrete-filled thin-walled steel tubes subjected to bending. *Thin-Walled Structures*, 47(3), 346-358. <https://doi.org/10.1016/j.tws.2008.07.004>
- Luo, Z., Shi, Y., Xue, X., Zhou, X., & Yao, X. (2023). Nonlinear patch resistance performance of hybrid titanium-clad bimetallic steel plate girder with web opening. *Journal of Building Engineering*, 65, Article 105703. <https://doi.org/10.1016/j.jobbe.2022.105703>
- Mander, J. B., Priestley, M. J., & Park, R. (1988). Theoretical stress-strain model for confined concrete. *Journal of Structural Engineering*, 114(8), 1804-1826. [https://doi.org/10.1061/\(ASCE\)0733-9445\(1988\)114:8\(1804\)](https://doi.org/10.1061/(ASCE)0733-9445(1988)114:8(1804))
- Manual, A. U. (2020). *Abaqus User Manual*. Abacus.
- Manual, A. S. U. S. (2012). *Abaqus 6.11*. Abacus.
- Rabbat, B., & Russell, H. (1985). Friction coefficient of steel on concrete or grout. *Journal of Structural Engineering*, 111(3), 505-515. [https://doi.org/10.1061/\(ASCE\)0733-9445\(1985\)111:3\(505\)](https://doi.org/10.1061/(ASCE)0733-9445(1985)111:3(505))
- Shao, Y., & Wang, Y. (2017). Experimental study on static behavior of I-girder with concrete-filled rectangular flange and corrugated web under concentrated load at mid-span. *Engineering Structures*, 130, 124-141. <https://doi.org/10.1016/j.engstruct.2016.10.002>

- Sim, J. G. (2019). Shear buckling behavior of a plate composite girder using concrete-filled steel tube structures. *International Journal of Advanced Structural Engineering*, 11, 377-384. <https://doi.org/10.1007/s40091-019-00239-5>
- Southern Steel Berhad. (2022). *A Comparison of Specification for PC Strand*. Southern Steel Berhad. [https://www.southsteel.com/upload/files/1691979722\\_Catalog\\_Spec\\_Rev\\_A\\_230811.pdf](https://www.southsteel.com/upload/files/1691979722_Catalog_Spec_Rev_A_230811.pdf)
- Wang, Z. Y., Li, X., Gai, W., Jiang, R., Wang, Q. Y., Zhao, Q., Dong, J., & Zhang, T. (2018). Shear response of trapezoidal profiled webs in girders with concrete-filled RHS flanges. *Engineering Structures*, 174, 212-228. <https://doi.org/10.1016/j.engstruct.2018.07.025>
- Yuan, H., Chen, X., Theofanous, M., Wu, Y., Cao, T., & Du, X. (2019). Shear behaviour and design of diagonally stiffened stainless steel plate girders. *Journal of Constructional Steel Research*, 153, 588-602. <https://doi.org/10.1016/j.jcsr.2018.11.015>
- Zhang, Z., Zou, P., Deng, E.-F., Ye, Z., Tang, Y., & Li, F.-R. (2023). Experimental study on prefabricated composite box girder bridge with corrugated steel webs. *Journal of Constructional Steel Research*, 201, Article 107753. <https://doi.org/10.1016/j.jcsr.2022.107753>

# Conversion Factor Estimation of Stacked Eucalypt Timber Using Supervised Image Classification with Artificial Neural Networks

Vinicius Andrade de Barros<sup>1</sup>, Carlos Pedro Boechat Soares<sup>1</sup>, Gilson Fernandes da Silva<sup>2</sup>, Gianmarco Goycochea Casas<sup>1\*</sup> and Helio Garcia Leite<sup>1</sup>

<sup>1</sup>Department of Forest Engineering, Federal University of Viçosa. Av. Purdue, s/n, University Campus, 36570-900 Viçosa, Minas Gerais, Brazil

<sup>2</sup>Department of Forest and Wood Sciences, Federal University of Espírito Santo, 29550 Jerônimo Monteiro, Espírito Santo, Brazil

## ABSTRACT

Stacked timber is quantified in-store units and then adjusted with a conversion factor for volume estimation in cubic meters, which is important for the wood trade in South America. However, measuring large quantities accurately can be challenging. Digital image processing and artificial intelligence advancements offer promising solutions, making research in this area increasingly attractive. This study aims to estimate conversion factors of stacked *Eucalyptus grandis* timber using supervised image classification with Artificial Neuronal Network (ANN). Measured data and photographs from an experiment involving thirty stacks of timber were used to achieve this. The conversion factor was determined using photographic methods that involved the applications of equidistant points and ANN and subsequently validated with values observed through the manual method. The ANN method produced more accurate conversion factor estimates than the equidistant points method. Approximately 97% of the ANN estimates were within the  $\pm 1\%$  error class, even when using low-resolution digital photographs.

## ARTICLE INFO

### Article history:

Received: 02 June 2023

Accepted: 02 November 2023

Published: 16 July 2024

DOI: <https://doi.org/10.47836/pjst.32.4.05>

### E-mail addresses:

vandradebx@gmail.com (Vinicius Andrade de Barros)

csoares.ufv@gmail.com (Carlos Pedro Boechat Soares)

gilson.silva@pq.cnpq.br (Gilson Fernandes da Silva)

gianmarco.casas@ufv.br (Gianmarco Goycochea Casas)

hglete@ufv.br (Helio Garcia Leite)

\* Corresponding author

*Keywords:* *Eucalyptus grandis*, forest inventory, forest management, image processing, machine learning

## INTRODUCTION

Quantifying the timber volume that arrives at processing yards and the quantity stored there is essential for planning forest activities in the field and for the company. It includes harvest planning, payment for

forest transportation, and standardization of the wood quality that will be converted into the final product.

Foresters have used a variety of methods to quantify the volume of logs, including mathematical expressions and conversion factors (Soares et al., 2011), weighing the load on trucks (Carvalho & Camargo, 1996), xylometry (Husch et al., 1993; Santana et al., 2023), laser scanning of truckloads (Nylinder et al., 2009), and software for digital image assessment (Campos & Leite, 2017).

Stacked timber quantified in stere units represents the combined timber volume and the air space between the logs. It must be converted to cubic meters using the conversion factor to isolate the timber volume only. Conversion factor estimation is used in the timber industry to determine the amount of space timber occupies when stacked. It is important for calculating transportation and storage costs, as well as for determining the amount of timber that can be transported in a single load. The conversion factor can vary depending on several issues, including the species of the tree, the size of the logs, the method of stacking, moisture content, temperature, and dimensions of timber stacks (Campos & Leite, 2017; Meyen & O'Connell, 2012; Soares et al., 2011). The significant challenge in determining the conversion factor is accurately calculating the actual volume of logs, particularly when dealing with large quantities. This process can consume a considerable amount of time for the forestry operator and can result in measurement errors due to the inherent complexities of the task.

Software tools such as Digitora and NeuroDIC quantify stacked timber through image analysis. Digitora employs an equidistant points method (Bertola et al., 2003; Gouveia Filho et al., 2022; Husch et al., 1993; Soares et al., 2003), while NeuroDIC utilizes artificial neural network (ANN) models to classify images (Campos & Leite, 2017; Silveira, 2014). Both tools enable the quantification of empty spaces and logs within stacked timber, which helps determine conversion factors.

The Trestima Stack mobile application is a valuable tool for quantifying the volume of a timber pile. Computer vision accurately determines the volume based on images captured through a smartphone or tablet. Actual volume is counted based on the surface area of the pile, log length, and an automatically generated coefficient factor. This user-friendly application proves especially helpful when conducting inventory assessments of timber stacks at roadside landing sites, particularly in cases involving multiple measurement batches (Kärhä et al., 2019). Furthermore, alternative applications like IFOVEA and Timbeter enable the measurement of timber volumes and the creation of panoramic views using multiple photographs. However, it is important to note that a known reference value, such as the width of the stacked timber, must be obtained using a tape measure (Moskalik et al., 2022).

ANNs are a type of artificial intelligence inspired by how the human brain works. ANNs are made up of interconnected nodes, which are like the neurons in the brain. These

nodes process and transmit information and can be trained to perform complex tasks such as classification and regression (Haykin, 2009; Montesinos López et al., 2022). ANNs are composed of input variables, the data the model is trained on, and output variables, which are the data the model tries to predict or classify. The model is structured in layers: the input layer, where data is initially received; hidden layers, which process information through weighted connections, with their quantity and neuron count determining model complexity; and the output layer, which produces predictions. The number of neurons in a layer influences its learning capacity, impacting the model's performance (Aggarwal, 2018; Campesato, 2020).

ANN models have been used in forestry to solve diverse problems such as height-diameter models (Bueno et al., 2020; Casas et al., 2022a; Da Rocha et al., 2021; Ercanlı, 2020), whole-stand models (Casas et al., 2022b; Cordeiro et al., 2022; De Andrade et al., 2022; De Freitas et al., 2020; De Oliveira Neto et al., 2022), stem taper (Da Cunha Neto et al., 2019; De Souza et al., 2023; Sandoval & Acuña, 2022; Seki, 2023; Tavares Júnior et al., 2021), survival and mortality (Bayat et al., 2019; Da Rocha et al., 2018; Reis et al., 2018) and timber price forecasting (Kožuch et al., 2023).

Image classification is a supervised learning task that involves the identification of target classes within images and can be used with ANN methods. A predefined set of classes is established, and a model is trained using images. ANN treats each pixel as an independent feature, and the spatial structure of the image is not considered (Aggarwal, 2018; Mather & Tso, 2016).

The digital processing of images using specialised software reduces the need for human intervention, which can lead to fewer errors and more accurate estimates (da Silva et al., 2005). ANNs have made significant progress in recent years, and one potential application is to use image classification to determine the conversion factor of stacked timber. This study aims to estimate the conversion factors of stacked eucalypt timber using supervised image classification using the ANN method.

## MATERIALS AND METHODS

### Experimental Description

This study utilised data from 30 stacks of *Eucalyptus grandis* timber that were carefully arranged and measured. The experiment was conducted in the Silviculture sector of the Department of Forestry Engineering at the Federal University of Viçosa, located in Viçosa, Minas Gerais. The data was collected as part of a study developed by Bertola et al. (2003).

For each stack, the actual volume of the log (m<sup>3</sup>) was determined using Smalian's formula (Equation 1) applied to each log:

$$V = \frac{A_1 + A_2}{2} L \quad (1)$$

Where  $V$  = Volume of the log ( $m^3$ );  $A_1$  = Area of the small end of the log ( $m^2$ );  $A_2$  = Area of the large end of the log ( $m^2$ ); and  $L$  = Length of the log (m).

The stack volume (st) was calculated by multiplying the dimensions of the stacks (Equation 2):

$$V = xyz \quad (2)$$

Where  $V$  = Stack volume (st);  $x$  = Width of the stack (m);  $y$  = Length of the stack (m); and  $z$  = Height of the stack (m).

In addition, photographs of both sides of each stack were taken using a Kodak DC 210 camera. A total of 60 photographs were taken at a resolution of  $1,152 \times 864$  dpi, zoomed to the maximum position, and with the observer positioned at 3 m. Consequently, the observed conversion factor was calculated as the ratio between the stack volume (st) and the actual log volume with bark ( $m^3$ ).

### Conversion Factor Estimation

The estimated conversion factors for each side of the stacks were calculated using the Digitora and NeuroDic software tools, and the final estimated conversion factors were obtained by averaging the factors from both sides.

### Conversion Factor Using the Equidistant Point Method

The Digitora software creates a grid of equidistant points that cover either a part or the entirety of the photograph (Figure 1). The conversion factor for each side of the stacks was obtained by manually counting the points that overlap with the logs and the empty spaces. Subsequently, the software calculates the percentage of empty spaces on the side of the stack, which was used to determine the conversion factor.

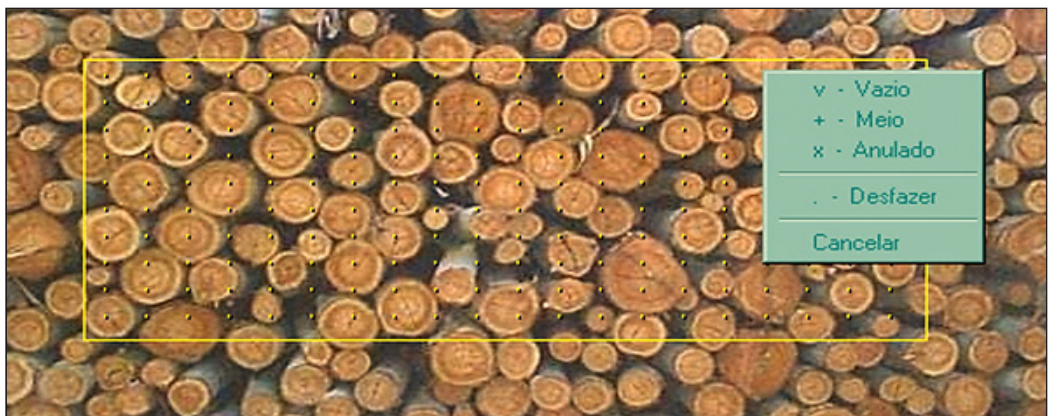


Figure 1. Processing of stacked eucalypt timber with equidistant points technique using Digitora software tools  
Note. Example of a low-resolution photograph processed in this studio

## Conversion Factor Using Artificial Neural Network Method

### *Image Processing and Classification*

The NeuroDIC software was used to calculate the conversion factors, following the method described by Silveira (2014). The software uses an artificial neural network to perform supervised image classification. After importing the photographs of the stack sides into the software, image filters were applied, and two classification classes were selected: wood and space, resulting in a black-and-white image representing each class (Figure 2).

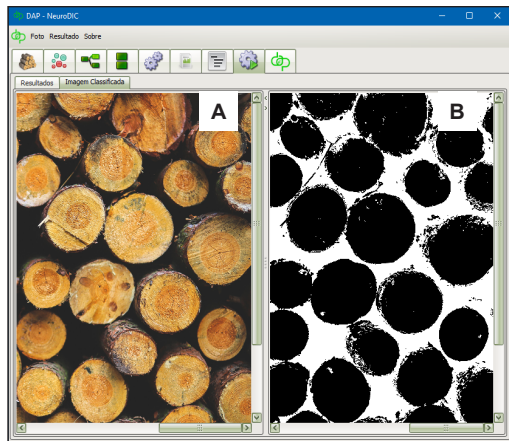


Figure 2. Processing of stacked eucalypt timber with the artificial neural network using NeuroDic software tools: Stacked timber before (A) and after (B) filter applications

### *Image Filter Selection*

The version of the software utilised in this study consisted of eight distinct filters, including *Contrast*, which adjusts the brightness and contrast of the image; *Curves*, which modifies points within the tonal range of an image; *Gain*, similar to the Contrast filter but with a wider range; *Invert*, which reverses the colours of the image, transforming it into its negative; *Solarize*, similar to the Invert filter, but with a “V” shaped transformation function; *Threshold*, which converts the original image into black and white, allowing for the determination of empty spaces or wood based on varying settings; *Black and White*, transforming the original image into grayscale; *GrayLevels*, which converts the original image into a grayscale scale (Silveira, 2014).

The selection of the best filters for training the artificial neural networks was based on analysing pixel histograms for each filter, focusing on identifying distribution patterns for the wood and space classes.

### *Input and Output Variables Selection*

The following input and output variables were defined to train the ANN model:

**Input variables:** The input variables are the pixel values from the images’ red, green, and blue (RGB) bands. The ANN learns to identify the patterns in the RGB bands associated with each class. Once the ANN model is trained, it can predict the class of the same or new image by feeding its pixel values into the network and getting the output prediction.

**Output variable:** The output variable is a binary class value, with 1 representing wood and 0 representing space. This variable represents the class of each pixel in the image.

### ANN Model Architecture and Configuration

The data were split into training (70%) and validation (30%) to establish the ANN models. Multilayer Perceptron (MLP) type was used with five neurons in the hidden layer and the sigmoid activation function (Equation 3). The stopping criterion was based on a mean error of 0.0001, 3,000 epochs and 20 convergence process numbers.

$$f(\alpha) = \frac{1}{(1 + e^{-\alpha})} \quad (3)$$

Note here that  $f$  is the function that represents the non-linear activation used in the entire neural network,  $b$  is the bias for the neuron activation threshold,  $x_i$  and  $w_i$  denote the input values of the unit or neuron and their weights;  $\alpha$  denotes the weighted combination (Equation 4):

$$\alpha = \sum_{j=1}^n w_j x_j + b \quad (4)$$

The Resilient Propagation (Rprop) algorithm (Equation 5) (Riedmiller & Braun, 1993) was used following the rule for each weight ( $\omega_{ij}$ ) an individual step-size ( $\Delta_{ij}$ ):

$$\Delta_{ij}^{(t)} = \begin{cases} \min(\eta^+ * \Delta_{ij}^{(t-1)}, \Delta_{\max}), & \text{if } \frac{\partial E^{(t-1)}}{\partial \omega_{ij}} * \frac{\partial E^{(t)}}{\partial \omega_{ij}} > 0 \\ \max(\eta^- * \Delta_{ij}^{(t-1)}, \Delta_{\min}), & \text{if } \frac{\partial E^{(t-1)}}{\partial \omega_{ij}} * \frac{\partial E^{(t)}}{\partial \omega_{ij}} < 0 \\ \Delta_{ij}^{(t-1)}, & \text{otherwise.} \end{cases} \quad (5)$$

where  $0 < \eta^- < 1 < \eta^+$  and each iteration, the new weights (Equation 6) are given by:

$$\omega_{ij}^{(t+1)} = \omega_{ij}^{(t)} + \Delta \omega_{ij}^{(t)} \quad (6)$$

If the partial derivative  $\partial E / \partial \omega_{ij}$  possesses the same sign for consecutive steps, the step size is increased, whereas if it changes the sign, the step size is decreased.

This study employed the positive, resilient propagation (Rprop+) algorithm (Equation 7) variation. The pseudocode below illustrates one iteration of the Rprop+ algorithm (Igel & Hüsken, 2003):

*Rprop+*  
 for each  $\omega_{ij}$  do {

$$\begin{aligned}
 &\text{if } \frac{\partial E^{(t-1)}}{\partial \omega_{ij}} * \frac{\partial E^{(t)}}{\partial \omega_{ij}} > 0 \text{ then } \{ \\
 &\quad \Delta_{ij}^{(t)} = \min(\Delta_{ij}^{(t-1)} * \eta^+, \Delta_{\max}) \\
 &\quad \Delta \omega_{ij}^{(t)} = -\text{sign}\left(\frac{\partial E^{(t)}}{\partial \omega_{ij}}\right) * \Delta_{ij}^{(t)} \\
 &\quad \omega_{ij}^{(t+1)} = \omega_{ij}^{(t)} + \Delta \omega_{ij}^{(t)} \\
 &\quad \} \\
 &\text{elseif } \frac{\partial E^{(t-1)}}{\partial \omega_{ij}} * \frac{\partial E^{(t)}}{\partial \omega_{ij}} < 0 \text{ then } \{ \\
 &\quad \Delta_{ij}^{(t)} = \max(\Delta_{ij}^{(t-1)} * \eta^-, \Delta_{\min}) \\
 &\quad \omega_{ij}^{(t+1)} = \omega_{ij}^{(t)} + \Delta \omega_{ij}^{(t-1)} \\
 &\quad \frac{\partial E^{(t)}}{\partial \omega_{ij}} = 0 \\
 &\quad \} \\
 &\text{elseif } \frac{\partial E^{(t-1)}}{\partial \omega_{ij}} * \frac{\partial E^{(t)}}{\partial \omega_{ij}} = 0 \text{ then } \{ \\
 &\quad \Delta \omega_{ij}^{(t)} = -\text{sign}\left(\frac{\partial E^{(t)}}{\partial \omega_{ij}}\right) * \Delta_{ij}^{(t)} \\
 &\quad \omega_{ij}^{(t+1)} = \omega_{ij}^{(t)} + \Delta \omega_{ij}^{(t)} \\
 &\quad \} \\
 &\} \tag{7}
 \end{aligned}$$

300 ANN models with the same architecture and configuration were trained, five models for each image to improve the model’s accuracy. The best model for each image was then selected, resulting in 60 models, two for each analysed stack. The statistical performance of each selected model can be seen in Supplementary Table 1.

### Comparative Analysis of Stacking Factors

The comparison between the conversion factors obtained from Digitora and NeuroDIC software tools was evaluated by considering the average of percentage deviations (APD%) (Equation 8), root mean square percentage error (RMSE%) (Equation 9), per cent relative error (RE%) (Equation 10), and the dependent samples t-test at a significance level of 5% (Soares et al., 2003).

$$APD\% = 100N^{-1} \sum_{i=1}^n \frac{\bar{Y}_i - Y_i}{Y_i} \quad (8)$$

$$RMSE\% = 100\bar{Y}_i^{-1} \sqrt{N^{-1} \sum_{i=1}^n (Y_i - \bar{Y}_i)^2} \quad (9)$$

$$RE\% = 100 \left( \frac{\bar{Y}_i - Y_i}{Y_i} \right) \quad (10)$$

Where  $\bar{Y}_i$  = Estimated conversion factor;  $Y_i$  = Observed conversion factor;  $\bar{Y}_i$  = Average of observed conversion factor; and N = Number of observations.

## RESULTS

The conversion factors estimated from the NeuroDIC and Digitora software tools did not show statistically significant (n.s.) variance compared to the observed factors (tcalc = -1.763 n.s. and -0.921 n.s., respectively). The conversion factors estimated from the NeuroDIC software were more accurate than those obtained from Digitora, as evidenced by the estimates of the APD (%) and RMSE (%) statistics (Table 1) and the distribution of percentage differences (Figure 3).

In Figure 3, stack number 13 showed the highest percentage difference for both evaluated software tools. Upon analysing the photograph of this stack (Figure 4), it is noticeable that a significant portion of it was shaded due to the weather conditions at the time, resulting in incorrect classification of the wood and space classes in the NeuroDIC software and visually misleading results in the Digitora software. Despite these conditions, the results were relatively desirable.

Table 1

*Observed and estimated conversion factors obtained from the NeuroDIC and Digitora software tools, along with corresponding statistics*

Number of Stack	Conversion Factors			RE (%)	
	Observed	NeuroDIC	Digitora	NeuroDIC	Digitora
1	1.3842	1.3758	1.3819	-0.6103	-0.1662
2	1.3666	1.3690	1.4147	0.1759	3.5197
3	1.3048	1.3063	1.2705	0.1157	-2.6288
4	1.3501	1.3320	1.2929	-1.3397	-4.2367
5	1.3318	1.3322	1.3505	0.0320	1.4041
6	1.3128	1.3117	1.2684	-0.0810	-3.3821
7	1.3034	1.3024	1.3019	-0.0737	-0.1151

Table 1 (continue)

Number of Stack	Conversion Factors			RE (%)	
	Observed	NeuroDIC	Digitora	NeuroDIC	Digitora
8	1.2998	1.3023	1.2954	0.1892	-0.3385
9	1.2968	1.2976	1.2785	0.0598	-1.4112
10	1.3081	1.3082	1.2647	0.0085	-3.3178
11	1.2967	1.3033	1.2346	0.5126	-4.7891
12	1.3037	1.3040	1.2934	0.0217	-0.7901
13	1.2465	1.2091	1.2959	-2.9983	3.9631
14	1.2887	1.2908	1.2425	0.1659	-3.5850
15	1.2799	1.2798	1.2830	-0.0069	0.2422
16	1.3249	1.3210	1.3092	-0.2937	-1.1850
17	1.2887	1.2927	1.2912	0.3108	0.1940
18	1.2676	1.2588	1.2394	-0.6968	-2.2247
19	1.2644	1.2568	1.2276	-0.5975	-2.9105
20	1.2534	1.2610	1.2290	0.6051	-1.9467
21	1.2761	1.2654	1.2912	-0.8400	1.1833
22	1.2520	1.2576	1.2481	0.4448	-0.3115
23	1.3344	1.3364	1.3102	0.1500	-1.8135
24	1.2632	1.2623	1.2970	-0.0676	2.6757
25	1.2534	1.2583	1.2588	0.3895	0.4308
26	1.2712	1.2669	1.2825	-0.3402	0.8889
27	1.2625	1.2631	1.2327	0.0453	-2.3604
28	1.2522	1.2471	1.2989	-0.4043	3.7294
29	1.2519	1.2370	1.2908	-1.1931	3.1073
30	1.2554	1.2492	1.2991	-0.4944	3.4810
APD (%)		-0.2270	-0.4231		
RMSE (%)		0.0151	0.6277		
Calculated t-value		-1.7337 <sup>ns</sup>	-0.9214 <sup>ns</sup>		

Note.  $t_{tab}$  (5%; 29df) = 2.040; ns = not significant

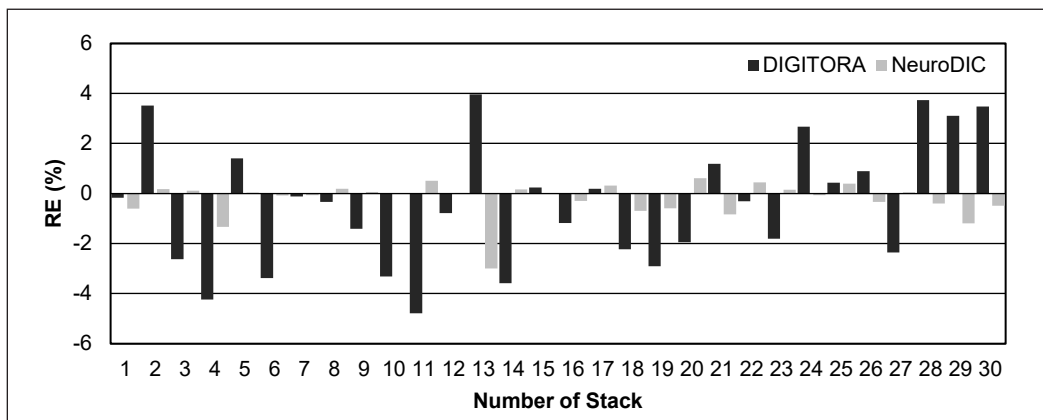


Figure 3. Percent relative error of conversion factor estimated from the NeuroDIC and Digitora software tools

The distribution of the relative percentage errors obtained with the NeuroDIC and Digitora software tools was compared (Figure 5). NeuroDIC had a narrower distribution of errors, with approximately 96.7% of the percentage differences between the observed and estimated factors concentrated in the  $\pm 1\%$  error class interval. It means that 50% of the NeuroDIC estimates were within 1% of the observed values, 40% were exactly equal, and 6.7% were within 1% below the observed values (Figure 5A). In contrast, Digitora had a wider distribution of errors, with only 43.3% of the percentage differences within the  $\pm 1\%$  error class interval (Figure 5B). The higher concentration of the percentage differences in the intervals of smaller error classes for NeuroDIC indicates that it is generally more accurate than Digitora. NeuroDIC is more likely to produce estimates close to the true values.



Figure 4. Photograph of stacked eucalypt timber number 13 exhibiting a higher relative error due to the image quality

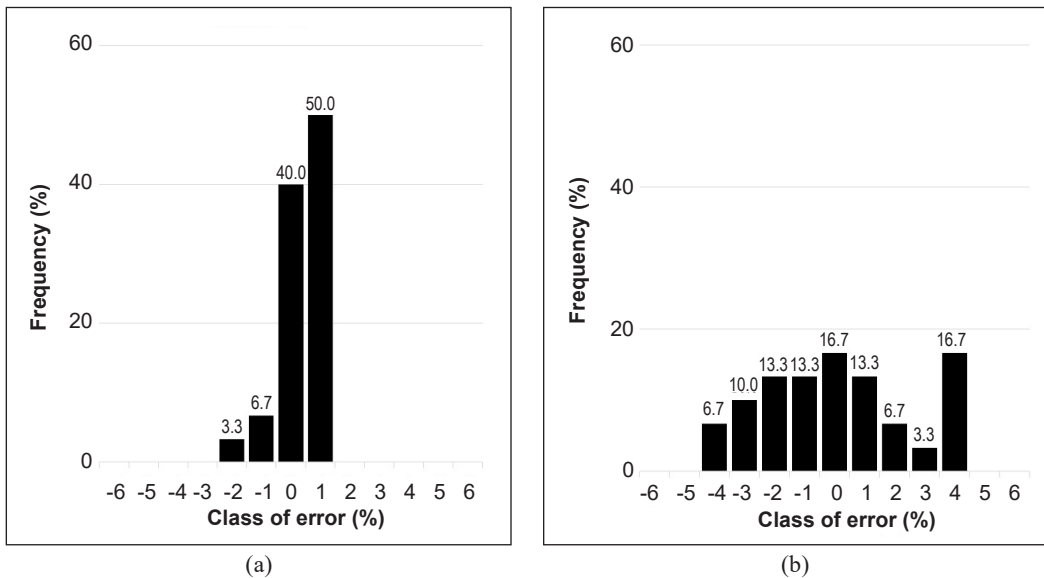


Figure 5. Error class plot between frequency in stacked eucalypt timber estimated: (a) NeuroDIC; and (b) Digitora software tools

## DISCUSSION

Stacked timber is quantified in in-store units, which are then adjusted using a conversion factor to more precisely estimate timber volume in cubic meters. This adjustment is necessary due to the prevalent use of cubic meters for wood commercialization, particularly in South America. The conversion factor measures the stacking efficiency and the space occupied by the stacking volume compared to the actual log volume. However, measurement inaccuracies can occur due to the challenges in accurately determining the volume of logs in large quantities. Digital image processing and significant advancements in artificial intelligence have shown remarkable efficacy in contributing to these cases, making research in this field more appealing and captivating.

Earlier studies have proven the accuracy of conversion factor estimation using low-resolution digital photographs (Bertola et al., 2003). The results of this study, which also used low-resolution digital photographs, further support the efficacy of Digitora (equidistant points method) and NeuroDic (ANN method) software tools in determining conversion factors. Despite the challenges posed by low natural lighting conditions, including cloud cover and variations in the time of day during image capture, the estimates were highly accurate.

When applied under controlled experimental conditions with manually stacked timber, Digitora accurately estimated conversion factors, with a mean difference (APD%) from observed factors of -0.4231% (Table 1). However, when evaluating mechanically stacked timber in a field condition at a forestry company, the mean difference increased to 3.2259% (Soares et al., 2003). It suggests that the accuracy of Digitora software tools may vary depending on the stacking method employed.

NeuroDic showed a mean difference (APD%) from observed factors of -0.2270% (Table 1), showing its superior accuracy compared to Digitora in this study. This finding was consistent with the research conducted by Silveira (2014), who found a 2.0% difference in the average estimation of conversion factors obtained by NeuroDic, once again proving its greater accuracy.

Additionally, da Silva et al. (2005) have used Matlab software to evaluate an image segmentation method for stacked eucalypt timber, which involves dividing the image into segments with uniform attributes based on pixel adjacency and similarity conditions (Andrade et al., 1994). They reported an average difference of 0.6370% between observed and estimated factors, higher than in the two software tools evaluated in this study. It highlights the effectiveness of the alternative method of determining conversion, such as the one in this study.

The traditional method of manual log scaling, which is relatively costly and time-consuming, can be replaced using NeuroDic. The adoption of NeuroDic enables increased sampling intensity with a cost reduction of up to 90%, as demonstrated by Silveira (2014).

In other words, digital image processing and artificial intelligence can improve the accuracy of timber volume measurement, which is important for commercialization purposes.

A study by Bertola et al. (2003) concluded that forest operator training influences the accuracy of the conversion factor. Therefore, the most knowledgeable forest operator in this study obtained the observed conversion factor. The influence of genetic factors on conversion factors further underlines the importance of accurate estimation methods. The study found significant differences in conversion factors between the two clones, while no significant differences were seen within the same clone (de Andrade Sandim et al., 2019). The conversion factors can vary depending on the mid-diameter and the crook, which show strong correlations between the factors (Heinzmann & Barbu, 2017)—according to De Miguel-Díez et al. (2023), who evaluated a detailed literature review, thirty parameters influence conversion factors. The conversion factor may vary according to the image quality due to field weather conditions. These conditions contribute to the variability of the conversion factors and highlight the importance of reliable estimation techniques offered by computer tools using photographic methods,

## CONCLUSION

The analysis of conversion factors using the NeuroDic (ANN) and Digitora (equidistant points method) software tools revealed no statistically significant variance compared to the observed factors. The ANN method provided more accurate conversion factor estimates than the equidistant points method. Both methods prove that an inferior quality photograph, affected by weather conditions, introduces errors in the estimations, albeit within acceptable limits.

## ACKNOWLEDGMENTS

The authors are grateful to the “Coordenação de Aperfeiçoamento de Pessoal de Nível Superior, Brasil—CAPES”—Financing Code 001 and Federal University of Viçosa.

## REFERENCES

- Aggarwal, C. C. (2018). *Neural networks and deep learning*. Springer International Publishing. <https://doi.org/10.1007/978-3-319-94463-0>
- Andrade, M., Peixoto, F. C., & Araújo, A. (1994). Segmentação de imagens através de rede neuronal por satisfação de restrições em ambiente paralelo [Image segmentation using a neural network that fulfils constraints in a parallel environment]. *Anais do VII SIBGRAPI*, 47-52.
- Bayat, M., Ghorbanpour, M., Zare, R., Jaafari, A., & Pham, B. T. (2019). Application of artificial neural networks for predicting tree survival and mortality in the Hyrcanian forest of Iran. *Computers and Electronics in Agriculture*, 164, Article 104929. <https://doi.org/10.1016/j.compag.2019.104929>

- Bertola, A., Soares, C. P. B., Ribeiro, J. C., Leite, H. G., & Souza, A. L. D. (2003). Determination of piling factors through Digitora software. *Revista Árvore*, 27(6), 837-844. <https://doi.org/10.1590/S0100-67622003000600010>
- Bueno, G. F., Costa, E. A., Cristina, A. N., Soares, A. A. V., de Miranda, R. O. V., & Schons, C. T. (2020). Effect of number of hidden layer neurons for height-diameter relationship of eucalyptus using artificial neural networks. *BIOFLX Scientific Journal*, 5(2), 222-230. <http://dx.doi.org/10.5380/biofix.v5i2.71374>
- Campeato, O. (2020). *Artificial Intelligence, Machine Learning, and Deep Learning*. Mercury Learning and Information.
- Campos, J. C. C., & Leite, H. G. (2017). *Mensuração florestal: Perguntas e respostas* (5. ed. atual. e ampl.) [Forest measurement: Questions and answers (5th ed.)]. Universidade Federal de Viçosa.
- Carvalho, A. M., & Camargo, F. R. A. (1996). Avaliação do método de recebimento de madeira por estere [Evaluation of the method of receiving wood by stere]. *Revista O Papel*, 57, 65-68.
- Casas, G. G., Fardin, L. P., Silva, S., de Oliveira Neto, R. R., Binoti, D. H. B., Leite, R. V., Domiciano, C. A. R., de Sousa Lopes, L. S., da Cruz, J. P., dos Reis, T. L., & Leite, H. G. (2022a). Improving yield projections from early ages in eucalypt plantations with the Clutter model and artificial neural networks. *Pertanika Journal of Science & Technology*, 30(2). <https://doi.org/10.47836/pjst.30.2.22>
- Casas, G. G., Gonzáles, D. G. E., Villanueva, J. R. B., Fardin, L. P., & Leite, H. G. (2022b). Configuration of the deep neural network hyperparameters for the hypsometric modeling of the Guazuma crinita Mart. in the Peruvian Amazon. *Forests*, 13(5), Article 697. <https://doi.org/10.3390/f13050697>
- Cordeiro, M. A., Arce, J. E., Guimarães, F. A. R., Bonete, I. P., Silva, A. V. D. S., Abreu, J. C. D., & Binoti, D. H. B. (2022). Volumetric estimates in eucalyptus stands using support vector machines and artificial neural networks. *Madera y bosques*, 28(1), Article e2812252. <https://doi.org/10.21829/myb.2022.2812252>
- Da Cunha Neto, E. M., Bezerra, J. C. F., Veras, H. F. P., Gouveia, D. M., Araujo, E. C. G., & Silva, T. C. (2019). Eucalyptus stem taper estimate through artificial intelligence techniques. *BIOFLX Scientific Journal*, 4(2), 166-171. <http://dx.doi.org/10.5380/biofix.v4i2.65831>
- Da Rocha, J. E. C., Junior, M. R. N., Júnior, I. D. S. T., de Souza, J. R. M., Lopes, L., & da Silva, M. L. (2021). Configuration of artificial neural networks for height-diameter relationship of Eucalyptus spp. *Scientia Forestalis*, 49(132), Article e3706.
- Da Rocha, S. J. S. S., Torres, C. M. M. E., Jacovine, L. A. G., Leite, H. G., Gelcer, E. M., Neves, K. M., Schettini, B. L. S., Villanova, P. H., Silva, L. F. D., Reis, L. P., & Zanuncio, J. C. (2018). Artificial neural networks: Modeling tree survival and mortality in the Atlantic Forest biome in Brazil. *Science of the Total Environment*, 645, 655-661. <https://doi.org/10.1016/j.scitotenv.2018.07.123>
- Da Silva, M. C., Soares, V. P., Pinto, F. D. A. C., Soares, C. P. B., & Ribeiro, C. A. Á. S. (2005). Determination of the volume wooden stacked through processing of digital images. *Scientia Forestalis*, 69, 104-114.
- De Andrade Sandim, A. S., Mota, A. C., dos Santos, M. L., dos Santos Barros, W., Costa, B. C., & de Andrade, V. M. S. (2019). Stacked volume conversion factor for geometric volume of Eucalyptus sp. *Revista Agro@ambiente On-line*, 13, 46-54. <https://doi.org/10.18227/1982-8470ragro.v13i0.5312>

- De Andrade, V. C. L., Cardoso, A. M., & Binotti, D. H. B. (2022). Growth and yield prognosis of *Corymbia citriodora* using artificial neural networks. *Advances in Forestry Science*, 9(2), 1735-1744. <https://doi.org/10.34062/afs.v9i2.12829>
- De Freitas, E. C. S., de Paiva, H. N., Neves, J. C. L., Marcatti, G. E., & Leite, H. G. (2020). Modeling of eucalyptus productivity with artificial neural networks. *Industrial Crops and Products*, 146, Article 112149. <https://doi.org/10.1016/j.indcrop.2020.112149>
- De Miguel-Diez F., Purfürst T., Acuna M., Tolosana-Esteban E., Cremer T. (2023). Estimation of conversion factors for wood stacks in landings and their influencing parameters: a comprehensive literature review for America and Europe. *Silva Fennica*, 57(1), Article 22018. <https://doi.org/10.14214/sf.22018>
- De Oliveira Neto, R. R., Leite, H. G., Gleriani, J. M., & Strimbu, B. M. (2022). Estimation of Eucalyptus productivity using efficient artificial neural network. *European Journal of Forest Research*, 141, 129-151. <https://doi.org/10.1007/s10342-021-01431-7>
- De Souza, J. R. M., de Oliveira Castro, R. V., Júnior, I. D. S. T., Marcelino, R. A. G., da Silva, R. M., & Moretti, S. D. A. (2023). Stem tapering of eucalyptus spp. using different configurations of artificial neural networks. *Floresta*, 53(2), 136-144. <http://dx.doi.org/10.5380/ufv.v53i2.78754>
- Ercanlı, İ. (2020). Innovative deep learning artificial intelligence applications for predicting relationships between individual tree height and diameter at breast height. *Forest Ecosystems*, 7, Article 12. <https://doi.org/10.1186/s40663-020-00226-3>
- Gouveia Filho, K. V., Soares, T. S., Cruz, E. S., & Mathias, R. A. M. (2022). Determinação de fatores de empilhamento e volume de madeira empilhada por meio do processamento de imagens digitais [Determination of stacking factors and wood volume stacked through digital image processing]. *Advances in Forestry Science*, 9(3), 1851-1858. <https://doi.org/10.34062/afs.v9i3.13470>
- Haykin, S. (2009). *Neural networks and learning machines* (3rd ed.). Pearson Education India.
- Heinzmann, B., & Barbu, M. C. (2017). Effect of mid-diameter and log-parameters on the conversion factor of cubic measure to solid measure concerning industrial timber. *Pro Ligno*, 13(1), 39-44.
- Husch, B., Miller, C. I., & Beers, T. W. (1993). *Forest mensuration* (3rd ed.). Krieger Publishing Company.
- Igel, C., & Hüsken, M. (2003). Empirical evaluation of the improved Rprop learning algorithms. *Neurocomputing*, 50, 105-123. [https://doi.org/10.1016/S0925-2312\(01\)00700-7](https://doi.org/10.1016/S0925-2312(01)00700-7)
- Kärhä, K., Nurmela, S., Karvonen, H., Kivinen, V. P., Melkas, T., & Nieminen, M. (2019). Estimating the accuracy and time consumption of a mobile machine vision application in measuring timber stacks. *Computers and Electronics in Agriculture*, 158, 167-182. <https://doi.org/10.1016/j.compag.2019.01.040>
- Kožuch, A., Cywicka, D., & Adamowicz, K. (2023). A comparison of artificial neural network and time series models for timber price forecasting. *Forests*, 14(2), Article 177. <https://doi.org/10.3390/f14020177>
- Mather, P., & Tso, B. (2016). *Classification methods for remotely sensed data*. CRC Press.
- Meyen, S., & O'Connell, K. (2012). *Stacked timber measurement*. The 2012 ITGA Forestry & Timber Yearbook. Teagasc Forestry Development Department. <https://www.forestry.ie/images/MiscDocs/2012YearbookArticles/StackedTimberMeasurement2012.pdf>

- Montesinos López, O. A., Montesinos López, A., & Crossa, J. (2022). Fundamentals of artificial neural networks and deep learning. In *Multivariate Statistical Machine Learning Methods for Genomic Prediction* (pp. 379-425). Springer. [https://doi.org/10.1007/978-3-030-89010-0\\_10](https://doi.org/10.1007/978-3-030-89010-0_10)
- Moskalik, T., Tymendorf, L., van der Saar, J., & Trzeciński, G. (2022). Methods of wood volume determining and its implications for forest transport. *Sensors*, 22(16), Article 6028. <https://doi.org/10.3390/s22166028>
- Nylinder, M., Kubénka, T., & Hultnäs, M. (2008). *Roundwood measurement of truck loads by laser scanning. A field study at Arauco pulp mill Nueva Aldea.*
- Reis, L. P., de Souza, A. L., dos Reis, P. C. M., Mazzei, L., Soares, C. P. B., Torres, C. M. M. E., Da Silva, L. F., Ruschel, A. R., Rêgo, L. J. S., & Leite, H. G. (2018). Estimation of mortality and survival of individual trees after harvesting wood using artificial neural networks in the amazon rain forest. *Ecological Engineering*, 112, 140-147. <https://doi.org/10.1016/j.ecoleng.2017.12.014>
- Riedmiller, M., & Braun, H. (1993). A direct adaptive method for faster backpropagation learning: The RPROP algorithm. *IEEE International Conference on Neural Networks*, 1, 586-591. <https://doi.org/10.1109/ICNN.1993.298623>
- Sandoval, S., & Acuña, E. (2022). Stem taper estimation using artificial neural networks for Nothofagus trees in natural forest. *Forests*, 13(12), Article 2143. <https://doi.org/10.3390/f13122143>
- Santana, A., Encinas, I., & Muñoz, R. (2023). Stacking factor in transporting firewood produced from a mixture of Caatinga biome species in Brazil. *International Journal of Forest Engineering*, 34(1), 54-63. <https://doi.org/10.1080/14942119.2022.2084674>
- Seki, M. (2023). Predicting stem taper using artificial neural network and regression models for Scots pine (*Pinus sylvestris* L.) in northwestern Türkiye. *Scandinavian Journal of Forest Research*, 38(1-2), 97-104. <https://doi.org/10.1080/02827581.2023.2189297>
- Silveira, D. D. P. (2014). *Estimation of the volume wooden stacked using digital images and neural networks* [Master dissertation]. Universidade Federal de Viçosa, Brazil. <http://locus.ufv.br/handle/123456789/3169>
- Soares, C. P. B., Ribeiro, J. C., Nascimento Filho, M. B. D., & Ribeiro, J. C. L. (2003). Determination of piling factors through digital photography. *Revista Árvore*, 27(4), 473-479. <https://doi.org/10.1590/S0100-67622003000400007>
- Soares, C.B.S., Paula Neto, F., & Souza, A.L. (2011). *Dendrometria e inventário florestal* (2nd ed.) [Dendrometry and forest inventory (2nd ed.)]. Universidade Federal de Viçosa.
- Tavares Júnior, I. D. S., de Souza, J. R. M., Lopes, L. S. D. S., Fardin, L. P., Casas, G. G., Oliveira Neto, R. R. D., Leite, R. V., & Leite, H. G. (2021). Machine learning and regression models to predict multiple tree stem volumes for teak. *Southern Forests: a Journal of Forest Science*, 83(4), 294-302. <https://doi.org/10.2989/20702620.2021.1994345>

**APPENDIX**

Supplementary Table 1

*Statistical performance of the best-selected models trained using artificial neural networks for each side of the staked timber*

Data splitting			Training			Validation		
Number of Stack	Stack side	ANN Model	bias	RMSE	r	bias	RMSE	r
1	A	2	0.0113	0.1840	0.9325	0.0149	0.1867	0.9307
1	B	5	0.0011	0.1972	0.9204	0.0074	0.1985	0.9191
2	A	1	0.0242	0.2081	0.9128	0.0176	0.2100	0.9099
2	B	5	0.0130	0.1769	0.9356	0.0114	0.1757	0.9372
3	A	3	0.0066	0.0908	0.9835	0.0045	0.1309	0.9656
3	B	1	-0.0026	0.1674	0.9436	0.0075	0.1991	0.9201
4	A	4	0.0059	0.1110	0.9753	0.0082	0.1198	0.9714
4	B	2	-0.0062	0.1368	0.9611	-0.0011	0.1081	0.9750
5	A	1	0.0013	0.0898	0.9838	-0.0041	0.0951	0.9819
5	B	1	0.0082	0.1454	0.9528	0.0134	0.1606	0.9428
6	A	4	0.0116	0.1525	0.9533	0.0107	0.1566	0.9504
6	B	1	0.0016	0.1246	0.9687	0.0053	0.1259	0.9676
7	A	4	0.0124	0.1777	0.9364	0.0174	0.1703	0.9402
7	B	2	0.0040	0.1263	0.9657	0.0063	0.1311	0.9625
8	A	3	0.0092	0.1679	0.9435	0.0147	0.1896	0.9284
8	B	3	-0.0065	0.1204	0.9711	-0.0057	0.1240	0.9692
9	A	4	0.0215	0.1783	0.9354	0.0234	0.1988	0.9192
9	B	1	-0.0075	0.1287	0.9661	-0.0015	0.1269	0.9673
10	A	1	0.0041	0.0830	0.9859	-0.0008	0.0751	0.9882
10	B	1	-0.0020	0.2072	0.9070	0.0032	0.2246	0.8913
11	A	3	0.0255	0.2955	0.8260	0.0437	0.3112	0.8089
11	B	2	0.0117	0.2339	0.8829	-0.0012	0.2137	0.9046
12	A	1	0.0194	0.2264	0.8957	0.0198	0.2413	0.8835
12	B	1	0.0021	0.2044	0.9159	0.0067	0.2074	0.9133
13	A	4	0.0045	0.2198	0.9027	0.0062	0.2281	0.8959
13	B	4	0.0069	0.3264	0.7752	0.0000	0.3618	0.7256
14	A	2	0.0203	0.2192	0.8929	0.0132	0.2263	0.8862
14	B	3	-0.0025	0.1613	0.9443	-0.0014	0.1600	0.9458
15	A	2	0.0338	0.2629	0.8544	0.0170	0.2461	0.8721
15	B	3	0.0038	0.1445	0.9561	0.0140	0.1795	0.9312
16	A	2	0.0366	0.2339	0.8865	0.0297	0.2437	0.8752
16	B	5	0.0181	0.2201	0.8971	0.0119	0.2144	0.9016

Data splitting			Training			Validation		
Number of Stack	Stack side	ANN Model	bias	RMSE	r	bias	RMSE	r
17	A	1	0.0257	0.2316	0.8932	0.0421	0.2673	0.8600
17	B	3	0.0108	0.1966	0.9220	0.0198	0.1971	0.9216
18	A	4	0.0226	0.2866	0.8366	0.0138	0.2866	0.8360
18	B	2	0.0149	0.1533	0.9514	0.0079	0.1151	0.9722
19	A	1	0.0126	0.1857	0.9268	0.0122	0.1784	0.9333
19	B	4	0.0160	0.3029	0.8166	0.0308	0.3038	0.8168
20	A	1	0.0298	0.2906	0.8303	0.0209	0.2973	0.8213
20	B	4	0.0077	0.2288	0.8935	0.0021	0.2320	0.8900
21	A	3	0.0162	0.2848	0.8379	0.0193	0.3134	0.8036
21	B	5	0.0079	0.2053	0.9095	0.0063	0.2273	0.8897
22	A	4	0.0184	0.2946	0.8247	0.0216	0.3217	0.7900
22	B	1	0.0024	0.0638	0.9913	0.0009	0.0534	0.9940
23	A	2	0.0309	0.2064	0.9166	0.0215	0.1938	0.9257
23	B	4	0.0024	0.1455	0.9577	0.0085	0.1594	0.9493
24	A	1	0.0367	0.2964	0.8230	0.0414	0.3099	0.8032
24	B	2	0.0056	0.1639	0.9456	0.0040	0.1620	0.9458
25	A	2	0.0348	0.2408	0.8848	0.0466	0.2505	0.8771
25	B	2	0.0228	0.1843	0.9330	0.0241	0.1946	0.9253
26	A	4	0.0099	0.1962	0.9225	0.0023	0.1894	0.9280
26	B	4	0.0035	0.1843	0.9296	-0.0040	0.1802	0.9328
27	A	3	0.0134	0.2721	0.8442	0.0110	0.2611	0.8557
27	B	1	0.0105	0.1912	0.9263	0.0061	0.1706	0.9411
28	A	2	0.0137	0.2528	0.8708	0.0070	0.2812	0.8399
28	B	4	0.0056	0.0799	0.9845	0.0038	0.1152	0.9673
29	A	1	0.0265	0.2445	0.8809	0.0453	0.2662	0.8588
29	B	3	0.0171	0.1711	0.9407	0.0175	0.1755	0.9377
30	A	1	0.0352	0.2959	0.8225	0.0273	0.2860	0.8338
30	B	3	0.0227	0.1425	0.9591	0.0130	0.1379	0.9621

Note. RMSE = Root Mean Square error and r = Coefcient Correlation



# Low Resource Malay Dialect Automatic Speech Recognition Modeling Using Transfer Learning from a Standard Malay Model

Tien-Ping Tan<sup>1\*</sup>, Lei Qin<sup>1</sup>, Sarah Flora Samson Juan<sup>2</sup> and Jasmina Yen Min Khaw<sup>3</sup>

<sup>1</sup>*School of Computer Sciences, Universiti Sains Malaysia, 11800 USM, Penang, Malaysia*

<sup>2</sup>*Faculty of Computer Science and Information Technology, Universiti Malaysia Sarawak, Sarawak, Malaysia*

<sup>3</sup>*Faculty of Information and Communication Technology, Universiti Tun Abdul Rahman, 31900 Kampar, Perak, Malaysia*

## ABSTRACT

Approaches to automatic speech recognition have transitioned from Hidden Markov Model (HMM)-based ASR to deep neural networks. The advantages of deep neural network approaches are that they can be developed quickly and perform better given large language resources. Nevertheless, dialect speech recognition is still challenging due to the limited resources. Transfer learning approaches have been proposed to improve speech recognition for low resources. In the first approach, the model is pre-trained on a large and diverse labeled dataset to learn the acoustic and language patterns from the speech signal. Then, the model parameters are updated with a new dataset, and the pre-trained model is fine-tuned on a low-resource language dataset. The fine-tuning process is usually completed by freezing the pre-trained layers and training the remaining layers of the model on the low-resource language corpus. Another approach is to use a pre-trained model to capture the compact and meaningful features as input to the encoder. Pre-training in this approach usually involves

using unsupervised learning methods to train models on a corpus of large amounts of unmarked data. It enables the model to learn the general patterns and relationships between the input speech signals. This paper proposes a training recipe using transfer learning and Standard Malay models to improve automatic speech recognition for Kelantan and Sarawak Malay dialects.

## ARTICLE INFO

### Article history:

Received: 25 June 2023

Accepted: 18 December 2023

Published: 16 July 2024

DOI: <https://doi.org/10.47836/pjst.32.4.06>

### E-mail addresses:

[tienping@usm.my](mailto:tienping@usm.my) (Tien-Ping Tan)

[qinlei@student.usm.my](mailto:qinlei@student.usm.my) (Lei Qin)

[sjsflora@unimas.my](mailto:sjsflora@unimas.my) (Sarah Samson Juan)

[khawym@utar.edu.my](mailto:khawym@utar.edu.my) (Jasmina Yen Min Khaw)

\* Corresponding author

**Keywords:** Automatic speech recognition, Malay dialects, Malay language, transfer learning

## INTRODUCTION

The performance of automatic speech recognition (ASR) has advanced rapidly in the past few decades, where the methods have transited from Hidden Markov Model (HMM)-based ASR to hybrid HMM/DNN (deep neural network) models, and now the focus is on end-to-end (E2E) deep neural networks. E2E deep neural networks have several advantages over other models. In general, the E2E deep neural networks can be developed faster compared to other models. For instance, the benchmark HMM-based models in Kaldi ASR (Povey et al., 2011) were developed by Johns Hopkins University and other institutions over an extended period since 2009. In contrast, a deep neural network model can be developed by a person in a few days. In addition, the performance of neural network models is also better than that of HMM when sufficient data is available for training (Watanabe et al., 2017). In an E2E deep neural network model, the joint modeling allows the entire system to be optimized to minimize the overall error, whereas in HMM-based ASR errors from one module can propagate through the system and accumulate, potentially degrading performance. Despite this, developing an ASR that performs well in low-resource languages is still very challenging. One of the challenges in low-resource ASR is dialect speech recognition.

Dialects occur as a result of culture, customs, and geography. With urbanization and social development, several dialects have become endangered or are spoken by only a small community. It means that most dialect corpora, if available, are small. In addition, it is difficult to transcribe dialect speech because no standard writing system exists for most dialects. Thus, dialect speakers who want to communicate in text may use different spelling rules. Hence, dialect speech recognition is a crucial and challenging problem in low-resource ASR.

One of the languages with many dialects is Malay. Malay belongs to the Austronesian family and is designated as the official language of Malaysia, Indonesia, Singapore, and Brunei. The Malay languages spoken in these countries may differ in pronunciation and vocabulary and are considered dialects. However, most Malay dialects do not have a written form. The formal Malay language recognized in Malaysia is Standard Malay, which originates from the Johor-Riau dialect (Asmah, 1991). The Johor-Riau dialect gained prominence due to the influence and importance of the empire during the 19th century. Malay dialects in Malaysia can be categorized based on their geographical distribution (Colins, 1989). The Malay dialects in Peninsular Malaysia are classified into seven groups: (1) the North-Western group, which includes Kedah, Perlis, Penang, and North Perak dialects; (2) the North-Eastern group, which is the Kelantan dialect; (3) the Eastern group, which is the Terengganu dialect, (4) the Southern group, which comprises Johor, Melaka, Selangor, and Perak (Southern), (5) the Negeri Sembilan group, (6) the Pahang dialect as a separate group, and (7) the Perak dialect, which covers the area of Central Perak.

Table 1 shows some text samples of Kelantan and Sarawak Malay compared to Standard Malay. There is no formal orthography for Malay dialects. The native speakers will write the dialect words based on how they are pronounced with reference from Standard Malay (Khaw et al., 2024). From these examples, we can see that the grammar of the dialect is similar. However, there are some insertions, deletions, and substitutions of letters in the dialect Malay words compared to the Standard Malay words. In addition, there are also unique vocabularies in Malay dialects that do not exist in Standard Malay.

Table 1

*Example of sentences in Kelantan dialect and Sarawak dialects and their translation in Standard Malay*

<b>Malay Dialects</b>	<b>Standard Malay</b>
kalu keno tange kito keno kulit mesti la gata (Kelantan Malay)	kalau kena tangan kita kena kulit mestilah gatal
cucuk pertama.. nunggu kitak lambat gilak. malas nak berbini (Sarawak Malay)	cucu pertama.. tunggu kamu lambat sangat. malas nak beristeri

There are many similarities between the Malay dialect and Standard Malay. In this study, we investigate using transfer learning in an end-to-end deep neural network to improve the performance of dialect Malay automatic speech recognition, specifically in Kelantan Malay and Sarawak Malay dialects.

### **Malay Automatic Speech Recognition**

There are a few studies on Malay automatic speech recognition. However, most of the works used HMM as their models. For example, Tan et al. (2008) trained a large vocabulary HMM/GMM ASR for read speech using Sphinx 3 ASR and obtained a WER of 14.6%. Chong et al. (2012) collected a Malay broadcast news and trained an HMM/GMM ASR using the Kaldi toolkit and obtained a WER of 17.1%. Juan et al. (2012) analyzed the speech recognition of Malay, Chinese, and Indian speakers and concluded that native Malay speakers have a lower WER compared to non-native speakers. Rahman et al. (2014) studied the Malay ASR for children. Their proposed approach achieves a WER of 24%.

### **Dialect Automatic Speech Recognition**

In general, automatic speech recognition models the acoustics, pronunciation, and language or word sequence given speech utterances and their respective transcription. In an HMM-based ASR, they are trained or built separately in different models: language, pronunciation, and acoustic (Koehn et al., 2007). A language model such as n-gram captures the linguistic context of a speech by modeling the relationship between words or sub-word tokens. A pronunciation dictionary normally models the relationship between the words and their pronunciations on phones, while an acoustic model contains the phones and their respective

acoustics features. However, in an E2E deep neural network ASR, such as the encoder-decoder model (Hori et al., 2017), the acoustics, pronunciation, and language representation are learned in a single deep neural network.

Several approaches can be applied to improve dialect ASR performance. First, collecting and augmenting dialect speech data can improve the result tremendously. It uses augmentation techniques such as pitch shifting, noise addition, and speed perturbation to create additional training examples (Renduchintala, 2018; Aitoulghazi et al., 2022). The approach is able to increase the size of the speech corpus more than one-fold. Second, studies show that acoustic modeling involving unsupervised learning of multilingual speech and transfer learning can improve ASR performance (Baevski et al., 2020). Third, modeling dialect words and their respective phones through grapheme-to-phoneme (G2P) can also improve accuracy. Fourth, including dialect-specific vocabulary, phrases, and text to model a separate language model for an E2E ASR can also be useful. This adaptation can involve incorporating dialect-specific language resources or adapting existing models using dialectal text data. Ali (2020) proposed to use a deep neural network consisting of a convolutional neural network (CNN), recurrent neural network, and a 4-gram language model for Arabic dialect speech recognition. A CTC beam search decoder guided by an n-gram language model was used for decoding. Next, we will focus on works that applied acoustic modeling approaches to improve the E2E ASR.

### **Acoustic Modeling in Dialect Automatic Speech Recognition**

A typical strategy to improve the performance of dialect ASR is to integrate dialect information into the model. Li et al. (2018) proposed using an encoder-decoder neural network to train an ASR model for seven English dialects: America, India, Britain, South Africa, Australia, Nigeria, Ghana, and Kenya. The authors proposed appending a tag that contains the dialect information to the transcription. It allows the system to perform automatic speech recognition and dialect classification at the same time. They also proposed using cluster adaptive training for their model. The size of the speech corpus in the study is very large, with about 40 thousand hours of noisy training data consisting of 35 million utterances. Compared with the dialect-independent models, the proposed model improves the word error rate (WER) by 1%–3%. Grace et al. (2018) proposed a similar approach, including the dialect information in the feature vector instead. They showed that the proposed model outperformed dialect-specific models.

Jain et al. (2018) proposed approaching the problem using dialect embedding inspired by x-vectors in speaker recognition (Snyder et al., 2018). They extracted the dialect embedding from a standalone time-delay neural network (TDNN) dialect classifier. The dialect embedding was used to augment the speech feature vectors consisting of MFCC and i-vectors. The authors trained a TDNN that jointly performs speech recognition and

dialect classification. The WER also improved in the range of 1%–3%. The approach of integrating dialect information is interesting. Nevertheless, this approach is suitable for training models with large speech resources.

Transfer learning has been proven to be an effective method to improve the performance of low-resource language ASR tasks because it allows models to learn from larger and more diverse data sets and transfer the knowledge to low-resource tasks. In E2E ASR, transfer learning can improve the performance of low-resource language tasks by leveraging the learned knowledge from high-resource language tasks. It is achieved by using a pre-trained model to improve the performance of the target model.

There are two approaches to implementing transfer learning. In the first approach, the model is pre-trained on a large and diverse labeled dataset to learn the acoustic and language patterns from the speech signal. Then, the model parameters are updated with a new dataset, and the pre-trained model is fine-tuned on a low-resource language dataset. The fine-tuning process is usually completed by freezing the pre-trained layers and training the remaining layers of the model on the low-resource language corpus.

Yan et al. (2018) used a Time Delay Neural Network with Long Short-Term Memory Projection (TDNN-LSTMP) for Tibetan dialects speech recognition. The speech corpus consists of Tibetan dialects U-Tsang and Amdo, with 62 hours and 52 hours of speech, respectively. The authors proposed using the Mandarin TDNN-LSTMP, trained using 1700 hours of speech, as the pre-trained model for Tibetan speech recognition. The experiments show that Mandarin to U-Tsang can achieve a remarkable performance, and the U-Tsang to Amdo is also effective. The approach obtains a relative improvement in WER, around 1%–4%.

Hou et al. (2020) transferred the large-scale E2E model trained using multilingual speech corpora from 42 languages as the pre-trained model to 14 low-resource languages. They used an encoder-decoder based on a transformer with hybrid CTC/attention for the ASR and language identification tasks. The pre-trained model contains speech data for around 1 to 7 hours. Their model achieved significantly superior results to the non-pre-trained baseline on the language-specific low-resource ASR task. The average WER for the 14 languages decreased from 83.4% to 60% for language-specific models.

Another approach is to use a pre-trained model to capture the compact and meaningful features as input to the encoder. Pre-training in this approach usually involves using unsupervised learning methods to train models on a corpus of large amounts of unmarked data. It enables the model to learn the general patterns and relationships between the input speech signals. One of the pre-trained models that received wide attention is the Wav2Vec2 (Baevski et al., 2020). The Wav2vec2 is the enhanced version of the Wav2Vec model that was trained using a self-supervised learning approach using a large dataset of 53,000 hours of unlabeled speech data from 53 languages. Once the model is trained on a large dataset, the representations learned by the acoustic encoder can be used as a starting point

for downstream speech recognition tasks. The idea is similar to fine-tuning large language models such as BERT for different natural language processing tasks. Baevski et al. (2020) trained a Wav2Vec2 model using LibriVox, and the pre-trained model was then fine-tuned with only 10 minutes of labeled data. Testing the trained model with Librispeech obtained a WER of 5.2% on the clean speech. The result is very promising, showing that ASR can be trained and performed well using a few minutes of speech data.

The raw speech is fed into a convolutional neural network (CNN) called the acoustic encoder to train the Wav2Vec2 model. The acoustic encoder then converts the raw audio waveform into a sequence of intermediate representations called acoustic features. The acoustic features are subsampled to reduce the temporal resolution. Context window masking encourages the model to learn representations that capture context. In this process, random subsequences of the subsampled acoustic features are masked, and the model is trained to predict the masked-out portions. The masked acoustic features are then passed through a stack of Transformer layers. The Transformer model learns to capture the relationships between different parts of the masked acoustic features and generate contextualized representations. The contextualized representations from the Transformer layers are used to calculate a contrastive loss. This loss encourages similar samples to have representations that are close together in the embedding space while pushing dissimilar samples apart. The model is trained using stochastic gradient descent (SGD). Figure 1 shows the Wav2Vec2 model.

Yi et al. (2021) applied Wav2Vec2 in speech recognition and obtained 20%–50% relative improvements in WER for low-resource languages. They used the CALLHOME telephone conversation speech corpus, which consists of six languages, namely Mandarin, English, Japanese, Arabic, German, and Spanish, with approximately 15 hours of labeled speech for fine-tuning.

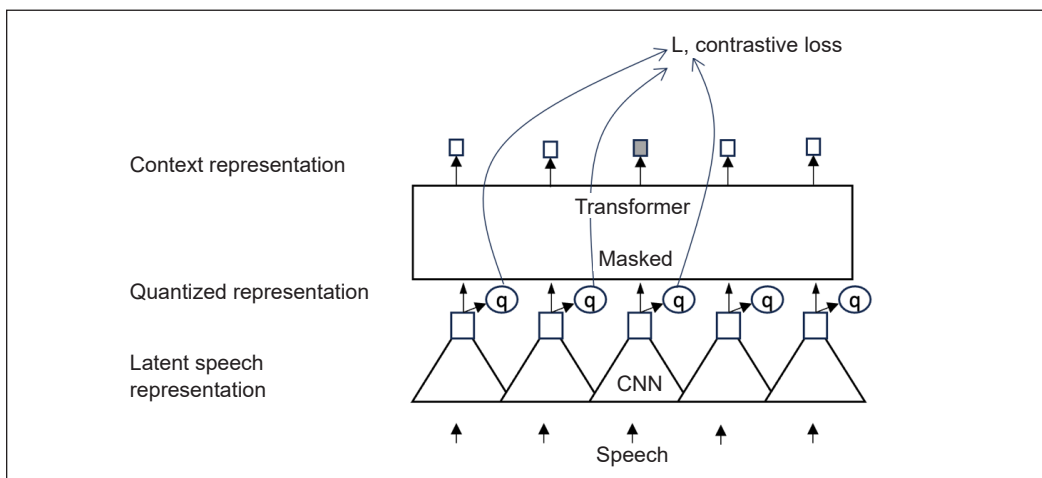


Figure 1. Wav2Vec2 (Baevski et al., 2020)

## MATERIALS AND METHODS

We first discuss the resources used in the study; then, we briefly analyze dialects in terms of the phonemes and the writing used in the dialects. Next, we propose the E2E ASR model used and the training steps to improve the E2E Malay dialect ASR model.

### Malay Dialect Speech Corpus

This study aims to investigate and propose an automatic speech recognition modeling for Malay dialects. We used the Malay dialect conversation speech corpus by Khaw et al. (2024) for training and testing. The speech corpus consists of dialogs in Kelantan Malay and Sarawak Malay. The corpus consists of many dialog conversations, each consisting of two Malay speakers who discuss a topic of interest for ten minutes in Malay dialect. The conversation was captured through the headset and recorded using the CoolEdit software, with the recording being set at 16 kHz/16 bits per sample. The speech was later transcribed to text by native speakers in the spoken dialect using Praat and translated into Standard Malay. Figure 2 shows a speech utterance transcribed in Kelantan Malay and Standard Malay. Table 2 describes the Malay dialect speech corpus.

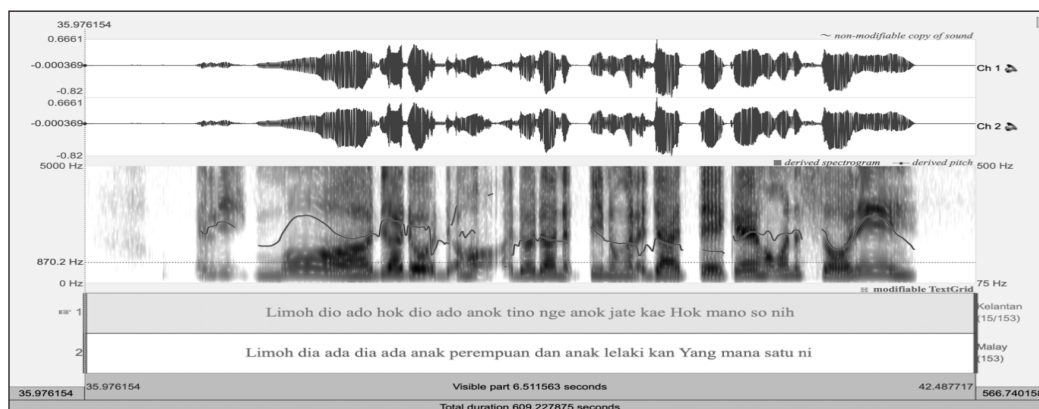


Figure 2. Praat was used to transcribe the conversation (Boersma, 2001)

Table 2  
Malay dialect conversation speech corpus

Description	Recorded Speech Conversation	
	Kelantan	Sarawak
<b>Age</b>	21–24	31
<b>Gender</b>	9 female, 1 male	1 female, 1 male
<b>Total Duration</b>	1 hour 40 mins	1 hour and 20 mins
<b>Number of Dialogs (2 speakers/dialog)</b>	10	8
<b>Training</b>	1 hour 20 mins, 8 speakers	1 hour, 2 speakers
<b>Testing</b>	20 mins, 2 speakers	20 mins, 2 speakers

## Malay Speech Corpus

Besides the Malay dialect speech corpus, we used a standard Malay speech corpus, MASS speech corpus, in our study. The MASS speech corpus (Tan et al., 2009) is a Standard Malay read speech corpus that consists of 199 speakers and about 140 hours of speech. Refer to Table 3 for information about the Standard Malay speech corpus speakers. About 120 hours of speech is used for training, while 20 hours is used for testing. The speakers consist of Malay, Chinese, Indian, and others.

Table 3  
*MASS speech corpus (Tan et al., 2009)*

	Speakers	Number	Hours	Age (mean, min, max)	Gender
Training	Malay	66	39	25.5, 10, 51	38F, 27M
	Chinese	98	73.5	27.3, 16, 38	65F, 34M
	Indian	8	5.5	24.4, 23, 28	1F, 7M
	Others	3	2	29.3, 28, 32	1F, 2M
Testing	Malay	8	6	28.8, 10, 48	4F, 4M
	Chinese	14	12	27.1, 20, 33	7F, 7M
	Indian	2	1.5	24.5, 23, 26	1F, 1M

## Linguistics

In terms of linguistics, Sarawak Malay and Kelantan Malay have similar phoneme sets to Standard Malay. Specifically, Sarawak Malay has all the phonemes in Standard Malay except /e/. Kelantan Malay also has all the phonemes in Standard Malay, and in addition, it has double consonants, which are not available in Standard Malay. Table 4 below shows the Standard Malay, Sarawak Malay, and Kelantan Malay phoneme sets. Nevertheless, the vocabulary used in Standard Malay and Malay dialects are different. The dialect speakers will insert, replace, or delete one or more letters in a Standard Malay word due to the difference in the pronunciation or phoneme in the dialect word. For instance, in Table 1, Kelantan dialect speakers insert the letter “k” into the word “*cucu*.” In addition, Kelantan dialect speakers delete the letter “l” from the word “*gatal*.” At the same time, Sarawak dialect speakers delete the second letter “a” from the word “*kalau*.” Kelantan dialect speakers may also substitute Standard Malay words that end

Table 4  
*Comparing the Standard Malay and Malay dialect phonemes (Khaw, 2017)*

	Phoneme
Standard Malay	p, b, t, d, k, g, ?, s, x, h, f, v, z, ʃ, tʃ, dʒ, l, r, m, n, ŋ, j, w, j, a, ə, e, i, o, u, ai, au, oi
Sarawak Malay	p, b, t, d, k, g, ?, s, x, h, f, v, z, ʃ, tʃ, dʒ, l, r, m, n, ŋ, j, a, ə, i, o, u, ai, au, oi
Kelantan Malay	p, b, t, d, k, g, ?, s, x, h, f, v, z, ʃ, tʃ, dʒ, l, r, m, n, ŋ, j, a, ə, e, i, o, u, ai, au, oi, pp, bb, tt, dd, kk, gg, ss, cc, jj, ll, mm, nn, ww

with “a” with “o.” In contrast, the Sarawak Malay speaker pronounces the Standard Malay word “*tunggu*” as “*nunggu*.”

On the other hand, if we analyze the distribution of letters in Sarawak Malay, Kelantan Malay, and Standard Malay, we can see that the letters in the dialect and Standard Malay have a positive correlation. Specifically, from Figure 3, we can see that Kelantan Malay has a lower percentage of “a” but a higher percentage of “k,” “o,” and “t” compared to Standard Malay. We can observe, for instance, in the Standard Malay words that end with the letter “a” or the last syllable that has a vowel “a,” the words in Kelantan Malay will substitute the letter “a” with “o.” Thus, words like “*nama*” and “*semak*” are written as “*namo*” and “*semok*”. Contrary to Sarawak Malay, the dialect has a lower percentage of “e,” “i,” “n,” “r,” and “u” but a higher percentage of “k” compared to Standard Malay. For Sarawak Malay, it can be observed that many words end with the letter “k” compared to Standard Malay.

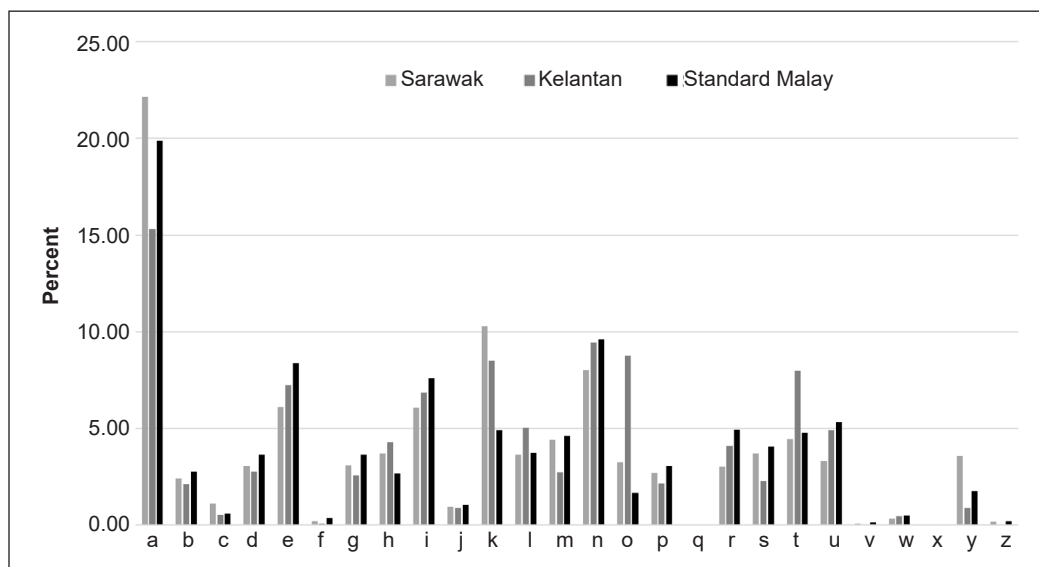


Figure 3. Distribution of letters in Malay Dialects and Standard Malay

Since there are many overlaps in the phoneme set, a positive correlation of letters between Malay dialect and Standard Malay, and abundant Standard Malay resources, we are interested in investigating using Standard Malay speech corpus to improve the dialect Malay speech corpus.

### E2E ASR Model

We propose an E2E deep neural network model that consists of a Wav2Vec2, an encoder model, and a classifier using CTC loss, as shown in Figure 4, for our automatic speech recognition. Wav2Vec2 is a pre-trained model that was self-supervised and trained using

a large amount of speech corpora. As for the encoder, we propose an encoder that consists of three deep neural network blocks, where each block consists of a linear layer, batch normalization layer, dropout layer, and leaky ReLU layer, as opposed to a more complex encoder such as a transformer encoder or encoder-decoder architecture for modeling Malay dialect because there are less than two hours of speech data available for training. The output layer is a linear layer of size 36 that will decode speech features to letters using Connectionist Temporal Classification (CTC) loss.

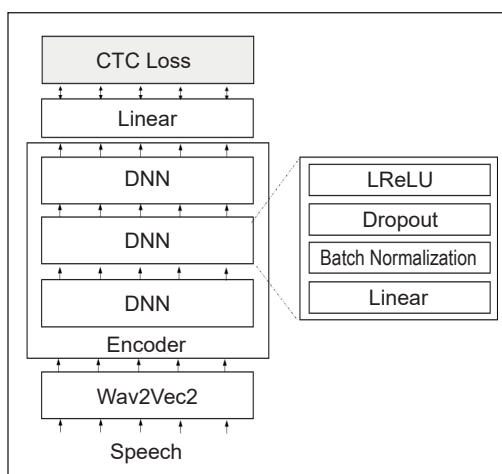


Figure 4. Wav2Vec2 and the encoder model were used

Since the amount of training data available is very small, we performed speech perturbation at the rate of 0.95% and 1.05% to the speech utterances to triple the amount of speech data available. We propose to train the pre-trained Wav2Vec2 and encoder model using Standard Malay speech data. Figure 5 shows our proposed modeling step. First, we used the training set of the MASS corpus, which consists of about 120 hours of Standard Malay read speech corpus to train the pretrained Wav2Vec2 (Wav2Vec2-XLSR-53) and

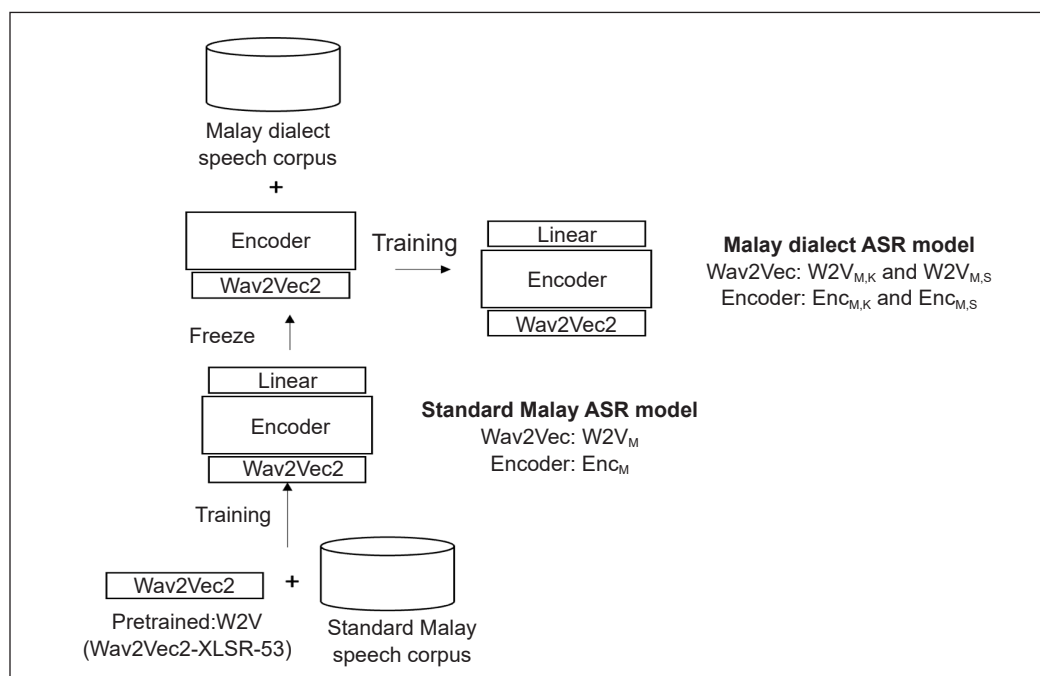


Figure 5. Proposed steps for Malay dialect ASR modeling

DNN model. It produces the trained Wav2Vec2 ( $W2V_A$ ) and encoder ( $Enc_A$ ) models. Besides, we also investigate the effect of using only the Standard Malay speech from native Malay speakers in the training. Thus, the subset of the MASS corpus that contains 39 hours of Standard Malay from native Malay speakers was used to train the pre-trained Wav2Vec2 and DNN model, which resulted in the  $W2V_M$  and  $Enc_M$  models. The weights of the Wav2Vec2 model and the encoder model produced were frozen. We then retrained the frozen models (either the Wav2Vec2 model or both the Wav2Vec2 model and encoder model) with dialect speech to produce Malay dialect ASR models. In Figure 5, we can use the Kelantan Malay dialect speech to train the pre-trained  $W2V_M$  model and the untrained encoder model to obtain the  $W2V_{M,K}$  and  $Enc_K$  models. Refer to the naming convention in Table 5 used for training the models.

Table 5  
The naming convention is used to train the different dialect models

Standard Malay speech	Dialect	Wav2Vec2	Encoder
Native and non-native Malay	-	$W2V_A$	$Enc_A$
Native Malay	-	$W2V_M$	$Enc_M$
-	Kelantan	$W2V_K$	$Enc_K$
-	Sarawak	$W2V_S$	$Enc_S$
Native and non-native Malay	Kelantan	$W2V_{A,K}$	$Enc_{A,K}$
Native Malay	Kelantan	$W2V_{M,K}$	$Enc_{M,K}$
Native and non-native Malay	Sarawak	$W2V_{A,S}$	$Enc_{A,S}$
Native Malay	Sarawak	$W2V_{M,S}$	$Enc_{M,S}$

## RESULTS AND DISCUSSION

The experiments used the Malay dialect conversation speech corpus (Khaw et al., 2024). Refer to Table 2 for information about the Malay dialect conversation speech corpus. The Malay dialect conversation speech recording and transcription were segmented using ffmpeg and script. For the training and testing and Kelantan Malay automatic speech recognition, eight dialogs from eight speakers (consisting of 1 hour 20 mins) were used for training (where two speakers took part in a dialog). In contrast, two separate dialogs from two speakers were used (consisting of 20 mins) for testing. There was no overlap in the speakers in the training and testing dataset. Since the amount of data available for training and testing is small, we used a cross-validation strategy to evaluate our model, where we rotated the training and testing data, as shown in Table 6. On the other hand, the training of Sarawak Malay was carried out using six dialogs (consisting of 1 hour), while two dialogs containing 20 mins were used for testing. Speakers overlap in training and testing for the Sarawak Malay dataset because we only have two speakers. The same cross-validation strategy was used to evaluate our model (Table 6).

Table 6

*Cross-validation strategy used to evaluate the model. The training and testing data are split as follows*

Dialect	Training set	Test set	Training Speakers	Testing Speakers
Kelantan Malay	Dialog 3, 4, 5, 6, 7, 8, 9 & 10	SET 1: Dialog 1 & 2	C, D, E, F, G, H, I, J	A, B
	Dialog 1, 2, 5, 6, 7, 8, 9 & 10	SET 2: Dialog 3 & 4	A, B, E, F, G, H, I, J	C, D
	Dialog 1, 2, 3, 4, 7, 8, 9 & 10	SET 3: Dialog 5 & 6	A, B, C, D, G, H, I, J	E, F
	Dialog 1, 2, 3, 4, 5, 6, 9 & 10	SET 4: Dialog 7 & 8	A, B, C, D, E, F, I, J	G, H
	Dialog 1, 2, 3, 4, 5, 6, 7 & 8	SET 5: Dialog 9 & 10	A, B, C, D, E, F, G, H	I, J
Sarawak Malay	Dialog 3, 4, 5, 6, 7 & 8	SET 1: Dialog 1 & 2	K, L	K, L
	Dialog 1, 2, 5, 6, 7 & 8	SET 2: Dialog 3 & 4	K, L	K, L
	Dialog 1, 2, 3, 4, 7 & 8	SET 3: Dialog 5 & 6	K, L	K, L
	Dialog 1, 2, 3, 4, 5 & 6	SET 4: Dialog 7 & 8	K, L	K, L

We were interested to know if there is any difference between Standard Malay and Standard Malay from only native Malay for the task. Thus, we used the MASS speech corpus (Tan et al., 2009), a Malay read speech corpus, for training the Standard Malay ASR models. The speechbrain toolkit was used in the experiments (Ravanelli et al., 2021). We trained two ASR models: a Standard Malay model using all the training sets of the MASS corpus (MASS<sub>A</sub>) and another Standard Malay model using only the Malay native speaker speech (MASS<sub>M</sub>). The MASS<sub>A</sub> described in Figure 1 was trained using about 120 hours of speech consisting of 191 speakers from the training set. Note that the pre-trained Wav2Vec2 model used in this training was Wav2Vec2-XLSR-53 from Huggingface. The result is a Standard Malay model: Wav2Vec2 model (W2V<sub>A</sub>) and encoder model (Enc<sub>A</sub>). To verify the effectiveness of the model proposed in Figure 1, we tested the model using about 20 hours of Standard Malay speech that consists of 22 speakers from the test set.

The word error rate (WER) was 16%. The result is very good, considering that we do not use any language model in the decoding, and the model used is simpler compared to an encoder-decoder model. We trained another Standard Malay model using about 39 hours of speech from 66 native Malay speakers. We trained the pre-trained Wav2Vec2-XLSR-53 model using the native Standard Malay speech in this case. The result is a Standard Malay model: Wav2Vec2 model (W2V<sub>M</sub>) and encoder model (Enc<sub>M</sub>). The Wav2Vec2 produces about 50 acoustic feature vectors for one second of speech. The size of the linear layer in the DNN was set at 1024, while the output linear layer was set at 36. The batch size is 6, and Adam optimizer was used. The maximum number of epochs was set at 30. The learning rate is set at  $10^{-3}$ . Greedy decoding was used to predict the best path for each utterance.

As described earlier, a cross-validation strategy was used in the experiments, where we rotate the speakers for training and testing. There were five test sets in the Kelantan Malay

experiment and four in the Sarawak Malay experiment, each consisting of two dialogs totaling 20 minutes. For the first baseline model, we tested the dialect models  $W2V_A+Enc_A$  and  $W2V_M+Enc_M$  on the dialect speech. Both models produced more than 90% WERs. The results show that the Standard Malay models cannot recognize the dialect words. Next, we trained the dialect ASR models depicted in Figure 5 using Kelantan dialect and Sarawak dialect speech, respectively, and the models produced are denoted as  $W2V_K+Enc_K$  and  $W2V_S+Enc_S$ , respectively. The initial pre-trained Wav2Vec2 model used in both cases was Wav2Vec2-XLSR-53. The baseline Kelantan Malay model and Sarawak Malay model have an average word error rate (WER) of 68.2% and 69.4%, respectively. Refer to Table 7 for the Kelantan Malay result and Table 8 for the Sarawak Malay result.

The results show that using a small amount of Malay dialect speech in training produces a better ASR model than Malay read speech. Nevertheless, the high WER was due to the very low resources used in the training, and the speech was spontaneous conversation. Nevertheless, the results were very good compared to the models trained using Standard Malay speech, where the WERs were more than 90%. We conducted three experiments to investigate the modeling steps proposed in Figure 5. In the first experiment, we train the pre-trained Standard Malay Wav2Vec model ( $W2V_A$ ) that we described earlier using the training set of Kelantan Malay speech and Sarawak Malay speech to produce the Kelantan Malay model ( $W2V_{A,K}$ ) and Sarawak Malay model ( $W2V_{A,S}$ ), respectively. The encoders were trained from scratch. Thus, the encoders produced for Kelantan Malay and Sarawak Malay were  $Enc_K$  and  $Enc_S$ , respectively. We tested the models using the Malay dialect speech test set using the same cross-validation strategy.

There is an improvement in the WER for Kelantan Malay and Sarawak Malay speech compared to the baseline, where the average WER was reduced to 65.6% and 62.1%, respectively. In the second experiment, we retrained the pre-trained Wav2Vec2 ( $W2V_A$ ) and pre-trained encoder ( $Enc_A$ , which were trained using Standard Malay speech). We obtained the Kelantan Malay model ( $W2V_{A,K}+Enc_{A,K}$ ) and the Sarawak Malay model ( $W2V_{A,S}+Enc_{A,S}$ ), respectively. We examined the models using the Malay dialect test sets using the cross-validation strategy, and the results show that the WER of both the Kelantan and Sarawak models slightly deteriorated compared to using only the Wav2Vec2 model. The result shows that pretraining Wav2Vec2 with Standard Malay speech can improve the WER of Malay dialect ASR, but pretraining the encoder with Standard Malay speech is not useful.

We repeated the previous experiment using the Wav2Vec2 pre-trained with Standard Malay speech from native speakers, which were  $W2V_M$ . Specifically, in experiment 3, we trained the pre-trained  $W2V_M$  using Kelantan Malay and Sarawak Malay speech and obtained  $W2V_{M,K}$  and  $W2V_{M,S}$ , respectively. Subsequently, we tested them using their respective test set. Interestingly, both models show lower WER compared to those trained using pre-trained  $W2V_A$  and those trained using native and non-native Malay speech. The

average WER for Kelantan Malay ASR drops more than 4%, while the average WER for Sarawak ASR improves by more than 7% compared to the baseline. Nevertheless, the improvement in the WER of Sarawak Malay ASR from using  $W2V_{M,S}$  is lower compared to the improvement in the WER of Kelantan Malay ASR from  $W2V_{M,K}$ . We did not evaluate the  $Enc_M$  since, in the previous experiment, combining the encoder showed no improvement in the WER.

First, the experiments show that training the pre-trained Wav2Vec2 using Malay speech is beneficial, as more discriminative features can be produced during feature extraction, which improves the WER. Furthermore, the results show that the pre-trained Wav2Vec2 that was trained with native Standard Malay speech,  $W2V_M$ , then used for training dialect models  $W2V_{M,K}$  and  $W2V_{M,K}$  give lower WERs compared to  $W2V_{A,K}$  and  $W2V_{A,K}$ , respectively. The non-native Malay speech may not be useful in adapting Wav2Vec2 to the Malay dialect ASR. On the other hand, since the writing of the dialect speakers is not the same, using the encoder model that is fine-tuned using Malay during training does not give a significant advantage, which can be seen in a drop in WER. The fourth observation is that the improvement in WER for the Malay dialect with a similar phoneme set to Standard Malay shows a higher improvement in WER when the native Malay Wav2Vec2 was used. Tables 7 and 8 show the complete results obtained in the experiments.

Table 7  
WER of the Kelantan Malay testing sets

Kelantan Malay					
Test set	Baseline: $W2V_A+Enc_A$	Baseline: $W2V_K+Enc_K$	$W2V_{A,K}+Enc_K$	$W2V_{A,K}+Enc_{A,K}$	$W2V_{M,K}+Enc_K$
SET 1	97.0%	66.4%	58.0%	58.5%	<b>57.2%</b>
SET 2	97.7%	68.4%	65.9%	66.1%	<b>64.3%</b>
SET 3	96.4%	64.0%	63.9%	64.9%	<b>60.5%</b>
SET 4	98.2%	76.3%	75.0%	75.1%	<b>74.1%</b>
SET 5	97.0%	65.9%	65.4%	65.0%	<b>63.9%</b>
Average	97.3%	68.2%	65.6%	65.9%	<b>64.0%</b>

Table 8  
WER of the Sarawak Malay testing sets

Sarawak Malay					
Test set	Baseline: $W2V_A+Enc_A$	Baseline: $W2V_S+Enc_S$	$W2V_{A,S}+Enc_S$	$W2V_{A,S}+Enc_{A,S}$	$W2V_{M,S}+Enc_S$
SET 1	95.2%	69.1%	65.4%	66.4%	<b>64.0%</b>
SET 2	93.5%	65.9%	58.5%	59.1%	<b>58.4%</b>
SET 3	93.4%	75.1%	<b>63.4%</b>	66.4%	63.6%
SET 4	95.1%	67.6%	61.3%	63.2%	<b>60.8%</b>
Average	94.3%	69.4%	62.1%	63.8%	<b>61.7%</b>

We further evaluate if the improvement is significant between the baselines and the proposed models ( $W2V_{M,K}+Enc_K$  or  $W2V_{M,S}+Enc_S$ ). We applied the T-Test known as the Matched Pairs Sentence-Segment Word Error (MAPSSWE) test to evaluate whether two ASR performances in WER are significantly different. Specifically, the null hypothesis is that the two systems have no performance difference. We used the Speech Recognition Scoring Toolkit (SCTK) version 2.4.12 (<https://www.nist.gov/itl/iad/mig/tools>) from the National Institute of Standards and Technologies (NIST), United States, to perform the tests. We performed a separate test for the Kelantan and Sarawak decoding/hypotheses. Since we experimented using cross-validation, the decoding from the respective model has to be merged and compared against the reference. For the Kelantan dialect models, the minimum p that the test finds a significant difference between  $W2V_K+Enc_K$  and  $W2V_{M,K}+Enc_K$  is  $p=0.004$  (99.6% confidence level), which is lower than the standard  $p=0.05$  (or higher than the 95% confidence level). On the other hand, for Sarawak dialect models, the minimum p that the test finds a significant difference between  $W2V_S+Enc_S$  and  $W2V_{M,S}+Enc_S$  is  $p=0.001$  (99.9% confidence level). Thus, both tests show that the results from the proposed models are statistically significant compared to the baseline results.

In addition, we select an utterance from Kelantan Malay and an utterance from Sarawak Malay for further analysis and discussion. We use word alignment for analysis as it is the commonly used approach in ASR. We conducted word alignment of the hypothesis and reference. The Kelantan Malay utterances were decoded using  $W2V_M+Enc_M$  and  $W2V_{M,K}+Enc_K$ . The following is the alignment of the decoding output (Kelantan\_001\_005\_002\_063.wav) that was produced using  $W2V_M+Enc_M$  (hypothesis) compared to the reference:

```

=====
Kelantan_001_005_002_063.wav, %WER 100.00 [ 6 / 6, 0 ins, 3
del, 3 sub ]
Ref: nok ;          gi          ; banyok ; banyok ;  tuh  ;  gok
      S  ;          S          ;  S    ;  D    ;  D    ;  D
Hyp: nur ; gibayebaannya ; tugu  ; <eps> ; <eps> ; <eps>
=====

```

The word alignment shows that the WER is 100%, which means none of the words produced is correct. However, we can see many characters are correct if we analyze the character alignment. The CER for the  $W2V_A+Enc_A$  is about 50% for the Kelantan Malay dialect and Sarawak Malay dialect using  $W2V_A+Enc_A$ . The result generally means that one in two characters are wrongly decoded, which is quite good compared to the word error rate. One of the reasons is due to the unseen phone in the Malay dialect. However, the average WER for the Kelantan Malay dialect and Sarawak Malay dialect of more than 90% show that the model has a problem with word segmentation. It is similar to human

auditory perception of an unknown language or dialect, where we have difficulty identifying words in the utterance even though we know all the sounds. When the model was trained with dialect speech, the same utterance was decoded by  $W2V_{M,K}+Enc_K$  to produce the following output:

```

=====
Kelantan_001_005_002_063.wav, %WER 16.67 [ 1 / 6, 0 ins, 0
del, 1 sub ]
Ref: nok ; gi ; banyok ; banyok ; tuh ; gok
    = ; = ; = ; = ; S ; =
Hyp: nok ; gi ; banyok ; banyok ; tu ; gok
=====

```

The WER of the utterance reduces to 16.67%, which means the dialect speech helps the model recognize unique phones in the dialect and word segmentation. Next, we analyze the alignment of the decoding output (Sarawak-03-96.wav) that was produced using  $W2V_M+Enc_M$  (hypothesis) compared to the reference:

```

=====
Sarawak-03-96.wav, %WER 125.00 [ 5 / 4, 1 ins, 0 del, 4 sub ]
Ref: umo ; baru ; brapa ; bulan ; <eps>
    S ; S ; S ; S ; I
Hyp: emua ; wa ; operwo ; ladn ; hinis
=====

```

The WER of the utterance is at 125%, which is very high. In the reference, we can see that some Sarawak Malay words are also Standard Malay words, such as “*baru*” and “*bulan*,” but the  $W2V_M+Enc_M$  model still has difficulty identifying these words. One of the reasons is that the dialect of Malay speech we are decoding is conversation speech, which is more spontaneous compared to read speech. Many ASR studies have shown that conversation speech has a higher WER compared to read speech. Second, the Standard Malay speech corpus is a read speech corpus. Thus, a mismatch in the training and testing speaking style may affect the decoding. After the model is trained with Kelantan Malay speech, the  $W2V_{M,S}+Enc_S$  model produces the following output. The WER of the utterance reduces to 50%, and the number of correctly decoded characters also increases.

```

=====
sarawak-03-96.wav, %WER 50.00 [ 2 / 4, 0 ins, 0 del, 2 sub ]
umo ; baru ; brapa ; bulan
  S ; S ; = ; =
rumo ; maok ; brapa ; bulan
=====

```

## CONCLUSION

In this study, we propose training steps that use the Wav2Vec2 that was fine-tuned using Standard Malay for subsequent modeling with Malay dialect speech for automatic speech recognition. The Wav2Vec2 that was fine-tuned using Standard Malay speech from native Malay speakers showed improved WER/CER for Kelantan and Sarawak Malay dialects. In contrast, the Standard Malay speech from all the speakers, including non-native speakers, only produces lower improvement in WER/CER in the Sarawak Malay speech recognition task. At the same time, there is no improvement in WER/CER in the Kelantan Malay speech recognition task.

The improvement in WER and CER is encouraging from Wav2Vec2; nevertheless, it is higher than the studies conducted by Yi et al. (2021) and Baevski et al. (2020). One possible reason may be that the amount of dialect speech used for training was smaller compared to Yi et al. (2021). Besides, we do not get a single-digit WER compared to Baevski et al. (2020) because the languages the authors tested were already modeled in the Wav2Vec2. On the other hand, the Malay dialects that were evaluated were not modeled in the Wav2Vec2. Nevertheless, Wav2Vec2 was trained in some Malay speech. The results show that the languages used to train the Wav2Vec2 affect the accuracy of the ASR. In addition, non-native Standard Malay speech does not seem useful in the Malay dialect ASR transfer learning.

## ACKNOWLEDGMENT

Oracle supported this research with a Research Grant. Award Number: CPQ-2746169, and Horizon 2020 research and innovation program under the Marie Skłodowska-Curie grant agreement No. 101007666.

## REFERENCES

- Aitoulghazi, O., Jaafari, A., & Mourhir, A. (2022). DarSpeech: An automatic speech recognition system for the Moroccan dialect. In *2022 International Conference on Intelligent Systems and Computer Vision (ISCV)* (pp. 1-6). IEEE Publishing. <https://doi.org/10.1109/ISCV54655.2022.9806105>
- Ali, A. R. (2020). Multi-dialect Arabic speech recognition. In *2020 International Joint Conference on Neural Networks (IJCNN)* (pp. 1-7). IEEE Publishing. <https://doi.org/10.1109/IJCNN48605.2020.9206658>
- Asmah, H. O. (1991). *Aspek bahasa dan kajiannya* [Aspects of language and its study]. Dewan Bahasa dan Pustaka.
- Baevski, A., Zhou, H., Mohamed, A., & Auli, M. (2020). wav2vec 2.0: A framework for self-supervised learning of speech representations. *ArXiv*, Article 2006.11477. <https://doi.org/10.48550/arXiv.2006.11477>
- Boersma, P. (2001). Praat: A system for doing phonetics by computer. *Glott International*, 5(9) 341-345.

- Chong, T. Y., Xiao, X., Xu, H., Tan, T. P., Chau-Khoa, P., Lyu, D. C., Chng, E. S., & Li, H., (2013). The development and analysis of a Malay broadcast news corpus. In *2013 International Conference Oriental COCODA held jointly with 2013 Conference on Asian Spoken Language Research and Evaluation (O-COCODA/CASLRE)* (pp. 1-5). IEEE Publishing. <https://doi.org/10.1109/ICSDA.2013.6709862>
- Colins, J. T. (1989). Malay dialect research in Malaysia: The issue of perspective. *Bijdragen tot de Taal-, Land- en Volkenkunde*, 235-264.
- Grace, M., Bastani, M., & Weinstein, E. (2018). Occam's adaptation: A comparison of interpolation of bases adaptation methods for multi-dialect acoustic modeling with LSTM. In *2018 IEEE Spoken Language Technology Workshop (SLT)*, (pp. 174-181). IEEE Publishing. <https://doi.org/10.1109/SLT.2018.8639654>
- Hori, T., Watanabe, S., Zhang, Y., & Chan, W. (2017). Advances in joint CTC-attention based end-to-end speech recognition with a deep CNN encoder and RNN-LM. *ArXiv*, Article 1706.02737. <https://doi.org/10.48550/arXiv.1706.02737>
- Hou, W., Dong, Y., Zhuang, B., Yang, L. Shi, J. & Shinozaki, T. (2020). Large-scale end-to-end multilingual speech recognition and language identification with multi-task learning. In *Interspeech* (pp. 1037-1041). ISCA Publishing. <https://doi.org/10.21437/Interspeech.2020-2164>
- Jain, A., Upreti, M. & P. Jyothi, P. (2018) Improved accented speech recognition using accent embeddings and multi-task learning. In *Proceedings of Interspeech* (pp. 2454-2458). ISCA Publishing.
- Juan, S. S., Besacier, L., & Tan, T. P. (2012). Analysis of Malay speech recognition for different speaker origins. In *2012 International Conference on Asian Language Processing* (pp. 229-232). IEEE Publishing. <https://doi.org/10.1109/IALP.2012.23>
- Khaw, J. Y. M. (2017). *Bootstrapping Kelantan and Sarawak Malay dialect models on text and phonetic analyses in text-to-speech system* [Doctorate Dissertation]. Universiti Sains Malaysia.
- Khaw, J. K. M., Tan, T. P. & Ranaivo-Malancon, B. (2024). Hybrid distance-statistical-based phrase alignment for analyzing parallel texts in standard Malay and Malay dialects. *Malaysian Journal of Computer Science*, 37(1), 89–106. <https://doi.org/10.22452/mjcs.vol37no1.5>
- Koehn, P., Hoang, H., Birch, A., Callison-Burch, C., Federico, M., Bertoldi, N., Cowan, B., Shen, W., Moran, C., Zens, R., Dyer, C., Bojar, O., Constantin, A., & Herbst, E. (2007). Moses: Open source toolkit for statistical machine translation. In *Proceedings of the 45th Annual Meeting of the Association for Computational Linguistics Companion Volume Proceedings of the Demo and Poster Sessions*, (pp. 177-180). Association for Computational Linguistics.
- Li, B., Sainath, T. N., Sim, K. C., Bacchiani, M., Weinstein, E., Nguyen, P., Chen, Z., Wu, Y. & Rao, K. (2018) Multi-dialect speech recognition with a single sequence-to-sequence model. In *2018 IEEE International Conference on Acoustics, Speech and Signal Processing (ICASSP)*, (pp. 4749-4753). IEEE Publishing. <https://doi.org/10.1109/ICASSP.2018.8461886>
- Povey, D., Ghoshal, A., Boulianne, G., Burget, L., Glembek, O., Goel, N., Hannemann, M., Motlíček, P., Qian, Y., Schwarz, P., Silovský, J., Stemmer, G. & Vesel, K. (2011). The Kaldi speech recognition toolkit. In *IEEE 2011 workshop on automatic speech recognition and understanding* (pp. 1-4). IEEE Signal Processing Society.

- Rahman, F. D., Mohamed, N., Mustafa, M. B., & Salim, S. S. (2014). Automatic speech recognition system for Malay speaking children. In *2014 Third ICT International Student Project Conference (ICT-ISPC)* (pp. 79-82). IEEE Publishing. <https://doi.org/10.1109/ICT-ISPC.2014.6923222>
- Ravanelli, M., Parcollet, T., Plantinga, P. W., Rouhe, A., Cornell, S., Lugosch, L., Subakan, C., Dawalatabad, N., Heba, A., Zhong, J., Chou, J., Yeh, S., Fu, S., Liao, C., Rastorgueva, E. N., Grondin, F., Aris, W., Na, H., Gao, Y., Mori, R. D., & Bengio, Y. (2021). SpeechBrain: A general-purpose speech toolkit. *ArXiv*, Article 2106.04624. <https://doi.org/10.48550/arXiv.2106.04624>
- Renduchintala, A., Ding, S., Wiesner, M., & Watanabe, S. (2018). Multi-modal data augmentation for end-to-end ASR. *ArXiv*, Article 1803.10299. <https://doi.org/10.48550/arXiv.1803.10299>
- Snyder, D., Garcia-Romero, D., Sell, G., Povey, D., & Khudanpur, S. (2018). X-Vectors: Robust DNN embeddings for speaker recognition. In *2018 IEEE International Conference on Acoustics, Speech and Signal Processing (ICASSP)*, (pp. 5329-5333). IEEE Publishing. <https://doi.org/10.1109/ICASSP.2018.8461375>
- Tan, T. P., Xiao, X., Tang, E. K., Chng, E. S., & Li, H. (2009). MASS: A Malay language LVCSR corpus resource. In *2009 Oriental COCODA International Conference on Speech Database and Assessments* (pp. 25-30). IEEE Publishing. <https://doi.org/10.1109/ICSODA.2009.5278382>
- Watanabe, S., Hori, T., Kim, S., Hershey, J. R., & Hayashi, T. (2017). Hybrid CTC/attention architecture for end-to-end speech recognition. In *IEEE Journal of Selected Topics in Signal Processing*, (Vol. 11, No. 8, pp. 1240-1253). IEEE Publishing. <https://doi.org/10.1109/JSTSP.2017.2763455>
- Yan, J., Yu, H., & Li, G. (2018). Tibetan acoustic model research based on TDNN. In *2018 Asia-Pacific Signal and Information Processing Association Annual Summit and Conference (APSIPA ASC)* (pp. 601-604). IEEE Publishing. <https://doi.org/10.23919/APSIPA.2018.8659584>
- Yi, C., Wang, J., Cheng, N., Zhou, S., & Xu, B. (2021). Transfer ability of monolingual Wav2vec.0 for low-resource speech recognition. In *2021 International Joint Conference on Neural Networks (IJCNN)* (pp. 1-6). IEEE Publishing. <https://doi.org/10.1109/IJCNN52387.2021.9533587>



## The Green Energy Effect on an HCCI Engine from Used Cooking Oil-based Biodiesel from Malaysia

Muntasser Abdulabbas Mossa\*, Abdul Aziz Hairuddin, Nuraini Abdul Aziz and Hasyuzariza Muhamad Tobib

*Department of Mechanical and Manufacturing Engineering, Faculty of Engineering, Universiti Putra Malaysia, 43400 UPM, Serdang, Selangor, Malaysia*

### ABSTRACT

Emissions from internal combustion engines (ICEs) significantly impact the environment, leading continents worldwide to work towards reducing them. The industry is increasingly leaning towards electric powertrains. However, power plants still utilize ICEs as generators, contributing to global pollution. Consequently, ICE emissions are garnering international attention. Alternatives like the Homogeneous Charge Compression Ignition (HCCI) engine and biodiesel fuels are being explored. HCCI engines have not been extensively tested with Used Cooking Oil (UCO) biodiesel. This study investigates the performance and emissions of HCCI engines using UCO-based biodiesel. This study tested an air-cooled, single-cylinder, 4-stroke diesel engine operating at 3600 rpm with a displacement of 0.219 liters. The HCCI mode was activated during preheating and run at 2700 rpm under varying biodiesel blend percentages and intake temperatures. In HCCI mode, brake-specific fuel consumption (BSFC) increased, peaking at a 90°C intake temperature. Diesel fuel in-cylinder pressure reached a maximum of 81 bars at 90°C, decreasing to 79 bars at 70°C. The HCCI mode resulted in lower NO<sub>x</sub>, CO, and UHC emissions. Higher biodiesel blend ratios further reduced CO emissions. Raising the intake air temperature to 90°C lowered NO<sub>x</sub> emissions by 96.66%, from 150 ppm to 5 ppm. Using green energy sources as fuel in HCCI engines significantly reduced emissions in this study, suggesting their potential as a future fuel for advanced engines.

### ARTICLE INFO

#### Article history:

Received: 25 June 2023

Accepted: 18 December 2023

Published: 16 July 2024

DOI: <https://doi.org/10.47836/pjst.32.4.07>

#### E-mail addresses:

[memo.alprince41@gmail.com](mailto:memo.alprince41@gmail.com) (Muntasser Abdulabbas Mossa)

[ahziz@upm.edu.my](mailto:ahziz@upm.edu.my) (Abdul Aziz Hairuddin)

[nuraini@upm.edu.my](mailto:nuraini@upm.edu.my) (Nuraini Abdul Aziz)

[hasyuzariza5914@gmail.com](mailto:hasyuzariza5914@gmail.com) (Hasyuzariza Muhamad Tobib)

\* Corresponding author

**Keywords:** Biodiesel, CI engine, emissions, HCCI, UCO

## INTRODUCTION

HCCI (Homogeneous Charge Compression Ignition) engines have a promising future in various applications. These engines are notable for their fuel efficiency and low NO<sub>x</sub> emissions. In certain HCCI engines, fuel is injected during the intake stroke to create a homogeneous mixture. Effective control of ignition and combustion in HCCI engines is crucial and requires specific techniques. Studies have shown that using particular fuel blends can control the combustion process in HCCI engines, enhancing efficiency while reducing emissions (Khandal et al., 2019; Özer et al., 2021; Thrlng, 2011). Fuel is injected into the inlet manifold, mixed with hot air, and the air temperature is further increased using an inlet air heater (Özer et al., 2021). The compression ratio is adjusted, and an EGR (Exhaust Gas Recirculation) system is employed to achieve HCCI mode. Challenges in premixed diesel-fueled HCCI engines include early ignition leading to knocking, increased liquid fuel presence in the intake manifold, and reduced combustion efficiency, resulting in higher HC emissions.

Several studies have reported reductions in NO<sub>x</sub> and other emissions using the premixed technique for diesel-HCCI (Christensen et al., 1999; Garcia et al., 2011; Gray & Ryan, 1997) also used the premixed technique for diesel-HCCI and reported a reduction in NO<sub>x</sub> and other emissions. Early direct injection in HCCI allows efficient fuel vaporization and mixing in hot compressed air. Engine combustion is influenced by several factors, including the homogeneity of the air-fuel mixture, inlet temperature, and chemical kinetics (Banapurmath et al., 2008). A lower percentage of biodiesel blend has been found to improve Brake Thermal Efficiency (BTE) and slightly decrease Brake Specific Fuel Consumption (BSFC). Other studies have experimented with methyl esters combined with Honge oil, jatropha oil, and sesame oil in DI diesel engines, often resulting in lower performance (Rashed et al., 2016). Methyl esters were used with Honge oil, jatropha oil, and sesame oil in a DI diesel engine, resulting in low performance. Puhan et al. (2005) improved Brake Power (BP) and BSFC performance in a typical diesel engine fueled with a blend of Pongamia Pinnanta methyl ester and diesel of up to 40% volume compared to just diesel. Further research indicates that biodiesel can be as effective as traditional diesel in CI engines (Abed et al., 2018; Banerjee et al., 2016; Tamilselvan et al., 2018).

However, a study by Rizvi (2009) noted that engine performance is often limited to specific parameters like BSFC, BP, and BTE. Factors such as fuel properties, injection timing and pressure, air-fuel blend, and fuel amount significantly affect engine performance. HCCI engines typically have lower BTE compared to CI engines. Many studies have explored methods to control the start of combustion in HCCI engines, employing techniques like varying inlet air temperature, pressure rates, equivalence ratios, EGR systems, ignition of fuels, compression ratios, and variable valve timing (Janecek et al., 2017; Puškár & Kopas, 2018; Strandh et al., 2004). Intake air heating is a common method to achieve HCCI

mode, where the hot mixture is obtained using an electronic air heater. Studies have also shown that methods like EGR can adjust combustion timing, influencing the temperature of the mixture and negative valve overlap (NVO) (Noh & No, 2017; Putrasari et al., 2017). A variable compression ratio (VCR) change can also affect combustion timing (Au et al., 2001; Christensen & Johansson, 1998).

Also, the change in variable compression ratio (VCR) to influence combustion timing was investigated by Mase et al. (1998) by examining the impact of temperature and equivalence ratio on HCCI engine performance, highlighting the control of ignition timing and combustion as primary challenges and examined the impact of temperature and equivalence ratio on HCCI engine performance, highlighting the control of ignition timing and combustion as primary challenges. Kimura et al. (2001) examined the impact of temperature and equivalence ratio on HCCI engine performance, highlighting the control of ignition timing and combustion as primary challenges. The study revealed that significantly varying the equivalence ratio affects in-cylinder pressure and temperature, with a shorter ignition delay leading to higher peak pressure and temperature (Bedoya et al., 2012). Heating the inlet air is a useful method for controlling ignition timing in HCCI engines, as it reduces air charge density and affects combustion quality (Rahbari, 2016). Heating the inlet air reduces the air charge density, affecting the combustion quality (Hasan & Rahman, 2016; Sundararajan et al., 2016).

However, many researchers prefer installing the heater because it is the easiest method to achieve HCCI mode (Strålin et al., 2003). Late direct ignition in HCCI involves high air-fuel mixing to enhance combustion characteristics. Port-injected HCCI engines create external mixtures operating at 0.6 MPa, and low injection pressure may hinder vaporization in the intake manifold. A homogeneous mixture requires fuel vapor (Urata et al., 2004). A homogenous combination requires fuel vapor (Ghorbanpour & Rasekhi, 2013). In their study, Channapattana et al. (2023) analyzed the energy and exergy of DI-CI engines using nickel oxide nanoparticle-enhanced *azadirachta indica* biofuel. They uncovered notable findings regarding the influence of fuel injection timing on engine efficiency, demonstrating the potential of advanced biofuels in improving the performance of such engines (Channapattana et al., 2023). Similarly, Srinidhi et al. (2022) explored the effects of fuel injection timing on CI engines fueled with neem biodiesel blends. Combining experimental data with numerical simulations provided insights into optimizing engine performance through precise fuel injection timing in the context of biodiesel usage (Srinidhi et al., 2022).

HCCI engine power depends on various operational factors, including engine thermal management, which controls combustion timing by regulating inlet air temperatures. Higher temperatures accelerate combustion and chemical processes. Factors like inlet pressure, fuel type, engine speed, and heat transfer influenced combustion timing (Rahbari, 2016).

Research on fuel injection strategies in HCCI engines suggests modes that enhance thermal efficiency compared to CI engines. Ganesh et al. (2008) found that using fuel injection techniques and an electromagnetic valve-train allows the HCCI engine to operate effectively at high and low loads. Direct fuel injection in the compression stroke improves engine performance significantly compared to port injection. Engine power depends on heating rates, and intake temperatures affect HCCI combustion (Sivarethinamohan et al., 2022). Running the HCCI engine with lean blends using a low compression ratio and high intake temperature can be effective.

Injecting fuel in the exhaust stroke with re-compression applied on the NVO leads to higher in-cylinder pressure and a high combustion temperature (Singh & Agarwal, 2012). Organized combustion can enhance ignition timing and improve temperatures, thereby improving HCCI combustion (Ganesh & Nagarajan, 2010). The Indicated Mean Effective Pressure (IMEP) is a uniform pressure measure required for an engine's stroke power, equivalent to the work done to achieve pressure inside the chamber. Research indicates that IMEP is an effective metric for evaluating engine performance (Sahu et al., 2021). Studies on four-stroke HCCI engines reveal the possibility of achieving higher IMEP using a lean blend fuel with a high compression ratio (Shi et al., 2006). One method for improving the lower load efficiency in HCCI mode operations is using DI and creating rich combustion (Hunicz et al., 2015; Sivarethinamohan et al., 2022).

The Brake Thermal Efficiency (BTE) of an HCCI (Homogeneous Charge Compression Ignition) engine, which is the output power divided by the input power, indicates the engine's effectiveness based on the energy provided by the fuel. BTE is a common measure of engine performance. CI (Compression Ignition) engines have been observed to have a lower BTE compared to HCCI engines (Ogawa et al., 2003). To address this issue, using a mixture of biodiesel and diesel has been shown to supply higher BTE, as demonstrated in previous studies (Mancaruso & Vaglieco, 2010). NO<sub>x</sub> production was found to be lower in diesel engines. In some experiments, engine performance using conventional diesel in HCCI engines was compared with CI engines (Sahu et al., 2021).

Different engines, specifically CI and HCCI, were investigated for operating performance (Hwang et al., 2016). Jafarmadar and Nemati (2017) discussed operating a direct injection, four-stroke, 4-cylinder, 16.5:1 compression ratio CI engine using diesel fuel and DME biofuel in both DI (Direct Injection) and HCCI modes. Biodiesel, an alternative renewable fuel made from the chemical reaction of various lipids such as animal fat, algae, soybean oil, vegetable oil, and palm oil with alcohol to produce fatty acid esters, has been researched extensively (Gharehghani, 2019). Biodiesel is easy to store and handle, similar to regular diesel fuel. It has a high flash point, is biodegradable, can help keep the fuel system clean, and has good lubricity with low emissions. Many countries are exploring biodiesel as a replacement for fossil fuels. The homogenous air-fuel combination in HCCI

engines reduces emissions and improves combustion. Various biodiesels, such as those derived from palm oil, algae, spent cooking oil, and soybean and animal fat waste, have been used in CI engines to minimize emissions (Fahd et al., 2013; Jiménez-Espadafor et al., 2012; Muhamad Tobib et al., 2021; Singh et al., 2014). Several studies have operated diesel engines on biodiesel to test emissions and performance (Iwashiro et al., 2002; Singh et al., 2014; Zhang et al., 2012), and many have examined biodiesel in HCCI engines to minimize emissions (Rajesh et al., 2020; Sanjid et al., 2013; Urata et al., 2004). Low-oxygen, nitrogen, and cetane fuels have been effective in engines (EL-Seesy et al., 2021; Gad et al., 2020; Tobib et al., 2019).

Hydrocarbon (HC) emissions result from two factors: excess fuel in the combustion chamber not being fully utilized and incomplete combustion in the engine's cold regions. As HCCI engine fuel is lean, HC is usually fully combusted. HC emissions in HCCI engines typically originate from cracks in the cylinder wall, especially near the piston rings. HCCI engines generally start HC formation at higher fuel-air ratios (Hasan et al., 2015; Khayum et al., 2021; Satyanarayana et al., 2018). The rate of HC can be reduced by blending diesel with biodiesel and using EGR (Exhaust Gas Recirculation). Ali et al. (2021) examined the effects of cooled external and internal EGR on the performance, combustion, and emissions of an HCCI engine, showing decreased cylinder pressure and NO<sub>x</sub> emissions but increased HC and CO emissions. Giakoumis et al. (2012) utilized a single-cylinder, four-stroke engine with a 19:1 compression ratio at 3000 rpm. The study tested different fuel spray angles and a dual injection strategy, with early timing injection for HCCI operation, resulting in reduced NO<sub>x</sub>, HC, and CO emissions but increased BSFC (Brake Specific Fuel Consumption).

Dharma et al. (2016), Gad and Ismail (2021) and Li et al. (2021) used Rapeseed methyl ester as fuel to run a CI engine in HCCI mode. The conditions included a constant speed with different EGR rates and loads. The engine, a single-cylinder, four-stroke direct injection diesel engine with a 17.5:1 compression ratio and 1500 rpm speed, showed improved NO<sub>x</sub> emissions but increased HC and CO emissions at varying EGR rates (0%, 10%, 20%, and 30%). CO emissions generally form in engines due to partial combustion of fuel. In HCCI engines, a high rate of CO is produced compared to CI engines, as demonstrated in various studies (Hasan et al., 2015; Kumar & Rehman, 2016). Blending diesel with biodiesel has somewhat reduced CI emissions (Ali et al., 2021; No, 2016), where low CO emissions in HCCI engines were observed.

In contrast, emission issues remain in both CI and SI (Spark Ignition) engines. Kumar and Rehman (2016) used a 17.5:1 compression ratio diesel engine with a single-cylinder at 1500 rpm, run at different loads and EGR rates. They used external mixture formation to increase fuel vapor in the HCCI engine, mixing with air in the intake stroke with an injection pressure of 200 bar. The results showed decreased peak pressure and reduced NO<sub>x</sub>,

HC, and CO emissions. Geng et al. (2017) investigated ways to reduce emissions in HCCI engines, which traditionally are inefficient and emit significant CO and UHC (Unburned Hydrocarbons). Using used cooking oil (UCO)--based biodiesel in HCCI engines is limited worldwide, and its emissions levels in HCCI mode have not been extensively researched. In Malaysia and some other countries, UCO is derived from palm oil-based biodiesel (Sahu et al., 2021). The main objective of this study is to reduce emission levels of HCCI engines fueled by UCO-based biodiesel.

## MATERIALS AND METHODS

This study employed a single-cylinder, 4-stroke, air-cooled diesel engine with a rotational speed of 3600 rpm. The engine, with a capacity of 0.219 liters, was converted to operate in HCCI (Homogeneous Charge Compression Ignition) mode. Engine power was measured using an eddy current dynamometer. A Port Fuel Injection (PFI) system and a preheater were installed in the intake manifold. Figure 1(a) depicts the engine setup and various sensors and actuators. The setup schematic and engine specifications are presented in Figure 2 and Table 1, respectively. Figure 2 illustrates the experimental engine configuration, including its connections to the fuel supply system with Direct Injection (DI), PFI, and return fuel lines. Figure 1(b) shows the connection of the dynamometer and the Engine Control Unit (ECU) to all the engine sensors. Exhaust gas emissions were analyzed using exhaust gas analyzers.

This study used two different fuel types: diesel and cooking oil (UCO). The properties of diesel and UCO-based biodiesel fuel are detailed in Table 2. The fuel was mixed in the laboratory to create a biodiesel blend, varying the diesel volume with UCO biodiesel percentages of 5%, 10%, 15%, and 20%. The biodiesel was tested up to B20 blend due to fuel stability issues and the current biodiesel market conditions in Malaysia, where B10 blended fuel will soon be introduced. Engine modifications for conversion to HCCI mode included the installation of a heater and PFI, as shown in Figure 2. A 5 kW heater was installed in the intake manifold to ensure high inlet temperatures entering the combustion chamber. A high-pressure (200 bar) Volkswagen injector with a 60° angle was used as the PFI to achieve a fine mist fuel spraying pattern. The ECU controlled the PFI, adjusting the amount of fuel injected by changing its pulse width. A temperature sensor was employed to measure the intake air temperature and was connected to a dedicated reader. The engine transition from DI to HCCI mode involved using the PFI and heater, where the direct injection valve was closed, and the PFI was opened to deliver fuel from the tank to the high-pressure port injector (Jiménez-Espadafor et al., 2012).

This experiment examined the performance and emissions of diesel and UCO (Used Cooking Oil)–based biodiesel in an HCCI (Homogeneous Charge Compression Ignition) engine. Various tests were conducted to determine the optimal intake temperature for

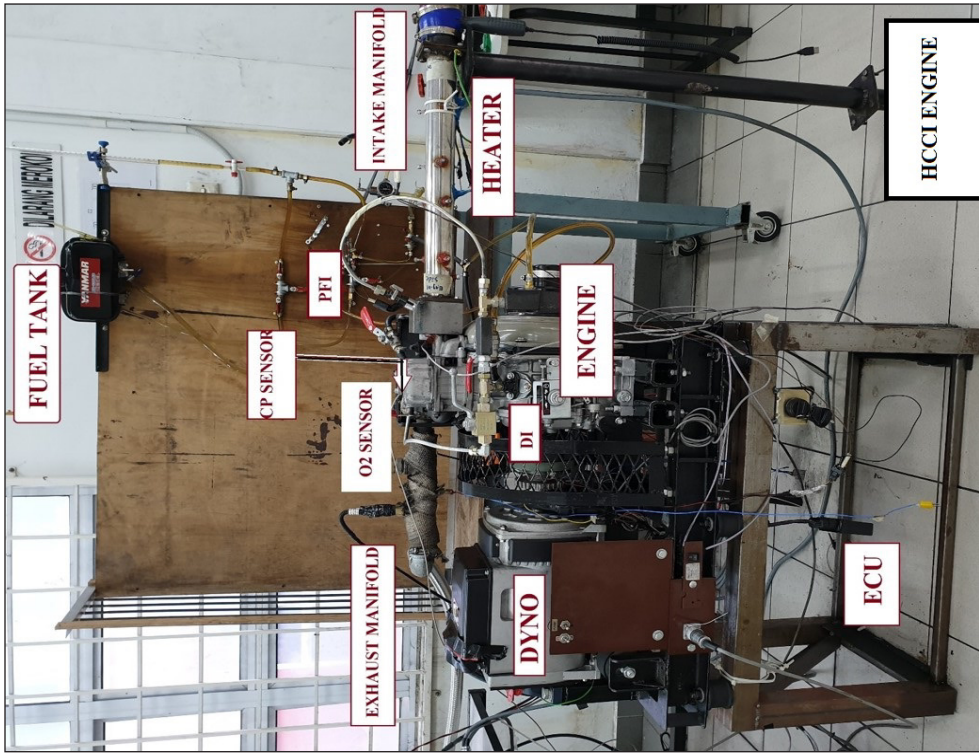


Figure 2. 10-kW dynamometer with a controller connected to the engine in the laboratory

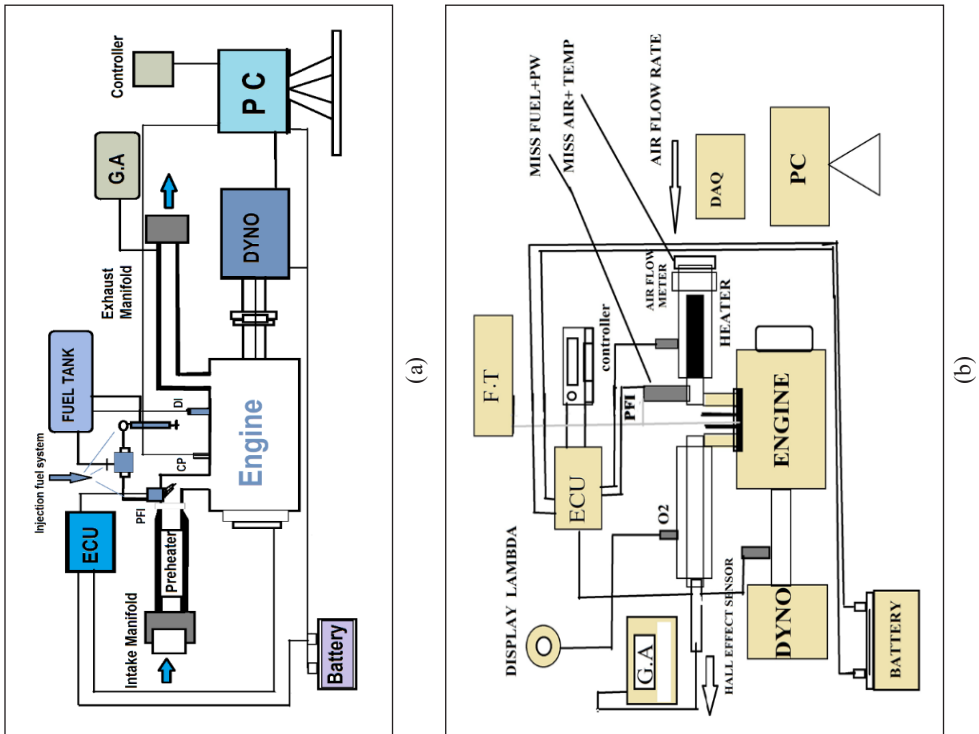


Figure 1. (a) Schematic representation of this study's experimental engine configuration; (b) ECU schematic coupled to sensors and PFI

the HCCI engine. The engine was preheated to 65°C using a pulse width of 2.5 ms. In HCCI mode, a consistent speed of 2700 rpm was maintained. The study evaluated the HCCI engine's speed stability under varying lambda conditions (air-fuel ratio), intake temperatures, and biodiesel mixtures. Each biodiesel blend was tested across four different lambda settings. After the warm-up phase, the direct injection valve was closed, and the PFI (Port Fuel Injection) system was engaged to supply fuel, thereby transitioning the engine to HCCI mode. Subsequently, the inlet temperature was maintained from 70°C to 90°C. It was necessary to reduce the intake temperature if it exceeded 95°C to avoid the engine entering the knocking region. Each set of operating conditions was replicated three times for each biodiesel blend (EL-Seesy et al., 2021; Rajesh et al., 2020).

Table 1  
*Specification of the diesel engine*

Engine model	Yanmar L48N
Engine type	Vertical cylinder, 4-stroke air-cooled diesel engine
Combustion	Direct Injection
Displacement	0.219 litres
Bore × Stroke	70 × 57 mm
Number of cylinders	1
Compression ratio	20.1

Table 2  
*Measured properties of diesel and used cooking oil*

Properties	Unit	Test Method	Diesel	B5	B10	B15	B20	B100
Density at 15°C	kg/L	ASTM D 4052-11	0.8409	0.8431	0.8449	0.8475	0.8495	0.885
Kinematic viscosity 40°C	mm <sup>2</sup> /s	ASTM D 445-14	3.650	3.698	3.759	3.820	3.921	5.285
Calorific value	MJ/kg	ASTM D 240-14	44.022	44.068	43.425	42.626	42.094	36.036
Cetane number	-	ASTM D 4737-10	55	50	47	45	43	-

## RESULTS AND DISCUSSION

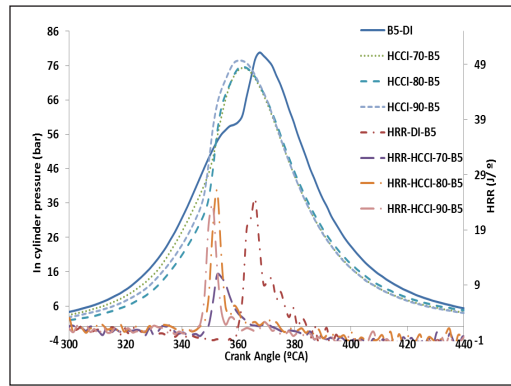
### Engine Performance

In diffusion mode, HCCI engines spontaneously ignite the mixture when it reaches the chemical activation energy point anywhere in the combustion chamber. A rich air-fuel mixture or high intake temperature can cause significant in-cylinder pressure and knock in HCCI engines. The in-cylinder pressure increases with load but decreases to its lowest at 0% load. Biodiesel blends affect in-cylinder pressure and Heat Release Rate (HRR) in both CI and HCCI engines. Figure 3 illustrates the impact of each mixture on in-cylinder pressure. An increase in intake temperature raises cylinder pressure. At 90°C in HCCI mode, the in-cylinder pressure reaches 81 bar. Diesel fuel raises in-cylinder pressure in CI and HCCI engines from 76 to 81 bar at varying input temperatures. The impact of the B5 blend on CI/HCCI cylinder pressure is notable.

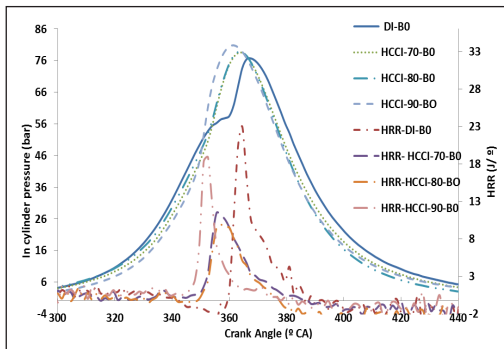
In HCCI mode, higher intake temperatures result in increased in-cylinder pressure and HHR. Biodiesel accelerates the combustion of hydrocarbons and oxygen. UCO B20 biodiesel

raises in-cylinder pressure from 77 to 79 bar and HRR from 13 to 25 J/°CA. The intake air temperature elevates the in-cylinder temperature during the compression stroke, facilitating earlier auto-ignition. Garcia et al. (2011) demonstrated the influence of varying intake air temperatures and lambda values on in-cylinder pressure using diethyl ether-ethanol fuel blends. Additional studies also observed that oxygen and hydrocarbons ignite more readily under these conditions (Gad et al., 2020; Singh et al., 2021; Sivarethinamohan et al., 2022).

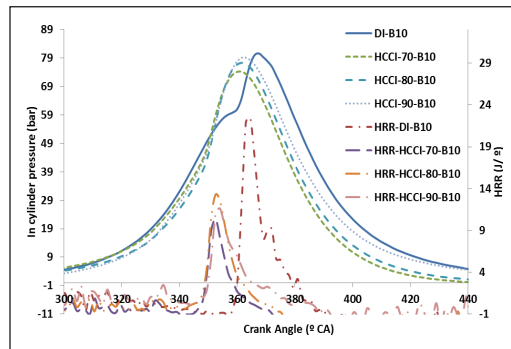
Figure 4 shows the peak pressure in the HCCI engine and examines the effects of varying intake temperatures and biodiesel blend ratios (B0, B5, B10, B15, and B20). The peak in-cylinder pressure of diesel fuel is 81 bars at 90°C, which decreases to 79 bars at 70°C. Both a lower intake temperature and a higher UCO-based biodiesel blend ratio contribute to a reduction in peak pressure across all fuels. With an increase in blend percentage, the



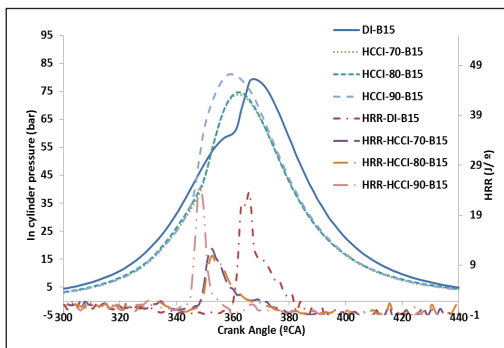
(a)



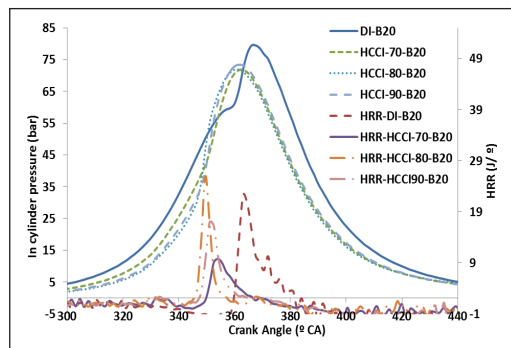
(b)



(c)



(d)



(e)

Figure 3. Intake temperatures and in-cylinder pressure in HCCI and CI modes at 2700 rpm, 2.4, and several biodiesel blends: (a)B0; (b)B5; (c)B10; (d)B15; and (e)B20

viscosity and density of biodiesel rise, making it more challenging to mix and combust. Intake temperature positively influences combustion chamber in-cylinder pressure (Gowthaman & Sathiyagnanam, 2016; Wei et al., 2017). This finding is further supported by additional studies, which varied air temperature control in an HCCI engine (Cinar et al., 2015; How et al., 2018; Hunicz et al., 2015; Khandal et al., 2019).

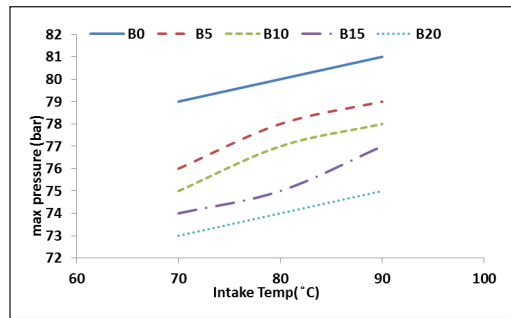


Figure 4. The effects of intake temperature on peak in-cylinder pressure in the HCCI engine for diesel and biodiesel fuel

The modes of CI/HCCI engines affect Brake Mean Effective Pressure (BMEP). In CI mode, diesel fuel exhibits the highest BMEP at 2.9 bars. Using B20 biodiesel results in a reduction of BMEP. However, an increase in intake temperature does not significantly impact BMEP. BMEP tends to be highest in Direct Injection (DI) mode. At low loads, HCCI engines operate efficiently. The energy in the fuel-air mixture enhances combustion temperature and consequently increases BMEP. The operating range of an HCCI engine is dependent on intake temperature and is typically constrained between misfiring and knocking, as shown in Figure 5 (Adam et al., 2017; Khandal et al., 2019; Krishnamoorthy et al., 2018; Zhang et al., 2012).

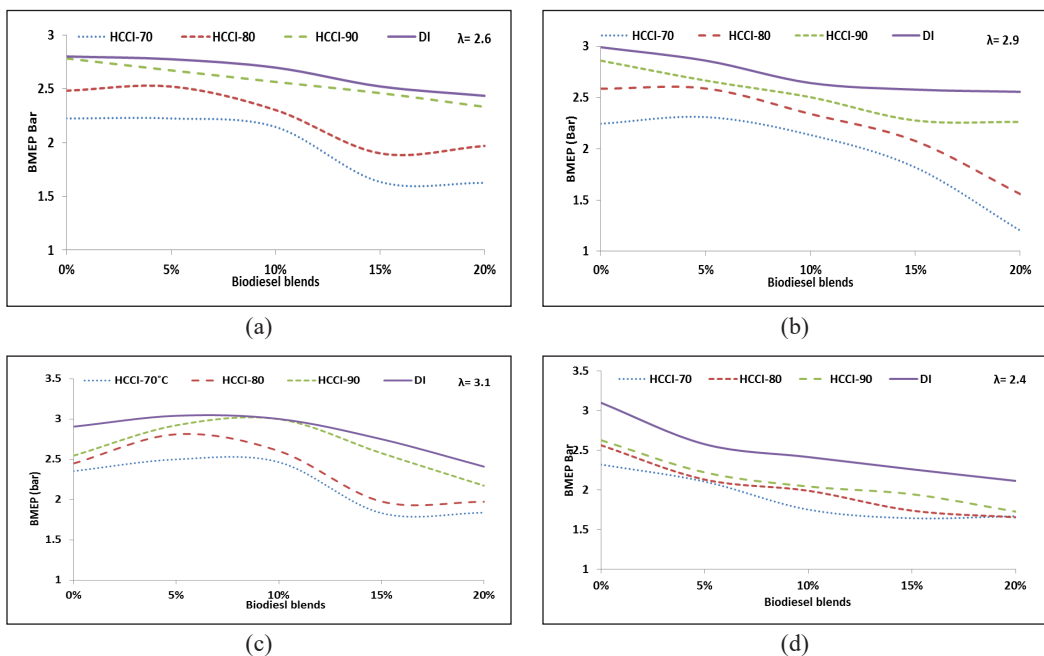


Figure 5. Different biodiesel mixes and intake temperatures and lambda affect BMEP in HCCI and CI modes at 2700 rpm: (a)  $\lambda = 3.1$ ; (b)  $\lambda = 2.9$ ; (c)  $\lambda = 2.6$ ; and (d)  $\lambda = 2.4$

Changes influence the brake-specific fuel consumption (BSFC) of the engine in terms of intake temperature and biodiesel blends. As depicted in Figure 6, the BSFC increases when the engine runs in HCCI mode. In HCCI mode at 70°C, the BSFC was 350 g/kWh, but it decreased to 256 g/kWh with B20 biodiesel. It was further reduced to 152 g/kWh in Direct Injection (DI) mode using B20 biodiesel. Additionally, higher air temperatures in the HCCI engine reduce volumetric efficiency and air mass flow rate, leading to advanced and uncontrolled combustion. The increased fuel consumption in HCCI mode is attributed to operating with reduced air density at all loads, which results in lower engine power due to the air's lower oxygen content. A study by Gowthaman and Sathiyagnanam (2016) focused on using biodiesel in HCCI mode and confirmed similar findings.

It aligns with other research indicating variations in BSFC (Godiño et al., 2018; Jafarmadar & Nemati, 2016; Sundararajan et al., 2016; Yousefi & Birouk, 2017). BSFC decreases in HCCI mode with increased intake temperature and biodiesel blend ratio, as shown in Figure 6, leading to higher fuel consumption at elevated temperatures. Port injection in HCCI mode consumes more fuel than in DI mode. Poor vaporization of biodiesel requires higher intake temperatures for improved combustion. Elevated

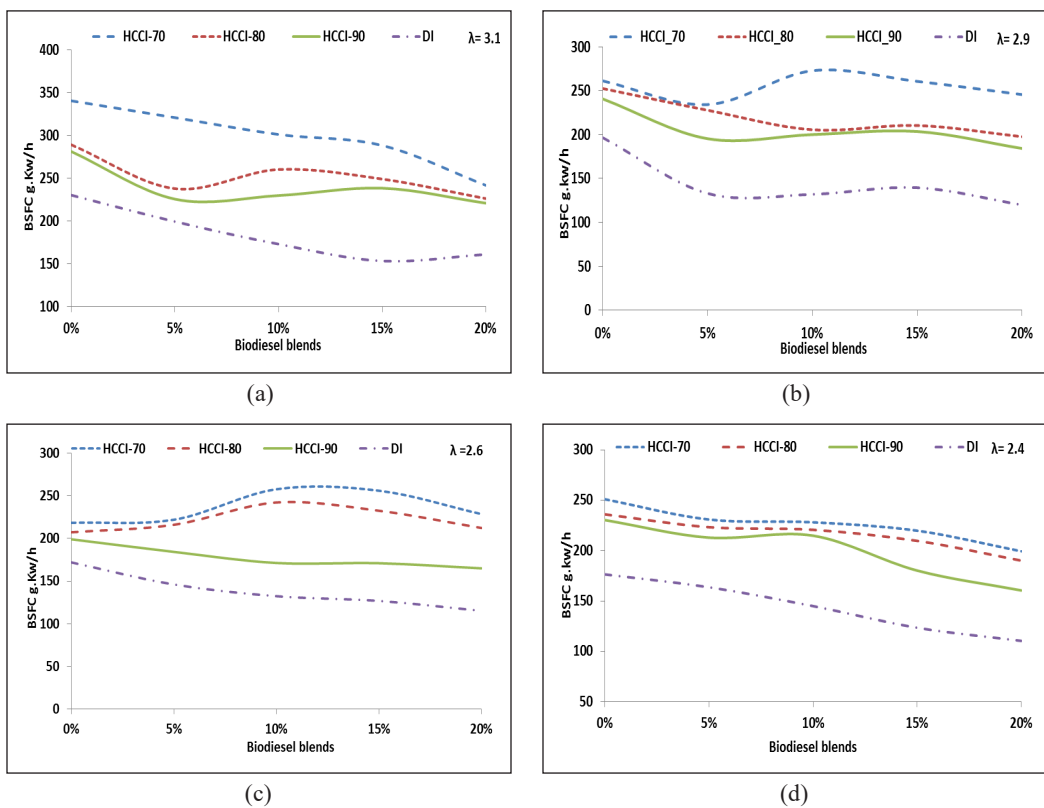


Figure 6. Different biodiesel blends and intake temperatures with lambda affect BSFC in HCCI and CI modes at 2700 rpm: (a)  $\lambda = 3.1$ ; (b)  $\lambda = 2.9$ ; (c)  $\lambda = 2.6$ ; and (d)  $\lambda = 2.4$

inlet air temperatures cause uncontrolled engine combustion and reduced engine power, necessitating a specific temperature range (Nalgundwar et al., 2016; Singh et al., 2017; Zhang et al., 2012).

Figure 7 shows the impact of varying lambda values on Brake Thermal Efficiency (BTE) in relation to intake temperature and biodiesel ratios. It is observed that biodiesel blends generally reduce BTE. A lower intake temperature also reduces BTE, whereas an intake temperature of 90°C increases BTE. Using diesel fuel in Direct Injection (DI) mode enhances engine BTE by 26.1%. In contrast, the Homogeneous Charge Compression Ignition (HCCI) mode, combined with UCO B20 biodiesel at an intake temperature of 70°C, decreases BTE to 14.2%—however, intake temperatures of 80°C and 90°C boost BTE. The decrease in BTE with biodiesel can be attributed to its higher viscosity, density, and cetane number, which complicates the fuel’s interaction with air and leads to less efficient vaporization and incomplete combustion prior to ignition. These factors contribute to reduced combustion efficiency, corroborating findings from previous studies (Hasan et al., 2015; Khandal et al., 2019; Zhang et al., 2012; Riyadi et al., 2023).

A high BTE of 27.1% was noted at an intake temperature of 70°C in DI mode. When lambda was adjusted from 2.4 to 3.1 at the same temperature, BTE decreased to 23.4%

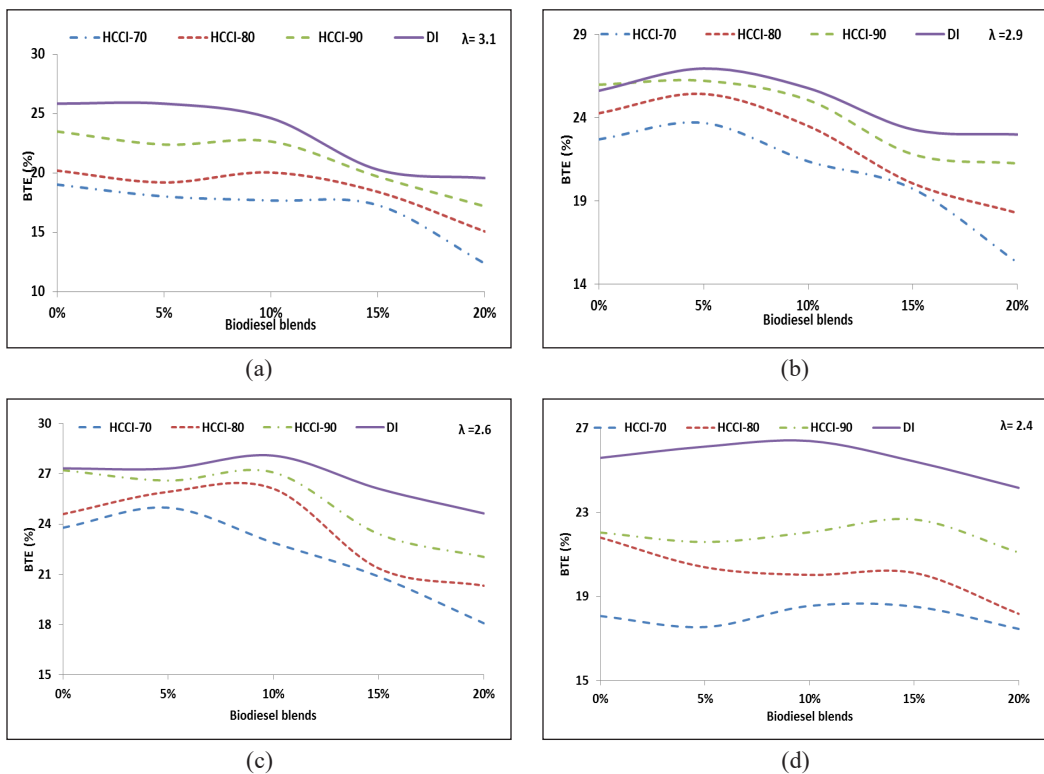


Figure 7. Different biodiesel blends and intake temperatures with lambda affect BTE in HCCI and CI modes at 2700 rpm: (a)  $\lambda = 3.1$ ; (b)  $\lambda = 2.9$ ; (c)  $\lambda = 2.6$ ; and (d)  $\lambda = 2.4$

and 19.8% at a lambda of 3.1. These results demonstrate the influence of lambda on BTE; specifically, biodiesel's high viscosity and density adversely affect fuel injection and combustion completeness. In the HCCI mode, the effect of biodiesel on BTE was analyzed at various blend ratios and intake temperatures. BTE was recorded at 25.1% with an intake temperature of 70°C, increasing to 28% at 90°C. A lower biodiesel rate corresponded with a higher BTE, which improved with increased intake temperature to 90°C. The HCCI engine mode shows enhanced combustion with higher intake temperatures, promoting more homogeneous fuel vaporization and thus increasing BTE. However, when running the engine on biodiesel, BTE is reduced due to the properties of UCO biodiesel at different blend rates. The study also observed that lambda significantly affects BTE. The fuel-air mixture is leaner at higher lambda values, leading to a reduced fuel supply. Conversely, a lower lambda value results in a richer mixture and an increased fuel supply to the chamber, facilitating better contact with air and enhancing the energy of combustion (Cinar et al., 2015; How et al., 2018; Krishnamoorthy et al., 2018; Satyanarayana et al., 2018; Singh et al., 2014; Sundararajan et al., 2016).

### The Emissions Levels

This study examines emission levels in both Compression Ignition (CI) and Homogeneous Charge Compression Ignition (HCCI) engines using different Used Cooking Oil (UCO) biodiesel blends and intake temperatures. HCCI engines are characterized by significant emissions of Unburned Hydrocarbons (UHC) and Carbon Monoxide (CO), but they emit lower levels of Nitrogen Oxides (NOx). Therefore, CI engine emissions were compared with HCCI engines operating at 2700 rpm.

The emission levels of CO and Carbon Dioxide (CO<sub>2</sub>), indicative of combustion efficiency, are discussed. Figure 8 shows that the CO emission levels vary depending on the biodiesel ratio and the engine mode, either HCCI or Direct Injection (DI). In HCCI mode, CO emissions tend to increase. An increase in intake temperature, however, reduces CO emissions. At an intake temperature of 90°C, CO emissions are low but rise with further temperature increases. In DI mode, CO emissions are at their lowest, 0.12%, but increase to 1.25% in HCCI mode when running on B20 biodiesel at 70°C. This increase is attributed to incomplete combustion due to the lower intake temperature.

Oxygen in UCO biodiesel also aids in lowering CO emissions by improving combustion (Ali et al., 2021; Khayum et al., 2021; Rajesh et al., 2020). Higher oxygen content in the fuel-air mixture reduces CO emissions as more oxidizers contact the fuel, facilitating in-cylinder combustion. The intake temperature significantly influences CO emissions in HCCI engines; higher inlet temperatures promote auto-ignition in the chamber, resulting in increased mixture fraction and easier ignition. This process leads to higher CO<sub>2</sub> emissions but lower CO emissions. These conditions influence the chemical reactions in

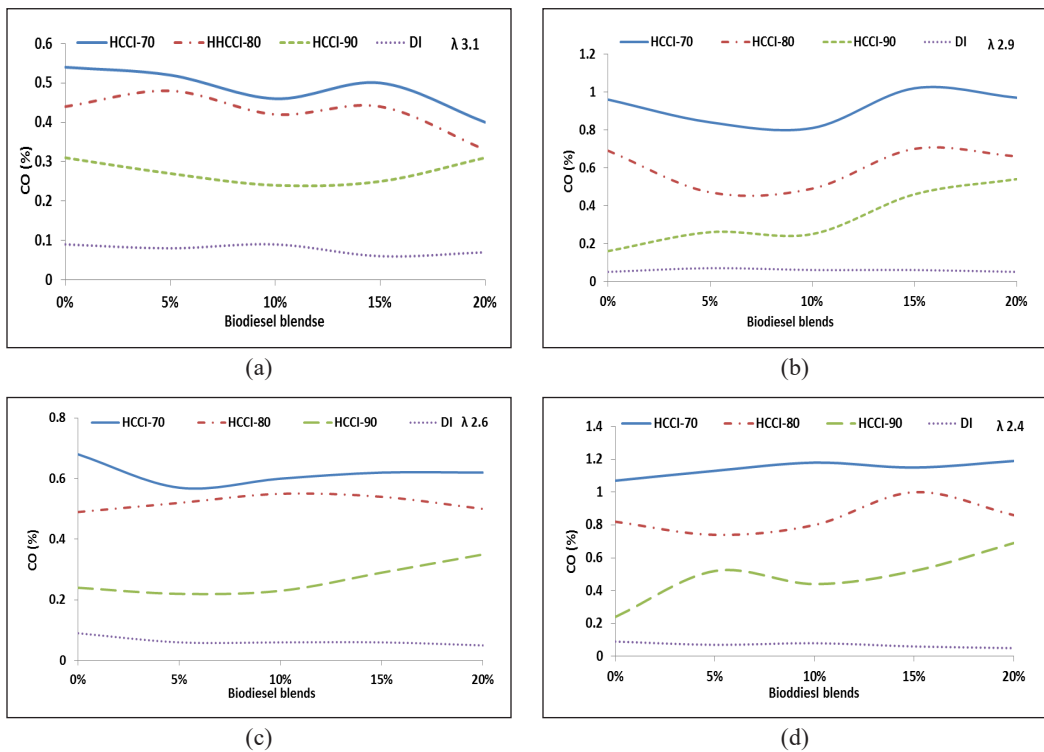


Figure 8. CO emissions in HCCI and CI modes at 2700 rpm with varying biodiesel blends and intake temperatures with lambda: (a)  $\lambda = 3.1$ ; (b)  $\lambda = 2.9$ ; (c)  $\lambda = 2.6$ ; and (d)  $\lambda = 2.4$

the combustion chamber, such as  $\text{CO} + \text{OH} = \text{CO}_2 + \text{H}$  and  $\text{CO} + \text{O}_2 = \text{CO}_2 + \text{O}$ . Higher intake temperatures reduce the engine’s volumetric efficiency and the concentration of oxygen molecules in the chamber, resulting in a greater quantity of OH radicals, which in turn lowers CO emission levels (Singh et al., 2014).

The levels of  $\text{CO}_2$  emissions are influenced by varying biodiesel blend ratios and intake temperatures in Direct Injection (DI) and Homogeneous Charge Compression Ignition (HCCI) modes. Generally,  $\text{CO}_2$  emissions decrease when operating in HCCI mode and diminish with increased biodiesel content. The highest and lowest  $\text{CO}_2$  emission levels recorded were 3.78% with diesel fuel in DI mode and 2.15% with B20 biodiesel at HCCI-70°C, respectively. Running the engine in HCCI mode reduces  $\text{CO}_2$  emissions, which decrease with rising biodiesel rates and varying intake temperatures (Gad & Ismail, 2021). Figure 9 shows the impact of biodiesel blend rates on  $\text{CO}_2$  emission levels. It shows that  $\text{CO}_2$  emissions increased from 2.6% to 4% with increased intake temperature, whereas  $\text{CO}_2$  emissions decreased with increasing biodiesel ratios of B0, B5, B10, B15, and B20. Specifically,  $\text{CO}_2$  emissions decreased to 1.95% but then increased to 2.55% when the intake temperature was raised to 90°C. These variations are attributed to different operating conditions, including lambda settings, intake temperatures, and biodiesel blend ratios. The

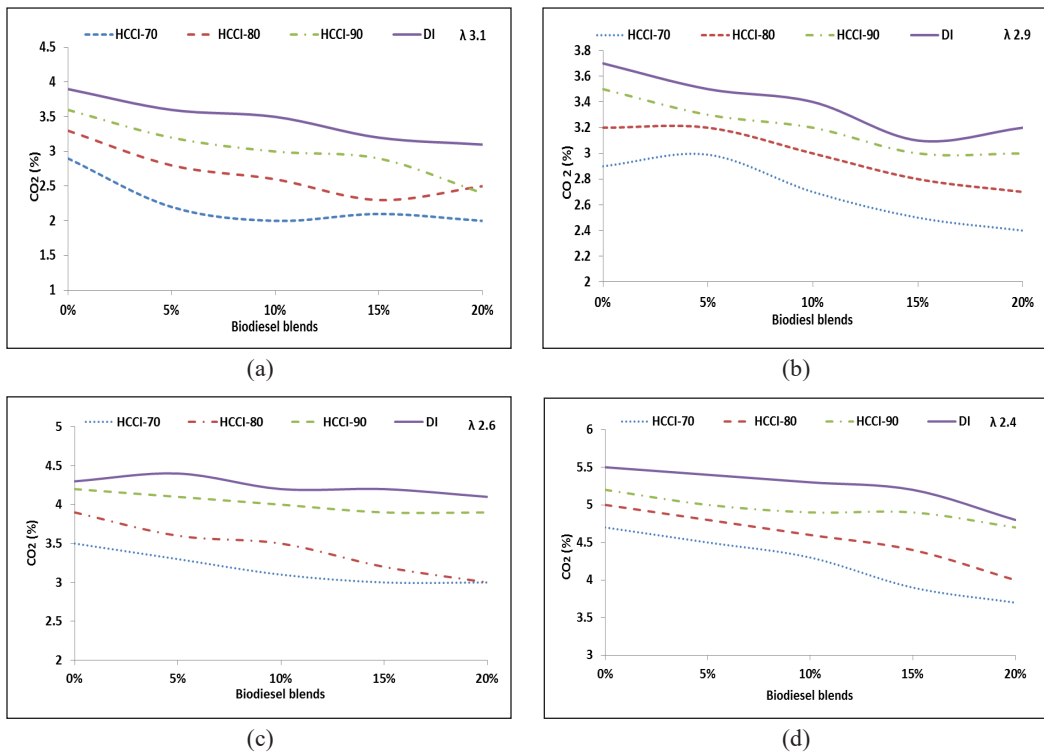


Figure 9. CO<sub>2</sub> emissions in HCCI and CI modes at 2700 rpm for varying biodiesel mix ratios and intake temperatures with lambda: (a)  $\lambda = 3.1$ ; (b)  $\lambda = 2.9$ ; (c)  $\lambda = 2.6$ ; and (d)  $\lambda = 2.4$

lambda influences the fuel-air mixture, shifting it from leaner to richer with a decrease in lambda value. This change also depends on the fuel supplied to the combustion chamber.

Furthermore, higher intake temperatures enhance air movement, facilitating easier contact and mixing between air and fuel. Consequently, these results indicate that using UCO biodiesel in HCCI mode reduces CO<sub>2</sub> emissions further due to the higher oxygen content in the biodiesel, which improves combustion efficiency. These findings are consistent with those reported in previous studies (Gowthaman & Sathiyaganam, 2016; Li et al., 2021; Etaiw et al., 2022).

Hydrocarbon (HC) emissions are released from unburned engine fuel mixtures. Figure 10 illustrates the effects of fuel mix ratios and intake temperatures on engine HC emissions in Direct Injection (DI) and Homogeneous Charge Compression Ignition (HCCI) modes. In DI mode, HC emissions were reduced from 31 ppm to 26 ppm when the biodiesel rate was increased from B0 to B20. The HC emission level initially was 83 ppm but dropped to 76 ppm as the temperature increased. Conversely, in HCCI mode, at an intake temperature of 70°C, HC emission levels increased as the biodiesel blend rate decreased. With an increase in the biodiesel ratio, HC emissions were reduced to 81 ppm at  $\lambda = 2.4$  and decreased to 62 ppm with B20 biodiesel. Specifically, when the engine was operated with B20 biodiesel

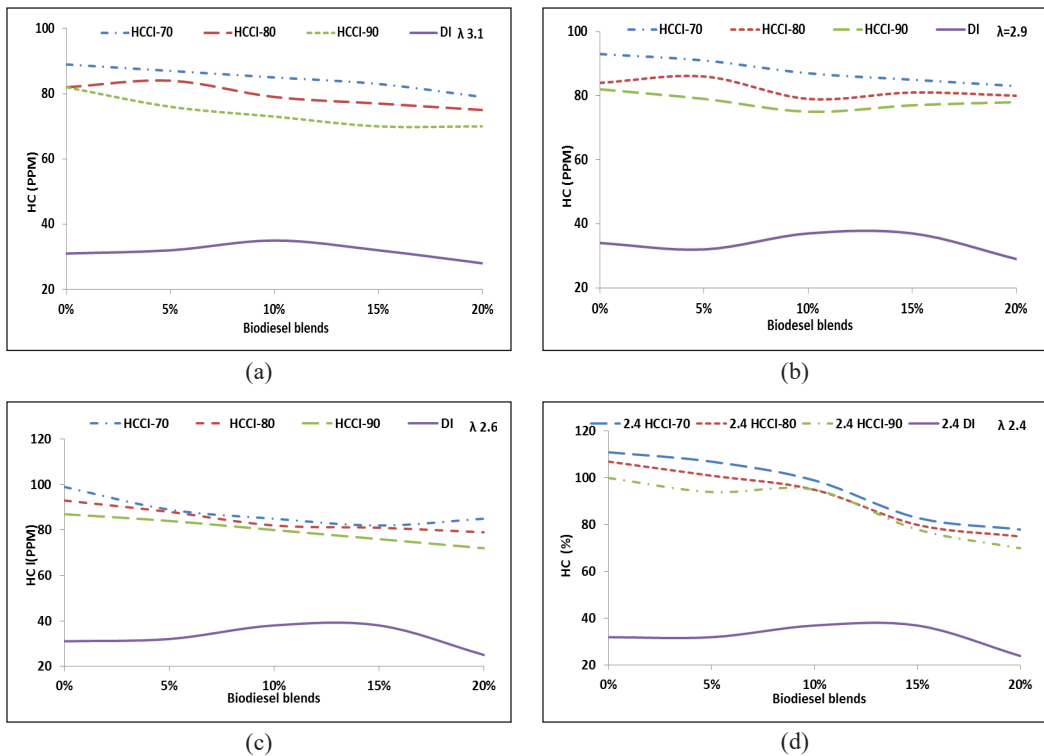


Figure 10. HC emission values in HCCI and CI modes at 2700 rpm for different biodiesel mixes and intake temperatures at lambda: (a)  $\lambda = 3.1$ ; (b)  $\lambda = 2.9$ ; (c)  $\lambda = 2.6$ ; and (d)  $\lambda = 2.4$

at 70°C, the HC emission level was 69 ppm, which then decreased to 65 ppm at an intake temperature of 90°C.

The reason for these variations is primarily the mode of operation. Running the engine in HCCI mode, coupled with the slow mixing velocity, typically resulted in higher HC emission levels. The reduction in HC emissions is attributed to a leaner air-fuel mixture, which creates a more homogeneous mix, thus facilitating better combustion. Additionally, using biodiesel reveals that higher blend ratios, which have a greater oxygen content, can lead to incomplete combustion. Other studies have reported similar findings when operating HCCI engines with biodiesel (Kumar & Rehman, 2016; Satyanarayana et al., 2018).

NOx emission production is a critical aspect frequently addressed in engine standards regulations. NOx is primarily produced in high-temperature combustion chamber reactions, where air nitrogen combines with oxygen to form nitric oxide (NO). In HCCI mode, low-temperature combustion effectively reduces NOx emissions. As depicted in Figure 11, different biodiesel mix ratios (B0, B5, B10, B15, and B20) affect the engine’s NOx emissions in HCCI mode at 70°C. Reducing the biodiesel blend rate and intake temperature in HCCI mode leads to lower NOx emissions. For example, increasing the input air temperature from 70°C to 90°C decreased NOx emissions from 8 ppm to 6 ppm.

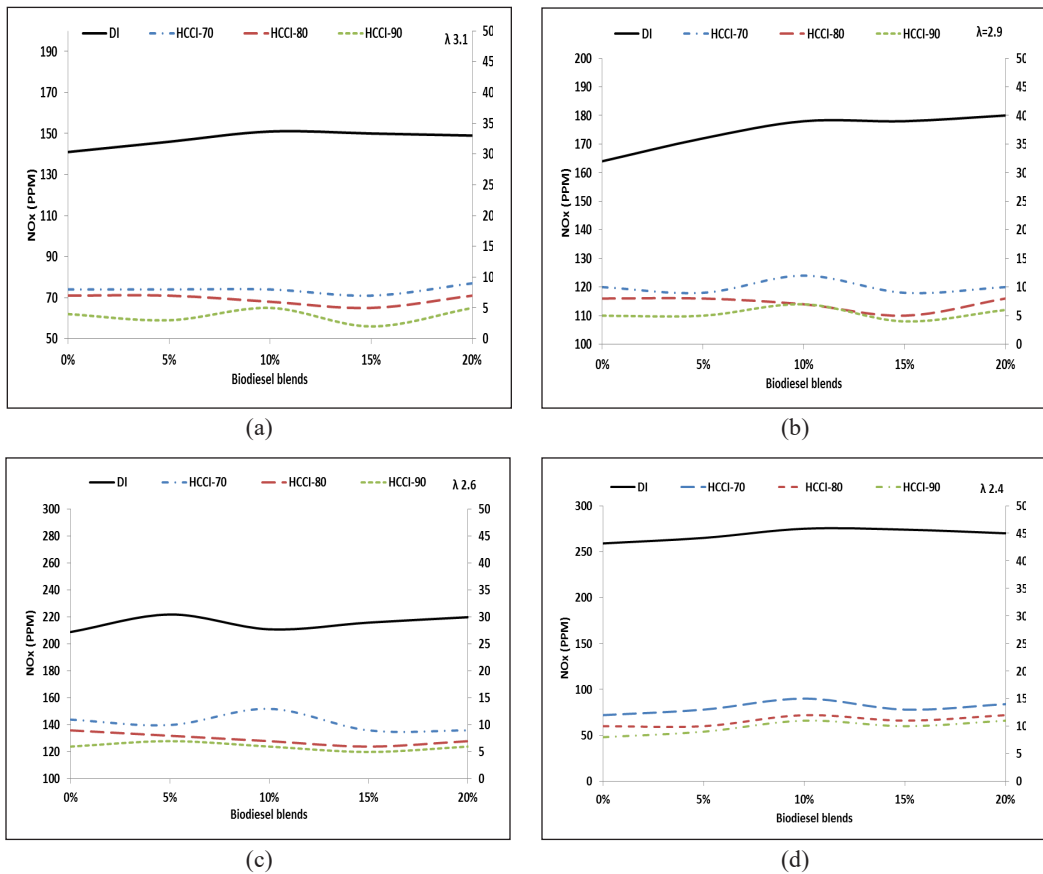


Figure 11. Different biodiesel mixes and intake temperature at lambda affect NOx emission levels in HCCI and CI modes at 2700 rpm: (a)  $\lambda = 3.1$ ; (b)  $\lambda = 2.9$ ; (c)  $\lambda = 2.6$ ; and (d)  $\lambda = 2.4$

When comparing diesel fuel and biodiesel fuel in HCCI mode, diesel fuel exhibits lower NOx emission levels: 4 ppm at 70°C and 3 ppm at 90°C. The lambda setting also plays a role in NOx emissions; a low lambda results in a richer blend with more fuel, thereby increasing NOx emissions. Higher combustion temperatures are known to increase NOx emissions, as temperature is a key factor in forming NOx. The increase in NOx emissions is correlated with combustion temperature and biodiesel concentration, which contains oxygen molecules. Nitrogen reacts with oxygen to form NO, further oxidizing to NO<sub>2</sub>. As the inlet air temperature rises, NOx emissions decrease. HCCI mode is effective in reducing NOx emissions, and this reduction is further enhanced with increased biodiesel blend rates. Conversely, NOx emissions tend to increase with a higher biodiesel blend ratio due to the high oxygen content in biodiesel. Moreover, the decrease in NOx emission levels when operating in HCCI mode has been corroborated by several studies (How et al., 2018; Khandal et al., 2019; Kumar & Rehman, 2016; Puškár & Kopas, 2018; Wei et al., 2017).

## CONCLUSION

This study evaluated the performance of Used Cooking Oil (UCO)-based biodiesel in a Homogeneous Charge Compression Ignition (HCCI) engine mode. The margin of error for each measured parameter was as follows: power ( $\pm 0.04$ ), HC (0.05%), NO<sub>x</sub> (0.2%), CO (0.06%), CO<sub>2</sub> (0.1%), and Brake Specific Fuel Consumption (BSFC) (+3%). In HCCI mode, diesel and UCO-based biodiesel have resulted in lower emissions compared to Direct Injection (DI) mode, suggesting that UCO-based biodiesel in HCCI engines could further reduce pollutants. HCCI mode led to lower in-cylinder pressures, decreased intake temperatures, and higher UCO biodiesel blend ratios. For instance, when operating with B20 biodiesel, the in-cylinder pressure dropped from 81 to 73 bar at 90°C.

The highest Heat Release Rate (HRR) recorded was 28 J/°CA in HCCI mode at an intake temperature of 70°C using diesel fuel. Engine power decreased when the intake temperature was raised from 2.5 kW to 2.3 kW in DI mode and dropped to 0.9 kW in HCCI mode using B20 biodiesel at 70°C. The Brake Mean Effective Pressure (BMEP) for the HCCI engine was lower due to its operation under low-load conditions. A higher BMEP was observed at full load with diesel fuel, reaching 3.32 bar. However, BMEP decreased with increasing engine speed and the introduction of UCO. The lowest BMEP, 1.5 bar, was noted at 3600 rpm using B20, likely due to UCO's lower energy content than diesel fuel.

Additionally, BSFC increased in HCCI mode, peaking at 90°C. At a lambda setting 2.4, the BSFC reached 340 g.kw/h in HCCI mode at 70°C using diesel fuel, marking the highest point. Brake thermal efficiency (BTE) declines when using biodiesel, which is attributed to the properties of UCO biodiesel (high viscosity and low calorific value). BTE decreased from 29% to 15% when operating the HCCI engine at an intake temperature of 90°C, primarily because HCCI engines run at low-load conditions.

CO emissions decreased with biodiesel fuel, while CO<sub>2</sub> and NO<sub>x</sub> emissions increased due to the accelerated combustion rate. CO emissions increased when switching from DI to HCCI mode but decreased with UCO biodiesel. CO emissions also declined with increased intake temperature and lambda for all fuels. Conversely, CO<sub>2</sub> production showed an opposite trend to CO. The HCCI engine yielded lower CO<sub>2</sub> emissions than the DI engine. The higher oxygen content in UCO-based biodiesel improved combustion, reducing CO and CO<sub>2</sub> emissions. However, the same high oxygen content increased NO<sub>x</sub> formation during combustion.

Regarding NO<sub>x</sub> emissions, the HCCI engine significantly reduced them, aligning with findings from numerous studies. Yet, increasing the blend ratio of UCO-based biodiesel only modestly improved NO<sub>x</sub> emissions. The higher oxygen content in higher biodiesel blends facilitated more rapid combustion, reducing Unburned Hydrocarbon (UHC) emissions. HC emissions were higher in HCCI engines compared to DI mode. A decrease in lambda

resulted in higher HC emissions due to the richer fuel mixture and increased fuel supply to the engine. Finally, UHC and CO<sub>2</sub> emissions decreased with an increased UCO content in the blend.

## ACKNOWLEDGEMENTS

Research grants and facilities from Universiti Putra Malaysia are appreciated. GP-IPS from UPM funds the study with project code GP-IPS 9706000 and is partly funded by the Malaysia Fundamental Research Grant Scheme (FRGS) under grant 5524734.

## REFERENCES

- Abed, K. A., El Morsi, A. K., Sayed, M. M., El Shaib, A. A., & Gad, M. S. (2018). Effect of waste cooking-oil biodiesel on performance and exhaust emissions of a diesel engine. *Egyptian Journal of Petroleum*, 27(4), 985-989. <https://doi.org/10.1016/j.ejpe.2018.02.008>
- Adam, A., Ramlan, N. A., Jaharudin, N. F., Hamzah, H., Othman, M. F., & Mrwan, A. A. G. (2017). Analysis of combustion characteristics, engine performance and exhaust emissions of diesel engine fueled with upgraded waste source fuel. *International Journal of Hydrogen Energy*, 42(28), 17993-18004. <https://doi.org/10.1016/j.ijhydene.2017.04.021>
- Ali, S. A., Hunagund, S., Hussain, S. S., & Bagwan, A. H. (2021). The effect of nanoparticles dispersed in waste cooking oil (WCO) biodiesel on thermal performance characteristics of VCR engine. *Materials Today: Proceedings*, 43(2), 888-891. <https://doi.org/10.1016/j.matpr.2020.07.214>
- Au, M. Y., Girard, J. W., Dibble, R., Flowers, D., Aceves, S. M., Martinez-Frias, J., Smith, R., Seibel, C., & Maas, U. (2001). 1.9-liter four-cylinder HCCI engine operation with exhaust gas recirculation (No. 2001-01-1894). SAE Technical Paper. <https://doi.org/10.4271/2001-01-1894>
- Banapurmath, N. R., Tewari, P. G., & Hosmath, R. S. (2008). Performance and emission characteristics of a DI compression ignition engine operated on Honge, Jatropha and sesame oil methyl esters. *Renewable Energy*, 33(9), 1982-1988. <https://doi.org/10.1016/j.renene.2007.11.012>
- Banerjee, R., Debbarma, B., Roy, S., Chakraborti, P., & Bose, P. K. (2016). An experimental investigation on the potential of hydrogen-biohol synergy in the performance-emission trade-off paradigm of a diesel engine. *International Journal of Hydrogen Energy*, 41(5), 3712-3739. <https://doi.org/10.1016/j.ijhydene.2015.12.140>
- Bedoya, I. D., Saxena, S., Cadavid, F. J., Dibble, R. W., & Wissink, M. (2012). Experimental study of biogas combustion in an HCCI engine for power generation with high indicated efficiency and ultra-low NO<sub>x</sub> emissions. *Energy Conversion and Management*, 53(1), 154-162. <https://doi.org/10.1016/j.enconman.2011.08.016>
- Channapattana, S. V., Campli, S., Madhusudhan, A., Notla, S., Arkerimath, R., & Tripathi, M. K. (2023). Energy analysis of DI-CI engine with nickel oxide nanoparticle added azadirachta indica biofuel at different static injection timing based on exergy. *Energy*, 267, Article 126622. <https://doi.org/10.1016/j.energy.2023.126622>

- Christensen, M., Hultqvist, A., & Johansson, B. (1999). Demonstrating the multi fuel capability of a homogeneous charge compression ignition engine with variable compression ratio. *Journal of Engines*, 108(3), 2099-2113. <https://doi.org/10.4271/1999-01-3679>
- Christensen, M., & Johansson, B. (1998). Influence of mixture quality on homogeneous charge compression ignition. *Journal of Fuels and Lubricants*, 107(4), 951-963. <https://doi.org/10.4271/982454>
- Cinar, C., Uyumaz, A., Solmaz, H., Sahin, F., Polat, S., & Yilmaz, E. (2015). Effects of intake air temperature on combustion, performance and emission characteristics of a HCCI engine fueled with the blends of 20% n-heptane and 80% isooctane fuels. *Fuel Processing Technology*, 130, 275-281. <https://doi.org/10.1016/j.fuproc.2014.10.026>
- Dharma, S., Ong, H. C., Masjuki, H. H., Sebayang, A. H., & Silitonga, A. S. (2016). An overview of engine durability and compatibility using biodiesel–bioethanol–diesel blends in compression-ignition engines. *Energy Conversion and Management*, 128, 66-81. <https://doi.org/10.1016/j.enconman.2016.08.072>
- EL-Seesy, A. I., Waly, M. S., He, Z., El-Batsh, H. M., Nasser, A., & El-Zoheiry, R. M. (2021). Influence of quaternary combinations of biodiesel/methanol/n-octanol/diethyl ether from waste cooking oil on combustion, emission, and stability aspects of a diesel engine. *Energy Conversion and Management*, 240, Article 114268. <https://doi.org/10.1016/j.enconman.2021.114268>
- Etaiw, S. E. H., Elkelawy, M., Elziny, I., Taha, M., Veza, I., & Bastawissi, H. A. E. (2022). Effect of nanocomposite SCP1 additive to waste cooking oil biodiesel as fuel enhancer on diesel engine performance and emission characteristics. *Sustainable Energy Technologies and Assessments*, 52(Part C), Article 102291. <https://doi.org/10.1016/j.seta.2022.102291>
- Fahd, M. E. A., Wenming, Y., Lee, P. S., Chou, S. K., & Yap, C. R. (2013). Experimental investigation of the performance and emission characteristics of direct injection diesel engine by water emulsion diesel under varying engine load condition. *Applied Energy*, 102, 1042-1049. <https://doi.org/10.1016/j.apenergy.2012.06.041>
- Gad, M. S., EL-Seesy, A. I., Radwan, A., & He, Z. (2020). Enhancing the combustion and emission parameters of a diesel engine fueled by waste cooking oil biodiesel and gasoline additives. *Fuel*, 269, Article 117466. <https://doi.org/10.1016/j.fuel.2020.117466>
- Gad, M., & Ismail, M. A. (2021). Effect of waste cooking oil biodiesel blending with gasoline and kerosene on diesel engine performance, emissions and combustion characteristics. *Process Safety and Environmental Protection*, 149, 1-10. <https://doi.org/10.1016/j.psep.2020.10.040>
- Ganesh, D., & Nagarajan, G. (2010). Homogeneous charge compression ignition (HCCI) combustion of diesel fuel with external mixture formation. *Energy*, 35(1), 148-157. <https://doi.org/10.1016/j.energy.2009.09.005>
- Ganesh, D., Nagarajan, G., & Ibrahim, M. M. (2008). Study of performance, combustion and emission characteristics of diesel homogeneous charge compression ignition (HCCI) combustion with external mixture formation. *Fuel*, 87(17-18), 3497-3503. <https://doi.org/10.1016/j.fuel.2008.06.010>
- Garcia, M. T., Aguilar, F. J. J. E., Villanueva, J. A. B., & Trujillo, E. C. (2011). Analysis of a new analytical law of heat release rate (HRR) for homogenous charge compression ignition (HCCI) combustion mode versus analytical parameters. *Applied Thermal Engineering*, 31(4), 458-466. <https://doi.org/10.1016/j.applthermaleng.2010.09.025>

- Geng, P., Mao, H., Zhang, Y., Wei, L., You, K., Ju, J., & Chen, T. (2017). Combustion characteristics and NOx emissions of a waste cooking oil biodiesel blend in a marine auxiliary diesel engine. *Applied Thermal Engineering*, *115*, 947-954. <https://doi.org/10.1016/j.applthermaleng.2016.12.113>
- Gharehghani, A. (2019). Load limits of an HCCI engine fueled with natural gas, ethanol, and methanol. *Fuel*, *239*, 1001-1014. <https://doi.org/10.1016/j.fuel.2018.11.066>
- Ghorbanpour, M., & Rasekhi, R. (2013). A parametric investigation of HCCI combustion to reduce emissions and improve efficiency using a CFD model approach. *Fuel*, *106*, 157-165. <https://doi.org/10.1016/j.fuel.2012.12.008>
- Giakoumis, E. G., Rakopoulos, C. D., Dimaratos, A. M., & Rakopoulos, D. C. (2012). Exhaust emissions of diesel engines operating under transient conditions with biodiesel fuel blends. *Progress in Energy and Combustion Science*, *38*(5), 691-715. <https://doi.org/10.1016/j.peccs.2012.05.002>
- Godiño, J. A. V., Aguilar, F. J. J. E., & García, M. T. (2018). Simulation of HCCI combustion in air-cooled off-road engines fuelled with diesel and biodiesel. *Journal of the Energy Institute*, *91*(4), 549-562. <https://doi.org/10.1016/j.joei.2017.04.002>
- Gowthaman, S., & Sathiyagnanam, A. P. (2016). Effects of charge temperature and fuel injection pressure on HCCI engine. *Alexandria Engineering Journal*, *55*(1), 119-125. <https://doi.org/10.1016/j.aej.2015.12.025>
- Gray, A. B., & Ryan, T (1997). Homogeneous charge compression ignition (HCCI) of diesel fuel. *Journal of Engines*, *106*(3), 1927-1935. <https://doi.org/10.4271/971676>
- Hasan, M. M., Rahman, M. M., & Kadirgama, K. (2015). A review on homogeneous charge compression ignition engine performance using biodiesel-diesel blend as a fuel. *International Journal of Automotive & Mechanical Engineering*, *11*, 2199-2211. <https://doi.org/10.15282/ijame.11.2015.3.0184>
- Hasan, M. M., & Rahman, M. M. (2016). Homogeneous charge compression ignition combustion: Advantages over compression ignition combustion, challenges and solutions. *Renewable and Sustainable Energy Reviews*, *57*, 282-291. <https://doi.org/10.1016/j.rser.2015.12.157>
- How, H. G., Masjuki, H. H., Kalam, M. A., & Teoh, Y. H. (2018). Influence of injection timing and split injection strategies on performance, emissions, and combustion characteristics of diesel engine fueled with biodiesel blended fuels. *Fuel*, *213*, 106-114. <https://doi.org/10.1016/j.fuel.2017.10.102>
- Hunicz, J., Geca, M. S., Kordos, P., & Komsta, H. (2015). An experimental study on a boosted gasoline HCCI engine under different direct fuel injection strategies. *Experimental Thermal and Fluid Science*, *62*, 151-163. <https://doi.org/10.1016/j.expthermflusci.2014.12.014>
- Hwang, J., Bae, C., & Gupta, T. (2016). Application of waste cooking oil (WCO) biodiesel in a compression ignition engine. *Fuel*, *176*, 20-31. <https://doi.org/10.1016/j.fuel.2016.02.058>
- Iwashiro, Y., Tsurushima, T., Nishijima, Y., Asaumi, Y., & Aoyagi, Y. (2002). *Fuel consumption improvement and operation range expansion in HCCI by direct water injection*. (No. 2002-01-0105). SAE Technical Paper. <https://doi.org/10.4271/2002-01-0105>
- Jafarmadar, S., & Nematy, P. (2016). Exergy analysis of diesel/biodiesel combustion in a homogenous charge compression ignition (HCCI) engine using three-dimensional model. *Renewable Energy*, *99*, 514-523. <https://doi.org/10.1016/j.renene.2016.07.034>

- Jafarmadar, S., & Nemat, P. (2017). Multidimensional modeling of the effect of exhaust gas recirculation on exergy terms in a homogenous charge compression ignition engine fueled by diesel/biodiesel. *Journal of Cleaner Production*, 161, 720-734. <https://doi.org/10.1016/j.jclepro.2017.05.182>
- Janecek, D., Rothamer, D., & Ghandhi, J. (2017). Investigation of cetane number and octane number correlation under homogenous-charge compression-ignition engine operation. *Proceedings of the Combustion Institute*, 36(3), 3651-3657. <https://doi.org/10.1016/j.proci.2016.08.015>
- Jiménez-Espadafor, F. J. J., Torres, M., Velez, J. A., Carvajal, E., & Becerra, J. A. (2012). Experimental analysis of low temperature combustion mode with diesel and biodiesel fuels: A method for reducing NOx and soot emissions. *Fuel Processing Technology*, 103, 57-63. <https://doi.org/10.1016/j.fuproc.2011.11.014>
- Khandal, S. V., Banapurmath, N. R., & Gaitonde, V. N. (2019). Performance studies on homogeneous charge compression ignition (HCCI) engine powered with alternative fuels. *Renewable Energy*, 132, 683-693. <https://doi.org/10.1016/j.renene.2018.08.035>
- Khayum, N., Anbarasu, S., & Murugan, S. (2021). Optimization of fuel injection parameters and compression ratio of a biogas fueled diesel engine using methyl esters of waste cooking oil as a pilot fuel. *Energy*, 221, Article 119865. <https://doi.org/10.1016/j.energy.2021.119865>
- Kimura, S., Aoki, O., Kitahara, Y., & Aiyoshizawa, E. (2001). Ultra-clean combustion technology combining a low-temperature and premixed combustion concept for meeting future emission standards. *Journal of Fuels and Lubricants*, 110(4), 239-246. <https://doi.org/10.4271/2001-01-0200>
- Krishnamoorthy, V., Dhanasekaran, R., Rana, D., Saravanan, S., & Kumar, B. R. (2018). A comparative assessment of ternary blends of three bio-alcohols with waste cooking oil and diesel for optimum emissions and performance in a CI engine using response surface methodology. *Energy Conversion and Management*, 156, 337-357. <https://doi.org/10.1016/j.enconman.2017.10.087>
- Kumar, P., & Rehman, A. (2016). Bio-diesel in homogeneous charge compression ignition (HCCI) combustion. *Renewable and Sustainable Energy Reviews*, 56, 536-550. <https://doi.org/10.1016/j.rser.2015.11.088>
- Li, H., Zhang, F., Feng, Z., Li, W., & Zou, X. (2021). Study on waste engine oil and waste cooking oil on performance improvement of aged asphalt and application in reclaimed asphalt mixture. *Construction and Building Materials*, 276, Article 122138. <https://doi.org/10.1016/j.conbuildmat.2020.122138>
- Mancaruso, E., & Vaglieco, B. M. (2010). Optical investigation of the combustion behaviour inside the engine operating in HCCI mode and using alternative diesel fuel. *Experimental Thermal and Fluid Science*, 34(3), 346-351. <https://doi.org/10.1016/j.expthermflusci.2009.10.010>
- Mase, Y., Kawashima, J., Sato, T., & Eguchi, M. (1998). Nissan's new multivalve DI diesel engine series. *Journal of Engines*, 107(3), 1537-1546. <https://doi.org/10.4271/981039>
- Muhamad Tobib, H., Hairuddin, A. A., Abdul Aziz, N., Al Anbagi, M., Md Noor, M., & Ayob, S. (2021). An experimental study of the performance of a homogeneous charge compression ignition (HCCI) engine fueled with palm oil-based biodiesel. *Automotive Science and Engineering*, 11(2), 3602-3625. <http://doi.org/10.22068/ase.2021.548>
- Nalgundwar, A., Paul, B., & Sharma, S. K. (2016). Comparison of performance and emissions characteristics of DI CI engine fueled with dual biodiesel blends of palm and jatropha. *Fuel*, 173, 172-179. <https://doi.org/10.1016/j.fuel.2016.01.022>

- No, S. Y. (2016). Application of biobutanol in advanced CI engines—A review. *Fuel*, *183*, 641-658. <https://doi.org/10.1016/j.fuel.2016.06.121>
- Noh, H. K., & No, S. Y. (2017). Effect of bioethanol on combustion and emissions in advanced CI engines: HCCI, PPC and GCI mode—A review. *Applied Energy*, *208*, 782-802. <https://doi.org/10.1016/j.apenergy.2017.09.071>
- Ogawa, H., Miyamoto, N., Kaneko, N., & Ando, H. (2003). *Combustion control and operating range expansion with direct injection of reaction suppressors in a premixed DME HCCI engine* (No. 2003-01-0746). SAE Technical Paper. <https://doi.org/10.4271/2003-01-0746>
- Özer, S., Akcay, M., & Vural, E. (2021). Effect of toluene addition to waste cooking oil on combustion characteristics of a CI engine. *Fuel*, *303*, Article 121284. <https://doi.org/10.1016/j.fuel.2021.121284>
- Puhan, S., Vedaraman, N., Ram, B. V. B., Sankarnarayanan, G., & Jeychandran, K. (2005). Mahua oil (Madhuca Indica seed oil) methyl ester as biodiesel-preparation and emission characteristics. *Biomass and Bioenergy*, *28*(1), 87-93. <https://doi.org/10.1016/j.biombioe.2004.06.002>
- Pušár, M., & Kopas, M. (2018). System based on thermal control of the HCCI technology developed for reduction of the vehicle NO<sub>x</sub> emissions in order to fulfil the future standard Euro 7. *Science of the Total Environment*, *643*, 674-680. <https://doi.org/10.1016/j.scitotenv.2018.06.082>
- Putrasari, Y., Jamsran, N., & Lim, O. (2017). An investigation on the DME HCCI autoignition under EGR and boosted operation. *Fuel*, *200*, 447-457. <https://doi.org/10.1016/j.fuel.2017.03.074>
- Rahbari, A. (2016). Effect of inlet temperature and equivalence ratio on HCCI engine performance fuelled with ethanol: Numerical investigation. *Journal of Central South University*, *23*, 122-129. <https://doi.org/10.1007/s11771-016-3055-7>
- Rajesh, A., Gopal, K., Victor, D. P. M., Kumar, B. R., Sathiyagnanam, A. P., & Damodharan, D. (2020). Effect of anisole addition to waste cooking oil methyl ester on combustion, emission and performance characteristics of a DI diesel engine without any modifications. *Fuel*, *278*, Article 118315. <https://doi.org/10.1016/j.fuel.2020.118315>
- Rashed, M. M., Kalam, M. A., Masjuki, H. H., Mofijur, M., Rasul, M. G., & Zulkifli, N. W. M. (2016). Performance and emission characteristics of a diesel engine fueled with palm, jatropha, and moringa oil methyl ester. *Industrial Crops and Products*, *79*, 70-76. <https://doi.org/10.1016/j.indcrop.2015.10.046>
- Riyadi, T. W. B., Spraggon, M., Herawan, S. G., Idris, M., Paristiawan, P. A., Putra, N. R., Faizullizam R, M., Silambarasan, R., & Veza, I. (2023). Biodiesel for HCCI engine: Prospects and challenges of sustainability biodiesel for energy transition. *Results in Engineering*, *17*, Article 100916. <https://doi.org/10.1016/j.rineng.2023.100916>
- Rizvi, S. Q. (2009). Chapter 4: Lubricant Additives. In S. Rizvi (Ed.), *A Comprehensive Review of Lubricant Chemistry, Technology, Selection, and Design* (pp. 100-211). ASTM International. <https://doi.org/10.1520/mnl11464m>
- Sahu, T. K., Sarkar, S., & Shukla, P. C. (2021). Combustion investigation of waste cooking oil (WCO) with varying compression ratio in a single cylinder CI engine. *Fuel*, *283*, Article 119262. <https://doi.org/10.1016/j.fuel.2020.119262>

- Sanjid, A., Masjuki, H. H., Kalam, M. A., Rahman, S. M. A., Abedin, M. J., & Palash, S. M. (2013). Impact of palm, mustard, waste cooking oil and Calophyllum inophyllum biofuels on performance and emission of CI engine. *Renewable and Sustainable Energy Reviews*, 27, 664-682. <https://doi.org/10.1016/j.rser.2013.07.059>
- Satyanarayana, P. A., Oleti, R. K., Uppalapati, S., & Sridevi, V. (2018). A comparative study on characterization of used cooking oil and mustard oil for biodiesel production: Engine performance. *Materials Today: Proceedings*, 5(9), 18187-18201. <https://doi.org/10.1016/j.matpr.2018.06.155>
- Shi, L., Cui, Y., Deng, K., Peng, H., & Chen, Y. (2006). Study of low emission homogeneous charge compression ignition (HCCI) engine using combined internal and external exhaust gas recirculation (EGR). *Energy*, 31(14), 2665-2676. <https://doi.org/10.1016/j.energy.2005.12.005>
- Singh, A. P., & Agarwal, A. K. (2012). Combustion characteristics of diesel HCCI engine: an experimental investigation using external mixture formation technique. *Applied Energy*, 99, 116-125. <https://doi.org/10.1016/j.apenergy.2012.03.060>
- Singh, D., Sharma, D., Soni, S. L., Inda, C. S., Sharma, S., Sharma, P. K., & Jhalani, A. (2021). A comprehensive review of biodiesel production from waste cooking oil and its use as fuel in compression ignition engines: 3rd generation cleaner feedstock. *Journal of Cleaner Production*, 307, Article 127299. <https://doi.org/10.1016/j.jclepro.2021.127299>
- Singh, G., Singh, A. P., & Agarwal, A. K. (2014). Experimental investigations of combustion, performance and emission characterization of biodiesel fuelled HCCI engine using external mixture formation technique. *Sustainable Energy Technologies and Assessments*, 6, 116-128. <https://doi.org/10.1016/j.seta.2014.01.002>
- Singh, V. P., Tiwari, S. K., Singh, R., & Kumar, N. (2017). Modification in combustion chamber geometry of CI engines for suitability of biodiesel: A review. *Renewable and Sustainable Energy Reviews*, 79, 1016-1033. <https://doi.org/10.1016/j.rser.2017.05.116>
- Sivarethinamohan, S., Hanumanthu, J. R., Gaddam, K., Ravindiran, G., & Alagumalai, A. (2022). Towards sustainable biodiesel production by solar intensification of waste cooking oil and engine parameter assessment studies. *Science of the Total Environment*, 804, Article 150236. <https://doi.org/10.1016/j.scitotenv.2021.150236>
- Srinidhi, C., Kshirsagar, P., Joshi, M., Kulkarni, A., Channapattana, S. V., Madhusudan, A., Aithal, K., & Gawali, S. (2022). Effect of fuel injection timing on CI engine fuelled with neem biodiesel blends—a comparative study of experimental and numerical simulation. *International Journal of Energy and Environmental Engineering*, 13, 395-406. <https://doi.org/10.1007/s40095-021-00429-6>
- Strålin, P., Wåhlin, F., & Ångström, H. E. (2003). *Effects of injection timing on the conditions at top dead center for direct injected HCCI* (No. 2003-01-3219). SAE Technical Paper. <https://doi.org/10.4271/2003-01-3219>
- Strandh, P., Bengtsson, J., Johansson, R., Tunestål, P., & Johansson, B. (2004). Cycle-to-cycle control of a dual-fuel HCCI engine. *Journal of Engines*, 113(3), 589-598. <https://doi.org/10.4271/2004-01-0941>
- Sundararajan, K., Janathanan, K., Pandian, V., Dhandapani, M., & Kanagara, K. (2016). *A performance, combustion and emission study on HCCI engine: Trends and innovations* (No. 2016-28-0013). SAE Technical Paper. <https://doi.org/10.4271/2016-28-0013>

- Tamilselvan, R., Rameshbabu, R., & Thirunavukkarasu, R. (2018). Effect of fuel injection timing on performance and emission characteristics of ceiba pentandra biodiesel. *Materials Today: Proceedings*, 5(2), 6770-6779. <https://doi.org/10.1016/j.matpr.2017.11.336>
- Thrlng, R. (2011). *Homogeneous-charge compression ignition (HCCI) engines* (No. 1989-09-01). SAE Technical Paper. <https://doi.org/10.4271/892068>
- Tobib, H. M., Rostam, H., Mossa, M. A. A., Hairuddin, A. A., & Noor, M. M. (2019). The performance of an HCCI-DI engine fuelled with palm oil-based biodiesel. In *IOP Conference Series: Materials Science and Engineering* (Vol. 469, Article 012079). IOP Publishing. <https://doi.org/10.1088/1757-899x/469/1/012079>
- Urata, Y., Awasaka, M., Takanashi, J., Kakinuma, T., Hakozaiki, T., & Umemoto, A. (2004). *A study of gasoline-fuelled HCCI engine equipped with an electromagnetic valve train* (No. 2004-01-1898). SAE Technical Paper. <https://doi.org/10.4271/2004-01-1898>
- Wei, L., Cheung, C. S., & Ning, Z. (2017). Influence of waste cooking oil biodiesel on combustion, unregulated gaseous emissions and particulate emissions of a direct-injection diesel engine. *Energy*, 127, 175-185. <https://doi.org/10.1016/j.energy.2017.03.117>
- Yousefi, A., & Birouk, M. (2017). Investigation of natural gas energy fraction and injection timing on the performance and emissions of a dual-fuel engine with pre-combustion chamber under low engine load. *Applied Energy*, 189, 492-505. <https://doi.org/10.1016/j.apenergy.2016.12.046>
- Zhang, S., Broadbelt, L. J., Androulakis, I. P., & Ierapetritou, M. G. (2012). Comparison of biodiesel performance based on HCCI engine simulation using detailed mechanism with on-the-fly reduction. *Energy & Fuels*, 26(2), 976-983. <https://doi.org/10.1021/ef2019512>



*Review Article*

## Computer Vision—The Frontier of Modern Environmental Diagnostics: A Review

Anna Sergeevna Olkova\* and Evgeniya Vladimirovna Tovstik

*Iyatka State University, 36 Moskovskaya St, Kirov, 610000, Russian Federation*

### ABSTRACT

Computer vision (CV), in combination with various sensors and image analysis algorithms, is a frontier direction in diagnosing the state of the environment and its biogenic and abiogenic objects. The work generalizes scientific achievements and identifies scientific and technical problems in this area of research based on the conceptual system of analysis on the time axis: from implemented achievements as part of the past and present to original new solutions—the future. Our work gives an idea of three areas of application of CV in diagnosing the state of the environment: phenotype recognition in digital images, monitoring of living and abiogenic objects, and development of new methods for identifying pollution and its consequences. The advantages of CV, which can be attributed to scientific achievements in this field of research, are shown: an increase in the volume of analyzed samples, simultaneous analysis of several parameters of the object of observation, and leveling of subjective evaluation factors. The main CV problems currently solved are the accuracy of diagnostics and changing quality of the survey, identification of the object of analysis with minimal operator participation, simultaneous

monitoring of objects of different quality, and development of software and hardware systems with CV. A promising direction for the future is to combine the capabilities of CV and artificial intelligence. Thus, the review can be useful for specialists in environmental sciences and scientists working in interdisciplinary fields.

### ARTICLE INFO

*Article history:*

Received: 10 July 2023

Accepted: 02 January 2024

Published: 16 July 2024

DOI: <https://doi.org/10.47836/pjst.32.4.08>

*E-mail addresses:*

[morgan-abend@mail.ru](mailto:morgan-abend@mail.ru) (Anna Sergeevna Olkova)

[tovstik2006@inbox.ru](mailto:tovstik2006@inbox.ru) (Evgeniya Vladimirovna Tovstik)

\* Corresponding author

*Keywords:* Bioassay, computer vision, deep learning, environmental quality, monitoring, phenotype

## INTRODUCTION

The scientific community supports an interdisciplinary strategy for assessing the quality of the environment since nature is a complex system of interrelated abiotic and biotic factors. One of the newest (frontline) directions in the biodiagnostics of natural and natural-technogenic systems is developing and implementing software and hardware systems using computer vision (CV). CV technologies are understood as a field of artificial intelligence associated with automatic and semi-automatic extraction of significant features from digital images obtained using automatic microscopes and cameras, drones, robotics, satellites and other equipment in order to detect, classify, segment, recognize objects of interest (Vaganov et al., 2021; Lurig et al., 2021).

At the initial stages of the development of the CV, it was engaged in solving such problems as reconstructing 3D scenes from 2D images, decomposition of images into their parts, recognizing and assigning labels to observed objects, deducing and describing relations among scene objects, matching stored descriptions to image representation (Fischler & Firschein, 2014). One of the first applications of CV in environmental research was the recognition of objects on satellite images of the Earth. Success in the work was achieved using the PASCAL VOC Challenge test (Everingham et al., 2010) and the Large Scale Visual Recognition Challenge (ILSVRC) (Russakovsky et al., 2015).

It should be noted that computer vision currently refers mainly to working with three-dimensional objects. At the same time, it, in some parts, exceeds the capabilities of biological vision. The term “machine vision” can also be met in the literature, which, for the most part, characterizes the ability of robotic machines to evaluate various visual parameters (linear dimensions, distance to an object) (Shapiro & Stockman, 2001). Machine learning is used to speed up and automate image analysis. At the same time, algorithms based on a new field of machine learning (deep learning) show more accurate performance compared to traditional approaches to tasks based on computer vision (Mochida et al., 2019). CV uses characteristics such as color, shape, and texture of the image to determine the content of an image (Weinstein, 2018).

Using computer vision to extract useful information from images and videos is becoming a key method for studying environmental objects. CV allows scientists to increase the volume of received and processed data and the number of measured parameters; it eliminates subjective assessments of biological macro- and micro-objects, reduces research costs, and makes it possible to develop new methods of diagnostics using IT. With the help of CV, it is possible to obtain biological and environmental data of a new generation with high speed, accuracy and reliability (Lopez-Marcano et al., 2020).

For example, digital holographic microscopy has become an alternative to conventional microscopy. Modern digital cameras have Charge-Coupled Device (CCD) or Complementary Metal Oxide Semiconductor (CMOS) sensors and digital image

processing tools. Multiple angles of digital holographic tomography and tomographic phase microscopy have rapidly evolved to recover a full three-dimensional (3D) refractive index map of intracellular structures or to estimate micro samples' three-dimensional morphology and shape (Monaldi et al., 2015).

The need to introduce CV in biodiagnostics was due to several reasons. Macroscale observations over large areas, such as forests, mountain systems, seas and oceans, and large man-made zones, in the 20th century mainly used methods of route descriptions and selection of representative sites (Ashikhmina et al., 2011). The obtained information was extrapolated to the entire macro-object, so there were risks of missing valuable data about the study area or even making incorrect scientific conclusions. The appearance of space and aero photography made it possible to “take a look” at large-scale natural objects and phenomena. When studying abiotic macro objects, information on the dynamics of the hydrological regime of water bodies (Kantor & Ashikhmina, 2014; Mu et al., 2022) and geothermal activity (Moraga et al., 2022; Xiong et al., 2022) is valuable. New methods of wildlife census appeared (Li et al., 2022; Norouzzadeh et al., 2020; Roy et al., 2023). As a result, studies of biotic processes were enriched with new data on the migration routes of terrestrial and marine animals (Zhou et al., 2022). Biogeographic maps with plant boundaries and biodiversity data can now be updated automatically (Wägele et al., 2022).

Biodiagnostics of the environment according to the characteristics of the meso- and macrocosm is still carried out on a representative sample of observed biological objects. However, the cost and complexity of data collection often limit the breadth and scope of environmental research (Weinstein, 2018). The main scientific approaches traditionally established in environmental biodiagnostics take into account several fields of view when microscopy of the studied object (Karl & Proctor, 2007; Ruiz-Santaquiteria et al., 2020), creating a model group of organisms in ecotoxicological tests (Gad, 2016), trapping a part of the natural population for studying (Abou-Donia, 2015), collecting biosamples for laboratory analysis (Ashikhmina et al., 2011). In each of these areas, it is practically impossible to bring information about the working sample of organisms closer to the characteristics of the entire population in the study area or the population of organisms in laboratory culture. As a result, part of experimental organisms' individual variability and sensitivity to various factors remains unaccounted for. CV methods cannot completely solve this problem, but they significantly increase the sample size and reliability of the received information. In addition, a CV allows new parameters into diagnostics that are inaccessible for visual and other classical accounting.

The purpose of this review is to demonstrate the application of computer vision for biodiagnostics of the state of the environment and to highlight the latest achievements in this interdisciplinary field and unsolved problems.

## MATERIALS AND METHODS

Scientific publications for review were selected in the international scientometric databases Web of Science, Scopus, ScienceDirect, and the Google Scholar search engine by thematic queries and subsequent filtering by year and type of publication. The criterion for selecting databases was the international coverage of authors and publications. At the same time, the principle of impartiality to publications was implemented: we did not filter magazines by rating. Keywords used were computer vision, environment, environmental quality, environmental pollution, deep learning, machine learning, artificial intelligence, monitoring, and phenotype. These keywords were used in different combinations according to the rules of the corresponding database.

The concept of the work was to consider the scientific foundations, the current state and the future of CV in the diagnosis of environmental quality on the time axis. We analyzed publications older than five years to include important original research and fundamental work in the CV field in the review. Among these works, preference was given to monographs and thematic books. In the books on diagnostics, we paid attention to the description of technical and methodological problems that are difficult to solve without a CV. The works published over the last five years (2019–2023) demonstrated the implemented technologies—these are already accomplished discoveries and achievements. The first criterion for using the works of 2019–2023 was the description in them of solutions to existing problems in the related field of “CV-biodiagnostics.” The second criterion is information about the implementation of the technology. These innovations informed us about the CV frontiers in the present time—generalization and analysis of unsolved problems we attributed to the future.

Studies were excluded if unrelated to digital phenotyping, biological objects and environmental resources monitoring, and environmental pollution research. We have not analyzed unpublished reports and conference materials not mentioned in Web of Science, Scopus, ScienceDirect.

In accordance with the concept, 70 sources covering current developments, experimental models and the introduction of computer vision-based software and hardware complexes in the diagnostics of natural and man-made systems were included in the review.

## RESULTS

### Directions for Using CV in the Environmental Diagnostics

#### *Digital Phenotyping*

Observations of the environment began with the formation of biological systematics and knowledge of the diversity of life forms. In the 20th century, a separate group of scientists consisted of specialists in the taxonomy of living organisms. Hardware and software

systems based on CV can partially facilitate their work. As a rule, they are aimed at automatic, accurate and high-throughput measurements, including the analysis of external signs and factors influencing the development of biota (Mochida et al., 2019).

A wide range of automated taxon accounting systems has been developed. Thus, plant phenotyping occurs based on their images, including in conjunction with the results of molecular genetic analysis of DNA (Stefen et al., 2022). At the same time, information processing can include the capture of both plant organs, including underground and aboveground, and the entire plant, including its three-dimensional phenotype (Li et al., 2020). High-throughput 3-D phenotyping according to the geometric parameters of tree crowns is implemented using two main technologies: mobile ground laser scanning based on light detection and ranging sensors (LiDAR) and digital aerial photogrammetry using images from unmanned aerial vehicles (UAVs) (Torres-Sanchez et al., 2023).

Recognition and search for botanical micro- and macroobjects using CV allows for obtaining fundamentally new phenotypic data for species classification and taxonomy and understanding plant processes and speciation (Vaganov et al., 2021). The solution to such problems is based on the interpretation of the plant surface's chromatic features, contour features, and textural features (Alam et al., 2022). Deep learning or transfer learning is the common approach for most of the studies (Hussein et al., 2021). Such technologies already make it possible to create digital herbariums.

Achievements in computer vision and deep learning make it possible to determine variations in phenotypic traits, behavior and interactions of insects and other invertebrates. Such non-invasive research methods make it possible to determine the abundance, biomass, and diversity of insects within the framework of the global problem of reducing their biodiversity (Høye et al., 2021), assess the foraging of honeybees (Ratnayake et al., 2021).

Phenotyping is especially difficult in the field of quantitative accounting of microorganisms. Microorganism image analysis technologies have progressed significantly from classical image processing and traditional machine learning to modern deep learning and potential visual transformation methods (Ma et al., 2023). Thus, when recognizing colonies of microorganisms on agar nutrient media, deep learning algorithms are applied that use geometric features, for example, the edge detection of colonies in a liquid nutrient medium—the watershed boundary between the globule formed by microorganisms and the liquid. Methods for identifying and enumerating microbial colonies on diagnostic culture media are usually based on various image enhancement methods: gray level contrast and image conversion to a three-channel (RGB) color model (Zhang et al., 2022; Boukouvalas et al., 2019).

A more advanced approach is deep learning technologies using Convolutional Neural Networks. The classification model created on its basis, in particular, of three types of stained bacteria, *Bacillus coagulans*, *Staphylococcus aureus* and *Clostridium perfringens*,

allows achieving training and testing accuracy of 96.75% and 81.35%, respectively (Rani et al, 2022).

The transition from algorithms and laboratory setups to devices for mass use is already beginning. Thus, the automated multiwell station Automated Open-Hardware Multiwell Imaging Station is proposed, which combines a microscope, a digital camera and a low-power single-board computer, which is capable of automatically collecting samples using 3D-printed pumps and capturing images with optical magnification up to 50 times (Gervasi et al., 2022).

Thus, the biological taxonomy of micro- and macroorganisms, which previously required a huge investment of time and material resources and highly qualified specialists, is now equipped with software and hardware systems with CV and elements of artificial intelligence.

CV helps to combine the study of the characteristics of biological species with the monitoring of biogenic and abiogenic objects.

### ***Monitoring of Biological Objects and Environmental Resources***

The second vector of using CV is monitoring living objects in the environment and their non-living components, which are valuable resources. It is known that monitoring—long-term and systematic observations—is the leading approach to studying the dynamics of ecosystems, which occurs under the influence of jointly acting natural and anthropogenic factors. It should be noted that monitoring is often associated with a large set of data, which creates difficulties in their interpretation. Software and hardware systems with CV can autofocus on biological objects of interest, capturing and analyzing images or videos, including those containing multiple objects of observation. Applying these technologies to systematic observations of populations and communities of organisms is an advance in ecological monitoring.

Monitoring animals, including protected species, their behavior, and the number of individuals in herds is extremely important for biodiversity conservation and managing invasive species. Combining remote sensing with unmanned aerial vehicles with CV technologies solves these problems in this study. Five animal species: (1) African elephant (*Loxodonta Africana*), (2) giraffe (*Giraffa camelopardalis*), (3) white rhinoceros (*Ceratotherium simum*), (4) wildebeest (*Connochaetes taurinus*), and (5) zebra (*Equus quaggas*) have shown that a new image analysis based on point pattern analysis allows picking up a drone from the height of 15 m to the height of 130 m, which increases the image capture area (Petso et al., 2021). The combination of computer vision camera traps, sensors, machine learning applied to satellite images, and GPS collar data can detect, track and localize animals in vast hunting areas (Dorfling et al., 2022). It will make it possible to combat the poaching of elephants and rhinos and then apply technology to protect other animals.

An invaluable tool for the high-throughput collection of species activity data is automated trackers, which are improved on the basis of CV and deep learning technologies. As a result, scientists provide software and hardware systems, including a portable motion activity monitor and a mobile activity detector. The monitored biological processes can include circadian rhythms, eclosion and diapause timing, and pollination. (Sondhi et al., 2022). Similar approaches are implemented by Bjerge et al. (2021). The authors developed an automatic moth trap with multiple light sources and a camera to attract and observe live insects at dusk and night. A computer vision algorithm based on a deep analysis of the captured images allows tracking and counting the number of insects and identifying their species.

CV makes it possible to observe populations of micro- and macro-organisms in the water column, which again was not possible with traditional methods. For example, CV technologies monitor ichthyofauna diversity in natural habitats (Ditria et al., 2021; Sheehan et al., 2020). Daily and seasonal monitoring of the vertical migration of cyanobacteria, which significantly affects water quality, has also become feasible with a CV-based instrument (Li et al., 2022). With the advent of high-speed digital cameras that feature large enough electronic sensors with small enough pixels, a time series of thousands of single holograms per second yielded some observations. They showed 3-D structures of the spatial distribution of marine plankton without further manual refocusing (Moreno et al., 2020).

A big threat to marine ecosystems and human health in recent years has been red tides caused by the reproduction of algae of the group of dinoflagellates. Their monitoring recognition and classification system based on CV was developed, which includes image segmentation, artificial feature extraction and classification based on a machine learning algorithm. Image segmentation allows for detecting the single algae's boundaries and getting its bounding rectangular areas as the sub-image from the original images, even if several objects stick together (Yang et al., 2020).

Monitoring plants and their communities on a micro- and macroscale has research and economic functions. The review (Keefe et al., 2022) reveals the advantages of monitoring forest resources using CV: mapping forest plantations with the possibility to take into account each seedling, optimizing logging routes, and introducing machine navigation, automation and robotics into the work of forestry. It was shown that CV provides an excellent opportunity to diagnose and monitor plant diseases (Xia et al., 2022; Patil et al., 2021). Thus, some algorithms allow registering plant damage by powdery mildew by visualizing *Erysiphe necator* hyphae directly on leaves without their preliminary sowing on a diagnostic nutrient medium (Bierman et al., 2019).

Monitoring invasive alien plants is relevant for preventing and controlling the biodiversity of agricultural and natural ecosystems. Using satellite images and expert processing is possible (Tovstik et al., 2019). More advanced are images taken with

intelligent UAVs (Qian et al., 2020). UAVs in a complex with “deep learning” are ideal for collecting, processing and extracting complex data obtained in real situations (Dudukcu et al., 2023). However, there is a problem with the high cost of global navigation satellite systems of the survey level (GNSSs). Yuan et al. (2022) proposed a novel approach for registering UAV-LiDAR data of level agricultural fields utilizing a colored iterative closest point algorithm, GNSS location, and inertial measurement unit orientation information from the UAV.

Thus, a fait accompli in monitoring the environment and its processes can be considered the need to use photo and video materials obtained using CV technologies. Innovative technologies with laboratory and single prototypes can be called hardware and software complexes with systems for navigation, information transmission, and primary processing. The future of monitoring research lies in improving the share of artificial intelligence in such products.

### ***Studying Environmental Pollution***

Thirdly, CV is very promising for assessing environmental pollution, especially in terms of neurobehavioral analysis of biological objects as their response to chemical impacts. Sensorimotor and cognitive-behavioral bioassays have enriched world science. For example, in the toxicological assessment of water by *Artemia franciscana* responses, the software detects organisms and analyzes their trajectory using image processing algorithms (Henry et al., 2019). For each specimen of *Daphnia magna*—a classic test organism—the following parameters are determined: swimming speed, height of the test object in the chamber, current and total distance traveled, size of the test object and its orientation in space, complexity of the movement trajectory (fractal dimension of the trajectory) (Nikitin et al., 2018).

Many physicochemical and biotic characteristics of water testify to its quality. These properties can also be determined using a CV. For example, a system for estimating water viscosity was created, making it possible to automatically judge water quality in real time. Its applied aspect is to ensure the health and safety of growing royal goldfish in small aquaculture (Ma & Wei, 2021). A simple detection and counting method for *Escherichia coli* in the water samples, including a combination of DNAzyme sensors, microfluidics, and computer vision strategies, was developed (Rauf et al., 2022). Attempts were made to assess climate change according to the biotic responses of butterflies through digital image processing (Wilson et al., 2021).

In ecotoxicological research, monitoring Earthworm behavior in the soil using deep learning is of particular value. Quantification of their activity is based on neural network model predictions made based on image sequences taken during exposure to an environmental factor or xenobiotic (Djerdj et al., 2020).

CV technologies provide rapid screening of contamination. For example, a digital image of an analyte drop is decomposed into three color components: red, green and blue. The concentration of colored substances is related to these color characteristics. The software processes the color signal to construct calibration curves and further chemical analysis (Fashi et al., 2020). This technology, with modifications, formed the basis of an Android application that determines the copper content in water, food and soil. An electromembrane extraction device with red-red-green-blue analysis based on a QR code has a detection limit and a quantitative determination limit of 0.1 µg/ml. Intra- and inter-assay relative standard deviations ranged between 2.0% and 2.3% and 3.1%–3.7 %, respectively (Zaroudi et al., 2023).

Combining the latest CV technologies (deep reinforcement learning, neural networks, and object recognition algorithms such as the dragonfly algorithm) makes it possible to observe and sort waste in real time (Al Duhaiyyim et al., 2022). With the help of independent machine learning models, it is possible to control water pollution sources by forming algae, floating impurities and changing the color of water bodies (Sharma et al., 2021). As a result, CV technologies, remote sensing and artificial intelligence technologies became one of the most sought-after strategies for automating environmental monitoring in terms of environmental pollution, especially in the face of global climate change problems (Yang et al., 2022).

## DISCUSSION

### Scientific Problems of CV in Environmental Diagnostics

Despite the many advantages of digital methods of environmental research, scientists have to solve a number of problems. A typical computer vision and signal processing workflow may include image pre-processing and segmentation—separating the “foreground” from the “background” to obtain a “binary mask,” measuring a parameter of interest (Lürig et al., 2021). At the same time, it is known that variability of such video file parameters as resolution, frame rate, file container types, codecs, and compression levels can be a source of experimental errors in behavioral analysis (Henry et al., 2019). These are the most common problems when using CV in environmental diagnostics. It is also possible to single out the scientific problems inherent in the scientific and practical areas discussed in this paper.

For digital phenotyping of living objects, it is extremely important to solve the problem of simultaneously tracking several significant parameters (Arya et al., 2022). A variation of this task is the acquiring and processing of volumetric (3D) images of living moving objects. Observation of unmarked animals in their natural habitat (in uncontrolled conditions) on video is reported to be difficult due to occlusion in the 3D environment (Ratnayake et al., 2021). However, the work of Kuswantori et al. (2022) shows progress toward fish digitization: accuracy increased to 72.65% with the landmarking technique, then increased to 76.64% with the subclassing technique, and finally increased to 77.42% by adding scale data.

The problems of biodiversity monitoring include problems resulting from a complex data structure, imperfection of statistical models, and communication of algorithms for different objects of study. Johnston et al. (2022) propose potential solutions to these problems: collecting additional data or metadata, analytically combining different data sets, and developing or refining statistical models. It should be noted that the quality of digital images of terrestrial (land) objects is still higher than that of underwater objects and the hydrosphere. Object crowding and occlusion reduce the latter’s quality, as well as the difficulty of obtaining large-scale data (Salman et al., 2020; Zhang et al., 2022).

The solution to these problems should be at the intersection of the efforts of biologists, ecologists and IT specialists. Some works devoted to CV for environmental research contain ideas that will be fully demanded and implemented in the future.

### Prospects for CV Technologies in Biodiagnostics

The most promising works have multiple interdisciplinary connections. Wägele et al. (2022) give the foundations for combining CV technologies and “computer hearing,” supplementing biodiversity data through decoding animal sounds. It also discusses the need to develop a database of barcodes of the DNA of organisms to collect even more complete and reliable information on biodiversity.

The prospects for CV are inextricably connected with improving artificial intelligence algorithms. Liu et al. (2022) note a significant scientific leap in developing neuromorphic patterns that simulate the functionality of the big brain. For deeper image processing by CV systems, a qualitative transition from two-dimensional neural networks to three-dimensional hierarchical neural networks, a biobrain characteristic, is required.

Figure 1 shows the development path of CV technologies in environmental diagnostics in the areas discussed in the review. From an idea, a prototype, or a pilot model to ordinary

	Yesterday	Today	Tomorrow
Digital phenotyping	Digital photography	Object recognition algorithms	Automatic identification of species of organisms
Monitoring of biological objects and environmental resources	Separate aero- and satellite images of the Earth’s surface	Continuous flow of information about the object of observation	3D survey with multiple data analysis
Assessing environmental pollution	Identification of pollution zones based on visible direct and indirect data	Sensorimotor and cognitive bioassaying	Combination of continuous chemical analysis and observation of responses of living organisms

Figure 1. Vector concept of CV technology development in environmental diagnostics

equipment, technologies are gradually bringing ecological research to a new scientific stage, distinguished by the transition from a point study of environmental objects to systems of total monitoring of their significant parameters.

## **CONCLUSION**

Thus, the scientific problems in the development of computer vision always come from practical problems that are solved with the help of such technologies.

The development and implementation of computer vision in environmental diagnostics is certainly a promising scientific direction, where the efforts of biologists, ecologists and IT specialists are needed. In the 20<sup>th</sup> century, the acquisition of satellite and aerial photographs was considered a breakthrough in visual environmental data. In the 21<sup>st</sup> century, digital processing of photo and video data will be applied to all objects in the micro and macro world.

Thanks to CV, 3-D herbariums, libraries of viruses and bacteria, non-invasive methods for determining species, and diagnostics of individual and population parameters of biological objects have become scientific achievements in phenotypization. Innovations in 3-D phenotyping, supplemented by other technologies, proved to be in demand in monitoring agricultural land, tracking moving objects, and monitoring processes in the water column. Environmental pollution assessment based on the CV family of technologies becomes rapid without losing analysis quality. At the same time, biotesting with short-circuit testing acquires consistency due to the variety of organisms' responses and the complexity of information processing.

Based on these scientific and technological achievements, databases of biological information will be created, new methods for studying biogenic and abiogenic objects, and algorithms for monitoring and managing environmental quality will be created. These achievements are important in solving global environmental problems of reducing species diversity and pollution.

The presented mini-review summarizes and structures the available information on using CV in environmental diagnostics and also suggests thinking about the future of environmental science methods and the role of scientists and artificial intelligence devices in bioecological and geocological research.

## **ACKNOWLEDGEMENT**

The authors acknowledge the research support provided by the Vyatka State University, Kirov, Russia, which made completing this work possible.

## REFERENCES

- Abou-Donia, M. (Ed.). (2015). *Mammalian Toxicology*. Wiley.
- Al Duhaiyyim, M., Marzouk, R., Al-Wesabi, F. N., Alrajhi, M., Hamza, M. A., & Zamani, A. S. (2022). An improved evolutionary algorithm for data mining and knowledge discovery. *CMC-Computers, Materials & Continua*, *71*(1), 1233-1247. <https://doi.org/10.32604/cmc.2022.021652>
- Alam, A., Chauhan, A., Khan, M. T., & Jaffery, Z. A. (2022). Drone-based crop product quality monitoring system: An application of smart agriculture. In R. S, Mor, D. Kumar, & A. Singh (Eds.), *Advanced Series in Management* (pp. 97-110). Emerald Publishing. <https://doi.org/10.1108/S1877-63612022000027007>
- Arya, S., Sandhu, K. S., Singh, J., & Kumar, S. (2022). Deep learning: As the new frontier in high-throughput plant phenotyping. *Euphytica*, *218*(4), Article 4. <https://doi.org/10.1007/s10681-022-02992-3>
- Ashikhmina, T. Ya., Alalykina, N. M., Domracheva, L. I., Shirokikh, I. G., Ogorodnikova, S. Yu., Kantor, G. Ya., Dabakh, E. V., Skugoreva, S. G., Vidyakin, A. I., Pestov, S. V., Golovko, T. K., Kondakova, L. V., Borodina, N. V., Domnina, E. A., Shirokikh, A. A., Tselishcheva, L. G., Kochurova, T. I., Adamovich, T. A., Kolupaev, A. V., Kondrukhova, S. V., Olkova, A. S., Panfilova, I. V., Timonyuk, V. M., Fokina, A. I., & Shulyateva, N. A. (2011). *Biological Monitoring of Natural and Man-Made Systems*. Syktyvkar: Institute of Biology of the Komi Scientific Center of the Ural Branch of the Russian Academy of Sciences.
- Bierman, A., LaPlumm, T., Cadle-Davidson, L., Gadoury, D., Martinez, D., Sapkota, S., & Rea, M. (2019). A high-throughput phenotyping system using machine vision to quantify severity of grapevine powdery mildew. *Plant Phenomics*, *2019*, Article 9209727. <https://doi.org/10.34133/2019/9209727>
- Bjerge, K., Nielsen, J. B., Sepstrup, M. V., Helsing-Nielsen, F., & Høye, T. T. (2021). An automated light trap to monitor moths (Lepidoptera) using computer vision-based tracking and deep learning. *Sensors*, *21*(2), Article 343. <https://doi.org/10.3390/s21020343>
- Boukouvalas, D. T., Prates, R. A., Leal, C. R. L., & Araújo, S. A. (2019). Automatic segmentation method for CFU counting in single plate-serial dilution. *Chemometrics and Intelligent Laboratory Systems*, *195*, Article 103889. <https://doi.org/10.1016/j.chemolab.2019.103889>
- Ditria, E. M., Lopez-Marcano, S., Sievers, M., Jinks, E. L., Brown, C. J., & Connolly, R. M. (2020). Automating the analysis of fish abundance using object detection: Optimizing animal ecology with deep learning. *Frontiers in Marine Science*, *7*, Article 429. <https://doi.org/10.3389/fmars.2020.00429>
- Djerdj, T., Hackenberger, D. K., Hackenberger, D. K., & Hackenberger, B. K. (2020). Observing earthworm behavior using deep learning. *Geoderma*, *358*, Article 113977. <https://doi.org/10.1016/j.geoderma.2019.113977>
- Dorfling, J., Siewert, S. B., Bruder, S., Aranzazu-Suescún, C., Rocha, K., Landon, P., Bondar, G., Pederson, T., Le, C., Mangar, R., Rawther, C., & Trahms, B. (2022). Satellite, aerial, and ground sensor fusion experiment for the management of elephants, rhinos, and poaching prevention. In *AIAA Science and Technology Forum and Exposition* (p. 1270). <https://doi.org/10.2514/6.2022-1270>
- Dudukcu, H. V., Taskiran, M., & Kahraman, N. (2023). UAV sensor data applications with deep neural networks: A comprehensive survey. *Engineering Applications of Artificial Intelligence*, *123* (Part C), Article 106476. <https://doi.org/10.1016/j.engappai.2023.106476>

- Everingham, M., Van Gool, L., Williams, C. K., Winn, J., & Zisserman, A. (2010). The pascal visual object classes (voc) challenge. *International Journal of Computer Vision*, 88, 303-338. <https://doi.org/10.1007/s11263-009-0275-4>
- Fashi, A., Cheraghi, M., Badiee, H., & Zamani, A. (2020). An analytical strategy based on the combination of ultrasound assisted flat membrane liquid phase microextraction and a smartphone reader for trace determination of malondialdehyde. *Talanta*, 209, Article 120618. <https://doi.org/10.1016/j.talanta.2019.120618>
- Fischler, M. A., & Firschein, O. (Eds.). (2014). *Readings in computer vision: Issues, problem, principles, and paradigms*. Elsevier.
- Gad, S. C. (Ed.). (2016). *Animal models in toxicology*. Routledge.
- Gervasi, A., Cardol, P., & Meyer, P. E. (2022). Automated open-hardware multiwell imaging station for microorganisms observation. *Micromachines*, 13(6), Article 833. <https://doi.org/10.3390/mi13060833>
- Henry, J., Rodriguez, A., & Wlodkowic, D. (2019). Impact of digital video analytics on accuracy of chemobehavioural phenotyping in aquatic toxicology. *Peer J*, 7, Article e7367. <https://doi.org/10.7717/peerj.7367>
- Høye, T. T., Ärje, J., Bjerger, K., Hansen, O. L. P., Iosifidis, A., Leese, F., Mann, H. M. R., Meissner, K., Melvad, C., & Raitoharju, J. (2021). Deep learning and computer vision will transform entomology. *PNAS*, 118(2), Article e2002545117. <https://doi.org/10.1073/pnas.2002545117>
- Hussein, B. R., Malik, O. A., Ong, W. H., & Slik, J. W. F. (2021). Automated extraction of phenotypic leaf traits of individual intact herbarium leaves from herbarium specimen images using deep learning based semantic segmentation. *Sensors*, 21(13), Article 4549. <https://doi.org/10.3390/s21134549>
- Johnston, A., Matechou, E., & Dennis, E. B. (2022). Outstanding challenges and future directions for biodiversity monitoring using citizen science data. *Methods in Ecology and Evolution*, 14(1), 103-116. <https://doi.org/10.1111/2041-210X.13834>
- Kantor, G. Y., & Ashikhmina, T. Y. (2014). Modeling of spring flood in the floodplain of the Vyatka River on the territory of the Kirovo-Chepetsky Branch Federal State Unitary Enterprise "RosRAO". *Theoretical and Applied Ecology*, 3, 29-35.
- Karl, D. M., & Proctor, L. M. (2007). Foundations of microbial oceanography. *Oceanography*, 20(2), 16-27.
- Keefe, R. F., Zimelman, E. G., & Picchi, G. (2022). Use of individual tree and product level data to improve operational forestry. *Current Forestry Reports*, 8, 148-165. <https://doi.org/10.1007/s40725-022-00160-3>
- Kuswatori, A., Suesut, T., Tangsrirat, W., & Nunak, N. (2022). Development of object detection and classification with YOLOv4 for similar and structural deformed fish. *Eureka: Physics and Engineering*, 2, 154-162. <https://doi.org/10.21303/2461-4262.2022.002345>
- Li, J., Li, Y., Bi, S., Xu, J., Guo, F., Lyu, H., Dong, X., & Cai, X. (2022). Utilization of GOCI data to evaluate the diurnal vertical migration of *Microcystis aeruginosa* and the underlying driving factors. *Journal of Environmental Management*, 310, Article 114734. <https://doi.org/10.1016/j.jenvman.2022.114734>

- Li, X., Li, N., Li, B., Sun, Y., & Gao, E. (2022). AbundanceR: A novel method for estimating wildlife abundance based on distance sampling and species distribution models. *Land*, 11(5), Article 660. <https://doi.org/10.3390/land11050660>
- Li, Z., Guo, R., Li, M., Chen, Y., & Li, G. (2020). A review of computer vision technologies for plant phenotyping. *Computers and Electronics in Agriculture*, 176, Article 105672. <https://doi.org/10.1016/j.compag.2020.105672>
- Liu, X., Wang, F., Su, J., Zhou, Y., & Ramakrishna, S. (2022). Bio-inspired 3D artificial neuromorphic circuits. *Advanced Functional Materials*, 32(22), Article 2113050. <https://doi.org/10.1002/adfm.202113050>
- Lopez-Marcano, S., Brown, C. J., Sievers, M., & Connolly, R. M. (2020). The slow rise of technology: Computer vision techniques in fish population connectivity. *Aquatic Conservation: Marine and Freshwater Ecosystems*, 31(1), 210-217. <https://doi.org/10.1002/aqc.3432>
- Lürig, M. D., Donoughe, S., Svensson, E. I., Porto, A., & Tsuboi, M. (2021). Computer vision, machine learning, and the promise of phenomics in ecology and evolutionary biology. *Frontiers in Ecology and Evolution*, 9, Article 642774. <https://doi.org/10.3389/fevo.2021.642774>
- Ma, P., Li, C., Rahaman, M., Yao, Y., Zhang, J., Zou, S., Zhao, X., & Grzegorzec, M. (2023). A state-of-the-art survey of object detection techniques in microorganism image analysis: From classical methods to deep learning approaches. *Artificial Intelligence Review*, 56, 1627-1689. <https://doi.org/10.1007/s10462-022-10209-1>
- Ma, Y., & Wei, W. (2021). Evaluate the viscosity of small aquaculture water by computer vision technology. *Journal of Physics: Conference Series*, 2010, Article 012022. <https://doi.org/10.1088/1742-6596/2010/1/012022>
- Mochida, K., Koda, S., Inoue, K., Hirayama, T., Tanaka, S., Nishii, R., & Melgani, F. (2019). Computer vision-based phenotyping for improvement of plant productivity: A machine learning perspective. *GigaScience*, 8(1), Article giy153. <https://doi.org/10.1093/gigascience/giy153>
- Monaldi, A. C., Romero, G. G., Alanís, E. E., & Cabrera, C. M. (2015). Digital holographic microscopy for microalgae biovolume assessment. *Optics Communications*, 336, 255-261. <https://doi.org/10.1016/j.optcom.2014.10.035>
- Moraga, J., Duzgun, H. S., Cavour, M., & Soydan, H. (2022). The geothermal artificial intelligence for geothermal exploration. *Renewable Energy*, 192, 134-149. <https://doi.org/10.1016/j.renene.2022.04.113>
- Moreno, G., Ascano, J. S., Ricardo, J. O., De La Cruz, L. T., Yaumel, A., Strickler, J. R., & Lopes, R. M. (2020). A new focus detection criterion in holograms of planktonic organisms. *Pattern Recognition Letters*, 138, 497-506. <https://doi.org/10.1016/j.patrec.2020.08.004>
- Mu, S., Yang, G., Xu, X., Wan, R., & Li, B. (2022). Assessing the inundation dynamics and its impacts on habitat suitability in Poyang Lake based on integrating Landsat and MODIS observations. *Science of the Total Environment*, 834, Article 154936. <https://doi.org/10.1016/j.scitotenv.2022.154936>
- Nikitin, O. V., Nasyrova, E. I., Nuriakhmetova, V. R., & Latypova, V. Z. (2018). Using computer vision algorithms to analyze the behavioral activity of daphnia. In *Proceedings of the XVI All-Russian Scientific and Practical Conference with International Participation*, 99. <https://elibrary.ru/item.asp?id=36586088>

- Norouzzadeh, M. S., Morris, D., Beery, S., Joshi, N., Jojic, N., & Clune, J. (2020). A deep active learning system for species identification and counting in camera trap images. *Methods in Ecology and Evolution*, *12*(1), 150-161. <https://doi.org/10.1111/2041-210X.13504>
- Patil, L. P., Ghante, P. H., Thomse, S. R., Navasare, M. G., & Pawar, S. Y. (2021). Robotic applications and management of plant diseases. *AgriCos e-Newsletter*, *2*(6), 36-40.
- Petso, T., Jamisola, R. S., Mpoeleng, D., Bennitt, E., & Mmereki, W. (2021). Automatic animal identification from drone camera based on point pattern analysis of herd behaviour. *Ecological Informatics*, *66*, Article 101485. <https://doi.org/10.1016/j.ecoinf.2021.101485>
- Qian, W., Huang, Y., Liu, Q., Fan, W., Sun, Z., Dong, H., Wan, F., & Qiao, X. (2020). UAV and a deep convolutional neural network for monitoring invasive alien plants in the wild. *Computers and Electronics in Agriculture*, *147*, Article 105519. <https://doi.org/10.1016/j.compag.2020.105519>
- Rani, P., Kotwal, S., & Manhas, J. (2022). An intelligent species level deep learning-based framework in automatic classification of microscopic bacteria images. In S. Roy, D. Sinwar, T. Perumal, A. Slowik, & J. M. R. S. Tavares (Eds.), *Innovations in Computational Intelligence and Computer Vision. Advances in Intelligent Systems and Computing*, (Vol. 1424). Springer. [https://doi.org/10.1007/978-981-19-0475-2\\_52](https://doi.org/10.1007/978-981-19-0475-2_52)
- Ratnayake, M. N., Dyer, A. G., & Dorin, A. (2021). Tracking individual honeybees among wildflower clusters with computer vision-facilitated pollinator monitoring. *PloS One*, *16*(2), Article e0239504. <https://doi.org/10.1371/journal.pone.0239504>
- Rauf, S., Tashkandi, N., Filho, J. I. O., Oviedo-Osornio, C. I., Danish, M. S., Hong, P. Y., & Salama, K. N. (2022). Digital *E. coli* counter: A microfluidics and computer vision-based dnazyme method for the isolation and specific detection of *E. coli* from water samples. *Biosensors*, *12*(1), Article 34. <https://doi.org/10.3390/bios12010034>
- Roy, A. M., Bhaduri, J., Kumar, T., & Raj, K. (2023). WilDect-YOLO: An efficient and robust computer vision-based accurate object localization model for automated endangered wildlife detection. *Ecological Informatics*, *75*, Article 101919. <https://doi.org/10.1016/j.ecoinf.2022.101919>
- Ruiz-Santaquiteria, J., Bueno, G., Deniz, O., Vallez, N., & Cristobal, G. (2020). Semantic versus instance segmentation in microscopic algae detection. *Engineering Applications of Artificial Intelligence*, *87*, Article 103271. <https://doi.org/10.1016/j.engappai.2019.103271>
- Russakovsky, O., Deng, J., Su, H., Krause, J., Satheesh, S., Ma, S., Huang, Z., Karpathy, A., Khosla, A., Bernstein, M., Berg, A.C., & Fei-Fei, Li. (2015). ImageNet large scale visual recognition challenge. *International Journal of Computer Vision*, *115*, 211-252. <https://doi.org/10.1007/s11263-015-0816-y>
- Salman, S., Shafait, F., Mian, M., Shortis, M. R., Khurshid, K., Ulges, A., Schwanecke, U. (2020). Automatic fish detection in underwater videos by a deep neuralnetwork-based hybrid motionlearning system. *ICES Journal of Marine Science*, *77*(4), 1295-12307. <https://doi.org/10.1093/icesjms/fsz025>
- Shapiro, L. G., & Stockman, G. C. (2001). *Computer vision*. Prentice Hall.
- Sharma, C., Isha, I., & Vashish, V. (2021). Water quality estimation using computer vision in UAV. In *2021 11th International Conference on Cloud Computing, Data Science & Engineering (Confluence)* (pp. 448-453). IEEE Publishing. <https://doi.org/10.1109/Confluence51648.2021.9377082>

- Sheehan, E. V., Bridger, D., Nancollas, S. J., & Pittman, S. J. (2020). PelagiCam: A novel underwater imaging system with computer vision for semi-automated monitoring of mobile marine fauna at offshore structures. *Environmental Monitoring and Assessment*, *192*, Article 11. <https://doi.org/10.1007/s10661-019-7980-4>
- Sondhi, Y., Jo, N. J., Alpizar, B., Markee, A., Dansby, H. E., Currea, J. P., Samuel, T. F., Ruiz, C., Barredo, E., Allen, P., DeGennaro, M., Kawahara, A. Y., & Theobald, J. C. (2022). Portable locomotion activity monitor (pLAM): A cost-effective setup for robust activity tracking in small animals. *Methods in Ecology and Evolution*, *13*(4), 805-812. <https://doi.org/10.1111/2041-210X.13809>
- Stefen, C., Wagner, F., Asztalos, M., Giere, P., Grobe, P., Hiller, M., Hofmann, R., Jähde, M., Lächele, U., Lehmann, T., Ortmann, S., Peters, B., Ruf, I., Schiffmann, C., Thier, N., Unterhitzberger, G., Vogt, L., Rudolf, M., Wehner, P., & Stuckas, H. (2022). Phenotyping in the era of genomics: MaTrics—A digital character matrix to document mammalian phenotypic traits. *Mammalian Biology*, *102*, 235-249. <https://doi.org/10.1007/s42991-021-00192-5>
- Torres-Sánchez, J., Escolà, A., de Castro, A. I., López-Granados, F., Rosell-Polo, J. R., Sebé, F., Jiménez-Brenes, F. M., Sanz, R., Gregorio, E., & Peña, J. M. (2023). Mobile terrestrial laser scanner vs. UAV photogrammetry to estimate woody crop canopy parameters—Part 2: Comparison for different crops and training systems. *Computers and Electronics in Agriculture*, *212*, Article 108083. <https://doi.org/10.1016/j.compag.2023.108083>
- Tovstik, E. V., Adamovich, T. A., & Ashikhmina, T. Y. (2019). Identification of sites of mass growth of *Heracleum sosnowskyi* Manden. using spectral indices according to Sentinel-2 images. *Theoretical and Applied Ecology*, *3*, 34-40. <https://doi.org/10.25750/1995-4301-2019-3-034-040>
- Vaganov, A.V., Krotova, O.S., & Khvorova, L.A. (2021). Processing and analysis of botanical micro- and macroobjects using computer vision technologies. *Journal of Physics: Conference Series*, *2142*(1), Article 012003. <https://doi.org/10.1088/1742-6596/2142/1/012003>
- Wägele, J. W., Bodesheim, P., Bourlat, S. J., Denzler, J., Diepenbroek, M., Fonseca, V., Frommolt, K. H., Geiger, M. F., Gemeinholzer, B., Glockner, F. O., Hauke, T., Kirse, A., Kolpin, A., Kostadinov, I., Kuhl, H. S., Kurth, F., Lasseck, M., Liedke, S., Losch, F., Muller, S., Petrovskaya, N., Piotrowski, K., Radig, B., Scherber, C., Schoppmann, L., Schulz, J., Steinhage, V., Tschan, G. F., Vautz, W., Velotto, D., Weigend, M., & Wildermann, S. (2022). Towards a multisensor station for automated biodiversity monitoring. *Basic and Applied Ecology*, *59*, 105-138. <https://doi.org/10.1016/j.baae.2022.01.003>
- Weinstein, B. G. (2018). A computer vision for animal ecology. *Journal of Animal Ecology*, *87*(3), 533-545. <https://doi.org/10.1111/1365-2656.12780>
- Wilson, R. J., Siqueira, A. F., Brooks, S. J., Price, B. W., Simon, L. M., Walt, S. J., & Fenberg, P. B. (2021). Applying computer vision to digitised natural history collections for climate change research: Temperature-size responses in British butterflies. *Methods in Ecology and Evolution*, *14*(2), 372-384. <https://doi.org/10.1111/2041-210X.13844>
- Xia, F., Xie, X., Wang, Z., Jin, S., Yan, K., & Ji, Z. (2022). A novel computational framework for precision diagnosis and subtype discovery of plant with lesion. *Frontiers in Plant Science*, *12*, Article 789630. <https://doi.org/10.3389/fpls.2021.789630>

- Xiong, Y., Zhu, M., Li, Y., Huang, K., Chen, Y., & Liao, J. (2022). Recognition of geothermal surface manifestations: A comparison of machine learning and deep learning. *Energies*, *15*(8), Article 2913. <https://doi.org/10.3390/en15082913>
- Yang, B., He, Y., & Yin, H. (2020). Research on data analysis and quality control based on P control chart. In *2020 13<sup>th</sup> International Congress on Image and Signal Processing, BioMedical Engineering and Informatics (CISP-BMEI)* (pp. 1098-1102). IEEE Publishing. <https://doi.org/10.1109/CISP-BMEI51763.2020.9263537>
- Yang, L., Driscoll, J., Sarigai, S., Wu, Q., Lippitt, C. D., & Morgan, M. (2022). Towards synoptic water monitoring systems: A review of AI methods for automating water body detection and water quality monitoring using remote sensing. *Sensors*, *22*(6), Article 2416. <https://doi.org/10.3390/s22062416>
- Yuan, W., Choi, D., & Bolkas, D. (2022). GNSS-IMU-assisted colored ICP for UAV-LiDAR point cloud registration of peach trees. *Computers and Electronics in Agriculture*, *197*, Article 106966. <https://doi.org/10.1016/j.compag.2022.106966>
- Zaroudi, F., Nasihatkon, B., Hosseinzadeh, R., Fakhar, A. R., & Seidi, S. (2023). Miniaturized on-chip electromembrane extraction with QR code-based red-green-blue analysis using a customized Android application for copper determination in environmental and food samples. *Food Chemistry*, *414*, Article 135667. <https://doi.org/10.1016/j.foodchem.2023.135667>
- Zhang, J., Li, C., Rahaman, M., Yao, Y., Ma, P., Zhang, J., Zhao, X., Jiang, T., & Grzegorzec, M. (2022). A comprehensive review of image analysis methods for microorganism counting: From classical image processing to deep learning approach. *Artificial Intelligence Review*, *55*, 2875-2944. <https://doi.org/10.1007/s10462-021-10082-4>
- Zhang, W., Miao, J., Li, M., & Liu, H. (2022). Research on underwater image registration method based on MSRCR and SIFT. In *International Conference on Computer Vision and Pattern Analysis (ICCPA 2021)* (Vol. 12158, pp. 74-80). SPIE Publishing. <https://doi.org/10.1117/12.2626893>
- Zhou, J., Yang, T., Chu, W., & Zhang, W. (2022). Underwater image restoration via backscatter pixel prior and color compensation. *Engineering Applications of Artificial Intelligence*, *111*, Article 104785. <https://doi.org/10.1016/j.engappai.2022.104785>



# A Deep Learning-based Classification Model for Arabic News Tweets Using Bidirectional Long Short-Term Memory Networks

Chin-Teng Lin<sup>1</sup>, Mohammed Thanoon<sup>2</sup> and Sami Karali<sup>1,2\*</sup>

<sup>1</sup>Australian AI Institute, Faculty of Engineering and Information Technology, University of Technology Sydney, Sydney, 2007, Australia

<sup>2</sup>Umm Al-Qura University, College of Engineering and Computing at Al-Lith, Makkah, 24382, Saudi Arabia

## ABSTRACT

This research develops a classification model for Arabic news tweets using Bidirectional Long Short-Term Memory networks (BiLSTM). Tweets about Arabic news were gathered between August 2016 and August 2020 and divided into five categories. Custom Python scripts, Twitter API and the GetOldTweets3 Python library were used to collect the data. BiLSTM was used to train and test the model. The results indicated an average accuracy, precision, recall, and f1-score of 0.88, 0.92, 0.88, and 0.89, respectively. The results could have practical implications for Arabic machine learning and NLP tasks in research and practice.

*Keywords:* Arabic, Arabic dataset, Arabic news, ML, NLP, Twitter

## INTRODUCTION

Social media platforms have changed the way people talk to each other and are now an important part of everyday life. Panagiotou et al. (2016) asserted that with the rise of social media, events can now reach a wider audience and create a buzz that was not possible earlier. Twitter users' tweets are a large source of unorganized and varied information. Aslam (2018) and Guzman et al. (2017) stated that around 326 million individuals log

onto Twitter monthly and generate around 500 million tweets. That is the equivalent of 6000 tweets per second. Tweets were initially intended as more of a light-hearted medium, but as researchers saw their potential, they quickly became one of the most researched platforms. Twitter does not enforce rules for its users, so anybody can post whatever they want.

### ARTICLE INFO

#### Article history:

Received: 16 July 2023

Accepted: 01 February 2024

Published: 16 July 2024

DOI: <https://doi.org/10.47836/pjst.32.4.09>

#### E-mail addresses:

[mithanoon@uqu.edu.sa](mailto:mithanoon@uqu.edu.sa) (Mohammed Thanoon)

[chin-teng.lin@uts.edu.au](mailto:chin-teng.lin@uts.edu.au) (Chin-Teng Lin)

[sami.karali@student.uts.edu.au](mailto:sami.karali@student.uts.edu.au) (Sami Karali)

\* Corresponding author

Tweets contain a wealth of data, yet some could be incorrect. In post-Trump politics, false news has taken the central stage, and social media platforms like Facebook and Twitter have been linked to its proliferation (Hunt, 2016). Automatically categorizing tweets is necessary to improve information retrieval for individual and institutional needs (e.g., news filtering, false news tracking, rumor mining). That is why training machine learning algorithms to properly categorize tweets is more important than ever. These algorithms may spot and remove hoaxes, rumors, and other nonsense from users' Twitter feeds.

Many challenges come with classifying Arabic tweets because of their vast potential. Another challenge is that Twitter has limited words for tweets, sometimes leading to ambiguous statements and unclear expressions, which can result in misclassifications in practical situations. Moreover, the Arabic language is multifaceted, including regional dialects and colloquialisms, adding another layer of complexity.

Natural Language Processing (NLP) methods like sentiment analysis, news categorization, and identifying rumor news can also analyze tweets. Alonso et al. (2021) observed that sentiment analysis is a good way to find and fight fake news. Kowsari et al. (2019) opined that putting news tweets into categories based on what they are about could help improve the quality of information people get and help the media share what news people are most interested in. People who work in the news will look at tweets and people's interests to get a picture of the population. When researchers classify texts, they can easily look for relevant information, look at it, and organize it for future use. Manual text categorization is possible, but it is a laborious process that takes a lot of effort and time. Text classification, which uses machine learning and deep learning, is a great way to automatically identify or classify text like news.

Many studies used machine-learning techniques (Ikonomakis et al. (2005); Buabin (2012). Yang and Pederson (1997) stated that classification is the process of putting a piece of text into one of many predetermined groups based on the information it contains. Al Sbou et al. (2018) stated that, as 6.6% of the world's population speaks Arabic, it is one of the most widely used languages. It is the fifth most popular language on the web, according to Albalooshi et al. (2011) and comes in three different forms, one of which is classical Arabic, which is used in religious and ancient scripts. A report by Raftery (2017) reveals that two-thirds of young Arabs use social media platforms like Facebook and Twitter as their primary sources of news, and the area is home to eleven million monthly active Twitter users who send out over 27.4 million tweets daily. Arabic tends to attach prepositions, pronouns, and the article to words. It makes the language very inflectional and agglutinative. It is important to know how they are put together syntactically to represent and change Arabic words to be used in a categorization system.

Arabic text categorization has received comparatively less attention than its English counterpart. Very few studies have focused on the categorization of short texts in Arabic.

In addition to the linguistic peculiarities of Arabic, the lack of open access to a small text corpus in the language is a limitation (Al-Tahrawi & Al-Khatib, 2015). There are only four other known papers that attempt to categorize Arabic tweets. Deep learning was utilized by Bdeir and Ibrahim (2020), and classical machine learning was employed by Bekkali and Lachkar (2014), Abdelaal et al. (2018) and Ibrahim et al. (2021).

As more and more Arabic news tweets are shared daily, the question now arises: How can we effectively classify and analyze them to meet the increasing need for accurate and reliable NLP models? By developing a deep learning-based categorization model for Arabic news tweets with Bidirectional Long Short-Term Memory (BiLSTM) networks, this research presents an approach to overcoming this challenge. By collecting and organizing tweets into broad categories like “general news,” “regional news,” “sports news,” “economic news,” and “quality of life news,” we were able to train and test our model to adequate levels across a variety of metrics, including accuracy, precision, recall, and f1-score.

Our research can aid in producing more targeted and relevant news material for Arabic speakers, and it can provide significant assistance for the development of natural language processing systems by providing insights into the precise categories of information that the population seems to be most interested in.

## **RELATED WORK**

According to Salloum et al. (2017a, 2017b), Alabbas et al. (2016), Salloum et al. (2018), and Elhassan and Ahmed (2015), automating the process of categorizing a collection of documents according to their content using technologies and algorithms is a text classification process. Elhassan and Ahmed (2015) noted that it is a technique for locating and navigating big datasets and organizing them into meaningful categories for later use. There has been a rise in specialized studies on the classification of texts as massive data are available from numerous sources, including websites, emails, news stories, social media posts, reports, and journals.

### **Twitter Dataset for NLP**

This study aims to learn how and why tweeted datasets have become so widely used for studying people’s opinions and responses. Twitter data is more useful than Facebook data for building 50 large corpora for natural language processing, as was pointed out by Ahmed et al. (2017). However, there is a dearth of data compared to the English dataset, as observed by Assiri et al. (2018). Existing dialects of Arabic, which vary from modern standard Arabic and even between Arab countries, further complicate matters. Data mining for Arabic sentiment analysis has greatly benefited from the efforts of Almuqren and Cristea (2021), which have created the gold-standard Saudi corpus AraCust and the Saudi lexicon AraTweet (ASA). AraSenCorpus is another repository of information; it includes 4.5 million tweets in both

standardized and colloquial varieties of Arabic. The widespread relevance and practicality of this dataset demonstrate the value of data. When organizing human opinion into a data set, Arabic Sentiment Analysis (ASA) and Arabic Text Classification (ATC) are crucial tools. Sentiment analysis is a method that can be used to calculate how the public feels about a topic. Feng and Kirkley (2021) researched the emotional response of the population to policies developed for dealing with COVID-19, and their findings suggest that tweets can be used to improve public health monitoring and crisis management. Jordan et al. (2018) determined that utilizing Twitter as a data source yields real-time information from various geographical regions. However, there is a lack of investigation into the potential of Twitter data for tracking and anticipating the public's reactions to issues. More research is required to validate the utility of datasets across disciplines.

### **Deep Learning Approaches**

Encoding textual features using bag-of-words, Ngrams, or Tf-IDF is common in text classification tasks, including Arabic. On the other hand, recent neural network-based models have dramatically surpassed these older approaches. Standard approaches, including gated neural network models like LSTM by Schmidhuber and Hochreiter (1997) and GRU by Chung et al. (2014), were able to circumvent these issues largely thanks to deep learning techniques. To consider context, Vaswani et al. (2017) observed that the Transformer Network architecture with self-attention layers has replaced all recurrent and convolutional layers as the state-of-the-art in many NLP tasks. It inspired the development of novel neural network architectures for contextual word embedding models like ELMO by Peters et al. (2018), ULmFit by Howard and Ruder (2018), and new hybrid Bidirectional Encoder Representations from Transformers (BERT) architectures by Devlin (2018). Even though deep learning models are powerful, many challenges may affect the model's performance, especially related to data quality on platforms like Twitter, due to brevity and ambiguity. Researchers have been addressing the scalability of these models in terms of both computational efficiency and adaptability to evolving news topics.

Self-attention layers shrank the model, improved training efficiency, and produced outstanding results in neural machine translation. Deep learning methods have been used in many areas of study, such as Arabic NLP and sentiment analysis. El-Alami and Alaoui (2016) used deep learning to improve Arabic text classification. They used a deep stacked auto-encoder and short reproduced codes to reduce the number of dimensions in the representation space. Sayed et al. (2017) examined how well Arabic text can be sorted using a deep neural network based on textual similarity and N-gram level. The results showed a deep learning classifier with an AR of 98.50%, a 75% similarity level, and a 3-gram outperforms the SVM, NB, and k-NN classifiers. Using a deep learning strategy, Boukil et al. (2018) improved the performance of their Arabic text classifier. They found 111,728

news documents on the web and put them into five categories to make a corpus. They used the TF-IDF method to choose which features to use and a vector-words strategy to show the text. With an accuracy of 92.94%, the CNN model outperformed both LR and SVM.

Galal et al. (2019) used CNN (Convolutional Neural Network) deep learning to classify Arabic texts. As a preprocessing step, they sorted all the Arabic words with the same root into groups using the proposed Gstem technique. The accuracy of the CNN improved to 92.42% with the help of Gstem from 88.75% without it. Elnagar et al. (2020) proposed and evaluated nine deep-learning methods for classifying single- and multi-label Arabic text. SANAD and NADiA, two massive Arabic text collections, were used to validate Arabic text classifiers. The best models for single-label classification tasks were HANGRU, CNN, BiGRU, and BiLSTM. These models have since been trained for multi-label classification. The models were evaluated based on their accuracy using the accuracy metric.

### Arabic Text Classification

Because of the nature of the Arabic language and the scarcity of adequate resources, categorizing Arabic text is more difficult. There is a big difference between the verbal and nominal sentences, where the latter do not need a verb, and the vocabulary size, and between the use of diphthongs and long vowels. A significant factor in using a particular methodological framework is the nature of classification, which may involve short versus long documents, multiclass versus binary classification, or multi-label classification. Studies of text classification in Arabic are in tandem with suitable benchmarks and corpora development.

Researchers have suggested many methods and approaches for classifying Arabic text. Using support vector machines, Moh'd Mesleh (2011) investigated the value of feature sub-set selection metrics and provided an empirical comparison of them (SVM). Hmeidi et al. (2015) studied the performance of such classifiers and examined how using different Arabic stems, like the light and root-based ones, affected the results. Embedding-based methods, such as word average and document embeddings like Doc2-vec and Glove, have been proposed by El Mahdaouy et al. (2016). Convolutional and recurrent neural networks have seen a rise in popularity and research due to their ability to model sentences based on sequences of context windows and capture local correlations. In contrast to RNN's ability to treat sequences of any length and capture long-term dependencies, CNN's emphasis on features at different sentence positions through convolutional filters and pooling sets it apart.

Dahou et al. (2016) proposed building a CNN for Arabic sentiment analysis on top of a model that used web-crawled corpus words to train embeddings for Arabic words. Both Alayba et al. (2018) and El-Alami et al. (2020) investigated convolutional neural networks (CNNs) and long short-term memories (LSTMs) and their hybrids for classifying Arabic text using a retrofitting technique that makes use of the semantic information embedded in Arabic Word-Net. Contextual embedding models like ELMo, ULMFiT, and BERT are

current developments in language modeling. The pre-trained Ara-BERT for Arabic was introduced by Antoun et al. (2020), and it was tested on a variety of natural-language understanding tasks and compared to the multilingual BERT. A large, evenly distributed Arabic short-text dataset is still lacking. Classifying news tweets is a challenging task related to short text classification tasks (Mohammed et al., 2020). Numerous languages, including Arabic, exhibit this property, as observed by Khoja et al. (2017). Despite recent progress in Arabic text classification, challenges like precise semantic capturing arise due to the complexity and ambiguity of Arabic text data.

## **METHODOLOGY**

A model was created with real data for news tweet topic classification. A hierarchical approach has been built and divided into four phases, as shown in Figure 1.

### **Tweets Harvesting Phase**

The first phase is news tweet collection. All news tweets were collected using self-made Python scripts for both the Twitter application programming interface (API) and the GetOldTweets3 Python library, allowing historical tweets to be collected beyond the 1-week limitation of the standard Twitter API. A larger set of tweets with a more diverse set enhances the robustness of the model.

### **Preprocessing Phase**

The second phase is cleaning the tweets of unwanted elements like non-Arabic words, symbols, URLs, emoticons, and stop words, especially those common in Arabic. The rationale of this phase is data cleaning to ensure that the model is trained on relevant content, improving its accuracy and efficiency. After collecting the news tweets, the preprocessing process was conducted. Only root tweets were considered, and retweets were excluded. All news tweets other than those in Arabic were excluded, including numbers. Then, all punctuation marks were removed. Furthermore, any URLs and emoticons were removed to obtain higher textual quality. Stop words were also excluded.

### **Features Extraction Phase**

The feature extraction phase is the process of transforming raw data into numerical features. This phase is responsible for a linear combination of the existing features. The recent state-of-the-art model, the AraBERT model, was used in this work. This model is a pre-trained BERT that is specifically for the Arabic language. This model tokenizes sentences and converts each token into embedding vectors. AraBERT is designed specifically for Arabic, which captures linguistic nuances that generic models may miss.

## Classification Phase

The final phase is decision-making, also known as the classification phase. The classifier in this phase acts on the sentence representation to get the decision and give each tweet a label belonging to one of the predefined classes. Various techniques can be used for text classification. Graves and Schmidhuber (2005) found BiLSTM suitable for text classification due to its effectiveness in NLP as well as its use of memory as specific hidden units. The BiLSTM model was implemented with specific configurations, including an embedding size of 256 words, a training batch size 64, and 5 epochs. BiLSTM is effective in text classification because of its ability to remember long-term dependencies, which makes it suitable for tweet classification.

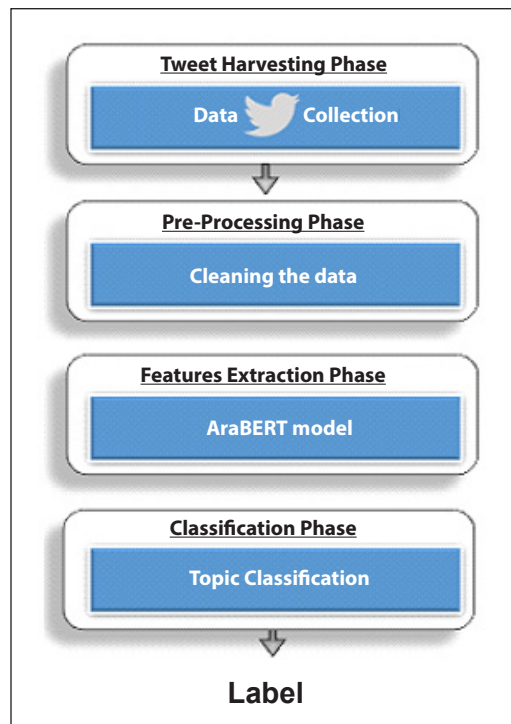


Figure 1. The flowchart of the model

## DESIGN AND IMPLEMENTATION

### Tweets Harvesting Phase

The target was to build a large Arabic news tweet dataset for Saudi Arabia. The dataset contained 89,179 news tweets related to Saudi Arabian news. News tweets were collected from verified users on Twitter, and all users were official news agencies of Saudi Arabia. These users had already categorized themselves into five classes: General News, Regional News, Sports News, Economic News and Quality of Life News. Moreover, they all posted tweets based on the class they belonged to. Therefore, each news tweet was labeled based on the user class from which the tweet was collected.

All news tweets were collected using self-made Python scripts for the Twitter application programming interface (API) and the GetOldTweets3 Python library. The Twitter API is a back-end server that stores all individuals' tweets. API provides a service where data can be collected for the public, but it has the limitation that data more than 1-week old cannot be accessed, as revealed by Search Tweets (<https://developer.twitter.com/en/docs/twitter-api/v1/tweets/search/guides/standardoperators>). However, there are many methods to extract the data that can be used, and there are no restrictions for collecting many tweets and accessing the historical tweets, like the GetOldTweets3 Python library

used in this study. GetOldTweets3 is an open-sourced Python library that can be used with specific keywords and periods to extract historical tweets, as averred by Jefferson (2018).

The collection period ranges from the day of the user creation (in general, August 2016) to August 1, 2020. Data were collected at different periods for each of the labels. Arabic filter was used to collect all data. Only root tweets were considered, and retweets were excluded. The data were formatted as Excel text files.

## Preprocessing Phase

This phase is one of the most important processes that go into a given dataset to obtain a clean version and prepare the dataset for the next phase. Even though the preprocessing phase is crucial for enhancing data quality, it might result in the loss of some relevant information. The dataset used in this research is substantial, reflecting the wide range of news topics. However, this diversity and the ever-evolving nature of news suggest that the dataset might still lack certain nuances.

After collecting the news tweets, the preprocessing process was conducted. Only root tweets were considered, and retweets were excluded. All news tweets other than those in Arabic were excluded, including numbers. Then, all punctuation marks were removed. Furthermore, any URLs and emoticons were removed to obtain higher textual quality. Stop words were also excluded.

The collected news tweets are publicly available (Karali et al., 2021). They were formatted into an Excel file containing labels, and all tweets were listed under their label with the posted date. The dataset contained only tweet IDs with their labels and posted days without any personally identifying information, using the user IDs to comply with Twitter's Developer Policy for the dataset, as extracted from Twitter's Developer Agreement and policy (<https://developer.twitter.com/en/developer-terms/agreement-and-policy>). Table 1 presents one example of the raw data before and after preprocessing and its translation.

Table 1

*One example of the raw data and its translation is before and after preprocessing*

Before processing	
Tweet	Translation
عاجل #مجلس الوزراء: الموافقة على اتفاقية# الخدمات الجوية بين حكومة المملكة وحكومة آيسلندا	# Urgent # Council of Ministers: The Air Services Agreement between the Kingdom of Saudi Arabia and the Icelandic governments has been approved.
After processing	
Tweet	Translation
عاجل مجلس وزراء موافق اتفاقي خدم جوي حكوم مملك حكوم آيسلندا	Urgent Council Ministers Air Service agreement Kingdom Saudi Arabia government Icelandic government approved.

Processing involved the removal of hashtags, prepositions, definite and indefinite articles, conjunctions and participles. The change in the content due to such processing is evident in Table 1.

### Features Extraction Phase

The feature extraction phase is the process of transforming raw data into numerical features. This transformation aims to process the numerical features and preserve the original dataset. The recent state-of-the-art model, the AraBERT model, was used in this work. The AraBERT model was used because it has proved its effectiveness with deep learning models, such as the BiLSTM model. This model is a pre-trained BERT that is specifically for the Arabic language. AraBERT uses the attention mechanism (Antoun et al., 2020). This mechanism learns contextual relations between words. Table 2 shows the structure of all versions of AraBERT (Matrane et al., 2021), and AraBERT base V2 was used in this study. AraBERT breaks up the sentences into sections (tokenization), and this method is relevant for Arabic as it is based on the Farasa Segmenter, as illustrated by Saeed (2021). After that, each token was converted to weights and embedding vectors. Table 2 summarizes the architectures of the AraBERT model (Elfaik & Nfaoui, 2021).

Table 2  
*AraBERT architectures details (Elfaik & Nfaoui, 2021)*

	AraBert	ArabicBERT T Mini	ArabuBERT Medium	ArabicBERT Base	ArabicBERT Large
Hidden layers	12	4	8	12	24
Attention heads	12	4	8	12	16
Hidden size	768	256	512	768	1024
Parameters	110 M	11 M	42 M	110 M	340 M

ArabicBert Large can identify 24 layers, 16 attention heads and a hidden size 1024 using 340 parameters. Thus, it is the most efficient feature extraction tool.

In Figure 2, a news tweet is divided into two parts: (1) sentence embedding and (2) positional embedding. AraBERT uses an encoder for each part of the news tweet and converts it into a vector. Then, in an activation layer, AraBERT uses a transformer decoder to calculate the score of each part.

### Classification Phase

Various techniques can be used for text classification. Graves and Schmidhuber (2005) found BiLSTM suitable for text classification due to its effectiveness in NLP as well as its use of memory as specific hidden units. In text classification, storing context history information and recalling the input words will support the model for classification

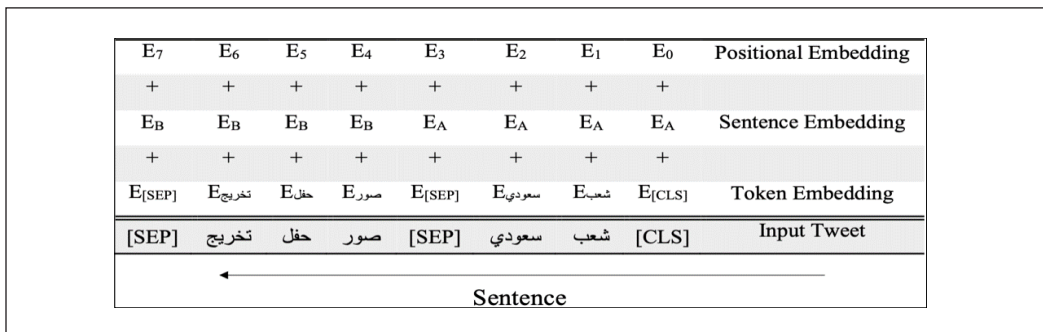


Figure 2. AraBERT model example of creating the input: Token, position, and sentence embeddings

and get higher results. BiLSTM has these characteristics, so this classifier was used in this research.

The BiLSTM model is based on the sequence-to-target concept and bidirectional architecture. BiLSTM makes the sequence information of a neural network in both directions, from front to back and in reverse. In regular LSTM, the input flow is in one direction, which is either forward or backward. On the other hand, both directions for the input flow in BiLSTM preserve past and future information.

Figure 2 illustrates the structure of the model. The embedding feeds the BiLSTM layer, and the dropout layer follows it to avoid overfitting. After that, dense layers are the following layers. The BiLSTM model is built using the following characteristics: 256-word embedding size, 64 training batch size, five epochs, 10 Max sentence length and Adam optimizer. In this study, after the BiLSTM model was built, it was applied to the dataset that has been collected to classify each news tweet to the class to which it belongs. Table 3 shows the BiLSTM text classification used in this research. The BiLSTM model started with an embedding technique to produce 256-dimensional word vectors for each word.

The pseudocode, presented later, provides a clear and structured representation of the methods used in this research.

## RESULTS

Machine learning models can be evaluated in several ways to see how well they perform. Automation-based evaluation is one such method. It employs objective metrics like recall, precision, and f1-score to conclude the quality of an evaluation’s results. In this research,

Table 3  
BiLSTM layer configuration and output shapes

Layer (type)	Output Shape
embedding (Embedding)	(None, 10, 256)
dropout (Dropout)	(None, 10, 256)
Bidirectional (Bidirectional)	(None, 10, 512)
dropout_1 (Dropout)	(None, 10, 512)
bidirectional_1 (Bidirectional)	(None, 256)
dropout_2 (Dropout)	(None, 256)
flatten (Flatten)	(None, 256)
dense (Dense)	(None, 32)
dropout_3 (Dropout)	(None, 32)
dense_1 (Dense)	(None, 5)

we used this method to test how well our algorithm could divide tweets into five distinct categories: (1) General News, (2) Regional News, (3) Sports News, (4) Economic News, and (5) Quality of Life News. For this purpose, we split our dataset into three parts: (1) training set, (2) validation set, and (3) testing set. The main goal was to train the model to properly categorize each tweet by its related label. After applying the BiLSTM model to the dataset, we used several methods to assess our classification model's efficacy. These included a receiver operating characteristic (ROC) curve, a confusion matrix, and a graphical representation of the false positive rate (FPR) at varying thresholds. Table 4 shows the calculation of the class-wise metrics for each class and the overall accuracy of 88%.

Table 4  
*Calculation of the class-wise metrics for each class and the overall accuracy*

Class	Precision	Recall	F1 score	Support
Economic News (C0)	0.99	0.97	0.98	688
General News (C1)	0.88	0.97	0.92	19276
Quality Life News (C2)	0.98	0.98	0.98	293
Regional News (C3)	0.79	0.47	0.59	4937
Sports News (C4)	0.97	0.99	0.98	1560
Accuracy	0.88			

Among the five categories, all evaluation variables were good for economic news, quality of news and sports news, as the values for precision, recall and f1-score were in the range of 0.97 to 0.99.

Furthermore, the area under the ROC curve (AUC) of 0.86 in Figure 3 demonstrates the model's overall performance, showing that it can distinguish between the positive and negative classes. The model's accuracy was broken down into true positives and false negatives predicted samples, as shown in the confusion matrix in Table 5. Additional insight into the model's performance was offered by the graphical representation of the FPR at different classification criteria (Figure 3), which showed that the model maintained a relatively low FPR even at high classification thresholds.

Table 5  
*Normalized confusion matrix for a multiclass dataset*

	Confusion Matrix					
	C <sub>0</sub>	C <sub>1</sub>	C <sub>2</sub>	C <sub>3</sub>	C <sub>4</sub>	1.0
C <sub>0</sub>	0.98	0.02	0	0.02	0	0.8
C <sub>1</sub>	0.01	0.97	0.01	0.04	0.01	0.6
C <sub>2</sub>	0	0.02	0.98	0	0.01	0.4
C <sub>3</sub>	0.01	0.53	0.01	0.48	0.01	0.2
C <sub>4</sub>	0	0.02	0	0	0.99	0.0

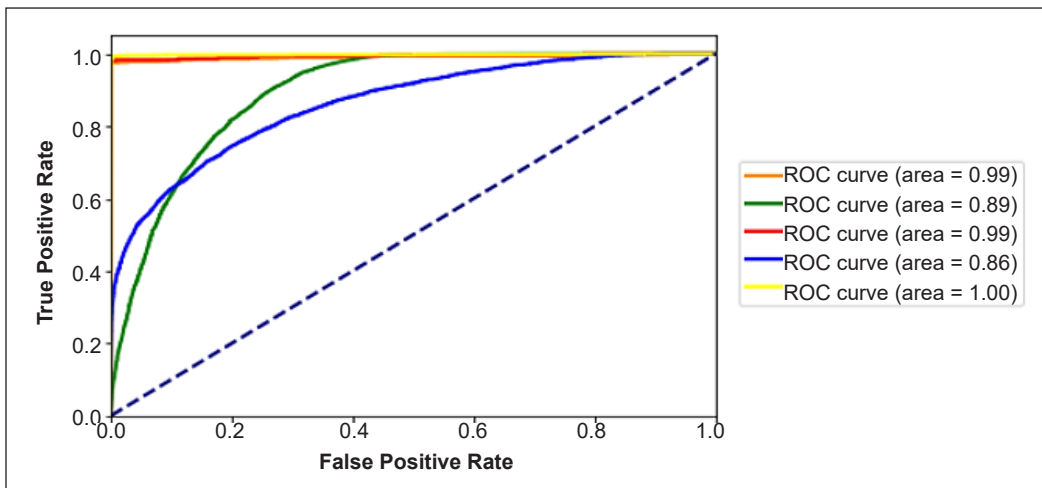


Figure 3. Receiver operating characteristic (ROC) (AUC) curves fitted to the data

Our results indicate that the model successfully classified the samples into their intended categories. Although there were a few false positives, the overall performance was good, as measured by a high AUC and a low FPR. The results demonstrate that the model performs reasonably well in accurately distinguishing between the positive and negative samples. However, there is room for improvement, particularly in reducing the number of false positives and false negatives.

## ANALYSIS OF ERRORS AND LIMITATIONS

While our model demonstrates promising results in classifying Arabic news tweets from Saudi Arabia, it is important to acknowledge its limitations and potential sources of errors:

1. Sources of False Positives and Negatives: False positives can arise from the inherent ambiguity of some tweets, where content may overlap between categories. For instance, a tweet discussing the economic impact of a regional sporting event might be misclassified between “Economic News” and “Sports News.” On the other hand, false negatives might result from unique linguistic structures or vernacular language for which the model has not been adequately trained.
2. Data Quality and Quantity: Data quality plays a pivotal role in the performance of any machine learning model. Although we sourced tweets from official, accredited news agencies, biases or inaccuracies in the data are always possible. Additionally, the volume of data, especially for underrepresented categories, might not be sufficient to capture all linguistic nuances.
3. Generalizability and Scalability: Our model is designed to fit Arabic news tweets from Saudi Arabia. This specificity ensures higher accuracy for this dataset, but it might not generalize well to tweets from other Arabic-speaking regions with different dialects

and sociocultural references. As for scalability, while the model efficiently handles the current dataset, its performance with much larger datasets remains untested.

4. **Ethical and Social Implications:** In Saudi Arabia's unique cultural, social, and political landscape, the ethical and social implications of a model analyzing tweets are crucial. For instance, consider a scenario where the model classifies tweets discussing an important cultural event in Riyadh as "general news" instead of "regional news." Furthermore, even though tweets are public, users in Saudi Arabia might have distinct privacy expectations. It is vital to ensure data collection respects these cultural norms and values. There is also potential regional bias if the model predominantly learns from tweets from specific Saudi regions, possibly leading to a skewed representation of national sentiments.
5. **Model Limitations:** While BiLSTM is effective, it has limitations. It might not capture very long-term dependencies in text as efficiently as some other architectures. Moreover, the model's complexity can lead to extended training times, especially with larger datasets.

Addressing these limitations and potential sources of errors is crucial for the model's applications and future iterations. In this research, we aim to pave the way for future models that are more resilient and inclusive.

## DISCUSSION

The research developed the model to classify Arabic news tweets in Saudi Arabia. This primary focus brings forth certain considerations. The linguistic and cultural distinctions of Saudi Arabia are different in many ways, even though Saudi Arabia represents a significant portion of the Arabic-speaking world. Due to this specificity, the model's performance may be influenced when exposed to tweets from other Arabic-speaking regions, as each region has its unique dialects and sociocultural references. Therefore, it is important to consider how well the model in this research would generalize and adapt to such diverse content. Moreover, tweets from verified and official news agencies that disseminate news in this research carry ethical weight.

News agencies on platforms like Twitter provide content intended for public consumption. The content often includes official statements, reports, or sensitive topics. Leveraging this kind of data for research purposes requires careful consideration. Ensuring the context, nuances, and intent behind the tweets are accurate is important. Misinformation or bias, even if unintentional, can have significant implications given the official nature of these sources. Therefore, researchers are responsible for approaching this data with the utmost integrity.

After identifying broader considerations, it is crucial to delve deeper into specific performance metrics and insights derived from our model. The results highlighted the

model's effectiveness in classifying Arabic news tweets from Saudi Arabia and pointed out areas for improvement, taking into account the challenges and ethical concerns mentioned above.

The classification of news articles is essential for machine learning and natural language processing tasks. Analyzing user-generated content, such as tweets, has become more crucial as social media platforms have proliferated. This paper used bidirectional long short-term memory (BiLSTM) networks to develop a deep learning-based classification model for Arabic news tweets. Analysis of the collected data suggests that we go over the categories of news stories that the Arabic-speaking population is most interested in, as evidenced by Rey (2019).

We investigated various definitions of general, regional, sports, economic, and quality of life news and how they relate to the Saudi people's interests and priorities. We also identified how our findings could be used in real-world applications like machine learning modeling and natural language processing.

We compiled a dataset of tweets about Arabic news from August 2016 to August 2020 and categorized them into five groups to achieve this goal. Custom Python scripts were used with the Twitter API and the GetOldTweets3 Python library to collect these data. According to our analysis, each news category has a significant relationship with Saudi Arabia's Vision 2030. In what follows, we will summarize the results of our study that looked at the news that Saudi Arabians tweeted about. The study examined the population's news preferences, revealing its interests. Now, let us put each paragraph into a category based on the type of news it contains:

### **General News**

According to the results of our study, the general news is what the population of Saudi Arabians is most interested in. Although Lehman-Wilzig and Seletzky's (2010) definition of general news as an intermediate category of news between hard (political, economic, or social topics) and soft (gossip, local scandal, and human interest), Rey (2019) defines general news as the most significant local and international news typically found on the front page with a big, bolded title called «banner headline,» and this is more appropriate for our study. We discovered that the Arabic population reads this news category the most.

### **Regional News**

This study distinguishes local/regional news as a distinct sector for analysis, even though national/international news does cover some local urgent or top events. «regional news» refers to feature articles that draw attention to relevant local events—the discussion centers on factors that may influence the population, including their choices and actions.

## **Economic News**

For many reasons, Saudis are concerned about the economy. The state's economy is extremely reliant on oil and its sales in the global market, as per the IMF (2016) report on economic diversification in oil-exporting Arab countries presented in the *Annual Meeting of Arab Ministers of Finance, Manama, Bahrain*. Washington, DC: IMF. The recent fluctuations in oil prices and consumption may worry the locals because they know the importance of oil. The fact that so many tweets deal with economic topics demonstrates that citizens of Saudi Arabia are interested in and eager to learn about the state of the economy and any developments in this regard.

## **Quality of Life News**

One of the goals of the Saudi Arabian government, Vision 2030, is to improve the citizens' standard of living. Changes in ecosystems, cultures, environments, and sports are highlighted as priorities in Saudi Vision 2030 (<https://www.vision2030.gov.sa>). The government's efforts to entice its citizens into these areas are motivated by a desire to raise the standard of living for its citizens. Participation in state life in various fields guarantees increased opportunities for people. According to a Ministry of Foreign Affairs report, social, cultural, and other services that improve quality of life are guaranteed. Therefore, it is reasonable and commendable that people care about hearing about improvements to their quality of life.

## **Sports News**

News about sports, the economy and quality of life have all been criticized for being uninteresting to people's needs. The people of Saudi Arabia care more about sports than they do about improving their standard of living or their country's economy. It might be explained by the government's heightened interest in sports development and expanding female sports nationwide, one of Vision 2030's objectives. Even though only a small portion of Saudi adults engage in physical activity, the local population actively participates in sports as spectators at the national and international levels.

## **CONCLUSION AND FUTURE WORK**

In conclusion, based on an analysis of what people in Saudi Arabia tweeted about, this study has given us important information about what kind of news they like. People in Saudi Arabia are most interested in reading about the country's progress toward the general, regional, sports, economic, and quality of life news goals set out in Saudi Vision 2030. It is shown by data collected from August 2016 to August 2020 using custom Python scripts and the Twitter API.

The dataset from this study can be used for many natural language processing (NLP) tasks and machine learning models. It makes it useful for the scientific community, educational institutions, students, and researchers who need a record of formal news from a certain time. Additionally, Bidirectional Long Short-Term Memory (BiLSTM) networks have been used to classify the dataset, leading to a model with a macro-average precision of 0.92, recall of 0.88 and f1-score of 0.89.

In terms of future work, more research could look at the news preferences of the Saudi Arabian population by looking at how they use social media and news sources other than those used in this study. Further understanding of the news' function in Saudi society may be gleaned by examining the influence of news sentiment on the public's attitudes and actions.

## ACKNOWLEDGEMENT

The authors sincerely thank University of Technology Sydney, Australia, for providing an enriching and supportive environment that greatly facilitated my academic endeavors and research.

## REFERENCES

- Abdelaal, H. M., Elmahdy, A. N., Halawa, A. A., & Youness, H. A. (2018). Improve the automatic classification accuracy for Arabic tweets using ensemble methods. *Journal of Electrical Systems and Information Technology*, 5(3), 363-370. <https://doi.org/10.1016/j.jesit.2018.03.001>
- Ahmed, W., Bath, P. A., & Demartini, G. (2017). Using Twitter as a data source: An overview of ethical, legal, and methodological challenges. In K. Woodfield (Ed.), *The Ethics of Online Research (Advances in Research Ethics and Integrity)*, (Vol. 2, pp. 79-107). Emerald Publishing Limited. <https://doi.org/10.1108/S2398-601820180000002004>
- Al Sbou, A. M., Hussein, A., Talal, B., & Rashid, R. A. (2018). A survey of Arabic text classification models. *International Journal of Electrical and Computer Engineering*, 8(6), 4352-4355. <https://dx.doi.org/10.11591/ijece.v8i6.pp4352-4355>
- Alabbas, W., Al-Khateeb, H. M., & Mansour, A. (2016). Arabic text classification methods: Systematic literature review of primary studies. In *2016 4th IEEE International Colloquium on Information Science and Technology (CiSt)* (pp. 361-367). IEEE Publishing. <https://doi.org/10.1109/CIST.2016.7805072>
- Alayba, A. M., Palade, V., England, M., & Iqbal, R. (2018). A combined CNN and LSTM model for Arabic sentiment analysis. In A. Holzinger, P. Kieseberg, A. Tjoa, E. Weippl (Eds.), *Machine Learning and Knowledge Extraction CD-MAKE 2018, Lecture Notes in Computer Science* (Vol 11015, pp. 179-191). Springer. [https://doi.org/10.1007/978-3-319-99740-7\\_12](https://doi.org/10.1007/978-3-319-99740-7_12)
- Albalooshi, N., Mohamed, N., & Al-Jaroodi, J. (2011). The challenges of Arabic language use on the Internet. In *2011 International Conference for Internet Technology and Secured Transactions* (pp. 378-382). IEEE Publishing.

- Almuqren, L., & Cristea, A. (2021). AraCust: A Saudi Telecom tweets corpus for sentiment analysis. *PeerJ Computer Science*, 7, Article e510. <https://doi.org/10.7717/peerj-cs.510>
- Alonso, M. A., Vilares, D., Gómez-Rodríguez, C., & Vilares, J. (2021). Sentiment analysis for fake news detection. *Electronics*, 10(11), Article 1348. <https://doi.org/10.3390/electronics10111348>
- Al-Tahrawi, M. M., & Al-Khatib, S. N. (2015). Arabic text classification using Polynomial Networks. *Journal of King Saud University-Computer and Information Sciences*, 27(4), 437-449. <https://doi.org/10.1016/j.jksuci.2015.02.003>
- Antoun, W., Baly, F., & Hajj, H. (2020). AraBERT: Transformer-based model for Arabic language understanding. *ArXiv*, Article 2003.00104. <https://doi.org/10.48550/arXiv.2003.00104>
- Aslam, S. (2018). *Twitter by the numbers: Stats, demographics & fun facts*. Omnicoreagency. com. <https://www.omnicoreagency.com/twitter-statistics/>
- Assiri, A., Emam, A., & Al-Dossari, H. (2018). Towards enhancement of a lexicon-based approach for Saudi dialect sentiment analysis. *Journal of Information Science*, 44(2), 184-202. <https://doi.org/10.1177/0165551516688143>
- Bdeir, A. M., & Ibrahim, F. (2020). A framework for Arabic tweets multi-label classification using word embedding and neural networks algorithms. In *Proceedings of the 2020 2nd International Conference on Big Data Engineering* (pp. 105-112). ACM Publishing. <https://doi.org/10.1145/3404512.3404526>
- Bekkali, M., & Lachkar, A. (2014). Arabic tweets categorization based on rough set theory. *International Journal of Computer Science & Information Technology*, 6, 83-96. <https://dx.doi.org/10.5121/csit.2014.41109>
- Boukil, S., Biniz, M., El Adnani, F., Cherrat, L., & El Moutaouakkil, A. E. (2018). Arabic text classification using deep learning technics. *International Journal of Grid and Distributed Computing*, 11(9), 103-114. <http://dx.doi.org/10.14257/ijgdc.2018.11.9.09>
- Buabin, E. (2012). Boosted hybrid recurrent neural classifier for text document classification on the Reuters news text corpus. *International Journal of Machine Learning and Computing*, 2(5), Article 588. <https://dx.doi.org/10.7763/IJMLC.2012.V2.195>
- Chung, J., Gulcehre, C., Cho, K., & Bengio, Y. (2014). Empirical evaluation of gated recurrent neural networks on sequence modelling. *ArXiv*, Article 1412.3555. <https://doi.org/10.48550/arXiv.1412.3555>
- Dahou, A., Xiong, S., Zhou, J., Haddoud, M. H., & Duan, P. (2016). Word embeddings and convolutional neural network for Arabic sentiment classification. In *Proceedings of coling 2016, the 26th international conference on computational linguistics: Technical papers* (pp. 2418-2427). The COLING 2016 Organizing Committee.
- Devlin, J., Chang, M. W., Lee, K., & Toutanova, K. (2018). Bert: Pre-training of deep bidirectional transformers for language understanding. *Arxiv*, Article 1810.04805. <https://doi.org/10.48550/arXiv.1810.04805>.
- El Mahdaouy, A., Gaussier, E., & El Alaoui, S. O. (2017). Arabic text classification based on word and document embeddings. In A. Hassanien, K. Shaalan, T. Gaber, A. Azar, M. Tolba (Eds.), *Proceedings of the International Conference on Advanced Intelligent Systems and Informatics 2016. Advances in Intelligent Systems and Computing* (Vol. 533). Springer. [https://doi.org/10.1007/978-3-319-48308-5\\_4](https://doi.org/10.1007/978-3-319-48308-5_4)

- El-Alami, F. Z., & El Alaoui, S. O. (2016). An efficient method based on a deep learning approach for Arabic text categorization. *International Arab Conference on Information Technology*, 1-7.
- El-Alami, F. Z., El Alaoui, S. O., & En-Nahnahi, N. (2020). Deep neural models and retrofitting for Arabic text categorization. *International Journal of Intelligent Information Technologies (IJIT)*, 16(2), 74-86. <https://dx.doi.org/10.4018/IJIT.2020040104>
- Elfaik, H., & Nfaoui, E. H. (2021). Combining context-aware embeddings and an attentional deep learning model for Arabic affect analysis on Twitter. *IEEE Access*, 9, 111214-111230. <https://doi.org/10.1109/ACCESS.2021.3102087>
- Elhassan, R., & Ahmed, M. (2015). Arabic text classification review. *International Journal of Computer Science and Software Engineering (IJCSSE)*, 4(1), 1-5.
- Elnagar, A., Al-Debsi, R., & Einea, O. (2020). Arabic text classification using deep learning models. *Information Processing & Management*, 57(1), Article 102121. <https://doi.org/10.1016/j.ipm.2019.102121>
- Feng, S., & Kirkley, A. (2021). Integrating online and offline data for crisis management: Online geolocalized emotion, policy response, and local mobility during the COVID crisis. *Scientific Reports*, 11, Article 8574. <https://doi.org/10.1038/s41598-021-88010-3>
- Galal, M., Madbouly, M. M., & El-Zoghby, A. D. E. L. (2019). Classifying Arabic text using deep learning. *Journal of Theoretical and Applied Information Technology*, 97(23), 3412-3422.
- Graves, A., & Schmidhuber, J. (2005). Framewise phoneme classification with bidirectional LSTM networks. In *Proceedings. 2005 IEEE International Joint Conference on Neural Networks*, 2005 (Vol. 4, pp. 2047-2052). IEEE Publishing. <https://doi.org/10.1109/IJCNN.2005.1556215>
- Guzman, E., Alkadhi, R., & Seyff, N. (2017). An exploratory study of Twitter messages about software applications. *Requirements Engineering*, 22, 387-412. <https://doi.org/10.1007/s00766-017-0274-x>
- Hmeidi, I., Al-Ayyoub, M., Abdulla, N. A., Almodawar, A. A., Abooraig, R., & Mahyoub, N. A. (2015). Automatic Arabic text categorization: A comprehensive comparative study. *Journal of Information Science*, 41(1), 114-124. <https://doi.org/10.1177/0165551514558172>
- Howard, J., & Ruder, S. (2018). Universal language model fine-tuning for text classification. *ArXiv*, Article 1801.06146. <https://doi.org/10.48550/arXiv.1801.06146>
- Hunt, E. (2016). *What is fake news? How to spot it and what you can do to stop it*. The Guardian. <https://www.theguardian.com/media/2016/dec/18/what-is-fake-news-pizzagate>
- Ibrahim, M. F., Alhakeem, M. A., & Fadhil, N. A. (2021). Evaluation of Naïve Bayes classification in Arabic short text classification. *Al-Mustansiriyah Journal of Science*, 32(4), 42-50.
- Ikonomakis, M., Kotsiantis, S., & Tampakas, V. (2005). Text classification using machine learning techniques. *WSEAS Transactions On Computers*, 4(8), 966-974.
- IMF. (2016). *Economic diversification in oil-exporting Arab countries*. International Monetary Fund. <https://www.imf.org/en/Publications/Policy-Papers/Issues/2016/12/31/Economic-Diversification-in-Oil-Exporting-Arab-Countries-PP5038>

- Jefferson, H. (2018). *Get old tweets programmatically*. Github. <https://github.com/Jefferson-Henrique/GetOldTweets-python>
- Jordan, S. E., Hovet, S. E., Fung, I. C. H., Liang, H., Fu, K. W., & Tse, Z. T. H. (2018). Using Twitter for public health surveillance from monitoring and prediction to public response. *Data*, 4(1), Article 6. <https://doi.org/10.3390/data4010006>
- Karali, S. M. Thanoon, C. T. Lin. (2021). Arabic news tweets. *Mendeley Data*, V3. <http://dx.doi.org/10.17632/9dxgbgx86k.3>
- Khoja, Y., Alhadlaq, O., & Alsaif, S. (2017). *Auto Generation of Arabic News Headlines*. Stanford University.
- Kowsari, K., Meimandi, K. J., Heidarysafa, M., Mendu, S., Barnes, L., & Brown, D. (2019). Text classification algorithms: A survey. *Information*, 10(4), Article 150. <https://doi.org/10.3390/info10040150>
- Lehman-Wilzig, S. N., & Seletzky, M. (2010). Hard news, soft news, ‘general’ news: The necessity and utility of an intermediate classification. *Journalism*, 11(1), 37-56. <https://doi.org/10.1177/1464884909350642>
- Matrane, Y., Benabbou, F., & Sael, N. (2021). Sentiment analysis through word embedding using AraBERT: Moroccan dialect use case. In *2021 International Conference on Digital Age & Technological Advances for Sustainable Development (ICDATA)* (pp. 80-87). IEEE. <https://doi.org/10.1109/ICDATA52997.2021.00024>
- Moh’d Mesleh, A. (2011). Feature subset selection metrics for Arabic text classification. *Pattern Recognition Letters*, 32(14), 1922-1929. <https://doi.org/10.1016/j.patrec.2011.07.010>
- Mohammed, P., Eid, Y., Badawy, M., & Hassan, A. (2020). Evaluation of different sarcasm detection models for Arabic news headlines. In A. Hassanien, K. Shaalan, & M. Tolba (Eds.), *Proceedings of the International Conference on Advanced Intelligent Systems and Informatics 2019. Advances in Intelligent Systems and Computing*, (Vol 1058). Springer. [https://doi.org/10.1007/978-3-030-31129-2\\_38](https://doi.org/10.1007/978-3-030-31129-2_38)
- Panagiotou, N., Katakis, I., & Gunopulos, D. (2016). Detecting events in online social networks: Definitions, trends and challenges. In S. Michaelis, N. Piatkowski, & M. Stolpe, M. (Eds.), *Solving Large Scale Learning Tasks. Challenges and Algorithms. Lecture Notes in Computer Science*, (Vol 9580). Springer. [https://doi.org/10.1007/978-3-319-41706-6\\_2](https://doi.org/10.1007/978-3-319-41706-6_2)
- Peters, M. E., Neumann, M., Iyyer, M., Gardner, M., Clark, C., Lee, K., & Zettlemoyer, L. (2018). Deep contextualized word representations. *ArXiv*, Article 1802.05365. <https://doi.org/10.48550/arXiv.1802.05365>
- Raftery, T. (2017). *Twitter Arab Word - Statistics Feb 2017*. <https://weedoo.tech/twitter-arab-world-statistics-feb-2017>
- Rey, M. V. (2019). *What are the eleven parts and their meaning*. Philippine News. [https://philnews.ph/2019/07/16/parts-of-newspaper/#google\\_vignette](https://philnews.ph/2019/07/16/parts-of-newspaper/#google_vignette)
- Saeed, M. (2021). Farasapy: *A Python wrapper for the well Farasa toolkit*. Github. <https://github.com/MagedSaeed/farasapy>
- Salloum, S. A., Al-Emran, M., & Shaalan, K. (2017a). Mining text in news channels: A case study from Facebook. *International Journal of Information Technology and Language Studies*, 1(1), 1-9.

- Salloum, S. A., Al-Emran, M., & Shaalan, K. (2017b). Mining social media text: Extracting knowledge from Facebook. *International Journal of Computing and Digital Systems*, 6(02), 73-81. <http://dx.doi.org/10.12785/IJCDS/060203>
- Salloum, S. A., Al-Emran, M., Monem, A. A., & Shaalan, K. (2018). Using text mining techniques for extracting information from research articles. In K. Shaalan, A. Hassanien, A., & F. Tolba (Eds.), *Intelligent Natural Language Processing: Trends and Applications. Studies in Computational Intelligence*, (Vol 740). Springer. [https://doi.org/10.1007/978-3-319-67056-0\\_18](https://doi.org/10.1007/978-3-319-67056-0_18)
- Sayed, M., Salem, R., & Khedr, A. E. (2017). Accuracy evaluation of Arabic text classification. In *2017 12th International Conference on Computer Engineering and Systems (ICCES)* (pp. 365-370). IEEE Publishing. <https://doi.org/10.1109/ICCES.2017.8275333>
- Schmidhuber, J., & Hochreiter, S. (1997). Long short-term memory. *Neural Comput*, 9(8), 1735-1780.
- Vaswani, A., Shazeer, N., Parmar, N., Uszkoreit, J., Jones, L., Gomez, A. N., Kaiser, L., & Polosukhin, I. (2017). Attention is all you need. In I. Guyon, U. Von Luxburg, S. Bengio, H. Wallach, R. Fergus, S. Vishwanathan, & R. Garnett (Eds.), *Advances in Neural Information Processing Systems 30 (NIPS 2017)* (pp. 1-11). NeurIPS Proceedings.
- Yang, Y., & Pedersen, J. O. (1997). A comparative study on feature selection in text categorization. ICML '97: Proceedings of the European Fourteenth International Conference on Machine Learning (pp. 412 - 420), Morgan Kaufmann Publishers Inc. <https://surdeanu.cs.arizona.edu/mihai/teaching/ista555-fall13/readings/yang97comparative.pdf>.

## Borderline-DEMNET: A Workflow for Detecting Alzheimer's and Dementia Stage by Solving Class Imbalance Problem

Neetha Papanna Umalakshmi<sup>1\*</sup>, Simran Sathyanarayana<sup>1</sup>, Pushpa Chicktotlikere Nagappa<sup>1</sup>, Thriveni Javarappa<sup>1</sup> and Venugopal Kuppanna Rajuk<sup>2</sup>

<sup>1</sup>Department of CSE, University of Visvesvaraya College of Engineering, Bangalore, 560001 Karnataka, India

<sup>2</sup>Bangalore University, Bangalore, 560001 Karnataka, India

### ABSTRACT

Alzheimer's Disease (AD) is the leading cause of dementia, a broad term encompassing memory loss and other cognitive impairments. Although there is no known cure for dementia, managing specific symptoms associated with it can be effective. Mild dementia stages, including AD, can be treated, and computer-based techniques have been developed to aid in early diagnosis. This paper presents a new workflow called Borderline-DEMNET, designed to classify various stages of Alzheimer's/dementia with more than three classes. Borderline-SMOTE is employed to address the issue of imbalanced datasets. A comparison is made between the proposed Borderline-DEMNET workflow and the existing DEMNET model, which focuses on classifying different dementia and AD stages. The evaluation metrics specified in the paper are used to assess the results. The framework is trained, tested, and validated using the Kaggle dataset, while the robustness of the work is checked using the ADNI dataset. The proposed workflow achieves an accuracy of 99.17% for the Kaggle dataset and 99.14% for the ADNI dataset. In conclusion, the proposed workflow outperforms previously identified models, particularly in terms of accuracy. It also proves that selecting a proper class balancing technique will increase accuracy.

### ARTICLE INFO

#### Article history:

Received: 27 July 2023

Accepted: 01 February 2024

Published: 16 July 2024

DOI: <https://doi.org/10.47836/pjst.32.4.10>

#### E-mail addresses:

neethapud@gmail.com (Neetha Papanna Umalakshmi)

simrankrithika@gmail.com (Simran Sathyanarayana)

pushpacn@gmail.com (Pushpa Chicktotlikere Nagappa)

drthrivenij@gmail.com (Thriveni Javarappa)

neethapuds@gmail.com (Venugopal Kuppanna Rajuk)

\* Corresponding author

*Keywords:* Alzheimer's disease, Borderline-SMOTE, dementia, DEMNET model, evaluation matrices

### INTRODUCTION

Alzheimer's Disease (AD) is a progressive neurological condition that gradually impairs memory, cognitive abilities, and eventually the capacity to perform basic tasks. In the United States, AD is presently classified as

the seventh most common cause of mortality (National Institute on Aging, 2021). The prevalence of AD in the United States is rapidly increasing. The number of Americans affected by this condition is on the rise, with over 6 million individuals of various age groups being affected. As of 2023, it is estimated that approximately 6.7 million Americans aged 65 and above are living with Alzheimer's (Alzheimer's Association, 2023).

Dementia refers to the decline in both behavioral and cognitive abilities, reaching a point where it hampers an individual's ability to carry out daily activities, such as thinking, remembering, and rationalizing. The severity of dementia varies, starting from mild stages, where it minimally impacts one's functioning, to the most advanced stages, where individuals require complete assistance from others to perform basic tasks in their daily lives (National Institute on Aging, 2021).

Presently, there is a global prevalence of over 55 million individuals diagnosed with dementia, with approximately 60% residing in low- and middle-income nations. Annually, nearly 10 million new cases are reported. Dementia arises due to a range of ailments and brain injuries. AD stands as the predominant type of dementia, accounting for approximately 60% to 70% of cases (World Health Organization, 2023). Tangles and plaques remain recognized as fundamental features of AD. The progress in brain imaging technology has enabled researchers to directly observe alterations in brain structure and function, as well as the development and dissemination of abnormal tau and amyloid proteins in the living brain (National Institute on Aging, 2021).

Traditional imaging methods have had limited involvement in detecting AD, but contemporary imaging technologies have gained prominence in AD diagnosis. These advanced techniques aid in diagnosing AD and serve as crucial tools for assessing treatment effectiveness, making prognosis judgments, and facilitating drug development (Zeng et al., 2021). AI has demonstrated great potential in medicine, especially in neuroimaging. It encompasses computer systems that can carry out tasks typically requiring human intelligence. Deep Learning (DL) algorithms enable computers to learn the most effective data representations for a given problem. Machine Learning (ML) and DL aim to replicate the neural networks found in the human brain, resulting in Artificial Neural Networks (ANNs) consisting of nodes arranged in input, hidden, and output layers (Litjens et al., 2017) (Monsour et al., 2022).

The progress of technology and the ready availability of digital medical data have led to the widespread utilization of computer techniques in the medical domain (Liu et al., 2022) (Neetha et al., 2022). Imbalanced datasets pose a common challenge in health-related applications. The classification of medical data often faces the issue of uneven data distribution, where at least one class is disproportionately represented, comprising a considerably smaller portion of the dataset (Kotsiantis et al., 2005).

When rare events occur infrequently, they are frequently misinterpreted as unexplored or overlooked cases or disregarded as noise or anomalies. Consequently, this results in a

greater occurrence of misclassifications for the positive class, especially when it represents the minority class, in contrast to the more prevalent class (Ali et al., 2013).

Many researchers have focused on addressing the classification challenges associated with multi-class imbalanced data in recent years. This particular task poses more significant obstacles when compared to binary imbalanced learning (Bi et al., 2019).

## **MOTIVATION**

Our experiment is driven by the investigation into the factors contributing to AD and its impact on human life, particularly in relation to dementia. AD is the leading cause of dementia, a condition that can ultimately result in mortality. The imbalance of classes is a prevalent issue often encountered in real-time medical datasets. However, achieving a balanced dataset and ensuring high accuracy can be challenging. ML and DL techniques have proven effective in resolving various challenges in real-time scenarios. Hence, we attempted to implement specific techniques to address the class imbalance problem while improving classification accuracy (Pushpa et al., 2013).

## **CONTRIBUTIONS**

### **Problem Statement**

Designing effective prediction models for Alzheimer's or dementia data presents a major challenge, particularly due to the issue of class imbalance. Imbalanced datasets occur when one class has considerably larger data points than the other. In the realm of ML, various techniques have been developed to address imbalanced data, but not all techniques are considered the best for all datasets. We utilized an advanced technique that performs better in image processing. This approach is combined with a modified DL algorithm called DEMNET, resulting in significant improvements compared to other sampling methods. Also, getting good accuracy in Multi-Class situations is challenging.

Here are several notable contributions made by the work:

1. We have introduced a new workflow structure known as Borderline-DEMNET (DEMENTia NETwork with Borderline SMOTE) to address the class imbalance challenge and enhance classification accuracy in four and five-class datasets.
2. The Borderline-DEMNET workflow has the potential to aid in the timely detection and diagnosis of diseases by focusing on class imbalance and multi-class classification issues sequentially.
3. Compared to previous studies on AD/dementia, our workflow demonstrates superior accuracy regarding four- and five-class problems.
4. It also demonstrates that employing an appropriate method for balancing class distribution can improve accuracy.

## Related Works

We have organized the relevant papers into two categories: Binary Classification and Multi-class problem. Many papers and outcomes are available in the field of Binary Classification. In contrast, only a few papers address the specific disease in the context of multi-class problems involving three or more classes.

### *Binary Classification*

In the study by (Prajapati et al., 2021), Deep Neural Network (DNN) was employed for AD classification across different stages. The dataset, sourced from the ADNI website, encompassed AD, Normal Control (CN), and Mild Cognitive Impairment (MCI) stages. However, the model was trained only on two classes at a time. Consequently, the model achieved an accuracy of 85.19% for AD vs. CN, 76.93% for MCI vs. CN, and 72.73% for AD vs. MCI.

Basaia et al. (2019) introduced the use of a Modified Convolutional Neural Network (CNN) for AD classification, utilizing a dataset from the ADNI source with Healthy Control (HC) and AD classes. Given the Binary classification, the model achieved an accuracy of 99%.

Wang et al. (2019) presented the application of the Ensemble Method for AD classification at various stages, utilizing a dataset from the ADNI website covering AD, Normal, and MCI stages. Similar to previous studies, the model was trained with two classes at a time, resulting in accuracies of 98.83% for AD vs. CN, 98.42% for MCI vs. CN, and 93.61% for AD vs. MCI.

CNN was employed for AD classification across stages using the ADNI dataset (Basheera et al., 2019). Although the dataset covered three stages, the model was trained with two classes simultaneously. Subsequently, it was trained with all three classes simultaneously, achieving a 100% accuracy for AD vs. Normal only.

Richhariya et al. (2020) utilized Universum Support Vector Machine-based Recursive Feature Elimination (USVM-RFE) for AD classification, employing a dataset from the ADNI website covering AD and Normal stages. Like other studies, the model was trained with two classes at a time, resulting in a 100% accuracy for AD vs. Normal.

Alinsaif et al. (2021) introduced Shearlet-based descriptors and deep features for AD classification using a dataset from the Open Access Series of Imaging Studies (OASIS) and ADNI, covering AD and Normal stages. The model, trained with two classes at a time, achieved an accuracy of 80% for AD vs. Normal.

Table 1 presents a summary of research papers focusing on Binary Classification. The Table 1 demonstrates that Binary Classification problems generally yield favorable performance results. However, the same model tends to underperform when it comes to higher classes.

Table 1

A compilation of studies focusing on the binary classification problem is presented in the following summary

Authors	Method	Dataset	Binary Class	Accuracy
<b>Prajapati et al., 2021</b>	DNN	ADNI	AD/CN	85.19%
			MCI/CN	76.93%
			AD/MCI	72.73%
<b>Basaia et al., 2019</b>	Modified CNN	ADNI	AD/HC	99%
<b>Wang et al., 2019</b>	Ensemble Method	ADNI	MCI/AD	93.61%
			MCI/Normal	98.42%
			AD/Normal	98.83%
<b>Basheera et al., 2019</b>	CNN	ADNI	AD/CN	100%
<b>Richhariya et al., 2020</b>	Universum Support Vector Machine-based Recursive Feature Elimination (USVM-RFE)	ADNI	CN/AD	100%
<b>Alinsaif et al., 2021</b>	Shearlet-based descriptors and deep features	OASIS	CN/AD	80%

### *Multi-Class Classification*

Murugan et al. (2021) introduced the DEMNET model for classifying four and five-class datasets from Kaggle and ADNI. The Kaggle dataset, with classes like Mild Dementia (MID), Non-Dementia (ND), Moderate Dementia (MOD), and Very Mild Dementia (VMD), achieved 95.23% accuracy, suggesting room for improvement.

Basheera et al. (2019) and (Wang et al., 2019) utilized CNN and ensemble methods, respectively, for AD classification in ADNI datasets. Accuracy for AD vs. Normal vs. MCI was 86.7% and 97.52%, indicating potential for further enhancement. (Neetha et al., 2022) employed D-DEMNET with DenseNet-121 for five class classifications from ADNI, obtaining 95.16% accuracy. However, it was comparatively less effective in five class classifications.

Raju et al. (2021) applied Transfer Learning with VGG16 using Fastai, achieving 99% accuracy in a four-class dataset. Suganthe et al. (2021) used a combination of Inception and ResNet V2, achieving 79.12% accuracy in a similar dataset, with plans to improve accuracy.

Raju et al. (2021) also presented Cascaded 3D CNN features and Multilayer Perceptron for ternary classification in a dataset covering AD, MCI, and NC, obtaining 96.66% accuracy.

Table 2 provides an overview of the studies focusing on Multi-Class Classification tasks. Several models mentioned in Table 1 are also mentioned here. Additionally, Table 2 presents the specific limitations addressed in this paper. Furthermore, it is observed that only a limited number of models in the Multi-Class classification domain accommodate datasets with more than three classes. As a result, there is a need to enhance the accuracy of classification problems involving four or more classes in the dataset.

Table 2  
*Synopsis of the studies focused on Multi-Class Classification*

Authors	Method	Dataset	Multi-Class	Accuracy	Drawbacks
<b>Murugan et al., 2021</b>	DEMNET	Kaggle	MID/MOD/ND/VMD	95.23%	Accuracy is yet to Increase.
<b>Basheera et al., 2019</b>	CNN	ADNI	AD/CN/MCI	86.7%	Accuracy is yet to increase.
<b>Neetha et al., 2022</b>	D-DEMNET	ADNI	AD/IMCI/MCI/eMCI/NC	95.16%	Comparatively, it is less effective in five class classifications.
<b>Raju et al., 2021 March</b>	Transfer Learning with VGG16 using Fastai	Kaggle	MID/MOD/ND/VMD	99%	Yet to try on higher class
<b>Wang et al., 2019</b>	Ensemble Method	ADNI	AD/Normal/MCI	97.52%	For three-Class.
<b>Suganthe et al., 2021</b>	Combination of Inception and ResNet V2	Kaggle	MID/MOD/ND/VMD	79.12%	Accuracy is yet to increase.
<b>Raju et al., 2021</b>	Cascaded 3D CNN features and Multilayer Perceptron classifier	ADNI	AD/MCI/NC	96.66%	For three-Class.

## MATERIALS AND METHODS

### Dataset Description

The standard datasets used in our study included the four-class dementia dataset sourced from Kaggle and the five-class AD dataset obtained from ADNI, also found in Kaggle(AD). These datasets were preprocessed and oversampled to extract their unique features. Additionally, we categorized the datasets into training, testing, and validation sets.

### *Kaggle*

Dementia is a progressive condition that tends to worsen over time. However, the progression of dementia varies from person to person. Nevertheless, most individuals experience symptoms that align with the different stages of dementia. The datasets used for AD analysis were obtained from Kaggle, a freely accessible platform. These datasets consist of a total of 6400 MR images, categorized into four groups: Mild Dementia (MID), Non-Dementia (ND), Moderate Dementia (MOD), and Very Mild Dementia (VMD). Each image in the dataset is 64 × 64 pixels in size. As dementia advances, individuals may require assistance from a loved one or a professional caregiver, as the condition can hinder daily tasks and activities (Sarvesh, 2019). There are varying quantities of images for each class in the dataset. Specifically, there are 2240 images for the Non-Demented (ND) class, 64 images for the Very Mild Demented (VMD) class, 896 images for the Mild Demented (MID) class, and 3200 images for the Moderate Demented (MOD) class.

## ADNI

The Alzheimer's Disease Neuroimaging Initiative (ADNI) is a long-term, multicenter project aiming to develop biomarkers to detect and monitor AD early on. These biomarkers are based on various factors such as clinical information, imaging data, genetics, and metabolism. Over a decade ago, this collaboration between public and private entities was established and has significantly contributed to AD research by facilitating global data exchange among researchers. The ADNI dataset consists of 1296 images and categorizes AD into five groups: EMCI, MCI, LMCI, AD, and NC. To accommodate the DEMNET model, the images in the ADNI dataset are resized to  $64 \times 64$  dimensions (Alzheimer's Disease Neuroimaging Initiative (Charan, 2022)). The dataset consists of different classes, each containing a different number of images. These classes include Normal Control (NC) with 49 images, early Mild Cognitive Impairment (eMCI) with 204 images, late Mild Cognitive Impairment (lMCI) with 61 images, Mild Cognitive Impairment (MCI) with 198 images, and AD with 145 images.

## Proposed Workflow

Our proposed methodology significantly enhances the accuracy of AD classification by employing the modified DEMNET approach to extract discriminative features. The suggested workflow is illustrated in Figure 1, encompassing several key phases: Data Pre-processing, Balancing the dataset using Borderline-SMOTE, the modified DEMNET phase, and Classification.

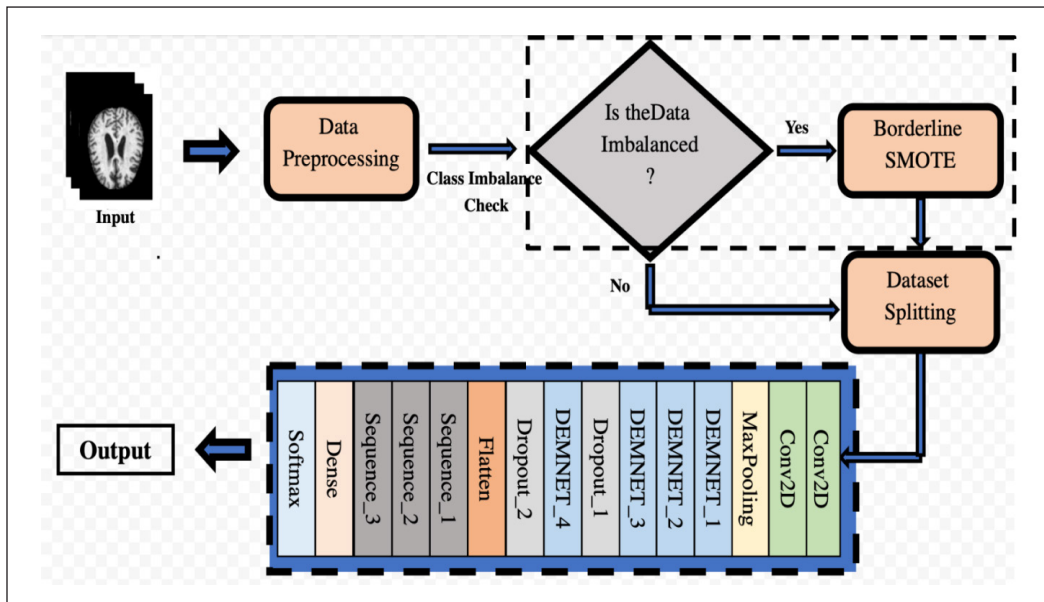


Figure 1. Proposed Borderline-DEMNET Workflow

### ***Borderline-SMOTE for Class Imbalance***

Certain DL techniques may struggle to effectively address the situation in cases of imbalance, leading to model malfunctions. Various balancing techniques can be employed to overcome this issue. Murugan et al. (2021) introduced the Synthetic Minority Over-sampling TEchnique (SMOTE) to tackle this problem, specifically in the context of images. However, utilizing SMOTE for image balancing was not widespread and was found best in text context. Consequently, we opted to implement Borderline SMOTE as specified in (Han et al., 2005), an extension of SMOTE that has proven effective in addressing image-related challenges.

Unlike alternative oversampling methods such as Random Oversampling or SMOTE (Synthetic Minority Over-sampling Technique), Borderline SMOTE often demonstrates advantages when addressing imbalanced datasets. This technique helps alleviate the risk of overfitting, commonly associated with generating synthetic examples for all instances in the minority class. Instead, it selectively enhances examples that pose greater challenges for the classifier to accurately classify. This targeted approach typically results in improved generalization performance and enhanced model robustness. Consequently, Borderline SMOTE proves to be a valuable tool in striving for a balanced and more precise classification in situations with imbalanced datasets. The Borderline SMOTE algorithm is presented in the accompanying Table 3.

Table 3  
*Borderline SMOTE algorithm*

Algorithm BorderlineSMOTE()
<p><i>Input:</i></p> <ul style="list-style-type: none"> <li>• <i>Training set T</i></li> <li>• <i>Number of nearest neighbors 'm' for each example in the minority class P</i></li> <li>• <i>Number of synthetic examples to generate 's'</i></li> <li>• <i>Number of neighbors to consider when generating synthetic examples 'k'</i></li> </ul> <p><i>Output:</i></p> <ul style="list-style-type: none"> <li>• <i>Synthetic examples for the minority class P</i></li> </ul> <p><i>Begin:</i></p> <p>Step 1: For each example <math>p</math> in the minority class <math>P</math> (<math>i = 1, 2, \dots, pnum</math>):</p> <ol style="list-style-type: none"> <li>1.1 Calculate the <math>m</math> nearest neighbors of <math>p</math> from the whole training set <math>T</math>.</li> <li>1.2 Count the number of majority examples among the <math>m</math> nearest neighbors (<math>m'</math>).</li> </ol> <p>Step 2: For each <math>p</math> in the minority class <math>P</math>:</p> <ol style="list-style-type: none"> <li>2.1 If <math>m = m'</math>, discard <math>p</math> as noise (not considered in the following steps).</li> <li>2.2 If <math>m / 2 \leq m' &lt; m</math>, add <math>p</math> to the set DANGER (easily misclassified).</li> <li>2.3 If <math>0 \leq m' &lt; m / 2</math>, mark <math>p</math> as safe (not participating in the following steps).</li> </ol> <p>Step 3: Set <math>DANGER = \{p^1, p^2, \dots, p^{dnum}\}</math> containing examples marked as DANGER.</p> <ol style="list-style-type: none"> <li>3.1 For each example <math>p^j</math> in DANGER, calculate its <math>k</math> nearest neighbors from <math>P</math>.</li> </ol> <p>Step 4: For each example, <math>p^j</math> in DANGER:</p> <ol style="list-style-type: none"> <li>4.1 Generate <math>s</math> synthetic examples:             <ul style="list-style-type: none"> <li>For <math>j = 1</math> to <math>s</math>:</li> </ul> </li> </ol>

- Randomly select  $s$  nearest neighbors from  $p$ 's  $k$  nearest neighbors in  $P$ .
- Calculate the differences  $\text{dif}_j$  between  $p'$  and its  $s$  nearest neighbors.
- Multiply  $\text{dif}_j$  by a random number  $r_j$  between 0 and 1.
- Generate a new synthetic minority example as  $p'' = p' + r_j * \text{dif}_j$ .

End:

Output: Set of synthetic minority examples for the minority class  $P$ .

Borderline SMOTE represents an enhanced oversampling technique rooted in SMOTE. It strategically incorporates a limited number of class samples located on the border to generate new samples, thereby enhancing the distribution of sample categories. The Borderline SMOTE samples are categorized into Safe, Danger, and Noise. Ultimately, the oversampling is selectively applied to a small subset of Danger samples (Sun et al., 2022).

Our project’s workflow illustrates the core functioning of our system. To begin, we acquired standard datasets: the four-class dementia dataset from Kaggle and the five-class AD dataset from ADNI. We then processed and oversampled these datasets to extract their unique characteristics. Additionally, we divided the dataset into three categories: training, testing, and validation. We employed the Borderline SMOTE approach for each dataset to create MRI images for minority groups. These images were utilized to train our modified DEMENT model, which underwent training with randomly selected images over 50 epochs.

Figure 2 represents some sample images generated by the method. Tables 4 and 5 give the list of images in count after passing to the method.

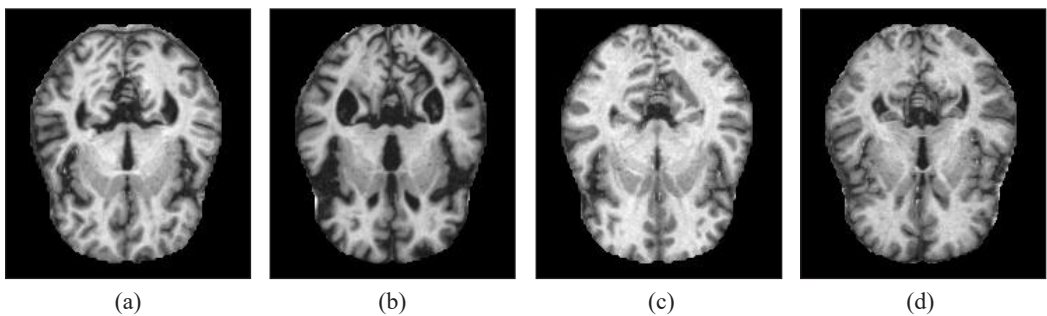


Figure 2. Sample images generated from borderline SMOTE: (a) MID; (b) MOD; (c) ND; and (d) VMD

Table 4  
Dataset description after generation for four class dataset

	Original image count	After generation
ND	2240	4717
VMD	64	4052
MID	896	4892
MOD	3200	4960

Table 5  
Dataset description after generation for four class dataset

	Original image count	After generation
MCI	198	2802
NC	493	2507
eMCI	204	2796
IMCI	61	2939
AD	145	2855

**DEMNET for Classification**

The task of the DNN is to automatically classify random MR images into different categories, leveraging the labeled images in the dataset for training. By analyzing the unique characteristics of each MR image and matching them with the appropriate dataset, the network progresses through its layers, transforming and transferring data from one layer to the next. This progressive learning makes the network more sophisticated and detailed with each layer. The most significant aspect of the DL model is its ability to learn independently, meaning it can quickly absorb information from the available data. Therefore, human knowledge or the quantity of minute features does not impact the network’s learning process. We considered the DEMNET concept from Murugan et al. (2021). Figure 3 represents the configuration of the modified DEMNET architecture.

1. Input Layer: The Input Layer of the augmented MRI images can be compared to the base model, allowing for their integration.
2. Convolution Layer: The initial layers of the convolutional network gather information from the input image by applying a filter to it.
3. Pooling Layer: The primary objective of this layer is to minimize computational expenses by decreasing the image’s spatial size and collecting trainable characteristics.
4. DEMNET Block: The DEMNET block is comprised of a series of two Convolutional Layers with ReLU activation, followed by a Batch Normalization Layer and a Maxpooling Layer.

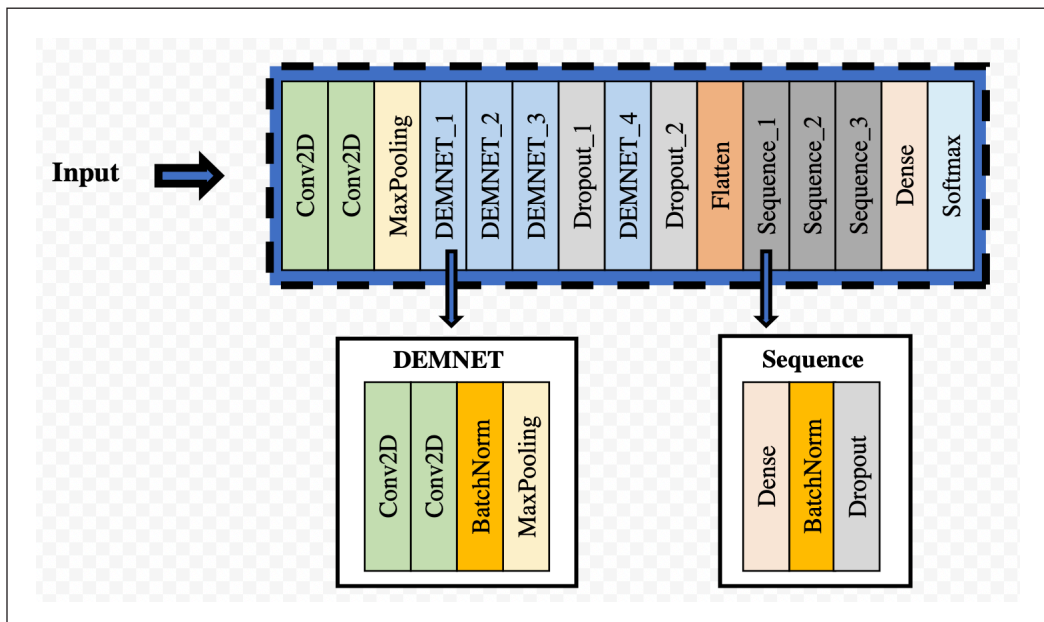


Figure 3. DEMNET Model with DEMNET block and sequence block

5. Dropout Layer: The dropout technique is a regularization method, miming the training process of multiple neural networks simultaneously, each with distinct architectures.
6. Sequence Block (Dense Block): The Sequence block is comprised of a Dense Layer with ReLU activation, followed by a Batch Normalization Layer and a Dropout Layer.
7. Dense Layer: The Dense Layer is a fully connected neural network layer where each neuron within the layer is intricately connected. It implies that every neuron in the Dense Layer receives input from all the neurons in the preceding layer.
8. Batch Normalization Layer: A CNN undergoes training using a gathered batch of input data rather than individual inputs. Similarly, Batch Normalization operates on batches, not singular inputs, to enhance the speed and stability of neural networks. This technique involves the addition of supplementary layers within a DNN.

To evaluate the performance of the modified DEMENT model, we employed a separate test dataset consisting of MRI data that was not used during the training phase. Samples from the training dataset were also utilized for validation purposes. In all scenarios, we generated results such as classification accuracy, AUC, loss, confusion matrix, and classification reports for both the Kaggle and ADNI datasets.

An overall workflow of the proposed framework is illustrated in Figure 1. The input undergoes the Data Preprocessing stage to resize the images for compatibility with the model. During this stage, we address the issue of Class-Imbalance by employing the Borderline technique to balance the dataset if any imbalance is detected. Once the dataset achieves class balance, it is divided into three sets: Training set, Validation set, and Test set, comprising 60%, 20%, and 20% of the dataset, respectively. After the dataset has been divided, the Training and Validation sets are forwarded to subsequent layers to train the model.

### **Borderline-DEMNET Flow**

Table 6 provides an overview of the steps involved in the process in the form of an Algorithm. The process begins by loading the input data. Once the data is loaded, the MRI images undergo pre-processing. During this pre-processing stage, techniques such as Data Augmentation are applied, which involve initializing necessary parameters, adjusting zoom, brightness, rescaling, and other settings. A critical step at this stage was checking the balance of classes. If an imbalance is detected, the dataset is subjected to the Borderline SMOTE technique to generate additional images. After achieving balance, the images were resized to 64 \* 64 dimensions. Table 7 gives the layers, kernel size, and parameters that workflow considers.

Table 6  
*Proposed Borderline-DEMNET flow*

---

Input: MRI images different classes.  
 Ouput: Classification results including Accuracy, Precision, Recall and F1 scores.

---

**begin**  
 Step 1:  
 Load the MRI data  
 Step 2:  
 Data pre-processing of the MRI images

- Perform Data Augmentation
- Initialize the parameters required for data augmentation
- For each image, call function ImageDataGenerator to perform Zoom, Brightness Range, Horz Flip and Rescaling of the MRI images.
- Store the augmented image in the working directory
- Image Normalization
- Perform Over-Sampling of the images using Borderline SMOTE, as the classes are imbalanced
- Store the re-sampled data in synthetic samples and synthetic labels
- Concatenate the synthetic labels to augmented labels and synthetic samples to augmented samples
- Resize the pixels of the augmented images to size 64 \* 64

Step 3:  
 Apply the Sequential() function to define the CNN model

- Building Model with ReLU as activation function
- Apply categorical-cross entropy
- RMSProp optimizer to train the model

Step 4:  
 Pass each MRI image to the convolution process

- Process each image of dimensions 64 \* 64 \* 3 processed depth-wise separate convolutions and convert the image into dimensions
- Drop Out the processed matrix/images by 0.5

Step 5:  
 The image is converted/fattened into a single-dimensional array

Step 6:  
 Apply the Dense layer with the softmax activation function and then apply dropout by 0.5 to the resultant array

Step 7:  
 Repeat Step 6 with a different set of neurons, apply dropout for repeated learning and activate the neurons

Step 8:  
 Plot the ACC and AUC curves for the trained model

Step 9:  
 Apply the confusion matrix, fetch the classification report results, and calculate the accuracy of test data

**end**

---

Table 7  
*The layers, kernel size and parameter details*

Layer (type)	Output Shape	Param #
Conv2D+ReLU	(None, 64, 64, 16)	448
Conv2D+ReLU	(None, 64, 64, 16)	2320
MaxPooling2D	(None, 32, 32, 16)	0

Table 7 (continue)

Layer (type)	Output Shape	Param #
DEMNET Block_1	(None, 16, 16, 32)	14016
DEMNET Block_2	(None, 8, 8, 64)	55680
DEMNET Block_3	(None, 4, 4, 128)	221952
Dropout	(None, 4, 4, 128)	0
DEMNET Block_4	(None, 2, 2, 256)	886272
Dropout	(None, 2, 2, 256)	0
Flatten	(None, 1024)	0
Sequential_1 (Dense Block)	(None, 512)	526848
Sequential_2 (Dense Block)	(None, 128)	66176
Sequential_3 (Dense Block)	(None, 64)	8512
Dense	(None, 4)	260
<b>Total params: 1,782,484</b>		
<b>Trainable params: 1,780,116</b>		
<b>Non-trainable params: 2,368</b>		

## RESULTS AND DISCUSSION

### Evaluation Metrics

Assessing the performance of a specific model is a crucial stage in creating a successful ML model. Various measures, known as Performance Metrics or Evaluation Metrics, are employed to gauge the model's effectiveness and quality. These performance indicators evaluate how effectively the model handles the provided data.

- Accuracy: Equation 1 is the primary metric to evaluate the model's performance in accurately predicting positive and negative events.

$$Accuracy = \frac{(TP + TN)}{(TP + TN + FP + FN)} \quad [1]$$

The value is classified as TP (True Positive) when the model accurately identifies the actual label and the image as normal. Similarly, the value is classified as TN (True Negative) when the algorithm correctly predicts an abnormal image and the actual label is also abnormal. In cases where the model predicts the image to be normal, but the actual label is incorrect, the value is classified as FP (False Positive). Conversely, when the algorithm predicts an abnormal image, but the actual label is normal, the value is classified as FN (False Negative).

- Precision: The Equation 2, denoted as PR, is determined by the proportion of accurately predicted positive observations compared to the total number of positive observations.

$$Precision = \frac{(TP)}{(TP+FP)} \quad [2]$$

- Recall: The parameter of Recall (REC) (Equation 3), alternatively referred to as sensitivity, evaluates the classifier’s ability to identify all positive samples effectively.

$$Recall = \frac{(TP)}{(TP+FN)} \quad [3]$$

- F1 score: The performance of a classification model is assessed by calculating the F-score (Equation 4) or F1 Score, which considers the model’s predictions specifically for the positive class.

$$F1score = \frac{(2*Precision *Recall )}{(Precision +Recall )} \quad [4]$$

### Experimental Setup

The proposed model was experimented with on Windows 10 edition with a device specification of Intel(R) Core(TM) i5-6200U CPU @ 2.30GHz–2.40 GHz with an 8.00 GB CPU. The suggested model underwent training using 50 epochs, a batch size 16, and an initial learning rate of 0.001. The required libraries for implementation were TensorFlow 2.7, Keras, Pandas, NumPy, and Matplotlib. The RMSProp optimizer was employed to train the algorithm. Additionally, the Area Under Curve (AUC) was computed for each epoch to evaluate the model’s ability to accurately differentiate between positive and negative classes.

### DEMNET with SMOTE and Borderline SMOTE for Four Class Dataset

The related work presents the DEMNET model, which is compared to the performance analysis of the Borderline-DEMNET model. The evaluation of these models includes metrics such as accuracy, precision, recall, and F1-measure. During the training phase, the four-class dataset yielded an accuracy of 98.97%, while the accuracy during the validation process was 99.17%.

In Figure 4, a comparison is presented between the training and validation percentages of the DEMNET model and the Borderline-DEMNET model in terms of accuracy. In Figure 5, a comparison is presented between the training and validation percentages of the DEMNET model and the Borderline-DEMNET workflow in terms of AUC parameters. Similarly, Figure 6 presents the comparison of loss parameters. The results indicate that our model performs at least as well as or better than the base model due to Borderline SMOTE. Borderline SMOTE tackles the problem of imbalanced class distribution by specifically targeting minority class samples located near the decision boundary.

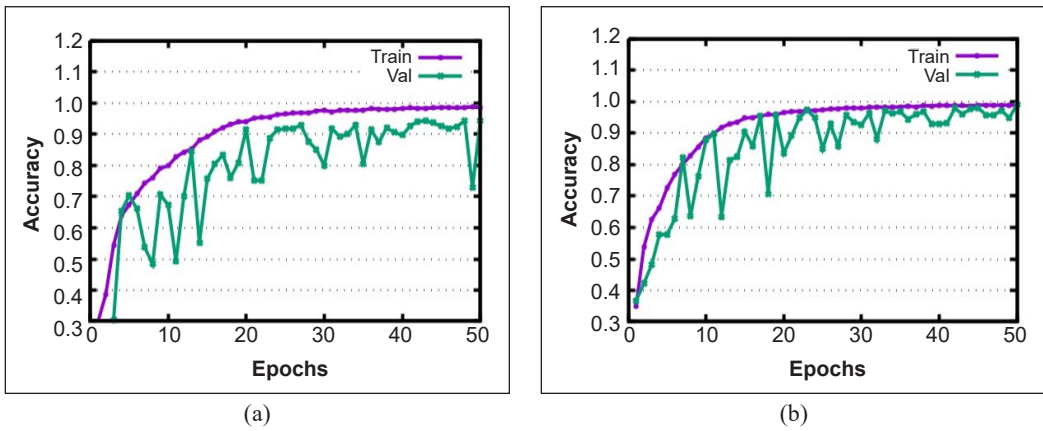


Figure 4. Training and validation curves of accuracy obtained: (a) DEMNET; and (b) Borderline-DEMNET Workflow

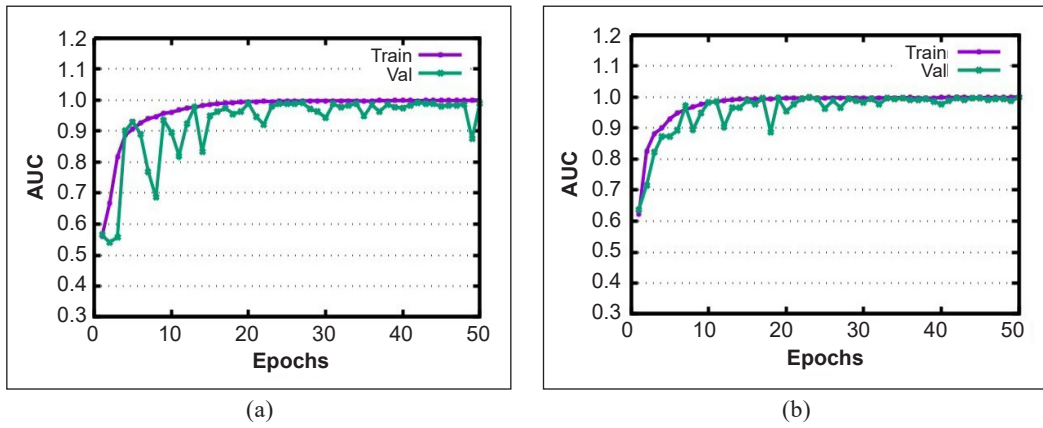


Figure 5. Training and validation curves of AUC obtained: (a) DEMNET; and (b) Borderline-DEMNET Workflow

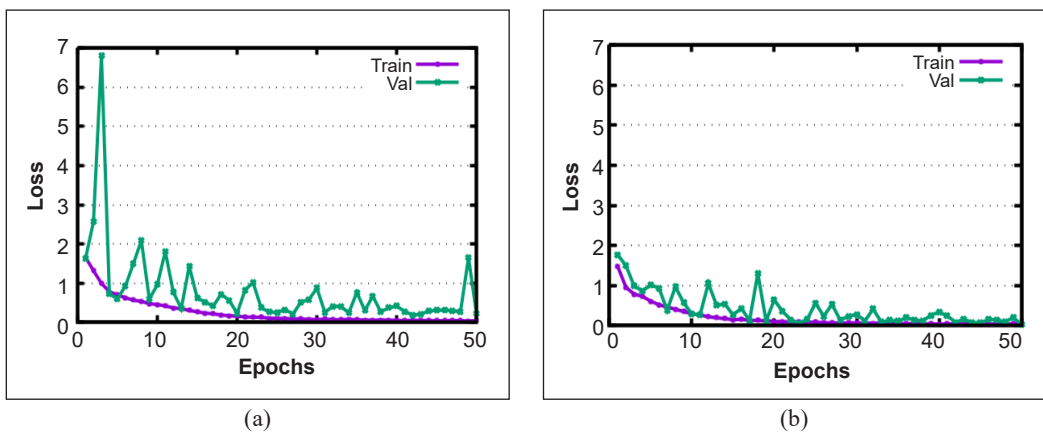


Figure 6. Training and validation curves of loss obtained: (a) DEMNET; and (b) Borderline-DEMNET Workflow

Figure 7 displays the average precision, recall, and F1-Score values, comparing the two workflows. Furthermore, the DEMNET model achieved a testing accuracy of 94% (Figure 8), while the Borderline-DEMNET workflow achieved a higher testing accuracy of 99.17% compared to the base model.

The performances of each class are presented in Tables 8 and 9, respectively, for both the workflows, which are used to calculate the average performance. The findings from classifying four separate categories indicate that the Borderline-DEMNET outperforms the DEMNET model in accuracy, precision, recall, and F1-measure.

Table 8  
Performance indices for individual classes in DEMNET are evaluated

	Precision	Recall	F1-score
ND	0.98	0.96	0.97
VMD	1.00	1.00	1.00
MID	0.91	0.93	0.92
MOD	0.91	0.90	0.91

Table 9  
Indices for the performance of individual classes in the new workflow

	Precision	Recall	F1-score
ND	1.00	1.00	1.00
VMD	1.00	1.00	1.00
MID	0.98	0.99	0.99
MOD	0.99	0.98	0.98

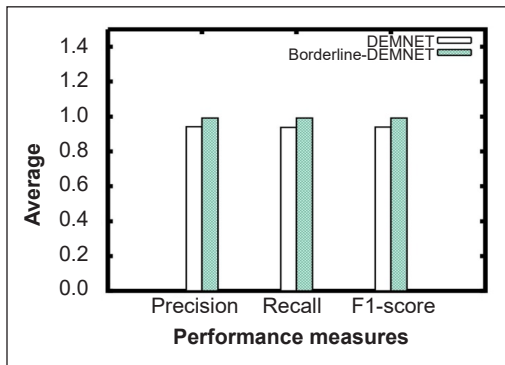


Figure 7. A comparison was conducted on the four-class dataset to evaluate the average precision, recall, and F1-score performance measures

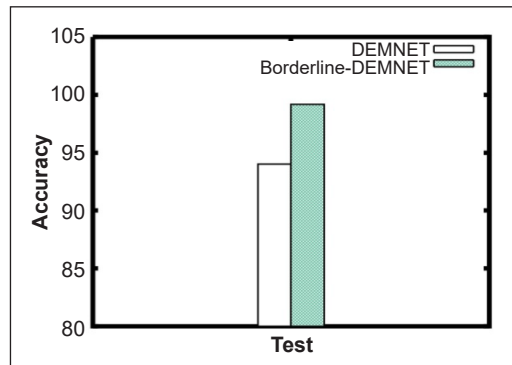


Figure 8. Comparison of testing accuracy among different workflows

### Comparison of DEMNET with SMOTE and Borderline SMOTE for Five Class Dataset

In order to assess the effectiveness of the Borderline-DEMNET framework on additional MRI datasets related to AD, subsequent to achieving improved outcomes on the four-class dataset, an experiment was conducted. The experiment involved a five-class classification of AD based on data obtained from the ADNI database. The five AD classes included in the analysis were NC, eMCI, MCI, IMCI, and AD.

The evaluation of models involves using metrics such as accuracy, precision, recall, and F1-measure (Pushpa et al., 2013). The Borderline-DEMNET model was trained using

a total of 1,780,181 parameters. During the training of the dataset, the model achieves a training accuracy of 99.25% and a validation accuracy of 99.14%. Figures 9, 10, and 11 illustrate both flows' training and validation curves. Upon comparing the two workflows, it is observed that our workflow performs on par with or better than the base model. Figure 12 comprehensively compares the average precision, recall, and F1-Score values.

The base architecture achieved training accuracy, validation accuracy, and testing accuracy rates of 97.89%, 73.74%, and 73.12%, respectively. In contrast, the proposed framework achieved higher accuracy rates, with 99.25% for training and 99.14% for validation and testing (Figure 13). In Figure 13, we added another model for comparison, which is known as D-DEMNET. It was our previous work on the same concept. Performance indices for individual classes can be found in Tables 10 and 11. The proposed workflow was also found to be effective in the five-class dataset.

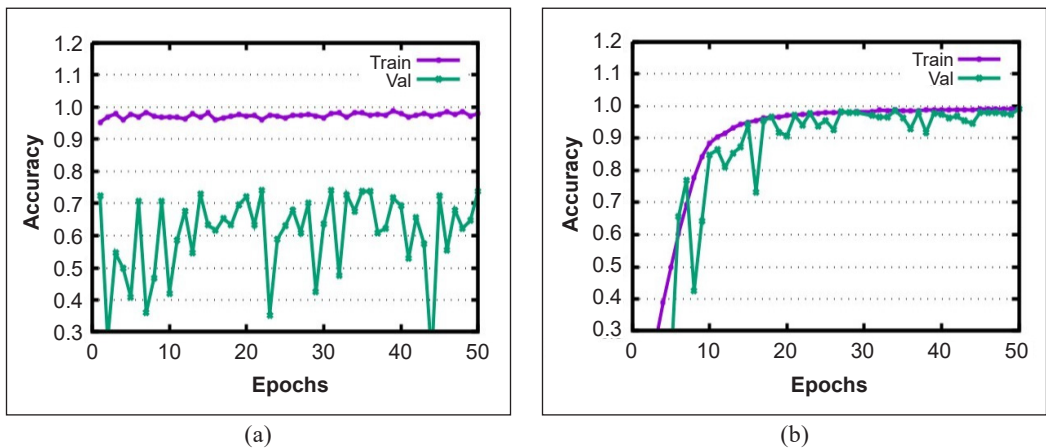


Figure 9. The accuracy training and validation curves of the five-class dataset were analyzed: (a) DEMNET; and (b) Borderline-DEMNET Workflow

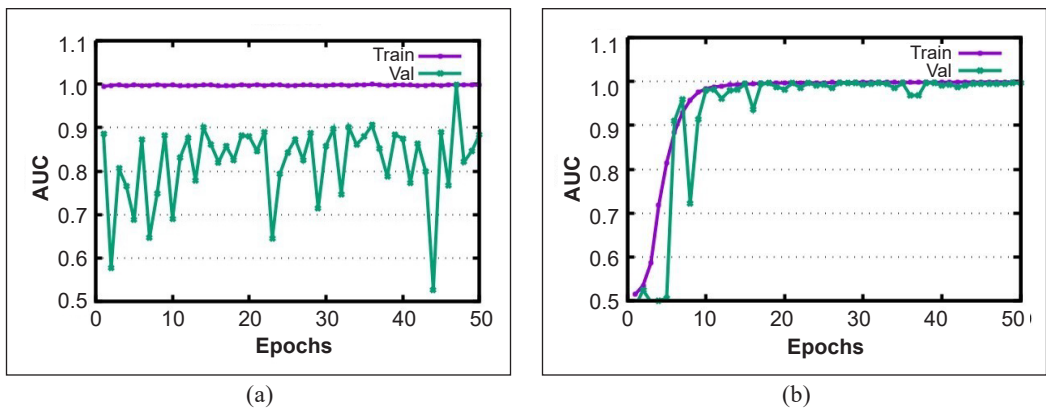


Figure 10. The AUC training and validation curves were generated using a five-class dataset: (a) DEMNET Model; and (b) Borderline-DEMNET Workflow

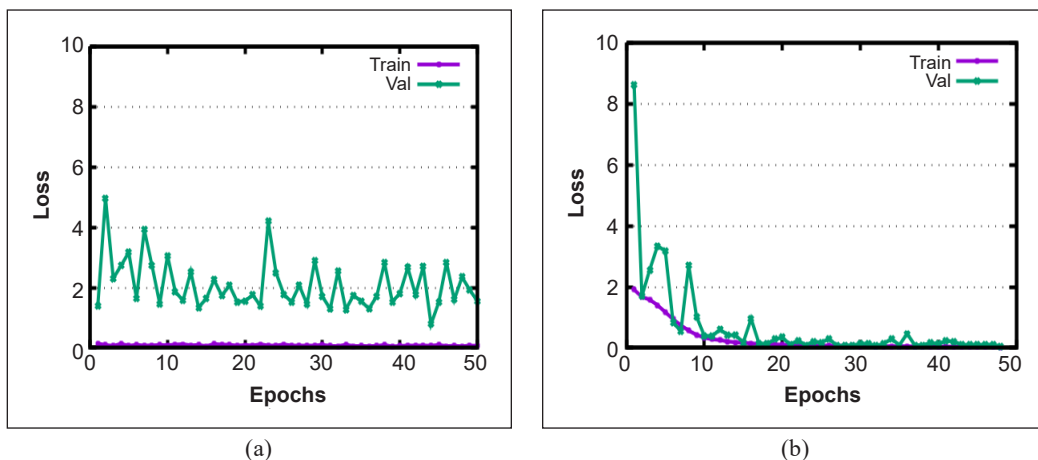


Figure 11. The loss training and validation curves were generated using a five-class dataset: (a) DEMNET Model; (b) and Borderline-DEMNET Workflow

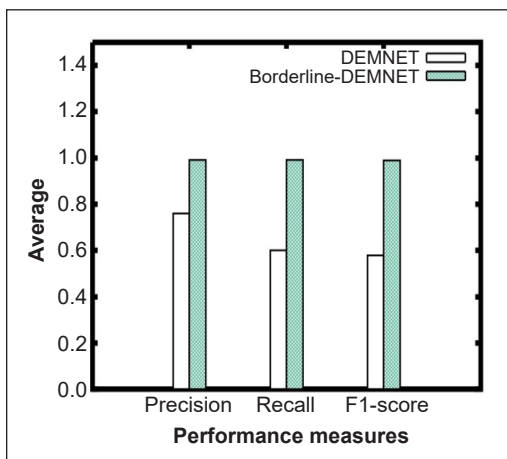


Figure 12. A study evaluated the performance of five-class datasets by comparing their average precision, recall, and F1-score

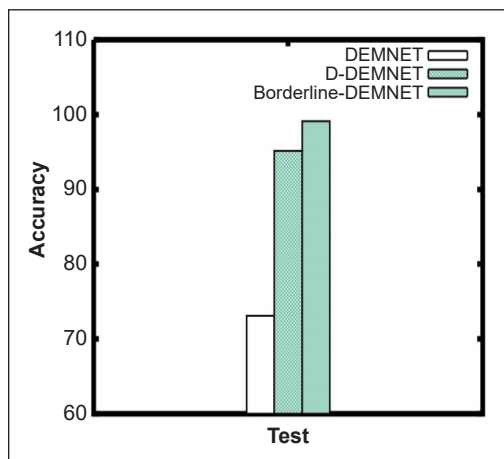


Figure 13. Comparison of testing accuracy among different workflows for a five-class dataset

Table 10

The performance indices for each class of the DEMNET Model were evaluated using a five-class dataset

	Precision	Recall	F1-score
AD	0.81	0.78	0.79
CN	0.38	0.89	0.53
eMCI	0.84	0.27	0.41
IMCI	0.87	0.91	0.89
MCI	0.94	0.15	0.27

Table 11

The performance metrics of the borderline-DEMNET architecture on a dataset consisting of five classes are evaluated

	Precision	Recall	F1-score
AD	1.00	0.99	1.00
CN	0.98	0.99	0.98
eMCI	0.99	1.00	0.99
IMCI	1.00	0.99	0.99
MCI	0.99	0.99	0.99

## CONCLUSION

The paper presents a novel framework named DEMentia NETwork with Borderline technique (Borderline-DEMNET) for Multi-Class classification problems to early diagnose or detect AD/dementia. This framework proves that using better techniques in class balancing can also improve the model's accuracy. It is considered an extension of DEMNET, which is used for classifying different stages of dementia and AD as specified in the related work. This Borderline-DEMNET framework is evaluated and compared using evaluation matrices such as accuracy, precision, recall, and F1-score. The framework results in 99.17% accuracy for the four-class dataset, whereas the framework gives 99.14% accuracy for the five-class dataset. So, from the results, the paper can conclude that the Borderline-DEMNET framework performs better in terms of evaluation matrices considered in the paper.

## ACKNOWLEDGEMENT

The collection and sharing of data for the Alzheimer's Disease Neuroimaging Initiative (ADNI) is funded by the National Institute on Aging through National Institutes of Health Grant U19 AG024904. The Northern California Institute for Research and Education serves as the grantee organization. ADNI has also historically received support from the National Institute of Biomedical Imaging and Bioengineering, the Canadian Institutes of Health Research, and private sector donations through the Foundation for the National Institutes of Health (FNIH). Generous contributions have been made by various organizations, including AbbVie, the Alzheimer's Association, the Alzheimer's Drug Discovery Foundation, Araclon Biotech, BioClinica, Inc., Biogen, Bristol-Myers Squibb Company, CereSpir, Inc., Cogstate, Eisai Inc., Elan Pharmaceuticals, Inc., Eli Lilly and Company, EuroImmun, F. Hoffmann-La Roche Ltd and its affiliate Genentech, Inc., Fujirebio, GE Healthcare, IXICO Ltd., Janssen Alzheimer Immunotherapy Research & Development, LLC., Johnson & Johnson Pharmaceutical Research & Development LLC., Lumosity, Lundbeck, Merck & Co., Inc., Meso Scale Diagnostics, LLC., NeuroRx Research, Neurotrack Technologies, Novartis Pharmaceuticals Corporation, Pfizer Inc., Piramal Imaging, Servier, Takeda Pharmaceutical Company, and Transition Therapeutics.

## REFERENCES

- ADNI. (2021). *Alzheimer's Disease Neuroimaging Initiative*. <https://adni.loni.usc.edu/>
- Charan, M. (2022). *Alzheimer's Disease 5 Class Dataset ADNI*. Kaggle. <https://www.kaggle.com/datasets/madhucharan/alzheimersdisease5classdatasetadni>
- Ali, A., Shamsuddin, S. M., & Ralescu, A. (2013). Classification with class imbalance problem: A review. *International Journal Advance Computing Application*, 5(3), 176-204.

- Alinsaif, S., & Lang, J. (2021). 3D shearlet-based descriptors combined with deep features for the classification of Alzheimer's disease based on MRI data. *Computers in Biology and Medicine*, 138, Article 104879. <https://doi.org/10.1016/j.combiomed.2021.104879>
- Alzheimer's Association. (2023). *Alzheimer's Disease Facts and Figures*. <https://www.alz.org/alzheimers-dementia/facts-figures>
- Basaia, S., Agosta, F., Wagner, L., Canu, E., Magnani, G., Santangelo, R., Filippi, M., & Alzheimer's disease neuroimaging initiative (2019). Automated classification of Alzheimer's disease and mild cognitive impairment using a single MRI and deep neural networks. *NeuroImage: Clinical*, 21, Article 101645. <https://doi.org/10.1016/j.nicl.2018.101645>
- Basheera, S., & Ram, M. S. S. (2019). Convolution neural network-based Alzheimer's disease classification using hybrid enhanced independent component analysis based segmented gray matter of T2 weighted magnetic resonance imaging with clinical valuation. *Alzheimer's & Dementia: Translational Research & Clinical Interventions*, 5(1), 974-986. <https://doi.org/10.1016/j.trci.2019.10.001>
- Bi, J., & Zhang, C. (2019). An empirical comparison on state-of-the-art multi-class imbalance learning algorithms and a new diversified ensemble learning scheme. *Knowledge-Based Systems*, 158, 81-93. <https://doi.org/10.1016/j.knosys.2018.05.037>
- Han, Hui., Wang, Wen-Yuan & Mao, Bing-Huan. (2005). Borderline-SMOTE: A new over-sampling method in imbalanced data sets learning. In D. S. Huang, X.P. Zhang, & G. B. Huang (Eds.), *Advances in Intelligent Computing. ICIC 2005. Lecture Notes in Computer Science* (Vol. 3644, p. 878-887). Springer. [https://doi.org/10.1007/11538059\\_91](https://doi.org/10.1007/11538059_91)
- Kotsiantis, S., Kanellopoulos, D., & Pintelas, P. E. (2005). Handling imbalanced datasets: A review. *GESTS International Transactions on Computer Science and Engineering*, 30(1), 25-36.
- Litjens, G., Kooi, T., Bejnordi, B. E., Setio, A. A. A., Ciompi, F., Ghafoorian, M., Laak, J. A. V. D., Ginneken, B. V., & Sánchez, C. I. (2017). A survey on deep learning in medical image analysis. *Medical Image Analysis*, 42, 60-88. <https://doi.org/10.1016/j.media.2017.07.005>
- Liu, L., Wu, X., Li, S., Li, Y., Tan, S., & Bai, Y. (2022). Solving the class imbalance problem using ensemble algorithm: Application of screening for aortic dissection. *BMC Medical Informatics and Decision Making Volume*, 22 Article 82. <https://doi.org/10.1186/s12911-022-01821-w>
- Monsour, R., Dutta, M., Mohamed, A. Z., Borkowski, A., & Viswanadhan, N. A. (2022). Neuroimaging in the era of artificial intelligence: Current applications. *Federal Practitioner*, 39(1), 14-20. <https://doi.org/10.12788/fp.0231>
- Murugan, S., Venkatesan, C., Sumithra, M. G., Gao, X. Z., Elakkiya, B., Akila, M., & Manoharan, S. (2021). DEMNET: A deep learning model for early diagnosis of Alzheimer diseases and dementia from MR images. *IEEE Access*, 9, 90319-90329. <https://doi.org/10.1109/ACCESS.2021.3090474>
- National Institute on Aging. (2021). *Alzheimer's disease fact sheet*. <https://www.nia.nih.gov/health/alzheimers-disease-fact-sheet>

- Neetha, P. U., Simran, S., Sunilkumar, G., Pushpa, C. N., Thriveni, J., & Venugopal, K. R. (2022). D-DEMNET framework for classifying the Alzheimer's disease for detection. In H. L. Gururaj, M. R. Pooja & F. Francesco (Eds.), *Recent trends in computational sciences. Proceedings of the Fourth Annual International Conference on Data Science, Machine Learning and Blockchain Technology* (pp. 1-5). CRC Press. <https://doi.org/doi: 10.1201/9781003363781-3>
- Prajapati, R., Khatri, U., & Kwon, G. R. (2021). An efficient deep neural network binary classifier for Alzheimer's disease classification. In *2021 International Conference on Artificial Intelligence in Information and Communication (ICAIIIC)* (pp. 231-234). IEEE Publishing. <https://doi.org/10.1109/ICAIIIC51459.2021.9415212>
- Pushpa, C. N., Patil, A., Thriveni, J., Venugopal, K. R., & Patnaik, L. M. (2013, December). Web page recommendations using radial basis neural network technique. In *2013 IEEE 8th International Conference on Industrial and Information Systems* (pp. 501-506). IEEE Publishing. <https://doi.org/10.1109/ICIInfS.2013.6732035>
- Pushpa, C. N., Thriveni, J., Venugopal, K. R., & LM, P. (2013). Web search engine based semantic similarity measure between words using pattern retrieval algorithm. *Computer Science & Information Technology*, 1-11. <https://doi.org/10.5121/csit.2013.3101>
- Raju, M., Gopi, V. P., & S., A. V. (2021). Multi-class classification of Alzheimer's disease using 3DCNN features and multilayer perceptron. In *2021 Sixth International Conference on Wireless Communications, Signal Processing and Networking (WiSPNET)* (pp. 368-373). IEEE Publishing. <https://doi.org/10.1109/WiSPNET51692.2021.9419393>
- Raju, M., Thirupalani, M., Vidhyabharathi, S., & Thilagavathi, S. (2021, March). Deep learning based multilevel classification of Alzheimer's disease using MRI scans. In *IOP Conference Series: Materials Science and Engineering* (Vol. 1084, No. 1, pp. 012017). IOP Publishing. <https://doi.org/10.1088/1757-899X/1084/1/012017>
- Richhariya, B., Tanveer, M., Rashid, A. H., & Alzheimer's disease neuroimaging initiative. (2020). Diagnosis of Alzheimer's disease using universum support vector machine based recursive feature elimination (USVM-RFE). *Biomedical Signal Processing and Control*, 59, Article 101903. <https://doi.org/10.1016/j.bspc.2020.101903>
- Sarvesh, D. (2019). *Alzheimer's dataset (4 class of images)*. Kaggle. <https://www.kaggle.com/datasets/tourist55/alzheimers-dataset-4-class-of-images>
- Suganthe, R. C., Geetha, M., Sreekanth, G. R., Gowtham, K., Deepakkumar, S., & Elango, R. (2021). Multiclass classification of Alzheimer's disease using hybrid deep convolutional neural network. *NVEO-Natural Volatiles & Essential Oils Journal*, 8(5), 145-153.
- Sun, Y., Que, H., Cai, Q., Zhao, J., Li, J., Kong, Z., & Wang, S. (2022). Borderline SMOTE algorithm and feature selection-based network anomalies detection strategy. *Energies*, 15(13), Article 4751. <https://doi.org/10.3390/en15134751>

Neetha Papanna Umalakshmi, Simran Sathyanarayana, Pushpa Chickotlikere Nagappa, Thriveni Javarappa and Venugopal Kuppanna Rajuk

Wang, H., Shen, Y., Wang, S., Xiao, T., Deng, L., Wang, X., & Zhao, X. (2019). Ensemble of 3D densely connected convolutional network for diagnosis of mild cognitive impairment and Alzheimer's disease. *Neurocomputing*, 333, 145-156. <https://doi.org/10.1016/j.neucom.2018.12.018>

World Health Organization. (2023). *Dementia*. <https://www.who.int/news-room/fact-sheets/detail/dementia>

Zeng, H. M., Han, H. B., Zhang, Q. F., & Bai, H. (2021). Application of modern neuroimaging technology in the diagnosis and study of Alzheimer's disease. *Neural Regeneration Research*, 16(1), 73-79. <https://doi.org/10.4103/1673-5374.286957>

# Novel Reactive Power Control Strategy for Mitigating Voltage Rise in the Malaysian Low Voltage Distribution Network with High PV Penetration

Mustafa Abo Alwez<sup>1,2\*</sup>, Jasronita Jasni<sup>1</sup>, Raghad Wahab<sup>3</sup>, Mohd Amran Mohd. Radzi<sup>1</sup> and Norhafiz Azis<sup>1</sup>

<sup>1</sup>Department of Electrical and Electronic Engineering, Faculty of Engineering, Universiti Putra Malaysia, 43400 UPM, Serdang, Selangor, Malaysia

<sup>2</sup>Department of Architecture Engineering, AL Muthanna University, 66001, AL Samawah, AL Muthanna, Iraq

<sup>3</sup>Department of Electrical Engineering, Kerbala University, 56001, Kerbala, Iraq

## ABSTRACT

Integrating renewable energy sources and distributed energy resources (DERs) in the Malaysian low voltage distribution network has introduced voltage stability challenges, particularly voltage rises, leading to detrimental impacts on network performance. This paper presents a novel reactive power control strategy for addressing these challenges. Unlike conventional methods with fixed reactive power references, the proposed technique dynamically adjusts the reactive power reference in real time, considering voltage and active power injection. It calculates the rate of change in reactive power reference ( $\Delta Q$ ) per second by analyzing Volt-VAR and Watt-VAR components and updates the reference accordingly. Simulations conducted on a low voltage distribution network in Taman Impian Putra, Malaysia, showcase the adverse effects of high photovoltaic (PV) penetration on voltage stability and highlight the success of the proposed strategy in mitigating voltage rise. The technique effectively reduces average voltage, maintains voltage regulation during

high sun irradiance and low load demand periods, and surpasses the adaptability of existing methods dependent on PV active injection or network voltage alone. The proposed strategy ensures accurate control and efficiently addresses dynamic network changes by accounting for both PV active power injection and network voltage. This approach offers enhanced voltage regulation, adaptability to varying network

## ARTICLE INFO

### Article history:

Received: 09 August 2023

Accepted: 02 January 2024

Published: 22 July 2024

DOI: <https://doi.org/10.47836/pjst.32.4.11>

### E-mail addresses:

mustafa.hussein@mu.edu.iq (Mustafa Abo alwez)

jas@upm.edu.my (Jasronita Jasni)

raghad.w@uokerbala.edu.iq (Raghad wahab)

amranmr@upm.edu.my (Mohd Amran Mohd.Radzi)

norhafiz@upm.edu.my (Norhafiz Azis)

\* Corresponding author

conditions, and reduced losses, making it a promising solution for mitigating voltage rise in the Malaysian low voltage distribution network. The simulations, validated using MATLAB Simulation and OpenDSS, confirm the strategy's efficacy and potential for real-world implementation.

*Keywords:* Distributed energy resources, low voltage distribution network, network voltage, PV active power injection, reactive power control, renewable energy integration, voltage regulation, voltage stability

---

## INTRODUCTION

The power distribution network in Malaysia has undergone a significant transformation in recent years, thanks to the integration of renewable energy sources and the increasing penetration of distributed energy resources (DERs) (Maghami et al., 2023). It is mainly driven by the decreasing cost of renewable sources (Alwez et al., 2020). While these developments have brought numerous environmental and economic benefits, they have also introduced new challenges concerning voltage stability in the low-voltage distribution network. Voltage rises, in particular, have emerged as a critical issue that requires effective mitigation strategies to ensure a reliable and efficient power supply (Tie & Gan, 2013).

The voltage rises when the power injected from DERs exceeds the local load demand in the distribution network, resulting in an unacceptable increase in voltage levels (Haque et al., 2017). This phenomenon can adversely affect the network's performance, including increased energy losses, reduced power quality, equipment damage, and compromised system stability (Hasheminamin et al., 2015). Conventional voltage control methods, such as tap-changing transformers and voltage regulators, have limitations in addressing these voltage rise challenges, especially in dynamic and unpredictable DER integration. The reactive power control ability in the smart inverter of PV systems can be utilized to overcome these limitations. Reactive power control can be based on either PV active power injection, which offers good voltage regulation but high losses, or the voltage at the point of common coupling of PV systems in the distribution network, which provides poor voltage regulation but low losses.

Many studies have proposed utilizing Volt/Var reactive power control of PV smart inverters to mitigate voltage rise on distribution networks with high PV penetration (Inaolaji et al., 2022; Singh et al., 2021). However, it is important to note that techniques solely dependent on network voltage tend to result in poor voltage regulation, as network voltage relies on the network's sensitivity to both active and reactive power. Demirok et al. (2011) proposed a reactive power control technique to mitigate voltage rise on low voltage distribution networks by combining PV active power injection and network voltage. This technique, referred to as PF (P, V), balances the two approaches. The study's results demonstrated improved voltage regulation compared to the Q(V) technique and lower

network losses compared to the PF(P) technique. However, it requires specific placement in areas with low voltage variations.

Kim and Song (2020) proposes a reactive power control technique to address voltage rise on low voltage distribution networks using PV active power injection (PF(P)) and network voltage (Q(V)). The weighting assigned to each technique varies based on the PV active power injection level. As a result, the proposed technique behaves like Q(V) when PV systems generate minimum power and acts like PF(P) when PV systems generate maximum power. However, this approach disregards load variations during high PV generation, potentially leading to unnecessary losses. Then, Inaolaji et al. (2022) present an algorithm for coordinating Volt-VAR and Watt-VAR control strategies. However, the initial algorithm failed to align peak load demand with peak PV generation. To resolve this issue, the author implemented an Energy Storage System. It is important to note that this solution has limitations, including high costs and potential impacts on network reliability.

This paper aims to study the effectiveness of a novel reactive power control technique in mitigating voltage rise on the Malaysian distribution network. The proposed reactive power control is based on simultaneous PV active power injection and network voltage. Unlike conventional methods, the proposed reactive power control does not directly correlate with PV active power injection or network voltage. Instead, it calculates the amount of reactive power change based on PV active power injection and network voltage, repeating this process every second. This control technique offers greater flexibility in managing reactive power to accommodate variations in network parameters. Furthermore, since it depends on both PV active power generation and voltage simultaneously, it ensures precise control over reactive power output. The proposed control technique is examined on the low voltage distribution network supplying a residential neighborhood in Taman Impian Putra PD, Malaysia. This study utilizes MATLAB simulation and OpenDSS simulation to simulate and evaluate the effectiveness of the proposed technique.

## METHODOLOGY

### Low Voltage Network Modelling

As presented by Tie and Gan (2013), the network used in this study is a low-voltage distribution network that supplies electricity to a residential area called Taman Impian Putra in Malaysia. The network data was collected from TNB, the company responsible for the transmission and distribution of electricity in Malaysia. The residential area and the distribution network are depicted in Figures 1 and 2, respectively. Furthermore, the network data is summarized in Table 1. The radial network comprises a  $4 \times 500 \text{ mm}^2$  PVC/PVC Aluminum (Al) cable that connects the transformer to the feeder pillar. The feeder pillar serves a total of five feeders. The cable between the feeder pillar and the poles is  $185 \text{ mm}^2$  4C Al XLPE. An Aerial Bundle Cable (ABC) with  $3 \times 185 \text{ mm}^2 + 120 \text{ mm}^2$  is

employed to distribute power from the poles to the houses. Among the feeders, Feeder 5 is the longest, spanning 332 meters, while Feeder 4 is the shortest at 186 meters. Each feeder serves approximately 27 to 33 terrace houses, assuming an average maximum demand of 2 kW per consumer, accounting for diversity. Mutual impedance and self-impedance are calculated using Equations 1 and 2, respectively (Ebrahimi et al., 2011).

$$Z_{ij} = 9.8696 * 10^{-4} \cdot f + j1.2566 * 10^{-3} \cdot f \cdot \left( \ln \frac{1}{D_{ij}} + 6.4905 + \frac{1}{2} \ln \frac{\rho}{f} \right) \Omega/\text{km} \quad [1]$$

$$Z_{ii} = r_i + 9.8696 * 10^{-4} \cdot f + j1.2566 * 10^{-3} \cdot f \cdot \left( \ln \frac{1}{GMR_i} + 6.4905 + \frac{1}{2} \ln \frac{\rho}{f} \right) \Omega/\text{km} \quad [2]$$

where  $D_{ij}$  = Distance between conductor i and j;  $r_i$  = Resistance of conductor ( $\Omega/\text{km}$ );  $f$  = System frequency 50 Hz;  $GMR_i$  = Geometric mean radius of conductor (cm); and  $\rho$  = earth resistivity ( $\Omega \cdot 100$ ).

Then, the subsequence and sequence impedance are calculated by Equations 3 and 4 (Kersting, 2020).

$$Z_o = Z_s + 2Z_m \quad [3]$$

$$Z_1 = Z_2 = Z_s - Z_m \quad [4]$$

Where  $Z_m$  and  $Z_s$  Can be calculated based on Equations 5 and 6 respectively (Kersting, 2020).

$$Z_m = \frac{Z_{ab} + Z_{ac} + Z_{ba} + Z_{bc} + Z_{ca} + Z_{cb}}{6} \quad [5]$$

$$Z_s = \frac{Z_{aa} + Z_{bb} + Z_{cc}}{3} \quad [6]$$

Table 1  
Summary of the network data

Characteristics	Amount
Number of customers	149
Area (km <sup>2</sup> )	0.75
Energy consumption (MWh/Year)	1572
Peal demand (kW)	298
Total network length (km)	1.5
Load density (MW/km <sup>2</sup> )	4
Transformer rating (KVA)	500



Figure 1. The residential area in Taman Impian Putra PD, Malaysia (<https://www.google.com/maps>)

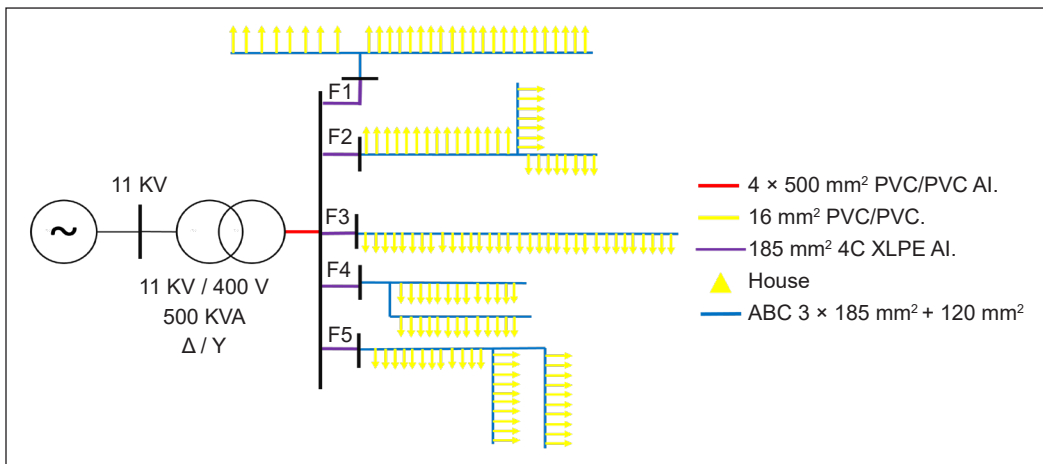


Figure 2. Low voltage distribution network of Taman Impian Putra (Tie & Gan, 2013)

### Load Demand and PV Generation

Figure 3 illustrates Malaysia’s aggregate load demand profile (Ebrahimi et al., 2011). It can be observed that the load demand experiences an increase at 5 p.m., reaching its peak at 8 p.m. This surge in demand is primarily attributed to the prevalent hot weather in Malaysia, leading to most customers’ higher usage of air conditioning systems. Conversely, the load demand is at its minimum between 7 a.m. and 5 p.m., as most customers are outdoors during this period. This load profile serves as a representative shape for all houses within the distribution network.

On the other hand, Figure 3 also presents the solar panel generation profile (Ebrahimi et al., 2011). Notably, the solar panels do not generate electricity during the night period from 8 p.m. to 8 a.m. due to the absence of sun irradiance. Subsequently, the PV generation gradually increases, reaching its maximum output at 1 p.m. It is important to highlight that this PV generation profile applies to all PV systems within the network.

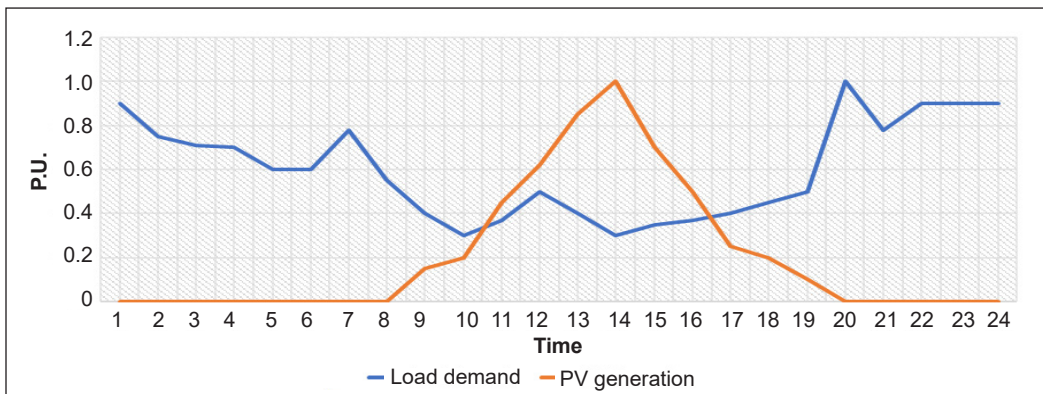


Figure 3. PV generation and load demand profile

### The Proposed Reactive Power Controls

The reactive power control algorithm alleviates voltage rise in distribution networks with high photovoltaic (PV) penetration. The algorithm relies on the smart inverter’s capacity to absorb or inject reactive power. Smart inverters that link PV systems to the national grid can regulate real power to meet national grid requirements and control reactive power through  $I_q$  and  $I_d$  for active power management. Additionally, voltage control is implemented to adhere to the voltage requirements of the national grid.

This study’s proposed reactive power control algorithm considers both PV active injection and the voltage simultaneously at the point of common coupling. In contrast to conventional approaches, the reactive power reference is not solely determined based on PV active injection or network voltage alone. Instead, this technique calculates the delta-reactive power and recalculates every second using Equation 7. This delta-reactive power is then utilized to determine the reactive power reference at a specific time using Equation 8. Consequently, the proposed reactive power control demonstrates enhanced adaptability to varying network parameters, continuously updating in real-time.

$$\Delta Q(t) = (VV * W) + (WV + (1 - W)) \tag{7}$$

$$Q(t) = Q(t-1) + \Delta Q (t) \tag{8}$$

The proposed technique commences by calculating the influence of PV active power injection on reactive power change (Watt-VAR). A modified fixed power factor method is employed, with the modification setting the starting point at 0.1 instead of 0. This adjustment implies that when there is no PV active power injection, the Watt-VAR aims to increase the reactive power reference by 0.1 per second towards the capacitive mode based on Equation 9. For a visual representation, please refer to Figure 4. Simultaneously, the proposed technique evaluates the impact of the voltage at the point of common coupling on reactive power change (Volt-VAR) in conjunction with Watt-VAR. Volt-VAR is computed using the conventional  $Q(V)$  technique, as illustrated in Figure 5 and Equation 10.

$$Watt - Var = \begin{cases} -1, & P \geq P_{max} \\ \frac{1.1 * P}{-P_{Max}} + 0.1, & 0 \leq P < P_{Max} \end{cases} \tag{9}$$

$$Q_{ref} = \begin{cases} Q_{lim}, & V < V_1 \\ \frac{Q_{lim}}{(V_1 - V_2)} (V - V_1), & V_1 \leq V < V_2 \\ 0, & V_2 \leq V < V_3 \\ \frac{Q_{lim}}{(V_3 - V_4)} (V - V_3), & V_3 \leq V < V_4 \\ -Q_{lim}, & V_4 \leq V \end{cases} \tag{10}$$

Furthermore, the technique determines the weight, signifying the relative significance of Volt-VAR and Watt-VAR in influencing reactive power change based on the voltage at the point of common coupling. As the voltage increases, the weight also increases, exerting more influence on the Volt-VAR algorithm to adjust reactive power, either increasing or decreasing it. This relationship is depicted in Figure 6 and defined in Equation 11. At 1.2 V (p.u.), the weight is 1, indicating that reactive power change depends entirely on Volt-VAR. Subsequently, the weight gradually decreases until it reaches 0 at 0.6 V (p.u.), signifying that reactive power change relies solely on Watt-VAR. Refer to Figure 6 for the weight calculation. Finally, Figure 7 illustrates the proposed reactive power control flow chart.

$$Weight = \begin{cases} 1, & V \geq V_{Max} \\ \frac{1}{(V_{Max} - V_{min})} (V - V_{min}), & V_{Min} < V < V_{Max} \\ 0, & V \leq V_{Min} \end{cases} \quad [11]$$

By considering both PV active injection and network voltage in the control strategy, the proposed approach ensures effective interaction with the dynamic changes in the network. This real-time updating capability enhances the system’s performance and stability, facilitating efficient reactive power control.

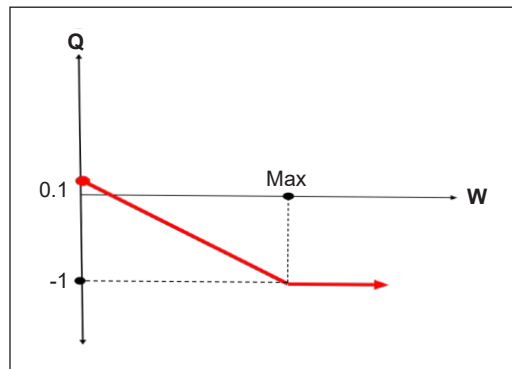


Figure 4. Proposed technique response to PV active power injection

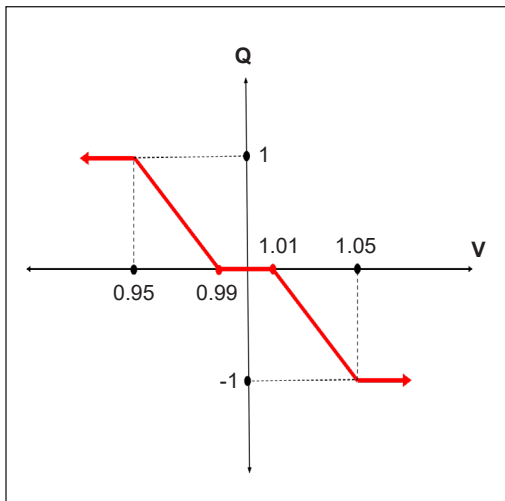


Figure 5. Proposed technique response to the voltage on the point of common coupling

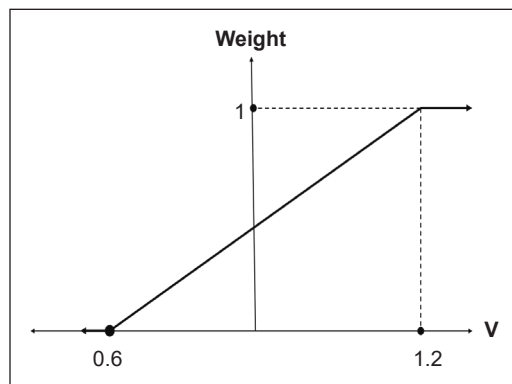


Figure 6. Weight calculation characteristic graph

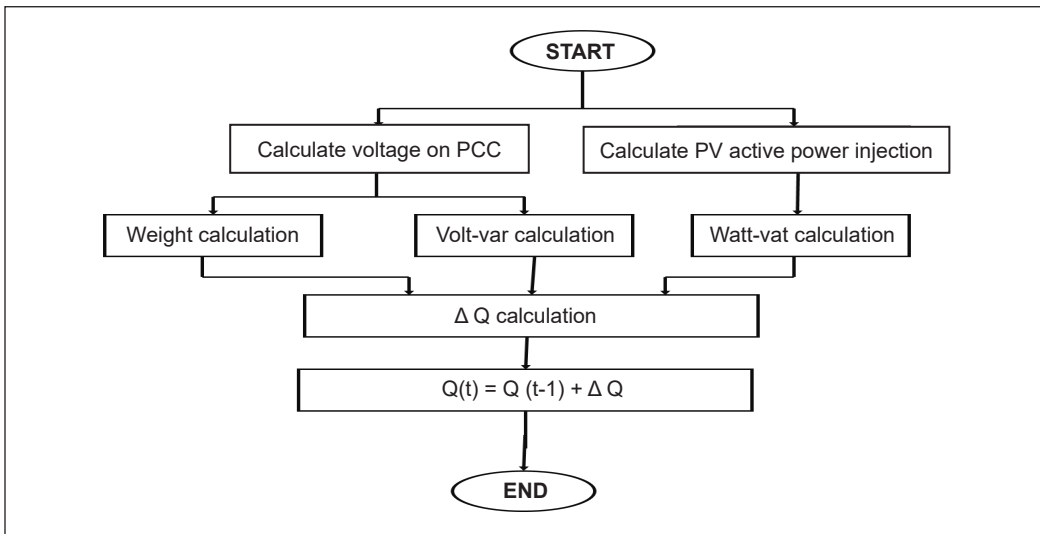


Figure 7. Proposed reactive power control technique flow chart

## SIMULATION AND RESULTS

The low voltage distribution network in the residential area of Taman Impian Putra PD in Malaysia, depicted in Figures 1 and 2, was not originally designed to accommodate the high number of distributed generation (DG) sources. Consequently, the increased penetration of PV systems brings numerous challenges to the network. One such challenge is voltage rise, discussed previously.

Simulations were conducted using MATLAB Simulation and OpenDSS on the network with varying levels of PV penetrations to analyze the impact of PV penetration. Figure 8 illustrates the voltages at the point of common coupling for a random house (the last householder of Feeder 3) without any reactive power control. It can be observed that the voltage starts to increase at 10 p.m. due to an increase in sun irradiance and a decrease in load demand. Subsequently, the voltage reaches its maximum at 1 p.m. The voltage declines as the sun irradiance decreases and householders return to their houses. Notably, the figure demonstrates that the level of PV penetration directly influences the maximum voltage increase.

Furthermore, Figure 9 provides insight into the highest and lowest average voltages observed on the distribution network at different penetration levels, all without any reactive power control implemented.

These simulation results highlight the adverse effects of high PV penetration on the network voltage. Without effective reactive power control measures, the voltage levels experience significant daily fluctuations influenced by sun irradiance and load demand variations. It is imperative to address these voltage issues to ensure the reliability and stability of the distribution network.

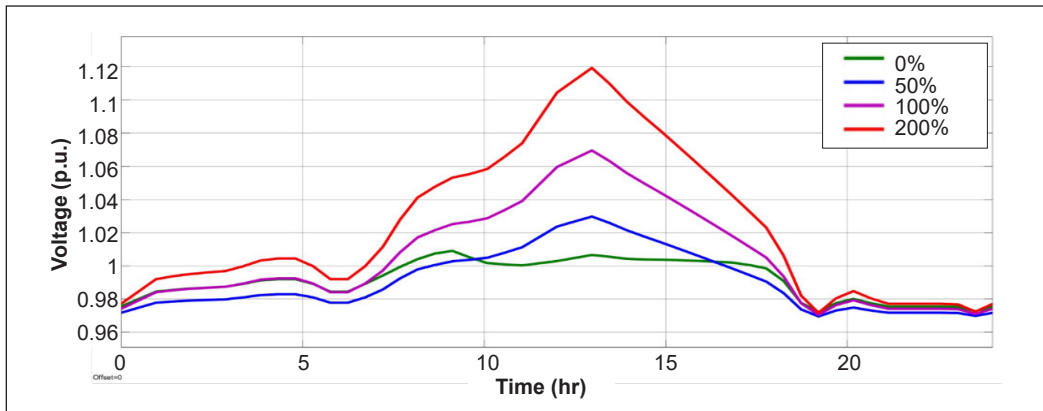


Figure 8. The voltage graph on the point of common coupling of the last customer on Feeder 3 for 24 h without reactive power control for a different level of penetration (0%, 50%, 100%, and 200%)

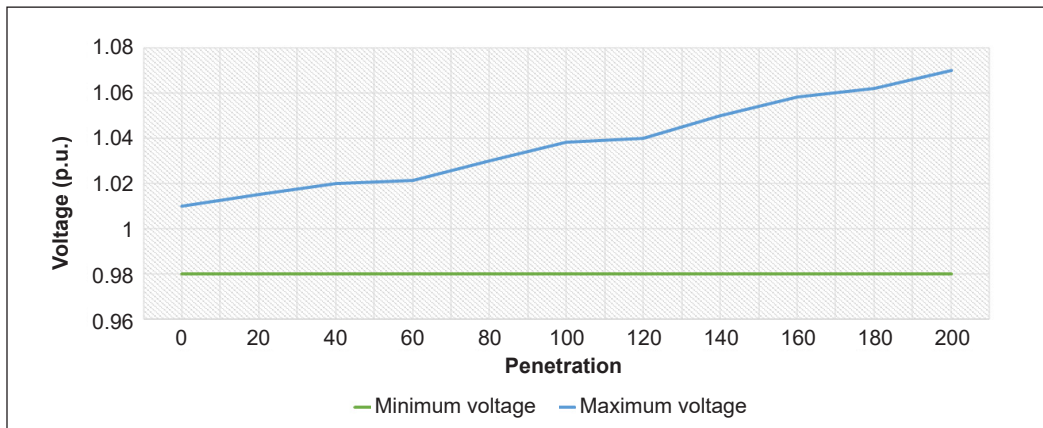


Figure 9. Highest and lowest voltage of distribution network for different levels of PV penetration without reactive power control

As a result, it is crucial to employ a voltage rise mitigation technique on the distribution network to address the challenges posed by high PV penetration. Fortunately, the proposed reactive power control technique demonstrates promising results in mitigating voltage rise and maintaining voltage within the permissible limits of 0.95 to 1.05 per unit (p.u.). Figure 10 presents the distribution network’s maximum and minimum average voltages when utilizing the proposed reactive power control at different levels of PV penetration. It is evident from the figure that the proposed technique effectively reduces the average voltage to a highly acceptable level.

The proposed reactive power control achieves this by mitigating the voltage during the mid-day period, characterized by maximum sun irradiance and minimum load demand, as depicted in Figure 11. The figure illustrates the voltage at the point of common coupling of the last customer on Feeder 3 over 24 hours, employing the proposed reactive power

control at different penetration levels. The control technique successfully mitigates voltage rise while minimizing losses. It accomplishes this by utilizing a novel control approach that does not rely directly on PV active injection or network voltage. Instead, the instantaneous values of PV active power injection and network voltage are used to calculate the required change in reactive power reference. This approach provides greater flexibility in adapting to variations in network parameters.

Moreover, this technique overcomes the limitations of other methods that solely depend on PV active injection and network voltage, which tend to overlook load variations and rely heavily on network voltage sensitivity. The proposed technique effectively addresses these limitations, improving voltage regulation and reducing losses.

Finally, Figure 12 illustrates the reactive power injection of the reactive power control at the last customer on Feeder 3, highlighting the effectiveness of the proposed control strategy.

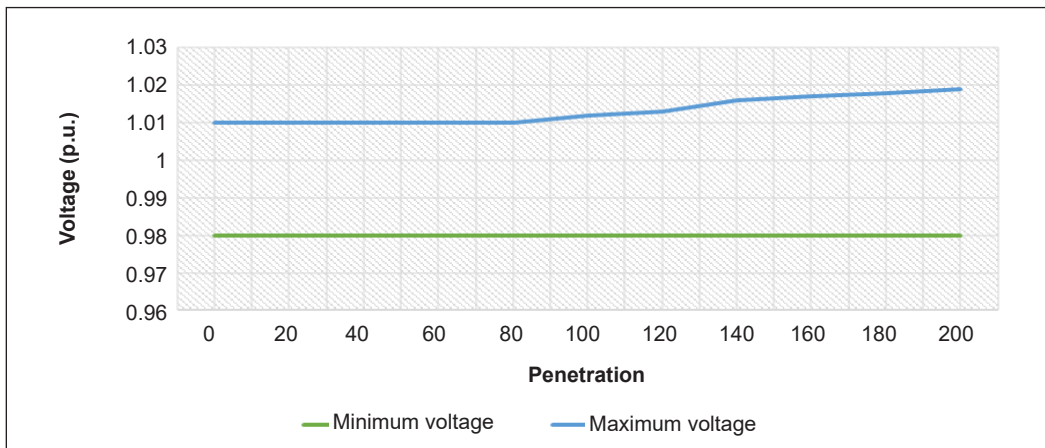


Figure 10. The highest and lowest voltage of the distribution network for different levels of PV penetration with the proposal reactive power control

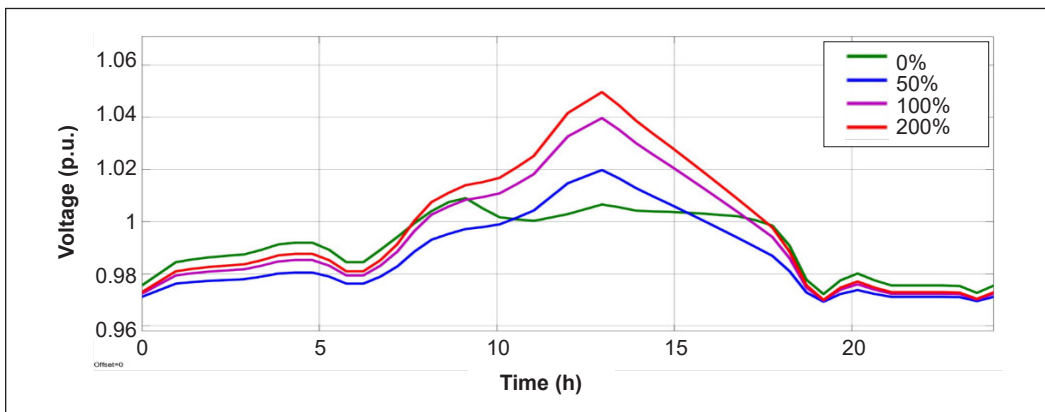


Figure 11. The voltage graph on the point of common coupling of the last customer on Feeder 3 for 24 hours with the proposal reactive power control for a different level of penetration (0%, 50%, 100%, 200%)

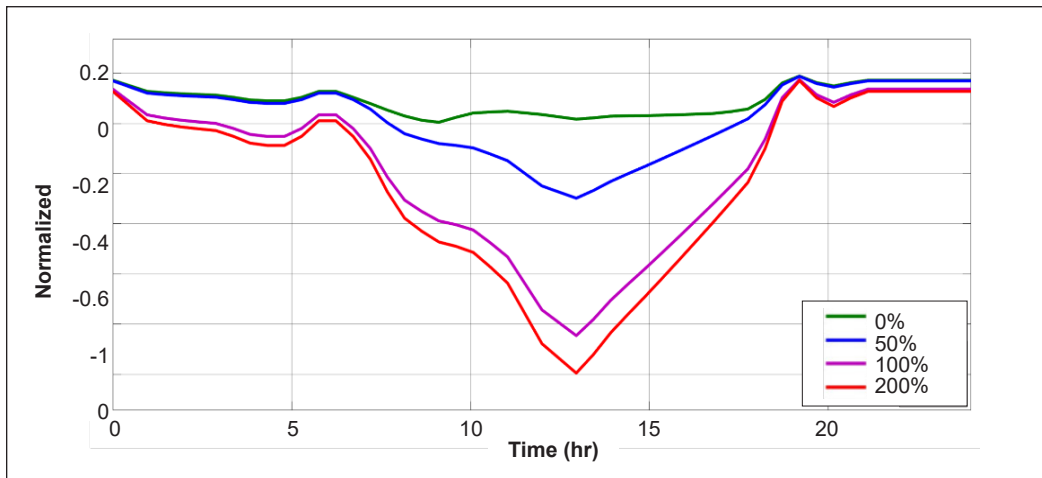


Figure 12. Reactive power injection of the proposal reactive power control for the last customer on Feeder 3 during 24 hours for different level of penetration (0%, 50%, 100%, 200%)

## DISCUSSION

This paper's proposed reactive power control technique combines both PV active power injection and the voltage at the point of common coupling. By considering these parameters and a weight determined by the network voltage, the technique calculates the necessary change in reactive power reference. This calculation is repeated every second to provide the control strategy with greater flexibility in adapting to changes in network parameters.

In contrast, existing reactive power control techniques typically depend on PV active power injection or network voltage at specific times. When relying solely on PV active power injection, the control technique is highly influenced by load variations. While this approach can achieve good voltage regulation, it may result in significant unnecessary losses when both PV injection and load demand are high. Moreover, this technique is based on a typical load shape assumption, which may not accurately represent the actual conditions.

On the other hand, network voltage-based reactive power techniques are directly proportional to the network voltage. However, the proponents of this technique overlooked that the network voltage in a specific location reacts differently to changes in active and reactive power, depending on the voltage-active/reactive sensitivity. This sensitivity increases as the distance from the feeder transformer increases. Consequently, this technique may demonstrate good voltage regulation only in high-sensitivity locations. This technique may result in poor voltage regulation for large-scale networks like the one presented in this paper.

However, the proposed technique incorporates active power injection and network voltage, allowing for a more accurate reactive power reference. The two parameters work together to correct each other, albeit at a slower rate compared to other techniques. Unlike these techniques, which have predetermined reactive power references for specific PV

active power or network voltage values, the proposed technique adjusts the reactive power reference every second based on the active power injection and network voltage until reaching a stability mode where the change in reference becomes zero. As variations in load demand and sun irradiance are typically not rapid, this technique yields better results compared to existing reactive power control techniques.

Hence, the presented simulation results offer a comprehensive analysis of the impact of photovoltaic (PV) penetration on distribution network voltage and the potential solutions to mitigate associated challenges. In Figure 8, the voltage variations at the point of common coupling for a random house show that increased sun irradiance and reduced load demand during the day result in voltage rise directly influenced by the level of PV penetration. These findings underscore the pressing need to mitigate voltage rise, as the proposed reactive power control technique addresses. The subsequent analysis in Figure 10 reveals that the proposed technique effectively reduces the average voltage to acceptable levels. This control strategy, illustrated in Figure 11, successfully combats voltage rise during peak sun irradiance, demonstrating adaptability to varying network parameters. Notably, this approach outperforms methods reliant solely on PV active injection and network voltage, as it considers load variations and reduces reliance on network voltage sensitivity. Figure 12 confirms the effectiveness of this strategy by showcasing the reactive power injection. In summary, these results emphasize the necessity of implementing innovative reactive power control measures to ensure the reliability and stability of distribution networks amidst high PV penetration, offering valuable insights for future grid management and renewable energy integration.

In summary, the proposed reactive power control technique uses both PV active power injection and network voltage, providing a more accurate reactive power reference. Although slower than other techniques, it achieves better results due to its adaptive nature. This approach surpasses the limitations of existing techniques by considering the dynamic changes in active power injection and network voltage, leading to improved voltage regulation in the distribution network.

## CONCLUSION

This paper addresses the pressing issue of voltage rise in low voltage distribution networks in Malaysia, driven by the increasing integration of renewable energy sources and distributed energy resources (DERs). While these developments offer substantial environmental and economic benefits, they bring new challenges, particularly regarding voltage stability. Voltage rises, triggered by the excessive power injection from DERs, can lead to increased energy losses, reduced power quality, equipment damage, and system instability. Conventional voltage control methods have limitations in effectively addressing these challenges, especially in dynamic DER integration.

This paper introduces a novel reactive power control strategy that simultaneously considers PV active power injection and network voltage to overcome these limitations. Unlike traditional approaches, this technique continuously updates its reactive power reference based on real-time changes in PV power generation and network voltage, offering greater flexibility to adapt to varying network parameters. Simulation results on a representative distribution network in Malaysia demonstrate the effectiveness of this technique in mitigating voltage rise and maintaining voltage within permissible limits under different penetration levels.

The proposed technique strikes the drawbacks of existing methods, which primarily rely on PV active injection or network voltage. Considering both parameters provides more precise control over reactive power output, ensuring improved voltage regulation and reduced losses. The technique's adaptability to variations in load demand and sun irradiance positions it as a promising solution for the challenges posed by high PV penetration in distribution networks. Overall, this research offers valuable insights into enhancing the reliability and stability of distribution networks in the face of increasing renewable energy integration and sets the stage for further developments in grid management and clean energy adoption.

## ACKNOWLEDGEMENT

The authors would like to express their sincere gratitude to Universiti Putra Malaysia for their invaluable support and supervision. Their scientific guidance and financial assistance were crucial to the completion of this study.

## REFERENCES

- Alwez, M. A., Jasni, J., Radzi, M. A. M., & Azis, N. (2020). PV system sizing to cover the electricity shortage in a residential quarter in Iraq. In *PECon 2020 - 2020 IEEE International Conference on Power and Energy* (pp. 214-218). IEEE Publishing. <https://doi.org/10.1109/PECON48942.2020.9314441>
- Demirok, E., González, P. C., Frederiksen, K. H. B., Sera, D., Rodriguez, P., & Teodorescu, R. (2011). Local reactive power control methods for overvoltage prevention of distributed solar inverters in low-voltage grids. *IEEE Journal of Photovoltaics*, 1(2), 174-182. <https://doi.org/10.1109/JPHOTOV.2011.2174821>
- Ebrahimi, R., Branch, B., Babae, A., & Hoseynpoor, M. (2011). Evaluation and calculation of overhead line impedance in distribution networks. *Australian Journal of Basic and Applied Sciences*, 5(8), 1278-1284.
- Haque, A. N. M. M., Nguyen, P. H., Vo, T. H., & Blied, F. W. (2017). Agent-based unified approach for thermal and voltage constraint management in LV distribution network. *Electric Power Systems Research*, 143, 462-473. <https://doi.org/10.1016/J.EPSR.2016.11.007>
- Hasheminamin, M., Agelidis, V. G., Salehi, V., Teodorescu, R., & Hredzak, B. (2015). Index-based assessment of voltage rise and reverse power flow phenomena in a distribution feeder under high PV penetration. *IEEE Journal of Photovoltaics*, 5(4), 1158-1168. <https://doi.org/10.1109/JPHOTOV.2015.2417753>

- Inaolaji, A., Savasci, A., & Paudyal, S. (2022). Distribution grid optimal power flow in unbalanced multiphase networks with volt-var and volt-watt droop settings of smart inverters. *IEEE Transactions on Industry Applications*, 58(5), 5832-5843. <https://doi.org/10.1109/TIA.2022.3181110>
- Kersting, W. H. (2020). Series impedance of overhead and underground lines. In W. H. Kersting & R. J. Kerestes (Eds.), *Distribution System Modeling and Analysis 5th Edition* (pp. 91-122). CRC Press. <https://doi.org/10.1201/9781003261094-4>
- Kim, S. B., & Song, S. H. (2020). A hybrid reactive power control method of distributed generation to mitigate voltage rise in low-voltage grid. *Energies*, 13(8), Article 2078. <https://doi.org/10.3390/en13082078>
- Maghami, M. R., Pasupuleti, J., & Ling, C. M. (2023). A Static and dynamic analysis of photovoltaic penetration into MV distribution network. *Processes* 2023, 11(4), Article 1172. <https://doi.org/10.3390/PR11041172>
- Singh, S., Veda, S., Singh, S. P., Jain, R., & Baggu, M. (2021). Event-driven predictive approach for real-time volt/VAR control with CVR in solar PV rich active distribution network. *IEEE Transactions on Power Systems*, 36(5), 3849-3864. <https://doi.org/10.1109/TPWRS.2021.3057656>
- Tie, C. H., & Gan, C. K. (2013). Impact of grid-connected residential PV systems on the Malaysia low voltage distribution network. In *Proceedings of the 2013 IEEE 7th International Power Engineering and Optimization Conference, PEOCO 2013* (pp. 670-675). IEEE Publishing. <https://doi.org/10.1109/PEOCO.2013.6564631>

*Review Article*

## Processing Plants Damage Mechanisms and On-stream Inspection Using Phased Array Corrosion Mapping—A Systematic Review

Jan Lean Tai<sup>1</sup>, Mohamed Thariq Hameed Sultan<sup>1,2,3\*</sup> and Farah Syazwani Shahar<sup>1</sup>

<sup>1</sup>Department of Aerospace Engineering, Faculty of Engineering, Universiti Putra Malaysia, 43400 UPM Serdang, Selangor, Malaysia

<sup>2</sup>Laboratory of Biocomposite Technology, Institute of Tropical Forest and Forest Product (INTROP), University Putra Malaysia, 43400 UPM Serdang, Selangor, Malaysia

<sup>3</sup>Aerospace Malaysia Innovation Centre, Prime Minister's Department, MIGHT Partnership Hub, 63600 Cyberjaya, Selangor, Malaysia

### ABSTRACT

This review aims to study the process plant damage mechanisms published by previous research, such as general corrosion, localised corrosion, and stress corrosion cracking. This review was conducted by analysing the current application of the common inspection method and technique and focusing on the phased array ultrasonic testing application. In order to further the current study, the review seeks direction on evaluating phased array corrosion mapping techniques to detect corrosion and metal loss during plant operation and minimise the plant's need for maintenance. This systematic literature review provides a better understanding of the current damage mechanisms and shows the possibility of an extended future study.

*Keywords:* General corrosion, localised corrosion, non-destructive testing (NDT), phased array ultrasonic testing (PAUT), pitting, stress corrosion cracking (SCC)

### INTRODUCTION

The in-line inspection activities of the petrochemical process plant are performed to carry out routine planned inspections of the plant's equipment to ensure that the entire system is in good working condition and avoid unexpected failure without the plant's shutdown.

Non-destructive testing (NDT) techniques have been widely utilised in

#### ARTICLE INFO

*Article history:*

Received: 16 August 2023

Accepted: 02 January 2024

Published: 25 July 2024

DOI: <https://doi.org/10.47836/pjst.32.4.12>

*E-mail addresses:*

taijanlean2008@hotmail.com (Jan Lean Tai)

thariq@upm.edu.my (Mohamed Thariq Hameed Sultan)

farahsyazwani@upm.edu.my (Farah Syazwani Shahar)

\* Corresponding author

the petrochemical industry. Conventional NDT methods, such as visual inspection (VT), magnetic particle testing (MT), penetrant testing (PT), and eddy current testing (ECT), are commonly used to detect surface defects. Ultrasonic testing (UT) and radiography testing (RT) are typically employed for internal flaws. The phased array corrosion mapping technique is a UT technique that provides image-based results and requires less testing time.

This systematic literature review aims to investigate the application of the phased array corrosion mapping technique for detecting corrosion and metal loss in high-temperature environments without shutting down the plant operation and minimising the plant's downtime for turnaround maintenance.

To better understand the subject matter, the first research question aims to identify the current plant damage mechanisms, in-service defects, and material distortions in equipment or piping systems studied by other researchers. The second research question sought to determine the materials involved in these damage mechanisms.

The third research question focuses on the current application stage of phased array ultrasonic testing and phased array corrosion mapping. The aim is to understand the advanced UT technique's capabilities and its application by other researchers. Finally, this review seeks to determine the feasibility of using phased array corrosion mapping in a plant's operating conditions.

## LITERATURE REVIEW

The search strategy employed in this literature review utilised the keyword "corrosion," encompassing various forms of corrosion such as general and localised corrosion, erosion corrosion, microorganism-induced corrosion, galvanic corrosion, and stress corrosion cracking. A total of 40 articles were selected based on these keywords, and articles that pertained to non-metal and non-process plants were excluded to address research questions one and two.

The second focus pertains to current inspection methods used in high-temperature plant operations. Specifically, the application of phased array ultrasonic testing (PAUT) is of interest, including its utilisation for corrosion mapping, weld inspection, application on non-metallic materials, and other phased array ultrasonic applications.

### The Process Plants Damage Mechanism

The cause of equipment deterioration or disintegration is known as the damage mechanism. Selecting the type of damage mechanism is done by screening the composition of the plant's equipment material, the fluid that is processed or stored in the equipment, the surrounding processing environment, and other conditions that affect the screening of the damage criteria (Siswanto et al., 2021).

Crude oil is a mixture of dissolved gases, water, and salts in the form of liquid hydrocarbons. It is an emulsion of water droplets dispersed throughout the continuous

hydrocarbon phase. Natural gas is a gaseous mixture of hydrocarbons, nitrogen, carbon dioxide, sulphur dioxide, water, and trace amounts of mercury, organic acids, and inert gases. CO<sub>2</sub>, H<sub>2</sub>S, H<sub>2</sub>O, mercury, and organic acids can cause metal corrosion in natural gas production, separation, processing, transportation, handling, and storage (Groysman, 2017).

Carbon dioxide causes corrosion called sweet corrosion. Sour corrosion occurs when H<sub>2</sub>S is the cause of corrosion. The corrosion caused by O<sub>2</sub> is called oxygen corrosion. Oxygen corrosion has a pitting appearance. Carbon steel, low alloy steels, copper, and its alloys are corroded by oxygen. However, oxygen is essential to maintain protective oxide layers on stainless steel, titanium, and aluminium.

Corrosion is responsible for 80% of total petrochemical plant failures. The corrosion rate increases 1–3 times for every 10°C increase in temperature, and pressure increases the solubility of corrosive gases, accelerating corrosion. Stainless steel (SS) is resistant to ordinary corrosion. However, pitting corrosion is still problematic (Wan & Yang, 2021).

Corrosion is generally classified into two primary categories, general corrosion and localised corrosion, which are determined by the appearance of corrosion. Stress corrosion cracking (SCC) is a notable damage mechanism that has garnered significant attention from researchers because of its detrimental effects. As depicted in Figure 1, this classification scheme highlights the crucial dissimilarities between various forms of corrosion.

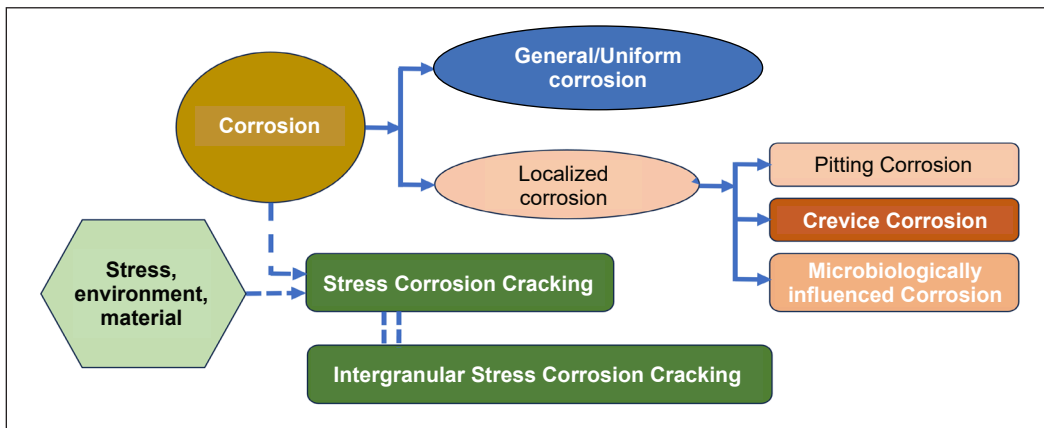


Figure 1. Classification of corrosion

### General Corrosion

Mazumder (2020) described corrosion as a localised electrochemical oxidation and reduction reaction occurring on the metal surface. An anode, cathode, and aqueous solution, or electrolyte, with positively and negatively charged ions with some conductivities, are used in the electrochemical corrosion process. When metals dissolve, electrons are moved to another location on the surface, causing slow degradation and eventual failure of the host metal (Fajobi et al., 2019).

Internal corrosion is linked to the gases or liquids that are stored or transferred. Continuous exposure to fluids causes corrosion under both anaerobic and aerobic conditions. Chemical reactions primarily cause internal piping corrosion, whereas electrochemical reactions cause material loss. Therefore, the corrosion type, depth and width, average corrosion rate, and vertical deviation are common indicators of corrosion damage (Shafeek et al., 2021).

Du et al. (2020) indicated that corrosion is the most common problem in atmospheric and vacuum distillation units, especially in low-temperature components because crude oil includes a lot of corrosive chemicals such as water, salt, sulphide, and acid. Therefore, the primary failure mechanisms of the atmospheric and vacuum distillation units can be regarded as internal corrosion thinning, including uniform and localised corrosion thinning wet hydrogen sulphide damage and exterior corrosion.

Colombo et al. (2018) studied the elements to determine why closed water-cooling systems fail at 270°C. The primary material for the cooling water system is a zinc-coated galvanised steel pipe. However, it still has corrosion issues, especially with high chloride and sulphate concentrations, temperature, and low pH.

Electrolytic corrosion and galvanic corrosion are two mechanisms that cause corrosion to occur. Due to its high mechanical properties, availability, and low cost, carbon steel has become the standard material for pipeline transportation (Ameh et al., 2018).

However, Kansara et al. (2018) believe uniform corrosion is defined as corrosion that occurs consistently across the exposed metal surface. It is generally easy to assess and anticipate, making catastrophic failures uncommon.

### ***Localised Corrosion***

Wang et al. (2021) introduced pitting corrosion, also known as localised corrosion or pinhole corrosion, as a kind of corrosion with a small diameter and considerable depth. Pitting pits form on the microscopic scale and cause metals and alloys to fail through perforation and stress corrosion cracking, among other failure modes.

Shekari et al. (2017) described pitting as a localised metal loss where the pitting diameter is on the order of the thickness of the plate or less, and the depth of pitting is less than the thickness of the plate. If not enough attention is paid to the enlarged pit, the damaged device can leak once the pit turns into a hole and penetrates the device housing.

Pitting is a corrosion mechanism in various pipeline steel grades used in the petroleum industry. Localised pits are produced by the differential cell, which expands by an autocatalytic mechanism known as self-stimulating and self-propagating (Subramanian, 2018).

Shekari et al. (2016) also introduced a fitness-for-service assessment method to determine plant equipment suffering from pitting corrosion. Pitting is a local corrosion

type that could penetrate the equipment wall and cause serious incidents. Salt in crude oil promotes pitting corrosion of metal structures in crude distillation overhead systems. It is also caused by hydrochloric acid in crude distillation overhead systems, particularly at temperatures of approximately 338°C (Fajobi et al., 2019).

Piri et al. (2021) indicated that failure and corrosion of carbon steel fire water pipes, predominantly localised corrosion, can cause pipeline leakage and rupture, resulting in costly repairs or replacement or even uncontrollable conditions during a plant's emergency. When the pressure of the fluid is lower than its vapour pressure, vapour pockets and bubbles can form on the pipe's inner surface, resulting in cavitation damage (Vanaei et al., 2017).

Khouzani et al. (2019) reported that microorganism-induced corrosion (MIC) is affected by microorganisms, including microalgae, bacteria, archaea, and fungi. MIC can occur in the absence of other corrosion or in combination with other corrosion failures.

MIC is an electrochemical phenomenon caused by microorganisms that can alter corrosion processes and increase localised corrosion. Bacteria, fungi, and microalgae are all microorganisms, but bacteria are the primary source of corrosion. MIC may arise during system operation or construction.

According to the results of many chemical and microbiological experiments from Chidambaram et al. (2018) study, they defined the fire water supply pipeline as ruptured by sulphide-reducing bacteria. Sulphide-reducing bacteria cause the MIC of fire-fighting water supply pipes.

Crevice corrosion is localised corrosion that occurs internally in the piping in either metal-to-metal or metal-to-non-metal grooves. Crevice corrosion is often used to describe the damage to passivating metals, but it can also refer to the failure of non-passivating metals caused by oxygen concentration cells (Cheshideh et al., 2021).

Austenitic stainless steels (ASS) are prone to pitting corrosion under chloride conditions. The critical pitting temperatures for 304 and 316 SS are approximately 30°C and 55°C, respectively (Martins et al., 2014).

Based on this review, the authors have identified four critical factors that influence corrosion: the pH and chemical composition of the product, the materials used in fabrication, temperature, and environmental conditions. In addition, the API Recommended Practice 571: Damage Mechanisms Affecting Fixed Equipment In The Refining Industry (2011), which is structured around both the environment and the product to classify corrosion mechanisms into various categories such as atmospheric corrosion, cooling water corrosion, and boiler water condensate corrosion (API, 2011).

Table 1 provides a selective overview of the critical damage mechanisms, highlighting the crucial factors and affected materials to understand better the four key factors influencing corrosion. Owing to space limitations, detailed information and explanations of all damage mechanisms have not been included (API, 2011).

Table 1  
Critical factors of damage mechanism

Damage Mechanism	Description Damage	Critical Factors	Affected Materials
Atmospheric Corrosion	Corrosion due to moisture in atmospheric conditions is a common phenomenon, particularly affecting marine environments and humid, polluted industrial areas. The dry rural environments, on the other hand, experience minimal corrosion. This corrosion can occur in the form of general deterioration or localised damage.	Factors impacting corrosion include environmental humidity levels, temperature fluctuations, and the presence of salts, sulphur compounds, and dirt. Corrosion rates increase with rising temperatures, peaking at 121°C, beyond which surfaces become too dry for corrosion.	Carbon steel, low alloy steels and copper alloyed aluminium.
Cooling Water Corrosion	Corrosion, whether general or localised, can have a detrimental impact on carbon steels and other metals due to the presence of dissolved salts, gases, organic compounds, or microbiological activity. Cooling water corrosion can result in various damage, including general and pitting corrosion, MIC, stress corrosion cracking, and fouling.	Cooling water corrosion and fouling are related issues that require consideration of factors such as temperature, water type, cooling system type, oxygen content, and fluid velocities. Higher process side temperatures and cooling water inlet temperatures increase the likelihood of scaling, which can occur if the water outlet temperature exceeds 46°C in brackish or saltwater.	Carbon steel, stainless steel, copper, aluminium, titanium and nickel base alloys.
Boiler Water Condensate Corrosion	The boiler system and condensate return piping are prone to general and localised pitting corrosion.	Dissolved gases like oxygen and carbon dioxide caused oxygen pitting and carbonic acid corrosion in boiler systems. Important factors like concentration, pH, temperature, feedwater quality, and treatment systems affect corrosion likelihood. Addressing these factors is crucial for prevention and mitigation.	Carbon steel, low alloy steel, 300 Series SS and copper-based alloys.
CO <sub>2</sub> Corrosion	Carbon dioxide corrosion occurs when carbon dioxide dissolves in water, forming carbonic acid. This acid can lower the pH, leading to general or pitting corrosion in carbon steel, resulting in localised thinning.	Elevated CO <sub>2</sub> partial pressures lower pH and accelerate corrosion, especially in liquid form. Higher temperatures increase corrosion rates until CO <sub>2</sub> vaporises. However, even with higher chromium levels in steels, improved corrosion resistance is not guaranteed until a minimum of 12% chromium is reached.	Carbon steel and low alloy steels.
Microbiologically Induced Corrosion (MIC)	MIC is corrosion caused by living organisms like bacteria, algae, or fungi. It often occurs with tubercles or organic substances, and the corrosion's characteristic feature is localised pitting beneath deposits or tubercles, where the organisms hide.	Microorganisms in aquatic environments often face stagnant or low-flow conditions that promote growth. They can thrive in harsh conditions, such as an oxygen deficit, exposure to light or darkness, high salt levels, a pH range from 0 to 12, and temperatures from -17°C to 113°C.	Carbon and low alloy steels, 300 and 400 Series SS, aluminium, copper and nickel base alloys.

### ***Erosion Corrosion***

Khan et al. (2019) introduced pipelines as one of the essential structural elements of refineries and petrochemical facilities. The pipe elbows with a rough surface will increase erosion-corrosion significantly.

Erosion corrosion is another possible result of the deterioration of metals caused by corrosion processes that occur directly or indirectly from the metabolic activities of MIC. Although pipeline corrosion is inevitable, it can be detected, assessed, controlled, and managed (Vanaei et al., 2017).

### ***Galvanic Corrosion***

Bimetallic corrosion is another name for galvanic corrosion. Galvanic corrosion occurs when one material comes into electrical contact with another in the presence of an electrolyte. The electrolyte contained two dissimilar materials, one serving as the anode and the other as the cathode. The electrical potential difference between the electrode reactions drives an accelerated attack on the anode metal, which dissolves into the electrolyte. As a result, the metal at the anode corrodes faster than otherwise, and the corrosion at the cathode is slowed (Kansara et al., 2018).

### ***Stress Corrosion Cracking***

SCC is a crack propagation process caused by the interaction of mechanical force with the environment. It occurs in various metallic materials and conditions and is often aided by pitting corrosion. The role of mechanical action is to accelerate and regulate the pit-to-crack transition in SS (Cui et al., 2021).

The SCC remains the leading cause of service failure in the chemical industry, affecting steam generator tubes, booster instrumentation penetrations, heater sleeves, nozzles, heat exchangers, and other components. For stress corrosion to occur, three essential components must be present: tensile stress, environment, and sensitive material. Changing these factors can often eliminate or reduce SCC susceptibility (Spisák & Szávai, 2019).

SCC is a frequent damage mechanism in ASS, and it is also the most typical mode of failure in 310S SS. The main influencing elements for the SCC of 310S SS are hydrogen and temperature. The SCC sensitivity index of 310S SS increases with temperature and peaks at 10 MPa and 160°C.

Intergranular stress corrosion cracking (IGSCC) is a corrosion attack that occurs primarily at grain boundaries. IGSCC is not apparent on the surface and must be identified by microstructural testing. Owing to the relatively high carbon concentration of the 304H base metal, the risk of IGSCC is higher than that of the lower carbon content of the 304 L grade. Sensitisation leads to IGSCC susceptibility in ASS.

Metals experienced intergranular corrosion within their interiors and at the grain boundaries. Destructive corrosion affects the metal's cross-sectional area, causing it to deteriorate (Fajobi et al., 2019).

Uchida et al. (2019) described SS IGSCC as one of plant facilities' most commonly reported material concerns. However, no significant accidents have been documented owing to meticulous inspections and maintenance, backed up by the tireless efforts of plant utilities and benders.

Table 2 shows that most metals were affected by both erosion and galvanic corrosion. Temperature and pH play crucial roles in the occurrence of erosional corrosion.

The classification of SCC damage mechanisms based on chemicals includes chloride SCC, caustic SCC, ammonia SCC, ethanol SCC, sulphate SCC, and others. However, owing to space limitations, significant information regarding these mechanisms is not provided in this discussion (API, 2011).

Table 2

*Erosion corrosion and galvanic corrosion*

<b>Damage Mechanism</b>	<b>Description Damage</b>	<b>Critical Factors</b>	<b>Affected Materials</b>
Erosion/ Erosion— Corrosion	Erosion-corrosion occurs when corrosion removes protective coatings, exposing metal surfaces, leading to a synergistic effect that amplifies erosion and corrosion. It can cause localised thinning of the metal surface, resulting in pits, grooves, gullies, waves, rounded holes, and valleys.	The amount of metal loss depends on factors like the velocity and hardness of the impacting medium, concentration, particle size and shape, density, and susceptibility to metal loss, which can be affected by temperature and pH.	All metals and alloys
Galvanic Corrosion	Galvanic corrosion occurs when two different metals are immersed in a suitably conductive electrolyte, such as a moist environment or soil with moisture—this form of corrosion results in crevices, grooves, or pits on the metal surface.	Galvanic corrosion requires the presence of an electrolyte, typically in a moist environment, as well as the direct contact between two different materials acting as the anode and cathode and an electrical connection between them.	Most metals are prone to corrosion, except for most noble metals.

### ***High-temperature Damage Mechanism***

High-temperature corrosion (temperatures above 220°C) is mainly caused by sulphur and acid components found in crude oil and its fractions. Sulfidation, or sulphide corrosion, is the reaction of steel and other alloys with reactive sulphur compounds such as H<sub>2</sub>S in crude oil at high temperatures.

The Sulfidation corrosion rate increases with temperature peaks around 450°C and can be observed at temperatures above around 260°C. This mechanism can affect

carbon/low alloy steels and stainless steels, reducing wall thickness generally (Schempp et al., 2016). However, Baby et al. (2016) believe high-temperature sulphide corrosion is uniform when operating temperatures above 204°C with sulphur oil.

Trimborn (2016) described another most common high-temperature damage mechanism. Methane generation by interaction with carbon in steel causes High-Temperature Hydrogen Attack (HTHA) deterioration. HTHA can occur in the parent material or the weld itself and can be found in various alloys. High-temperature hydrogen corrosion is a kind of corrosion that occurs when steel is subjected to high-pressure hydrogen at a high temperature. Hydrogen atoms diffuse into the steel, combine with carbon, and generate methane gas inside the material, causing decarburisation and microcracking.

The high-temperature damage mechanism related to the material grade is also an exciting area of research. Aliprandi et al. (2020) experimented on the A335 P5 steel to determine the relationship between corrosion and temperature. They found that the remaining life of steel could be many years up to 600°C, reduce the remaining life to 700°C, and drastically reduce to a few hundred hours at 800°C.

Microstructural analyses and hardness testing findings revealed no metal matrix creep or degradation signs. This analysis eliminates the likelihood of tube failure caused solely by long-term or localised high-temperature overheating. In a nutshell, fireside corrosion is the primary cause of failure in X20CrMoV12-1 steel pipes (Almazrouee et al., 2018).

Jordan and Maharaj (2020) stated that five common damage mechanisms damage stainless steel in high-temperature service.

Creep embrittlement—Fracture ductility is an important mechanical property when stress concentrations and local imperfections (such as notches) are considered in the design. It is inversely proportional to creep and fracture strength, affecting the design of the propagation of cracks and, thus, the material's notch toughness.

Reheat cracking, also known as stress relaxation cracking, occurs in metals due to stress relaxation during post-weld heat treatment or in service at temperatures above 400°C and is most commonly seen in heavy-wall and coarse-grained areas of a welded heat-affected zone.

Sigma-phase embrittlement (SPE) is the most prevalent intermetallic phase in ASSaustenitic stainless steel. SPE is a typical high-temperature problem for austenitic alloys, as high-temperature service promotes the creation of this hard, brittle, nonmagnetic phase over time. When exposed to temperatures in the range of 595°C to 760°C, the formation of a sigma-phase in ASS of series 304H is unavoidable. The amount of sigma-phase formation and the rate at which the sigma-phase forms are faster and more significant in stabilised grades 321H and 347H SS than in 304H and 316H SS.

Sensitisation is the degradation of the alloy's integrity, and chromium depletion occurs near carbides precipitated at grain boundaries during welding in this situation. ASS becomes sensitised when subjected to temperatures between 400°C and 815°C.

## The Process Plants Inspection Method/Technique

Many inspection methods are applied to the existing plant monitoring and inspection, aligned with the previously extracted damage mechanism information from API Recommended Practice 571: Damage Mechanisms Affect Fixed Equipment in the Refining Industry (API, 2011). The recommendations for prevention, mitigation, inspection, and monitoring of these specific damage mechanisms are detailed in Table 3 for the benefit of readers (API, 2011).

Table 3

*Damage mechanism prevention, mitigation, inspection and monitoring methods*

Damage Mechanism	Prevention/Mitigation	Inspection and Monitoring
Erosion/Erosion–Corrosion	Improve pipe design by altering shape, geometry, and material. Increase pipe diameter, streamline bends, thicken walls, and add replaceable baffles. Enhance erosion resistance with harder alloys, hard-facing, or surface treatments for harder substrates.	VT, UT, RT, IR and on-line electrical resistance probes.
Galvanic Corrosion	To prevent and reduce corrosion, use proper design. Avoid touching different metals in conductive areas unless they have an excellent anode/cathode ratio.	VT, UTG
Atmospheric Corrosion	Surface preparation and coatings application play a pivotal role in ensuring the longevity of materials in corrosive environments through long-term protection.	VT, UT
Cooling Water Corrosion	Prevention of cooling water corrosion and fouling requires proper design, operation, and chemical treatment of cooling water systems while maintaining process side inlet temperatures below 60°C.	ECT or IRIS Monitor pH, oxygen, temperatures, and hydrocarbon.
Boiler Water Condensate Corrosion	Implement oxygen scavenging treatments like catalysed sodium sulphite and hydrazine according to system pressure. Ensure proper operation of the mechanical deaerator, as a residual of the oxygen scavenger can carry oxygen into the steam generation system. If inadequate, consider an amine inhibitor treatment if scale control treatment does not manage carbon dioxide in the condensate return system.	MT and Water Analysis
CO2 Corrosion	Minimise corrosion in steam condensate systems with corrosion inhibitors, significantly condensing vapours with vapour phase inhibitors. Raising condensate pH above 6 reduces corrosion. The 300 Series SS has high corrosion resistance, but upgrading to stainless steel is needed for CO2 removal. CO2 corrosion causes operational issues, and the 400 and duplex SS exhibit corrosion resistance.	VT, UT, RT and water analyses
Microbiologically Induced Corrosion (MIC)	Microorganisms thrive in water-based systems, requiring biocides like chlorine, bromine, ozone, ultraviolet light, or customised compounds. While biocides hinder microorganism growth, ongoing treatment is vital. Maintain appropriate flow velocities, minimise low flow or stagnant zones, and keep non-water containment systems clean and dry.	visual appearance, monitor fouling

The literature review on process plant inspection focuses on high-temperature applications that could be inspected during plant operation. PAUT is another focus area that includes corrosion mapping, weld inspection, and other applications.

### ***High-Temperature Inspection Application***

Zhang et al. (2016) introduced the NDT method, which can be used to perform inspections during plant operations in a high-temperature environment. Infrared thermal imaging (IR), UT, and pulsed eddy currents can perform well at high temperatures, but PT and MT have limitations.

The solution for detecting plant corrosion during plant operation is to use ultrasonic thickness gauging (UTG), which can be used at temperatures up to 200°C. However, the uncertainties of different technicians and equipment may not be accurate at the same UTG point. The study points out that the challenge of piezoelectric and couplant is challenging to work with high temperatures, and the solution by the paper is to mount a fixed point UTG on the pipe with a waveguide and gold plate to undertake piezo material and a couplant challenge to continue corrosion monitoring up to 200°C. However, it shows productivity and only a spot thickness measurement that cannot detect localised corrosion (Cheong et al., 2017).

On the other hand, Jory (2019) reported that UTG can measure materials with surface temperatures approaching 500°C. However, Inspection of refinery equipment poses challenges owing to the high temperatures. Elevated heat levels can compromise the accuracy and efficiency of measurements. Improper handling of heat may lead to damage and the restriction of transducer life, as many can only tolerate temperatures up to 52°C.

Turcu et al. (2018) determine a workable solution for PAUT corrosion mapping during plant operation; the study approach uses a Dual Linear Probe to experiment with test samples with flat-bottom holes (FBH) up to 150°C. The results show that it is challenging when the temperature rises to 150°C. The challenge includes couplant selection, the probe contact to the hot surface time, velocity change when the temperature changes, and the PAUT scanner selection. These challenges include couplant selection, probe contact to the hot surface time, velocity change when the temperature changes, and PAUT scanner selection.

### ***Phased Array Ultrasonic Corrosion Mapping***

Turcotte, Rioux, and Lavoie (2016) compared conventional UT, PAUT and 3d scanners for tank corrosion mapping inspection. Whereas traditional UT beams report only one thickness at a time, phased array scans can generate a range of thicknesses. One of the main benefits of using a phased array for corrosion mapping is that it works the same way as an array of traditional UT probes, all aligned with precise overlap and working

simultaneously. In addition to the frequency, the size and number of probe elements were the main drivers.

The advantage of the PAUT compared to conventional ultrasonic thickness measurement in terms of time and coverage emphasises that the Total focusing method (TFM) provides a more accurate image than the electronic sector scanning. It takes 2.7 hours to cover the 100 mm × 100 mm grid with a 1 mm grid, assuming one second for each measurement step with conventional ultrasonic thickness measurement. Phased array corrosion mapping can cover the same area in seconds (Ber et al., 2016).

Njelle et al. (2019) carried out the actual PAUT corrosion mapping on two separators made of carbon steel. They recorded the findings to calculate the corrosion rate and remaining life of the inspection intervals.

Jamil and Yahya (2019) experimented on a carbon steel test piece with different drill holes designed and showed that the corrosion mapping results provide good detectability. Collect and analyse basic metrics from A, B, and C scan displays in results.

Mohan et al. (2019) used the HydroFORM scanner to perform PAUT corrosion mapping because of the low productivity and low efficiency of manual UTG and because the UTG may not detect localised corrosion.

Tangadi et al. (2015) studied replacing UTG with PAUT on the corrosion mapping with a carbon steel block. Scanning speed is one of the main advantages of PAUT corrosion mapping. A single SA2-0L wedge and 5L64 probe arrangement can cover a grid width of 30 mm at a time. Compared to PAUT, based on the point scan principle, UTG requires a longer scan time to cover the same 30 mm width. The limitation of this study is the test specimen design with % wall loss in simulating the general corrosion and the absence of an experiment on the localised corrosion application.

### **Phased Array Ultrasonic Weld Inspection**

Kim et al. (2021) studied the application of PAUT on ASS welds. NDT using ultrasound is complex due to the anisotropy and inhomogeneity of austenitic steels in the weld. Because of their complex microstructure, it is challenging to describe actual welds accurately, and they are known to contain coarse grains. Based on simulation and experimental results for six defects, only a frequency of 4 MHz can provide a reliable A-scan signal for the top crack. The lack of fusion at the top portion is identified using shear waves but not longitudinal ones. However, it can be challenging to assess faults when using shear waves due to scattered and diffracted signals.

Fousianis et al. (2018) focused on two case studies of the PAUT technique on-stream inspection to detect hydrogen-induced crack (HIC) at weldments. PAUT could provide faster inspection speed, detailed defect orientation, and recoverability, and HIC damage usually comes in three stages or types. Examples include hydrogen blisters, sparse laminar

discontinuities, and massive clusters of in-plane discontinuities, which add to a surface-breaking structure.

Small-diameter pipes in power plants have small outer diameters and thin pipe walls. The conventional ultrasonic inspection makes scanning the welds difficult, leading to missed inspections. Liu et al. (2021) applied a PAUT technique to work on small diameter pipes, and the experiment concluded that the PAUT inspection could detect a 1 mm profound defect below the pipe's surface.

### ***Phased Array Ultrasonic in Non-metallic Material***

The high-density polyethylene (PE) pipe is the alternative to replace metallic pipes in nuclear power plants because it has lower maintenance costs. When applying PAUT to the PE pipe, ultrasonic waves cause dispersion and attenuation because of the velocity. The PAUT detected PE defects such as cracks, poor fusion interface, void, structural deformity, and cold welding (Zheng et al., 2018).

Thorpe et al. (2018) studied the application of PAUT to PE pipe weld (butt fusion and electrofusion joints) and demonstrated the detectability and reliability.

De Almeida and Pereira (2019) experimented with the PAUT for glass fibre-reinforced polymer pipe laminated joints. The inherent anisotropy and heterogeneity of composite materials and the high absorption capacity of polymers lead to significant energy losses through scattering, deflection, and absorption, especially in thicker parts of the assembly. The experiment revealed that five out of the six artificial defects were detected. Defect six may be due to its proximity to the surface, and it was only partially spotted by the PAUT.

Like other researchers, Fetzer (2021) described the challenge of PAUT applied to carbon fibre-reinforced polymer material owing to the non-homogeneous material's properties and countered the challenge with beam steering the incident angle of PAUT. The steering angle was compensated for attenuation and a high standard deviation in the ramping zone.

### ***Phased Array Ultrasonic in Other Applications***

Singh et al. (2017) experimented on low-carbon steel (ASTM Number SA516 Gr 70) with different heat-treated samples with machined 1.5 mm side drill holes (SDH). The result shows that the noise and attenuation factor is changed with different heat treatments. The reflected amplitude signal varies in different heat-treated. It is required to apply to average and filtering for detectability improvement.

Gunasekar and Sastikumar (2020) compared the PAUT calibration by SDH and electrical discharge machining (EDM) notch. Based on ASME Section V code recommendations, the ultrasonic testing operator chooses SDH for flat components and surface notches for curved structures like pipes and tubes. Drilling SDH in curved pieces is challenging. However, this is practically doable for jobs with larger diameters and thicknesses. Only a notch is

used for tubes with lesser diameters. The experiment revealed that the SDH response was good, but the notch varied up to 20 decibels (dB) depending on the probe angle.

Lozev et al. (2020) experimented on the actual HTHA defect specimens, and the results show that it can be optimised by using PAUT FMC/TFM methods. The HTHA is complicated damage that occurs locally. In carbon and low-alloy steels exposed to the high partial pressure of hydrogen at extreme temperatures, HTHA forms in welds, weld heat-affected zones, and base materials.

Galán-Pinilla et al. (2021) experimented on eight ASTM A36 carbon steel test specimens with EDM slots and a welded specimen without penetration defect to determine the PAUT signal accuracy and dimension characterisation. They found that the PAUT beam, the same as conventional UT, will get an optimised signal perpendicular to the beam and less amplitude if parallel to the sound beam.

Caulder (2018) introduced the benefit of applied PAUT FMC/TFM techniques and the evolved types, such as Advanced FMC/TFM, Adaptive TFM, and TFMp. Signal imaging is more transparent and precise than PAUT imaging. FMC is a data-collecting method, whereas TFM is a postprocessing image reconstruction procedure used for FMC data.

Bergman et al. (2018) introduced a GE Un-bored Rotor Ultrasonic system (URIST<sup>TM</sup> technology) to inspect steam turbine rotors. It shows the broad application of the PAUT technique. Both UT and PAUT require a smooth surface to carry out an inspection. Mirchev et al. (2021) introduced a scan PAUT on the rough surface by immersion technique using a water bath to serve as a couplant.

Holloway and Ginzel (2020) sought a new PAUT technique (Phased array composite angle technique) to detect corrosion under pipe support. The theory has been proven, and the researcher works on hardware and software development. Reverdy et al. (2016) introduced the most advanced PAUT technique, the TFM/FMC application and its advantages. It has an excellent ability to detect fine cracks, and the thickness measurement accuracy is about 0.5 mm.

## Literature Review Summary

Figure 2 summarises the types of damage mechanisms studied by other researchers. General corrosion comprises 20% of the overall damage mechanism and is considered the second largest group of damage mechanisms. Localised corrosion includes pitting at 26%, crevice corrosion at 6%, intergranular cession at 2%, and CO<sub>2</sub> corrosion and naphthenic corrosion at 1%.

The pie chart shows 77% corrosion types of damage mechanisms, with galvanic corrosion at 8%, MIC at 7%, sulfidic corrosion at 3%, and erosion-corrosion at 4%. Cracks related to corrosion consist of SCC 10% and other SCC 7%. Hence, 94% of the reviewed literature revolves around corrosion type or corrosion-related damage mechanisms to answer research question one.

Similar to other research, Liu et al. (2018) studied plant failure cases between 1990 and 2017 and found that about 46% of the total failures were caused by corrosion. The most affected material by corrosion is stainless steel, which consists of 41%, followed by carbon steel, 14%, and alloy steel, 14%.

The stainless-steel summaries in this literature review consist of 26% compared with the majority of 51% of carbon steel. Other materials, such as ferritic alloy steel, low alloy steel, martensitic steel, duplex stainless steel, and copper alloys, are shown in Figure 3 for a better understanding of research question two.

PAUT is already at a mature stage and is widely recognised by the public. Currently, it is not only the initial weld inspection. It is also widely used for corrosion mapping and different base materials such as alloy and composite materials.

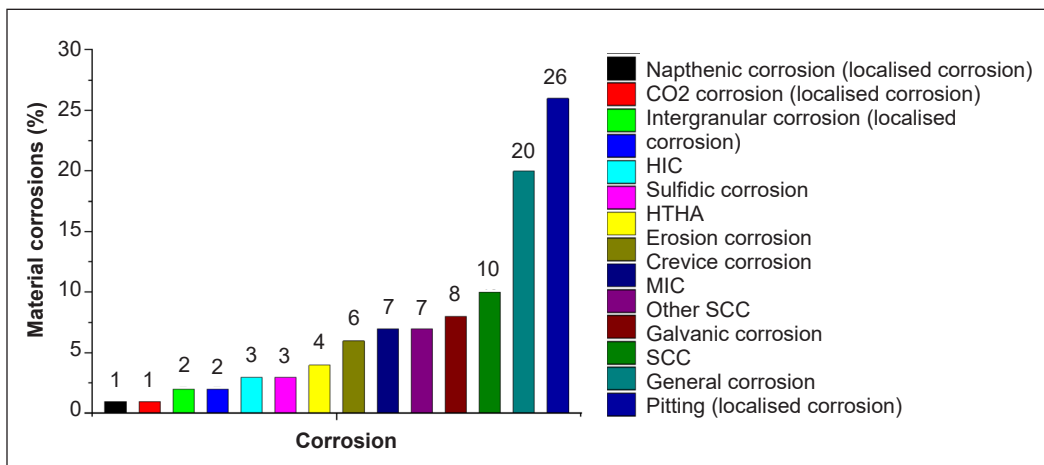


Figure 2. Type of damage mechanism studies by other researchers

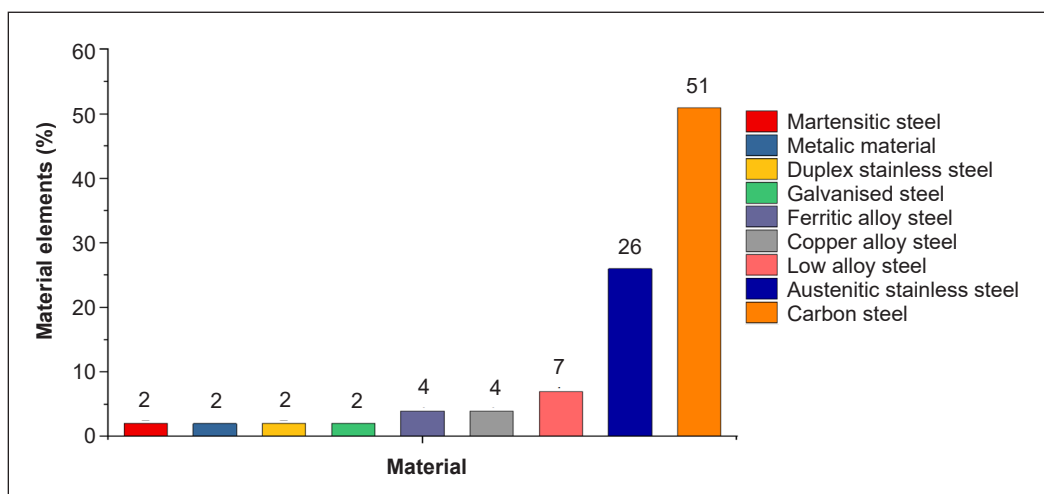


Figure 3. Damage affected material grade summaries

This review suggests a prevalent trend among researchers to substitute UTG with phased array corrosion mapping. However, it is noteworthy that most of these studies concentrate on a singular material, carbon steel, and are limited to ambient-temperature applications. It highlights a potential avenue for further exploration, as corrosion impacts various materials, and real-world plant operations often involve non-ambient temperature applications.

The typical methodology used by other researchers is to experiment on the fabricated specimen with SDH or FBH to determine the detectability. In addition, some papers introduced the new PAUT TFM/FMC application that could produce better image presentations for future studies.

## CONCLUSION

In petrochemical process plant maintenance, the piping system is a larger compartment that some plant owners usually overlook among all the damage mechanisms at the process plant, either in general corrosion or localised corrosion. The corrosion-related damage, such as stress corrosion cracking, is over 80%. The affected material includes carbon steel, 300 & 310 series SS, and super duplex material.

Some UTGs that can inspect the hot material surface up to 500°C have been reported (Jory, 2019). The advantage of the UTG is that it requires less training and is easy to operate, and the equipment's cost is lower than that of other testing techniques. However, drawing and taking readings grid by grid requires more time if targeted to detect localised corrosion, which is the main disadvantage. The reading may also vary because of the probe pressure applied by the different technicians during the inspection.

On the other hand, PAUT has recently gained wide application in different industries and various materials. PAUT corrosion mapping, with the advantage of faster speed, detects general and localised corrosion reported by other researchers. The majority of the PAUT corrosion mapping is conducted at ambient temperature. Only Turcu et al. (2018) reported that the experiment on corrosion mapping carried out by Dual Linear Probe achieved up to 150°C.

The challenge in the following research on applying phased array corrosion mapping in elevated temperatures may need to be studied further by highlighting the ultrasound principle and the support from the current equipment and accessories. However, this literature review has provided a better understanding of the current damage mechanism and shows that an extended study in this area is possible.

## ACKNOWLEDGEMENT

The authors thank Universiti Putra Malaysia for the financial support through Geran Inisiatif Putra Siswazah (GP-IPS) with grant number 9739200. The authors also express

their gratitude to the Department of Aerospace Engineering, Faculty of Engineering, Universiti Putra Malaysia, and the Laboratory of Biocomposite Technology, Institute of Tropical Forestry and Forest Product (INTROP), Universiti Putra Malaysia (HICoE) for their close collaboration in this study.

## REFERENCES

- Aliprandi, P., Guglielmino, E., & Sili, A. (2020). Mechanical characterisation of the ASTM A335 P5 steel and reliability of radiant tubes after long operating time in a petrochemical industry furnace. *Metallurgia Italiana*, 112(10), 45-53.
- Almazrouee, A. I., Al-Fadhlah, K. J., Alhajeri, S. N., & Alfheid, S. (2018). High temperature corrosion of martensitic steel of reheater pipes in a desalination power plant. *Engineering Failure Analysis*, 85, 89-96. <https://doi.org/10.1016/j.engfailanal.2017.12.003>
- Ameh, E. S., Ikpeseni, S. C., & Lawal, L. S. (2018). A review of field corrosion control and monitoring techniques of the upstream oil and gas pipelines. *Nigerian Journal of Technological Development*, 14(2), 67-73. <https://doi.org/10.4314/njtd.v14i2.5>
- API. (2011). *API recommended practice 571: Damage mechanisms affecting fixed equipment in the refining industry*. American Petroleum Institute. [https://www.apiwebstore.org/standards/571?\\_\\_hstc=23321061.45041909c1713c2f47776c88c555a58e.1717118461018.1717118461018.1717118461018.1&\\_\\_hssc=23321061.1.1717118461019&\\_\\_hsfp=1989271524](https://www.apiwebstore.org/standards/571?__hstc=23321061.45041909c1713c2f47776c88c555a58e.1717118461018.1717118461018.1717118461018.1&__hssc=23321061.1.1717118461019&__hsfp=1989271524)
- Baby, N. V., Paricha, B., & Naik, S. J. (2016). Determination of corrosion rates and remaining life of piping using API and ASME standards in oil and gas industries. *International Research Journal of Engineering and Technology*, 3(6), 772-777.
- Ber, L. L., Benoist, G., & Dainelli, P. (2016). Corrosion detection and measurement improvement using advanced ultrasonic tools. *19th World Conference on Non-Destructive Testing*, 554, 1-8.
- Bergman, R., Mauro, A. S., & Brian, M. (2018). Advanced volumetric phased array inspection for un-bored steam turbine rotors. In *27th ASNT Research Symposium* (pp. 27-30). The American Society for Nondestructive Testing. <https://doi.org/10.32548/rs.2018.002>
- Caulder, A. (2018). Full matrix capture and total focusing method: The next evolution in ultrasonic testing. *Materials Evaluation*, 76(5), 591-597.
- Cheong, Y. M., Kim, K. M., & Kim, D. J. (2017). High-temperature ultrasonic thickness monitoring for pipe thinning in a flow-accelerated corrosion proof test facility. *Nuclear Engineering and Technology*, 49(7), 1463-1471. <https://doi.org/10.1016/j.net.2017.05.002>
- Cheshideh, H., Nasirpouri, F., Mardangahi, B., & Jabbarpour, A. (2021). Failure analysis and preventive recommendations against corrosion of steel tubes of gas risers in natural gas urban distribution lines. *Engineering Failure Analysis*, 122, Article 105240. <https://doi.org/10.1016/j.engfailanal.2021.105240>
- Chidambaram, S., Ashok, K., Karthik, V., & Venkatakrishnan, P. G. (2018). Microbiological corrosion of ASTM SA105 carbon steel pipe for industrial fire water usage. *IOP Conference Series: Materials Science and Engineering*, 314, Article 012027. <https://doi.org/10.1088/1757-899X/314/1/012027>

- Colombo, A., Oldani, L., & Trasatti, S. P. (2018). Corrosion failure analysis of galvanised steel pipes in a closed water cooling system. *Engineering Failure Analysis*, 84, 46-58. <https://doi.org/10.1016/j.engfailanal.2017.10.008>
- Cui, C., Ma, R., & Martínez-Pañeda, E. (2021). A phase field formulation for dissolution-driven stress corrosion cracking. *Journal of the Mechanics and Physics of Solids*, 147, Article 104254. <https://doi.org/10.1016/j.jmps.2020.104254>
- De Almeida, P. D., & Pereira, G. R. (2019). Phased array inspection of glass fiber reinforced polymers pipeline joints. *Journal of Materials Research and Technology*, 8(5), 4736-4740. <https://doi.org/10.1016/j.jmrt.2019.08.020>
- Du, L., Wang, Q., Li, X., & Yan, H. (2020). Cause analysis and suggestion on corrosion leakage of pipe in atmospheric and vacuum pressure unit. *IOP Conference Series: Materials Science and Engineering*, 711, Article 012015. <https://doi.org/10.1088/1757-899X/711/1/012015>
- Fajobi, M. A., Loto, R. T., & Oluwole, O. O. (2019). "Crude distillation overhead system": Corrosion and control. *Journal of Physics: Conference Series*, 1378, Article 042090. <https://doi.org/10.1088/1742-6596/1378/4/042090>
- Fetzer, B. (2021). *Phased array beam steering techniques used for composite inspection*. The American Society for Nondestructive Testing.
- Fousianis, P., Anastasopoulos, A., Bouchagier, L., Kastanis, P., Papasalouros, D., Ladis, I., & Kourousis, D. (2018, October 22-23). *Ultrasonic detection of hydrogen induced cracking (HIC) in oil and gas industry* [Conference session]. 1st International Conference on Welding & NDT, of HSNT and WGI, Athens, Greece.
- Galán-Pinilla, C. A., Quintero-Ortiz, L. A., & Herrera-Ortiz, J. O. (2021). Dimensional characterisation with phased array ultrasonic testing of induced discontinuities in ASTM A36 steel by EDM and SMAW welding processes. *UIS Engineering Magazine*, 20(3), 147-154. <https://doi.org/10.18273/revuin.v20n3-2021010>
- Groysman, A. (2017). Corrosion problems and solutions in oil, gas, refining and petrochemical industry. *Corrosion and Material Protection Journal*, 61(3), 100-117. <https://doi.org/10.1515/kom-2017-0013>
- Gunasekar, S., & Sastikumar, D. (2020). Comparison of side drilled holes and surface notch response for phased array sectorial beams calibration process. *Journal of Non Destructive Testing and Evaluation (JNDE)*, 19(2), 22-27.
- Holloway, P., & Ginzl, R. (2020). Ultrasonic phased array approach to detection and measurement of corrosion at pipe supports. *e-Journal of Nondestructive Testing*, 25(3), 1-10.
- Mazumder, M. A. J. (2020). Global impact of corrosion: occurrence, cost and mitigation. *Global Journal of Engineering Sciences*, 5(4), 1-5. <https://doi.org/10.33552/gjes.2020.05.000618>
- Jamil, J., & Yahya, S. Y. S. (2019). Corrosion assessment using advanced ultrasonic measurement technique. *IOP Conference Series: Materials Science and Engineering*, 554, Article 012004. <https://doi.org/10.1088/1757-899X/554/1/012004>
- Jordan, P., & Maharaj, C. (2020). Asset management strategy for HAZ cracking caused by sigma-phase and creep embrittlement in 304H stainless steel piping. *Engineering Failure Analysis*, 110, Article 104452. <https://doi.org/10.1016/j.engfailanal.2020.104452>

- Jory, C. (2019). Tips for internal corrosion using the echo to echo technique with compression. *The NDT Technician*, 18(3), 8-11.
- Kansara, D. P., Sorathiya, A. P., & Patel, H. R. (2018). Corrosion monitoring and detection techniques in petrochemical refineries. *IOSR Journal of Electrical and Electronics Engineering (IOSR-JEEE)*, 13(2), 85-93.
- Khan, R., Ya, H. H., Pao, W., & Khan, A. (2019). Erosion–corrosion of 30°, 60°, and 90° carbon steel elbows in a multiphase flow containing sand particles. *Materials*, 12(23), Article 3898. <https://doi.org/10.3390/ma12233898>
- Khouzani, M. K., Bahrami, A., Hosseini-Abari, A., Khandouzi, M., & Taheri, P. (2019). Microbiologically influenced corrosion of a pipeline in a petrochemical plant. *Metals*, 9(4), Article 459. <https://doi.org/10.3390/met9040459>
- Kim, Y. L., Cho, S., & Park, I. K. (2021). Analysis of flaw detection sensitivity of phased array ultrasonics in austenitic steel welds according to inspection conditions. *Sensors*, 21(1), Article 242. <https://doi.org/10.3390/s21010242>
- Liu, S. W., Lv, J. H., & Wang, W. Z. (2018). Failure cases analysis in petrochemical industry. *International Journal of Civil and Environmental Engineering*, 11(5), 1-5. <https://doi.org/10.5281/zenodo.1316600>
- Liu, X. Y., Su, J. L., Zhang, L., & Su, X. Y. (2021). Power plant small-diameter tube phased array inspection verification and inspection technology. *Journal of Physics: Conference Series*, 2005, Article 012198. <https://doi.org/10.1088/1742-6596/2005/1/012198>
- Lozev, M., Neau, G. A., Yu, L., Eason, T. J., Orwig, S. E., Collins, R. C., Mammen, P. K., Reverdy, F., Lonne, S., Wassink, C., Cence, H., & Chew, J. (2020). Assessment of high temperature hydrogen attack using advanced ultrasonic array techniques. *Materials Evaluation*, 78(11), 1223-1238. <http://dx.doi.org/10.32548/2020.me-04183>
- Martins, C. M. B., Moreira, J. L., & Martins, J. I. (2014). Corrosion in water supply pipe stainless steel 304 and a supply line of helium in stainless steel 316. *Engineering Failure Analysis*, 39, 65-71. <https://doi.org/10.1016/j.engfailanal.2014.01.017>
- Mirchev, Y., Mihovski, M., & Chukachev, P. (2021). Ultrasonic testing of rough surfaces using phased array probe. *Engineering Sciences*, LVIII (1), 64-79. <https://doi.org/10.7546/engsci.lviii.21.01.05>
- Mohan, B. C., & Jeyasekhar, M. C. (2019). Oil and gas assets condition monitoring by high sensitive paut hydroform corrosion monitoring technique for integrity assessment.
- Njelle, V., Ikeh, O., Cornelius, O., & Obiukwu-ifeanyi, N. (2019). Study of corrosion rate of low and medium carbon steel pressure vessel in Nigeria oil and gas industry using ultrasonic testing (UT). *Engineering Sciences*, 15(3), 151-158.
- Piri, B., Amini, R., Asadinia, E., Vardak, S., Mehdilouee, R., & Mojarrad, A. (2021). Investigation of failure mechanisms and remaining life prediction of firewater pipelines used in industrial applications. *Engineering Failure Analysis*, 124, Article 105301. <https://doi.org/10.1016/j.engfailanal.2021.105301>
- Reverdy, F., Benoist, G., & Ber, L. L. (2016). Advantages and complementarity of phased-array technology and total focusing method. *19th World Conference on Non-Destructive Testing 2016*, 1-8.

- Schempp, P., Preuß, K., & Tröger, M. (2016). About the correlation between crude oil corrosiveness and results from corrosion monitoring in an oil refinery. *Corrosion*, 72(6), 843-855. <https://doi.org/10.5006/1940>
- Shafeek, H., Soltan, H. A., & Abdel-Aziz, M. H. (2021). Corrosion monitoring in pipelines with a computerised system. *Alexandria Engineering Journal*, 60(6), 5771-5778. <https://doi.org/10.1016/j.aej.2021.04.006>
- Shekari, E., Khan, F., & Ahmed, S. (2016). A predictive approach to fitness-for-service assessment of pitting corrosion. *International Journal of Pressure Vessels and Piping*, 137, 13-21. <https://doi.org/10.1016/j.ijpvp.2015.04.014>
- Shekari, E., Khan, F., & Ahmed, S. (2017). Economic risk analysis of pitting corrosion in process facilities. *International Journal of Pressure Vessels and Piping*, 157, 51-62. <https://doi.org/10.1016/j.ijpvp.2017.08.005>
- Singh, D., Banerjee, A., & Das, S. (2017, December 14-16). *A comparative study of PAUT and TOFD responses with the changes in microstructure of various materials - A step towards reliable detection* [Conference session]. NDE 2017 Conference & Exhibition of the Indian Society for NDT (ISNT), West Bengal, India.
- Siswanto, N., Priyanta, D., & Ramadhan, J. (2021). Implementation of risk-based inspection (RBI) in condensate separator and storage vessel: A case study. *International Journal of Marine Engineering Innovation and Research*, 6(1), 1-10. <https://doi.org/10.12962/j25481479.v6i1.7565>
- Spisák, B., & Szávai, S. (2019, May 23-24). *Mechanisms of stress corrosion cracking* [Conference session]. MultiScience-XXXIII MicroCAD International Multidisciplinary Scientific Conference, University in Miskolc, Hungary.
- Subramanian, C. (2018). Localised pitting corrosion of API 5L grade A pipe used in industrial fire water piping applications. *Engineering Failure Analysis*, 92, 405-417. <https://doi.org/10.1016/j.engfailanal.2018.06.008>
- Tangadi, S., Telidevara, N. K. S. P., & Maddi, H. K. (2015). PAUT as tool for corrosion damage monitoring. *Special Issue of e-Journal of Nondestructive Testing*, 22(6), 1-7.
- Thorpe, N., Acebes, M., Wylie, D., Troughton, M., Gilmour, O., Roy, O., Benoist, G., & Dweik, R. (2018). Ultrasonic phased array non-destructive testing and in-service inspection system for high integrity polyethylene pipe welds with automated analysis software. *Special Issue of e-Journal of Nondestructive Testing (eJNDT)*, 23(8), 1-9.
- Trimborn, N. (2016). Detecting and quantifying high temperature hydrogen attack (HTHA). *Special Issue of e-Journal of Nondestructive Testing (eJNDT)*, 21(7), 1-4.
- Turcotte, J., Rioux, P., & Lavoie, J. (2016). Comparison corrosion mapping solutions using phased array, conventional UT and 3D scanners. *Special Issue of e-Journal of Nondestructive Testing (eJNDT)*, 21(7) 1-10.
- Turcu, F., Jedamski, T., & Treppmann, DR. D. (2018). In-service corrosion mapping—Challenges for the chemical industry. *Special Issue of e-Journal of Nondestructive Testing (eJNDT)*, 23(8), 1-8.
- Uchida, S., Chimi, Y., Kasahara, S., Hanawa, S., Okada, H., Naitoh, M., Kojima, M., Kikura, H., & Lister, D. H. (2019). Improvement of plant reliability based on combining of prediction and inspection of crack growth due to intergranular stress corrosion cracking. *Nuclear Engineering and Design*, 341, 112-123. <https://doi.org/10.1016/j.nucengdes.2018.10.021>

- Vanaci, H. R., Eslami, A., & Egbewande, A. (2017). A review on pipeline corrosion, in-line inspection (ILI), and corrosion growth rate models. *International Journal of Pressure Vessels and Piping*, *149*, 43-54. <https://doi.org/10.1016/j.ijvp.2016.11.007>
- Wan, Z., & Yang, J. (2021). Research on corrosion management technology of petroleum pipeline and pressure vessel. *IOP Conference Series: Earth and Environmental Science*, *692*(4), Article 042057. <https://doi.org/10.1088/1755-1315/692/4/042057>
- Wang, F., Shan, Q., Zhang, F., Lu, F., Li, J., Yu, T., & Qu, C. (2021). Pitting corrosion behavior of metal materials and research methods. *IOP Conference Series: Earth and Environmental Science*, *651*(3), Article 032039. <https://doi.org/10.1088/1755-1315/651/3/032039>
- Zhang, Z. G., Feng, H. X., & Zhao, W. H. (2016). The NDT methods under high temperature service environment. *MATEC Web of Conferences*, *40*, Article 04001. <https://doi.org/10.1051/mateconf/20164004001>
- Zheng, J., Zhang, Y., Hou, D., Qin, Y., Guo, W., Zhang, C., & Shi, J. (2018). A review of non-destructive examination technology for polyethylene pipe in nuclear power plant. *Frontiers of Mechanical Engineering*, *13*, 535-545. <https://doi.org/10.1007/s11465-018-0515-9>



## Effects of Unavailability of Conventional Energy Units on Power Generation System Adequacy

Athraa Ali Kadhem<sup>1,2\*</sup> and Noor Izzri Abdul Wahab<sup>1</sup>

<sup>1</sup>Faculty of Engineering, University Putra Malaysia, 43400 UPM, Serdang, Selangor, Malaysia

<sup>2</sup>General Directorate of Educational Planning, Ministry of Education, Baghdad, Iraq

### ABSTRACT

Presently, aside from conventional power, wind energy is considered an important power source in electrical power supply systems. The prime factor affecting electrical power supply systems is the blackout of electrical power for load demand-supply. Therefore, the safe operation of interconnected large power systems integrated with wind energy cannot be carried out without understanding the system's behavior during abnormal and emergencies. In power generation systems, failure of the conventional generating units (CGUs) and wind turbine generating units (WTGUs) will lead to service interruption and subsequent disconnection of load points. This paper analyzes the impact of frequent failures of the CGUs and WTGUs on the output power systems. A Sequential Monte Carlo Simulation (SMCS) method and the Frequency and Duration (F&D) method are extremely effective for estimating the variation of risk indices when additional wind turbine generators are incorporated into the generation system. The results demonstrate the variation of reliability indices in the adequacy systems when additional WTGUs are incorporated into the generation system.

*Keywords:* Conventional generating unit, component failure, power system adequacy, sequential Monte Carlo simulation, wind turbine unit

### ARTICLE INFO

*Article history:*

Received: 21 August 2023

Accepted: 02 January 2024

Published: 25 July 2024

DOI: <https://doi.org/10.47836/pjst.32.4.13>

*E-mail addresses:*

[athraaonoz2007@yahoo.com](mailto:athraaonoz2007@yahoo.com) (Athraa Ali Kadhem)

[izzri@upm.edu.my](mailto:izzri@upm.edu.my) (Izzri Abdul Wahab)

\* Corresponding author

### INTRODUCTION

The numerous adequacy problems in future power systems have been addressed (Alham et al., 2023). Generation system reliability is an important aspect and a big challenge in the planning for future system capacity expansion to ensure that the total installed capacity is sufficient to provide adequate

electricity when needed (Khoo et al., 2020a; Khoo et al., 2020b; Almutairi et al., 2015). Wind power is clean, renewable, and sustainable (Kadhem et al., 2017a). The growth rate and global installed wind power capacity (WPC) worldwide from 2015 to 2021 are shown in Table 1 and Figure 1, respectively. Where a growth rate is about (43%), and 705 MW of capacity had been installed worldwide by the end of 2022. Accordingly, when the percentage of wind penetration arrives at (>30%), the maximum penetration level for wind power in the system grid is indicated (Baloch et al., 2017). Therefore, the consumption of wind power farms is between 17 and 39 times as much as the consumption of conventional power.

Table 1  
Growth rate (%) of wind power installation from 2015–2021

Countries	China	US	Germany	India	Spain	United Kingdom	Brazil	France	Canada	Italy
Growth Rate (%)	43	53	69	62	79	54	37	56	79	50
Total Growth Rate	43 %		Total Installed Wind Capacity					705 MW		

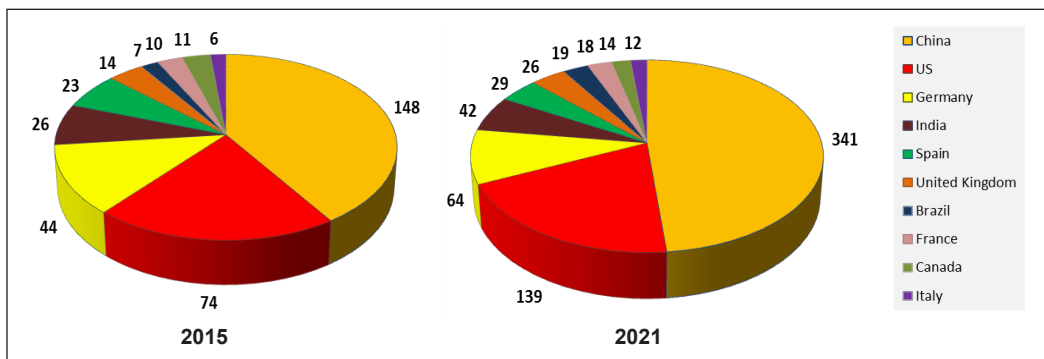


Figure 1. Total wind power cumulative installed capacity by country (website “Top 10 countries with largest wind energy capacity”) in 2015 and 2021

The electrical grid is a vital component of modern society that requires significant and cost-effective investments to ensure its reliability (Lai et al., 2023). Various methods can be used to evaluate the reliability of power systems. One approach involves using energy consumption as a “benchmark,” while others focus on determining the performance of individual system components and identifying instances of success or failure (Ibrahim, 2017). The effectiveness of these methods on various systems depends on the system’s intricacy and the desired precision level. Consequently, the failure of any component in a power system will cause the entire system to fail (Kadhem et al., 2017b; Abdalla et al., 2020). The reliability assessment approaches for adequacy systems are generally divided into the analytical technique, the Monte Carlo simulation technique, and the intelligent

search technique (Kadhem et al., 2017d). Reliability indices are considered for system adequacy assessment (Roy et al., 2017; Arabali et al., 2014). This study employs the simulation method, whereby the state of all the CGUs is considered.

The increasing flexibility of active distribution systems coupled with the high penetration of renewable distributed generators leads to an increase in the complexity of power systems (Su & Teh, 2023). Many works of literature have focused on studying the availability of renewable generation units in electric power systems integrated with wind energy (Ma et al., 2023; Ziegler et al., 2023). Meanwhile, the problem of measuring the unavailability of CGU in electric power systems integrated with wind energy has not been sufficiently addressed in the literature by using the SMCS method. Accordingly, this paper aims to find out the weaknesses of the CGU of the power supply system integrated with wind energy and also to figure out the amount of loss of capacity caused by the failure of CGU. Therefore, measuring system unit availability is vital and is considered the basic aspect of most reliability-related studies (Li et al., 2019; Peeters et al., 2018). This paper evaluates the efficiency of generating systems that use wind energy. Two models are used: one for the CGUs and one for the WTGUs. Additionally, a load model is used to serve as a reliability indicator. This paper examines the reliability of these systems when undesirable failures occur during their lifespan. To conduct this study, the researchers adopted the SMCS technique, a powerful tool for assessing the safety and reliability of power systems. The findings of this study can help to identify areas for improvement.

When integrating WTGUs with conventional generating plants, certain considerations need to be considered for adequacy assessment (Kadhem et al., 2016). In this report, we utilize the Weibull Distribution Probability (WDP) model to generate and duplicate wind speed data for each hour of the year in the SMCS simulation process. The attainable power generated from the CGUs and WTGUs during power systems operation is computed, and the reliability index of the suggested technique indicates the efficiency of estimating the power output. The SMCS method is extremely effective for estimating the variation of risk indices when additional wind turbine generators are incorporated into the generation system. The proposed algorithm has been tested on Standard MRTS, IEEE-79, and IEEE-96 test systems.

## **RELIABILITY ASSESSMENT OF ADEQUACY SYSTEM WITH WTGUS**

It is crucial to consider certain important factors to ensure the successful integration of wind energy systems into the adequacy assessment of conventional generating plants. Figure 2 presents a concise overview of these factors, which primarily includes the development of a model for conventional generation and creating an appropriate wind velocity model. Both steps are essential for achieving optimal results. The output energy from WTGUs and conventional generators differ significantly in their characteristics. Conventional generators

supply power at their rated values unless they experience partial or complete failure. However, WTGUs generate power output that varies due to the wind speed fluctuation and the power curve’s design characteristics.

Reliability indices are utilized as design constraints for generating system adequacy assessment to ensure reliable system operation. These concepts are discussed in Wang and Singh (2007) and Wang et al. (2007). Two important indices are employed to compute the reliability of the power system adequacy, represented by Equations 1 and 2. The functions of these indices can be summarized as follows:

LOLE (hr/yr or days/yr): To determine the required time to be considered when the system’s power capacity does not satisfy the load demand.

LOEE (MWh/year): To determine the required power capacity to be considered when the system’s power capacity is less and does not satisfy the load demand.

$$LOLE = \frac{i}{n} \sum_{i=1}^{8736 \times n} LOLE_i \quad [1]$$

$$LOEE = \frac{i}{n} \sum_{i=1}^{8736 \times n} LOEE_i \quad [2]$$

A level of LOLE is usually used as the reliability criteria of the generation systems. The standard level of LOLE is one-day-in ten years or less (Phoon, 2006). It does not mean a full day of shortages once every ten years; rather, it refers to the total accumulated time of shortages that should not exceed one day in ten years. Now, LOLE represents the reliability standard utilized in various countries. The reliability standard adopted in various countries is presented in Table 2 (Shi, 2014). The LOLE is also smaller than the popularly used criterion ( $LOLE \leq 2.4$  hours/year) (Gao, 2013).

Table 2  
Reliability standard LOLE in 10 countries

Countries	LOLE value (days/year)	LOLE value (hours/year)
Australia		(5 ≈ 7)
Belgium		(16)
Brazil	(2.5)	
Canada	(0.1)	
France		(3)
Japan	(0.3)	
Republic of Ireland		(8)
Spain	(0.1)	
China	(1 ≈ 2)	
UK		(3)

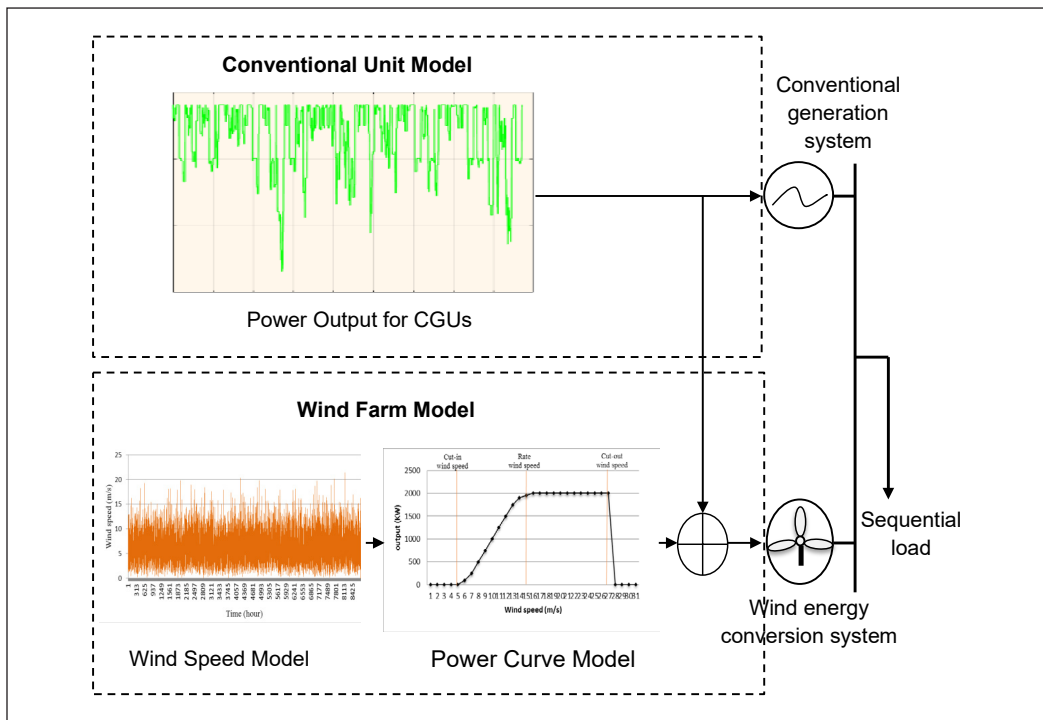


Figure 2. Adequacy systems modeling

## METHODOLOGY

### Conventional Unit Model

The available capacity of all system-generating units is added together to determine the adequacy of the system's power capacity. Each generating unit in power systems has two states (2-states), "where the generating units are regarded as either being entirely out of service (down, or MW =0) or totally in service (up, or MW = total power output of unit)" (Billinton & Li, 1994). Figure 3 shows the operation cycle for each generating unit in the MRTS test system and the relationship between the reliability parameters. In this study, the Capacity Outage Probability Table (COPT) has been adopted as the methodology of system adequacy assessment, in addition to knowing the relationships between the FOR value of CGUs and the reliability parameters of units, which are  $\lambda$ ,  $\mu$ , MTTF, MTTR, and MTBF.

In this manner, the status of all system components is sampled between 0 and 1 in each simulation interval (Wang et al., 2007). Each simulation interval of sampled system states is randomly selected and independent from the preceding and succeeding samples (Hou et al., 2016). The operation cycle per hour per year of the CGUs for the MRTS system is demonstrated in Figure 3. In the case of a two-state model, the value of a random number is compared with the FOR of the system units, where the generation unit is presented as either a fully rated state ( $U_p = 1$ ) or a failed state ( $Down = 0$ ).

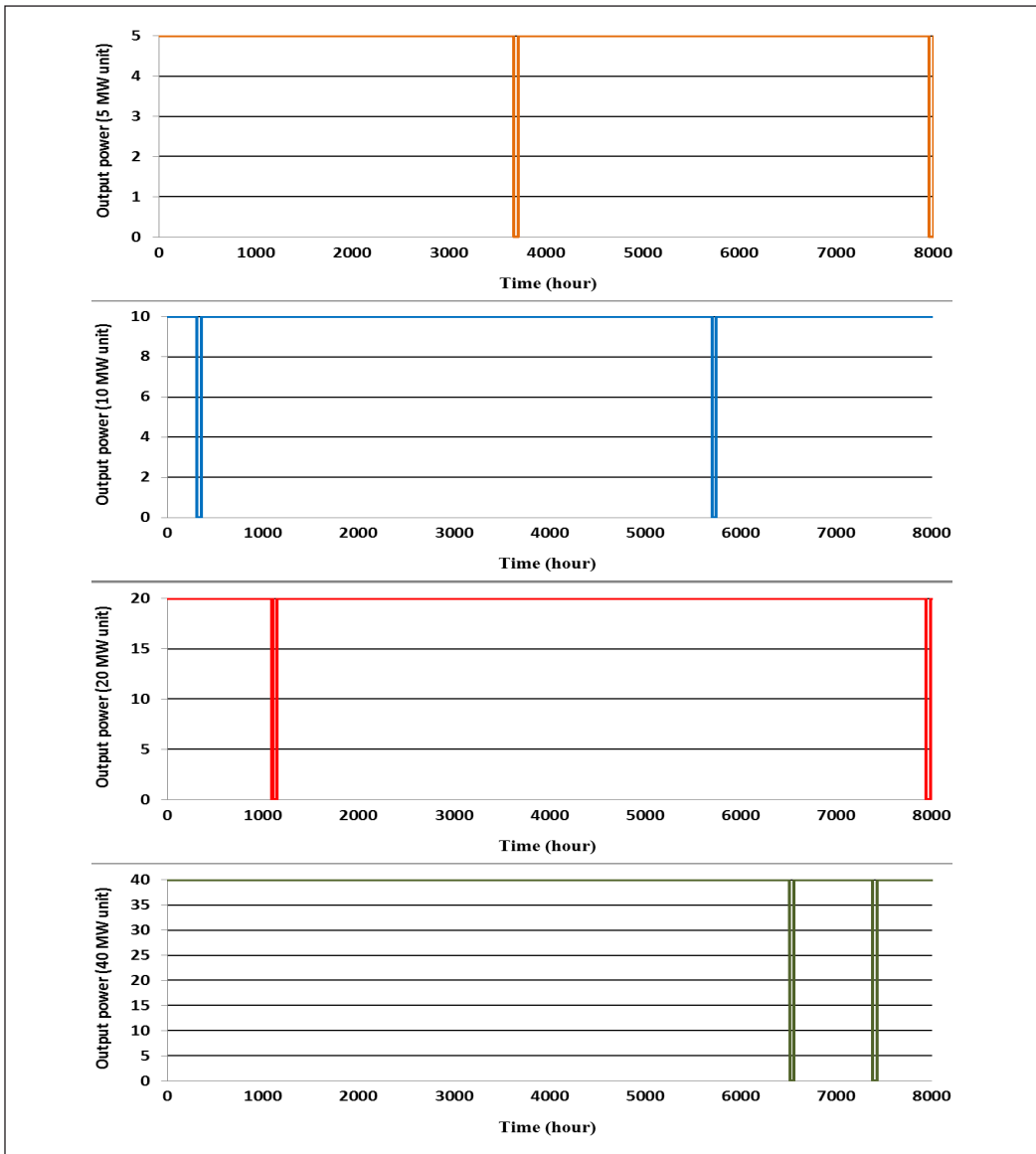


Figure 3. The operation cycle per hour year of some generating units for the MRTS test system

## Wind Farm Model

### Wind Speed Model

Obtaining accurate wind speed data for wind resource estimation can be difficult (Chauhan & Saini, 2015). Therefore, an effective model for estimating wind power is necessary for power system reliability evaluation (Saltani et al., 2014; Soleymani et al., 2015). However, wind speed data forecasting is still a problem that requires a distribution math model. This paper utilizes the Weibull Distribution model (WDM), which consists of two

parameters: scale parameter  $c$  and shape parameter  $k$ . These parameters effectively depict wind speed data and frequency distribution and predict wind energy output from a wind turbine (Kadhem et al., 2017c). Figure 4 displays the representation of the two Weibull distribution parameters with different values.

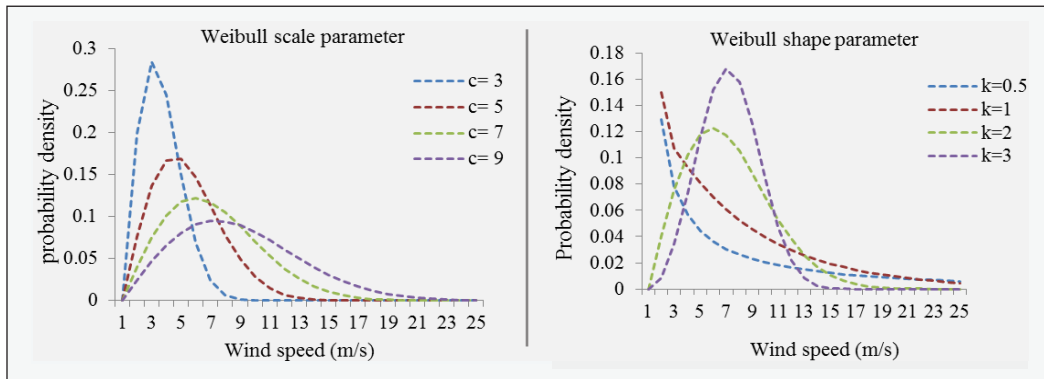


Figure 4. Different values of the  $k$  and  $c$  of the Weibull Distribution density

The shape parameter  $k$  controls the shape of the WDM. Therefore, the parameter  $k$  shows the width of the wind speed distribution ( $I$ ). Meanwhile, in the wind simulation,  $c$  is the “mean value” of the speed. By applying Equation 3, wind can be reproduced “artificially,” which can be used to generate a power output of the WTGUs by setting the value  $k=2$  and  $c=7$ .

$$V = C \left[ -\text{Ln}(U) \right]^{1/k} \tag{3}$$

In Equation 3, the WD parameters are set to  $c = 7$  and  $k = 2$  (Azad et al., 2014). The wind speed profile in Figure 5 shows hourly variations over ten years. Moderate winds are common, with rare occurrences of strong or weak winds. The available wind data measurements for one year and ten years show convergence. Wind speed data in the time series are commonly arranged in a frequency distribution format due to easier interpretation using statistical analysis. Table 3 reanalyzes the simulation for all-time series average wind speed using Weibull cumulative distribution functions, demonstrating that the average wind speed measurements are reliable. Based on the data presented in Figure 5, it is evident that wind speeds are predominantly distributed within the range of 6 to 15 m/s. As a result, the Weibull Model can effectively simulate the wind speed profile by appropriately adjusting its scale and shape parameters.

Table 3  
Shows a reanalysis of the simulation for average wind speed

Years	1	2	3	4	5	6	7	8	9	10
Wind (m/s)	7.21	7.22	7.22	7.17	7.22	7.25	7.22	7.23	7.15	7.21

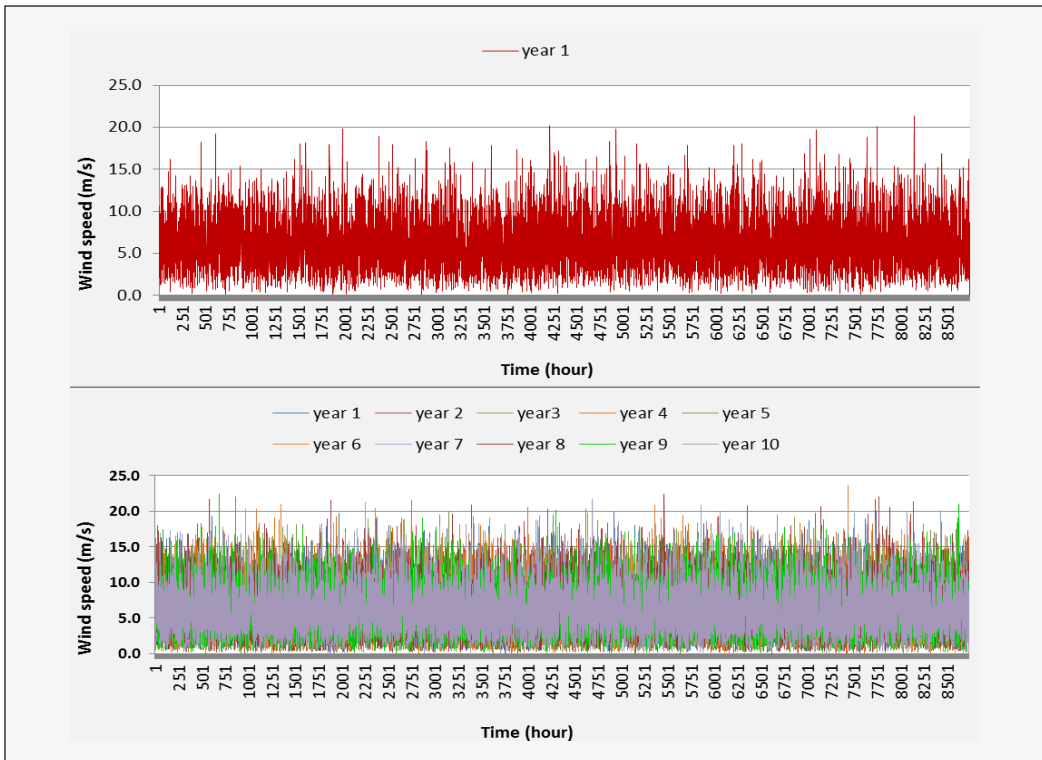


Figure 5. Picture of simulated wind speed an hour per year and an hour per for ten years

**Power Curve Model (Wind Turbine Model)**

Because the WTGUs can supply power with no fuel cost, wind energy is considered economically effective. In this study, the WDM represents the wind speed model expressing the WTGU realized output power based on wind speed variations for a specific site. Estimating wind energy can be challenging due to the random nature of wind velocity and variation in wind turbine power curves, which lead to uncertainties. During simulation, the power output from WTGUs can be determined based on the wind speed input using Equation 4.

$$P_{WTGUs} = \begin{cases} 0 & w < V_{ci} \\ (a + b + w + c * w) \times P_r & V_{ci} \leq w < V_r \\ P_r & V_r \leq w < V_{co} \\ 0 & w > V_{co} \end{cases} \quad [4]$$

This study explores the potential for generating wind energy at varying levels that correspond to fluctuations in wind speed. As a result, the wind power model can produce energy with different levels of capacity, ranging from instantaneous to hourly. Simulation of the profiles of the wind speed was employed to simulate the ability of WTGUs to generate wind output power. From Equation 4, the values *a*, *b*, and *c* are constants presented in Khare

et al. (2016) and Chauhan and Saini (2015). Based on this equation, the WTGU does not produce any value energy “when the wind speed  $w$  (m/s) is less than the cut-in rate  $V_{ci}$  (m/s) of the turbine speed and shuts down power production from WTGU when the wind speed exceeds the cut-out speed  $V_{co}$  (m/s) from the turbine speed .”The output power ( $Pr$ ) increases as the wind speed increases within the range where the rated speed of the wind  $V_r$  (m/s) remains fixed, and WTGU generates a rate of output power.

This study focuses on the characteristics of WTGU, specifically the ”cut-in-speed, cut-out-speed, and rate speed of 4, 25, and 19 m/s, respectively, with a rated power of 2 MW” (Kadhem et al., 2019b). Figures 6 and 7 show the hourly wind speed forecast and simulated wind power output of a WTGU with a 2 MW power rate for a year.

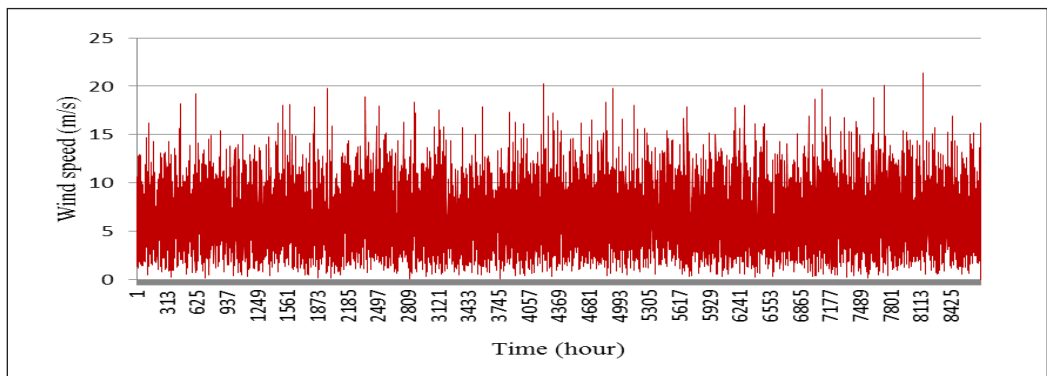


Figure 6. Shows the forecast for hourly wind speed over a year

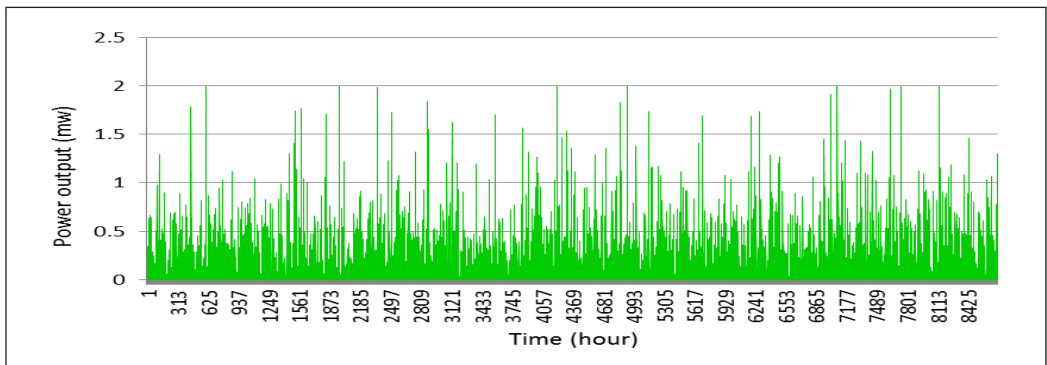


Figure 7. Indicates for the simulation wind power output for WTGU with a power rate of 2 MW for a similar period

### Steps of Evaluation Procedure

When assessing the adequacy of power generation involving wind energy, the first step is to create a capacity model based on the operational characteristics of the CGUs and WTGs. This process is illustrated in Figure 8. The capacity and load models are used to develop a

risk model. This paper presents a power systems reliability assessment that combines the SMCS method with the F&D method (Shi & Lo, 2012). The F&D technique offers insights into the frequency and length of the insufficient capacity situation. Here are the primary steps involved in carrying out the procedures for assessing the adequacy of generation systems:

Step 1: Input the reliability data for the CGUs ( $\lambda$ ,  $\mu$ , MTTF, MTTR) to create a system components capacity and total system capacity model.

Step 2: Input the sequential load duration curve level to create values of load demand hourly states—the annual SLDC models for MRTS and IEEE-RTS-79.

Step 3: Run the system to calculate probability values of the COPT of the system units, select failed states for the CGUs, and additionally know the system contingency state and determine the priority order of the unit’s more failed states.

Step 4: Calculate the reliability indices using Equations 1 and 2 for a number of sample years.

Step 5: Adjust the power system parameters again, the parameters of WTGUs and wind farm conditions.

Step 6: Obtain the power output for WTUGs using Equations 3 and 4. Repeat steps 1–5.

Step 7: Generate a capacity outage probability table for both conventional generating units and wind farm units using the SMCS and F&D methods.

Step 8: Calculate the results of the reliability indices.

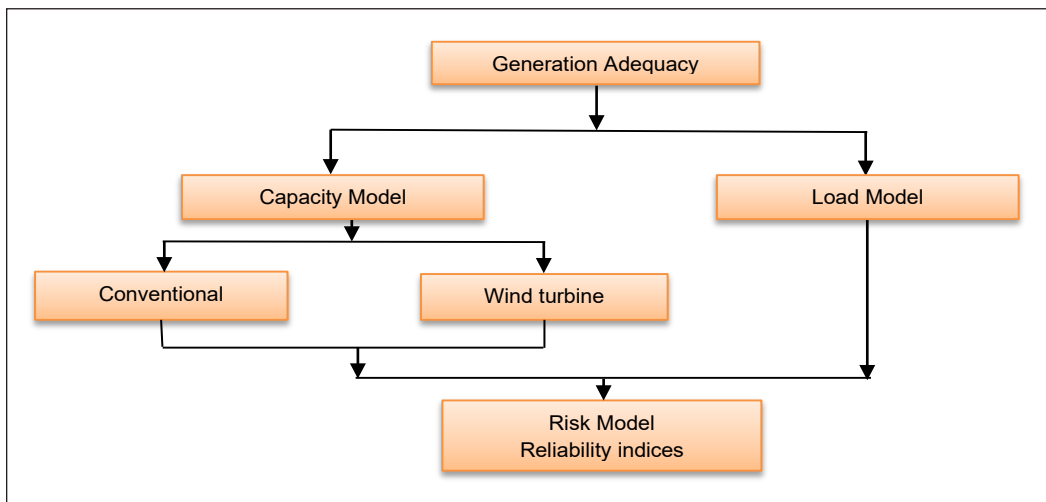


Figure 8. The risk model for assessing the adequacy of a generating system

### SEQUENTIAL LOAD MODEL

The system’s reliability is analyzed using the Time Series Load forecasting technique. Load designs can be either non-sequential or sequential paradigms with various algorithmic approaches. The Sequential Load Duration Curve (SLDC) method can produce hourly

load demand state values. Around “8736 hours” of separate states can be recorded yearly (Kadhem et al., 2019b). The annual SLDC models for MRTS & IEEE-RTS-79-96 are shown in Figure 9.

As shown in Table 4, the test systems of the reliability indexes consist of total power output, peak load, and generation units (Grigg & Wong, 1999).

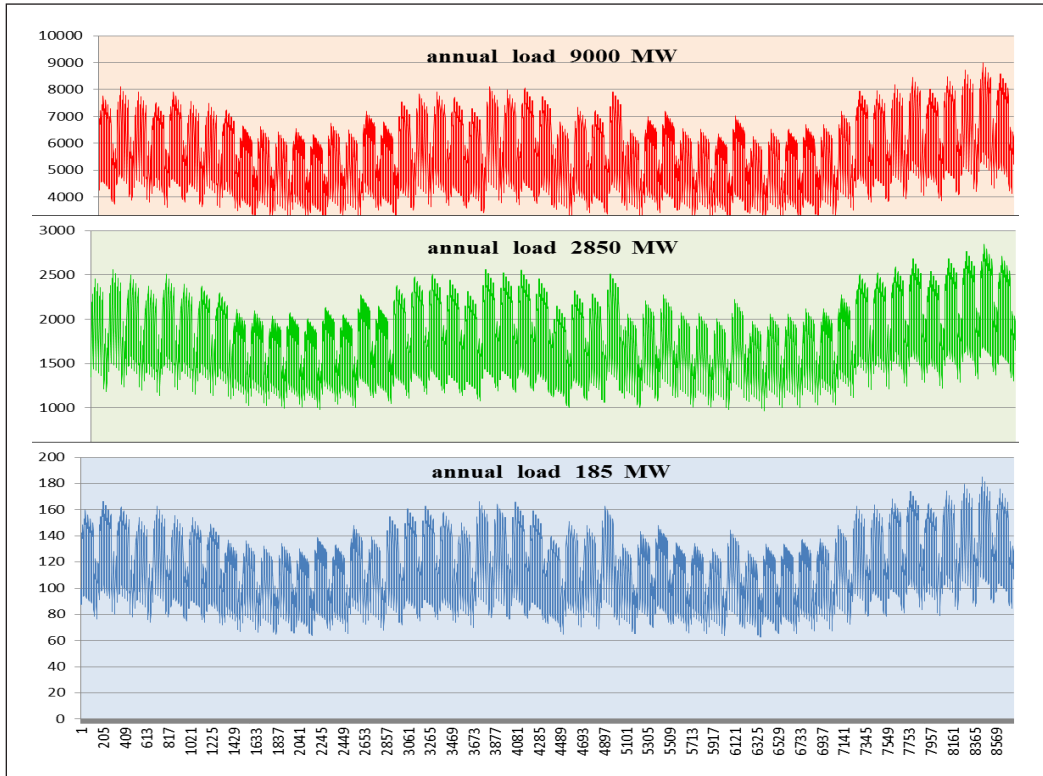


Figure 9. Annual SLDC model for MRTS and IEEE-79-96

Table 4

Total power output, peak load, and generation units for reliability test systems

Test System	Load (MW)	Capacity (MW)	No. units	MIM Cap. unit	MAX Cap. unit
MRTS	185	240	11	5	40
IEEE-79	2850	3405	32	12	400
IEEE-96	9000	10215	96	12	400

## RESULTS AND DISCUSSION

This paper presents a method developed and tested using two different test systems: MRTS and IEEE-RTS-79-96. These systems are used to validate the performance of the SMCS method in assessing the reliability of generating systems' adequacy.

### Case (1): System with only CGUs

As shown in Table 4, the test systems of the reliability indexes applied in this paper consist of total power output, peak load, and generation units. The SMCS and F & D methods calculate generation systems' adequacy by iterative selection and measurement of system failure states. Because it relies on proportionate sampling, it is very efficient in locating failure states.

In this search, the threshold probability ( $t_p$ ) equals  $t_p = 1e-6$ ,  $t_p = 1e-15$  and  $t_p = 1e-20$  for MRTS and IEEE-79-96 test systems, respectively. As the system size increases, the threshold probability is predicted to decrease.

The system's capacity adequacy is determined by adding up the available capacities of all the units that generate power. Each generating unit in power systems is in one of two states, either out of service (MW = 0) or totally in service (MW = total power output of unit). Figures 10 and 11 explain the operation cycle for each CGU in the test systems and the relationship between the reliability parameters. By combining reliability parameters ( $\lambda$ , MTTR) for a certain duration (usually one year), the operation cycle of every system unit can be estimated. Consequently, Figures 10 and 11 show a simulated scenario for the most frequent test system failure run for several years (800 years). In addition, these figures show the results recorded in Tables 6 and 7.

When simulating the system, running over a large number of years is more useful to identify additional cases of failure that happen or are repeated. Figures 10 and 11 depict the operation cycle per hour per year of the generating units for the MRTS and IEEE-79 test systems running with a number of samples between 100–800. From these figures, we can conclude that the units with a capacity of 40 MW and 400 MW for MRTS and IEEE-79-96 test systems, respectively, have more repeated failed states.

As seen in Table 5, in the case where the sample number is 800, we can see that available units in the system operation cycle are  $2 \times 5$ ,  $1 \times 10$ ,  $4 \times 20$ , and  $1 \times 40$  MW, with a total capacity of 140 MW and failure probabilities value of 0.0013. Meanwhile, the unavailable units in the system operation cycle are  $1 \times 20$  and  $2 \times 40$  MW. In Table 6, for the IEEE-79 test system in the case where the sample number is 800, we can see that available units in the system operation cycle are  $5 \times 12$ ,  $2 \times 20$ ,  $6 \times 50$ ,  $4 \times 76$ ,  $3 \times 100$ ,  $4 \times 155$ ,  $3 \times 197$ ,  $0 \times 350$ , and  $0 \times 400$  MW, with a total capacity of 2215 MW and failure probabilities value of 0.0017. Meanwhile, the unavailable units in the system operation cycle are  $2 \times 20$ ,  $1 \times 350$ , and  $2 \times 400$  MW. In Table 7, for the IEEE-96 test system, where the sample number is 800, we can see that available units in the system operation cycle are  $15 \times 12$ ,  $11 \times 20$ ,  $17 \times 50$ ,  $10 \times 76$ ,  $9 \times 100$ ,  $9 \times 155$ ,  $9 \times 197$ ,  $3 \times 350$ , and  $2 \times 400$  MW, with a total capacity of 7928 MW and failure probabilities value of 0.00608. Meanwhile, the unavailable units in the system operation cycle are  $1 \times 20$ ,  $1 \times 50$ ,  $2 \times 76$ ,  $3 \times 155$ , and  $4 \times 400$  MW.

Calculations of the COPT for the system units are set out in Tables 5, 6 and 7. The results show the contingency state and priority order of the units' more failed states. The reliability

assessment indices generated by the system are compared with other methods reported in the literature to validate the effectiveness of the proposed method. This comparison is shown in Table 8 (Kadhem et al., 2019a).

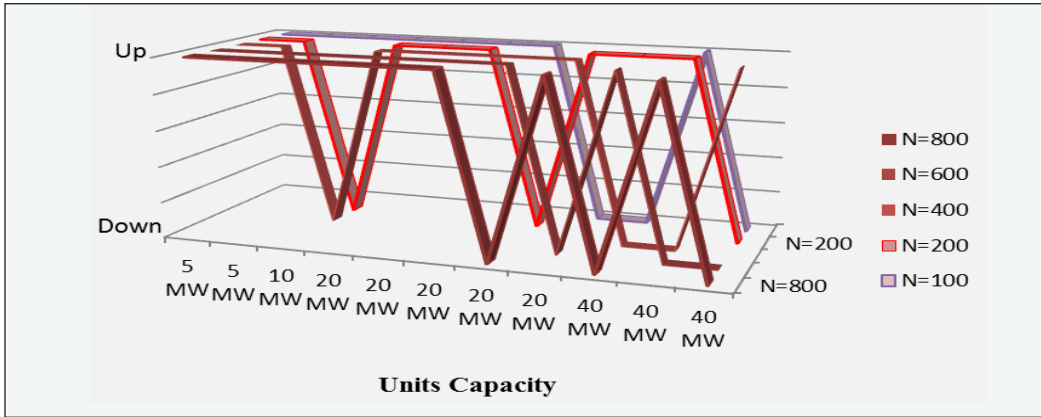


Figure 10. The operation cycle per hour per year of the generating units for the MRTS test system with a number of samples between (100–800) without wind power

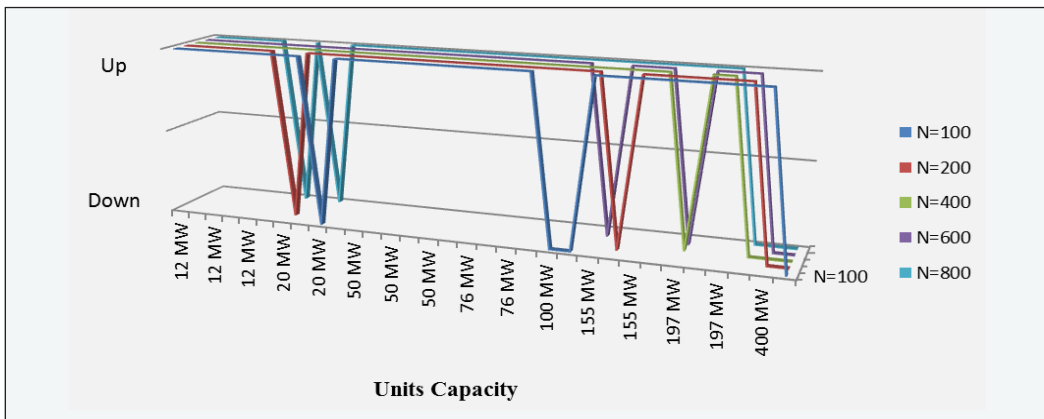


Figure 11. The operation cycle per hour per year of the generating units for the IEEE 79 test system with a number of samples between 100–800) without wind power

Table 5  
The COPT from the SMCS for MRTS-System

No. of samples	Unit number and capacity				Failure Prob.	Total (MW)
	2 × 5 MW	1 × 10 MW	5 × 20 MW	3 × 40 MW		
N=100	2	1	4	1	0.0013	140
N=200	2	0	4	2	0.0012	170
N=400	2	0	5	1	0.0017	150
N=600	2	1	4	1	0.041	160
N=800	2	1	4	1	0.0013	140

Table 6  
The COPT from the SMCS for IEEE-RTS-79-System

No of samples	Unit number and capacity									Failure Prob.	Total (MW)
	5×12 MW	4×20 MW	6×50 MW	4×76 MW	3×100 MW	4×155 MW	3×197 MW	1×350 MW	2×400 MW		
N=100	5	3	6	4	1	4	3	1	1	0.0024	2785
N=200	5	3	6	4	2	4	3	0	1	0.0038	2535
N=400	5	4	6	4	3	4	2	0	0	0.0033	2058
N=600	5	4	6	4	3	3	2	1	0	0.0029	2253
N=800	5	2	6	4	3	4	3	0	0	0.0017	2215

Table 7  
The COPT from the SMCS for IEEE-RTS-96-System

No of samples	Unit number and capacity									Failure Prob.	Total (MW)
	15×12 MW	12×20 MW	18×50 MW	12×76 MW	9×100 MW	12×155 MW	9×197 MW	3×350 MW	6×400 MW		
N=100	15	7	18	12	7	9	7	3	2	0.00471	7456
N=200	15	8	17	11	7	9	7	3	3	0.00154	7750
N=400	15	7	18	10	7	9	9	3	2	0.00081	7698
N=600	15	8	17	10	8	10	7	3	2	0.00035	7529
N=800	15	11	17	10	9	9	9	3	2	0.00608	7928

Table 8  
Reliability indices of the MRTS and IEEE-RTS-79-96 system

Test System		Reliability Indices			
		LOLE	LOEE	LOFE	LOLD
MRTS-System	Ref. (Kadhem et al., 2017d)	1.161	10.32	0.239	4.856
	Compute	1.232	11.61	0.333	3.698
IEEE-79-System	Ref. (Soleymani et al., 2015)	9.385	1120.3	2.72	3.45
	Compute	9.355	2311.5	2.019	4.633
IEEE-96-System	Ref. (Kadhem et al., 2019a)	0.140	23.97	-	-
	Compute	0.160	17.11	-	-

## Case (2): System with CGUs and WTGUs

The WTGUs installed in wind farms have the following specifications:  $V_{ci} = 5.3$ ,  $V_{co} = 21$ , and  $V_r = 12$  m/s. The rated output power of every WTGU is given as  $P_r = 2.5$  MW (Almutairi et al., 2015; Billinton & Gan, 1993). A wind farm with 16 identical 2.5 MW and a total wind power capacity of 40 MW is added into the MRTS, whereby the wind power penetration level is about 16.6 %. For IEEE-79, wind farms include 160 identical 2.5 MW and a total capacity of 400 MW is added with a wind power penetration level of about 11.6%. With the installation of 16 and 160 WTGUs of 2.5 MW, the total installed capacity is 40 and 400

MW, respectively. Figures 12 and 13 show the simulated output power with the associated failure of individual units for the MRTS and IEEE-79 test system running with a number of samples between 100–800. From these figures, we can conclude that the units with a capacity of 40 MW and 350 MW for MRTS and IEEE-79 test systems, respectively, have more repeated failed states even with wind power penetration.

It is well known that a 40-MW and 400-MW wind farm cannot replace the same size CGU with a capacity of 40 MW and 400 MW, respectively, due to the intermittent wind speed characteristics. Therefore, the capacity credit of a wind farm is required to replace a given number of CGUs for the same system reliability (Billinton & Chen, 1998; Castro & Ferreira, 2001).

From Table 9, in the case where the sample number is 800, we can see that available units in the MRTS system operation cycle are  $2 \times 5$ ,  $1 \times 10$ ,  $4 \times 20$ , and  $2 \times 40$  MW, with a total capacity of 180 MW and failure probabilities value of 0.0334. Meanwhile, the unavailable

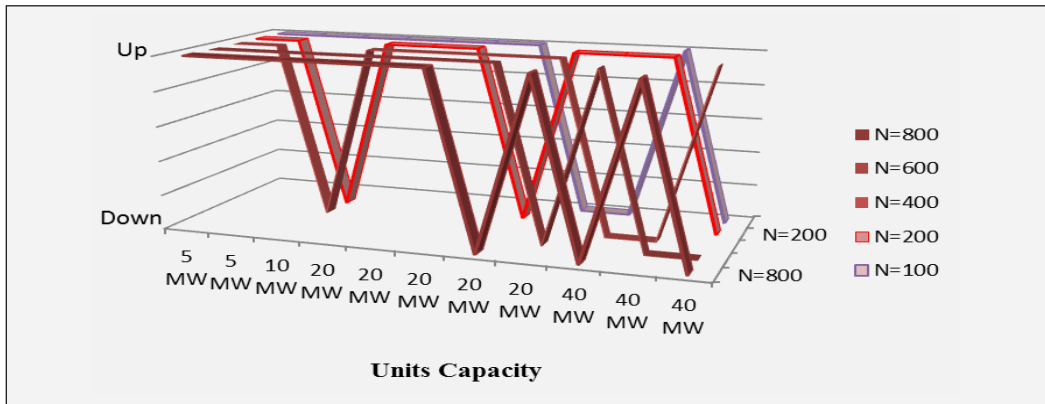


Figure 12. The operation cycle per hour per year of the generating units for the MRTS test system with number samples between 100–800 with added wind power (40 MW)

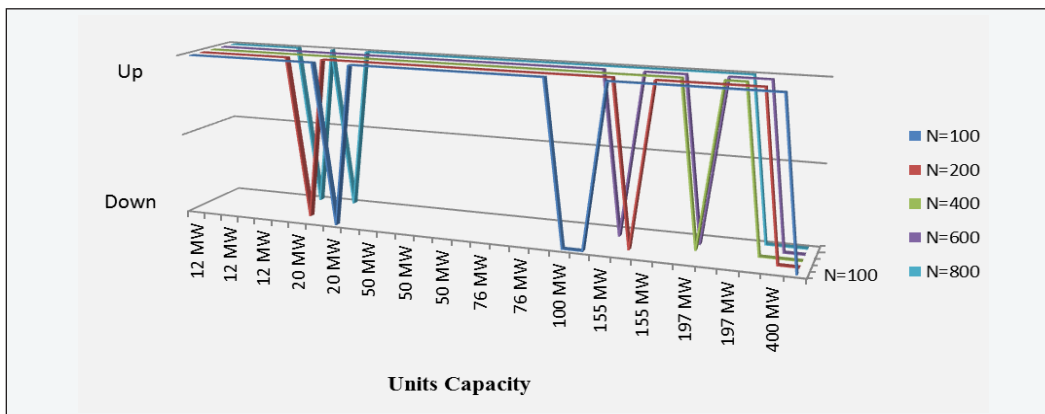


Figure 13. The operation cycle per hour per year of the generating units for the IEEE 79 test system with number samples between 100–800 with added wind power (400 MW)

units in the system operation cycle are 1×20 and 1×40 MW. In Table 10, for the IEEE-79 test system in the case where the sample number is 800, we can see that available units in the system operation cycle are 5×12, 3×20, 6×50, 4×76, 3×100, 4×155, 2×197, 0×350, and 2×400 MW, with a total capacity of 2838 MW and failure probabilities value of 0.0273. Meanwhile, the unavailable units in the system operation cycle are 1×20, 1×197, and 1×350 MW.

Table 9  
The COPT from the SMCS for MRTS-System with wind power

No. of samples	Unit number and capacity with wind power (40 MW)				Failure Prob.	Total (MW)
	2 ×5 MW	1×10 MW	5×20 MW	3×40 MW		
N=100	2	1	4	2	0.0452	180
N=200	2	1	5	1	0.0461	160
N=400	2	1	5	1	0.0362	160
N=600	2	1	4	2	0.0258	180
N=800	2	1	4	2	0.0334	180

The Capacity Outage Probability Table (COPT) calculations for the system units are shown in Tables 9 and 10. The results show the contingency state and priority order of the more failed states of the unit. Additionally, to confirm the effectiveness of our proposed method, we compared the results of our system’s reliability assessment indices with those of other methods presented in the literature (Table 11).

Table 10  
The COPT from the SMCS for IEEE-RTS-79-System with wind power

No. of samples	Unit number and capacity with wind power (400 MW)									Failure Prob.	Total (MW)
	5×12 MW	4×20 MW	6×50 MW	4×76 MW	3×100 MW	4×155 MW	3×197 MW	1×350 MW	2×400 MW		
N=100	5	4	6	4	2	4	3	0	1	0.0113	2555
N=200	5	3	6	4	3	4	3	0	1	0.0338	2635
N=400	5	4	6	4	3	3	3	1	0	0.0206	2450
N=600	5	4	6	4	3	2	3	1	1	0.0153	2695
N=800	5	3	6	4	3	4	2	0	2	0.0273	2838

Table 11  
Reliability indices of the MRTS and IEEE-RTS-79 system

Test System		Reliability Indices			
		LOLE	LOEE	LOFE	LOLD
MRTS-System	Ref. (Almutairi et al., 2015)	0.98	7.36	0.22	4.48
	Compute	0.85	12.66	0.17	4.99
IEEE-79-System	Ref. (Kadhem et al., 2017c)	7.43	823.78	0.29	25.6
	Compute	7.18	989.94	0.31	23.3

## CONCLUSION

One of the most common problems in calculating the adequacy of generation systems is stochastic conventional units' failure, which could expose an electrical network to unexpected power outages. This paper presents the impact of the conventional generation units' failure frequency on the output power systems. The sequential Monte Carlo simulation method (SMCSM) is utilized to assess the reliability of power systems. When the simulation of generation systems runs over many years, it is more useful to identify additional failure cases that happen or are repeated. In this paper, the assessment of reliability indices in the adequacy systems is carried out in two scenarios, where the test system without wind turbine units is treated as the base case, and the test system with wind turbine units is the subsequent case. In the first scenario (System With Only CGUS), Figures 10 and 11 depict the operation cycle per hour per year of the generating units for the MRTS and IEEE-79 test system running with a number of samples between 100–800.

From these figures, we can conclude that the units with 40 MW and 400 MW capacity for MRTS and IEEE-79 test systems have more repeated failed states. In the second scenario (System With CGUs & WTGUs), Figures 12 and 13 show the simulated output power with the associated failure of individual units for the MRTS and IEEE-79 test system running with a number of samples between 100–800. From these Figures, we can conclude that the units with a capacity of 40 MW and 350 MW for MRTS and IEEE-79 test systems have more repeated failed states even with wind power penetration. The attainable power generated from the CGUs and WTGUs during power systems operation was computed, and the reliability index of the suggested technique indicates the efficiency of estimating the power output. This paper's proposed reliability model and SMCS method can generate comprehensive reliability indexes based on the findings. The proposed method has been tested on Standard MRTS, IEEE-79, and IEEE-96 test systems.

## ACKNOWLEDGMENTS

The authors would like to thank University Putra Malaysia (UPM) for supporting this study.

## REFERENCES

- Abdalla, A. N., Nazir, M. S., Jiang, M., Kadhem, A. A., Izzri, N., Wahab, A., & Cao, S. (2020). Metaheuristic searching genetic algorithm based reliability assessment of hybrid power generation system. *Energy Exploration & Exploitation*, 39(1), 488-501. <https://doi.org/10.1177/0144598720959749>
- Alham, M. H., Gad, M. F., & Ibrahim, D. K. (2023). Potential of wind energy and economic assessment in Egypt considering optimal hub height by equilibrium optimizer. *Ain Shams Engineering Journal*, 14(1), Article 101816. <https://doi.org/10.1016/j.asej.2022.101816>
- Almutairi, A., Ahmed, M. H., & Salama, M. M. A. (2015). Probabilistic generating capacity adequacy evaluation: Research roadmap. *Electric Power Systems Research*, 129, 83-93. <https://doi.org/10.1016/j.epsr.2015.07.013>

- Arabali, A., Ghofrani, M., Etezadi-Amoli, M., & Fadali, M. S. (2014). Stochastic performance assessment and sizing for a hybrid power system of Solar/Wind/Energy Storage. *IEEE Transactions on Sustainable Energy*, 5(2), 363-371. <https://doi.org/10.1109/TSTE.2013.2288083>
- Azad, A. K., Rasul, M. G., & Yusaf, T. (2014). Statistical diagnosis of the best Weibull methods for wind power assessment for agricultural applications. *Energies*, 7(5), 3056-3085. <https://doi.org/10.3390/en7053056>
- Baloch, M. H., Abro, S. A., Kaloi, G. S., & Mirjat, N. H., Tahir, S., Nadeem, M. H., Gul, M., Memon, Z. A., & Kumar, M. (2017). A research on electricity generation from wind corridors of Pakistan (two provinces): A technical proposal for remote zones. *Sustainability*, 9(9), Article 1611. <https://doi.org/10.3390/su9091611>
- Billinton, R., & Chen, H. (1998). Assessment of risk-based capacity benefit factors associated with wind energy conversion Systems. *IEEE Transactions on Power Systems*, 13(3), 1191-1196. <https://doi.org/10.1109/59.709119>
- Billinton, R., & Gan, L. (1993). Wind power modeling and application in generating adequacy assessment. In *IEEE WESCANEX 93 Communications, Computers and Power in the Modern Environment Conference Proceedings* (pp. 100-106). IEEE Publishing. <https://doi.org/10.1109/wescan.1993.270560>
- Billinton, Roy, & Li, W. (1994). *Reliability Assessment of Electric Power Systems Using Monte Carlo Methods*. Springer. <https://doi.org/10.1007/978-1-4899-1346-3>
- Castro, R. M. G., & Ferreira, L. A. F. M. (2001). A comparison between chronological and probabilistic methods to estimate wind power capacity credit. *IEEE Transactions on Power Systems*, 16(4), 904-909. <https://doi.org/10.1109/59.962444>
- Chauhan, A., & Saini, R. P. (2015). Statistical analysis of wind speed data using Weibull Distribution Parameters. In *2014 1st International Conference on Non-Conventional Energy (ICONCE 2014)* (pp. 160-163). IEEE Publishing. <https://doi.org/10.1109/ICONCE.2014.6808712>
- Gao, Z. (2013). *Reliability Management of Power Systems with Wind Power Generation and Energy Storage* [Doctoral dissertation, Nanyang Technological University]. NTU Library.
- Grigg, C., & Wong, P. (1999). The IEEE reliability test system-1996 a report prepared by the reliability test system task force of the application of probability methods subcommittee. *IEEE Transactions on Power Systems*, 14(3), 1010-1020. <https://doi.org/10.1109/59.780914>
- Hou, K., Jia, H., Yu, X., Li, Y., Xie, C., & Yan, J. (2016). Composite generation and transmission system reliability assessment using impact increment based state enumeration method. In *2016 International Conference on Probabilistic Methods Applied to Power Systems (PMAPS)* (pp. 1-6). IEEE Publishing. <https://doi.org/10.1109/PMAPS.2016.7764119>
- Ibrahim, H. (2017). Electrical engineering 398. In H. Ibrahim, S. Iqbal, S. S. Teoh, & M. T. Mustaffa (Eds.), *9th International Conference on Robotic, Vision, Signal Processing and Power Applications* (pp. 37-45). Springer.
- Kadhem, A., Wahab, N. I. A., Bin Aris, I., Bt Jasni, J., & Abdalla, A. N. (2016). Effect of wind energy unit availability on power system adequacy. *Indian Journal of Science and Technology*, 9(28), 1-7. <https://doi.org/10.17485/ijst/2016/v9i28/97962>

- Kadhem, A. A., Izzri, N., Wahab, A., Aris, I., Jasni, J., & Abdalla, A. N. (2017a). Advanced wind speed prediction model based on a combination of Weibull Distribution and an artificial neural network. *Energies*, *10*(11), Article 1744. <https://doi.org/10.3390/en10111744>
- Kadhem, A. A., Wahab, N. I. A., Aris, I., Jasni, J., & Abdalla, A. N. (2017b). Reliability assessment of power generation systems using intelligent search based on disparity theory. *Energies*, *10*(3), Article 343. <https://doi.org/10.3390/en10030343>
- Kadhem, A. A., Wahab, N. I. A., Aris, I., Jasni, J., Abdalla, A. N., & Matsukawa, Y. (2017c). Reliability assessment of generating systems with wind power penetration via BPSO. *International Journal on Advanced Science, Engineering and Information Technology*, *7*(4), 1248-1254.
- Kadhem, A., Wahab, N. I. A., Aris, I., Jasni, J., & Abdalla, A. N. (2017d). Computational techniques for assessing the reliability and sustainability of electrical power systems: A review. *Renewable and Sustainable Energy Reviews*, *80*, 1175-1186. <https://doi.org/10.1016/j.rser.2017.05.276>
- Kadhem, A. A., Wahab, N. I. A., & Abdalla, A. N. (2019a). Differential evolution optimization algorithm based on generation systems reliability assessment integrated with wind energy. In *5th International Conference on Power Generation Systems and Renewable Energy Technologies, PGSRET 2019* (pp. 1-6). IEEE Publishing. <https://doi.org/10.1109/PGSRET.2019.8882705>
- Kadhem, A. A., Wahab, N. I. A., & Abdalla, A. N. (2019b). Wind energy generation assessment at specific sites in a Peninsula in Malaysia based on reliability indices. *Processes*, *7*(7), Article 399. <https://doi.org/10.3390/pr7070399>
- Khare, V., Nema, S., & Baredar, P. (2016). Solar-wind hybrid renewable energy system: A review. *Renewable and Sustainable Energy Reviews*, *58*, 23-33. <https://doi.org/10.1016/j.rser.2015.12.223>
- Khoo, W. C., Teh, J., & Lai, C. M. (2020a). Demand response and dynamic line ratings for optimum power network reliability and ageing. *IEEE Access*, *8*, 175319-175328. <https://doi.org/10.1109/ACCESS.2020.3026049>
- Khoo, W. C., Teh, J., & Lai, C. M. (2020b). Integration of wind and demand response for optimum generation reliability, cost and carbon emission. *IEEE Access*, *8*, 183606-183618. <https://doi.org/10.1109/ACCESS.2020.3029273>
- Lai, C. M., Teh, J., Alharbi, B., AlKassem, A., Aljabr, A., Alshammari, N. (2023). Optimisation of generation unit commitment and network topology with the dynamic thermal rating system considering N-1 reliability. *Journal of Electric Power Systems Research*, (221), Article 109444. <https://doi.org/10.1016/j.epr.2023.109444>
- Li, K., Yang, Q., Cui, Z., Zhao, Y., & Lin, S. (2019). Reliability evaluation of a metro traction substation based on the Monte Carlo method. *IEEE Access*, *7*, 172974-172980. <https://doi.org/10.1109/ACCESS.2019.2957151>
- Ma, J., Liu, Y., Zhang, S., Wu, L., & Yang, Z. (2023). Comprehensive probabilistic assessment on capacity adequacy and flexibility of generation resources. *International Journal of Electrical Power and Energy Systems*, *145*, Article 108677. <https://doi.org/10.1016/j.ijepes.2022.108677>
- Peeters, J. F. W., Basten, R. J. I., & Tinga, T. (2018). Improving failure analysis efficiency by combining FTA and FMEA in a recursive manner. *Reliability Engineering and System Safety*, *172*, 36-44. <https://doi.org/10.1016/j.rss.2017.11.024>

- Phoon, H. Y. (2006). Generation System Reliability Evaluations with Intermittent Renewables [Master dissertation, University of Strathclyde]. University of Strathclyde.
- Roy, A., Sahoo, S. S., & Chatterjee, K. (2017). A reliability assessment model of a wind farm for generation adequacy studies of wind integrated power system. In *3rd IEEE International Conference on Science Technology, Engineering and Management (ICONSTEM 2017)* (pp. 566-570). IEEE Publishing. <https://doi.org/10.1109/ICONSTEM.2017.8261386>
- Saltani, S., Mahmood-Reza Haghifam, N. S., & Jahromi, and M. Z. (2014). Novel method for feasibility study of wind farm installation based on reliability indices. In *2014 International Conference on Probabilistic Methods Applied to Power Systems (PMAPS)* (pp. 1-6). IEEE Publishing. <https://doi.org/10.1109/PMAPS.2014.6960654>.
- Shi, S. (2014). *Operation and Assessment of Wind Energy on Power System Reliability Evaluation Declaration of Author's Right* [Master dissertation, University of Strathclyde]. University of Strathclyde.
- Shi, S., & Lo, K. L. (2012). Reliability assessment of power system considering the impact of wind energy. In *2012 47th International Proceedings of the Universities Power Engineering Conference* (pp. 1-6). IEEE Publishing. <https://doi.org/10.1109/UPEC.2012.6398666>
- Soleymani, S., Mosayebian, M. E., & Mohammadi, S., (2015). A combination method for modeling wind power plants in power systems reliability evaluation. *Computers and Electrical Engineering*, *41*, 28-39. <https://doi.org/10.1016/j.compeleceng.2014.12.005>
- Su, Y., & Teh, J. (2023). Two-stage optimal dispatching of AC/DC hybrid active distribution systems considering network flexibility. *Journal of Modern Power Systems and Clean Energy*, *11*(1), 52-65. <https://doi.org/10.35833/MPCE.2022.000424>
- Wang, L., & Singh, C. (2007). Adequacy assessment of power-generating systems including wind power integration based on ant colony system algorithm. In *2007 IEEE Lausanne Power Tech* (pp. 1629-1634). IEEE Publishing. <https://doi.org/10.1109/PCT.2007.4538559>
- Wang, L., Singh, C., & Tan, K. C. (2007). Reliability evaluation of power-generating systems including time-dependent sources based on binary particle swarm optimization. In *2007 IEEE Congress on Evolutionary Computation* (pp. 3346-3352). IEEE Publishing. <https://doi.org/10.1109/CEC.2007.4424904>
- Ziegler, D. U., Pretico, G., Mateo, C., & Gómez San Román, T. (2023). Methodology for integrating flexibility into realistic large-scale distribution network planning using Tabu search. *International Journal of Electrical Power and Energy Systems*, *152*, Article 109201. <https://doi.org/10.1016/j.ijepes.2023.109201>

# Single Deformation Occurrence During Testing of Kenaf Composite Through Momentum Trapping Modification on Split Hopkinson Pressure Bar

Muhammad Fauzinizam Razali, Sareh Aiman Hilmi Abu Seman\*, Mohd Syakirin Rusdi and Siti Nuha Majiddah Abdul Aziz

*School of Mechanical Engineering, Universiti Sains Malaysia, 14300 Nibong Tebal, Pulau Pinang, Malaysia*

## ABSTRACT

In dynamic applications, the effective use of kenaf composite materials necessitates comprehensive and precise elucidation of their mechanical response under high strain rate loading conditions. Accurately measuring the sample's deformation can only be achieved using a pulse-trapping technique. In this study, a dynamic momentum trapping mechanism that is simple to assemble and configure was constructed and affixed to a conventional Split Hopkinson Pressure Bar (SHPB) system. The effectiveness of the verified momentum trap approach was shown when the secondary wave of compression was decreased by 50 percent in the application of momentum trapping that stopped the specimen from coming in contact with the incident bar, resulting in a much-improved correlation between various strain rates and the failure of kenaf composite microstructure.

*Keywords:* Failure correlation, momentum trapping, Split Hopkinson pressure bar, strain rates

## ARTICLE INFO

### Article history:

Received: 08 September 2023

Accepted: 18 January 2024

Published: 25 July 2024

DOI: <https://doi.org/10.47836/pjst.32.4.14>

### E-mail addresses:

[mefauzinizam@usm.my](mailto:mefauzinizam@usm.my) (Muhammad Fauzinizam Razali)

[sarehaiman@usm.my](mailto:sarehaiman@usm.my)\* (Sareh Aiman Hilmi Abu Seman)

[syakirin@usm.my](mailto:syakirin@usm.my) (Mohd Syakirin Rusdi)

[nuha.abdulaziz99@gmail.com](mailto:nuha.abdulaziz99@gmail.com) (Siti Nuha Majiddah Abdul Aziz)

\* Corresponding author

## INTRODUCTION

Based on its strong mechanical properties, low density, excellent properties of damping and biodegradability, kenaf fiber reinforced composite has attracted a great deal of interest (Mansingh et al., 2022). It has been documented that kenaf composite has a high cellulose content (70.4wt%), contributing to its high strength (Millogo et al., 2015). Even so, the kenaf fiber showed good mechanical properties, thermal stability and a strong

fiber-matrix adhesion compared to other natural fibers (Alshammari et al., 2023; Arjmandi et al., 2021). The kenaf composite has recently been used increasingly for automotive secondary structural parts (Uzoma et al., 2023; Wazeer et al., 2023). For example, Toyota Boshoku Corp. has used kenaf composite as the interior components of its newly developed electric concept car, Toyota LQ (Vasilash, 2020), while its European division, Lexus, has applied kenaf composite as package shelves (Holbery & Houston, 2006). Another leading car maker, General Motors, has also used kenaf composite in Saturn L300s and Opel Vectra's as packaging trays and door panel inserts (Holbery & Houston, 2006). In addition, a study made by Arockia Dhanraj et al. (2019) on kenaf composites' mechanical properties has also approved its suitability for automotive structural applications such as front modules, door panels and bumper beams.

In order to design components or structures built of kenaf composites, one needs to have a comprehensive grasp of the mechanisms of dynamic deformation and failure, particularly in the event of impact loading events like car collisions. Hence, to improve the design for structural components better suited to this specific application in the automotive sector, it is particularly necessary to characterize kenaf composite under loading conditions that are close to those experienced in real life (Abidin et al., 2023; Tamrakar et al., 2021).

Kenaf composite has been widely investigated for its mechanical response either at quasi-static (Bhambure et al., 2023; Ochi, 2008; Saba et al., 2015) or at dynamic loading rates (Bhambure et al., 2023; Omar et al., 2010). The relationship between loading rates, the mechanical properties and the type of failure observed macroscopically (Omar et al., 2010) and microscopically (Seman et al., 2019b; Sharba et al., 2016) has been found in several studies. However, the kenaf composite is not reportedly interrupted during dynamic loading, where specimens are only individually loaded (Omar et al., 2010). At higher stress rates, a lack of interrupted tests can lead to an inaccurate relationship between various stress rate levels and failure in the microstructure.

The standard Hopkinson pressure bar (SHPB) configuration should usually not be used for disrupted tests as stress wave reflections from the free ends reload the specimen several times (Omar et al., 2010; Zhang et al., 2020). Nemat-Nasser et al. (1991) first eliminated reflected stress waves by using a momentum trap technique applied to two different split Hopkinson pressure bars working in compressive and tensile directions. The momentum trap in a compressive SHPB consisted of transfer flanges, an incident tube, and a rigid mass, all with the same impedance as the input bar and was co-axial to it. Using SHPB, Song and Chen (2004) recorded another set-up for interrupted compressive dynamic testing conducted on soft materials. The momentum trap in these configurations consisted only of a transfer flange and a large rigid mass passed through the input bar. Therefore, the reaction mass was compensated for by a small gap that had accuracy regulated by a collar located at the free end of the input bar. A tandem momentum trap has been developed by Prot

and Cloete (2016) to avoid the effort of adjusting the gap between the rigid mass and the flange. This design, which can provide a single specimen loading event, comprises a pair of concentric tubes that are impedance matched, co-axially aligned with, and configured to function sequentially with the input bar.

The methods above included the rigid mass or second momentum trap to create a returning tensile wave when it was impacted by the incident tube or flange. However, attaching a huge rigid mass to the existing SHPB setup might be complicated as it would affect the movement of the incident bar if it were not properly installed. On top of that, even though a tandem momentum trap developed by Prot and Cloete (2016) did not need a precision gap, implementation of this technique is quite complicated as different diameters of momentum traps and bushing were needed in this design. Thus, a simple dynamic testing technique was developed in this research, based on a momentum trap concept, to provide an exact correlation between different stress rate levels and microstructural damages to a kenaf composite. The technique was based on Nemat Nasser 's work, but different working theories, designs and dimensions of the momentum trap components were used to fit the current SHPB. The method of the energy trap modified for the Split Hopkinson Pressure Bar was examined in depth. Data from several dynamic recovery experiments performed on kenaf composites and high-speed images are presented to demonstrate the validity of the hypothesis.

## METHODOLOGY

### Split Hopkinson Pressure Bar

The kenaf composite was dynamically characterized by a compression SHPB (Figure 1) available in Universiti Sains Malaysia. Key elements of the setup included bearings and a



Figure 1. Split Hopkinson pressure bar

sturdy support system for the input bar, the output bar, and the striker bar to keep the three bars in uniaxial alignment under the intense impact of a pressurized nitrogen gas gun with a power of up to 70 psi. All bars are 12 mm in diameter but different in length, where input and output bars are 1500 mm long, whereas the striker bar is 152 mm long. In addition, to avoid superimposing the incident and reflected pulses, the ratio of length to diameter of 20 of the input and output bars was required. The bars had a density of 8000 kg/m<sup>3</sup>, Young’s modulus of 200 GPa, and a bar wave velocity of 5000 m/s; they were crafted from high-carbon chromium alloy steel.

### Momentum Trapping Design

Components of the momentum trap were made from high-strength steel tubing, with inner tube diameters chosen to match those of the incident bar and outer tube diameters processed so that the tubes’ cross-sectional areas meet the impedance requirement. The length of the momentum traps has been selected to be as long as the striker so that the strain gauges mounted to the middle are not interfered with. Finally, the 60 mm long flange was also made of high-strength steel, which can achieve strength and rigidity while maintaining a low mass. The momentum trap and Split Hopkinson Pressure Bar (SHPB) specification are given in Table 1.

Table 1  
SHPB and momentum trap component specifications

	Input bar	Output bar	Striker	Rigid mass	Incident tube	
<b>Material</b>	High carbon chromium alloy steel	High carbon chromium alloy steel	High carbon chromium alloy steel	High strength steel	High strength steel	High strength steel
<b>Length (mm)</b>	1500	1500	152	152	152	25
<b>Inner diameter (mm)</b>	–	–	–	12	12	12
<b>Outside diameter (mm)</b>	12	12	12	24	24	24
<b>Impedance (kPa.s/m)</b>	13,941	13,941	13,941	13,941	13,941	13,941
<b>Density (kg/m<sup>3</sup>)</b>	8000	8000	8000	7800	7800	7800

As shown in Figure 2, the momentum trapping device includes a flange attached as a momentum trap to the end of the incident bar, an incident tube and a rigid mass through which the incident bar passes. The rigid mass was attached at a fixed position to prevent any movement. The momentum trap parts are arranged concentrically with the incident bar and aligned with each other. The stress waves are transmitted through a flange fixed on the incident bar between the momentum trap pieces.

The gap between the incident bar and the rigid mass had been established. This default gap has been correctly managed so that if the secondary loading wave reflected

in the incident bar emerges, the incident bar will unexpectedly stop due to the reversed compressive pulse impact from the incident tube. Since the excessive momentum is trapped to ensure a single load on the sample, the condition of the specimen under the identified load is well established, and the development of damage inside the specimen is easier to interpret.

The working mechanism of a modified SHPB is shown in Figure 2. In the first stage, the activation of the gas gun resulted in a collision between the striker and the flange connected to the input bar. This phenomenon gives rise to two separate compression waves, with the first wave propagating through the incident bar and the subsequent wave propagating through the tube (Figure 3a). Following the collision, the striker will experience little rebound due to encountering an impedance lower than the combined impedance of the incident bar and flange (Figure 3a).

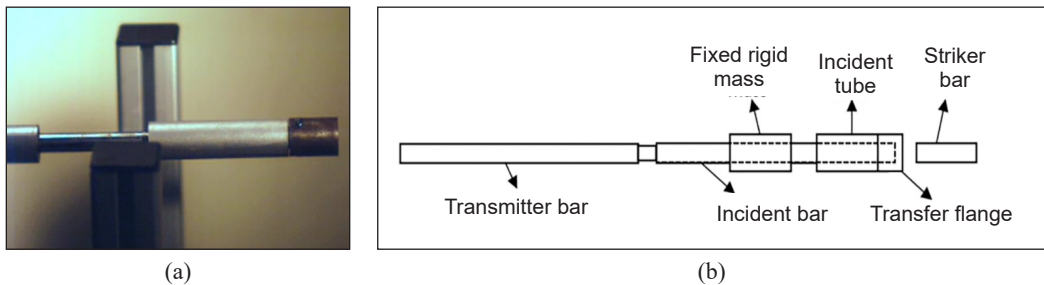


Figure 2. (a) Implementation of a momentum trapping on a SHPB; and (b) Schematic illustration of momentum trapping on a SHPB

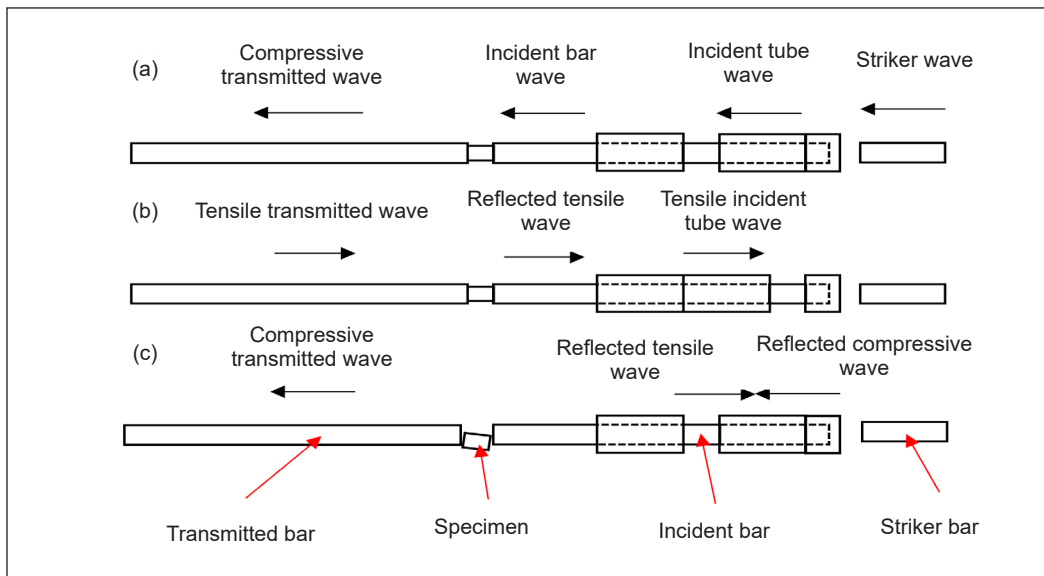


Figure 3. Schematic illustration of the operating principle of a standard SHPB with a momentum trap

Due to the matched impedance of all components comprising the momentum trap and the input bar, the second wave is transmitted to the rigid mass without reflection. Upon the arrival of the compressive wave at the unfixed end of the immovable rigid mass, it underwent reflection as a tensile wave, subsequently being transmitted back into the incident tube (as seen in Figure 3b). This transmission resulted in the detachment of the incident tube from the rigid mass, as illustrated in Figure 3c. The incident tube then impacted the transfer flange, which stopped the movement of the incident bar toward the specimen (Figure 3c). Consequently, the specimen only experienced a single load of known amplitude and duration. In the meantime, the impacts of the incident tube on the transfer flange created a reflected compressive wave that collided and superposed with the reflected tensile wave, which formed a resultant wave of lower amplitude (Figure 3c).

### High-speed Camera

In order to verify whether the momentum trapping mechanism connected to the SHPB system is correct and reliable, high-speed real-time video pictures were needed. This analysis recorded the incident bar movement within five frames when the specimen was struck. The high-speed camera is synchronized manually with the first movement of the projectile to allow the camera to capture the whole deformation process.

A high-speed image sequence with a frame rate of about 5000 fps and higher was acquired during dynamic experiments. A strong light source at this speed was sufficient to minimize exposure time and obtain “frozen” images. Two light sources were used at the same frequency as the camera’s frame rate. The light exposure was checked to avoid thermal effects on the mechanical properties of the tested material. Figure 4 shows a high-speed camera and light source setup during the SHPB experiment.

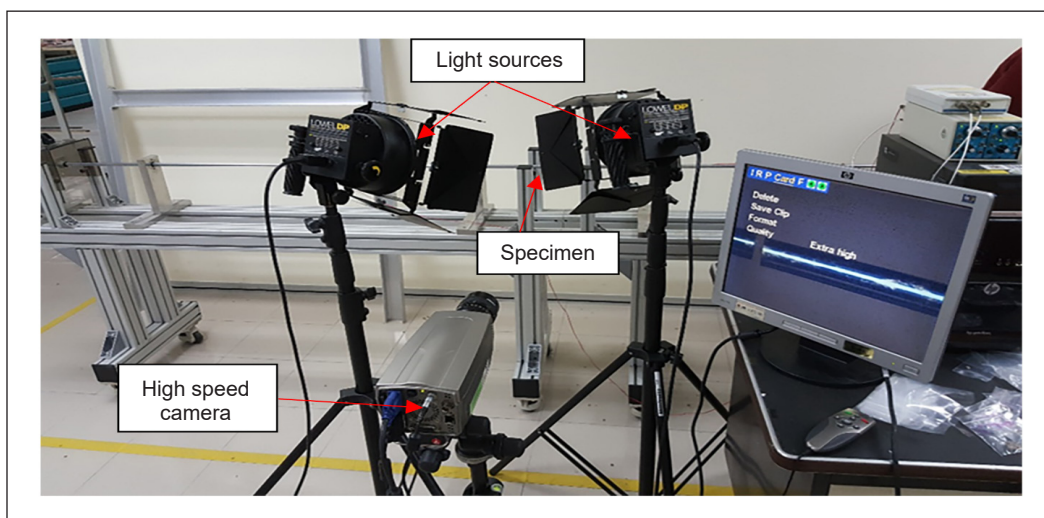


Figure 4. High speed camera setup during impact loading

## Materials

Long unidirectional fiber yarns of tex 1400 used were supplied by JUTEKO Bangladesh, Pvt. Ltd. Bangladesh. The tex number of the yarn refers to the diameter size of the yarn used for the pultrusion process. Tex is defined as a unit of measurement for the linear mass density of fibers and the mass in grams per 1000 meters. Unsaturated polyester resin (Crystic P9901) was purchased from the Revertex Company, Malaysia. Other mixtures for resin, such as benzoyl peroxide (BPO) as initiator, calcium carbonate ( $\text{CaCO}_3$ ) as filler and the release agent powder, were supplied by Revertex Company as well. A thermoset pultrusion machine model no. SVS-PUL-6T at the School of Materials and Mineral Resources Engineering, Universiti Sains Malaysia, produced the pultruded kenaf fiber reinforced composites samples. By using 55 kenaf yarns tex of 1400, a pultruded kenaf composite with 70% volume fractions (v/v %) has been produced, as shown in Figure 5. A pultruded kenaf composite with a diameter size of 12.7 mm that has been produced was then cut into 7 mm of length.



Figure 5. Kenaf composite specimen

## RESULTS AND DISCUSSION

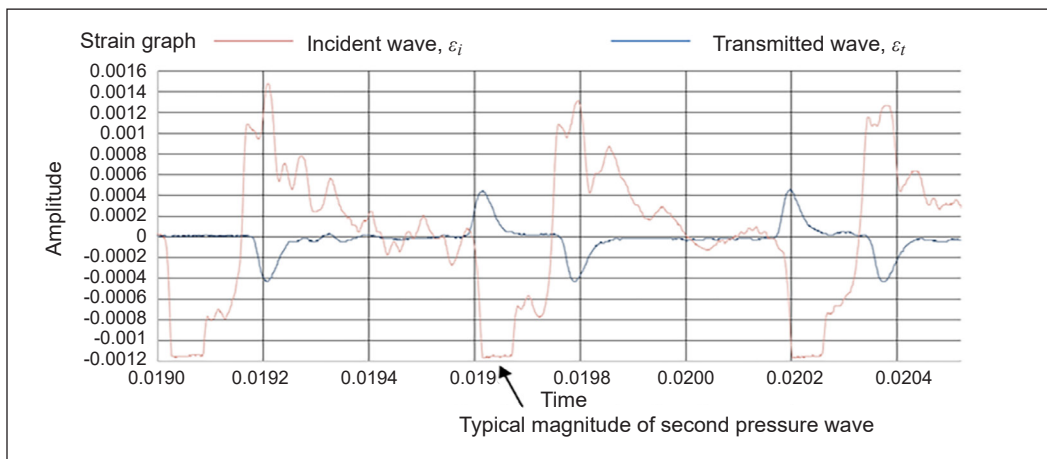
Figure 6 shows the example of two waves reported for experimentation in the Hopkinson bars without (a) and with (b) the momentum trap. In general, with and without a momentum trap, the incoming wavelength is similar to the minimal effect of the transfer flange. In an untrapped Split Hopkinson Pressure Bar, the incident bar hit the specimen several times, as shown in Figure 7a, where the second and third waves are held at a strain magnitude of 0.0012 at the time of 0.0196s and 0.0202s, respectively.

Contrariwise, the secondary wave of compression was decreased by 50 percent in the application of momentum trapping (refer to the difference in incident bar signals of around 0.0196 $\mu\text{s}$  to 0.0198 $\mu\text{s}$ ). The second compression wave's changes in magnitude indicate that the tensile wave reflected in the input bar was disturbed by the wave induced by the impact of the flange tube. The remaining tensile wave was then reflected as the second compressive wave at the free end of the incident bar. Although the second compressive wave was not completely isolated or returned as a tensile wave, the effect of the incident tube on the flange was sufficient to ensure that the specimen was not in contact with the tube and, thus, was loaded only once. A similar result has also been reported by Xia and Yao (2015), where the second compressive wave has been reduced by implementing a momentum trapping system in SHPB.

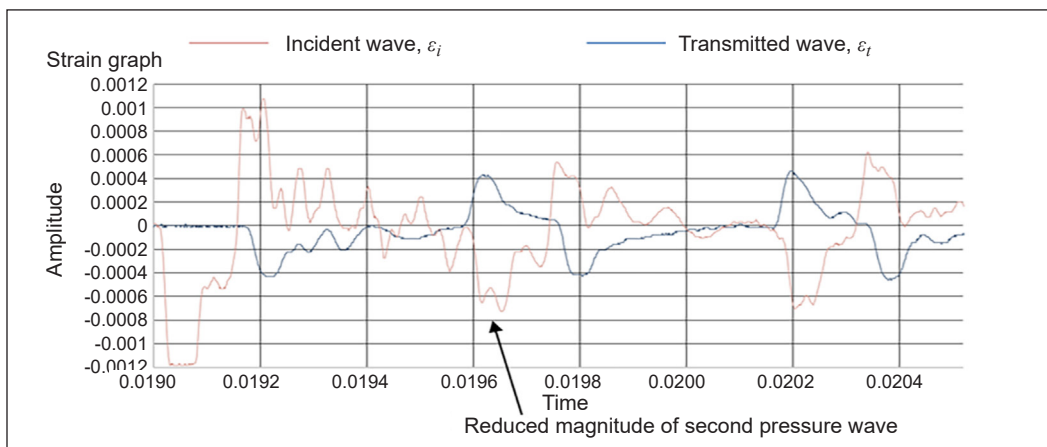
The data from the high-speed camera were utilized to distinguish between the condition of the specimen with and without the momentum trapping. In Figure 7a, from the time

of 0.0190s to 0.0198s, where the momentum trapping was excluded from the SHPB, the specimen was loaded four times, and the input bar moved further towards the specimen. This unnecessary movement of the incident bar has created additional damage to the specimen, as shown in Figure 9. However, as shown in Figure 7b from the time range of 0.0190s until 0.0198s, it is evident that, when using the momentum trapping, after the loading of the specimen at a time of 0.0192s, the output bar, which does not include a momentum trap, goes away while the input bar's face stays still. Therefore, it is established that the specimens experienced a single loading event.

An incident tube and a rigid mass were separated by a predetermined gap, as depicted in Figure 8a. After the incident tube has made contact with the rigid mass (Figure 8d), a secondary loading wave reflected in the incident bar will arrive and cause the gap



(a)



(b)

Figure 6. Strain-time history graphs in incident and transmitter bars (a) without momentum trap, and (b) with momentum trap

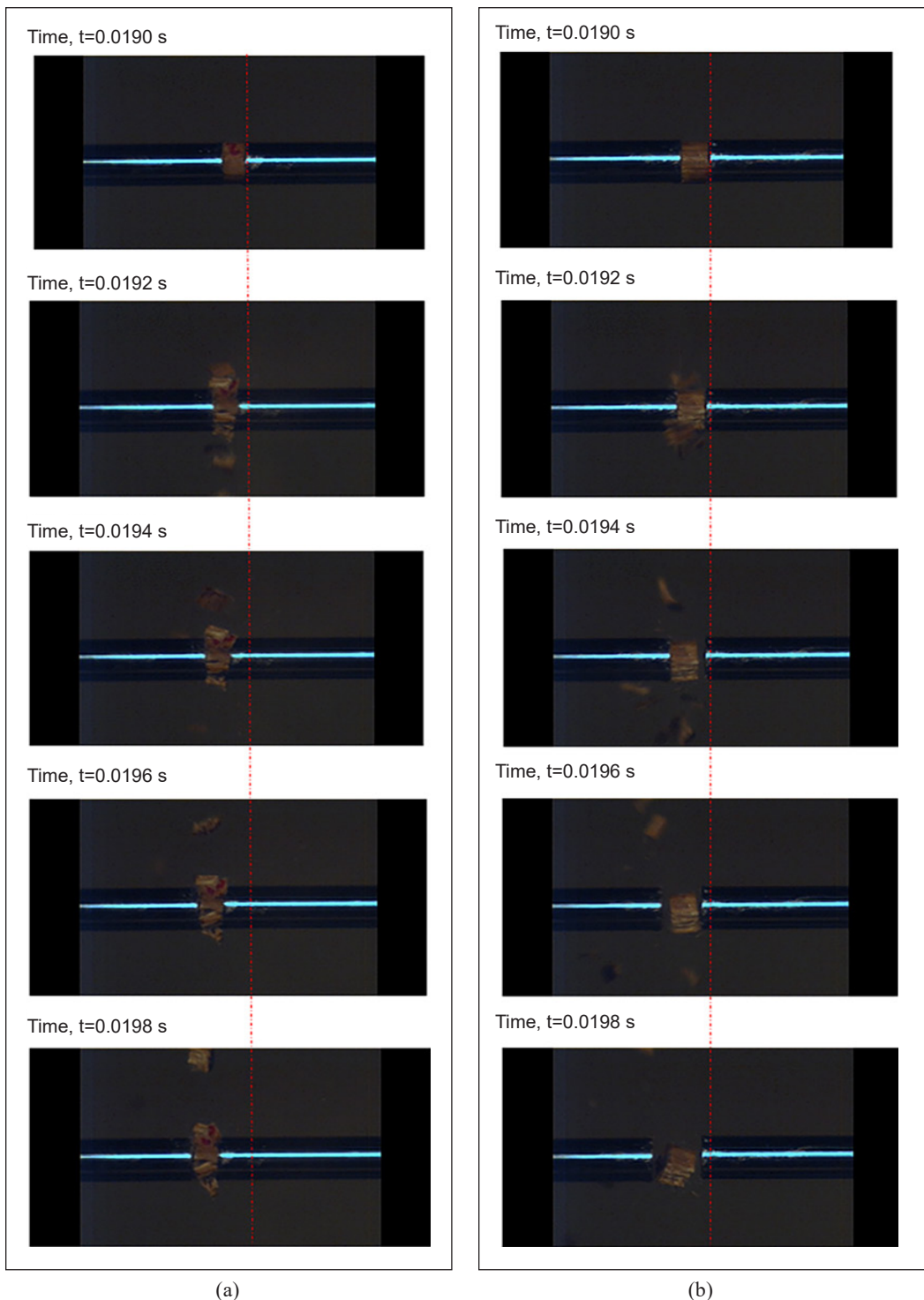


Figure 7. High speed images of specimen's condition during impact loading (a) without momentum trap (b) with momentum trap

between the incident tube and the transfer flange to close (Figure 8e). As the gap was closed (Figure 8d), a reverse compressive pulse resulted from the impact of the incident tube on the flange, causing the incident bar to stop abruptly. As the needless momentum was extracted to ensure a single load on the specimen, the state of the specimen was established by the defined load, and the development of damage within a specimen was easier to identify. The movement of the incident tube during the impact is shown in Figures 8a to 8e.

Proper care should be taken to establish the precise distance between the transfer flange and the stiff mass to achieve satisfactory results. To be precise, if the distance is too great, the effect of the incident tube on the transfer flange would not be sufficient to prevent further specimen loading by the incident bar. On the other hand, if the gap is too short, a reflected secondary load wave in the incident bar might arrive even at the incident tube position, and the flange is not closed. It may impact the stress pulse, shift the incident tube to an incorrect location, or do both, resulting in unwanted results.

Figure 9 shows the stress-strain curves of the kenaf composite under strain rates of 1000/s until 1400/s. As strain rates increased, both stiffness and compressive strength decreased. Reductions in both properties were relatable to the failure images of kenaf composite specimens (Figure 10), where specimens have endured

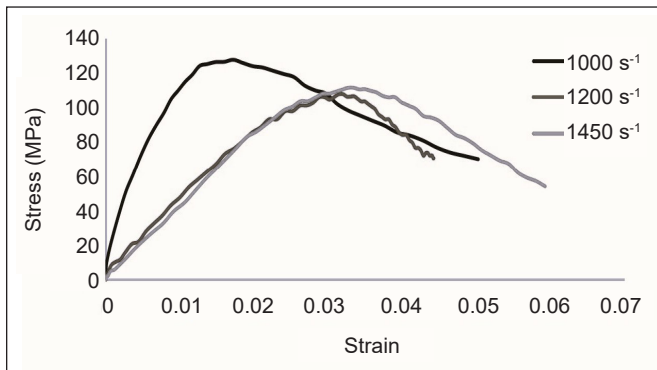
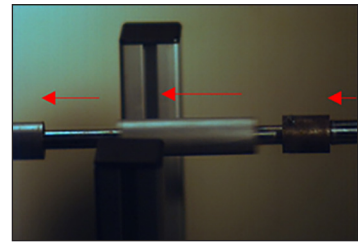


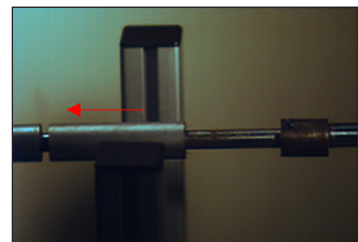
Figure 9. Compressive stress-strain curve of kenaf composite under different strain rates



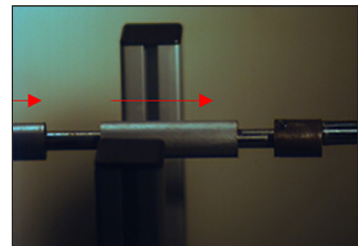
(a)



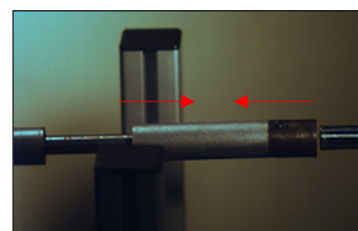
(b)



(c)



(d)



(e)

Figure 8. Sequence of movement of momentum trap during impact loading

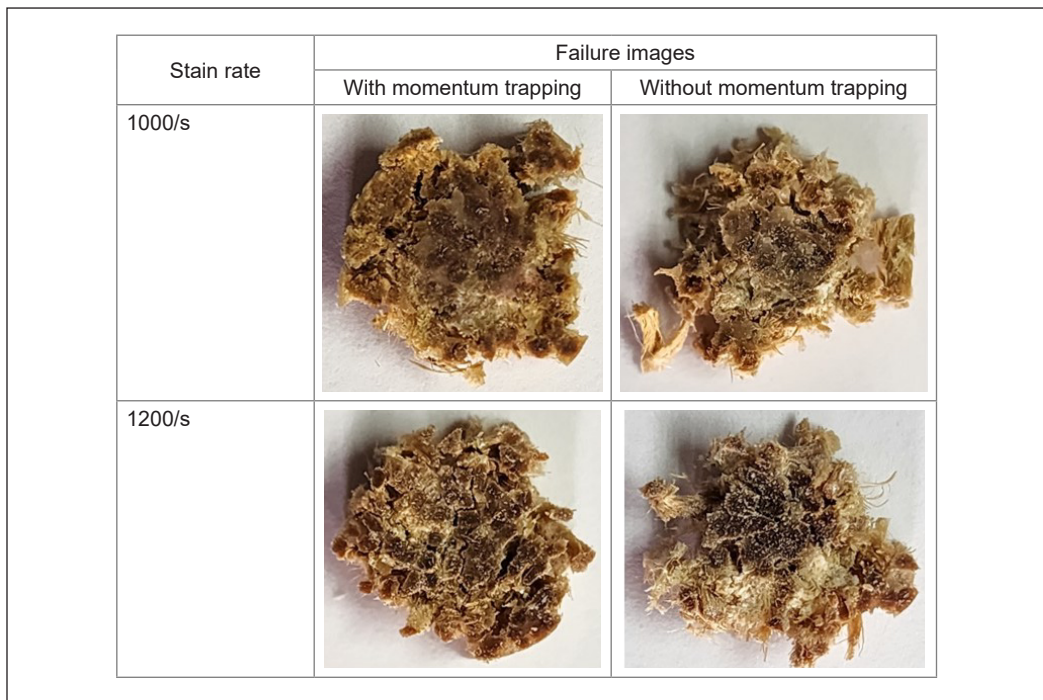


Figure 10. Failures of kenaf composite under different strain rates with and without momentum trapping

more extensive matrix cracking and fiber fracture damages as strain rates increased. According to Seman et al. (2019a), heat generated during impact has increased the molecular mobility of resin, which has contributed to a reduction in compressive properties and values.

The correlation between different strain rate levels and microstructural damages to a kenaf composite with and without momentum trapping is shown in Figure 10. Under strain rates of 1000/s and 1200/s, kenaf composite specimens have endured more catastrophic damages as the incident bar repeatedly impacted it when momentum trapping was not installed (Figure 7). Meanwhile, the installation of momentum trapping has helped to abstain from the secondary and subsequent movement of the incident bar toward the specimen, and less damage has been found on the specimen, as shown in Figure 10. By eliminating the repeated movement of the incident bar, unnecessary damage to specimens can be avoided. Thus, an exact correlation between different strain rate levels and microstructural damages to a kenaf composite can be made.

## CONCLUSION

The classical split Hopkinson pressure bar and a unique and simple momentum trapping method for recovering dynamic specimens were introduced. The technique enables dynamic specimen recovery with a much smaller rigid mass and less complicated momentum trap

arrangement, thus facilitating the installation and commissioning of the test. An effective dynamic process has successfully realized the recovery of kenaf composite specimens through a single deformation event. This achievement is confirmed by the significant reduction of the secondary wave by approximately 50%, which stopped the repeated movement of the incident bar and additional damage to the specimens. Therefore, an exact correlation between different stress rate levels and microstructural damages to kenaf composites has been obtained.

## ACKNOWLEDGEMENT

The authors would like to thank the Ministry of Higher Education, Malaysia, under the Fundamental Research Grant Scheme (FRGS) ref: FRGS/1/2023/STG05/USM/03/1 and Universiti Sains Malaysia Short Term Grant 304/PMEKANIK/6315493 for supporting this research.

## REFERENCES

- Abidin, N. M. Z., Sultan, M. T. H., Shah, A. U. M., Shahar, F. S., Najeeb, M. I., Ali, M. R., Basri, A. A., Baloor, S. S., Gaff, M., & Hui, D. (2023). The evaluation of the mechanical properties of glass, kenaf, and honeycomb fiber-reinforced composite. *Reviews on Advanced Materials Science*, 62(1), Article 20220299. <https://doi.org/10.1515/rams-2022-0299>
- Alshammari, M. B., Ahmad, A., Jawaid, M., & Awad, S. A. (2023). Thermal and dynamic performance of kenaf/washingtonia fibre-based hybrid composites. *Journal of Materials Research and Technology*, 25, 1642-1648. <https://doi.org/10.1016/j.jmrt.2023.06.035>
- Arjmandi, R., Yıldırım, I., Hatton, F., Hassan, A., Jefferies, C., Mohamad, Z., & Othman, N. (2021). Kenaf fibers reinforced unsaturated polyester composites: A review. *Journal of Engineered Fibers and Fabrics*, 16, Article 15589250211040184. <https://doi.org/10.1177/15589250211040184>
- Arockia Dhanraj, J., G, D., Kumar, S., Sivakumar, S., & Vishnuvardhan, R. (2019). *Experimental investigation on mechanical properties and vibration damping frequency factor of kenaf fiber reinforced epoxy composite*. SAE Technical Papers, 2019-28-0167. <https://doi.org/10.4271/2019-28-0167>
- Bhambure, S. S., Rao, A. S., & Senthilkumar, T. (2023). Analysis of mechanical properties of kenaf and kapok fiber reinforced hybrid polyester composite. *Journal of Natural Fibers*, 20(1), Article 2156964. <https://doi.org/10.1080/15440478.2022.2156964>
- Holbery, J., & Houston, D. (2006). Natural-fiber-reinforced polymer composites in automotive applications. *The Journal of The Minerals, Metals & Materials Society*, 58, 80-86. <https://doi.org/10.1007/s11837-006-0234-2>
- Mansingh, B. B., Binoj, J. S., Manikandan, N., Sai, N. P., Siengchin, S., Rangappa, S. M., Bharath, K. N., & Indran, S. (2022). Chapter 12 - Kenaf fibers, their composites and applications. In S. M. Rangappa, J. Parameswaranpillai, S. Siengchin, T. Ozbakkaloglu, & H. Wang (Eds.), *Plant Fibers, Their Composites, and Applications* (pp. 283-304). Woodhead Publishing. <https://doi.org/https://doi.org/10.1016/B978-0-12-824528-6.00011-4>

- Millogo, Y., Aubert, J. E., Hamard, E., & Morel, J. C. (2015). How properties of kenaf fibers from Burkina Faso contribute to the reinforcement of earth blocks. *Materials*, 8(5), 2332-2345. <https://www.mdpi.com/1996-1944/8/5/2332>
- Nemat-Nasser, S., Isaacs, J. B., & Starrett, J. E. (1991). Hopkinson Techniques for dynamic recovery experiments. *Proceedings: Mathematical and Physical Sciences*, 435(1894), 371-391. <http://www.jstor.org/stable/51971>
- Ochi, S. (2008). Mechanical properties of kenaf fibers and kenaf/PLA composites. *Mechanics of Materials*, 40(4-5), 446-452. <https://doi.org/https://doi.org/10.1016/j.mechmat.2007.10.006>
- Omar, M. F., Akil, H. M., Ahmad, Z. A., Mazuki, A. A. M., & Yokoyama, T. (2010). Dynamic properties of pultruded natural fibre reinforced composites using split Hopkinson pressure bar technique. *Materials & Design*, 31(9), 4209-4218. <https://doi.org/https://doi.org/10.1016/j.matdes.2010.04.036>
- Prot, M., & Cloete, T. J. (2016). A tandem momentum trap for dynamic specimen recovery during split Hopkinson pressure bar testing of cancellous bone. *Journal of Dynamic Behavior of Materials*, 2, 50-58. <https://doi.org/10.1007/s40870-016-0046-6>
- Saba, N., Paridah, M. T., & Jawaid, M. (2015). Mechanical properties of kenaf fibre reinforced polymer composite: A review. *Construction and Building Materials*, 76, 87-96. <https://doi.org/https://doi.org/10.1016/j.conbuildmat.2014.11.043>
- Seman, S. A. H. A., Ahmad, R., & Akil, H. M. (2019a). Experimental and numerical investigations of kenaf natural fiber reinforced composite subjected to impact loading. *Polymer Composites*, 40(3), 909-915. <https://doi.org/10.1002/pc.24758>
- Seman, S. A. H. A., Ahmad, R., & Akil, H. M. (2019b). Meso-scale modelling and failure analysis of kenaf fiber reinforced composites under high strain rate compression loading. *Composites Part B: Engineering*, 163, 403-412. <https://doi.org/10.1016/j.compositesb.2019.01.037>
- Sharba, M., Salman, S., Leman, Z., Sultan, M., Ishak, M., & Hanim, M. (2016). Effects of processing method, moisture content, and resin system on physical and mechanical properties of woven kenaf plant fiber composites. *Bioresources*, 11(1), 1466-1476.
- Song, B., & Chen, W. (2004). Loading and unloading split Hopkinson pressure bar pulse-shaping techniques for dynamic hysteretic loops. *Experimental Mechanics*, 44, 622-627. <https://doi.org/10.1007/BF02428252>
- Tamrakar, S., Kiziltas, A., Mielewski, D., & Zander, R. (2021). Characterization of kenaf and glass fiber reinforced hybrid composites for underbody shield applications. *Composites Part B: Engineering*, 216, Article 108805. <https://doi.org/https://doi.org/10.1016/j.compositesb.2021.108805>
- Uzoma, A. E., Nwaeche, C. F., Al-Amin, M., Muniru, O. S., Olatunji, O., & Nzeh, S. O. (2023). Development of interior and exterior automotive plastics parts using kenaf fiber reinforced polymer composite. *Eng*, 4(2), 1698-1710. <https://www.mdpi.com/2673-4117/4/2/96>
- Vasilash, G. S. (2020). *Natural fiber-reinforced composite developed for Toyota EV concept*. Gardner Business Media. <https://www.gardnerweb.com/articles/natural-fiber-reinforced-composite-developed-for-toyota-ev-concept>

- Wazeer, A., Das, A., Abeykoon, C., Sinha, A., & Karmakar, A. (2023). Composites for electric vehicles and automotive sector: A review. *Green Energy and Intelligent Transportation*, 2(1), Article 100043. <https://doi.org/https://doi.org/10.1016/j.geits.2022.100043>
- Xia, K., & Yao, W. (2015). Dynamic rock tests using split Hopkinson (Kolsky) bar system – A review. *Journal of Rock Mechanics and Geotechnical Engineering*, 7(1), 27-59. <https://doi.org/https://doi.org/10.1016/j.jrmge.2014.07.008>
- Zhang, K., Sun, Y., Wang, F., Liang, W., & Wang, Z. (2020). Progressive failure and energy absorption of chopped bamboo fiber reinforced polybenzoxazine composite under impact loadings. *Polymers*, 12(8), Article 1809. <https://doi.org/10.3390/polym12081809>

## Application of Fuzzy Analytic Network Process in Selection of Bio-composite Filament for Fused Deposition Modeling Process

Hazliza Aida Che Hamid<sup>1</sup>, Mastura Mohammad Taha<sup>2\*</sup>, Syahibudil Ikhwan Abdul Kudus<sup>2</sup>, Noryani Muhammad<sup>1</sup>, Mohd Adrinata Shaharuzaman<sup>1</sup>, Loh Yueh Feng<sup>3</sup> and Ahmad Ilyas Rushdan<sup>4,5,6,7</sup>

<sup>1</sup>Faculty of Mechanical Technology and Engineering, Universiti Teknikal Malaysia Melaka, Hang Tuah Jaya, 76100 Durian Tunggal, Melaka, Malaysia

<sup>2</sup>Faculty of Industrial and Manufacturing Technology and Engineering, Universiti Teknikal Malaysia Melaka, Hang Tuah Jaya, 76100 Durian Tunggal, Melaka, Malaysia

<sup>3</sup>Lembaga Perindustrian Kayu Malaysia, Pusat Pembangunan Fiber dan Biokomposit, Kompleks Perabot Olak Lempit, 42700, Banting, Selangor, Malaysia

<sup>4</sup>Sustainable Waste Management Research Group (SWAM), School of Chemical and Energy Engineering, Faculty of Engineering, Universiti Teknologi Malaysia, 81310 UTM Johor Bahru, Johor, Malaysia

<sup>5</sup>Centre for Advanced Composite Materials (CACM), Universiti Teknologi Malaysia, 81310 UTM Johor Bahru, Johor, Malaysia

<sup>6</sup>Institute of Tropical Forest and Forest Products, Universiti Putra Malaysia, 43400 Serdang, Selangor, Malaysia

<sup>7</sup>Centre of Excellence for Biomass Utilization, Universiti Malaysia Perlis, 02600, Arau, Perlis, Malaysia

### ABSTRACT

The concurrent engineering approach necessitates integrating material selection into the product design to effectively align with client specifications. Premature product failure, leading to substantial losses, frequently arises as a consequence of inadequate material selection due to conflicting demands. The Multi-Criteria Decision Making (MCDM) procedures are essential for making wise decisions since choosing materials is complicated. This study employs fuzzy analytic network process (FANP) techniques to determine which

bio-composite filaments will be the most effective for Fused Deposition Modeling (FDM). The requirements and available factors of egg carton packaging material determine the selection criteria for bio-composite filaments. These factors serve as the foundation for identifying ten essential features. The acquired data showed that the sugar palm fiber/poly(lactic acid) composite (SPF/PLA) 7.5 wt.% fiber loading exhibited the highest priority score, 19.80%. The

#### ARTICLE INFO

##### Article history:

Received: 14 September 2023

Accepted: 02 January 2024

Published: 22 July 2024

DOI: <https://doi.org/10.47836/pjst.32.4.15>

##### E-mail addresses:

[hzlizaaida24@gmail.com](mailto:hzlizaaida24@gmail.com) (Hazliza Aida Che Hamid)

[mastura.taha@utem.edu.my](mailto:mastura.taha@utem.edu.my) (Mastura Mohammad Taha)

[syahibudil@utem.edu.my](mailto:syahibudil@utem.edu.my) (Syahibudil Ikhwan Abdul Kudus)

[noryani@utem.edu.my](mailto:noryani@utem.edu.my) (Noryani Muhammad)

[adrinata@utem.edu.my](mailto:adrinata@utem.edu.my) (Mohd Adrinata Shaharuzaman)

[loh@mtib.gov.my](mailto:loh@mtib.gov.my) (Loh Yueh Feng)

[ahmadilyas@utm.my](mailto:ahmadilyas@utm.my) (Ahmad Ilyas Rushdan)

\* Corresponding author

kenaf/acrylonitrile butadiene styrene (Kenaf/ABS) composite, with a fiber loading of 7.5%, exhibited the lowest ranking, scoring 4.4%. Subsequently, a sensitivity analysis was conducted to further corroborate the findings. It was observed that the SPF/PLA 7.5 wt.% fiber loading consistently ranked highest throughout all four examined scenarios. The study determined that a bio-composite filament material with a weight ratio of 7.5% SPF/PLA fiber loading is the optimal choice for utilizing FDM technology in the design of egg carton packaging.

*Keywords:* Bio-composites filaments, fused deposition modeling (FDM), fuzzy analytic network process, material selection process

## INTRODUCTION

The Fused Deposition Modeling (FDM) technique is extensively used in Three-dimensional (3D) printing because it can generate a wide variety of complicated pieces at a lower production cost and with various customizable materials. FDM typically employs a thermally controlled technique in which a melted thermoplastic filament is placed onto a build platform. Most FDM filament comprises thermoplastics like polylactic acid (PLA) or acrylonitrile-butadiene-styrene (ABS). Their favorable thermal and rheological qualities facilitate the production phase (Mohan et al., 2017). FDM material feedstock typically consists of rolled filaments between 1.75 and 3 mm diameter (Mohd Pu'ad et al., 2019). When the filament melts, the substance comes out of a nozzle. The liquidizer head moves along the X and Y axes, while the building platform moves along the Z axis. Figure 1 shows how an FDM printer creates an object by fusing filament spools to make layers.

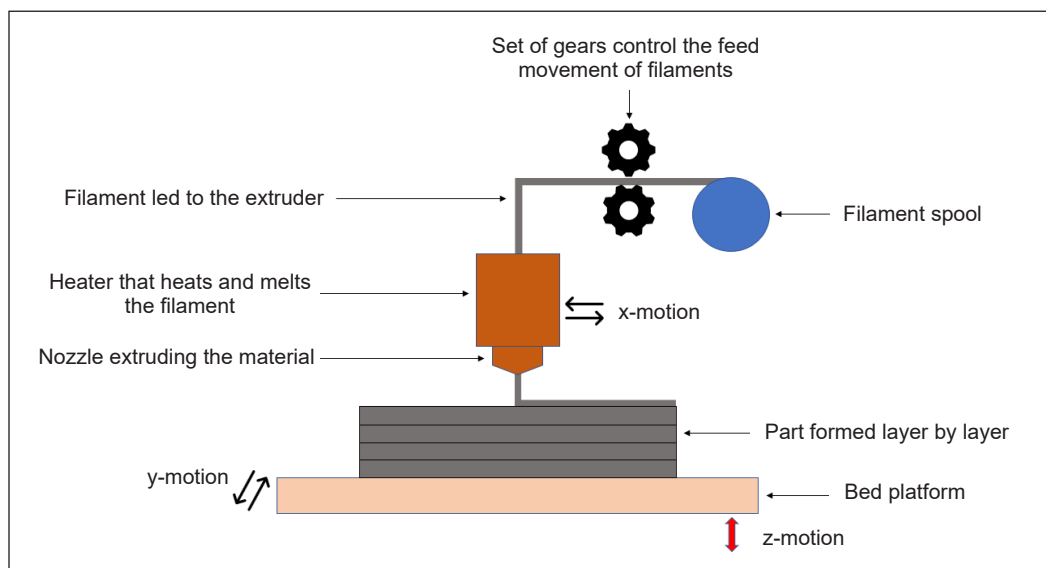


Figure 1. FDM process schematically

Filaments come in various materials, with bio-composite filaments being one option. Bio-composites consist of two distinct elements: (1) natural fiber and (2) matrix. Recent studies revealed that plant-based natural fibers are the most often used material in bio-composites. Plant-based natural fibers such as jute, flax, hemp, coir, and sisal are gaining popularity in the composite sector due to stricter laws concerning their usage. According to Noryani et al. (2018), plant-based natural fiber is far simpler to work with than animal or mineral fiber, making it ideal for experimental and installation settings. Table 1 shows that natural fiber can come from different types of cellulose, animals, and minerals. Every natural fiber category possesses distinct attributes that render it appropriate for diverse purposes. As an illustration, cotton is renowned for its inherent softness and breathability, wool is esteemed for its exceptional insulating properties, and silk is highly regarded for its rich tactile sensation.

A comprehensive comprehension of the origin and characteristics of diverse natural fibers is crucial in selecting appropriate materials for certain applications. The numerous advantages of these natural fibers include cheap cost, flexibility, high strength-to-weight ratios, low densities, high recycling rates, and minimum environmental effect. These have led to their widespread usage throughout the years (Safri et al., 2018). However, selecting suitable processing conditions to enhance the performance of the composites is essential when using natural fibers as reinforcing elements in conjunction with thermoplastics (Kabir et al., 2020; Ngo et al., 2018).

The essential part of the bio-composite manufacturing process is selecting the appropriate natural fiber. The characteristics of the material determine the choice of natural fiber. Natural fiber's effectiveness is heavily dependent on the plant's age. Fibers'

Table 1  
*Sources of natural fibers*

	Group	Fiber	Source
Natural fibers	Animal	Hair	Come from hairy mammals and animals
		Avian	Feathers of birds
		Silk	Dried saliva of bugs or insects
	Cellulose	Bast	Jute, Flax, Hemp, Ramies, Kenaf, Roselle, Mesta
		Leaf	Sisal, Banana, Abaca, Pina
		Seed	Kapok, Cotton, Luffa. Milkweed
		Fruit	Coir, Oil palm
		Wood	Softwood, Hardwood
		Stalk	Rice, Wheat, Barley, Maize, Oat, Rye
		Grass	Bamboo, Bagasse, Corn, Sabai, Rape, Esparto, Cancry
	Mineral	Asbestos cloth	Asbestos
		Glass	Mixed silicates

Source: Gholampour and Ozbakkaloglu (2020)

chemical components varied depending on their origin, but cellulose, hemicellulose, and lignin were among the more prevalent ones (Xanthos, 2005). The internal structure of the cellulose fibers is shown in Figure 2. The fiber reinforcement's physical and chemical characteristics significantly impact the final bio-composite material's qualities. The composition of natural fibers is the primary factor in determining their mechanical qualities (especially the non-cellulosic components like hemicellulose, lignin, waxes, and pectin). Removing these non-cellulosic components from the fiber increases the composite material's

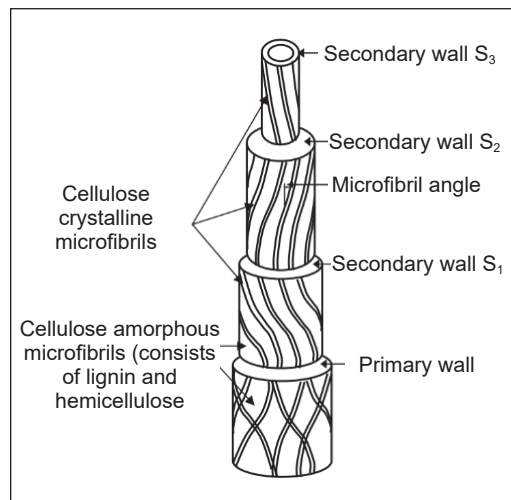


Figure 2. Diagrammatic representation of natural fiber composition (Kabir et al., 2012)

mechanical strength since the bonding ability of the fiber and matrix is not hindered (Vigneshwaran et al., 2020). Due to their hydrophilicity, most natural fibers have poor bonding properties. These advantages may decrease the bio-mechanical composite's strength (Faruk et al., 2012). Natural fibers offer adequate reinforcements in the composite industry for a variety of applications, including those involving transportation, interior components, buildings, airplanes, and the construction sector (Alsubari et al., 2021; Amir et al., 2021; Asyraf et al., 2020; Hanan et al., 2020).

Developing eco-friendly FDM-based natural fiber-reinforced polymer bio-composites has drawn much interest from both industries and researchers. Natural fibers have been viewed as crucial components in the creation of a green and sustainable economy because of their low density, high specific strength and modulus, lighter weight, high affinity, and biodegradability in contrast to glass and other synthetic fiber-reinforced composite materials (Bi & Huang, 2022). In addition, they have drawn a lot of rivals and market platforms (Stoof et al., 2017). Le Duigou et al. (2020) claimed that faults (such as porosity and misalignment), mechanical hygro-thermal deterioration, and residual stress are produced during the manufacturing stages of semi-finished goods (filament), which affect the performance characteristics of composite materials. According to research by Šafka et al. (2016), ABS/Coconut bio-composites have a slightly higher modulus of elasticity (+16%) but much lower strength (-50%) and strain (-15%) when compared to a pure matrix. According to Dong et al. (2018), tensile strength decreased by 60%, Charpy impact strength decreased by 55%, and flexural strength decreased by 60%. PLA-based bio-composites tensile modulus, strength, and impact resistance are all impacted by the addition of cork powder (Daver et al., 2018).

A standard extrusion method using fibers and polymer creates the filament for FDM. More attention is being paid to the extrusion parameters used to make filaments. The filaments were hemp fiber, hemp hurds, bamboo fiber and powder, flax fiber, bagasse fiber, cork powder, cocoa shell, coconut fiber, cotton fiber, wood fiber, wood pulp, wood flour, Harakeke fiber, waste macadamia nutshell (Coppola et al., 2018; Depuydt et al., 2019; Liu et al., 2019; Milosevic et al., 2017; Montalvo Navarrete et al., 2018; Pop et al., 2019; Stoof et al., 2017; Stoof & Pickering, 2018; Xiao et al., 2019). According to Mazzanti et al. (2019), manufacturing filament is a crucial step in the FDM process, and defects at this stage (such as porosity) are passed on to the printed parts. Due to that, design engineers have a difficult choice when attempting to optimize the manufacturing process of a particular design by determining which materials to utilize among the many conceivable fiber and matrix combinations (Noryani et al., 2018).

The attributes of the finished composites rely on their components, for which some data are accessible; moreover, composites do not share the same features as metal-based materials. Thus, design engineers need to proceed with care when selecting materials. In addition, we may fine-tune the composites' attributes by modifying the constituent parts' properties. For this reason, material selection is essential to the manufacturing process since it may save high costs incurred during product design testing. The effectiveness of a substance may be evaluated using several different approaches, and it can be affected by a wide range of variables. The design engineer is responsible for deciding which composite material combinations best achieve the intended design goals. As a result, material selection is a crucial stage in the design process, necessitating attention to product specifications, budget, and ecological impact, as AL-Oqla and Salit (2017) stated.

Therefore, this study aims to use the multi-criteria decision-making (MCDM) strategy with the fuzzy analytical network process (FANP) technique to determine which bio-composite filament material would be ideal for the FDM process. These filaments are the most eco-friendly option since they can be used several times, recycled, and thrown away without harm. The FANP study considered their tensile strength, flexural strength, impact strength, and printability to choose which bio-composite filaments to utilize. Using SuperDecisions V3.X, the FANP material selection algorithm is implemented.

## **MATERIALS AND METHODS**

Material selection is significant in product development, manufacturing, and marketing stages. Nonetheless, the work is time-consuming and requires careful consideration because of several competing criteria. Material selection is often motivated by the need to enhance performance while minimizing costs; however, other variables, such as resistance to failure and reduced weight, may also be powerful motivators (Emovon & Oghenenyero, 2020). If the wrong materials are used, it might be challenging

to meet the needs of both consumers and producers. It may also cause an assembly to fail or a product's performance to degrade, harming productivity, profit, and an organization's credibility.

The MCDM technique is one of the most popular to solve the material selection problem. MCDM offers a systematic procedure that considers the decision criteria and the knowledge of the advantages and disadvantages of the decision-makers to assist in selecting the best choice from a group of options. MCDM tools like the analytical hierarchy process (AHP), the analytical network process (ANP), the Vlse Kriterijumska Optimizacija Kompromisno Resenje (VIKOR), the multi-attribute utility theory (MAUT), the Elimination and Choice Expressing the Reality (ELECTRE), the Preference Ranking Organization Method for Enrichment Evaluations (PROMETHEE), and the technique of ranking preferences by the similarity of the ideal solutions (TOPSIS) have all been used for materials research and development (Emovon & Oghenyerovwho, 2020; Noryani et al., 2018). Using the several criteria for making a choice, each of which can be measured differently, the tools framework ranks the available options. Table 2 provides a comprehensive overview of several well-known MCDM tools, including information on their underlying decision-making principles, inventors, invention dates, advantages and disadvantages.

Table 2  
*Comprehensive overview of MCDM*

MCDM method	Decision-making philosophy	Inventor/Year	Advantages	Disadvantages
AHP	Weighting criteria and options attain optimal results according to importance. Before sorting through possible solutions, the issue is often organized hierarchically.	Thomas Saaty, 1970	There is no need for a separate instrument to calculate criterion weights.	Adding additional criteria and options makes the method more difficult to implement.
ANP	The hierarchical structure of AHP is transformed into a network consisting of components such as criteria, sub-criteria, and alternatives. Feedback and dependency links inside and between clusters connect all network elements.	Thomas Saaty, 1996	Able to prioritize both dependent and independent needs. The outcomes are dependable and error-tolerant. The outcomes are reliable.	The prioritization process is complex. Tool support is needed to minimize the complexity and time consumption while prioritizing requirements.
VIKOR	Finding the best answer by contrasting choices based on how closely they resemble the ideal.	S. Opricovic, 1990	An improved version of TOPSIS.	Conflicting situations provide challenging opportunities for developing and applying methods.

Table 2 (continue)

MCDM method	Decision-making philosophy	Inventor/Year	Advantages	Disadvantages
<b>TOPSIS</b>	It uses distances between the positive and negative solutions to determine preferable ones.	Hwang and Yoon, 1981	The process is simple, and the strategy for finding a solution does not change.	The assessment of Euclidean distance does not consider the connection between the criteria. Additionally, vector normalization could be needed to solve multidimensional problems.
<b>PROMETHEE</b>	It is an outranking strategy for solving decision-making problems considering the divergence of choice concerning decision criteria.	J. P. Brans and P. Vicke, 1982	Score normalization is unnecessary.	A separate method is required for assessing criteria weight. A preference function must also be defined.
<b>ELECTRE</b>	Creates a solution by establishing an outranking connection between two possible choices.	Benayoun Roy, 1968	They can give a solution in the absence of the required information.	The complicated assessment techniques involved make the approach computationally challenging without dedicated software.

Source: Emovon and Oghenenyero, 2020; Kumar et al., 2017

MCDM issues may be solved in several ways, including using the ANP technique. Thomas L. Saaty (1996) created it, using it extensively to solve MCDM issues across several disciplines. It considers a wide range of interactions, relationships, and feedback between higher and lower-level components and makes decisions based on the sometimes-unreliable preferences of humans. Saaty’s ANP has two significant flaws, according to Ayağ and Yücekaya (2019): it is only helpful for simple choice situations and generates and manages a very asymmetrical judgment scale. Furthermore, the ANP technique ranks slightly imprecisely since it does not consider the uncertainty in translating one’s judgment to a number. However, outcomes are heavily influenced by the decision-makers biased assessment, choices, and preferences. To address this shortcoming, “fuzzy ANP” has been suggested, using ANP pairwise comparisons and fuzzy logic.

In 1965, Zadeh created the first iteration of what would become known as a fuzzy set theory to solve the difficulties associated with the study of “fuzzy phenomena,” which include issues of vagueness, ambiguity, and incompleteness (Mohaghar et al., 2012). The FANP approach fits the subjectivity of human judgment as it is conveyed in everyday language. Getting precise conclusions in pairwise comparisons may sometimes be elusive

and unpractical (Senvar et al., 2018). Promentilla (2008) argued that acquiring accurate assessments in pairwise comparisons is difficult due to human judgments' complexity, ambiguity, and intrinsic subjectivity. When making a subjective evaluation, spoken judgments are more accessible or natural. Conventional qualification needs to work on explaining circumstances that seem complicated or complex to characterize adequately. Linguistic variables may be employed. Fuzzy-level language measures are shown in Table 3. It is important to note that the membership function of the linguistic scale is set by the three parameters of the symmetric triangular fuzzy number. In his 2011 article, Balmat explained how fuzzy set theory is an extension of classical set theory that helps solve numerous problems involving inaccurate and uncertain data works. Table 4 outlines the advantages and disadvantages of the theory of fuzzy sets.

There are few examples of research using the FANP method for product creation or choice in the existing literature (Zavadskas et al., 2016). Using the manufacturing of lithium-iron phosphate batteries as an example, Chen et al. (2015) combined a FANP method with interpretative structural modeling (ISM) to assess several new product

Table 3  
The linguistic scales with the fuzzy level scale

Gradients of language	Degree of significance	Fuzzy triangular scale	Triangle-shaped fuzzy-ratio scale	Details
<b>Equally important/significant</b>	1	(1, 1, 1)	(1, 1, 1)	Two actions contribute similarly to the goal.
<b>Intermediate</b>	2	(1, 2, 3)	(1/3, 1/2, 1)	There is a minor advantage in one activity over another, according to experience and judgment.
<b>Moderately important/significant</b>	3	(2, 3, 4)	(1/4, 1/3, 1/2)	
<b>Intermediate</b>	4	(3, 4, 5)	(1/5, 1/4, 1/3)	Based on one's knowledge, experience, and judgment, one activity is superior to another.
<b>Strongly important/significant</b>	5	(4, 5, 6)	(1/6, 1/5, 1/4)	
<b>Intermediate</b>	6	(5, 6, 7)	(1/7, 1/6, 1/5)	Strong preference is shown toward one action over another.
<b>Very strongly important/significant</b>	7	(6, 7, 8)	(1/8, 1/7, 1/6)	
<b>Intermediate</b>	8	(7, 8, 9)	(1/9, 1/8, 1/7)	A fair assumption can be made that one course of action is preferable because of the overwhelming weight of information in its favor.
<b>Extremely important/significant</b>	9	(9, 9, 9)	(1/9, 1/9, 1/9)	

Note that on a reciprocal scale, if nonzero values were given into the i activity above, compare it to activity j, and the j would have the typical value.

Source: Bathaei et al. (2019); Senvar et al. (2018)

Table 4

*Advantages and disadvantages of fuzzy set theory*

<b>Advantages</b>	<b>Disadvantages</b>
Fuzzy logic considers uncertainty and the development of current understanding.	Creating a reliable fuzzy system is not always straightforward.
Fuzzy logic allows imprecise input.	It needs to be tested in a virtual environment before being employed in the real world.
Fuzzy logic permits a small number of rules to cover a wide range of complexity.	

*Source:* Velasquez and Hester (2013); Balmat (2011)

development approaches. Based on a FANP assessment technique, Senvar et al. (2018) provided a strategy for choosing the best renewable energy investment project. Ayağ and Yücekaya (2019) suggested using the FANP and the grey relational analysis (GRA), two of the most used MCDM approaches, to assess various ERP software options. Many studies have recently focused on integrating QFD with MCDM and fuzzy logic. To establish essential technical qualities that would improve the quality of a suggested wheelchair, Mistarihi et al. (2020) combined the QFD model with the FANP technique.

The significance of the FANP method is shown by using two real-world examples involving the selection of materials for turbine blades, and the rankings of the available materials are provided. The first scenario involves evaluating the best material for a wind turbine blade out of five possibilities (steel, aluminum, e-glass, carbon, and aramid) based on five characteristics (stiffness, tensile strength, density, elongation at break, and minimum temperature) (Babu et al., 2006). In contrast, Thakker et al. (2008) evaluated the properties of eight materials: titanium alloy, nickel alloy, aluminum alloy, glass fiber-reinforced plastics, silicon nitride, copper alloy, stainless steel, and carbide across four dimensions to identify the optimal material for a wave energy turbine blade. Another case in point is the recommendation of FANP to choose the optimal material for a super-critical boiler by Maity and Chakraborty (2012a), who emphasized the need to consider the interplay and interdependencies of the many variables involved in this process.

Several published works have attempted to include the FANP method in the product development/selection process; however, customer needs-to-engineering characteristics mapping has yet to be made, and a single criteria decision-making strategy has always been used. The primary contribution of this work is that it is the first to apply the FANP method to pick bio-composite materials, specifically FDM filaments. SuperDecision V3.X's algorithm was used to determine the weighted average of each pairwise comparison matrix.

Data collection is crucial to every research project since it yields information. The information provided should be as thorough as possible to provide accurate results. The data on the criteria and sub-criteria were all gathered from reliable sources as a result. The methodology steps are shown in Figure 3. The following phases were involved in

implementing the suggested FANP model. The first phase was to specify the primary objective and available alternatives for choosing the best bio-composite material for filaments that comply with the FDM process specifications. The information chose the possibilities for bio-composite filament materials from previous studies that were readily available. After that, the mechanical properties analysis from several technical references was used to establish the FANP model's criteria. Natural fiber is crucial in producing bio-composite filaments with improved mechanical qualities, including tensile strength, flexural strength, impact strength, toughness, durability, and hardness (Rajendran Royan et al., 2021).

The second phase was choosing the essential material selection criterion. To do this, a questionnaire that included the material's primary selection criteria was created and distributed to experts. The critical criteria were categorized based on the findings of the first phase, and the experts suggested the final criteria for the second session. Experts then organized the last criteria, connections, and interdependencies between the elements for use in the FANP model. The FANP model was created in three phases (Figure 4).

Professor Saaty made the first proposal for the ANP in 1996. For ANP to be able to study systems with impact and feedback, the concepts of indirect priority and supermatrix

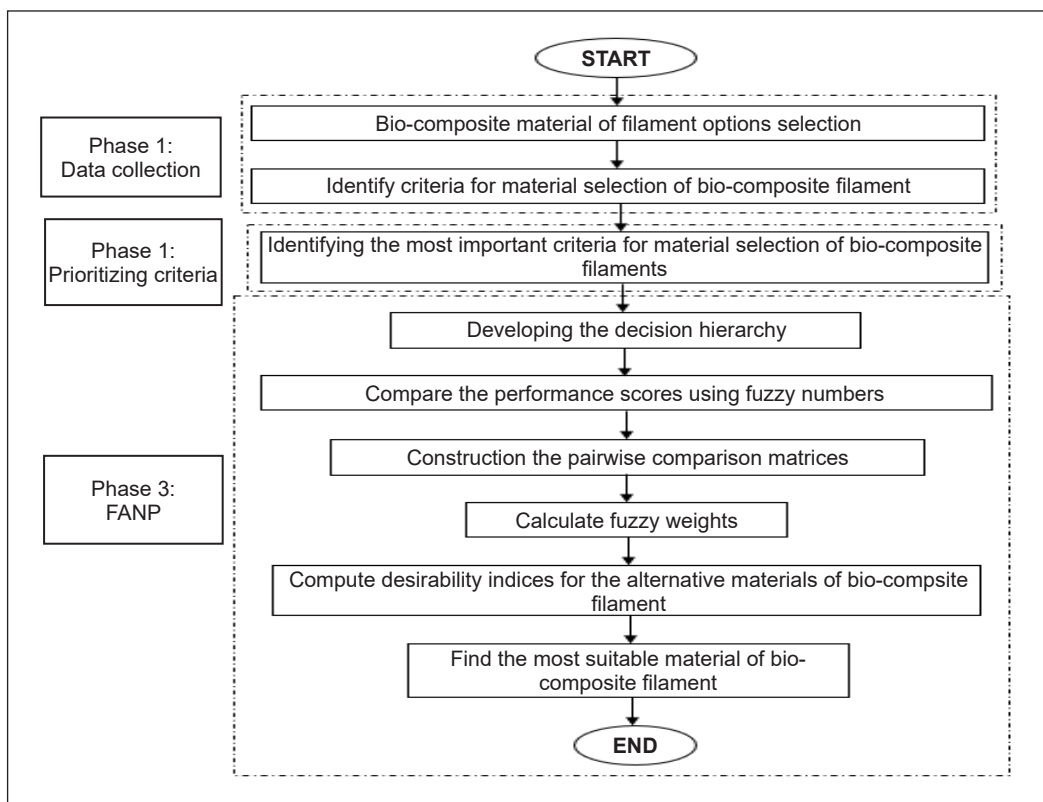


Figure 3. The fundamental structure of the best-suggested model of a bio-composite filament for use in material selection

are brought into play (Maity & Chakraborty, 2012b). There are two layers in an ANP network: control and network. Goals and independent principles, or only one objective, are included in the control layer. Groups of objects that communicate with one another make up the network layer.

The FANP expands upon the conventional approach suggested in this study. How the comparison matrix is constructed and solved is the primary distinction between FANP and ANP. The enhanced technique generates the linguistic variable-fuzzy number table as the basis for the fuzzy comparison matrix. The fuzzy preference programming (FPP) algorithm calculates the weight vector using the suggested FANP approach. Following are the steps that can be utilized to analyze the predicted performance of various kinds of bio-composite filaments using the FANP method:

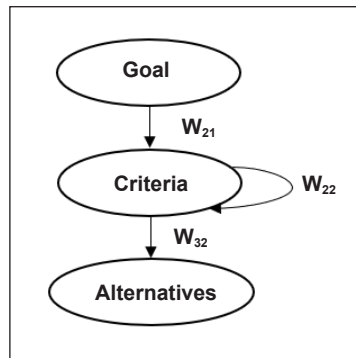


Figure 4. The proposed FANP model

**Step 1: Creating the Fuzzy Comparison Matrix**

It was assumed that there was only one target *G* in the control layer and that there were *N* element groups (*C*<sub>1</sub>, *C*<sub>2</sub>, ..., *C*<sub>*N*</sub>) in the network layer. Experts, *k* were asked to evaluate the relative effects of elements *SC*<sub>*i*1</sub>, *SC*<sub>*i*2</sub>, ..., *SC*<sub>*i**m*</sub> in group *C*<sub>*i*</sub> (*i* = 1, 2, ..., *N*) on elements *SC*<sub>*jl*</sub> (*l* = 1, ..., *n*<sub>*j*</sub>), with *SC*<sub>*jl*</sub> as the primary criterion and target *G* as the secondary criterion. From what the *k* experts said, a fuzzy judgment matrix was made. Each element was first shown as a linguistic variable. Then, the formula in Table 3 turned it into a triangular fuzzy number. The fuzzy comparison matrix then looked like what is shown in Table 5.

Table 5  
Fuzzy comparison matrix

<i>SC</i> <sub><i>jl</i></sub>	<i>SC</i> <sub><i>i</i>1</sub>	<i>SC</i> <sub><i>i</i>2</sub>	...	<i>SC</i> <sub><i>i</i><i>n</i></sub>
<i>SC</i> <sub><i>i</i>1</sub>	<i>e</i> <sub><i>i</i>11</sub>	<i>e</i> <sub><i>i</i>12</sub>	...	<i>e</i> <sub><i>i</i>1<i>n</i></sub>
<i>SC</i> <sub><i>i</i>2</sub>	<i>e</i> <sub><i>i</i>21</sub>	<i>e</i> <sub><i>i</i>22</sub>	...	<i>e</i> <sub><i>i</i>2<i>n</i></sub>
.	.	.	.	.
.	.	.	.	.
.	.	.	.	.
<i>SC</i> <sub><i>i</i><i>n</i></sub>	<i>e</i> <sub><i>i</i><i>n</i>1</sub>	<i>e</i> <sub><i>i</i><i>n</i>2</sub>	...	<i>e</i> <sub><i>i</i><i>n</i><i>n</i></sub>

Source: Pang et al. (2021)

**Step 2: Calculate the Comparative Synthetic Matrix**

Expert opinions were put together in this work using an average geometric method. This medium eliminated the effect of combining opinions on the reliability of the comparison

matrix. In  $C_i$  ( $i = 1, 2, \dots, N$ ), the elements  $SC_{iu}$  and  $SC_{iv}$  were compared, and the results were shown as  $(l_{iuv}, m_{iuv}, u_{iuv})$ . Using the fuzzy number's lower limit,  $l_{iuv}$ , as an example, below is the formula for determining  $l_{iuv}$  (Equation 1):

$$l_{iuv} = (l_{iuv}^{(1)} \times l_{iuv}^{(2)} \times \dots \times l_{iuv}^{(k)})^{1/k} \quad [1]$$

### Step 3: Compute the Weight Vector Using the FPP Technique

The weight of elements  $SC_{iu}$  and  $SC_{iv}$  were denoted by  $w_u$  and  $w_v$ , respectively. Equation 2 determines the membership degree of  $(w_u / w_v)$ , and  $s_{iuv}$  stands for the unity between the solution weight and expert opinion.

$$s_{iuv} \left( \frac{w_u}{w_v} \right) = \begin{cases} \frac{w_u/w_v - l_{iuv}}{m_{iuv} - l_{iuv}}, & \frac{w_u}{w_v} \leq m_{iuv} \\ \frac{u_{iuv} - (w_u/w_v)}{u_{iuv} - m_{iuv}}, & \frac{w_u}{w_v} \geq m_{iuv} \end{cases} \quad s_{iuv} \left( \frac{w_u}{w_v} \right) = \begin{cases} \frac{w_u/w_v - l_{iuv}}{m_{iuv} - l_{iuv}}, & \frac{w_u}{w_v} \leq m_{iuv} \\ \frac{u_{iuv} - (w_u/w_v)}{u_{iuv} - m_{iuv}}, & \frac{w_u}{w_v} \geq m_{iuv} \end{cases} \quad [2]$$

### Step 4: Create the Unweight Supermatrix

The weight vector  $(w_{i1}^{(j1)}, w_{i2}^{(j2)}, \dots, w_{ini}^{(jl)})^T$  of the judgment matrix was constructed. In this case, the column vector denoted the weight vector of the impacts of components  $SC_{jl}$  ( $l = 1, \dots, n_j$ ) in  $C_i$  on elements  $SC_{i1}, SC_{i2}, \dots, SC_{ini}$ . They observed that the submatrix  $W_{ij}$  was computed using Equation 3.

$$W_{ij} = \begin{bmatrix} w_{i1}^{(j1)} & w_{i1}^{(j2)} & \dots & w_{i1}^{(jn_j)} \\ w_{i2}^{(j1)} & w_{i2}^{(j2)} & \dots & w_{i2}^{(jn_j)} \\ \vdots & \dots & \ddots & \vdots \\ w_{ini}^{(j1)} & w_{ini}^{(j2)} & \dots & w_{ini}^{(jn_j)} \end{bmatrix} \quad W_{ij} = \begin{bmatrix} w_{i1}^{(j1)} & w_{i1}^{(j2)} & \dots & w_{i1}^{(jn_j)} \\ w_{i2}^{(j1)} & w_{i2}^{(j2)} & \dots & w_{i2}^{(jn_j)} \\ \vdots & \dots & \ddots & \vdots \\ w_{ini}^{(j1)} & w_{ini}^{(j2)} & \dots & w_{ini}^{(jn_j)} \end{bmatrix} \quad [3]$$

$W_{ij} = 0$  if the elements in  $C_i$  did not affect  $C_j$ . The following formula was the unweighted supermatrix,  $W$ , made up of the sub-matrix (Equation 4):

$$W = \begin{matrix} & \begin{matrix} 1 & \dots & n_1 & 1 & \dots & n_2 & \dots & 1 & \dots & n_N \end{matrix} \\ \begin{matrix} 1 & \dots & n_1 \\ 1 & \dots & n_2 \\ \dots \\ 1 & \dots & n_N \end{matrix} & \begin{bmatrix} W_{11} & W_{12} & \dots & W_{1N} \\ W_{21} & W_{22} & \dots & W_{2N} \\ \vdots & \dots & \ddots & \vdots \\ W_{N1} & W_{N2} & \dots & W_{NN} \end{bmatrix} \end{matrix} \quad [4]$$

### Step 5: Create the Weighted Supermatrix $\overline{W}$ and Determine the Weighing Matrix $A$

$W$  still has to be column normalized even if the sub-matrix  $W_{ij}$  had already been done. On element group  $C_j$  ( $j = 1, 2, \dots, N$ ), the influence degree of element group  $C_i$  ( $i = 1, 2, \dots, N$ ) was

compared. A fuzzy comparison matrix was created using target G as the criteria and element group  $C_j$  ( $j = 1, 2, \dots, N$ ) as the sub-criterion. The FPP method created the weight vector for the judgment matrix  $(a_1^{(j)}, a_2^{(j)}, \dots, a_N^{(j)})^T$  ( $j = 1, 2, \dots, N$ ).  $a_1^{(j)}, a_2^{(j)}, \dots, a_N^{(j)}$  ( $j = 1, 2, \dots, N$ ). The weight of the element group  $C_i$  ( $i = 1, 2, \dots, N$ ) impact on element group  $C_j$  ( $j = 1, 2, \dots, N$ ) was shown in this case by the column vector. A computation was conducted, which is noteworthy (Equation 5), to generate the weighting matrix.

$$A = \begin{matrix} C_1 \\ C_2 \\ \dots \\ C_N \end{matrix} \begin{bmatrix} a_1^{(1)} & a_1^{(2)} & \dots & a_1^{(N)} \\ a_2^{(1)} & a_2^{(2)} & \dots & a_2^{(N)} \\ \vdots & \dots & \ddots & \vdots \\ a_N^{(1)} & a_N^{(2)} & \dots & a_N^{(N)} \end{bmatrix} \tag{5}$$

**Step 6: Compute the Super-weighted Matrix,  $\bar{W} = (a_i^{(j)} w_{ij}). \bar{W} a_i^{(j)} w_{ij}$**

**Step 7: Determine the Limit Supermatrix**

Assuming there were  $T$  indications at the network layer, a one-step priority ordering can be represented by the element  $w_{pq}$  in  $\bar{W}, w_{pq} \bar{W}$ , which indicated the degree to which indicator  $p$  ( $p = 1, 2, \dots, T$ ) influenced indicator  $q$  ( $q = 1, 2, \dots, T$ ). Another way to determine  $p$ 's influence on  $q$  is using the two-step priority formula  $\sum_{k=1}^T w_{pk} w_{kq}, \sum_{k=1}^T w_{pk} w_{kq}$ , where  $p$  and  $q$  are vectors. If there is a limit matrix  $\bar{W}^\infty = \lim_{t \rightarrow \infty} \bar{W}^t, \bar{W}^\infty \lim_{t \rightarrow \infty} \bar{W}^t$ , then the column vector in  $\bar{W}^\infty \bar{W}^\infty$  is the weight vector of all indicators in the network layer aiming for  $G$ .

**Step 8: Compute the Total Worth Assessment**

Experts were polled to rate potential unit schemes in terms of  $T$  indicators using this method. The final assessment value was calculated by multiplying the weight vector by the experts' ratings.

Sensitivity analysis has been increasingly prevalent in engineering and research, as it is considered an essential procedure for evaluating the feasibility of a model or approach (Ionescu-Bujor & Cacuci, 2004). Conducting a sensitivity analysis of the FANP approach is crucial to ascertain the stability of the derived order of preference. According to Saltelli et al. (2005), sensitivity determines the extent to which a certain model, whether numerical or otherwise, is influenced by its input factors. Li et al. (2013) conducted a sensitivity analysis on the criteria weights for the TOPSIS technique used to evaluate water quality. Their findings suggest that the TOPSIS approach is suitable for this purpose, as it demonstrates sensitivity to changes in the criteria weights. The stability of the derived order of preference for this study was assessed using a similar technique, with a little adjustment in the criteria weights. The weights assigned to the criterion were manipulated to evaluate the sensitivity of the FANP analysis. In this context, a perturbation is defined as introducing a disturbance of the

criteria weights  $\omega_k$ , where  $k$  ranges from 1 to  $n$ . The perturbed criteria weights are denoted as  $\acute{\omega}_k$ . The relationship between  $\omega_k$  and  $\acute{\omega}_k$  is formally expressed as the unitary ratio  $\beta_k$ . This study employed seven variations of the  $\beta_k$  method, with  $\beta_k$  values of 0.01, 0.02, 0.05, 0.1, 0.2, 0.5, and 1.0. Following the adjustment of weights resulting from adopting  $\beta_k$ , a reevaluation of performance scores and rankings was conducted, allowing for a comparative analysis. The criteria weights were systematically manipulated over time, resulting in disruptions. Subsequently, the resulting variations in rankings were examined for each case.

## RESULTS AND DISCUSSION

Fabricating bio-composite filament entails adding reinforcement and matrix ingredients to a printed filament. Here, the matrix material will be one of the 3D printed polymeric materials, such as PLA, ABS, and nylon, and the reinforcing material may be continuous or discontinuous fibers. While the matrix shields the reinforcing material from toxic environments like abrasion, the reinforcement provides filament strength and stiffness. According to Matsuzaki et al. (2016), the choice of matrix and reinforcing materials should be made in a manner that both are compatible in terms of physical adhesion, chemical inertness, and comparable thermal expansion coefficients. Because there are so many different materials, choosing the ideal one requires the design engineers to spend significant time and money. As a result, FANP may be regarded as the most practical method to tackle this issue since it can handle the interactions and interdependencies between the selection criteria under consideration. Therefore, the relevant decision matrix in Table 6 was created to apply the FANP technique to this bio-composite filaments material selection issue and demonstrate its viability.

This selection matrix includes ten bio-composite filaments and four main selection criteria. The values of all criteria in Table 6 are derived from data acquired from conducted assessments. Table 7 lists the specifics of these four selection criteria.

The interfacial adhesion between the resin and fibers profoundly influences the

Table 6  
*Decision matrix for bio-composite filaments material selection problem*

SI No.	C1	C2	C3	C4
A1	20.9	36.5	12586.6	760
A2	19.2	39.2	12291.3	840
A3	20.7	42.4	6568.4	800
B1	37.9	68.2	10084.8	760
B2	27.8	39.5	4913.4	840
B3	33.9	49.7	11485.9	988
C1	20.6	14.4	31293	852
C2	16.4	12.1	25963.2	918
D1	21.5	18.2	30852.9	852
D2	20.4	16.7	31683	918

Table 7  
*Criteria for bio-composite filaments material selection*

Properties of bio-composite filament materials	Symbol
Tensile strength, MPa	C1
Flexural strength, MPa	C2
Impact strength, kJ/m <sup>2</sup>	C3
Printability, mm	C4

tensile characteristics of bio-composites. Both physical and chemical modifications of the fiber and resin can improve the tensile characteristics of composites. The tensile characteristics of bio-composites are susceptible to the fiber volume fraction in the matrix resin (Gholampour & Ozbakkaloglu, 2020). When the volume percentage of the fibers is increased below the optimal amount, the load is distributed to more fibers. The matrix can support the applied stress even after the fibers have fractured. The tensile characteristics of composites typically increase with increasing fiber volume percentage. However, some studies have indicated otherwise. This fiber volume fraction can increase the composite's tensile strength (Ku et al., 2011). One of the most critical measures of a composite's durability is its flexural stiffness, which indicates how well it can withstand deformation when bent (Faruk et al., 2012). The composite material's modulus and moment of inertia are significant in determining its flexural characteristics. Optimal fiber composition in bio-composites has the potential to increase their flexural strength. Defects in the wetting of fibers may cause stress concentration areas in composites, which reduces the flexural strength as the fiber content grows further. Composites' flexural modulus also improves as their fiber content rises.

Bio-composites' behavior is very sensitive to the degree of bonding between the matrix and fiber. Bio-composites rely heavily on this characteristic during their useful lives. Techniques of modification can be used to enhance the impact characteristics of bio-composites. Bumps, collisions, and falling items or debris may all contribute to impact loading. Compatibility of bonding, fiber pull-out, energy absorption, and adhesiveness are all factors that affect the impact resistance of composites. The quality of an FDM print job depends on the filaments' feedability or how easily they can be fed into the printing head and melted there (Nasereddin et al., 2018). The filament in FDM printers is fed by being pushed between two counter-rotating gears. The printing head may jam if the filament is too fragile to resist the mechanical stress of compression and pressing. It will wrap as it is moved forward, reblocking the head if it is too pliable.

Alternative bio-composite filament materials are listed in detail in Table 8. Powdered kenaf (*Hibiscus cannabinus*) fibers and ABS pellets made from 100 % pure ABS were provided. Han et al. (2022) employed kenaf fibers with a mean length of 120  $\mu\text{m}$ . The 1.75 mm diameter filament was produced by compounding kenaf fiber and ABS pellets in an HTGD-20 twin screw extruder. Different kenaf fiber-reinforced ABS (KRABS) composite volume percentages were used: 0%, 2.5%, 5%, 7.5%, and 10%.

The sugar palm fiber (*Arenga Pinnata*) was sourced from Jempol, Negeri Sembilan's rainforests on the western peninsular of Malaysia (Nasir et al., 2022). Sugar palm plants were used to create SPF after being cut into 1/3-centimeter pieces; the long fiber was washed under running water to remove leftover dirt and filth. Polylactic acid (PLA) was employed as the polymer matrix with a 1.24 g/cm<sup>3</sup> density. Pellets of Ingeo™ Biopolymer

2003D (pure, 100% PLA), Acetic acid (glacial), methanol, sodium hydroxide pellets for EMSURE® analysis and 3-Aminopropyl triethoxysilane were provided. Lab Tab Engineering Company Ltd., located in Muang, Samutprakarn, Thailand, supplied the twin screw extruder used for the extrusion process, which rotated at 70 rpm and included 26 mm twin screws with a 40:1 L/D. A sugar palm fiber/PLA (SPF/PLA) composite sample was fed into the barrel of a twin-screw extruder. Before entering the twin screw, the mixing mechanism thoroughly combined the SPF particles and PLA pellets, which were transported to the melting chamber and extruded via a die.

There is potential for recycling and reusing wood fibers, with industry sectors like woodworking and papermaking being the sources. Pine grove and tongue wood are the primary types of scrap wood generated by SME furniture factories (Nahfis et al., 2022; Azali et al., 2022). Plastic manufacturing tiny 2 mm pellets were purchased as a source of recycled PP polymer that was separated into three fiber loadings of 1%, 3%, and 5% for wood dust and sized between 1.5–1.75 mm. Recycled wood PP polymer (r-WoPPC) was produced utilizing a LABTECH twin screw extruder, resulting in composites of covalently linked fiber with polymers in filament form suitable for FDM commercial use. Coir, or coconut fiber, is a natural fiber extracted from coconut husk and processed into bales after washing.

The fibrous husk (mesocarp) of the coconut (*Cocos Nucifera*) on the coconut palm, which is a member of the palm family (Palme), is processed to produce coconut fiber, which is classified as a fiber/fibrous substance (Reddy, 2013). The number 5 in the resin identification code indicates that polypropylene can be recycled (Ariffadzilah et al., 2022). The matrix and fibers work together to produce a biodegradable material that is both ecologically friendly and recyclable; this filament is made from polypropylene reinforced with coconut fiber. The coconut husk was selected because it is readily available and has desirable fiber characteristics, as determined by surveys of the local populace in Malaysia.

For use in the FANP model, a complete set of criteria was established, together with their interconnections and dependencies. The finalized FANP model consisted of three distinct components (Figure 5). The remaining dependencies in the model between the control criteria and the hierarchy network between the four fundamental criteria and the alternatives are shown in Figure 6.

The decision matrix from Table 6 was transformed into the fuzzy decision matrix from Table 9 using the triangular fuzzy

Table 8  
*Bio-composite filament materials*

Fiber	Polymer	Fiber loading (%)	Symbol
<b>Kenaf</b>	ABS	2.5	A1
		5	A2
		7.5	A3
<b>Sugar palm</b>	PLA	2.5	B1
		5	B2
		7.5	B3
<b>Wood dust</b>	r-PP	3	C1
		5	C2
<b>Coconut husk</b>	PP	3	D1
		5	D2

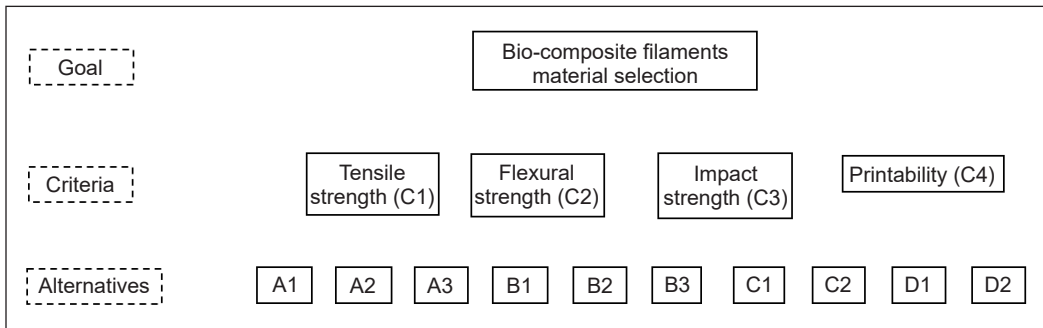


Figure 5. FANP model

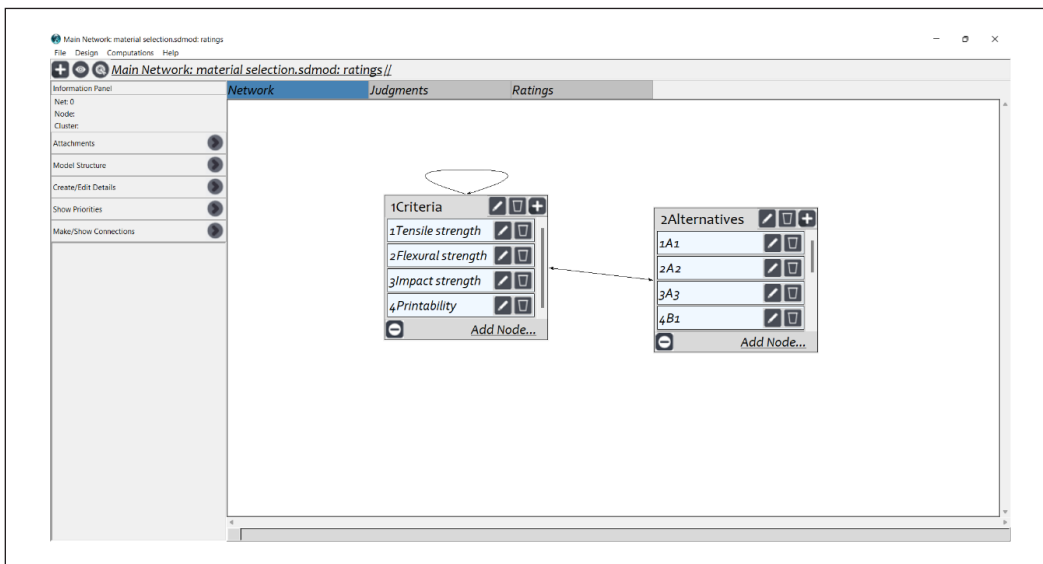


Figure 6. Network structure of the bio-composite filament material selection problem

Table 9

Fuzzy decision matrix for bio-composite filament material selection problem

SI. No.	C1	C2	C3	C4
A1	(15.3, 20.9, 24.6)	(29.1, 36.5, 47.4)	(6099.4, 12586.6, 18816)	(600, 760, 1000)
A2	(11.6, 19.2, 26.4)	(25.8, 39.2, 46.8)	(8219.9, 12291.3, 20697.8)	(600, 840, 1000)
A3	(18.2, 20.7, 21.7)	(36.2, 42.4, 46.3)	(4819.4, 6568.6, 7964.3)	(600, 800, 1000)
B1	(28.2, 37.9, 43)	(60.9, 68.2, 82.6)	(7432.9, 10084.8, 13517.4)	(600, 760, 1000)
B2	(14.9, 27.8, 37)	(29.8, 39.5, 51.4)	(2354.4, 4913.4, 8135.4)	(600, 840, 1000)
B3	(23.7, 33.9, 61.2)	(27.6, 49.7, 63.8)	(9128.4, 11485.9, 15300)	(960, 988, 1000)
C1	(19.4, 20.6, 22.4)	(5.3, 14.4, 18.7)	(8108.1, 31293, 89172.4)	(750, 852, 970)
C2	(13.7, 16.4, 17.3)	(2.4, 12.1, 23.1)	(12483.9, 25963.2, 40092.5)	(800, 918, 1000)
D1	(18, 21.5, 25.8)	(13.3, 18.2, 25.8)	(18984.4, 30852.9, 43386.4)	(750, 852, 970)
D2	(17.1, 20.4, 24)	(15.1, 16.7, 20)	(3004.6, 31683, 46133.3)	(800, 918, 1000)

membership function to solve the bio-composite filament material selection issue via the FANP approach. Priority vectors were created by constructing a pairwise comparison matrix for the selection criteria under consideration, as illustrated in Table 10. There was a clear hierarchy of material properties, with impact strength and printability of the potential material coming in first, then flexural strength.

After this, four pairwise comparison matrices of criteria were built to consider the interdependency connection between the four selection criteria (Figures 7, 8, 9 and 10). It is necessary to use the priority vectors of the pairwise comparison matrices for various criteria to create the supermatrix, highlighting the significance of the other criteria.

Table 10  
Various criteria pairwise comparison matrix

Criteria	C1	C2	C3	C4	Priority vector
C1	(1, 1, 1)	(1/3, 1/2, 1)	(1/4, 1/3, 1/2)	(1/4, 1/3, 1/2)	0.106
C2	(1, 2, 3)	(1, 1, 1)	(1/4, 1/3, 1/2)	(1/4, 1/3, 1/2)	0.151
C3	(2, 3,4)	(2, 3, 4)	(1, 1, 1)	(1, 1, 1)	0.371
C4	(2, 3, 4)	(2, 3, 4)	(1, 1, 1)	(1, 1, 1)	0.371

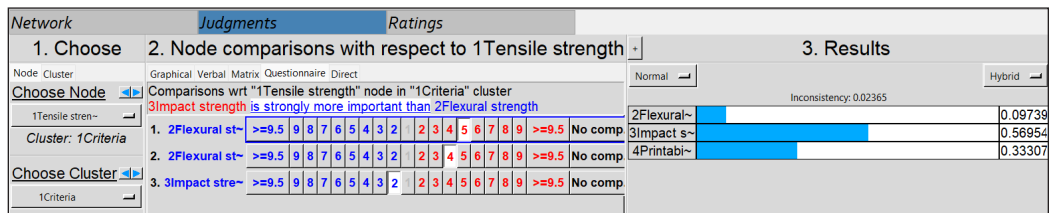


Figure 7. Comparison matrix for ‘tensile strength’ that compares several criteria in terms of their pairwise similarities and differences

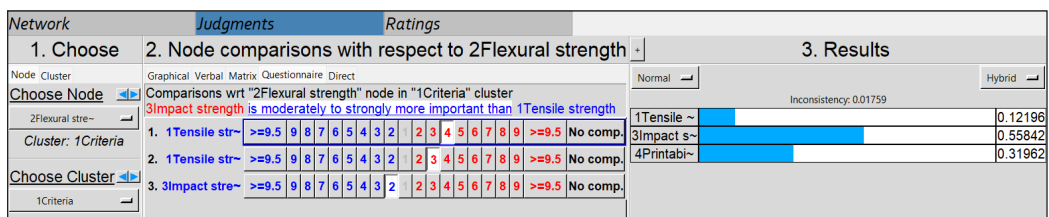


Figure 8. Matrix of pairwise comparisons based on several measures of ‘flexural strength’

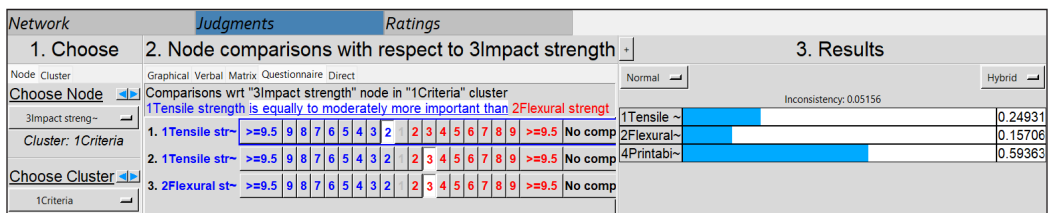


Figure 9. Impact strength comparison matrix with any criteria

Network		Judgments	Ratings																			
1. Choose		2. Node comparisons with respect to 4Printability				3. Results																
Node Cluster	Graphical Verbal Matrix Questionnaire Direct				Normal	Hybrid																
Choose Node	Comparisons wrt "4Printability" node in "1Criteria" cluster				Inconsistency: 0.01759																	
4Printability	2Flexural strength is equally to moderately more important than 1Tensile streng				1Tensile ~	0.13650																
Cluster: 1Criteria	1. 1Tensile str~	>=9.5	9	8	7	6	5	4	3	2	2	3	4	5	6	7	8	9	>=9.5	No com	2Flexural~	0.23849
Choose Cluster	2. 1Tensile str~	>=9.5	9	8	7	6	5	4	3	2	2	3	4	5	6	7	8	9	>=9.5	No com	3Impact s~	0.62501
1Criteria	3. 2Flexural st~	>=9.5	9	8	7	6	5	4	3	2	2	3	4	5	6	7	8	9	>=9.5	No com		

Figure 10. Various printability measures are compared in a pairwise matrix

Pairwise comparison matrices were built for the materials under consideration to determine the nature of the interdependency between the alternatives, with each matrix displaying the relevance of a particular criterion. In this step, the unweighted supermatrix was figured out when all comparisons and weighting produced were completed (Table 11).

Before determining the limit, the unweighted supermatrix should be reduced to a matrix with each column sum equalling unity. This matrix is then referred to as a stochastic column matrix. The normalized or weighted supermatrix was made by multiplying stochastic matrices several times in a row until the column in each block settles and becomes the same (Table 12).

A limited supermatrix is made by multiplying each block until the columns are stable and identical. It is necessary to normalize them to keep the unweighted supermatrix's columns' randomness. Then, the overall priorities can be decided by setting the normalized supermatrix to a limiting power. Each element in a row was ranked according to significance by the value that defined it. It was found that the selection issue was affected by the best option that met the greatest priority overall, which was also the selection criteria with the highest priority overall. The limited supermatrix would be obtained using the normalized supermatrix's 19<sup>th</sup> power. The limited supermatrix can be seen in Table 13.

The supermatrix is boosted to a high enough power until convergence occurs. The supermatrix was then increased to limit power to be  $W^{2n+1}W^{2n+1}$ , yielding a steady-state outcome, with  $n$  being an arbitrarily huge number that included all interactions. The next step was to choose the choice with the highest overall relevance. The absolute priority for alternatives was presented, and the alternative with the most significant value was selected as the best alternative to normalizing every column in the restricted supermatrix. Table 14 normalized values of the alternatives demonstrated that SPF/PLA 7.5 wt.% with 19.80% importance was the best material for bio-composite filaments in the FDM process. In other words, SPF/PLA 7.5 wt.% with 20% importance was chosen as the best bio-composite filament material of FDM for the egg carton packaging project after the FANP method was used for the issue under consideration. The sequence of the criteria according to the priority is shown in Figure 11.

Table 11  
The unweighted supermatrix

Clusters	Nodes	C1	C2	C3	C4	A1	A2	A3	B1	B2	B3	C1	C2	D1	D2
<b>Criteria</b>	C1	0	0.122	0.2493	0.1365	0.305	0.305	0.305	0.305	0.305	0.305	0.305	0.305	0.305	0.305
	C2	0.0974	0	0.1571	0.2385	0.1131	0.1131	0.1131	0.1131	0.1131	0.1131	0.1131	0.1131	0.1131	0.1131
	C3	0.5695	0.5584	0	0.625	0.305	0.305	0.305	0.305	0.305	0.305	0.305	0.305	0.305	0.305
	C4	0.3331	0.3196	0.5936	0	0.2469	0.2469	0.2469	0.2469	0.2469	0.2469	0.2469	0.2469	0.2469	0.2469
<b>Alternatives</b>	A1	0.0741	0.0785	0.0579	0.0174	0	0	0	0	0	0	0	0	0	0
	A2	0.0376	0.0923	0.0596	0.0524	0	0	0	0	0	0	0	0	0	0
	A3	0.0614	0.1039	0.0248	0.0274	0	0	0	0	0	0	0	0	0	0
	B1	0.2499	0.3847	0.0407	0.0174	0	0	0	0	0	0	0	0	0	0
	B2	0.1358	0.0923	0.0178	0.0524	0	0	0	0	0	0	0	0	0	0
	B3	0.2295	0.1624	0.0358	0.3775	0	0	0	0	0	0	0	0	0	0
	C1	0.0523	0.0213	0.2218	0.059	0	0	0	0	0	0	0	0	0	0
	C2	0.0263	0.0193	0.1341	0.1687	0	0	0	0	0	0	0	0	0	0
D1	0.0864	0.0238	0.2037	0.059	0	0	0	0	0	0	0	0	0	0	
D2	0.0469	0.0217	0.2037	0.1688	0	0	0	0	0	0	0	0	0	0	

Table 12  
The weighted supermatrix

Clusters	Nodes	C1	C2	C3	C4	A1	A2	A3	B1	B2	B3	C1	C2	D1	D2
<b>Criteria</b>	C1	0	0.061	0.1274	0.0683	0.305	0.305	0.305	0.305	0.305	0.305	0.305	0.305	0.305	0.305
	C2	0.0487	0	0.0785	0.1192	0.1131	0.1131	0.1131	0.1131	0.1131	0.1131	0.1131	0.1131	0.1131	0.1131
	C3	0.2848	0.2792	0	0.3125	0.305	0.305	0.305	0.305	0.305	0.305	0.305	0.305	0.305	0.305
	C4	0.1665	0.1598	0.2968	0	0.2769	0.2769	0.2769	0.2769	0.2769	0.2769	0.2769	0.2769	0.2769	0.2769
<b>Alternatives</b>	A1	0.037	0.0392	0.0289	0.0087	0	0	0	0	0	0	0	0	0	0
	A2	0.0188	0.0461	0.0298	0.0262	0	0	0	0	0	0	0	0	0	0
	A3	0.0307	0.052	0.0124	0.0137	0	0	0	0	0	0	0	0	0	0
	B1	0.1249	0.1923	0.0204	0.0087	0	0	0	0	0	0	0	0	0	0
	B2	0.0679	0.0461	0.0089	0.0262	0	0	0	0	0	0	0	0	0	0

Table 12 (continue)

Clusters	Nodes	C1	C2	C3	C4	A1	A2	A3	B1	B2	B3	C1	C2	D1	D2
B3		0.1147	0.0812	0.0179	0.1887	0	0	0	0	0	0	0	0	0	0
C1		0.0262	0.0106	0.1109	0.0295	0	0	0	0	0	0	0	0	0	0
C2		0.0131	0.0096	0.067	0.0844	0	0	0	0	0	0	0	0	0	0
D1		0.0432	0.0119	0.1019	0.0295	0	0	0	0	0	0	0	0	0	0
D2		0.0234	0.0108	0.1019	0.0844	0	0	0	0	0	0	0	0	0	0

Table 13  
The limit supermatrix

Clusters	Nodes	C1	C2	C3	C4	A1	A2	A3	B1	B2	B3	C1	C2	D1	D2
<b>Criteria</b>	C1	0.1494	0.1494	0.1494	0.1494	0.1494	0.1494	0.1494	0.1494	0.1494	0.1494	0.1494	0.1494	0.1494	0.1494
	C2	0.0869	0.0869	0.0869	0.0869	0.0869	0.0869	0.0869	0.0869	0.0869	0.0869	0.0869	0.0869	0.0869	0.0869
	C3	0.2308	0.2308	0.2308	0.2308	0.2308	0.2308	0.2308	0.2308	0.2308	0.2308	0.2308	0.2308	0.2308	0.2308
	C4	0.1996	0.1996	0.1996	0.1996	0.1996	0.1996	0.1996	0.1996	0.1996	0.1996	0.1996	0.1996	0.1996	0.1996
<b>Alternatives</b>	A1	0.0174	0.0174	0.0174	0.0174	0.0174	0.0174	0.0174	0.0174	0.0174	0.0174	0.0174	0.0174	0.0174	0.0174
	A2	0.0189	0.0189	0.0189	0.0189	0.0189	0.0189	0.0189	0.0189	0.0189	0.0189	0.0189	0.0189	0.0189	0.0189
	A3	0.0147	0.0147	0.0147	0.0147	0.0147	0.0147	0.0147	0.0147	0.0147	0.0147	0.0147	0.0147	0.0147	0.0147
	B1	0.0418	0.0418	0.0418	0.0418	0.0418	0.0418	0.0418	0.0418	0.0418	0.0418	0.0418	0.0418	0.0418	0.0418
	B2	0.0214	0.0214	0.0214	0.0214	0.0214	0.0214	0.0214	0.0214	0.0214	0.0214	0.0214	0.0214	0.0214	0.0214
	B3	0.066	0.066	0.066	0.066	0.066	0.066	0.066	0.066	0.066	0.066	0.066	0.066	0.066	0.066
	C1	0.0363	0.0363	0.0363	0.0363	0.0363	0.0363	0.0363	0.0363	0.0363	0.0363	0.0363	0.0363	0.0363	0.0363
	C2	0.0351	0.0351	0.0351	0.0351	0.0351	0.0351	0.0351	0.0351	0.0351	0.0351	0.0351	0.0351	0.0351	0.0351
	D1	0.0369	0.0369	0.0369	0.0369	0.0369	0.0369	0.0369	0.0369	0.0369	0.0369	0.0369	0.0369	0.0369	0.0369
	D2	0.0448	0.0448	0.0448	0.0448	0.0448	0.0448	0.0448	0.0448	0.0448	0.0448	0.0448	0.0448	0.0448	0.0448

Table 14  
The final outcomes

Alternatives	Ideals	Limited values	Real values	Ranking
A1	0.263090	0.017362	0.052086 (5.2%)	9
A2	0.286758	0.018924	0.056772 (5.7%)	8
A3	0.222665	0.014694	0.044083 (4.4%)	10
B1	0.633646	0.041816	0.125448 (12.5%)	3
B2	0.324771	0.021433	0.064298 (6.4%)	7
B3	1.000000	0.065993	0.197978 (19.80%)	1
C1	0.550412	0.036323	0.108970 (10.9%)	5
C2	0.532019	0.035109	0.105328 (10.5 %)	6
D1	0.558969	0.036888	0.110664 (11.1%)	4
D2	0.678726	0.044791	0.134373 (13.4%)	2

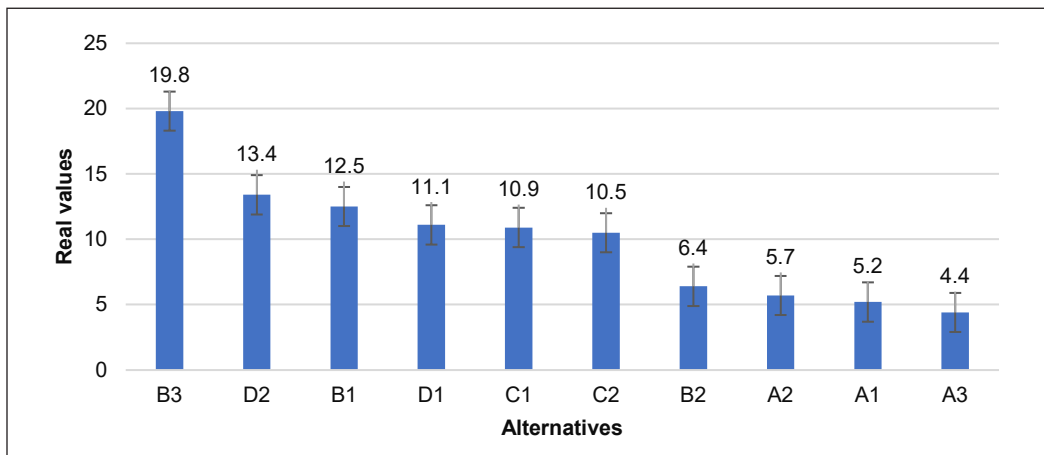


Figure 11. Priorities of the criteria

MCDM is a systematic and analytical approach that considers various criteria or factors to assess and compare alternatives. Within the framework of material selection, various aspects may come into play, including but not limited to cost, durability, environmental impact, and additional considerations. MCDM facilitates a methodical evaluation and prioritization of many possibilities, considering predetermined criteria. Fuzzy logic pertains to handling ambiguity and imprecision within the context of decision-making. In the realm of material selection, it is common for factors to lack specific definitions or ease of quantification. The notion of fuzziness enables the depiction of imprecise or unclear data, rendering it appropriate for addressing the inherent vagueness in decision-making scenarios seen in the actual world.

The integration of MCDM with fuzzy theory serves to augment the decision-making process. Fuzzy logic can accommodate the inherent uncertainties present in the criterion,

but MCDM offers a structured approach for concurrently managing several criteria. The use of this integration facilitates a more accurate portrayal of decision-making situations. In conclusion, integrating MCDM with fuzzy theory offers a viable and efficient framework for addressing the intricate challenges associated with material selection. This methodology recognizes and confronts the ambiguities and many factors inherent in making decisions, resulting in more knowledgeable and resilient choices regarding material selection.

In order to do the sensitivity analysis of the FANP approach, a study was undertaken to examine the impact of altering the unitary ratio of the fuzzy criteria weights. Figure 12 illustrates the sensitivity of the ranking of each bio-composite filament material to disturbances caused by variations in criteria weights for FANP techniques. The radar

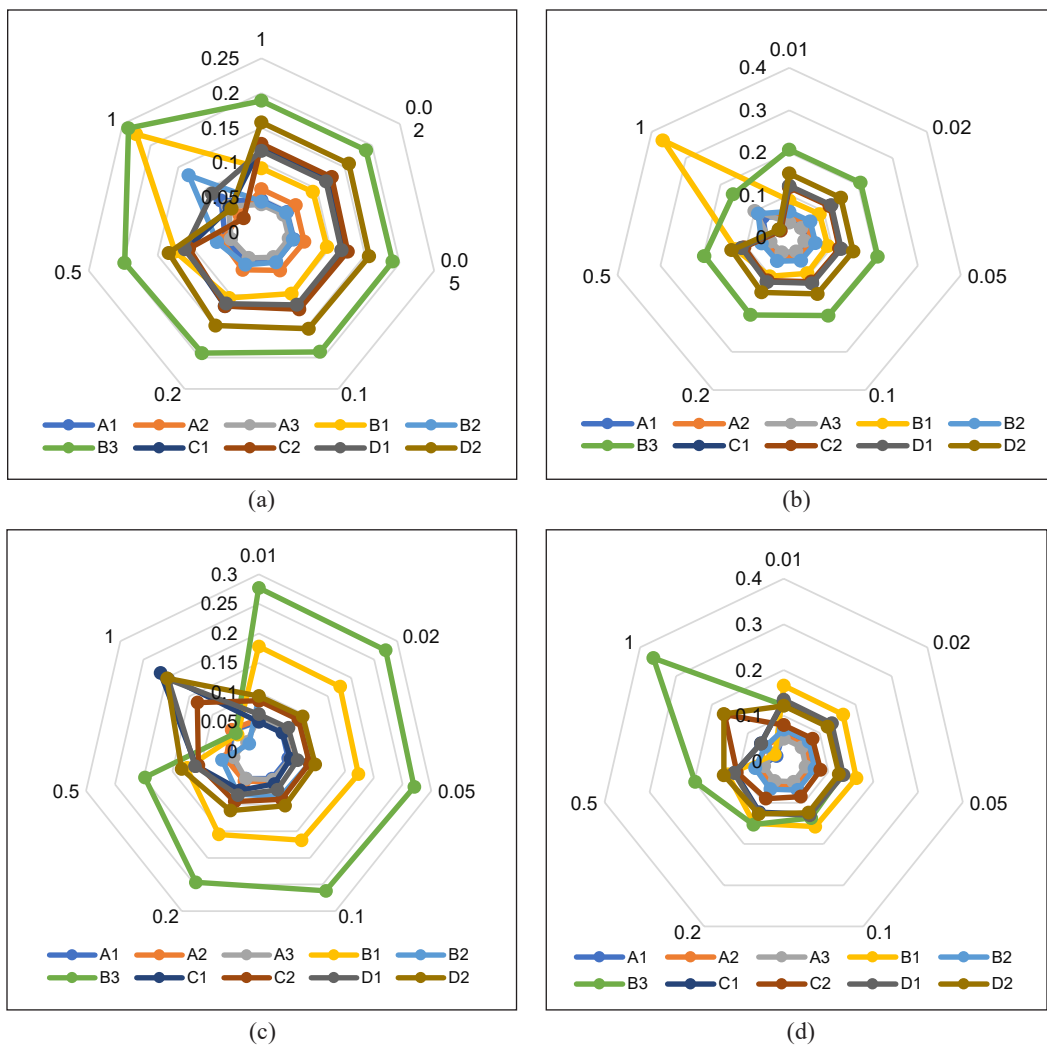


Figure 12. Ranking of the bio-composite filaments material with induced disturbance on the FANP-derived weights of (a) tensile strength, (b) flexural strength, (c) impact strength, and (d) printability

diagrams represent variable  $\beta$  by utilizing radii on the chart, while the ranking is conveyed by the distances observed within these radii.

In Figure 12(a), it can be shown that the relative ordering of the ten bio-composite filament materials began to undergo alterations when the value of  $\beta_1$  reached 0.2. The rankings of all materials were modified due to a change in the weighting of criteria for tensile strength. Following the value of  $\beta_1$  being set to 0.5, it was seen that the variability in rankings became more pronounced. It can be attributed to the rapid increase in the weights assigned to the criteria of tensile strength as  $\beta_1$  increased. Slight fluctuations in the ranking were noted for A2, B3, and D1 bio-composite filaments. The remaining bio-composite filaments exhibited sensitivity to changes in the weightage assigned to tensile strength. The sensitivity of the FANP study was examined by employing similar methodologies to assess the influence of varying weights on flexural strength, impact strength, and printability. Figure 12(b) demonstrates that the disruption imposed on the flexural strength weights resulted in consistent rankings of the bio-composite filaments material up to a value of  $\beta_2 = 0.2$ . Subsequently, a marginal alteration in the hierarchy of B1 bio-composite filament occurred, reaching a value of  $\beta_2 = 0.50$ . after that, there was a noticeable alteration in the ranking score of the B1 bio-composite filament. The rest of the filaments were also sensitive to the weight variation of flexural strength.

According to Figure 12(c), it can be observed that the B1, B3, C1, C2, D1, and D2 bio-composite filaments exhibited a high level of sensitivity to the disturbance caused by variations in impact strength weights. Conversely, the A1 and A2 bio-composite filaments displayed no sensitivity to such disturbances. The ranks of all the filaments exhibited consistency up to a value of  $\beta_3$  equal to 0.2. Figure 12(d) illustrates that all the filaments exhibited a degree of sensitivity to the perturbation caused by changes in printability weights. The filaments' rankings remained unchanged until  $\beta_4$  reached a value of 0.1. subsequently, a progressive shift in the bio-composite filament ranks occurred as a result of a significant alteration solely in the ranking of the B3 bio-composite filament. B3 filament exhibits a significantly greater level of printability than alternative filaments. As the value of  $\beta_4$  increased, there was a corresponding increase in the weight assigned to printability. Consequently, an enhancement was observed in the ranking of the B3 filament. The summary of sensitivity analysis results can be seen in Table 15.

The B3 fiber composite was chosen as the optimal material for enhancing the strength of bio-composite filaments used in fused deposition modeling technology, specifically for egg carton packaging. Furthermore, it was revealed that B1 and D2 fiber composite exhibited a high frequency of occurrence within the top three ranks. In contrast, A2, A3, and C1 consistently ranked among the lowest three in all scenarios. Based on the findings, it was determined that A3 exhibited the lowest level of preference among bio-composite filaments when utilized as in FDM technology, specifically with regard to the designated design purpose.

Table 15

*Summary of sensitivity analysis results based on four circumstances*

Rank	Original results	Increment of "Tensile strength," $\beta_1=1.0$	Increment of "Flexural strength," $\beta_1=1.0$	Increment of "Impact strength," $\beta_1=1.0$	Increment of "Printability," $\beta_1=1.0$
#1	B3	B3	B1	C1	B3
#2	D2	B1	B3	D2	D2
#3	B1	B2	A3	D1	C2
#4	D1	D1	A2	C2	C1
#5	C1	A1	B2	A2	D1
#6	C2	A3	A1	A1	A2
#7	B2	C1	D1	B3	B2
#8	A1	D2	D2	B1	A3
#9	A2	A2	C1	A3	B1
#10	A3	C2	C2	B2	A1

## CONCLUSION

This study addresses the issues of selecting a bio-composite filament material by presenting a methodology based on FANP. This methodology takes into account both quantitative and qualitative aspects in the evaluation of bio-composite filament material options. The conventional ANP technique facilitates feedback among hierarchical levels and is a comparatively recent approach demonstrating superiority over the AHP method. The scale utilized consists of nine points. The use of the nine-point scale pairwise comparison in the standard ANP may not adequately and appropriately reflect the accurate assessment of decision-makers due to ambiguity and uncertainty surrounding their evaluations. Due to this rationale, the integration of conventional ANP with fuzzy logic was pursued. The utilization of the FANP entails more effort than the fuzzy AHP due to the necessity of constructing several pairwise comparison matrices based on triangular fuzzy numbers for a typical research investigation. Conversely, the advantage of utilizing the FANP lies in its ability to capture potential interdependencies that may arise inside decision hierarchies. Hence, unlike the fuzzy AHP, the FANP provides a more reliable solution.

The findings of this study are significant for future research endeavors. The integration of MCDM approaches is of utmost importance when considering the selection of materials. This claim is supported by previous studies investigating alternate methods for selecting materials, going beyond the conventional mean and variance approach. The main aim of the present study was to introduce a new approach for assessing many elements involved in the material selection process. This study also carries implications for professionals, policymakers, and individuals in leadership positions. Evaluating and choosing materials can be understood as a methodical approach that encompasses several steps, including

identifying criteria, determining their relative significance, applying the criteria using the FANP technique, and subsequent analysis of the results. This method holds substantial promise for use in a range of real circumstances. Engineering, management, and invention professionals can apply this study's metrics, research structure, and technique to make well-informed decisions regarding selecting ideal industrial stock materials.

Exploring other MCDM models to facilitate material selection may benefit future investigations. It would enable a comparative comparison of their outcomes in relation to the present study's findings. In addition, factor analysis and confirmatory factor analysis can be utilized to define precise criteria for selecting materials. In conclusion, future research efforts may utilize flexible decision-support systems, such as software based on MCDM, to comprehensively assess all aspects related to the choice of materials. In summary, the FANP methodology demonstrates greater benefits in selecting bio-composite filament materials when a thorough assessment of several parameters is taken into account, along with the possible impact of interconnections among these elements. The study outcomes indicate that using SPF/PLA 7.5 wt.% fiber loading in FDM is a recommended strategy for producing egg carton packaging. The assignment of the highest position to prioritize impact strength can be attributed to its crucial significance in package design. Further research is needed to enhance the effectiveness of the proposed FANP technique through an in-depth examination of various bio-composite materials and the numerous aspects that require careful attention.

## ACKNOWLEDGEMENT

The authors thank Universiti Teknikal Malaysia Melaka and the Ministry of Higher Education of Malaysia for providing the financial support and grant scheme FRGS/1/2020/TK0/UTEM/02/26 to the principal author of this project.

## REFERENCES

- AL-Oqla, F. M., & Salit, M. S. (2017). Introduction. *Materials Selection for Natural Fiber Composites* (pp. 1-21). Woodhead Publishing. <https://doi.org/10.1016/b978-0-08-100958-1.00001-3>
- Alsubari, S., Zuhri, M. Y. M., Sapuan, S. M., Ishak, M. R., Ilyas, R. A., & Asyraf, M. R. M. (2021). Potential of natural fiber reinforced polymer composites in sandwich structures: A review on its mechanical properties. *Polymers*, 13(3), Article 423. <https://doi.org/10.3390/polym13030423>
- Amir, A. L., Ishak, M. R., Yidris, N., Zuhri, M. Y. M., & Asyraf, M. R. M. (2021). Potential of honeycomb-filled composite structure in composite cross-arm component: A review on recent progress and its mechanical properties. *Polymers*, 13(8), Article 1341. <https://doi.org/10.3390/polym13081341>
- Ariffadzilah, M. L. M., Yusuf, Y., & Mustafa, N. (2022). *Physical, mechanical and morphological properties of recycled polypropylene (PP) reinforced with coconut fiber*. [Final Year Degree Dissertation]. Universiti Teknikal Malaysia Melaka, Melaka, Malaysia. <http://digitalcollection.utem.edu.my/id/eprint/28160>

- Asyraf, M. R. M., Ishak, M. R., Sapuan, S. M., Yidris, N., Ilyas, R. A., Rafidah, M., & Razman, M. R. (2020). Potential application of green composites for cross arm component in transmission tower: A brief review. *International Journal of Polymer Science*, 2020, Article 8878300. <https://doi.org/10.1155/2020/8878300>
- Ayağ, Z., & Yücekaya, A. (2019). A fuzzy ANP-based GRA approach to evaluate ERP packages. *International Journal of Enterprise Information Systems*, 15(1), 45-68. <https://doi.org/10.4018/IJEIS.2019010103>
- Azali, N. S. Z., Mustafa, N., Jumaidin, R., Kudus, S. I. A., Razali, N., Taha, M. M., Yusuf, Y., & Ali, M. R. (2022). Thermal properties of wood dust fibre and recycled polypropylene (r-WoPPc) for development of thermoplastic composites filaments of fused deposition modeling. *Journal of Advanced Research in Fluid Mechanics and Thermal Sciences*, 96(2), 42-50. <https://doi.org/10.37934/arfmts.96.2.4250>
- Babu, K. S., Raju, N. S., Reddy, M. S., & Rao, D. N. (2006, June 19-23). The material selection for typical wind turbine blades using a MADM approach & analysis of blades. In *Multiple Criteria Decision Making* (pp. 1-12). Chania, Greece.
- Balmat, J. F., Lafont, F., Maifret, R., & Pessel, N. (2011). A decision-making system to maritime risk assessment. *Ocean Engineering*, 38(1), 171-176. <https://doi.org/10.1016/j.oceaneng.2010.10.012>
- Bathaei, A., Mardani, A., Baležentis, T., Awang, S. R., Streimikiene, D., Fei, G. C., & Zakuan, N. (2019). Application of fuzzy analytical network process (ANP) and VIKOR for the assessment of green agility critical success factors in dairy companies. *Symmetry*, 11(2), Article 250. <https://doi.org/10.3390/sym11020250>
- Bi, X., & Huang, R. (2022). 3D printing of natural fiber and composites: A state-of-the-art review. *Materials and Design*, 222, Article 111065. <https://doi.org/10.1016/j.matdes.2022.111065>
- Chen, W. C., Wang, L. Y., & Lin, M. C. (2015). A hybrid MCDM model for new product development: Applied on the Taiwanese LiFePO<sub>4</sub> Industry. *Mathematical Problems in Engineering*, 2015, Article 462929. <https://doi.org/10.1155/2015/462929>
- Coppola, B., Garofalo, E., Di Maio, L., Scarfato, P., & Incarnato, L. (2018). Investigation on the use of PLA/hemp composites for the fused deposition modelling (FDM) 3D printing. *AIP Conference Proceedings*, 1981(1), 1-5. AIP Publishing. <https://doi.org/10.1063/1.5045948>
- Daver, F., Lee, K. P. M., Brandt, M., & Shanks, R. (2018). Cork-PLA composite filaments for fused deposition modelling. *Composites Science and Technology*, 168, 230-237. <https://doi.org/10.1016/j.compscitech.2018.10.008>
- Depuydt, D., Balthazar, M., Hendrickx, K., Six, W., Ferraris, E., Desplentere, F., Ivens, J., & Van Vuure, A. W. (2019). Production and characterization of bamboo and flax fiber reinforced polylactic acid filaments for fused deposition modeling (FDM). *Polymer Composites*, 40(5), 1951-1963. <https://doi.org/10.1002/pc.24971>
- Dong, Y., Milentis, J., & Pramanik, A. (2018). Additive manufacturing of mechanical testing samples based on virgin poly (lactic acid) (PLA) and PLA/wood fibre composites. *Advances in Manufacturing*, 6, 71-82. <https://doi.org/10.1007/s40436-018-0211-3>
- Emovon, I., & Oghenyerovwho, O. S. (2020). Application of MCDM method in material selection for optimal design: A review. *Results in Materials*, 7, Article 100115. <https://doi.org/10.1016/j.rinma.2020.100115>

- Faruk, O., Bledzki, A. K., Fink, H. P., & Sain, M. (2012). Biocomposites reinforced with natural fibers: 2000–2010. *Progress in Polymer Science*, 37(11), 1552-1596. <https://doi.org/10.1016/j.progpolymsci.2012.04.003>
- Gholampour, A., & Ozbakkaloglu, T. (2020). A review of natural fiber composites: properties, modification and processing techniques, characterization, applications. *Journal of Materials Science*, 55(3), 829-892. <http://doi.org/10.1007/s10853-019-03990-y>
- Han, S. N. M. F., Taha, M. M., Mansor, M. R., & Rahman, M. A. A. (2022). Investigation of tensile and flexural properties of kenaf fiber-reinforced acrylonitrile butadiene styrene composites fabricated by fused deposition modeling. *Journal of Engineering and Applied Science*, 69, Article 52. <https://doi.org/10.1186/s44147-022-00109-0>
- Hanan, F., Jawaid, M., & Md Tahir, P. (2020). Mechanical performance of oil palm/kenaf fiber-reinforced epoxy-based bilayer hybrid composites. *Journal of Natural Fibers*, 17(2), 155-167. <https://doi.org/10.1080/15440478.2018.1477083>
- Ionescu-Bujor, M., & Cacuci, (2004). A comparative review of sensitivity and uncertainty analysis of large-scale systems-I: Deterministic methods. *Nuclear Science and Engineering*, 147(3), 189-203. <https://doi.org/10.13182/NSE03-105CR>
- Kabir, M. M., Wang, H., Lau, K. T., & Cardona, F. (2012). Chemical treatments on plant-based natural fibre reinforced polymer composites: An overview. *Composites Part B: Engineering*, 43(7), 2883-2892. <https://doi.org/10.1016/j.compositesb.2012.04.053>
- Kabir, S. M. F., Mathur, K., & Seyam, A. F. M. (2020). A critical review on 3D printed continuous fiber-reinforced composites: History, mechanism, materials and properties. *Composite Structures*, 232, Article 111476. <https://doi.org/10.1016/j.compstruct.2019.111476>
- Ku, H., Wang H., Pattarachaiyakoop N., & Trada M. (2011) A review on the tensile properties of natural fiber reinforced polymer composites. *Composites Part B: Engineering*, 42(4), 856-873. <https://doi.org/10.1016/j.compositesb.2011.01.010>
- Kumar, A., Sah, B., Singh, A. R., Deng, Y., He, X., Kumar, P., & Bansal, R. C. (2017). A review of multi criteria decision making (MCDM) towards sustainable renewable energy development. *Renewable and Sustainable Energy Reviews*, 69, 596-609. <https://doi.org/10.1016/j.rser.2016.11.191>
- Le Duigou, A., Correa, D., Ueda, M., Matsuzaki, R., & Castro, M. (2020). A review of 3D and 4D printing of natural fibre biocomposites. *Materials and Design*, 194, Article 108911. <https://doi.org/10.1016/j.matdes.2020.108911>
- Li, P., Qian, H., Wu, J., & Chen, J. (2013). Sensitivity analysis of TOPSIS method in water quality assessment: I. Sensitivity to the parameter weights. *Environmental Monitoring and Assessment*, 185, 2453-2461. <https://doi.org/10.1007/s10661-012-2723-9>
- Liu, H., He, H., Peng, X., Huang, B., & Li, J. (2019). Three-dimensional printing of poly(lactic acid) bio-based composites with sugarcane bagasse fiber: Effect of printing orientation on tensile performance. *Polymers for Advanced Technologies*, 30(4), 910-922. <https://doi.org/10.1002/pat.4524>
- Maity, S. R., & Chakraborty, S. (2012a). Super-critical boiler material selection using fuzzy analytic network process. *Management Science Letters*, 2(4), 1083-1096. <https://doi.org/10.5267/j.msl.2012.03.012>

- Maity, S. R., & Chakraborty, S. (2012b). Turbine blade material selection using fuzzy analytic network process. *International Journal of Materials and Structural Integrity*, 6(2–4), 169-189. <https://doi.org/10.1504/IJMSI.2012.049954>
- Matsuzaki, R., Ueda, M., Namiki, M., Jeong, T. K., Asahara, H., Horiguchi, K., Nakamura, T., Todoroki, A., & Hirano, Y. (2016). Three-dimensional printing of continuous-fiber composites by in-nozzle impregnation. *Scientific Reports*, 6, Article 23058. <https://doi.org/10.1038/srep23058>
- Mazzanti, V., Malagutti, L., & Mollica, F. (2019). FDM 3D printing of polymers containing natural fillers: A review of their mechanical properties. *Polymers*, 11(7), Article 1094. <https://doi.org/10.3390/polym11071094>
- Milosevic, M., Stoof, D., & Pickering, K. L. (2017). Characterizing the mechanical properties of fused deposition modelling natural fiber recycled polypropylene composites. *Journal of Composites Science*, 1(1), Article 7. <https://doi.org/10.3390/jcs1010007>
- Mistarihi, M. Z., Okour, R. A., & Mumani, A. A. (2020). An integration of a QFD model with Fuzzy-ANP approach for determining the importance weights for engineering characteristics of the proposed wheelchair design. *Applied Soft Computing Journal*, 90, Article 106136. <https://doi.org/10.1016/j.asoc.2020.106136>
- Mohaghar, A., Fathi, M. R., Faghieh, A., & Turkayesh, M. M. (2012). An integrated approach of Fuzzy ANP and Fuzzy TOPSIS for R&D project selection: A case study. *Australian Journal of Basic and Applied Sciences*, 6(2), 66-75.
- Mohan, N., Senthil, P., Vinodh, S., & Jayanth, N. (2017). A review on composite materials and process parameters optimisation for the fused deposition modelling process. *Virtual and Physical Prototyping*, 12(1), 47-59. <https://doi.org/10.1080/17452759.2016.1274490>
- Mohd Pu'ad, N. A. S., Abdul Haq, R. H., Mohd Noh, H., Abdullah, H. Z., Idris, M. I., & Lee, T. C. (2019). Review on the fabrication of fused deposition modelling (FDM) composite filament for biomedical applications. *Materials Today: Proceedings*, 29(Part 1), 228-232. <https://doi.org/10.1016/j.matpr.2020.05.535>
- Montalvo Navarrete, J. I., Hidalgo-Salazar, M. A., Escobar Nunez, E., & Rojas Arciniegas, A. J. (2018). Thermal and mechanical behavior of biocomposites using additive manufacturing. *International Journal on Interactive Design and Manufacturing*, 12, 449-458. <https://doi.org/10.1007/s12008-017-0411-2>
- Nahfis, S. Z. A., Nuzaimah, M., Abdul Kudus, S. I., Ahmad, M. N., & Shaharuzaman, M. A. (2022). Chemical treatment has an influence on the strengthening of recycle wood pp composite ( r-WoPPC ) filament. *Proceedings of Mechanical Engineering Research Day 2022*, 70-72.
- Nasereddin, J. M., Wellner, N., Alhijaj, M., Belton, P., & Qi, S. (2018). Development of a simple mechanical screening method for predicting the feedability of a pharmaceutical FDM 3D printing filament. *Pharmaceutical Research*, 35, Article 151. <https://doi.org/10.1007/s11095-018-2432-3>
- Nasir, M. H. M., Taha, M. M., Razali, N., Ilyas, R. A., Knight, V. F., & Norrahim, M. N. F. (2022). Effect of chemical treatment of sugar palm fibre on rheological and thermal properties of the PLA composites filament for FDM 3D printing. *Materials*, 15(22), Article 8082. <https://doi.org/10.3390/ma15228082>
- Ngo, T. D., Kashani, A., Imbalzano, G., Nguyen, K. T. Q., & Hui, D. (2018). Additive manufacturing (3D printing): A review of materials, methods, applications and challenges. *Composites Part B: Engineering*, 143, 172-196. <https://doi.org/10.1016/j.compositesb.2018.02.012>

- Noryani, M., Sapuan, S. M., & Mastura, M. T. (2018). Multi-criteria decision-making tools for material selection of natural fibre composites: A review. *Journal of Mechanical Engineering and Sciences*, 12(1), 3330-3353. <https://doi.org/10.15282/jmes.12.1.2018.5.0299>
- Noryani, M., Sapuan, S. M., Mastura, M. T., Zuhri, M. Y. M., & Zainudin, E. S. (2018). A statistical framework for selecting natural fibre reinforced polymer composites based on regression model. *Fibers and Polymers*, 19, 1039-1049. <https://doi.org/10.1007/s12221-018-8113-3>
- Pang, N., Nan, M., Meng, Q., & Zhao, S. (2021). Selection of wind turbine based on fuzzy analytic network process: A case study in China. *Sustainability (Switzerland)*, 13(4), Article 1792. <https://doi.org/10.3390/su13041792>
- Pop, M. A., Croitoru, C., Bedó, T., Geaman, V., Radomir, I., Coşniţa, M., Zaharia, S. M., Chicoş, L. A., & Miloşan, I. (2019). Structural changes during 3D printing of bioderived and synthetic thermoplastic materials. *Journal of Applied Polymer Science*, 136(17), Article 47382. <https://doi.org/10.1002/app.47382>
- Rajendran Royan, N. R., Leong, J. S., Chan, W. N., Tan, J. R., & Shamsuddin, Z. S. B. (2021). Current state and challenges of natural fibre-reinforced polymer composites as feeder in fdm-based 3d printing. *Polymers*, 13(14), Article 2289. <https://doi.org/10.3390/polym13142289>
- Reddy, T. B. (2013). Open access mechanical performance of green coconut fiber/HDPE composites. *International Journal of Engineering Research and Applications*, 3(6), 1262-1270.
- Šafka, J., Ackermann, M., Bobek, J., Seidl, M., Habr, J., & Běhálek, L. (2016). Use of composite materials for FDM 3D print technology. *Materials Science Forum*, 862, 174-181. <https://doi.org/10.4028/www.scientific.net/MSF.862.174>
- Safri, S. N. A., Sultan, M. T. H., Jawaaid, M., & Jayakrishna, K. (2018). Impact behaviour of hybrid composites for structural applications: A review. *Composites Part B: Engineering*, 133, 112-121. <https://doi.org/10.1016/j.compositesb.2017.09.008>
- Saltelli, A., Ratto, M., Tarantola, S., & Campolongo, F. (2005). Sensitivity analysis for chemical models. *Chemical. Review*, 105 (7), 2811-2828. <https://doi.org/10.1021/cr040659d>
- Senvar, O., Vayvay, O., & Hamal, S. (2018). Selection of optimal renewable energy investment project via fuzzy ANP. *Journal of Economics, Finance and Accounting*, 5(2), 224-233. <https://doi.org/10.17261/pressacademia.2018.827>
- Stoof, D., & Pickering, K. (2018). Sustainable composite fused deposition modelling filament using recycled pre-consumer polypropylene. *Composites Part B: Engineering*, 135, 110-118. <https://doi.org/10.1016/j.compositesb.2017.10.005>
- Stoof, D., Pickering, K., & Zhang, Y. (2017). Fused deposition modelling of natural fibre/polylactic acid composites. *Journal of Composites Science*, 1(1), Article 8. <https://doi.org/10.3390/jcs1010008>
- Velasquez, M., & Hester, P. (2013). An analysis of multi-criteria decision making methods. *International Journal of Operations Research*, 10(2), 56-66.
- Vigneshwaran, S., Sundarakannan, R., John, K. M., Joel Johnson, R. D., Prasath, K. A., Ajith, S., Arumugaprabu, V., & Uthayakumar, M. (2020). Recent advancement in the natural fiber polymer composites: A

comprehensive review. *Journal of Cleaner Production*, 277, Article 124109. <https://doi.org/10.1016/j.jclepro.2020.124109>

Xanthos, M. (Ed). (2005). *Functional fillers for plastics*. Wiley. <https://doi.org/10.1002/3527605096>

Xiao, X., Chevali, V. S., Song, P., He, D., & Wang, H. (2019). Polylactide/hemp hurd biocomposites as sustainable 3D printing feedstock. *Composites Science and Technology*, 184, Article 107887. <https://doi.org/10.1016/j.compscitech.2019.107887>

Zavadskas, E. K., Antucheviciene, J., Turskis, Z., & Adeli, H. (2016). Hybrid multiple-criteria decision-making methods: A review of applications in engineering. *Scientia Iranica*, 23(1), 1-20. <https://doi.org/10.24200/sci.2016.2093>



## Optimizing Bagged Trees in an Ensemble Classifier for Improved Prediction of Diabetes Prevalence in Women

Jose Candia Jr.\* , Airish Mae Adonis and Jesica Perlas

*Department of Computer Science, North Eastern Mindanao State University – Tagbina Campus, Poblacion, Tagbina, 8308 Surigao del Sur, Philippines*

### ABSTRACT

This study aims to optimize the performance of the bagged tree in an ensemble classifier for predicting diabetes prevalence in women. The study used a dataset of 1,888 women with six features: age, BMI, glucose level, insulin level, blood pressure, and pregnancy status. The dataset was divided into training and testing sets with a 70:30 ratio. The bagged tree ensemble classifier was used for the analysis, and five-fold cross-validation was applied. The study found that using all features during training resulted in a 92.3% training accuracy and a 99.5% testing accuracy. However, applying optimization techniques such as feature selection, parameter tuning, and a maximum number of splits improved model performance. Feature selection optimized the accuracy performance by 0.2%, while parameter tuning improved the test accuracy by 0.2%. Moreover, decreasing the maximum number of splits from 1322 to 800 or 600 resulted in an optimized model with 0.1% higher validation accuracy. Finally, the optimized bagged tree models were evaluated using various performance metrics, including accuracy, precision, recall, and F1 score. The study found that Model 1, which used 800 maximum number of splits and 50 learners, outperformed Model 2 in terms of recall and F1 score, while Model 2, which used 600 maximum number

of splits and 50 learners, had a higher precision score. The study concludes that optimization techniques can significantly improve the performance of the bagged tree in predicting diabetes prevalence in women.

### ARTICLE INFO

#### Article history:

Received: 07 March 2023

Accepted: 12 September 2023

Published: 22 July 2024

DOI: <https://doi.org/10.47836/pjst.32.3.16>

#### E-mail addresses:

[jqcandia@nemsu.edu.ph](mailto:jqcandia@nemsu.edu.ph) (Jose Candia Jr.)

[airishadonis09@gmail.com](mailto:airishadonis09@gmail.com) (Airish Mae E. Adonis)

[perlasjesica09@gmail.com](mailto:perlasjesica09@gmail.com) (Jesica Perlas)

\*Corresponding author

**Keywords:** Bagged trees, diabetes prevalence, ensemble classifier, feature selection, model optimization, parameter tuning

## INTRODUCTION

Diabetes is a major public health problem worldwide, affecting millions of people and imposing a significant economic burden on healthcare systems. In the Philippines, diabetes is a growing concern, with a prevalence rate of 7.5% among women aged 20–79 years. The high prevalence of diabetes in the Philippines can be attributed to various factors, including sedentary lifestyles, unhealthy diets, and genetic predisposition. Therefore, an urgent need is to develop accurate and reliable methods for predicting diabetes prevalence in women to prevent complications and improve health outcomes.

Machine learning algorithms have shown promise in predicting diabetes prevalence in women (Nishat et al., 2021). Decision trees and ensemble classifiers are popular techniques for classification and prediction tasks because of their simplicity, interpretability, and ability to handle both categorical and numerical data. Ensemble classifiers, in particular, are known to improve the accuracy and robustness of the model by combining the predictions of multiple decision trees. Bagged trees are an ensemble classifier that has gained popularity in recent years. Bagging is a resampling method that involves randomly selecting subsets of the training data and training decision trees on each subset. The predictions of the individual trees are then combined through a voting or averaging scheme to produce a final prediction. Bagged trees have improved the accuracy and stability of decision tree models, particularly for complex and noisy datasets.

Several studies have used machine learning algorithms to predict diabetes prevalence in the Philippines. For instance, Tan et al. (2019) used decision trees and logistic regression to predict the risk of type 2 diabetes among Filipino adults. The study found that the most important predictors of diabetes were age, body mass index (BMI), waist circumference, and family history of diabetes. Similarly, a study by Abayadeera et al. (2019) used decision trees and logistic regression to predict the risk of type 2 diabetes among urban Filipinos. The study found that the most important predictors of diabetes were age, BMI, physical activity, and education level. However, few studies have used bagged trees to predict diabetes prevalence in the Philippines. One study by Pang et al. (2017) used bagged trees to predict the risk of diabetes among Chinese adults, achieving an accuracy of 78.4%. Another study by Jia et al. (2018) used bagged trees to predict the risk of diabetes among urban Chinese residents, achieving an accuracy of 84.2%. These studies demonstrate the potential of bagged trees in predicting diabetes prevalence and risk factors.

This study aims to optimize the bagged tree ensemble classifier for predicting diabetes prevalence in women in the Philippines. We will use data from the 2019 Philippine National Nutrition Survey, a nationally representative survey that collects information on Filipinos' health and nutrition status. We will focus on six key predictors of diabetes prevalence in women: pregnancies, glucose levels, blood pressure, BMI, age, and diabetes pedigree function. By optimizing the parameters of the bagged tree algorithm, we aim to improve

the accuracy and robustness of the model. The results of this study could have important implications for the early detection and prevention of diabetes in women, as well as for the development of more effective machine-learning algorithms for predicting chronic diseases in resource-limited settings.

### Conceptual Framework

The conceptual framework for this study on optimizing bagged trees in an ensemble classifier for improved prediction of diabetes prevalence in women is presented in the diagram below:

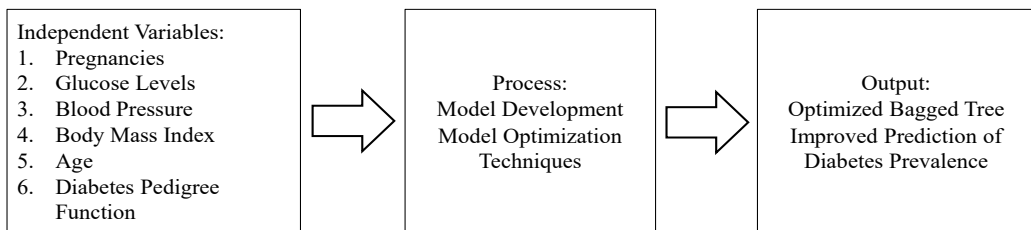


*Figure 1.* Conceptual framework of optimizing bagged trees in an ensemble classifier for improved prediction of diabetes prevalence in women

The independent variables in this study include the predictive factors of diabetes prevalence in women: pregnancies, glucose, blood pressure, BMI, age, and diabetes pedigree function. These variables will be used as input features for the bagged trees in the ensemble classifier. The dependent variable is the prediction of diabetes prevalence in women.

The bagged trees algorithm will be used as the main classifier for predicting diabetes prevalence in women. The bagged trees algorithm is an ensemble learning method that combines multiple decision trees to improve prediction accuracy and reduce the risk of overfitting. The bagged trees algorithm will be optimized using various parameters such as the number of trees, maximum depth, and minimum number of samples required to split a node.

The study will also employ feature selection techniques to determine the most important predictive factors for diabetes prevalence in women. The feature selection process will be performed using wrapper methods, specifically the recursive feature elimination algorithm. The recursive feature elimination algorithm is a backward selection method that recursively removes features from the model and evaluates their impact on model performance. The output of the bagged trees algorithm will be evaluated using performance metrics such as accuracy, precision, recall, and F1 score.

## MATERIALS AND METHODS

This study used ensemble classifier model development and optimization techniques to predict diabetes prevalence in women. The study was conducted in the following phases:

### Phase 1: Data Collection

The dataset used for this study was obtained from the Philippine Statistics Authority's National Nutrition Survey 2019 (Philippine Statistics Authority 2020), which includes information on women diagnosed with diabetes. The dataset will be preprocessed to remove missing values and normalize the data.

Table 1  
*Factors affecting maternal risk during pregnancy*

Factors	Descriptions
Pregnancies	Number of pregnancies a woman has had
Glucose Level	Blood glucose levels in terms of molar concentration, mmo/L
Blood Pressure	Lower value of blood pressure in mmHg
Body Mass Index	Measure of body fat based on a person's height and weight
Diabetes Pedigree Function	Measure of diabetes family history
Age	Age in years

The collected data was divided into two sets: a training set comprising 70% of the data and a testing set comprising 30%. The training set was utilized to construct and train a machine learning model, while the testing set was used to assess the model's performance based on previously unseen data.

Table 2 presents the data distribution between the training and testing datasets for predicting diabetes prevalence in women. The training dataset comprises 1,323 data points, while the testing dataset contains 565.

Table 2  
*Training and testing datasets of diabetes prevalence in women*

Diabetes Prevalence	Training 70%	Testing 30%	Total
Yes	457	182	639
No	866	383	1,249
Total	1,323	565	1,888

### Phase 2: Feature Selection

In this phase, a wrapper method using the Recursive Feature Elimination algorithm will be utilized to select the most important features to predict diabetes prevalence in women. Recursive Feature Elimination works by removing one feature at a time and evaluating the impact of the feature on the model's performance until the best subset of features is determined. This method aims to

increase the model's accuracy and reduce overfitting by removing irrelevant features. The selected features will train the model in the next phase.

### **Phase 3: Parameter Tuning**

The Bagged Trees algorithm will be used as the primary classifier for predicting diabetes prevalence in women. In this phase, the Bagged Trees algorithm will be optimized by varying its parameters, such as the maximum number of splits and learners. This phase aims to improve the model's performance by determining the parameters' optimal values. Parameter tuning is crucial as it can significantly impact the model's accuracy and generalization ability.

### **Phase 4: Performance Evaluation**

In this phase, the performance of the Bagged Trees algorithm will be evaluated using performance metrics such as accuracy, precision, recall, and F1 score. The evaluation will involve splitting the dataset into training and testing sets using a 5-fold cross-validation approach. Since the dataset had skewed data with many more observations of one class, a stratified 5-fold cross-validation was applied. The metrics will be used to evaluate the model's ability to predict diabetes prevalence in women accurately. Accuracy is the proportion of true predictions out of all predictions made, while precision is the proportion of true positive predictions out of all positive predictions made. Recall is the proportion of true positive predictions out of all actual positive cases, and the F1 score is the harmonic mean of precision and recall. The higher the values of these metrics, the better the model's performance.

The study will use MATLAB software, specifically the Statistics and Machine Learning Toolbox. MATLAB is a powerful programming language and software environment widely used for scientific computing and data analysis. The bagged tree ensemble classifier will be optimized and trained on the diabetes dataset using this toolbox. The resulting model will then be used to predict diabetes prevalence in women in the Philippines, which could have important implications for early detection and prevention of diabetes in this population.

## **RESULTS**

The results and discussion present the study's findings on optimizing bagged trees in an ensemble classifier for improved prediction of diabetes prevalence in women. It highlights the performance of the optimized model in predicting diabetes prevalence based on the selected features and tuned parameters. It also discusses the implications of the study's findings for the early detection and prevention of diabetes in women in the Philippines and for developing more effective machine-learning algorithms for predicting chronic

diseases in resource-limited settings. Overall, the results and discussion aim to provide a comprehensive understanding of the effectiveness of the optimized bagged trees model in predicting diabetes prevalence in women and its potential impact on public health.

Table 3  
*Ensemble classifier model summary*

Model Type	Ensemble Method	Learner Type	Validation Method	Training Accuracy	Testing Accuracy
Bagged Tree	Bag	Decision Tree	5-fold Cross Validation	92.3%	99.5%
Bagged Tree	Bag	Decision Tree	Stratified 5-fold Cross Validation	81.4%	82.5%

The primary goal of this research is to construct a robust machine-learning model capable of accurately predicting the prevalence of diabetes among women in the Philippines. To fulfill this objective, we employed an ensemble classifier model trained on the entire feature set and evaluated using standard and stratified 5-fold cross-validation techniques. An overview of the model's performance can be found in Table 3.

The outcomes reveal that our bagged tree ensemble classifier model demonstrated a remarkable performance, achieving a notable accuracy of 92.3% during training and an impressive 99.5% accuracy during testing. When addressing the imbalanced data issue through stratified cross-validation, the accuracy rates for training and testing slightly decreased to 81.4% and 82.5%, respectively.

Table 4  
*Bagged tree model optimization using feature selection*

Bagged Tree Model	Feature Selection	Validation Accuracy	Test Accuracy	Remarks
1	All features were used in the model (6/6)	81.4%	82.5%	Initial Model
2	All features used except: Pregnancy (5/6)	81.5%	81.9%	Unoptimized
3	All features used except: Blood Pressure (5/6)	81.0%	82.5%	Unoptimized
4	All features used except: Pregnancy and Blood Pressure (4/6)	81.4%	81.1%	Unoptimized
5	All features used except: Blood Pressure and Age (4/6)	79.5%	80.9%	Unoptimized

The findings from the experiments provide insights into the relationship between feature selection and the performance of the bagged tree model in predicting the likelihood of diabetes prevalence. Here is a summary of the observations:

Model 1 (Initial Model): The model trained with all features achieved a validation accuracy of 81.4% and a test accuracy of 82.5%. It serves as the baseline for comparison. Removing the "Pregnancy" feature (Model 2) while retaining the rest resulted in a slightly decreased validation accuracy of 81.5% and a test accuracy of 81.9%. It indicates a minor reduction in model performance, suggesting that "Pregnancy" might play a role in accurate predictions. Excluding the "Blood Pressure" feature (Model 3) while keeping others led to a validation accuracy of 81.0% and a test accuracy of 82.5%, consistent with the initial model's performance. Removing both "Pregnancy" and "Blood Pressure" features (Model 4) caused a validation accuracy of 81.4% and a test accuracy of 81.1%. The performance drop suggests that both features somewhat contribute to model accuracy. Omitting "Blood Pressure" and "Age" features (Model 5) resulted in a validation accuracy of 79.5% and a test accuracy of 80.9%, representing the least optimized configuration among the tested scenarios.

Table 5  
*Optimization of bagged tree model through varying learners*

Bagged Tree Model	Number of Learners	Validation Accuracy	Test Accuracy	Remarks
1	30	81.4%	82.5%	Initial Model
2	40	81.5%	82.5%	Unoptimized
3	50	82.5%	81.6%	Unoptimized
4	60	82.2%	82.3%	Unoptimized
5	70	82.2%	82.8%	Optimized

The optimization of the developed model was also carried out using parameter tuning. Table 5 summarizes the results of the bagged tree model optimization by varying the number of learner parameters, which determines the number of decision trees in the ensemble. The optimization technique increased training and test accuracy by 0.8% and 0.3%, respectively, when the number of learners was increased from 30 to 70. The improvement in accuracy suggests that the increase in the number of learners resulted in a more robust and accurate model.

The study also investigated the impact of varying the maximum number of splits in optimizing the bagged tree model's performance. Table 6 summarizes the results of the experiment. It shows that increasing the maximum number of splits from 20 to greater than 100 improved the validation accuracy by at least 9.3% and test accuracy by 15.4%.

This result suggests that setting a higher value for maximum splits can prevent the model from overfitting and improve its generalization performance.

Table 6  
*Optimization of bagged tree model through varying splits*

Bagged Tree Model	Maximum Number of Splits	Validation Accuracy	Test Accuracy	Remarks
1	20	82.2%	82.8%	Initial Model
2	50	88.2%	91.0%	Optimized
3	100	91.5%	98.2%	Optimized
4	200	91.9%	99.5%	Optimized
5	300	91.8%	99.8%	Most Optimized
6	500	92.3%	99.6%	Most Optimized

Table 7  
*Performance metrics of the optimized bagged tree model*

Metrics	Model 1 Splits: 300 Learner: 70		Model 2 Splits: 500 Learner: 70	
	Validation	Test	Validation	Test
Accuracy	91.8%	99.8%	92.3%	99.6%
Precision	92.7%	99.7%	93.4%	99.5%
Sensitivity (Recall)	94.7%	100%	94.7%	100%
Specificity	86.7%	99.5%	87.8%	98.9%
F1 Score	93.7%	99.9%	94.1%	99.7%

The performance metrics of the optimized Bagged Tree model, evaluated on both the validation and test datasets, are presented in Table 7. The model was tested using Model 1 with 300 splits and Model 2 with 500 splits while maintaining a constant learner count of 70.

Model 1 achieved an accuracy of 91.8% on the validation set and an impressive 99.8% on the test set. Model 2 exhibited similar performance, with an accuracy of 92.3% on the validation set and a slightly lower accuracy of 99.6% on the test set.

The precision values for both models were consistently high as well. For Model 1, precision was recorded at 92.7% on the validation set and an exceptional 99.7% on the test set. Model 2 displayed slightly improved precision, with values of 93.4% on the validation set and 99.5% on the test set.

Sensitivity (recall), which measures the model's ability to correctly identify positive instances, was remarkably high for both models. Model 1 exhibited a sensitivity of 94.7%

on both the validation and test sets, indicating its strong capability to identify positive cases. Similarly, Model 2 achieved a perfect sensitivity of 100% on both datasets.

Regarding specificity, which reflects the model's ability to correctly identify negative instances, both models displayed respectable values. Model 1 recorded a specificity of 86.7% on the validation set and a noteworthy 99.5% on the test set. Model 2 showed a slight increase in specificity, with values of 87.8% on the validation set and 98.9% on the test set.

The F1 score, which balances precision and recall, showcased consistent and high values for both models. Model 1 attained an F1 score of 93.7% on the validation set and an impressive 99.9% on the test set. Model 2's F1 score was slightly higher, with values of 94.1% on the validation set and 99.7% on the test set.

## DISCUSSION

The study aimed to optimize the bagged tree ensemble classifier model to improve the prediction of diabetes prevalence in women. Through the analysis of the four findings, several important insights were uncovered.

First, the high accuracy results collectively indicate a performance exhibited by the model, showcasing its ability to provide accurate predictions regarding the likelihood of diabetes prevalence among women. It lends substantial support to the practical applicability of machine learning algorithms, particularly emphasizing the efficacy of the bagged tree ensemble classifier in forecasting diabetes prevalence among women in resource-constrained settings such as the Philippines, which is consistent with previous studies that used machine learning algorithms for diabetes prediction. For instance, a study by Mujumdar and Vaidehi (2019) used a machine learning approach based on decision trees and random forest algorithms to predict diabetes and achieved an accuracy of 91.78%. Another study by Zhao et al. (2019) applied a support vector machine (SVM) algorithm to predict diabetes and reported an accuracy of 95.03%. These studies demonstrate the potential of machine learning algorithms in accurately predicting diabetes prevalence.

Second, while prior studies have consistently highlighted the enhanced performance of machine learning models through the application of feature selection techniques (Nguyen et al., 2020; Zhang et al., 2018), the current investigation presents a unique scenario where each predictor included in the model appears to bear significant relevance to the predictive outcomes.

Third, the finding is consistent with the literature on ensemble methods, which suggests that increasing the number of trees in an ensemble generally improves the model's accuracy up to a certain point (Biau, 2012). Additionally, other studies on parameter tuning in bagged tree models have also shown that increasing the number of trees can lead to improved performance (Chen et al., 2004; Wang et al., 2018). However, it is important to note that increasing the number of learners beyond a certain point can also lead to overfitting,

where the model becomes too complex and starts to memorize the training data rather than generalize it to new data. Therefore, finding the optimal number of learners that maximizes the model's accuracy without overfitting is important.

Fourth, the finding is consistent with the related literature, which showed that increasing the maximum number of splits can reduce overfitting and improve the performance of decision tree-based algorithms (Breiman et al., 1984; Quinlan, 1993). In a study by Han and Kamber (2001), the authors demonstrated that maximizing the depth of decision trees in a bagged ensemble model can improve its generalization performance. The finding highlights the importance of fine-tuning the hyperparameters of machine learning models to optimize their performance.

Overall, the findings of this study provide valuable insights into optimizing the bagged tree ensemble classifier model for predicting diabetes prevalence in women. The study highlights the importance of feature selection, parameter tuning, and a maximum number of split optimizations in improving the model's performance. Future studies may further explore these techniques and other potential methods for optimizing the bagged tree ensemble classifier model for predicting diabetes prevalence in women.

## **CONCLUSION**

In conclusion, this study aimed to optimize the bagged tree ensemble classifier for improved prediction of diabetes prevalence in women. The study found that applying feature selection and parameter tuning techniques increased model accuracy, precision, recall, specificity, and F1 score. Specifically, the optimized bagged tree model using 300 splits and 70 learners showed the best performance of the model based on various evaluation metrics in a test dataset, while the optimized model using 500 maximum number of splits and 70 learners showed the best performance in the validation dataset. These findings suggest that using bagged tree ensemble classifiers and optimization techniques can provide improved predictions for diabetes prevalence in women. The insights gained from this study could significantly improve healthcare outcomes for women at risk of diabetes. Further research can be conducted to test the applicability of this approach to other datasets and populations.

## **ACKNOWLEDGEMENTS**

The authors express heartfelt gratitude to the following individuals for their invaluable support and guidance throughout this research: Dr. Ariston O. Ronquillo, Campus Director, of North Eastern Mindanao State University -Tagbina Campus, Philippines, for his unwavering support and encouragement and for providing us the necessary resources and creating a conducive environment for research; Dr. Born Christian Isip, Dean of the College of Information Technology Education, North Eastern Mindanao State University -Main Campus, Philippines, for her insightful feedback and expertise in enhancing the

quality of this work; Dr. Myelinda Baldelovar, Department Chair of the Computer Science Department of North Eastern Mindanao State University -Tagbina Campus, Philippines, for her crucial guidance and support within the department; and Dr. Rolly Salvaleon, the Vice-President for Research and Extension of North Eastern Mindanao State University, Philippines, for approving the financial support for the publication of this research. Thank you all for your significant contributions to this research.

## REFERENCES

- Abayadeera, N., Jayawardena, R., & Byrne, N. M. (2019). Machine learning-based models for diabetes risk prediction in urban Filipinos. *Journal of Diabetes Research*, 2019, 1-8. <https://doi.org/10.1155/2019/3709346>
- Biau, G. (2012). Analysis of a random forests model. *Journal of Machine Learning Research*, 13(1), 1063-1095.
- Breiman, L., Friedman, J., Stone, C. J., & Olshen, R. A. (1984). *Classification and regression trees*. CRC press.
- Chen, T., Li, Z. H., Yuan, C. X., & Wong, K. C. (2004, July 4-8). *Improving bagging algorithms: Anti-overfitting by bagging adaptive boosting*. [Paper presentation]. Proceedings of the Twenty-first International Conference on Machine Learning (ICML), Alberta, Canada.
- Han, J., & Kamber, M. (2001). *Data mining: Concepts and techniques*. Morgan Kaufmann Publishers.
- International Diabetes Federation. (2019). *IDF diabetes atlas* (9th ed.). International Diabetes Federation. [https://www.diabetesatlas.org/upload/resources/material/20200302\\_133351\\_IDFATLAS9e-final-web.pdf](https://www.diabetesatlas.org/upload/resources/material/20200302_133351_IDFATLAS9e-final-web.pdf)
- Jia, Q., Chen, F., Wang, Y., Huang, B., & Chen, Y. (2018). Application of bagged decision trees for predicting diabetes mellitus in urban Chinese residents. *Journal of Healthcare Engineering*, 2018, 1-10.
- Mujumdar, A., & Vaidehi, V. (2019). Diabetes prediction using machine learning algorithms. *Procedia Computer Science*, 165, 292-299. <https://doi.org/10.1016/j.procs.2020.01.047>
- Nguyen, T. T., Tran, T. H., & Nguyen, H. H. (2020, November 12-14). *Feature selection techniques for diabetes prediction*. [Paper presentation]. Proceedings of the International Conference on Advanced Data Mining and Applications, Foshan, China.
- Nishat, M. M., Faisal, F., Mahbub, M. A., Mahbub, M. H., Islam, S., & Hoque, M. A. (2021). Performance assessment of different machine learning algorithms in predicting diabetes mellitus. *Bioscience Biotechnology Research Communications*, 14(1), 74-82. <https://doi.org/10.21786/bbrc/14.1/10>
- Pang, B., Wang, C., Lu, Y., Cao, J., Zhang, Y., & Jing, L. (2017). Predicting the risk of diabetes mellitus using machine learning techniques. *Frontiers in Genetics*, 8, 1-8.
- Philippine Statistics Authority. (2020). *2019 National nutrition survey final results*. Philippine Statistics Authority. <https://psa.gov.ph/nutrition-statistics/2019NNSTables>
- Quinlan, J. R. (1993). *C4.5: Programs for machine learning*. Morgan Kaufmann Publishers.
- Tan, C., Ona, E. T., Yu, W., Garabiles, M. R., & Sy, R. G. (2019). Predictive modeling of type 2 diabetes risk among Filipinos using decision trees and logistic regression. *Diabetes Research and Clinical Practice*, 153, 177-185.

- Wang, Y., Cao, Y., & Zhang, Y. (2018). An adaptive bagging algorithm for imbalanced data classification. *Applied Soft Computing*, 71, 1018-1030.
- Zhang, Y., Liu, L., & Li, Q. (2018, July 16-20). *A feature selection method based on PSO-SVM for diabetes prediction*. [Paper presentation]. IEEE International Conference on Software Quality, Reliability and Security Companion, Lisbon, Portugal.
- Zhao, Y., Feng, X., Li, L., Liu, Y., & Zhang, X. (2019). Prediction of diabetes using support vector machine algorithm based on medical examination data. *BMC Medical Informatics and Decision Making*, 19(2), 1-9.

## Determining Process Variability Using Fuzzy Triangular Distribution in Dynamic Value Stream Mapping

**Thulasi Manoharan, Faieza Abdul Aziz\*, Zulkiffle Leman and Siti Azfanizam Ahmad**

*Department of Mechanical & Manufacturing Engineering, Faculty of Engineering, Universiti Putra Malaysia, 43400 UPM, Serdang, Selangor, Malaysia*

### ABSTRACT

One of the lean tools is value stream mapping (VSM), which is used to visually map and analyze the flow of materials, information and processes required to deliver a product or service to the customer. VSM is widely used to streamline processes, reduce lead time and enhance overall operational performance. While VSM is a powerful tool, some challenges are associated with its conventional application in the manufacturing industry. Conventional VSM typically represents a snapshot of the value stream at a specific point in time. This static representation might not capture modern manufacturing environments' dynamic and evolving nature. Hence, this research addresses the problem of static representation of conventional VSM by applying Fuzzy Triangular Distribution (TFN) in the manufacturing industry by introducing a more flexible and dynamic approach. A conveyor manufacturing company was selected as a case study based on the wide variety and low volume type of manufacturing process. TFN approach was used to analyze variabilities in process parameters to identify their mean, minimum, and maximum values and remove all the outliers. Integrating TFN with VSM gives dynamic behavior to the conventional VSM. Based on the identifications, appropriate lean improvement tools were applied to develop an optimized future VSM. As a result, the future state map shows a 71.74%

and 19.45% improvement ratio in terms of production lead time and value-added time, respectively, compared to the current VSM. This study can be further extended by investigating how the reduction of lead time and WIP inventory can help reduce costs for a company.

### ARTICLE INFO

#### Article history:

Received: 15 March 2023

Accepted: 22 September 2023

Published: 22 July 2024

DOI: <https://doi.org/10.47836/pjst.32.3.17>

#### E-mail addresses:

[thulasimanoharan1@gmail.com](mailto:thulasimanoharan1@gmail.com) (Thulasi Manoharan)

[faieza@upm.edu.my](mailto:faieza@upm.edu.my) (Faieza Abdul Aziz)

[zleman@upm.edu.my](mailto:zleman@upm.edu.my) (Zulkiffle Leman)

[s\\_azfanizam@upm.edu.my](mailto:s_azfanizam@upm.edu.my) (Siti Azfanizam Ahmad)

\*Corresponding author

**Keywords:** Dynamic, lead time, triangular fuzzy number, value stream mapping, variability

## INTRODUCTION

In today's competitive business landscape, organizations strive to optimize their processes to ensure efficiency, reduce waste, and enhance overall performance. Value Stream Mapping (VSM) has emerged as a valuable tool for visualizing and analyzing the end-to-end processes within an organization (Lugert, Völker et al., 2018). VSM plays a crucial role in the lean production system by emphasizing activities that add value and pinpointing opportunities to eliminate waste (Lugert, Batz et al., 2018). This tool can be described as a graphical representation used to depict the current state of an organization, determine areas where waste can be reduced, and make decisions on necessary improvements to eliminate waste. It has become a widely adopted technique across various industries and domains and is considered a crucial aspect of lean production (Mudgal et al., 2020; Valencia et al., 2019).

VSM helps identify bottlenecks, inefficiencies, and opportunities for improvement. However, conventional static VSM may fall short of capturing the dynamic nature of processes and the inherent variability that occurs in real-time operations (Krishnan et al., 2018). Product variation due to increasing customer demand refers to the process of adapting or modifying a product to meet customers' changing needs and preferences (Womack et al., 1990). It can include introducing new features, changing the design, or offering different sizes, colors, or styles.

Product variation can be a good way for companies to stay competitive and meet the evolving needs of their customers (Abdulmalek & Rajgopal, 2017). While static VSM provides a snapshot of the process, it often fails to capture the variations that naturally occur due to changing demands, machine breakdowns, workforce availability and other unpredictable factors (Romero & Arce, 2017). These variations can lead to inefficiencies, lower productivity and increased operational costs. Therefore, there is a need to develop a methodology that integrates the concept of process variability into the existing framework of VSM (Venkataraman et al., 2014).

Variability significantly impacts the duration of each stage's cycle time and the work-in-process (WIP) between stages, causing extended wait periods, congestion, and a lack of predictability in terms of input and processing times (Woehrle & Abou-Shady, 2010). This difference arises from numerous factors, including product characteristics, workforce, equipment, and the environment in the value stream (Busert & Fay, 2019).

Thus, obtaining definite values when collecting data on time, inventory, and control parameters is challenging. The ambivalence and inherent variability of data contribute to waste and significant sources of noise in pull systems (Li & Wang, 2017). The failure to consider real variability in VSM is a significant drawback, and this article suggests a fuzzy VSM technique to overcome this weakness by incorporating uncertainty into value stream analysis and improvement (Azizi & Manoharan, 2015).

## BACKGROUND STUDY

The primary objective of dynamic VSM is to enhance the conventional VSM approach by incorporating real-time data and variability analysis. The goal is to create a more accurate and holistic representation of the process that takes into account the dynamic nature of operations. It involves capturing the average state of the process and its fluctuations and how those impact the overall performance metrics. Thus, this research presents a comprehensive approach that considers the unique characteristics of the production environment, such as its dynamic impact on the value stream. It is achieved by employing dynamic VSM with triangular fuzzy numbers (TFN) to drive ongoing enhancements in the face of uncertainty. By addressing variability and uncertainty, they can achieve sustained operational excellence.

### Value Stream Mapping (VSM)

Value stream mapping (VSM) is a lean tool that helps identify value-added and non-value-added activities in a production process with the goal of continuous improvement by eliminating waste. It is regarded as the most effective and widely used visual tool (Roessler et al., 2015; Tabanlı & Ertay, 2013). VSM is used to map the current and future states of a production process and to control variability and uncertainty in the dynamic production process (McDonald et al., 2002). However, the uncertainty inherent in dynamic and complex products, such as the Order (MTO) manufacturing environment, limits the use of traditional VSM in this area (Rahani & Al-Ashraf, 2012; Tasdemir & Hiziroglu, 2019). A fuzzy VSM approach is proposed that considers the inherent vagueness and uncertainty of dynamic production and reflects this uncertainty using fuzzy set theory to address this issue. Fuzzy VSM can visualize uncertainty in a wide range of industrial applications, making it a suitable tool for this purpose. Table 1 shows the lean manufacturing applications and VSM in various industries.

Table 1  
*Lean manufacturing applications and VSM in various industries*

Author/year	Objective	Case Sectors	Results	Contribution
Zahraee (2016)	Integrating the Lean tool of VSM with computer simulation to identify the underlying sources of waste and enhance production rates to meet customer demand	Small-scale heater industry	The production lead time (PLT) was shortened from 17.5 days to 11 days, accompanied by a reduction in value-added time from 3412 seconds to 2415 seconds. Additionally, the takt time experienced a decrease from 250 seconds to 192 seconds.	Future studies could focus on incorporating green manufacturing principles to minimize waste and pollution, fostering economic growth, and establishing mechanisms for recycling industrial waste generated during operational activities.

Table 1 (Continue)

Author/year	Objective	Case Sectors	Results	Contribution
Liu and Yang (2020)	This study employs commonality analysis to discern shared processes within a Make-to-Order (MTO) context, aiming to underscore unique characteristics inherent to the MTO environment.	Cast stone manufacturing company based in the UK	The approach presented in the paper, commonality analysis, introduces an additional step to the conventional methodology for creating future value streams. This extra step enhances data analysis for improved insights.	The effectiveness of commonality analysis has been demonstrated, and conducting a more comprehensive analysis could yield even more satisfactory results.
de Paula Ferreira et al. (2020)	To introduce an expansion of the VSM idea that involves calculating the costs linked to essential operations and the overall expenses of the complete production process	Production of ceramic capacitors	The suggested approach for evaluating the efficiency and flexibility of a production process relies on cost-based Value Stream Mapping (VSM), portfolio analysis, and simulating the impact of enhancements on the economic effectiveness of the production system.	Extending conventional VSM to capture time and cost analysis through a simulation program
Busert and Fay (2019)	The goal is to introduce an innovative method for creating a Lean Service System within the India Post service sector. This method involves using Simulation to simplify the system and reduce its complexity.	India Post service industry	The discovery reveals a 9.62 percent improvement in the delivery of items per individual.	This research marks the first instance of merging Value Stream Mapping with Simulation (VSM-Sim) to model and enhance the operational performance factors of mailing service operations.
Ghobakhloo and Fathi (2019)	To analyze the role of VSM in healthcare services by eliminating everything that adds no value to the organization	Healthcare services	VSM helps reduce patients' waiting time in healthcare lines by synchronizing different activities. Secondly, VSM helps to standardize symbols and make them easier to understand.	As the lean approach has been introduced in healthcare organizations, VSM and other tools related to process improvement have been incorporated into these organizations.

Table 1 (Continue)

Author/year	Objective	Case Sectors	Results	Contribution
Mudgal et al. (2020)	The objective is to expand the application of Value Stream Mapping into the context of Industry 4.0, focusing on supporting Industry 4.0 efforts in manufacturing firms, particularly in smaller and medium-sized enterprises (SMEs).	Small and mid-size enterprises (SMEs)	VSM combined with hybrid simulation can assist Industry 4.0 roadmap development and help companies understand changes in materials, equipment, processes, and information flows associated with Industry 4.0 application scenarios.	This study explores the integration of the Lean practice value stream mapping (VSM) with hybrid simulation (HS), which combines discrete event and agent-based modeling and simulation, contributing to reducing this research gap.

## FUZZY VSM

Fuzzy VSM is used to convert ambivalence into fuzzy numbers to deal with the uncertainty of value stream parameters in a computational manner (Stadnicka & Litwin, 2019). A subset of the real number set is known as a fuzzy set that denotes unsure figures (Liu & Yang, 2020). Zadeh (1965) denotes a class of items with a variety of degrees of membership as what is meant by a fuzzy set. The degree draws attention to whether a piece of equipment is entirely inside the set, entirely outside, or halfway inside and halfway outside. This set's membership is promoted rather than connected to a probability distribution.

According to Liu and Yang (2020), inventories, periods, and other operating factors in a value stream, such as TFN and NFN, were acquired to represent inventories, periods, and other operating factors in a value stream. A commercial strategy demonstrates the applicability and efficacy of the suggested A production lot for incorporating variability in VSM analysis for both TFN and NFN forms. Based on the results, Liu and Yang (2020) conclude that Triangular fuzzy VSM chooses, in a complex manufacturing environment with complex operational procedures, to misinterpret the unpredictability of the process. The author suggests that to improve the accuracy of VSM analysis, fuzzy VSM should be analyzed through a simulative approach.

## Integration of VSM with Fuzzy Algorithm

According to Braglia et al. (2009), the traditional VSM procedure is not able to provide an actual illustration of the production process ambiguity issues related to the analysis. Besides, variability is one of the main elements affecting the work-in-process (WIP) between side-by-side processes and the cycle time of each stage. The variability impacts the queuing time and leads to blocking and unreliability in inputs and time of the process (Chen et

al., 2013). Uncertainty occurs in many aspects, including WIP, equipment, manpower, and the environment of the value stream (Faulkner & Badurdeen, 2014). Hence, it causes difficulty when collecting data related to time, inventories, and other operating variables (Zahraee, 2016). Additionally, one of the main causes of waste is the inaccuracy of data and the inherent fluctuation in such statistics (Stadnicka & Litwin, 2019), and it stands out when it comes to pulling system inputs, outputs, processes, unpredictable breakdowns, and random setup times (Dai et al., 2012).

Given the problems, one of the key drawbacks of VSM is the inadequate treatment of actual variability in the value stream (Liu & Yang, 2020). To overcome this weakness, Braglia et al. (2009) suggested a few substitute methods based on fuzzy algebra and statistics, respectively. Both approaches were created to ease the users' understanding and applied to company practices. Pacchini et al. (2019) mapped the value stream using fuzzy set theory and chose the optimum future-state VSM. Although they suggest a fuzzy VSM method to manage variability in value stream analysis and enhancement, these two studies solely utilize triangular fuzzy numbers to represent values in VSM. They do not explore the appropriateness of other fuzzy expressions in diverse production settings. (Deshkar et al., 2018).

### **Triangular Fuzzy Number (TFN)**

A mathematical arithmetic framework is required to control the uncertainty of value stream specifications in a computation method. According to Zadeh (1965), a fuzzy distribution has been established based on the theory of fuzzy sets as a possible methodology for the mathematical control of variability and unreliability (Galan et al., 2007; Karim et al., 2012).

Due to varying membership degrees, Zadeh (1965) denotes a fuzzy set as a class of objects. This set is organized by the membership function  $\mu(x)$ , which maintains a membership degree for each object class between zero and one. It also implies that an object or element is probably "a little" included in the set, whether it exists inside the set or not. This set's membership changes frequently and is irrelevant to a probabilistic function (Guo et al., 2019; Gurumurthy & Kodali, 2011).

Triangular fuzzy numbers are used for further modeling. More complicated membership functions increase computational demands without enhancing any appreciable returns (Braglia et al., 2009). Triangular fuzzy numbers are likewise simple to use and reasonably depict the circumstances being examined (Ferreira et al., 2020). Fuzzy numbers express the uncertain aspects of value stream indicators such as cycle times, inventories, and lead times (Dety & Yingling, 2000). Since value stream analyses cannot produce probabilities due to their qualitative nature, utilizing theoretical variables is not considered in this scenario.

The purpose of applying fuzzy set theory is to translate the unpredictability of value stream features into fuzzy numbers for computational management. A fuzzy set is a subset

of real numbers that represent uncertain values. It is defined by a membership function  $\mu(x)$  that assigns a membership degree from zero to one to each object class. Based on this degree, an element can be fully inside, entirely outside, or partially within the set. The membership degree is graded and is not linked to a probability distribution. This research introduces a triangular fuzzy number (TFN) to illustrate the variability in value stream management (VSM).

Data collecting must be done properly to express the process and waiting times with the suitable TFNs. This study gives a parameter identical to the previous study and is used to calculate the values of a, b, and c, as suggested by Liu and Yang (2020).

## **MATERIALS AND METHODS**

The integration of Fuzzy Triangular Numbers with Value Stream Mapping was introduced to build a dynamic VSM that can capture variability and uncertainty in a complex and more customized production operation such as an MTO manufacturing industry. It consists of a set of steps: (1) Collection of manufacturing process data, (2) analysis of process variability using Triangular Fuzzy Number, (3) Implementation of lean improvement tool, and (4) Design of future state VSM.

### **Case Study**

A conveyor chain manufacturing company, referred to as CM, is studied to display the utilization of fuzzy value stream mapping to integrate variability/uncertainty in value stream analysis. CM is a make-to-order manufacturing company with an average production rate of 1,500 m of chain per week. The production process comprises a shop flow system that is segmented into six primary stages: (1) coining, (2) drilling, (3) chamfering, (4) welding, (5) heat treatment/coating/plating (sub-cont), (6) sub-assembly, (7) main assembly and (8) quality check and packaging. All these activities are carried out within the company except for heat treatment/ plating or ed-coating, which are outsourced to various subcontractors. The choice of a conveyor manufacturing company as a case study is attributed to its ability to operate in a wide variety of processes and low volume. The production process is made-to-order, and a wide range of goods have various process parameters. Its unchanging and rigid nature characterizes a VSM and is inefficient in capturing varying process parameters. Hence, this research demonstrates controlling variability using fuzzy algorithms and mapping the current value stream.

### **Designing Current Value Stream Map**

In order to progress a current state map, it is relevant to collect information regarding shipment frequency and quantity, client orders, processes involved in product manufacturing

processes, for instance, changeover times (COs), cycle times (CTs), variables such as the number of operators, the frequency and amount of materials received, the quantity and storage locations of inventory, and working time related to the manufacturing system data collection involved gathering and meticulously reviewing 100 data sets to create a sufficient sample for subsequent analysis. Additionally, data pertaining to the quantities of raw materials, work-in-progress (WIP), and finished products were collected according to the flow chart shown in Figure 1 to build the Current VSM.

The time was taken to measure the cycle time (C/T) when the worker had finished repeating a particular task. The measurements include the manual cycle time and machine cycle time. The machine cycle time indicated on value-added actions and the manual cycle time measured are non-value-added actions but necessary. Manual and machine cycle time are considered for the calculations in all the workstations. Although there was available

cycle time stated in the production job sheet, the researcher conducted a time study using a stopwatch. Since it is not distinguished that the recorded cycle times were measured in the condition of the machine and the status of the workers, according to the Rother and Shook (2003) recommendation, cycle times were measured at the time of investigation to explore the real condition of the value stream.

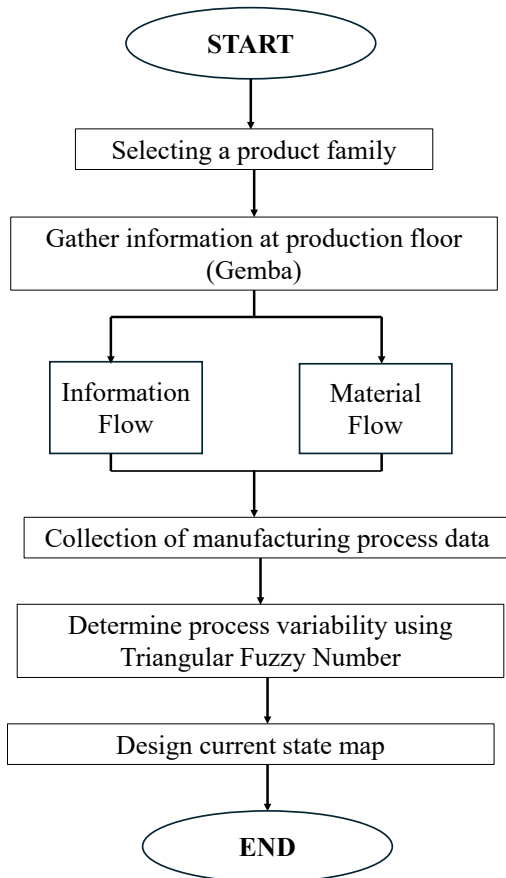


Figure 1. Flowchart to build Current VSM

### Analyze Process Variability Using Triangular Fuzzy Number

The Conveyor Manufacturing (CM) facility is overseen by an ERP production control system, which transmits a daily schedule to individual workstations. The first method uses TFN to show how long an item spends at each stage of manufacture. While TFNs offer a compromise between computational cost and the accuracy of the final ranking, their use in the context of VSM seems reasonable. An ordered quartet = (a, b, c) defines a generic TFN, where a and c stand for the lower and upper bounds, respectively. The fuzzy degree is indicated by c-a, with

larger values indicating a higher degree of fuzziness. TFNs provide a favorable trade-off between computation  $c$ . If  $a=b=c$ , TFN diverges into a real number. The interval  $[a, c]$  is represented as the support of  $\tilde{A}$  as shown in Equations 1 to 4.

The following relation details the bilinear relation that constitutes the membership function  $\mu_{\tilde{A}}(x)$ :

$$\mu_{\tilde{A}}(x) = \begin{cases} 0, & x \leq a, \\ \frac{x - a}{b - a}, & a < x \leq b \\ \frac{c - x}{c - b}, & b < x \leq c, \\ 0, & x > c, \end{cases} \quad [1]$$

- (i)  $\alpha = 1$ :  $\mu(x) = 1$  denotes the value  $x$  unequivocally falls within the range of potential values.
- (ii)  $\alpha = \lambda$ :  $\mu(x) > \lambda$  means that the value  $\lambda$  has a possibility of  $\mu(x) > \lambda$  falls within the range of potential values

Hence, the value of  $b$  is established as the average of the sample data for condition  $\alpha$ -cut  $\alpha_1 = 1$ . The sample's minimum and maximum values correlate to an  $\alpha$ -cut  $\alpha_2 = 0.1$  rather than to 0 to integrate other possible maximum values that are unable to be expressed by inspection to incorporate more potential maximum values that cannot be conveyed by inspection.

$$a = \frac{(\min(\text{sample}) - 0.1b)}{0.9} \quad [2]$$

$$b = \mu(\text{sample}), \quad [3]$$

$$c = \frac{(\max(\text{sample}) - 0.1b)}{0.9} \quad [4]$$

### Implement Lean Improvement Tools

After identifying waste by mapping the current state, actions need to be taken to reduce or eliminate the waste in the next stage. Waste can occur in two different stages: one at the managerial level and another at the worker level. The waste that occurs at the worker level is selected for further improvements using the Value Stream Mapping (VSM) tool. The causes of waste can be grouped into two classes: behavioral and information factors. The root of each waste is distinguished by using the number of questions and the trace of causes, including behavioral and information factors (Romero & Arce, 2017).

A future state map is then created by eliminating waste at the worker level. In the future state map, it is tried to make the flow continue through waste elimination. It can dramatically

reduce throughput time and almost always reduces costs substantially. Achieving frequent, continuous flow requires brainstorming, but the straightforward road map for mapping the future state is answering several questions stated by Rother and Shook (2003).

Answering these questions gives us an idea of the future state's mapping needs. The step-by-step answering of these questions leads the researcher to map the optimized state map. Hence, to answer the questions, the appropriate data was collected to map the current state. The first five questions concern "basic" issues in constructing the future state map, as shown below.

1. What is the Takt time for the projected product family at the conveyor manufacturing company?
2. Should the products produced be directly shipped or sent to a finished goods supermarket?
3. Where will CM use a pull system supermarket inside the value stream?
4. Where can continuous flow be used?
5. What process improvement tools will be needed to achieve the future state design?

### Design Future State Value Stream Map

The fuzzy set theory is performed to context preceding data sets at the beginning to determine the most appropriate future state, which is practical. It is carried out to convert the vectors to make the input data for the following decision-making process more comprehensible. Therefore, for every output  $C = \{c_1, c_2, \dots, c_j\}$  associated with each future state  $A = \{a_1, a_2, \dots, a_i\}$ , a fuzzy number must be constructed from the  $n$  unique data sets ( $X_{ks} = ck(as)$ )  $n$ . The values of  $m$ ,  $\alpha$ , and  $\beta$  must be determined, as shown in Equations 5 and 6, to express each column of simulation results as a fuzzy number.

The triangular form is used to depict data as the middle value ( $m$ ), and the median (also known as the 50%-quantile or  $Q_{0.5}$ -value) from the set of  $n$  results is considered the best approximation. The median separates the set into two parts, one with larger numbers and the other with smaller numbers. Additionally, the median is considered the best choice for elaborating accumulations in sets (Zahraee, 2016). The lower and upper spreads are measured by incorporating the 5% and 95% quantiles to minimize the impact of outliers on the fuzzy sets' absolute spread. Figure 2 shows the holistic view of the methodology used in this study, and Figure 3 shows the representation of Triangular Fuzzy Distribution.

$$\begin{array}{ll}
 m \text{ for all } n & m = Q_{0.5} \{X_{id0}, \dots, X_{idn}\} & [5] \\
 a \text{ and } b \text{ for all } n & a = m - Q_{0.05} \{X_{id0}, \dots, X_{idn}\} \\
 & b = Q_{0.95} \{X_{id0}, \dots, X_{idn}\} - m & [6]
 \end{array}$$

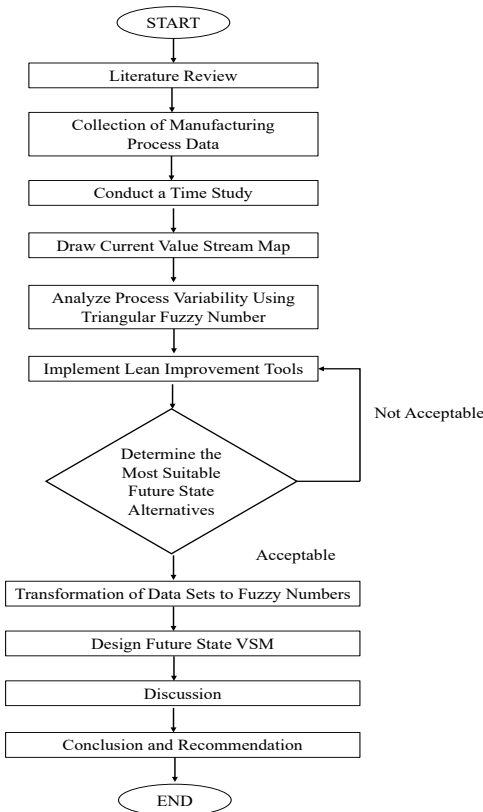


Figure 2. A holistic view of the methodology

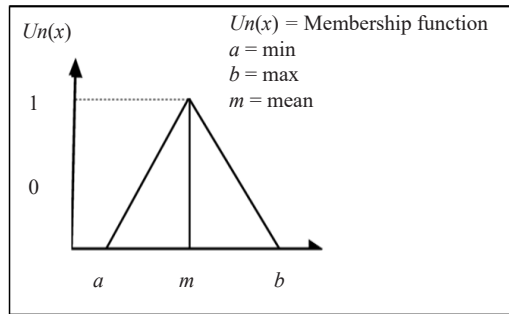


Figure 3. Representation of Triangular Fuzzy Distribution

## RESULTS

The proposed methodology is implemented in a real case study for the dynamic value stream mapping conducted by integrating with fuzzy triangular distribution and providing manufacturing process data.

### Current State Analysis

Current state analysis and their processes are explained in detail. The processes are grouped into two main categories: value-added activities (VA) and non-value-added activities (NVA).

- i. A product family was selected to prevent complexity in mapping the value stream of CM. Three family products are identified in this conveyor manufacturing company: single former chain, double former chain, and condom chain. Among these three, only one product family is chosen based on their common process and high customer demand, as shown in Table 2.

Table 2  
Product family selection

Product/ Workstation	STP 1	MAC	WEL	STP 2	Sub- Cont	ASY 1	ASY 2
Single former chain	X	X			X	X	X
Double former chain	X	X	X	X	X	X	X
Condom chain	X	X			X	X	X

- ii. Information flows from upstream, which begins with receiving customer orders. Production Planning and Control (PPC) creates production orders and bills of materials based on the sales orders.
- iii. Material flows from downstream to upstream, starting from receiving goods from suppliers. Figure 4 shows the sequence of material flow at CM.
- iv. Manufacturing process data were collected by measuring the cycle time (C/T), including manual and machine cycle times.
- v. Other than C/T, other process parameters include machine changeover time (C/O), every part every x (time) (EPEX), the number of operators, and the number of inventories between stations.
- vi. Average daily output is calculated as Equation 7.

$$\text{Average daily output} = \frac{\text{Demand}}{\text{Working Days}} = \frac{84,240 \text{ meter}}{156 \text{ Days}} = 540 \text{ meters/day} \quad [7]$$

- vii. Takt time is calculated based on the available production capacity over customer daily demand, which is 780 minutes, as shown in Equation 8.

$$\begin{aligned} \text{Takt Time} &= \frac{\text{Net Available for Production}}{\text{Customer's Daily Demand}} \\ &= \frac{780 \text{ minutes}}{270 \text{ coil}} \\ &= 173 \text{ seconds/coil} \end{aligned} \quad [8]$$

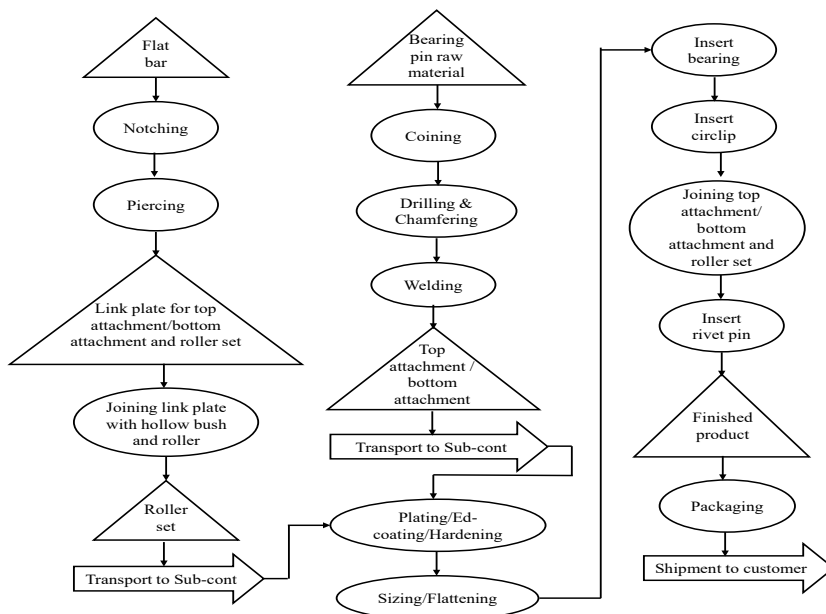


Figure 4. Sequence of material flow at CM

Triangular fuzzy numbers were used to distribute process data to (min, mean, and max) and standard variables using mean and variance based on the 100 groups of data sets. Table 3 shows the data distribution for five different processes.

Table 3  
Triangular Distribution for measured cycle time and buffer/WIP for five workstations

	Standard Variable		Observed Value			TFN
	Mean	Std. Dev	Min	Mean	Max	
Raw material inventory (days)	6.03	2.37	1.1	6.03	12	(1.1, 6.03, 12.0)
Coining (s)	89.84	6.74	68.02	89.84	100.01	(68.02, 89.84, 100.01)
Buffer 1 (days)	3.42	1.72	1.2	3.42	7.01	(1.2, 3.42, 7.01)
*Drilling (s)	208.13	7.66	191.1	208.13	225.01	(191.10, 208.13, 225.01)
Buffer 2 (days)	5.78	2.09	1.2	5.78	9.10	(1.2, 5.78, 9.10)
Chamfering (s)	89.97	7.06	68.01	89.97	100.01	(68.01, 89.97, 100.01)
Buffer 3 (days)	4.02	1.85	1.11	4.02	8.20	(1.11, 4.02, 8.20)
Welding (s)	97.52	8.67	90.1	97.52	122	(90.1, 97.52, 122)
Buffer 4 (days)	2.42	1.72	1.11	2.01	4.2	(1.11, 2.01, 4.2)
*Assembly (s)	331.07	12.97	288.2	331.07	375	(288.2, 331.07, 375)
Buffer 5 (days)	3.42	1.68	1.01	3.42	7.03	(1.01, 3.42, 7.03)

- viii. Table 3 depicts the current value stream of the conveyor manufacturing in Figure 5. The timelines for the standard and triangular fuzzy number (TFN) approaches are demonstrated in Figure 5.
- ix. The present state map (Figure 5) illustrates that the overall production lead time (TPLT) is 28 days, while the total value-added time (TVAT) is only 13 minutes, which leaves a significant gap for improvement.
- x. Using the triangular fuzzy timeline, TPLT (days) denoted as  $\mu_A(x) \sim (11.01, 28.87, 54.24)$  and TVAT (min) denoted as  $\mu_B(x) \sim (11.73, 13.61, 15.37)$  with the following Equations 9 and 10, respectively.

$$\mu_A(x) = \begin{cases} 0, & x < 11.01 \\ \frac{x - 11.01}{17.86}, & 11.01 \leq x \leq 28.87 \\ \frac{54.24 - x}{25.37}, & 28.87 \leq x \leq 54.24 \\ 0, & x > 54.24. \end{cases} \quad [9]$$

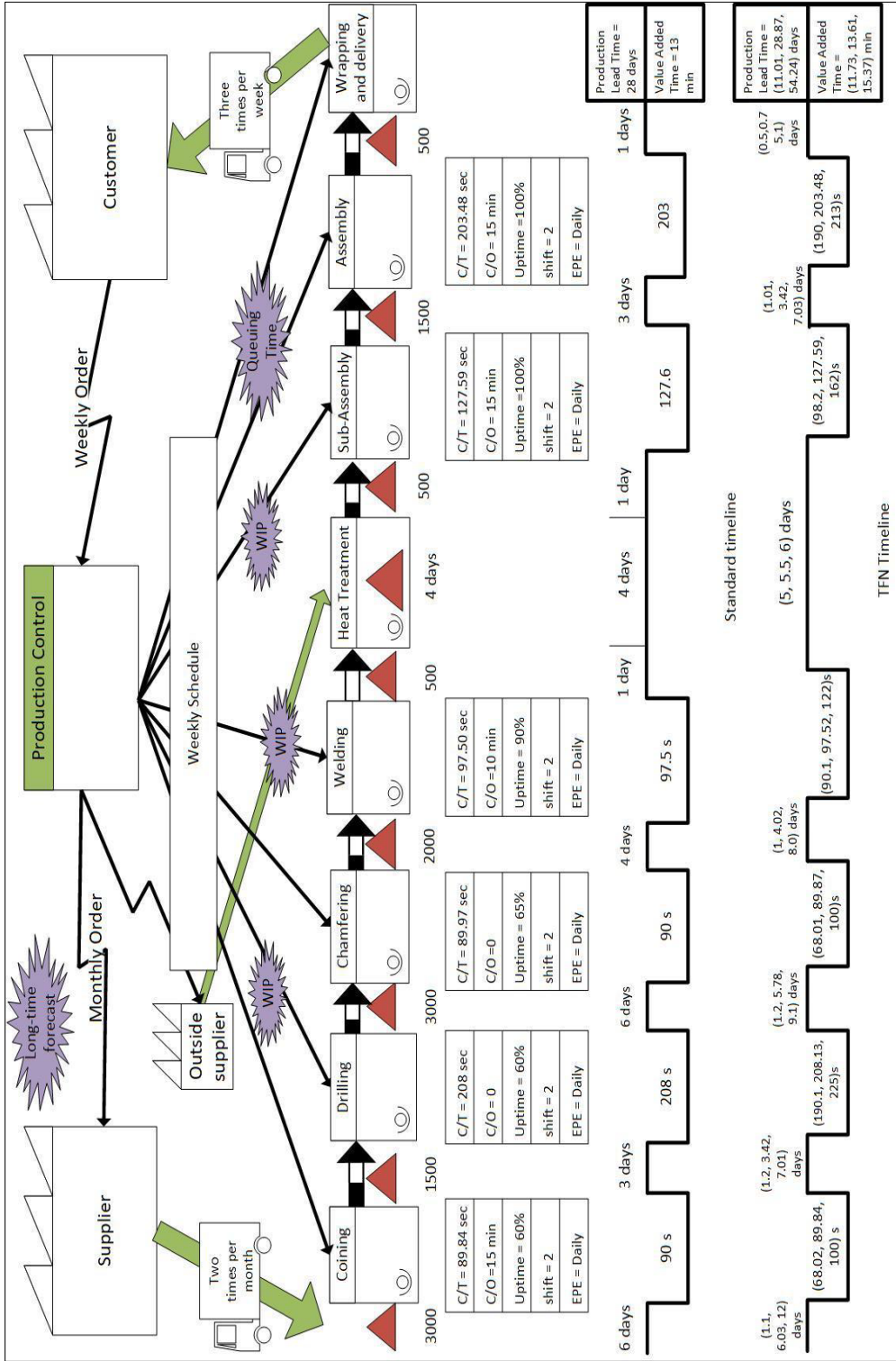


Figure 5. Current value stream map

$$\mu_B(x) = \begin{cases} 0, & x < 11.73 \\ \frac{x-11.73}{1.88}, & 11.73 \leq x \leq 13.61 \\ \frac{15.37-x}{1.76}, & 13.61 \leq x \leq 15.37, \\ 0, & x < 15.37. \end{cases} \quad [10]$$

### Developing Future State Mapping

In order to create a future state map, the areas of improvement in the current state map must be determined. As listed below, several problems are identified on the production floor, mainly due to unsystematic process flow lines.

1. Large amounts of inventories and WIP are in each processing department.
2. There are big differences between the total production lead time (28 days) and value-added time (13 min)
3. High process variabilities, such as in cycle time and setup time due to different product models
4. Unbalanced utilization of workers
5. Complexity in production planning and a high amount of inventory
6. Delayed in the arrival of subparts from subcontractors after the heat-treatment/plating/ Ed-coating process.

Lean manufacturing aims to improve production efficiency by producing quality output according to specifications and delivering it to customers on time. Although the purpose of this research is to focus on reducing total production lead time, the lead time and inventory are two equivalent factors.

### Implement Lean Improvement Tools

Waste is identified by analyzing the material and information flow in the value stream based on the current state map. In order to redesign the current state map and develop an improved future state map, a set of questions needs to be answered. There are five questions in total related to the basics of the construction of a future state map. Below are descriptions of the answers to the questions from 1 to 5.

**Question 1:** What is the Takt time for the proposed product family of the CM?

- i. Takt time is calculated based on Equation 8, which is 173 seconds/coil.

**Question 2:** Where will the supermarket system be used inside the value stream by the CM?

ii. A "supermarket" is similar to a storage area (a space allocated to keep finished goods) packed and ready to be shipped. Supermarkets aim to control the process, which cannot be linked to the continuous flow. The supermarkets enable CM to minimize the inventory. As a result, the lead time was reduced, and the turnover ratio increased. In similar orders, supermarkets can be dedicated with similar planning. So that once a coined bearing pin becomes full, the workstations are arranged to produce other orders.

**Question 3:** Where will CM use a pull system supermarket inside the value stream?

iii. The pull system works as a channel where the welding department is located at the beginning and the sub-contractor at the end of the value stream. Hence, any excess inventory or disturbance caused by the push system at this channel can be controlled easily.

**Question 4:** Where is the continuous flow technique applied?

iv. The balance chart, as shown in Figure 6, indicates the variabilities for cycle times at CM.

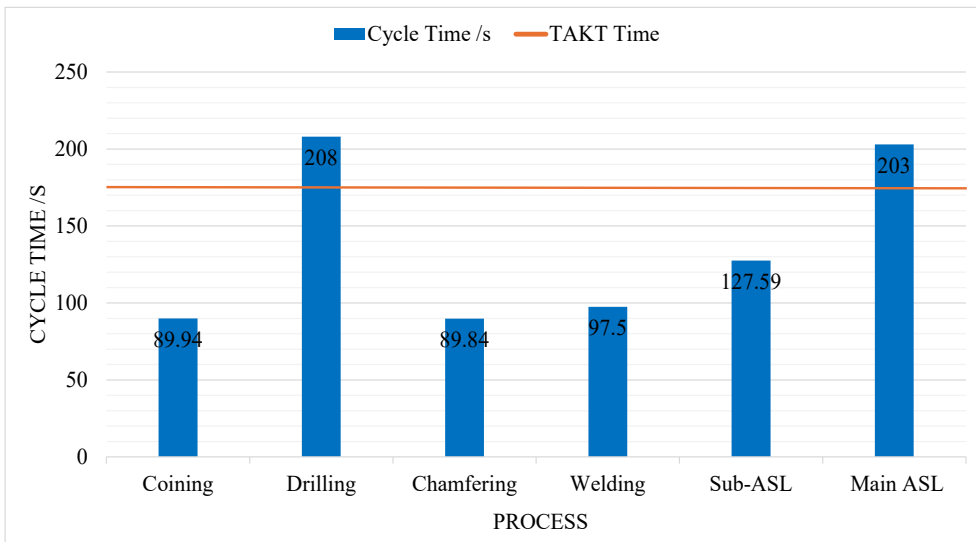


Figure 6. Balancing chart of current value stream

v. Figure 6 shows that the major obstacles to balancing the cycle times are the drilling and main assembly stations, which have higher cycle times than takt time.

- a. Two different areas are drilled separately on the bearing pin at the drilling station, called the center drill and top drill. The setting time taken by the current operator to change the chuck is 3.26 minutes or 196 seconds on average, plus 7 seconds taken to clean the burr. If the current worker changes with an expert worker, it can help to reduce the manual setting time from 3.26 minutes to 2.5 minutes on average. Eventually, the cycle time at this station can be reduced to 157 seconds, and the output can be increased from 1125 units to 1400 units per day.
  - b. The main assembly department has particular production features and can be improved by balancing skilled and unskilled workers evenly between night and morning shifts. The cycle time in this department is 203 seconds, which is higher than the takt time. In order to increase the current output at the main assembly department, the unskilled workers must work alongside the skilled workers. As such, the workers are rebalanced by arranging three skilled and two unskilled workers in the morning shifts and two skilled and three unskilled workers in the night shift. Through these arrangements, the current output from 230 units per day to 280 units can reduce the cycle time to 167 seconds.
- vi. Figure 7 shows the improved cycle times for the stations. The workloads for each station are balanced according to the following explanations.

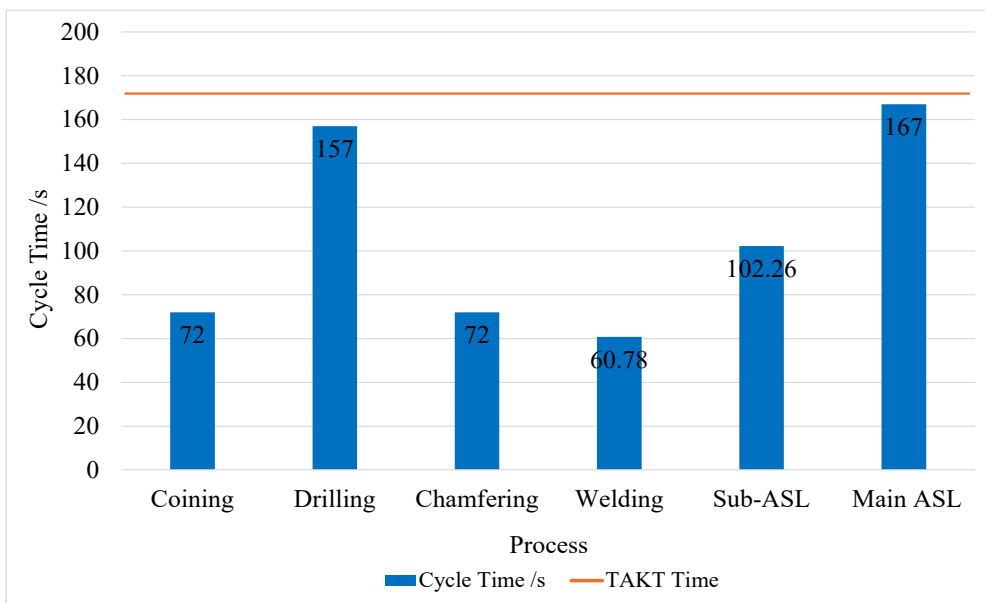


Figure 7. Balancing chart of future value stream

**Question 5:** What process improvement will be needed to achieve the future state design?

vii. Using the transfer of Kanban cards is the most effective tool for designing a smooth flow. The Heijunka box decides when the Kanban card should be released. FIFO and the one-piece-in-flow method manage the continuous flow before sending it to sub-contractors and welding workstations. So, the production Kanban cards should be sent to the coining workstation directly at every pitch. The pitch is calculated by multiplying the Takt time or coefficient by the quantity of finished goods transferred. At every pitch, one production Kanban was dispatched to the welding department. In each turn, the orders are released at a fast pace, and the finished products are stocked at the FIFO channel before delivery to the subcontractors. So, the pace of production is maintained a constant role.

The type improvements for the future state map are summarized in Table 4.

Table 4  
*Improvement for future state map*

Improvement in	Information Flow	Reduction of monthly order from 250k of raw materials to 150k based on actual monthly output
Material Flow		<p>Controlling information flow using heijunka box instead of sending individual production orders from production control</p> <p>Use Kanban cards to send order schedules between stations to control the pull system at CM.</p> <p>Routinely check and fix the production order schedule on the CM shop floor.</p> <p>Minimizing raw material and parts delivery from a weekly to monthly.</p> <p>Standardize and control buffer inventory between each station using the supermarket.</p> <p>Overproduction is removed at each station, and buffer inventory is predefined based on the demand in the next station and Takt time.</p> <p>Reduction of cycle time in drilling machine using controllers and sensors (TPM technique) and use of expert operator</p> <p>Using the one-piece-in- flow technique in the sub-assembly department</p> <p>Using the First-In-First-Out (FIFO) technique before sending products to outside suppliers to prevent overproduction</p> <p>Fixing the lot size delivery to 20 pallets equivalent to 270 units of conveyor chain</p>

Based on the lean improvement tools described in Table 4, a future state value stream was developed and depicted in Figure 8, which includes all information transfer, material movement, and recommended kaizen.

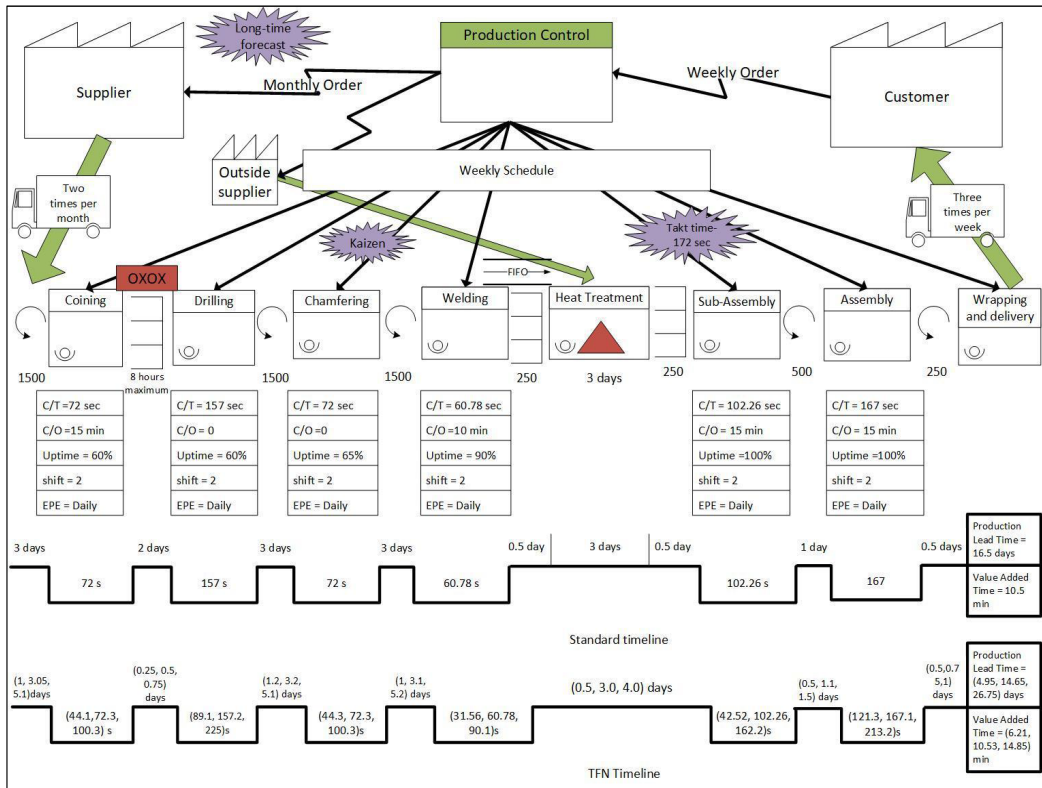


Figure 8. Future value stream mapping

### Analysis of Future VSM using Triangular Fuzzy Number

Data representation in the triangular form as a middle value (m) uses the median (also referred to as the 50% quantile or Q- 0.5 value) from the set of n results as the most suitable approximation. The median splits the set into two number groups, one with larger values and one with smaller ones. Furthermore, the median is ideal for describing accumulations within sets (de Paula Ferreira et al., 2020). The information regarding the approximation of future state designs, FVSM, and their transformation into fuzzy numbers is detailed in Table 5 based on Equations 5 and 6. The visualization of triangular fuzzy numbers is denoted in Figure 9.

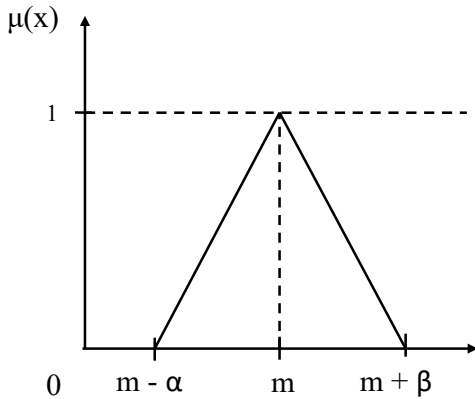


Figure 9. Visualization of triangular fuzzy numbers (TFN) (Liu & Yang, 2020)

## DISCUSSION

Integration of Value Stream Mapping with Triangular Fuzzy Analysis aligns with the growing trend of incorporating uncertainty analysis into process improvement methodologies. Similar studies have utilized fuzzy logic, Monte Carlo simulations, and other probabilistic methods to capture the inherent variability present in operational processes. While different studies employ varied techniques, this study contributes by applying Triangular Fuzzy Analysis to Value Stream Mapping, enabling it to address uncertainties in process time, inventory, and resource availability.

Table 5  
TFN for calculated cycle time and WIP for FVSM

Cycle Time and WIP	Stock at a defined minimum	Stock at physical maximum	Fuzzy stock (m;α;β)
Raw material inventory (days)	1	5	(3; 2; 2)
Coining (s)	44	100	(72; 28; 28)
Buffer 1 (days)	0.25	0.75	(0.5; 0.25; 0.25)
Drilling (s)	89	225	(157; 68; 68)
Buffer 2 (days)	1	5	(3; 2; 2)
Chamfering (s)	44	100	(72; 28; 28)
Buffer 3 (days)	1	5	(3; 2; 2)
Welding (s)	31.56	90	(60.78; 29.22; 29.22)
Sub-Assembly (s)	42.52	162	(102.26; 59.74; 59.74)
Buffer 5 (days)	0.5	1.5	(1; 0.5; 0.5)
Main-Assembly (s)	121	213	(167; 46; 46)

Incorporating Triangular Fuzzy Analysis enhances the accuracy of decision-making processes by explicitly considering uncertainties. It equips managers with more robust insights to develop adaptable strategies that perform well under various scenarios. For instance, they can allocate additional resources to critical process stages that exhibit high variability due to uncertain factors.

Consider a manufacturing company aiming to optimize its production line. Traditional VSM identifies a bottleneck in the assembly stage, suggesting increased machine capacity as a solution. However, fuzzy analysis reveals that machine breakdowns and variations in worker efficiency significantly impact assembly time. The managerial implication is investing in machine capacity, developing preventive maintenance schedules, and cross-training workers to mitigate uncertainties. This holistic approach ensures consistent production even when unexpected events occur.

## CONCLUSION

The study's integration of Value Stream Mapping (VSM) with Triangular Fuzzy Numbers (TFN) has substantially contributed to process optimization and uncertainty management. Based on the identifications, appropriate lean improvement tools were applied to develop an optimized future VSM. As a result, the future state map shows a 71.74% and 19.45% improvement ratio in terms of production lead time and value-added time, respectively, compared to the current VSM.

While the study presents a novel approach, it is important to acknowledge its limitations. One potential limitation is the complexity associated with determining appropriate membership functions for TFN. The accuracy of results heavily depends on the selection of membership function parameters, which might be challenging to establish in some contexts.

Future studies can build upon the work to further refine and expand the application of VSM with TFN. Exploring alternative methods for membership function determination, such as data-driven or expert-driven approaches, could help mitigate uncertainties associated with TFN modeling. Furthermore, research could delve into integrating TFN with other process improvement methodologies, such as Six Sigma or Lean Thinking. Investigating how TFN can contribute to optimizing processes within the context of broader quality and efficiency improvement initiatives could open new avenues for research.

The principles of VSM are universally applicable and widely recognized as effective tools for identifying process inefficiencies. Similarly, TFN, as a representation of uncertainty, is a concept that transcends industry boundaries.

In summary, the study's integration of VSM with TFN offers a novel pathway for addressing uncertainty in process optimization. Its significant contribution lies in combining systematic process mapping with a quantitative representation of uncertainty, resulting in more informed decision-making. As the industrial landscape continues to evolve, this work is a foundation for fostering resilient and adaptable operations in diverse industries worldwide.

## ACKNOWLEDGEMENT

The authors deeply acknowledge Universiti Putra Malaysia (UPM) financial support (Vote Number: GP-IPS/2022/9735100), Research and Management Centre of UPM.

## REFERENCES

- Abdulmalek, F. A., & Rajgopal, J. (2017). Analyzing the benefits of lean manufacturing and value stream mapping via simulation: A process sector case study. *International Journal of Production Economics*, 107(1), 223–236. <https://doi.org/10.1016/j.ijpe.2006.09.009>
- Azizi, A., & Manoharan, T. (2015). Designing a future value stream mapping to reduce lead time using SMED-A case study. *Procedia Manufacturing*, 2, 153–158. <https://doi.org/10.1016/j.promfg.2015.07.027>
- Braglia, M., Frosolini, M., & Zammori, F. (2009). Uncertainty in value stream mapping analysis. *International Journal of Logistics Research and Applications*, 12(6), 435–453. <https://doi.org/10.1080/13675560802601559>
- Busert, T., & Fay, A. (2019). Extended value stream mapping method: Harmonizing information flows for the control of production processes. *IFAC-PapersOnLine*, 52(13), 54–59. <https://doi.org/10.1016/j.ifacol.2019.11.129>
- Chen, J. C., Cheng, C. H., & Huang, P. B. (2013). Supply chain management with lean production and RFID application: A case study. *Expert Systems with Applications*, 40(9), 3389–3397. <https://doi.org/10.1016/j.eswa.2012.12.047>
- Dai, Q., Zhong, R., Huang, G. Q., Qu, T., Zhang, T., & Luo, T. Y. (2012). Radiofrequency identification-enabled real-time manufacturing execution system: A case study in an automotive part manufacturer. *International Journal of Computer Integrated Manufacturing*, 25(1), 51–65. <https://doi.org/10.1080/0951192X.2011.562546>
- Deshkar, A., Kamle, S., Giri, J., & Korde, V. (2018). Design and evaluation of a Lean Manufacturing framework using value stream mapping (VSM) for a plastic bag manufacturing unit. *Materials Today: Proceedings*, 5(2), 7668–7677. <https://doi.org/10.1016/j.matpr.2017.11.442>
- de Paula Ferreira, W., Armellini, F., & De Santa-Eulalia, L. A. (2020). Simulation in industry 4.0: A state-of-the-art review. *Computers & Industrial Engineering*, 149, Article 106868. <https://doi.org/10.1016/j.cie.2020.106868>
- Detty, R. B., & Yingling, J. C. (2000). Quantifying benefits of conversion to lean manufacturing with discrete event simulation: A case study. *International Journal of Production Research*, 38(2), 429–445. <https://doi.org/10.1080/002075400189509>
- Faulkner, W., & Badurdeen, F. (2014). Sustainable value stream mapping (Sus-VSM): Methodology to visualize and assess manufacturing sustainability performance. *Journal of Cleaner Production*, 85, 8–18. <https://doi.org/10.1016/j.jclepro.2014.05.042>
- Galan, R., Racero, J., Eguia, I., & Garcia, J. M. (2007). A systematic approach for product families formation in reconfigurable manufacturing systems. *Robotics and Computer-Integrated Manufacturing*, 23(5), 489–502. <https://doi.org/10.1016/j.rcim.2006.06.001>

- Ghobakhloo, M., & Fathi, M. (2019). Corporate survival in Industry 4.0 era: the enabling role of lean-digitized manufacturing. *Journal of Manufacturing Technology Management*, 31(1), 1-30. <https://doi.org/10.1108/JMTM-11-2018-0417>
- Guo, W., Jiang, P., Xu, L., & Peng, G. (2019). Integration of value stream mapping with DMAIC for concurrent Lean-Kaizen: A case study on an air-conditioner assembly line. *Advances in Mechanical Engineering*, 11(2), Article 1687814019827115. <https://doi.org/10.1177/1687814019827115>
- Gurumurthy, A., & Kodali, R. (2011). Design of lean manufacturing systems using value stream mapping with simulation: A case study. *Journal of Manufacturing Technology Management*, 22(4), 444–473. <https://doi.org/10.1108/17410381111126409>
- Karim, A. N. M., Jaafar, A. A. B., Abdullah, M. A. I., Haque, M., Ali, M. Y., & Azline, S. A. (2012). Applying value stream mapping for productivity improvement of a metal stamping industry. *Advanced Materials Research*, 576, 727–730. <https://doi.org/10.4028/www.scientific.net/AMR.576.727>
- Krishnan, S., Dev, A. S., Suresh, R., Sumesh, A., & Rameshkumar, K. (2018). Bottleneck identification in a tire manufacturing plant using simulation analysis and productivity improvement. *Materials Today: Proceedings*, 5(11), 24720–24730. <https://doi.org/10.1016/j.matpr.2018.10.270>
- Li, M., & Wang, Z. (2017). An integrated replenishment and production control policy under inventory inaccuracy and time delay. *Computers and Operations Research*, 88, 137-149. <https://doi.org/10.1016/j.cor.2017.06.014>
- Liu, Q., & Yang, H. (2020). Incorporating variability in lean manufacturing: a fuzzy value stream mapping approach. *Mathematical Problems in Engineering*, 2020, Article 1347054. <https://doi.org/10.1155/2020/1347054>
- Lugert, A., Batz, A., & Winkler, H. (2018). An empirical assessment of the future adequacy of value stream mapping in manufacturing industries. *Journal of Manufacturing Technology Management*, 29(5), 886–906. <https://doi.org/10.1108/136>
- Lugert, A., Völker, K., & Winkler, H. (2018). Dynamization of value stream management by technical and managerial approach. *Procedia CIRP*, 72, 701-706. <https://doi.org/10.1016/j.procir.2018.03.284>
- McDonald, T., Aken, E. M. V., & Rentes, A. F. (2002). Utilizing simulation to enhance value stream mapping: A manufacturing case application. *International Journal of Logistics Research and Applications*, 5(2), 213-232. <https://doi.org/10.1080/13675560210148696>
- Mudgal, D., Pagone, E., & Salonitis, K. (2020). Approach to value stream mapping for make-to-order manufacturing. *Procedia CIRP*, 93, 826–831. <https://doi.org/10.1016/j.procir.2020.04.084>
- Pacchini, A. P. T., Lucato, W. C., Facchini, F., & Mummolo, G. (2019). The degree of readiness for the implementation of industry 4.0. *Computers in Industry*, 113, Article 103125. <https://doi.org/10.1016/j.compind.2019.103125>
- Rahani, A. R., & Al-Ashraf, M. (2012). Production flow analysis through value stream mapping: A lean manufacturing process case study. *Procedia Engineering*, 41, 1727–1734. <https://doi.org/10.1016/j.proeng.2012.07.375>

- Roessler, M. P., Kleeberg, I., Kreder, M., Metternich, J., & Schuetzer, K. (2015). Enhanced value stream mapping: Potentials and feasibility of IT support through manufacturing execution systems. In M. Gen, K. J. Kim, X. Huang & Y. Hiroshi (Eds.), *Industrial engineering, management science and applications* (pp. 393-402). Springer. [https://doi.org/10.1007/978-3-662-47200-2\\_42](https://doi.org/10.1007/978-3-662-47200-2_42)
- Romero, L. F., & Arce, A. (2017). Applying value stream mapping in manufacturing: A systematic literature review. *IFAC-PapersOnLine*, 50(1), 1075–1086. <https://doi.org/10.1016/j.ifacol.2017.08.385>
- Rother, M., & Shook, J. (2003). *Learning to see: Value stream mapping to create value and eliminate muda*. Lean Enterprise Institute.
- Stadnicka, D., & Litwin, P. (2019). Value stream mapping and system dynamics integration for manufacturing line modeling and analysis. *International Journal of Production Economics*, 208, 400–411. <https://doi.org/10.1016/j.ijpe.2018.12.011>
- Tabanlı, R. M., & Ertay, T. (2013). Value stream mapping and benefit-cost analysis application for value visibility of a pilot project on RFID investment integrated to a manual production control system - A case study. *International Journal of Advanced Manufacturing Technology*, 66, 987–1002. <https://doi.org/10.1007/s00170-012-4383-x>
- Tasdemir, C., & Hiziroglu, S. (2019). Achieving cost efficiency through increased inventory leanness: Evidence from oriented strand board (OSB) industry. *International Journal of Production Economics*, 208, 412–433. <https://doi.org/10.1016/j.ijpe.2018.12.017>
- Valencia, E. T., Lamouri, S., Pellerin, R., Dubois, P., & Moeuf, A. (2019). Production planning in the fourth industrial revolution: A literature review. *IFAC-PapersOnLine*, 52(13), 2158–2163. <https://doi.org/10.1016/j.ifacol.2019.11.525>
- Venkataraman, K., Ramnath, B. V., Kumar, V. M., & Elanchezhian, C. (2014). Application of value stream mapping for reduction of cycle time in a machining process. *Procedia Materials Science*, 6, 1187–1196. <https://doi.org/10.1016/j.mspro.2014.07.192>
- Woehrl, S. L., & Abou-Shady, L. (2010). Using dynamic value stream mapping and lean accounting box scores to support lean implementation. *American Journal of Business Education (AJBE)*, 3(8), 67-76. <https://doi.org/10.19030/ajbe.v3i8.472>
- Womack, J. P., Jones, D. T., & Roos, D. (1990). *The machine that changed the world: the story of lean production, Toyota's secret weapon in the global car wars that is now revolutionizing world industry*. Free Press.
- Zadeh, L. A. (1965). Fuzzy sets. *Information and Control*, 8(3), 338-353. [https://doi.org/10.1016/S0019-9958\(65\)90241-X](https://doi.org/10.1016/S0019-9958(65)90241-X)
- Zahraee, S. M. (2016). A survey on lean manufacturing implementation in a selected manufacturing industry in Iran. *International Journal of Lean Six Sigma*, 7(2), 136-148. <https://doi.org/10.1108/IJLSS-03-2015-0010>

*Review Article*

## The Importance of Vegetation Landscape in Firefly Habitats

Nurhafizul Abu Seri and Azimah Abd Rahman\*

*Geoinformatic Unit, Geography Section, School of Humanities, Universiti Sains Malaysia, 11800 USM, Pulau Pinang, Malaysia*

### ABSTRACT

This study explores the importance of vegetation (display trees) in shaping the habitat preferences, mating behaviours, and survival strategies of *Pteroptyx* fireflies in Southeast Asia, especially Malaysia. The research highlights the crucial role of diverse plant species, tree characteristics, and specific plant components in influencing firefly behaviour, emphasising the impact of vegetation composition, structure, and function. The findings underscore the essential role of vegetation in providing resources such as food, shelter, and suitable breeding sites, thereby shaping the distribution and abundance of firefly populations in their natural habitats. Moreover, the study elucidates the significant influence of plant-related chemical compounds and emissions on firefly behaviour and ecosystem dynamics, underscoring the intricate interplay between plant life and insect populations. This comprehensive understanding of the intricate dynamics between fireflies and their vegetation landscape has substantial implications for conservation efforts and the sustainable management of their habitats.

*Keywords:* Chemical compounds, display trees, fireflies, Malaysia, *Pteroptyx*, sustainable management, vegetation

### ARTICLE INFO

*Article history:*

Received: 20 March 2023

Accepted: 18 December 2023

Published: 22 July 2024

DOI: <https://doi.org/10.47836/pjst.32.3.18>

*E-mail addresses:*

[nurhafizul.abuseri97@gmail.com](mailto:nurhafizul.abuseri97@gmail.com) (Nurhafizul Abu Seri)

[azimahrahman@usm.my](mailto:azimahrahman@usm.my) (Azimah Abd Rahman)

\*Corresponding author

### INTRODUCTION

Fireflies (Coleoptera: Lampyridae), also known as lightning bugs, are charismatic insects that attract many people worldwide because of their bioluminescence (Faust, 2004), which enables them to light up the night sky. Yet, these insects experience threats to their ecosystem, and the vegetation landscape is a vital determinant in their

survival. Vegetations are vital in firefly ecosystems because they offer these insects food, shelter, and breeding grounds (Jusoh et al., 2010a; Kaiser et al., 2017; Sriboonlert et al., 2015; Wattanachaiyingcharoen et al., 2011).

Firefly habitats range from mangroves to rivers, inland to highlands (Ballantyne et al., 2011). The abundance of vegetation not only provides them with a suitable habitat but also allows them to hide during the day and increases their chances of finding a mate when females respond to male signals from perches in vegetation (Lewis & Cratsley, 2008; Wang et al., 2007). Unfortunately, the population of fireflies has been declining recently (Lauff, 2017). One of the main causes is the destruction of their environment brought on by urbanisation and deforestation (Nadirah et al., 2020; Thancharoen, 2007).

On a variety of temporal scales, the vegetation landscape influences biogeochemical functions (such as production and nutrient cycling, controlling soil condition), ecological functions (such as habitats for organisms at various tropical levels), and anthropogenic functions (such as sediment management) (Bouillon et al., 2008; Field et al., 1998; McKee & Faulkner, 2000). However, little is known about the specific vegetation characteristics that support firefly populations in different habitats. Understanding the vegetation landscape of firefly habitats can provide insights into the ecology and conservation of these insects.

Several key research gaps warrant attention in the pursuit of understanding fireflies' display tree preferences in Malaysia. Firstly, there remains a need for a comprehensive and systematic assessment of the underlying ecological and environmental factors influencing the selection of specific display trees by fireflies. Investigating the precise role of vegetation composition, structure, and function in shaping the display tree preferences of fireflies could provide valuable insights into the intricacies of their habitat selection.

Furthermore, a deeper exploration of the chemical and physical attributes of favoured display trees and their potential influence on firefly behaviour is essential. Understanding the specific plant-related compounds or emissions that attract fireflies to certain tree species could illuminate the interplay between plant chemistry and firefly ecological dynamics.

Lastly, Lampyridae's genetic foundation and evolutionary traits lead to a lack of comprehensive information in public databases regarding firefly species. Despite their ecological significance and potential as umbrella species for conservation efforts, the paucity of genetic data and comprehensive knowledge limits effective strategies for their preservation.

## **THE ROLE OF VEGETATION LANDSCAPE (COMPOSITION, STRUCTURE, AND FUNCTION)**

### **Vegetation Landscape (Composition)**

The overall physical appearance of an area primarily defined by its vegetation is referred to as a vegetation landscape. The plant community's composition, structure, and function

can be used to describe a vegetation landscape. Vegetation landscape refers to an area's physical and visible features determined by the types of plants that grow in that area. It encompasses the natural distribution and patterns of different plant species and the ecosystems and habitats they create. Fireflies inhabit many habitats, including mangrove forests, rivers, inland, and the highlands (Ballantyne et al., 2011), particularly along elevational ranges, and are most prevalent in locations with high humidity and extensive vegetation (Branham, 2010; Branham, 2015). Figure 1 highlights the interconnectedness of composition, structure, and function in vegetation landscape, emphasising the importance of balanced, diverse landscapes for supporting firefly populations and holistic habitat management for conservation.

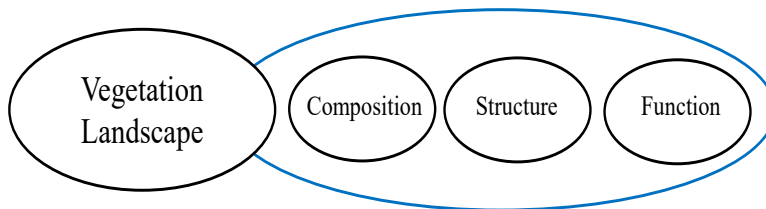


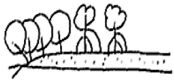
Figure 1. Three elements of vegetation landscape in firefly habitat

The vegetation landscape may include a variety of plants native to the region, such as trees, shrubs, grasses, and other types of vegetation. It is known as composition in the vegetation landscape, which refers to the various types of plants available in a certain ecosystem or geographical area. The composition of the vegetation landscape within firefly habitats refers to the diverse array of plant species that play a crucial role in providing the necessary resources for the survival and thriving of firefly populations. Understanding the intricate composition of vegetation is essential for comprehending the complex ecological dynamics that govern firefly habitats. In the context of firefly ecosystems, the composition of the vegetation landscape encompasses various aspects, including the types of plants present, their distribution patterns, and their ecological significance for fireflies. For example, in the firefly's habitat area, they are found on certain species of riparian vegetation, including *Sonneratia caseolaris*, *Hibiscus tiliaceus*, *Nypa fruticans*, *Acrotichum aureum*, *Areca cathechu*, *Oncosperma tigillarum*, and *Ficus* sp., especially in Peninsular Malaysia and Thailand (Juliana et al., 2012; Khoo et al., 2012; Prasertkul, 2018). Figure 2 illustrates five vegetation assemblages related to *Pteroptyx tener* abundance. Vegetation Group A (*Sonneratia caseolaris*-*Rhizophora*); Vegetation Group B (*Sonneratia caseolaris*-*Nypa fruticans*); Vegetation Group C (*Sonneratia caseolaris*-*Rhizophora*-*Nypa fruticans*); Vegetation Group D (*Sonneratia caseolaris*-*Rhizophora*-*Acrostichum Aureum*); Vegetation

Group E (*Sonneratia caseolaris*-*Rhizophora*-*Nypa fruticans*-*Acrostichum Aureum*) (Jusoh et al., 2010b).

In addition, fireflies were found appearing in other vegetation species in riparian areas, including *Rhizophora apiculata*, *Clerodendrum inerme*, *Glochidion littorale*, *Bruguiera parviflora*, and *Excoecaria indica* (Chey, 2004; Mahadimenakbar & Saikim, 2016) proving that tree selection the display of these species is not necessarily from the same vegetation species (Chey, 2004; Ohba & Wong, 2004).

Table 1  
 Classification of vegetation assemblages in firefly areas (Jusoh et al., 2010b)

Vegetation Assemblage	Vegetation Species	Diagram of Vegetation Assemblage	Vegetation Profile
A	<ul style="list-style-type: none"> <li>• <i>Sonneratia caseolaris</i></li> <li>• <i>Rhizophora</i> sp.</li> </ul>		
B	<ul style="list-style-type: none"> <li>• <i>Sonneratia caseolaris</i></li> <li>• <i>Nypa fruticans</i></li> </ul>		
C	<ul style="list-style-type: none"> <li>• <i>Sonneratia caseolaris</i></li> <li>• <i>Rhizophora</i> sp.</li> <li>• <i>Nypa fruticans</i></li> </ul>		
D	<ul style="list-style-type: none"> <li>• <i>Sonneratia caseolaris</i></li> <li>• <i>Rhizophora</i> sp.</li> <li>• <i>Acrotischum aureum</i></li> </ul>		
E	<ul style="list-style-type: none"> <li>• <i>Sonneratia caseolaris</i></li> <li>• <i>Rhizophora</i> sp.</li> <li>• <i>Nypa fruticans</i></li> <li>• <i>Acrotischum aureum</i></li> </ul>		

Note:

-  *Sonneratia caseolaris*
-  *Acrotischum aureum*
-  *Nypa fruticans*
-  *Rhizophora* sp.

Within firefly habitats, various plant species contribute to creating a suitable environment for fireflies, offering essential resources such as food, shelter, and breeding sites. Certain vegetation types are more favourable for firefly populations, indicating a specific preference for plant species. Previous research (Chey, 2010; Jusoh et al., 2010b; Norela et al., 2017) have identified several key plant species that serve as favoured habitats for fireflies, such as *Sonneratia caseolaris*, *Rhizophora apiculata*, *Nypa fruticans*, and many others, emphasising the importance of specific plant compositions for firefly survival.

Furthermore, the diversity of vegetation composition within firefly habitats is critical in supporting the broader ecosystem, fostering a rich and balanced environment for various flora and fauna. The presence of specific plant species, especially those with high ecological significance, contributes to the habitat's overall biodiversity and ecological stability. For instance, as one of the initial trees to emerge on tidal mudflats, *Sonneratia caseolaris* helps to stabilise the riverbanks and coastal areas, creating a more conducive environment for the growth of other varieties of trees and plants. Studies have indicated that the spontaneous regrowth of *Sonneratia caseolaris* is highly effective, often eliminating the necessity for deliberate planting efforts (Aziz et al., 2012).

### **Vegetation Landscape (Structure)**

The structure of the vegetation landscape refers to the physical arrangement and spatial distribution of plant communities within a particular landscape or ecosystem. It encompasses various characteristics such as the type and abundance of vegetation, the height and size of plants, the arrangement and spacing of plant communities, and the distribution of plant species and their associated habitats. *Sonneratia caseolaris*, a firefly's favourite display tree, has a distinct structural architecture that distinguishes it from other trees. It has a more complex structure and larger plants, providing more resources for insects to thrive, particularly food sources, such as leaves and litter (Abdullah et al., 2019).

Due to unique tree characteristics/structures such as height, crown size, leaf density, and stem diameter, Jusoh et al. (2010a) assumed that fireflies only occupied young *Sonneratia caseolaris* trees. This research suggests that the specific characteristics and structure of *Sonneratia caseolaris* trees, including their height, crown size, leaf density, and stem diameter, play a significant role in the habitat preferences of fireflies. The study implies that fireflies tend to occupy or prefer young *Sonneratia caseolaris* trees, likely due to certain advantageous features offered by these trees. Young trees may provide an ideal environment for mating and breeding fireflies, offering suitable conditions such as manageable heights for light signalling, appropriate crown sizes for shelter, optimal leaf density for protection and food sources, and stem diameters that may facilitate various life cycle activities.

An optimal foliage density within these landscapes fosters a rich insect population, ensuring an essential food supply for firefly larvae and adults. Moreover, maintaining a balanced foliage density creates a favourable microclimate that sustains firefly populations' healthy development and activity. The unique combination of these three characteristics is thought to create an environment conducive to the specific requirements of fireflies, which may explain their preference for young *Sonneratia caseolaris* trees over other tree types or age groups. Further exploration of these tree characteristics and their relationship with firefly behaviour and habitat selection can provide valuable insights into the intricate dynamics of their ecological interactions, contributing to a deeper understanding of the factors influencing the distribution and abundance of firefly populations within their natural habitats.

Moreover, *Pteroptyx olivier* was also found in numerous mangrove swamp shrub trees (Jusoh et al., 2018). There was a reason why this species of firefly preferred mangrove trees, such as the fact that *Pteroptyx* fireflies preferred trees with a greater proportion of apertures or open spaces in the canopy. In contrast, trees surrounded by 0 to 25% open space are seldom chosen as display trees. *Pteroptyx* fireflies never inhabit trees with a dense canopy (Jaikla et al., 2020). Unfortunately, the conversion of mangrove swamp forests to other land use land cover (LULC) led to a reduction of more than half of the number of display trees inhabited by fireflies in the Rembau-Linggi estuary. This development will certainly jeopardise the firefly population in the area (Jusoh & Hashim, 2012).

Fireflies are bioluminescent insects that survive and reproduce by relying on vegetation cover and structure. Thus, their abundance, distribution, and behaviour can be influenced by the type and distribution of vegetation in their habitats. *Pteroptyx* larvae that feed on snails and reside in moist, frequently flooded soils are vulnerable to events such as rain, and many prey are likely to harm both larval and adult populations (Loomboot, 2007). It results from adult females depositing eggs in wetlands in river intertidal zones. Mangrove snails and other soft-bodied animals are firefly larvae prey (Barrows et al., 2008; Lewis et al., 2020). Prasertkul (2018) hypothesises that the trees that have attracted large numbers of *Pteroptyx* may be adjacent to the oviposition or eclosion site of the female pupa, which may be related to the larval feeding site. Yet, there is currently insufficient evidence to support any hypothesis.

Vegetation landscape structure becomes more important to fireflies because daytime resting sites for terrestrial larvae have been postulated in the soil, leaf litter, and rock crevices (Vaz et al., 2020; Vaz, Manes et al., 2021). These larvae are visible at night on the surface, creeping through the weeds and grass and occasionally climbing a few inches up the stem, especially under humid conditions (Faust, 2017). The larvae prepare for pupation by creating a dirty chamber in the soil, where they will reside for six to ten days until emerging as adult fireflies (Nallakumar, 2003).

## Vegetation Landscape (Function)

Plants' ecological roles in the ecosystem are referred to as functions in the vegetation landscape, such as providing food and habitat for wildlife. According to Jusoh et al. (2010b), firefly populations are ecologically linked to ground cover with display trees and/or specific plant assemblages. For instance, the vegetation landscape in the forest area, especially mangrove forests, plays a critical role in maintaining a healthy ecosystem for fireflies. A healthy ecosystem for fireflies includes food for them to consume. Although the nutritional requirements of adult *Pteroptyx tener* are unknown, it is assumed that this insect feeds on the nectar and sap of mangrove trees (Cheng et al., 2017). Some congregating firefly species, notably *Photinus pallens*, may have resource-related leks (mating swarms), such as nectar or plant sap (Lloyd, 1998).

However, research shows that this vegetation provides important food sources for fireflies, such as sugar in the nectar/sap from trees for adults to feed (Jusoh et al., 2010a, 2010b; Othman et al., 2018). It is uncertain how much Southeast Asian *Pteroptyx* lekking behaviour is related to food because the main display tree plant, *Sonneratia caseolaris*, does not flower and fruit year-round, unlike *Hibiscus tiliaceus*. While *Terminalia catappa*, another non-primary display tree, blossoms and bears fruit twice a year (Prasertkul, 2018). Hence, it may be inferred that the appearance of flowers or fruits on trees is not a prerequisite for forming a firefly's colonies. Prasertkul (2018) reveals that *Pteroptyx malacca* and *Pteroptyx valida* may select plants based on seasonal suitability and broad-leaved species such as *Terminalia catappa* or *Acacia mangium*. These plant species may be protected from wind and rain.

In addition to providing food and shelter, the vegetation landscape is also essential for fireflies' mating and breeding behaviour (Kaiser et al., 2017). Fireflies use their light signals to communicate with potential mates (Fallon et al., 2019), and the vegetation landscape provides a suitable platform for them to do so. The light signals are also used to attract prey (Bechara & Stevani, 2018), so the presence of vegetation helps to ensure enough food for the fireflies to survive and reproduce.

Jusoh et al. (2010b) proposed that suitable display trees for *Pteroptyx* include those that are (1) near the water's edge, (2) sturdy trees, (3) near larval food sources, (4) provide nectar or rubber for the adults' diet, and (5) have a leaf arrangement that is easy for flash communication. Meanwhile, Ohba and Wong (2004) proposed that several factors influence firefly species' selection of display trees, including (1) the display tree should be near the water's edge, as this facilitates firefly communication, (2) each display tree's leaf arrangement must be ideal for mating, (3) the display tree must be in good health, (4) must contain nectar or rubber for an adult if they eat, and (5) the larval prey food.

Furthermore, the vegetation landscape is important for maintaining the quality of the habitat because vegetation helps to prevent soil erosion, filter pollutants, and maintain

water quality in streams and rivers. It is important for firefly habitats, as water sources are essential for the survival of firefly larvae. Adult fireflies and their larvae may also be affected by saltwater intrusion resulting from water pollution caused by pesticides from agricultural landfills and illegal emissions (Lewis et al., 2020). It is evident when the number of fireflies is decreasing due to changes in river water quality caused by river pollution, diesel use, and development around firefly habitat areas (Jusoh et al., 2010b).

Vegetation provides shelter and hiding places for fireflies during the day. Fireflies are found in the butterfly larvae nests left out during the day (Ohba & Wong, 2004). It is due to the high light intensity during the day, forcing the fireflies to seek a dark environment. Therefore, it can be concluded that a suitable vegetation landscape to be used as a habitat for fireflies must have these characteristics. It is recommended that future research be done to observe the behaviour of these fireflies during the day, especially in areas exposed to sunlight.

The vegetation also helps to maintain humidity levels in the habitat, which is important for the survival of firefly eggs and larvae. Without the proper vegetation landscape, firefly habitats become dry and inhospitable, leading to a decline in firefly populations. Jusoh et al. (2010a) stated that firefly eggs needed wet soil and a shaded location to survive heat and dryness. Fireflies preferred plants from *Rhizophora* species (*Rhizophora Mucronata* and *Rhizophora Apiculata*) to deposit their eggs (Norela et al., 2017).

## **FIREFLY DISPLAY TREES IN MALAYSIA**

Table 1 shows the tabulation of firefly display trees in Malaysia. This table displays the firefly display trees plants, highlighting the diverse range of plant species that serve as habitats for different firefly species. In Malaysia, firefly display trees are those specifically favoured by fireflies for their light signalling behaviours and reproduction. These trees, typically found in mangrove areas and other suitable habitats, play a crucial role in supporting the life cycle of fireflies. Some common firefly display trees in Malaysia include *Sonneratia caseolaris* and other mangrove species like *Rhizophora apiculata* and *Nypa fruticans*. These trees provide an essential environment for fireflies to thrive, offering suitable surfaces for light signalling, shelter, and food sources. Understanding the significance of these specific trees in the context of firefly habitats is essential for conserving and managing firefly populations in Malaysia, contributing to preserving this natural wonder for future generations.

Since Malaysia has a vast area of mangrove forest, a favoured habitat for fireflies, this may be one of the reasons why many species of fireflies have been identified in Malaysia, and there may be even more undocumented species. The total mangrove forest cover worldwide is 15.62 million hectares, with 577,940 hectares (3.7%) in Malaysia. Although this percentage is small, mangrove swamp forests are among Malaysia's most important

forest types. In Peninsular Malaysia, the area of mangrove swamp forest is 98,249.8 hectares (17%), Sabah has the largest mangrove swamp forest area in Malaysia at 338,672.8 hectares (58.6%), and Sarawak covers 141,017.4 hectares (24.4%) of the total (Ahmad et al., 2018). The comprehensive presence of mangrove swamp forests across the country underscores their critical role in supporting diverse flora and fauna, including firefly populations. Understanding the distribution and extent of these forests aids in implementing effective conservation strategies. It underscores the significance of preserving these crucial habitats for the sustained well-being of various species, including fireflies. Further research and documentation of firefly species within these mangrove habitats is essential for developing comprehensive conservation efforts and ensuring the long-term survival of these unique and fascinating insects in Malaysia.

Meanwhile, *Nypa fruticans* and *Metroxylon sago* are important for firefly larvae because their food sources, which are snail prey, live in that area (Nada & Kirton, 2004). The density of firefly larvae is higher in sago plantations than in oil palm trees (Kirton et al., 2006), which may be related to more snails in sago plantations. Tiny snails (*Cyclotropis carinata*) are prey of firefly larvae that inhabit the riverbanks (Nada & Kirton, 2004) and are becoming increasingly endangered because of human activities or natural disasters (Foo & Mahadimenakbar, 2015).

It also serves as a habitat for their prey, such as snails, an essential food source for firefly larvae. The survival of fireflies in their larval stage depends on the tiny snails that live in the damp areas of mangrove swamps. Fireflies spend a substantial amount of time in this stage, which lasts 97.83 days, depending on the river water (Loomboot et al., 2007). The larvae, which feed on river snails, are frequently found 5 to 30 metres from Nipah and Sago palm trees (Loomboot et al., 2007).

Table 1  
Firefly display trees in Malaysia

Scientific Name	Vernacular name	Sources
<i>Acrostichum aureum</i>	Coarse Swamp Fern	Jusoh et al. (2010b); Juliana et al. (2012); Foo and Mahadimenakbar (2015)
<i>Aegiceras floridum</i>	Black Mangrove	Foo and Mahadimenakbar (2016)
<i>Areca catechu</i>	Pinang	Nada et al. (2009)
<i>Avicennia alba</i> Blume	Api-api Hitam	Chey (2006); Jusoh et al. (2011); Foo and Mahadimenakbar (2015); Foo and Mahadimenakbar (2017);
<i>Avicennia marina</i>	Api-api Jambu	Abdullah et al. (2020)
<i>Avicennia rumphiana</i>	Api-api Bulu	Abdullah et al. (2020)
<i>Barringtonia</i> sp.	-	Ohba and Wong (2004); Mahmud et al. (2018)

Table 1 (Continue)

Scientific Name	Vernacular name	Sources
<i>Barringtonia racemosa</i> (L.) Spreng.	Putal Kedul	Jusoh et al. (2011)
<i>Brownlowia argentata</i>	-	Jusoh et al. (2011)
<i>Bruguiera gymnorhiza</i>	Tumu Merah	Ohba and Wong (2004); Jusoh et al. (2011)
<i>Bruguiera parviflora</i>	-	Mahadimenakbar et al. (2007); Abdullah et al. (2020)
<i>Ceriops decandra</i>	Tengar	Jusoh et al. (2011)
<i>Clerodendrum inerme</i> (Verbenaceae)	-	Chey (2010)
<i>Derris</i> sp.	-	Abdullah et al. (2020)
<i>Derris trifoliata</i> Lour	Common Derris	Jusoh et al. (2011)
<i>Excoecaria agallocha</i> L.	Bebuta	Jusoh et al. (2011); Foo and Mahadimenakbar (2017)
<i>Excoecaria indica</i> L.	-	Foo and Mahadimenakbar (2017)
<i>Excoecaria indica</i> (Willd.) Muell. Arg. (Euphorbiaceae)	-	Chey (2004); Mahadimenakbar et al. (2007)
<i>Ficus binjamina</i>	-	Mahadimenakbar et al. (2007)
<i>Ficus microcarpa</i> (Moraceae)	Jejawi	Chey (2010)
<i>Ficus</i> sp.	-	Ohba and Wong (2004); Juliana et al. (2012); Shahara et al. (2017)
<i>Glochidion littorale</i> (Euphorbiaceae)	Selunsur	Chey (2010)
<i>Gluta velutina</i> Blume	Rengas Air	Ohba and Wong (2004); Jusoh et al. (2011)
<i>Guilandina bonduc</i> L.	Grey Nicker	Mahmod et al. (2018)
<i>Heritiera littoralis</i> Dry. ex W. Ait. (Sterculiaceae)	Dungun	Chey (2004)
<i>Hibiscus tiliaceus</i> / <i>Talipariti tiliaceum</i>	Bebaru Tree	Ohba and Wong (2004); Mahadimenakbar et al. (2007); Jusoh et al. (2011); Juliana et al. (2012); Abdullah et al. (2020); Cheng et al. (2017); Foo and Mahadimenakbar (2017); Jusoh et al. (2018); Mahmod et al. (2018)

Table 1 (Continue)

Scientific Name	Vernacular name	Sources
<i>Lumnitzera littorea</i> (Combretaceae)	Teruntum Merah	Chey (2008); Chey (2009); Foo and Mahadimenakbar (2016); Jusoh et al. (2018)
<i>Metroxylon sagu</i>	Pokok Sagu	Nada et al. (2009)
<i>Nypa fruticans</i> Wurmbr		Ohba and Wong (2004); Mahadimenakbar et al. (2007); Jusoh et al. (2010b); Jusoh et al. (2011); Juliana et al. (2012); Foo and Mahadimenakbar (2015); Foo and Mahadimenakbar (2017); Mahmud et al. (2018)
<i>Oncosperma tigillarum</i>	Nibung Palm	Nada et al. (2009); Juliana et al. (2012)
<i>Pandanus</i> sp.	-	Abdullah et al. (2020)
<i>Rhizophora apiculata</i> Blume	Bakau Minyak	Chey (2004); Chey (2006); Mahadimenakbar et al. (2007); Chey (2008); Chey (2010); Chey (2011); Jusoh et al. (2011); Foo and Mahadimenakbar (2015); Foo and Mahadimenakbar (2017); Jusoh et al. (2018); Abdullah et al. (2020)
<i>Rhizophora mucronata</i>	Bakau Kurap	Chey (2008); Chey (2011); Foo and Mahadimenakbar (2016)
<i>Rhizophora</i> sp.	Bakau	Jusoh et al. (2010b)
<i>Rhizophora stylosa</i>	Bakau Kurap	Chey (2011)
<i>Scyphiphora hydrophyllacea</i>	Chengam	Chey (2006); Chey (2008); Chey (2009); Chey (2011)
<i>Sonneratia alba</i>	Perepat	Jusoh et al. (2011); Foo and Mahadimenakbar (2017); Jusoh et al. (2018)
<i>Sonneratia caseolaris</i> (L.) Engl.	Berembang	Jusoh et al. (2010b); Jusoh et al. (2011); Juliana et al. (2012); Cheng et al. (2017); Hazmi and Sagaff (2017); Shahara et al. (2017); Jusoh et al. (2018); Mahmud et al. (2018)
<i>Thespesia populnea</i>	Bebaru	Abdullah et al. (2020)
<i>Xylocarpus granatum</i> J. König	Nyireh Bunga	Chey (2006); Jusoh et al. (2011); Jusoh et al. (2018); Abdullah et al. (2020)

## FIREFLY DISPLAY TREES CHEMICAL COMPOUND

Three varieties of cuticular wax (crustose, granules, and flake cuticular wax) were detected on the leaf epidermal surfaces of four tree species, namely *Sonneratia caseolaris*, *Barringtonia racemosa*, *Gluta renghas*, and *Hibiscus tiliaceus*, potentially contribute to the influencing factors in the selection of display trees by fireflies. All four tree species exhibited flake cuticular wax except for *Sonneratia caseolaris*, which displayed granular and crustose cuticular wax on its epidermal surface (Norela et al., 2020). Cuticular wax constitutes a lipid-based covering that envelops the external surface of leaves and other plant structures. It comprises a blend of lipids, encompassing fatty acids, alcohols, and hydrocarbons. This shielding layer serves to safeguard the plant from diverse threats, including loss of moisture (Sevanto, 2020), ultraviolet (UV) radiation (Krauss et al., 1997), damage caused by herbivores (Eigenbrode & Espelie, 1995), elevated temperatures (Salem-Fnayou et al., 2011), and physical strain (Dominguez et al., 2011; Khanal & Knoche, 2017).

The presence and composition of cuticular wax on plant surfaces are vital in influencing the abundance of insects, including fireflies, in their selected habitats. This protective wax layer serves as a physical barrier against pathogens (Wang et al., 2020), creating a safer environment for these insects by minimising the risk of pathogen invasion. Additionally, as a reservoir of signals triggering plant defence responses, cuticular wax indicates a healthier and more resilient ecosystem, potentially attracting insects like fireflies to habitats with robust defence mechanisms. Moreover, the cues provided by the cuticular wax layer, which pathogens could exploit, have implications for the overall health of the plant population. Well-maintained cuticular wax layers in habitats effectively regulating these cues can foster a more balanced and sustainable ecosystem, consequently drawing a higher abundance of insects, such as fireflies, reliant on a thriving plant environment for their survival and reproduction. Hence, the integrity and functionality of the cuticular wax layer in plant-pathogen interactions indirectly influence the presence and population density of insects, including fireflies, as they tend to favour habitats with effective protective mechanisms, contributing to a sustained presence in these environments.

Trichomes were observed exclusively on *Gluta renghas* and *Hibiscus tiliaceus* leaf epidermal surfaces. However, no trichomes were detected on the epidermal surface of *Sonneratia caseolaris* and *Barringtonia racemosa*. Consequently, *Sonneratia caseolaris* and *Barringtonia racemosa* may possess diminished leaf resistance (Norela et al., 2020). The absence of trichomes on the epidermal surface of *Sonneratia caseolaris* and *Barringtonia racemosa* may suggest lower resistance to environmental stressors and herbivores. Consequently, these plants could be more attractive to fireflies for laying their eggs, as the lack of trichomes might provide easier access to suitable locations for their reproductive activities. However, when considering the findings by Norela et al. (2020) that plants without trichomes might be more attractive to fireflies for egg-laying, it is

essential to reconcile this with the observation that female fireflies typically deposit their eggs on the soil behind display trees, not directly on the trees themselves. This nuance raises questions about the direct association between plant trichome absence and firefly egg-laying preferences.

Furthermore, there appears to be a potential contradiction within their study's findings. While it suggests that fireflies may prefer plants with lower resistance due to the absence of trichomes, it contradicts earlier research (e.g., Jusoh et al., 2010a, 2010b; Norela et al., 2017; Ohba & Wong, 2004) indicating that fireflies tend to favour habitats with effective protective mechanisms. This article raises a question regarding the consistency of firefly habitat preferences. As stated earlier, do fireflies indeed prefer habitats with effective protective mechanisms, or are they more attracted to plants with lower resistance, as suggested by the absence of trichomes? It may be necessary to consider a more comprehensive understanding of firefly habitat selection, acknowledging that multiple factors beyond trichome presence or absence can influence their preferences to resolve this apparent contradiction. Further research and a nuanced exploration of the interplay between firefly behaviour, plant characteristics, and habitat dynamics may clarify this.

*Excoecaria agallocha*, commonly called the blind-your-eye mangrove, is a unique mangrove plant belonging to the Euphorbiaceae family. Notably, the milky latex produced by this plant contains various phytotoxins, particularly the excoecariatoxins, which possess potent irritant properties affecting the skin, eyes, and mucous membranes. These phytotoxins are attributed to three distinct groups of diterpene esters of the daphnane and tiglane types, which are responsible for the toxic effects exhibited by *Excoecaria agallocha* (Chan et al., 2018). The presence of phytotoxins in the *Excoecaria agallocha* plant's latex significantly impacts the behaviour and interactions of various insects, including fireflies, within the surrounding ecosystem. The irritant properties of the latex serve as a natural defence mechanism, deterring potential predators and herbivores from feeding on the plant, indirectly creating a safer environment for fireflies to thrive and reproduce. Additionally, the existence of these toxic compounds in the environment, particularly in regions abundant with *Excoecaria agallocha*, can alter the foraging behaviour of fireflies, potentially leading them to favour other plant species or habitats, thus influencing their distribution and population dynamics. Moreover, the toxic nature of the plant's latex may impact the selection of suitable breeding and mating sites for fireflies, as they may actively avoid areas with high concentrations of *Excoecaria agallocha* to safeguard themselves from potential harm.

According to the National Parks Board of Singapore (2022), *Sonneratia caseolaris* is recognised for its ability to attract fireflies through its aromatic flowers and emission of volatile organic compounds (VOCs). The tree exhibits striking red flowers that bloom at dusk, emitting a fragrance resembling sour milk that persists for a single night. While the

precise mechanism by which the VOCs of *Sonneratia caseolaris* entice fireflies is not yet entirely comprehended, it is suggested that these organic compounds function as a signal for the fireflies, potentially aiding them in locating and recognising potential mates. This fascinating correlation between the plant's emissions and the behavioural patterns of fireflies illuminates the intricate workings of the natural world, underscoring the diverse ways in which different organisms communicate and interact within their shared ecosystems. Further investigation into this dynamic relationship has the potential to yield valuable insights into the broader ecological significance of such interactions and their impact on the overall biodiversity and sustainability of the surrounding environment.

Fireflies have also been found in *Guilandina bonduc* L. and *Barringtonia* sp. vegetation, though not with the best synchronisation (Mahmod et al., 2018). The presence of the plant *Barringtonia racemosa* in a habitat or ecosystem can repel the presence of insects because this plant species is known to contain the insecticide Saponin (Osman et al., 2017), potentially leading to a reduced presence of insects, including fireflies, within its vicinity. This repellent effect is linked to the plant's ability to release Saponin, a natural defence mechanism against insect infestations and herbivory. The implications of *Barringtonia racemosa*'s presence on insect populations underscore the intricate relationships between plant chemistry and the ecological balance of a habitat. While the protective characteristics of Saponin contribute to the plant's resilience and survival, they can also inadvertently impact the broader ecosystem by influencing the abundance and distribution of insects, including those crucial to the ecosystem's biodiversity.

## **SIGNIFICANCE OF FIREFLY CONSERVATION IN TROPICAL ENVIRONMENTS**

There are numerous Lampyridae species, and efforts to conserve them from extinction, such as making fireflies into enigmatic umbrella species, have been made. Still, the endeavour has come to a halt. Lampyridae's genetic foundation and evolutionary traits are still unknown, and public databases have relatively little information regarding fireflies (Fu et al., 2017). Several international treaties protect mangrove trees, which are crucial to reaching the Paris Climate Agreement's targets (Taillardat et al., 2018). Insects must be protected by being viewed as distinct species with specific survival mechanisms focusing on tropical insects and their environments (Basset & Lamarre, 2019). The species of fireflies must be conserved since they belong to the insect kingdom. Insects are the most varied group of multicellular animals on Earth, as purveyors of ecological services including pollination, pest control (biocontrol), decomposition, and energy transfer through the food chain, and many more (Chowdhury et al., 2017).

In this firefly conservation initiative, species distribution models (SDMs) are one of the modelling approaches that might be considered and utilised. Modelling SDMs can establish

conservation guidelines by forest remnant and firefly protection rules. The outcomes of this modelling can combine taxonomic and ecological knowledge and contribute to filling in significant gaps in firefly biology (Vaz, Guerrazzi et al., 2021). This modelling also entails mapping the possible distribution of fireflies in their habitat areas to evaluate pressure changes over time. Then, the categorisation of potential distribution ranging from 0% to 100% suitable into three increasing suitability criteria, which corresponds to the projected fitness with the event location to determine the lowest fitness value at which any firefly is detected in the field (Vaz, Guerrazzi et al., 2021). This model can forecast biodiversity's spatial and temporal distribution in response to environmental stressors.

Malaysia is rich in natural resources, but if they are not managed and do not have solid and efficient protection or conservation strategy, it is no surprise that the country's biodiversity cannot last for a very long time. Thus, for the efficient protection of firefly populations, a thorough comprehension of their distribution, abundance, and habitat requirements is needed (Takeda et al., 2006). The conservation of these fireflies strongly relies on preserving their natural habitats, which are vital to their life cycle. Therefore, it is extremely important to conserve the habitat of fireflies, the mangrove forest, because this will indirectly protect the firefly species that inhabit the area. Among the successful and necessary conservation efforts to be followed by state and national forestry agencies are, as Goessens et al. (2014) proposed, mangroves replanting at Matang Mangrove Forest Reserve (MMFR) handled precisely with best practices in the world since 1902. Since Malaysia's independence in 1957, the MMFR has been maintained sustainably based on five work programs (Ibharim et al., 2015).

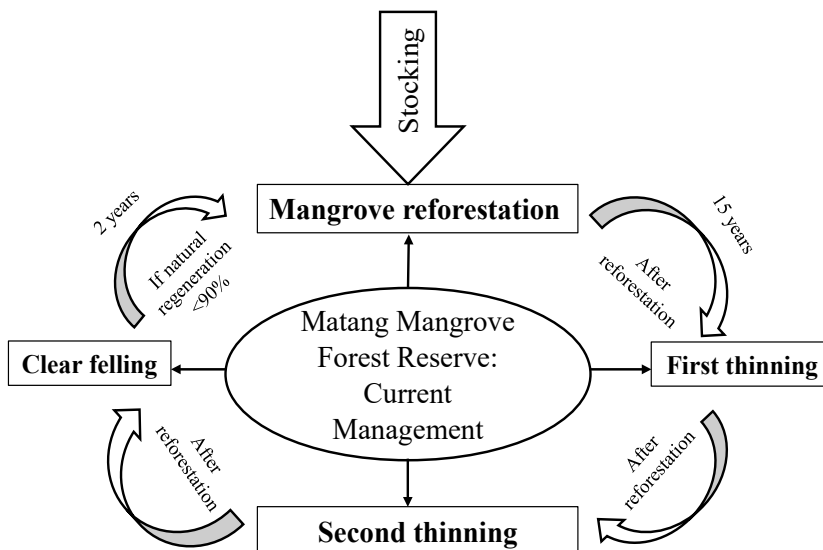


Figure 3. Matang Mangrove Forest Reserve (MMFR) management system (Goessens et al., 2014)

Figure 3 depicts the Matang Mangrove Forest Reserve in Perak-West Coast, Peninsular Malaysia. The yellow circle with red dots indicates the location of the Virgin Forest Reserve (VJR). At the same time, the block of Managed Mangrove Forest (marked with MF and including vegetation that is 15, 20, and 30 years old) is considered for silvometric measures. Including silvicultural approaches in managing mangrove resources could result in more sustainable management (Roy, 2016; Santos & Lana, 2017).

## CONCLUSION

In conclusion, fireflies, known as lightning bugs, hold a charismatic allure with their bioluminescent displays, capturing people's global fascination. However, their existence is threatened by various ecological pressures, predominantly stemming from human-induced changes in their natural habitats. The vegetation landscape plays a pivotal role in the survival and well-being of firefly populations, offering essential resources such as food, shelter, and breeding grounds. A thorough understanding of the vegetation landscape's composition, structure, and function is crucial for comprehending the complex ecological dynamics that govern firefly habitats.

The diversity of firefly habitats, ranging from mangroves to rivers and inland to highlands, underscores the significance of various vegetation types in supporting firefly populations. While the destruction of their habitats due to urbanisation and deforestation remains a primary concern, the specific characteristics of the vegetation landscape that support firefly populations are not yet fully understood. Research gaps persist, necessitating comprehensive assessments of the ecological and environmental factors influencing firefly preferences for specific display trees.

The chemical and physical attributes of favoured display trees, including the role of cuticular wax, trichomes, and plant emissions, are integral to firefly behaviour and habitat selection. Understanding the intricate interplay between vegetation characteristics and firefly ecology can illuminate the nuanced relationships between plants and insects, offering valuable insights into the underlying mechanisms shaping firefly habitats.

Furthermore, the conservation of fireflies is crucial for preserving the charismatic appeal of these insects and safeguarding the broader ecosystem. Given the limited genetic data and knowledge of firefly species, comprehensive conservation efforts are necessary to protect these insects from extinction. Species distribution models (SDMs) offer a promising approach to establishing effective conservation guidelines and mapping the potential distribution of fireflies in response to environmental changes. Implementing sustainable management practices, such as mangrove reforestation and silvicultural measures, can contribute to the long-term preservation of firefly habitats and the biodiversity they support.

By prioritising the conservation of fireflies and their habitats, especially within the rich tropical environments of countries like Malaysia, it is possible to ensure the sustained

well-being of these captivating insects and the broader ecosystems they inhabit. Effective conservation strategies should aim to protect and restore the vegetation landscape, promoting the coexistence of fireflies and other vital organisms in these unique and diverse ecosystems.

## ACKNOWLEDGEMENT

This research was financed by the Ministry of Higher Education Malaysia under the Fundamental Research Grant Scheme with project code FRGS/1/2020/SS0/USM/02/6.

## REFERENCES

- Abdullah, N. A., Radzi, S., Asri, L. N., Idris, N. S., Husin, S., Sulaiman, A., Khamis, S., Sulaiman, N., & Hazmi, I. R. (2019). Insect community in riparian zones of Sungai Sepetang, Sungai Rembau and Sungai Chukai of Peninsular Malaysia. *Biodiversity Data Journal*, 7, Article e35679. <https://doi.org/10.3897/BDJ.7.e35679>
- Abdullah, N. A., Asri, L. N., Radzi, S. N. F., Musbah, M., Hazmi, I. R., & Sulaiman, N. (2020). Abiotic factors influencing diversity and abundance of congregating fireflies (*Coleoptera: Lampyridae*) in Miri, Sarawak, Malaysia. *Oriental Insects*, 55(2), 149-164. <https://doi.org/10.1080/00305316.2020.1757529>
- Ahmad, W. J. W., Ahmad, N., & Mohamed, A. L. (2018). *Mangrove flora of Malaysia: Malaysia biodiversity information system (MyBIS)*. Malaysia Biodiversity Information System (MyBIS).
- Aziz, H. K., Hamdan, O., Azahari, F. M., Shah, I. A., Nasir, H. M., & Annuar, N. S. (2012). Mapping the distribution of display trees for conservation of firefly habitat - A case study of the mangrove tree *Sonneratia caseolaris* in Selangor, Malaysia. *Lampyrid: The Journal of Bioluminescent Beetle Research*, 2, 156-161.
- Ballantyne, L., Xin, H. F., Shih, C. H., Cheng, C. Y., & Yiu, V. (2011). *Pteroptyx maipo* Ballantyne, a new species of bent-winged firefly (Coleoptera: Lampyridae) from Hong Kong, and its relevance to firefly biology and conservation. *Zootaxa*, 2931(2011), 8- 34. <https://doi.org/10.11646/ZOOTAXA.2931.1.2>
- Barrows, E. M., Arsenault, S. B., & Grenier, N. P. (2008). Firefly (Coleoptera: Lampyridae) flight periods, sex ratios, and habitat frequencies in a United States Mid-Atlantic freshwater tidal marsh, low forest, and their ecotone. *Banisteria*, 31, 47-52
- Basset, Y., & Lamarre, G. P. (2019). Toward a world that values insects. *Science*, 364(6447), 1230-1231. <https://doi.org/10.1126/science.aaw7071>
- Bechara, E. J., & Stevani, C. V. (2018). Brazilian bioluminescent beetles: Reflections on catching glimpses of light in the Atlantic Forest and cerrado. *Anais da Academia Brasileira de Ciências*, 90(1), 663-679. <https://doi.org/10.1590/00013765201820170504>
- Bouillon, S., Connolly, R. M., & Lee, S. Y. (2008). Organic matter exchange and cycling in mangrove ecosystems: Recent insights from stable isotope studies. *Journal of Sea Research*, 59(1-2), 44-58. <https://doi.org/10.1016/j.seares.2007.05.001>
- Branham, M. A. (2010). 4.15. Lampyridae Latreille, 1817. In R. A. B. Leschen., R. G. Beutel & J. F. Lawrence (Eds.), *Coleoptera, beetles. volume 2: Morphology and systematics (Elateroidea, Bostrichiformia, Cucujiformia partim)* (pp. 141-149). Walter de Gruyter. <https://doi.org/10.1515/9783110911213.141>
- Branham, M. A. (2015). Beetles (Coleoptera) of Peru: A survey of the families. Lampyridae. *Journal of the Kansas Entomological Society*, 88(2), 248-250. <https://doi.org/10.2317/kent-88-02-248-250.1>

- Chan, E. W. C., Oshiro, N., Kezuka, M., Kimura, N., Baba, K., & Chan, H. T. (2018). Pharmacological potentials and toxicity effects of *Excoecaria agallocha*. *Journal of Applied Pharmaceutical Science*, 8(5), 166-173. <https://doi.org/10.7324/JAPS.2018.8.523>
- Cheng, S., Chan, K. M., Ishak, S. F., Khoo, V., & Chew, M. Y. (2017). Elucidating food plants of the aggregative, synchronously flashing Southeast Asian firefly, *Pteroptyx tener* Olivier (Coleoptera, Lampyridae). *BioRisk*, 12, 25-39. <https://doi.org/10.3897/biorisk.12.14061>
- Chey, V. K. (2004). Fireflies of Sungai Klias and their display trees. *Sepilok Bulletin*, 1, 67-69.
- Chey, V. K. (2006). Fireflies of Sungai Paitan. *Sepilok Bulletin* 5, 1-6.
- Chey V. K. (2008). Fireflies of Kionsom. *Sepilok Bulletin*, 8(1), 15-22.
- Chey, V. K. (2009). Fireflies of Tuaran. *Sepilok Bulletin* 10, 25-33.
- Chey, V. K. (2010). Fireflies of Beaufort with special reference to Sungai Garama and Sungai Klias. *Sepilok Bulletin*, 12(1), 13-19.
- Chey, V. K. (2011). Fireflies of Pulau Sakar. *Sepilok Bulletin*, 13 & 14, 27-32.
- Chowdhury, G. R., Datta, U., Zaman, S., & Mitra, A. (2017). Ecosystem services of insects. *Biomedical Journal of Scientific & Technical Research*, 1(2), 1-2.
- Domínguez, E., Heredia-Guerrero, J. A., & Heredia, A. (2011). The biophysical design of plant cuticles: An overview. *New Phytologist*, 189(4), 938-949. <https://doi.org/10.1111/j.14698137.2010.03553.x>
- Eigenbrode, S. D., & Espelie, K. E. (1995). Effects of plant epicuticular lipids on insect herbivores. *Annual Review of Entomology*, 40(1), 171-194.
- Fallon, C., Hoyle, S., Lewis, S., Owens, A., Black, S. H., & Jepsen, S. (2019). *Conserving the jewels of the night guidelines for protecting fireflies in the United States and Canada*. The Xerces Society for Invertebrate Conservation.
- Faust, L. F. (2004). Fireflies as a catalyst for science education. *Integrative and Comparative Biology*, 44(3), 264-265. <https://doi.org/10.1093/icb/44.3.264>
- Faust, L. F. (2017). *Fireflies, glow-worms, and lightning bugs: identification and natural history of the fireflies of the eastern and central United States and Canada*. University of Georgia Press.
- Field, C., Osborn, J., Hoffman, L., Polsenberg, J., Ackerly, D., Berry, J., Björkman, O., Held, A., Matson, P., & Mooney, H. (1998). Mangrove biodiversity and ecosystem function. *Global Ecology & Biogeography Letters*, 7(1), 3-14. <https://doi.org/10.1111/j.1466-8238.1998.00278.x>
- Foo, K., & Mahadimenakbar, M. D. (2015). Diversity of fireflies (Coleoptera: Lampyridae) of Sungai Teratak, Sabah, Malaysia. *Journal of Tropical Biology & Conservation (JTBC)*, 12, 1-11. <https://doi.org/10.51200/jtbc.v12i.2621>
- Foo, K., & Mahadimenakbar, M. D. (2016). Short notes on fireflies of Sungai Kawang, Sabah. *Journal of Tropical Biology and Conservation*, 13, 125-128. <https://doi.org/10.51200/jtbc.v13i.402>
- Foo, K., & Mahadimenakbar, M. D. (2017). Diversity of *Pteroptyx* fireflies (Coleoptera: Lampyridae) and their display trees at Klias peninsula, Sabah, Malaysia. *Journal of Tropical Biology & Conservation (JTBC)*, 14, 95-103. <https://doi.org/10.51200/jtbc.v14i0.891>
- Fu, X., Li, J., Tian, Y., Quan, W., Zhang, S., Liu, Q., Liang, F., Zhu, X., Zhang, L., Wang, D., & Hu, J. (2017). Long-read sequence assembly of the firefly *Pyrocoelia pectoralis* genome. *GigaScience*, 6(12), 1-7. <https://doi.org/10.1093/gigascience/gix112>

- Goessens, A., Satyanarayana, B., Van der Stocken, T., Quispe Zuniga, M., Mohd-Lokman, H., Sulong, I., & Dahdouh-Guebas, F. (2014). Is Matang Mangrove Forest in Malaysia sustainably rejuvenating after more than a century of conservation and harvesting management? *PloS one*, *9*(8), Article e105069. <https://doi.org/10.1371/journal.pone.0105069>.
- Hazmi, I. R., & Sagaff, S. A. S. (2017). Fireflies population and the aquaculture industry (Coleoptera: Lampyridae) of the Sungai Sepetang, Kampung Dew, Perak, Malaysia. *Serangga*, *22*(2), 217-237.
- Ibharim, N. A., Mustapha, M. A., Lihan, T., & Mazlan, A. G. (2015). Mapping mangrove changes in the Matang Mangrove Forest using multi temporal satellite imageries. *Ocean & Coastal Management*, *114*, 64-76. <https://doi.org/10.1016/j.ocecoaman.2015.06.005>
- Jaikla, S., Thancharoen, A., & Pinkaew, N. (2020). Biology and rearing technique for the mangrove firefly, *Pteroptyx valida* (Coleoptera: Lampyridae) Olivier, with discussion of additional instar in female. *Journal of Asia-Pacific Biodiversity*, *13*(3), 367-371. <https://doi.org/10.1016/j.japb.2020.05.002>
- Juliana, W. A. W., Shahril, M. H. M., Rahman, N. A. N. A., Nurhanim, M. N., Maimon, A., & Norela, S. (2012). Vegetation profile of the firefly habitat along the riparian zones of Sungai Selangor at Kampung Kuantan, Kuala Selangor. *Malaysian Applied Biology Journal*, *41*(1), 55-58.
- Jusoh, W. F. A. W., Hashim, N. R., & Ibrahim, Z. Z. (2010a). Distribution and abundance of *Pteroptyx* fireflies in Rembau-Linggi estuary, Peninsular Malaysia. *Environment Asia*, *3*(special issue), 56-60. <https://doi.org/10.14456/EA.2010.40>
- Jusoh, W. F. A. W., Hashim, N. R., & Ibrahim, Z. Z. (2010b). Firefly distribution and abundance on mangrove vegetation assemblages in Sepetang estuary, Peninsular Malaysia. *Wetlands Ecology and Management*, *18*(3), 367-373. <https://doi.org/10.1007/s11273-009-9172-4>
- Jusoh, W. F. A. W., & Hashim, N. R. (2011). The effect of habitat modification on firefly populations at the Rembau-Linggi estuary, Peninsular Malaysia. *Lampyrid*, *2*, 149-155.
- Jusoh, W. F., Ballantyne, L., Lambkin, C. L., Hashim, N. R., & Wahlberg, N. (2018). The firefly genus *Pteroptyx* Olivier revisited (Coleoptera: Lampyridae: Luciolinae). *Zootaxa*, *4456*(1), 1-71. <https://doi.org/10.11646/zootaxa.4456.1.1>
- Kaiser, L., Ode, P., van Nouhuys, S., Calatayud, P. A., Colazza, S., Cortesero, A. M., Thiel, A., & van Baaren, J. (2017). The plant as a habitat for entomophagous insects. *Advances in Botanical Research*, *18*, 179-223. <https://doi.org/10.1016/bs.abr.2016.09.006>
- Khanal, B. P., & Knoche, M. (2017). Mechanical properties of cuticles and their primary determinants. *Journal of Experimental Botany*, *68*(19), 5351-5367. <https://doi.org/10.1093/jxb/erx265>
- Khoo, V., Nada, B., Kirton, L. G., & Phon, C. K. (2012). Monitoring the population of the firefly *Pteroptyx tener* along the Selangor River, Malaysia for conservation and sustainable ecotourism. *Lampyrid*, *2*, 162-173.
- Kirton, L. G., Nada, B., Tan, S. A., Ang, L. H., Tang, L. K., Hui, T. F., & Ho, W. M. (2006). The Kampung Kuantan firefly project: A preliminary assessment of the habitat requirements of *Pteroptyx tener* (Coleoptera: Lampyridae). In Y. F. Ho & K. A. Sharifah (Eds.), *Highlights of FRIM's non-IRPA Projects* (pp. 1-4). Forest Research Institute Malaysia.
- Krauss, P., Markstädter, C., & Riederer, M. (1997). Attenuation of UV radiation by plant cuticles from woody species. *Plant, Cell & Environment*, *20*(8), 1079-1085. <https://doi.org/10.1111/j.1365-3040.1997.tb00684.x>
- Lauff, R. (2017). "Fireflies, glow-worms, and lightning bugs: Identification and natural history of the fireflies of the Eastern and Central United States and Canada" by Lynn Frierson Faust, 2017. *The Canadian Field Naturalist*, *131*(2), 191-192. <https://doi.org/10.22621/cfn.v131i2.2002>

- Lewis, S. M., & Cratsley, C. K. (2008). Flash signal evolution, mate choice, and predation in fireflies. *Annual Review of Entomology*, 53, 293-321. <https://doi.org/10.1146/annurev.ento.53.103106.093346>
- Lewis, S. M., Wong, C. H., Owens, A., Fallon, C., Jepsen, S., Thancharoen, A., Wu, C., De Cock, R., Novák, M., López-Palafox, T., Khoo, V., & Reed, J. M. (2020). A global perspective on firefly extinction threats. *BioScience*, 70(2), 157-167. <https://doi.org/10.1093/biosci/biz157>
- Lloyd, J. E. (1998). On research and entomological education II: A conditional mating strategy and resource-sustained lek(?) in a classroom firefly (Coleoptera: Lampyridae; Photinus). *The Florida Entomologist*, 81(3), 261-272. <https://doi.org/10.2307/3495917>
- Loomboot, S. (2007). The biology and rearing of firefly *Pteroptyx malaccae* Gorham. *Environment and Natural Resources Journal*, 5(1), 35-43.
- Mahadimenakbar, M. D., Mahsol, H. H., & Ghani, M. A. (2007). The distribution and phenology of *Pteroptyx* fireflies (Coleoptera; Lampyridae) along Garama River, Sabah, Malaysia. *Journal of Tropical Biology & Conservation (JTBC)*, 3, 1-9. <https://doi.org/10.51200/jtbc.v3i>
- Mahadimenakbar, M. D., & Saikim, F. H. (2016). Studies on congregating fireflies (Coleoptera; Lampyridae; *Pteroptyx* sp.) in Sabah, Malaysia: A Review. *Journal of Tropical Biology & Conservation*, 13, 13-25. <https://doi.org/10.51200/jtbc.v13i.394>
- Mahmod, A. M., Sulaiman, A., Asri, L. N., Abdullah, N. A., Husin, S. M., Shukor, A. M., Darbis, N. D. A., Satiman, E. M. F. E. N., & Norela, S., (2018). Kelimpahan kelip-kelip bersinkroni di Sungai Chukai, Kemaman, Terengganu [Abundance of synchronize firefly at Sungai Chukai, Kemaman, Terengganu]. *Undergraduate Research Journal for Integrative Biology*, 2, 117-123.
- McKee, K. L., & Faulkner, P. L. (2000). Restoration of biogeochemical function in mangrove forests. *Restoration Ecology*, 8(3), 247-259. <https://doi.org/10.1046/j.1526-100x.2000.80036.x>
- Nada, B., & Kirton, L. G. (2004). The secret life of fireflies. *IRBM Newsletter*, 3, 2-4.
- Nada, B., Kirton, L. G., & Norma-Rashid, Y. (2009). The fireflies of Kuala Selangor: Conservation of Berembang alone won't save them. *Conservation Malaysia*, 10, 4-5.
- Nadirah, R., Zaiton, S., & Wan Norhidayah, W. M. (2020). Local community and visitor awareness of firefly conservation in Kuala Selangor, Malaysia. *The Malaysian Forester*, 83(2), 178-193.
- Nallakumar, K. (2003). The synchronously flashing aggregative fireflies of Peninsular Malaysia. *Biodiversity*, 4(2), 11-16. <https://doi.org/10.1080/14888386.2003.9712684>
- National Parks Board of Singapore. (2022, August 17). *Sonneratia caseolaris* (L.) Engl. [Review of *Sonneratia caseolaris* (L.) Engl.]. Flora and Fauna Web. <https://www.nparks.gov.sg/florafaunaweb/flora/3/3/3343>
- Norela, S., Loo, M. C., & Abdullah, M. (2017). Association between the firefly population and some biotic and abiotic factors along the Sungai Sepetang river banks at Kampung Dew. *Malayan Nature Journal*, 69(3), 110-118.
- Norela, S., Amirul-Aiman, A. J., Noraini, T., & Ismail, B. S. (2020). Leaf ultrastructure of firefly display trees. *Malayan Nature Journal*, 72(1), 93-102.
- Ohba, N., & Wong, C. H. (2004). External morphology and ecological study of the firefly, *Pteroptyx tener* at Kampong Kuantan, Selangor, Malaysia. *Science Report of Yokosuka City Museum*, 51, 1-33.

- Osman, N. I., Sidik, N. J., & Awal, A. (2017). Ethnobotanical profiles and phytochemical constituents of *Barringtonia racemosa* L. for potential scrutiny of bioactive compounds through plant biotechnology. *Journal of Natural Remedies*, 17(2), 57-68. <https://doi.org/10.18311/jnr/2017/15945>
- Othman, N. W., Sulaiman, N., Abdullah, N. H., & Ramli, R. (2018). Mouthpart and digestive tract morphology of the synchronised firefly, *Pteroptyx tener* (Coleoptera: Lampyridae). *Serangga*, 23(2), 170-182.
- Prasertkul, T. (2018). Characteristics of *Pteroptyx* firefly congregations in a human dominated habitat. *Journal of Insect Behavior*, 31(4), 436-457. <https://doi.org/10.1007/s10905-018-9687-8>
- Roy, A. K. D. (2016). Local community attitudes towards mangrove forest conservation: Lessons from Bangladesh. *Marine Policy*, 74, 186-194. <https://doi.org/10.1016/j.marpol.2016.09.021>
- Salem-Fnayou, A. B., Bouamama, B., Ghorbel, A., & Mliki, A. (2011). Investigations on the leaf anatomy and ultrastructure of grapevine (*Vitis vinifera*) under heat stress. *Microscopy Research and Technique*, 74(8), 756-762. <https://doi.org/10.1002/jemt.20955>
- Santos, N. M. D., & Lana, P. (2017). Present and past uses of mangrove wood in the subtropical Bay of Paranaguá (Paraná, Brazil). *Ocean & Coastal Management*, 148, 97-103. <https://doi.org/10.1016/j.ocecoaman.2017.07.003>
- Shahara, A., Nura, A. M. R., Maimon, A., & Norela, S. (2017). Assessment of firefly abundance at a new ecotourism site of Sungai Bernam, Selangor, Malaysia. *Malayan Nature Journal*, 69(2), 67-74.
- Sevanto, S. (2020). Why do plants have waxy leaves? Do we know after all? *Tree Physiology*, 40(7), 823–826. <https://doi.org/10.1093/treephys/tpz117>
- Sriboonlert, A., Swatdipong, A., Wonnapijit, P., Teerasak, E., & Thancharoen, A. (2015). New record of *Pteroptyx tener* olivier (Coleoptera: Lampyridae: Luciolinae) in Thailand. *The Coleopterists Bulletin*, 69(2), 332-336. <http://dx.doi.org/10.1649/0010-065X-69.2.332>
- Taillardat, P., Friess, D. A., & Lupascu, M. (2018). Mangrove blue carbon strategies for climate change mitigation are most effective at the national scale. *Biology letters*, 14(10), Article 20180251. <https://doi.org/10.1098/rsbl.2018.0251>
- Takeda, M., Amano, T., Katoh, K., & Higuchi, H. (2006). The habitat requirement of the Genji firefly *Luciola cruciata* (Coleoptera: Lampyridae), a representative endemic species of Japanese rural landscapes. In D. L. Hawksworth & A. T. Bull (Eds.), *Arthropod Diversity and Conservation* (pp. 177-189). Springer. [https://doi.org/10.1007/978-1-4020-5204-0\\_12](https://doi.org/10.1007/978-1-4020-5204-0_12)
- Thancharoen, A. (2007). *The biology and mating behavior of an aquatic firely species, Luciola Aquatilis Sp. Nov. Thancharoen* (Coleoptera: Lampyridae) [Unpublish doctoral dissertation]. Mahidol University.
- Vaz, S., Silveira, L. F. L. D., & Rosa, S. P. (2020). Morphology and life cycle of a new species of *Psilocladus Blanchard*, 1846 (Coleoptera, Lampyridae, Psilocladinae), the first known bromeliad-inhabiting firefly. *Papéis Avulsos de Zoologia*, 60, 1-15. <https://doi.org/10.11606/1807-0205/2020.60.special-issue.24>
- Vaz, S., Manes, S., Gama-Maia, D., Silveira, L., Mattos, G., Paiva, P. C., Figueirido, M., & Lorini, M. L. (2021). Light pollution is the fastest growing potential threat to firefly conservation in the Atlantic Forest hotspot. *Insect Conservation and Diversity*, 14(2), 211-224. <https://doi.org/10.1111/icad.12481>
- Vaz, S., Guerrazzi, M. C., Rocha, M., Faust, L., Khattar, G., Mermudes, J., & da Silveira, L. F. L. (2021). On the intertidal firefly genus *Micronaspis* Green, 1948, with a new species and a phylogeny of *Cratomorphini* based on adult and larval traits (Coleoptera: Lampyridae). *Zoologischer Anzeiger*, 292, 64-91. <https://doi.org/10.1016/j.jcz.2021.01.00>

- Wang, Y., Fu, X., Lei, C., Jeng, M. L., & Nobuyoshi, O. (2007). Biological characteristics of the terrestrial firefly *Pyrocoelia pectoralis* (Coleoptera: Lampyridae). *The Coleopterists Bulletin*, 61(1), 85-93. <https://doi.org/10.1649/907.1>
- Wang, X., Kong, L., Zhi, P., & Chang, C. (2020). Update on cuticular wax biosynthesis and its roles in plant disease resistance. *International Journal of Molecular Sciences*, 21(15), Article 5514. <http://dx.doi.org/10.3390/ijms21155514>
- Wattanachaiyingcharoen, W., Nak-eiam, S., & Thancharoen, A. (2011). Distribution and habitat of the firefly, *asymmetricata circumdata* (Motsch.) (Coleoptera: Lampyridae: Luciolinae) in the North of Thailand. *NU International Journal of Science*, 8(2), 12-18.

## Vision-Based Multi-Stages Lane Detection Algorithm

Fayez Saeed Faizi<sup>1,2\*</sup> and Ahmed Khorsheed Al-sulaifanie<sup>1</sup>

<sup>1</sup>Department of Electrical and Computer Engineering, College of Engineering, University of Duhok, Zakho Road - Duhok, Iraq

<sup>2</sup>Department of Energy Engineering, Technical College of Engineering, Duhok Polytechnic University, 61 Zakho Road, 1006 Mazi Qr - Duhok, Iraq

### ABSTRACT

Lane detection is an essential task for autonomous vehicles. Deep learning-based lane detection methods are leading development in this sector. This paper proposes an algorithm named Deep Learning-based Lane Detection (DLbLD), a Convolutional Neural Network (CNN)-based lane detection algorithm. The presented paradigm deploys CNN to detect line features in the image block, predict a point on the lane line part, and project all the detected points for each frame into one-dimensional form before applying K-mean clustering to assign points to related lane lines. Extensive tests on different benchmarks were done to evaluate the performance of the proposed algorithm. The results demonstrate that the introduced DLbLD scheme achieves state-of-the-art performance, where F1 scores of 97.19 and 79.02 have been recorded for TuSimple and CU-Lane benchmarks, respectively. Nevertheless, results indicate the high accuracy of the proposed algorithm.

*Keywords:* Autonomous cars; deep learning; lane detection; vision-based CNN

### INTRODUCTION

Autonomous driving has received much attention in recent years, which has led to rapid development in this technology. Artificial intelligence is increasingly utilized and considered the leading technique for self-driving and advanced driver-assistant systems

(Tabelini et al., 2021a). For these systems to work efficiently, lane detection is an essential problem that needs to be addressed.

It has a pivotal impact on the driving system's performance and accuracy. It is also important in applications such as lane-keeping assistants, driving route planning, and real-time vehicle positioning (Al-Jarrah et al., 2018).

#### ARTICLE INFO

##### Article history:

Received: 13 April 2023

Accepted: 20 November 2023

Published: 22 July 2024

DOI: <https://doi.org/10.47836/pjst.32.3.19>

##### E-mail addresses:

[fayez.faizi@dpu.edu.krd](mailto:fayez.faizi@dpu.edu.krd) (Fayez Saeed Faizi)

[ahmed.khorsheed@uod.ac](mailto:ahmed.khorsheed@uod.ac) (Ahmed Khorsheed Al-sulaifanie)

\*Corresponding author

Conventional lane detection algorithms mainly extract features through hand-crafted operators (Aly, 2008; Jiang et al., 2009; Kim, 2008), followed by fitting a line via methods such as random sampling consensus (Kim, 2008) and Hough transforms (Liu et al., 2010). Nevertheless, such methods lack accuracy in the actual environment because they depend on low-level hand-crafted features (Ko et al., 2022). Conversely, deep learning was deployed in recent studies, which resolved some shortcomings of traditional methods and gave better results (Abualsaud et al., 2021). The Deep Learning (DL)-based methods showed better accuracy than traditional methods, resulting in efficient process handling by deep learning. In addition, the generalization option provided by AI-based methods is missing in traditional algorithms because the conventional systems depend on hand-crafting low-level feature extraction. Segmentation was the earliest method proposed for lane detection through deep learning. Other paradigms have been presented lately, such as row-wise detection, anchored-based, and parametric prediction methods (Tabelini et al., 2021a). Deep learning-based lane detection methods have made significant progress and present robust algorithms; however, many challenges must be addressed.

Most lane detection methods depend on predicting points on the lane line and fitting a line to these points. Detecting and then aggregating points into line(s) is challenging. According to recent references in the lane detection field, deep learning-based algorithms show significant results from accuracy, speed, and total efficiency points of view. The fast development of AI technology helps to present reliable self-driving systems. Nevertheless, these methods still face some challenges. The key point challenge is recognizing the lane line(s) and determining points on that line(s) that can be utilized later for different purposes, including steering angle prediction, speed control, or a complete self-driving system (Ko et al., 2022; Tabelini et al., 2021a). Road condition and light intensity play essential roles in the vision-based detection process because they make the features difference to distinguish between lane line and background very small. Rain on the road, shadows on the lane line, dazzle, or dim light are common issues the system needs to face (Zang et al., 2018). Assigning the predicted points to the related lines is another challenging problem, especially because the lanes' shape and number change over the road (Neven et al., 2018; Tang et al., 2021).

This study proposes a new lane detection algorithm named DLbLD to overcome the mentioned challenges. The high learning ability of CNN is associated with a new network architecture to predict the presence of lane line parts in the incoming image block. The proposed network can recognize the features that lead to a binary classification of the incoming block as Lane or Background. A Gaussian filter eliminates pepper and salt noise in determining a point on the lane line for each block labeled Lane from the last stage. The DLbLD algorithm projects all the predicted points from the previous step into a one-dimensional form before applying the K-mean machine learning (ML) clustering method to improve assigning the detected points to the related lane line.

Different Lane detection methods have been presented in recent years; these methods can be divided into four types according to the strategy used in describing line shapes: segmentation-based methods, parametric prediction methods, row-wise detection methods, and anchor-based methods (Abualsaud et al., 2021; Tabelini et al., 2021a).

From a Segmentation point of view, the predictions are made on a pixel level, where each pixel is marked as a Lane or Background. Unlike a general segmentation process, instance-level discrimination is needed for the lane detection task. Pan et al. (2018) proposed the SCNN paradigm, which deploys the multi-class classification technique for instance discrimination. SCNN performs efficiently in long, thin structures but at the cost of speed. It is slow and achieves 7.5 frames per second (FPS), limiting its real-time application. A large backbone is an essential cause of low-speed performance. Also, Hou et al. (2019) present a self-attention distillation (SAD) scheme to obtain rich contextual information from a frame, where a high-level feature map is used to build the low-level feature maps. However, to generate the segmentation map, a post-processing phase is required to translate it into different lane lines. At the same time, Lee and Kim (2022) propose a multi-task learning paradigm, including a lane detection function. Their experiments illustrate promising results with a speed of 37 FPS. All the experiments were run on TITAN RTX NVIDIA, an expensive and high-powered GPU.

On the other hand, the Anchor-based methods overcome the problems that segmentation-based modules face (Liu, Chen et al., 2021). Anchored methods deploy a top-to-down methodology and determine the affined coordinates by optimizing the lane shape. In their work, Tabelini et al. (2021a) proposed an algorithm with slender anchors because the normal box anchor used in object detection does not suit their paradigm. With the predefined anchors, the proposed method limits the effect of the no-vision-clue issue and emphasizes instance discrimination ability. Another lane detection framework was presented by Xu et al. (2022) that shows a high-speed performance due to its light backbone network size. The pipeline addresses the curve lane issue by capturing accurate curve information and long-ranged coherence while preserving an efficient computational division. Nevertheless, fixed anchor shapes have described lane line shapes with a low degree of freedom.

From the Row-Wise detection method perspective, the input image as grid divisions is used to predict the location of the cell that contains a lane line part. Only the cell with the highest probability is selected on each row, which is why this process must be repeated for every lane in the image. As in segmentation-based methods, row-wise detection-based methods require a post-processing step to aggregate the detected cells into a line. Yoo et al. (2020) proposed an idea to avoid dense prediction at the pixel level. Their results show promising efficiency after testing the proposed algorithm on two datasets. Phillion (2019) and Qin et al. (2020) present other schemes to achieve higher speed. They reach 90 FPS and more than 310 FPS, respectively, but at the cost of losing some accuracy.

The above methods are based on modules that predict points on the lane line and then, through post-processing, regress these points into line(s). The algorithm directly outputs a curve equation representing a lane line using Parametric prediction methods. Tabelini et al. (2021b) and Liu, Yuan et al. (2021) proposed different lane detection algorithms by directly predicting quadratic or cubic polynomials representing different lane lines in the image. Both methods show a high-speed performance with 115 FPS and 420 FPS, respectively. However, the parametric prediction-based paradigms did not overtop other methods from an accuracy perspective. Generally, methods based on the Parametric prediction method show a high FPS with lower accuracy than other methods.

In contrast to what was presented before, our study makes the following contributions. First, the detection of lane features in challenging environmental conditions should be improved, and the incoming image blocks should be classified into Lane or Background groups. Second, each Lane labeled block is represented with a single coordinate representing a pixel on the line. Third, the detected points are categorized into the related lane lines.

**PROPOSED METHOD**

Deep learning is an efficient method of recognizing patterns after it is trained (Chen & Xiang, 2022). The proposed algorithm combines CNN, Gaussian filter, ML clustering, and curve fitting to detect a lane line. Figure 1 shows the flow diagram of the proposed algorithm applied in each incoming frame.

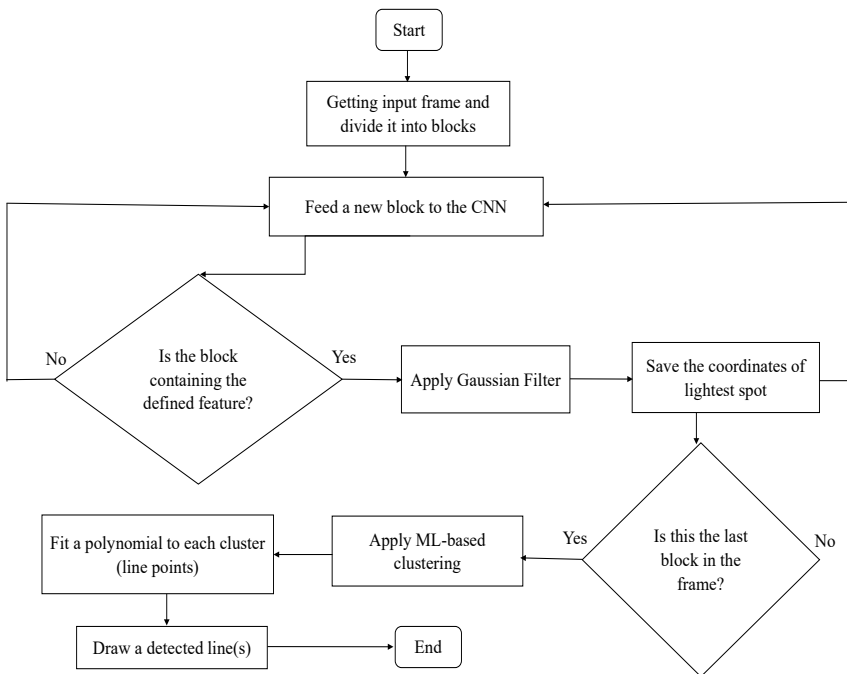


Figure 1. General flow diagram of the DLbLD algorithm

## Network Architecture

TensorFlow (Abadi et al., 2016) and Keras (Chollet, n.d.) are used to build the deep learning network of the proposed algorithm. The DLbLD network consists of three convolutional layers, each having a rectified linear unit (ReLU) activation function. The last two are followed by a Max-pooling size  $2 \times 2$  layer. The depth of the first layer is 16, the second is 32, and the last is 128. All utilize a  $3 \times 3$  kernel size. Next comes a flattened layer, followed by the dense layer with a depth of 128 and ReLU activation function, a 50% dropout layer, and a final dense layer with a single output and a Sigmoid activation function. Figure 2 illustrates the architecture of the network architecture used in this work.

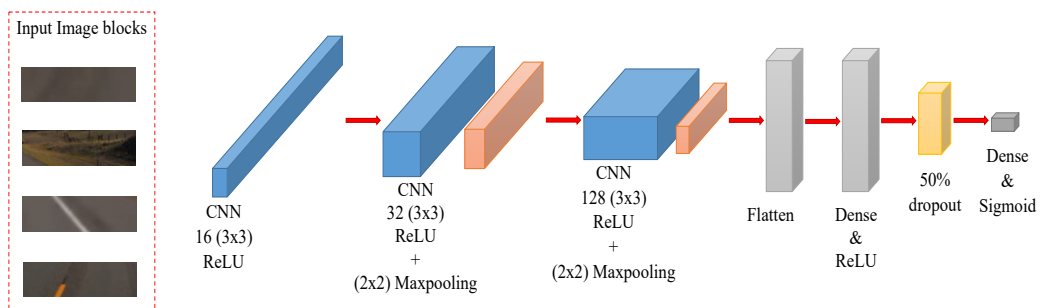


Figure 2. Proposed network architecture

First, the image is divided into smaller blocks, each having a 20-pixel height and 80-pixel width, as shown in the left part of Figure 2. The two upper blocks represent a sample of Background images, while the lower two are image blocks with a part of the Lane line. The network receives an RGB image block with a  $20 \times 80 \times 3$  dimension as an input—obtained from a camera located on the vehicle—and divided into blocks. Then, each convolution layer extracts features from the input image, resulting in a high-dimensional feature map of height  $\times$  width  $\times$  channel dimension. The feature map is flattened, fully connected, and 50% dropped. It outputs a single binary value indicating whether the input image block has the required feature (lane line part).

The network used in this work is a modified form of the common network used by He et al. (2016) and Zang et al. (2018). The version deployed here contains different layers with different parameters and outputs a binary decision. It contrasts with other works that result in Detection Loss or other required features depending on the system task. Such networks have a relatively simple architecture and still perform efficiently in feature extraction and recognizing the required characteristics (He et al., 2016; Tang et al., 2021).

In contrast to the work presented by Liu, Yuan et al. (2021), who used the Transformer encoder-decoder network, the idea behind using such common architecture is to show the power of the proposed idea. The incoming image is divided into small blocks and fed to a trained CNN that searches for one particular matter—the existence of a lane line part.

The network searches for features that indicate whether the incoming block contains a lane line part. Based on the network's prediction, the system decides whether to discard the incoming block if it is a background image block with no lane line or pass it to the next phase in the algorithm if it contains a lane line part.

### Identifying Points on the Line

The network output represents a label that indicates if the input image block contains lane line features. The block labeled with a binary value of "1" indicates the presence of a line segment, while the "0" label refers to the absence of a line segment in that block (image part). The system stores the coordinates of the top-left corner of the block labeled "1" as it represents (with the offset 80 x 20) a specific block that feeds to the network. But the coordinates of a point on the line (PO) inside the block that belongs to group "1" are needed. The idea utilized in this work to detect a single point on the labeled block located on the lane line part is considering the intensity difference between the lane color and the background. It is known that the lane line color is either white or yellow, while the background (road) is black. In digital images, the lighter colors have a higher intensity than the darker ones. The pixels of the line part have a higher intensity value than the background pixels so that the PO can be calculated as the maximum intensity in the block. Nevertheless, not all the incoming blocks are clean, but they are distorted by a noise similar to pepper and salt noise. In this case, the salt noise point is selected as a PO. The proposed algorithm utilizes the Gaussian blur filter of 5 x 5 to solve this issue and get the real point coordinates on the line. The blur kernel applied to the block labeled "1" is generated using the 2D Gaussian equation shown in Equation 1:

$$G_{(x,y)} = \frac{1}{2\pi\sigma^2} e^{-\frac{x^2+y^2}{2\sigma^2}} \quad [1]$$

where x and y specify the distance from the center point (0,0). For the kernel used in this work, x and y range from -5 to 5.  $\sigma$  is the standard deviation, indicating how significantly the pixels around the center pixel affect the computation result. Figure 3 illustrates the effect of deploying this filter.

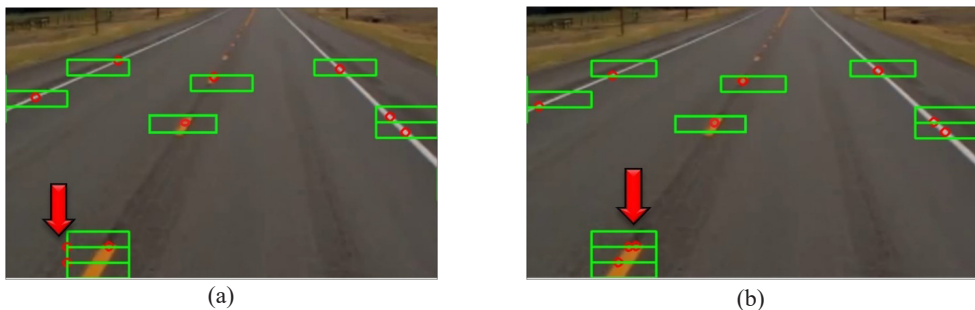


Figure 3. Location of PO, (a) without using Gaussian kernel, (b) with the use of Gaussian kernel

In Figure 3(a), the two down-left blocks give the wrong PO points due to the presence of a salt noise. In Figure 3(b), the system determines the correct PO points on the line after deploying the Gaussian blur filter.

**Assigning PO Points to the Related Lane Lines**

All the detected points on the line POs are saved as raw data points for each video frame. These data must be classified according to the lane line they belong to, which is used to draw the polynomial that fits that set of points. Because the detected POs seem ‘Scattered’ on the image, it is essential to specify each PO to the related Lane line. Conventional methods that depend on simple ‘Center point dividing’ were used in other works to perform this task. Such methods try to anchor a point between the two-lane lines and assign the points located on the left of the anchored point to the left line and the remaining detected points to the right lane line. These methods are suffused from an accuracy perspective, which applies only to two-lane line cases. On the other hand, in this work, the well-known K-mean (Lloyd, 1982), the ML-based clustering method, is used to achieve this goal. Deploying K-mean clustering directly on the raw data assigns some points belonging to one line to another. The proposed method performs a pre-processing step, making the clustering process more accurate. The idea is to put all the detected points (the raw data points) on one y-level instead of being distributed over the y-axis (i.e., project the points into a one-dimensional form). Figure 4 shows this process, where, first, the system detects the points on the line. Then, y-values for all POs are set to the center y-value of the POs using Equations 2 and 3.

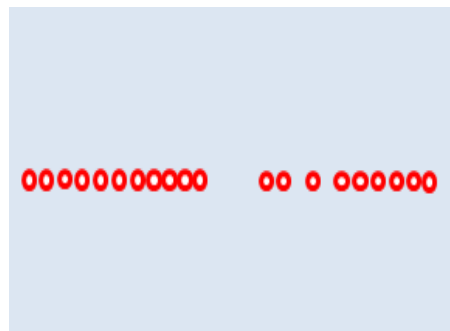
$$y_{center} = \frac{y_{max} + y_{min}}{2} \tag{2}$$

$$PO_{new} = (x, y_{center}) \tag{3}$$

K-mean clustering is applied to all new (POs), which produces an efficient grouping. Finally, return the original y-value to each PO.



(a)



(b)

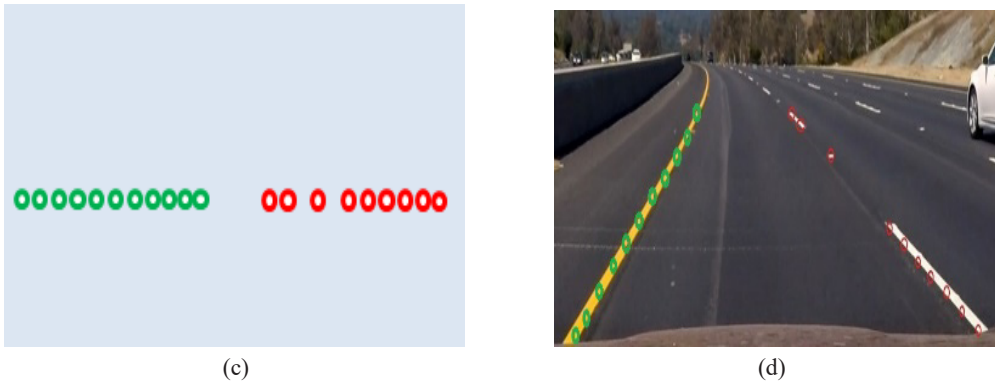


Figure 4. K-mean clustering, (a) detected pos, (b) new pos with new y-value, (c) deploying k-mean clustering, (d) returning original y-values and setting each PO to its line

The method explained in Figure 4 improved the clustering results significantly and put each PO into its correct lane line. The next step depends on this, so ensuring that each PO belongs to the correct group is important.

### Creating the Lane Lines

After the clustering, the proposed algorithm fits all the POs belonging to a specific line via a quadratic polynomial shown in Equation 4.

$$f(x) = a_2x^2 + a_1x + a_0 \tag{4}$$

Using Python (Rossum & Drake, 1995), the command `coef = np.poly1d(np.polyfit(x,y,2))` returns the coefficient of the quadratic equation that will be used in building each lane line, where x and y represent a list of x and y values for each line group, respectively. Finally, a line is drawn over each set of POs belonging to each line with a different color.

## RESULTS AND DISCUSSION

Several experiments were performed using different benchmarks to evaluate the proposed algorithm. The results were compared to those of other recent works to gauge the impact of the proposed method.

### Datasets

Two benchmarks, TuSimple (Pizzati et al., 2020) and CU-Lane (Pan et al., 2018), were utilized to evaluate the DLbLD algorithm. TuSimple is a widely used dataset consisting of 6,766 frames of highways with different weather conditions and daytimes. A one-second video of this benchmark is formed from 20 frames. The CU-Lane dataset is a larger and

more challenging benchmark, consisting of 133,235 frames divided into nine categories for both urban and highway roads. The summary of these benchmarks is illustrated in Table 1.

Table 1  
*Details of used datasets*

Dataset	Train	Test	Validation	Road
TuSimple	3.63K	2.78K	0.36K	Highways
CU-Lane	88.88k	34.68k	9.68k	Highways and urban

## Evaluation Method

F1 measurement was considered by applying the method used by Pan et al. (2018) to judge the algorithm's accuracy in detecting lane lines. Intersect of union (IoU) between prediction and the ground truth is calculated (for a fixed-line width) to determine whether the sample is a true positive (PT), false negative (FN), or false positive (FP). The F1 measure is evaluated according to Equation 7, which utilizes precision and recall, as in Equations 5 and 6.

$$Precision = \frac{TP}{TP+FP} \quad [5]$$

$$Recall = \frac{TP}{TP+FN} \quad [6]$$

$$F1 = \frac{2 \times Precision \times Recall}{Precision + Recall} \quad [7]$$

For the TuSimple dataset tests, the accuracy metric is also considered, according to Equation 8, to evaluate the accuracy of the proposed method.

$$Accuracy = \frac{\sum_{frame} POs}{\sum_{frame} TPOs} \quad [8]$$

Where POs are the number of detected points on the line, and TPOs are the total number of points on the line for that frame.

## Implementation Details

The proposed CNN was first trained with a dataset of 8,500 images, divided equally into two groups containing Lane Line and Background. The RMSprop with a learning rate inspired by the strategy Loshchilov and Hutter (2017) used, equal to 0.001, was an optimizer and utilized “binary\_crossentropy” as a loss augment. The presented paradigm preserving data augmentation needs a long learning time, so we chose 200 training epochs for both datasets. Results recorded in this paper for comparison were performed using an NVIDIA GeForce GTX 1080 card.

## Experiment Results

Before evaluating the proposed system, several experiments were done to attain the best possible results. A main aspect considered was the block-size image parts fed to CNN. Selecting the dimensions of the block has a significant impact on the results. A program was built that divided the incoming image into smaller blocks and fed it to the network to choose the block size with optimal prediction accuracy. This program divided the incoming image into blocks of 10 x 10 pixels. Then, it took all the probabilities for width and height—by an increasing step of 10 pixels—until it reached a block size of 120 x 120 pixels. It took 144 different block sizes. The system fed the blocks to the network at each probability and calculated the prediction accuracy. Figure 5 summarizes the results of this process.

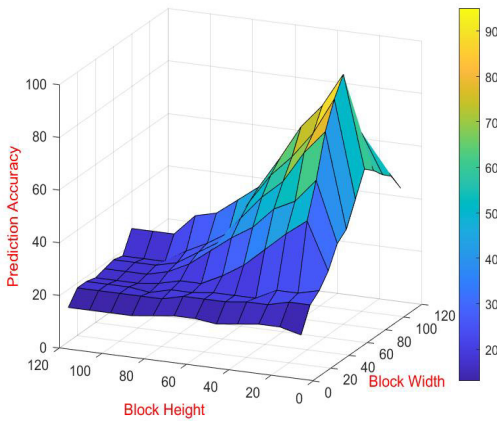


Figure 5. Accuracy for different block-size

It is clear from Figure 5 that a block size of width=80 pixels x height=20 pixels gives the highest prediction accuracy, which explains why these dimensions have been chosen in this work. The proposed algorithm was tested on both the TuSimple and CU-Lane benchmarks, and the results were compared to some of the recent methods proposed in this research, including Tabelini et al. (2021a), Hou et al. (2019), Pan et al. (2018), Phillion (2019), Yoo et al. (2020) and Qin et al. (2020).

### Using the TuSimple Dataset

The TuSimple dataset was used to evaluate the proposed algorithm in the first experiment set. The comparison results on deploying the TuSimple benchmark are illustrated in Table 2. The proposed algorithm achieved a new F1 score of 97.19 with a low FP of 2.0.

Table 2  
Comparing DLbLD to different methods using the TuSimple dataset

Method	Accuracy	FP	FN	F1
DLbLD (ours)	96.56	2.0	3.52	97.19
SCNN (Pan et al., 2018)	96.53	6.17	1.8	95.97
ENet-SAD (Hou et al., 2019)	96.64	6.02	2.05	95.92
FastDraw (Phillion, 2019)	95.2	7.6	4.5	93.92
UFAST-ResNet34 (Qin et al., 2020)	95.86	18.91	3.75	88.02

Table 2 (Continue)

Methods	Accuracy	FP	FN	F1
UFAST-ResNet18 (Qin et al., 2020)	95.82	19.05	3.92	87.87
LanATT-ResNet18 (Tabelini et al., 2021a)	95.57	3.56	3.01	96.71
LanATT-ResNet 34 (Tabelini et al., 2021a)	95.63	3.53	2.92	96.77
LanATT-ResNet122 (Tabelini et al., 2021a)	96.1	5.64	2.17	96.06
ERF-E2E (Yoo et al., 2020)	96.02	3.21	4.28	96.25
ERFNet-HESA (Lee et al., 2022)	96.01	3.29	4.58	-
Lane-Detection (Yao & Chen, 2022)	95.11	6.95	4.9	-
MLP (Yao et al., 2023)	94.36	5.5	5.6	-
Lane method (Xin et al., 2023)	95.92	2.41	4.29	96.64
HAM (Xie et al., 2023)	96.1	2.29	4.0	96.84
4-head self-attention (Shengli et al., 2023)	95.55	3.39	3.29	-
XR34 (Yanga et al., 2023)	<b>96.71</b>	2.82	3.24	-
Res (Yang et al., 2023)	-	-	-	97.15

Testing the proposed algorithm on the TuSimple benchmark shows the highest F1 score of (97.19) while the previous best result was registered by Tabelini et al. (2021a) with an F1 score of (96.77). Nevertheless, the presented method recorded one of the best accuracy scores after the one registered by Yanga et al. (2023) and then Hou et al. (2019) with a very small lack of (0.16 %) compared to the best accuracy recorded.

### Using the CU-Lane Dataset

Considering seven categories, DLbLD achieved the best F1 score results in five scenarios, indicating the robustness of the proposed method under differing conditions. A new state-of-the-art F1 average total score of 79.02 has been achieved. Table 3 shows the results when utilizing the CU-Lane benchmark.

Table 3

Comparing DLbLD to different methods using the CU-Lane dataset

Method	Average	Normal	Crowd	Dazzle	Shadow	Arrow	Curve	Night
DLbLD (Ours)	<b>79.02</b>	<b>94.03</b>	70.4	<b>70.17</b>	<b>81.26</b>	84.75	<b>77.43</b>	<b>75.1</b>
SCNN (Pan et al., 2018)	71.47	90.60	69.70	58.50	66.90	84.10	64.40	66.10
ENet-SAD (Hou et al., 2019)	71.53	90.1	68.8	60.2	65.9	84	65.7	66

Table 2 (Continue)

Method	Average	Normal	Crowd	Dazzle	Shadow	Arrow	Curve	Night
FastDraw (Philion, 2019)	68.4	85.9	63.6	57	69.9	79.4	65.2	57.8
UFAST- ResNet34 (Qin et al., 2020)	73.09	90.7	70.2	59.5	69.3	85.7	69.5	66.7
UFAST- ResNet18 (Qin et al., 2020)	67.99	87.7	66	58.4	62.8	81	57.9	62.1
LanATT- ResNet18 (Tabelini et al., 2021a)	73.98	91.17	72.71	65.82	68.03	87.82	63.75	68.58
LanATT- ResNet 34 (Tabelini et al., 2021a)	76.94	92.14	75.03	66.47	78.15	88.38	67.72	70.72
LanATT- ResNet122 (Tabelini et al., 2021a)	76.4	91.74	<b>76.16</b>	69.47	76.31	86.29	64.05	70.81
ERF-E2E (Yoo et al., 2020)	75.46	91	73	64.5	74.1	85.8	71.9	67.9
ERFNet- HESA (Lee et al., 2022)	75.69	92	73.1	63.1	75.1	88.1	68.8	69.6
Lane- Detection (Yao & Chen, 2022)	68.64	88.5	67.6	62.4	62	81.2	56.9	61.9
MLP (Yao et al., 2023)	69.03	89.6	67.1	59.9	60.3	83.0	61.4	61.9
Lane method (Xin et al., 2023)	76.8	92.6	74.9	65.6	75.5	88.2	69.8	70.9
HAM (Xie et al., 2023)	76.47	92.1	74.1	63.1	77.1	88.3	69.3	71.3

Table 2 (Continue)

Method	Average	Normal	Crowd	Dazzle	Shadow	Arrow	Curve	Night
4-head self-attention (Shengli et al., 2023)	74.38	91.43	73.56	66.18	66.81	86.79	65.6	70.3
XR34 (Yanga et al., 2023)	78.52	92.83	75.96	69.48	77.86	<b>88.66</b>	71.14	73.74
Res (Yang et al., 2023)	74.39	91.3	70.0	61.4	72.1	84.6	74.8	66.5

The results on the CU-Lane dataset show the best F1 score in five scenarios out of seven, including the Normal, Dazzle, Shadow, Curve, and Night cases, with scores of 94.03, 70.17, 81.26, 77.43, and 75.1, respectively. The system can 'see' the road and analyze the image to accurately predict lane line location for all these scenarios. Although the proposed method recorded state-of-the-art results in the cost of the need for a GPU. On the other hand, in the Crowd scenario, the presented paradigm recorded a low F1 score because it could not see the road clearly, whereas other cars were blocking the lane lines. Knowing that the DLbLD algorithm was designed to extract lane features from an image block of the total image and indicate its coordinates to be used later in creating the lane line. So, being unable to see some lane parts blocked by other cars leads to a drop in the efficiency of the presented system.

In the seventh scenario that considered the Arrows case, the DLbLD algorithm registered a low F1 score; the reason behind that is to return to the design idea of the proposed scheme where it searches for lane parts in the incoming blocks and replaces them with a single point located on that line part to be utilized later in forming the related lane line, and not searching for Arrows drawn on the road, as it is not designed or trained to do so. Results shown in Table 3 indicate that the proposed method is efficient in dealing with most scenarios when the camera can see the road; it also shows the superiority of this method compared to other works. Nevertheless, the introduced system's performance degrades when obstacles, such as cars in the crowd scenario, block the lane lines. In addition, the results depicted in Table 3 show a low F1 score in the arrow case due to the design of the DLbLD algorithm, which was designed to deal with lane lines and not recognize arrows on the road.

Deploying the proposed method on two standard benchmarks with different environmental conditions demonstrates its impact and superiority over the recently available methods in most environments. Even in challenging Night and Shadow conditions, the proposed algorithm illustrates an improvement of more than 6% and almost 4%, respectively, and a total average improvement of 2.7%. From a real-time performance perspective, the proposed system was tested to indicate this metric. First, an Intel® Core™

i7 Control Processing Unit (CPU) was used to run the system and process the incoming images. Results indicated a low FPS rate of 3.2. Another test used the NVIDIA GeForce GTX 1080 card. Real-time performance improved significantly and recorded 67.8 FPS. These results can be interpreted as the effect of using a graphic processing unit (GPU) that handles image processing better than a CPU (Qin et al., 2020). Table 4 compares other works from the FPS point of view.

Table 4  
*Comparing the speed of DLbld with GPU to different methods*

Method	DLbLD (Ours)	SCNN [12]	ENet-SAD [13]	UFAST- ResNet [19]	LanATT- ResNet18 [1]	ERF-E2E [17]
FPS	67.8	7.5	75	322.5	250	90.31

Table 4 indicates the performance of the proposed algorithm compared to other related works in terms of processing speed using the FPS measure. Although the presented system achieved a 67.8 FPS, which is not the highest in Table 4, it is still considered a very good result as it is more than enough for real-time applications. It is worth mentioning that the recorded FPS can be significantly improved by using a powerful GPU. The proposed paradigm is superior to other systems as a total trade-off between the recorded accuracy and the achieved speed.

## CONCLUSION

This work presents a new CCN-based lane detection algorithm. The proposed system utilized a single vision sensor as an input; the camera takes video frames and feeds them to the system. The processing starts by dividing the incoming images into smaller blocks with 20x80 pixels. The blocks are presented to the proposed neural network to check the presence of a lane line segment. The image block will then be classified in a binary base; if the paradigm predicts that the block contains a part of a lane line, that block will be labeled as '1'; otherwise, it will be labeled as '0'. After applying the Gaussian blur filter, a point-on-line (PO) for each block in the frame is determined. K-mean clustering then assigns each PO of the projected points to the related lane line. The results of applying the proposed DLbLD algorithm to TuSimple and CU-Lane benchmarks indicate its robustness and superiority to recent works. Nevertheless, GPU is needed to speed up the process and give a better FPS rate.

## ACKNOWLEDGEMENTS

This work was supported by the (UoD) and (DPU)/Ministry of Higher Education (MHE)/Kurdistan Region Government (KRG)/Iraq. As a part of the higher studies program/Ph.D. plan for the studying years 2020–2023.

## REFERENCES

- Abadi, M., Barham, P., Chen, J., Chen, Z., Davis, A., Dean, J., Devin, M., Ghemawat, S., Irving, G., Isard, M., Kudlur, M., Levenberg, J., Monga, R., Moore, S., Murray, D. G., Steiner, B., Tucker, P., Vasudevan, V., Warden, P., ... & Zheng, X. (2016, November 2-4). *TensorFlow: A system for large-scale machine learning*. [Paper presentation]. Proceedings of the 12th USENIX Symposium on Operating Systems Design and Implementation (OSDI), Savannah, USA.
- Abualsaud, H., Liu, S., Lu, D., Situ, K., Rangesh, A., & Trivedi, M. M. (2021). LaneAF: Robust multi-lane detection with affinity fields. *IEEE Robotics and Automation Letters*, 6(4), 7477–7484. <https://doi.org/10.1109/lra.2021.3098066>
- Al-Jarrah, R., Al-Jarrah, M., & Roth, H. (2018). A novel edge detection algorithm for mobile robot path planning. *Journal of Robotics*, 2018, Article 1969834. <https://doi.org/10.1155/2018/1969834>
- Aly, M. (2008, June 4-6). *Real time detection of lane markers in urban streets*. [Paper presentation]. IEEE Intelligent Vehicles Symposium, Eindhoven, Netherlands. <https://doi.org/10.1109/IVS.2008.4621152>
- Chen, Y., & Xiang, Z. (2022). Lane mark detection with pre-aligned spatial-temporal attention. *Sensors*, 22(3), Article 794. <https://doi.org/10.3390/s22030794>
- Chollet, F. (n.d.). *Keras* [Python]. Github.com. <https://github.com/keras-team/keras>
- He, K., Zhang, X., Ren, S., & Sun, J. (2016, June 27-30). *Deep residual learning for image recognition*. [Paper presentation]. IEEE Conference on Computer Vision and Pattern Recognition (CVPR), Las Vegas, USA. <https://doi.org/10.1109/cvpr.2016.90>
- Hou, Y., Ma, Z., Liu, C., & Loy, C. C. (2019, October 27-November 2). *Learning lightweight lane detection CNNs by self attention distillation*. [Paper presentation]. IEEE/CVF International Conference on Computer Vision (ICCV), Seoul, Korea. <https://doi.org/10.1109/iccv.2019.00110>
- Jiang, R., Klette, R., Vaudrey, T., & Wang, S. (2009, September 2-4). *New lane model and distance transform for lane detection and tracking*. [Paper presentation]. Computer Analysis of Images and Patterns: 13th International Conference (CAIP), Munster, Germany. [https://doi.org/10.1007/978-3-642-03767-2\\_127](https://doi.org/10.1007/978-3-642-03767-2_127)
- Kim, Z. (2008). Robust lane detection and tracking in challenging scenarios. *IEEE Transactions on Intelligent Transportation Systems*, 9(1), 16–26. <https://doi.org/10.1109/TITS.2007.908582>
- Ko, Y., Lee, Y., Azam, S., Munir, F., Jeon, M., & Pedrycz, W. (2022). Key points estimation and point instance segmentation approach for lane detection. *IEEE Transactions on Intelligent Transportation Systems*, 23(7), 8949–8958. <https://doi.org/10.1109/tits.2021.3088488>
- Lee, D. G., & Kim, Y. K. (2022). Joint semantic understanding with a multilevel branch for driving perception. *Applied Sciences*, 12(6), Article 2877. <https://doi.org/10.3390/app12062877>
- Lee, M., Lee, J., Lee, D., Kim, W., Hwang, S., & Lee, S. (2022, January 3-8). *Robust lane detection via expanded self attention*. [Paper presentation]. IEEE/CVF Winter Conference on Applications of Computer Vision (WACV), Waikoloa, USA.
- Liu, G., Worgotter, F., & Markelic, I. (2010, June 21-24). *Combining statistical Hough transform and particle filter for robust lane detection and tracking*. [Paper presentation]. IEEE Intelligent Vehicles Symposium, La Jolla, USA. <https://doi.org/10.1109/IVS.2010.5548021>

- Liu, L., Chen, X., Zhu, S., & Tan, P. (2021, October 10-17). *CondLaneNet: A top-to-down lane detection framework based on conditional convolution*. [Paper presentation]. IEEE/CVF International Conference on Computer Vision (ICCV), Montreal, Canada. <https://doi.org/10.1109/iccv48922.2021.00375>
- Liu, R., Yuan, Z., Liu, T., & Xiong, Z. (2021, January 3-8). *End-to-end lane shape prediction with transformers*. [Paper presentation]. IEEE/CVF Winter Conference on Applications of Computer Vision (WACV), Waikoloa, USA. <https://doi.org/10.1109/WACV48630.2021.00374>
- Lloyd, S. (1982). Least squares quantization in PCM. *IEEE Transactions on Information Theory*, 28(2), 129–137. <https://doi.org/10.1109/TIT.1982.1056489>
- Loshchilov, I., & Hutter, F. (2017). *SGDR: Stochastic gradient descent with warm restarts*. arXiv. <https://doi.org/10.48550/arXiv.1608.03983>.
- Neven, D., De Brabandere, B., Georgoulis, S., Proesmans, M., & Van Gool, L. (2018, June 26-30). *Towards end-to-end lane detection: An instance segmentation approach*. [Paper presentation]. IEEE Intelligent Vehicles Symposium (IV), Changshu, China. <https://doi.org/10.1109/ivs.2018.8500547>
- Pan, X., Shi, J., Luo, P., Wang, X., & Tang, X. (2018). Spatial as deep: Spatial CNN for Traffic scene understanding. *Proceedings of the AAAI Conference on Artificial Intelligence*, 32(1), Article 7277. <https://doi.org/10.1609/aaai.v32i1.12301>
- Phillion, J. (2019, June 15-20). *Fastdraw: Addressing the long tail of lane detection by adapting a sequential prediction network*. [Paper presentation]. IEEE/CVF Conference on Computer Vision and Pattern Recognition (CVPR), Long Beach, California. <https://doi.org/10.1109/cvpr.2019.01185>
- Pizzati, F., Allodi, M., Barrera, A., & García, F. (2020). Lane detection and classification using cascaded CNNs. In R. Moreno-Diaz, F. Pichler & A. Quesada-Arencibia (Eds.) *Computer aided systems theory—EUROCAST 2019* (pp. 95–103). Springer. [https://doi.org/10.1007/978-3-030-45096-0\\_12](https://doi.org/10.1007/978-3-030-45096-0_12)
- Qin, Z., Wang, H., & Li, X. (2020). Ultra fast structure-aware deep lane detection. In A. Vedaldi, H. Bischof, T. Borx & J. Frahm (Eds.) *Computer vision—ECCV 2020* (pp. 276–291). Springer. [https://doi.org/10.1007/978-3-030-58586-0\\_17](https://doi.org/10.1007/978-3-030-58586-0_17)
- Rossum, G. V., & Drake, F. L. (1995). *Python reference manual*. Centrum voor Wiskunde en Informatica.
- Shengli, F., Yuzhi, Z., & Xiaohui, B. (2023). Lane marker detection based on multihead self-attention. *Mobile Information Systems*, 2023, Article 2075022. <https://doi.org/10.1155/2023/2075022>
- Tabelini, L., Berriel, R., Paixão, T. M., Badue, C., De Souza, A. F., & Oliveira-Santos, T. (2021a, June 20-25). *Keep your eyes on the lane: Real-time attention-guided lane detection*. [Paper presentation]. IEEE/CVF Conference on Computer Vision and Pattern Recognition (CVPR), Nashville, Tennessee. <https://doi.org/10.1109/cvpr46437.2021.00036>
- Tabelini, L., Berriel, R., Paixão, T. M., Badue, C., De Souza, A. F., & Oliveira-Santos, T. (2021b, January 10-15). *Polylanenet: Lane estimation via deep polynomial regression*. [Paper presentation]. 25th International Conference on Pattern Recognition (ICPR), Milan, Italy. <https://doi.org/10.1109/icpr48806.2021.9412265>
- Tang, J., Li, S., & Liu, P. (2021). A review of lane detection methods based on deep learning. *Pattern Recognition*, 111, Article 107623. <https://doi.org/10.1016/j.patcog.2020.107623>

- Xie, T., Yin, M., Zhu, X., Sun, J., Meng, C., & Bei, S. (2023). A fast and robust lane detection via online re-parameterization and hybrid attention. *Sensors*, 23(19), Article 8285. <https://doi.org/10.3390/s23198285>
- Xin, L., Yingping, H., & Zhenming, L. (2023). Axial attention-guided anchor classification lane detection. *Opto-Electronic Engineering*, 50(7), Article 230079-1. <https://doi.org/10.12086/oe.2023.230079>
- Xu, H., Wang, S., Cai, X., Zhang, W., Liang, X., & Li, Z. (2022). Curvelane-NAS: Unifying lane-sensitive architecture search and adaptive point blending. In A. Vedaldi, H. Bischof, T. Brox & J. Frahm (Eds.) *Computer vision—ECCV 2020* (pp. 689–704). Springer. [https://doi.org/10.1007/978-3-030-58555-6\\_41](https://doi.org/10.1007/978-3-030-58555-6_41)
- Yang, Q., Ma, Y., Li, L., Su, C., Gao, Y., Tao, J., Huang, Z., & Jiang, R. (2023). Lightweight lane line detection based on learnable cluster segmentation with self-attention mechanism. *IET Intelligent Transport Systems*, 17(3), 522–533. <https://doi.org/10.1049/itr2.12277>
- Yanga, J., Zhang, L., & Lu, H. (2023). Lane detection with versatile atrousformer and local semantic guidance. *Pattern Recognition*, 113, Article 109053. <https://doi.org/10.1016/j.patcog.2022.109053>
- Yao, X., Wang, Y., Wu, Y., He, G., & Luo, S. (2023). MLP-Based efficient convolutional neural network for lane detection. *IEEE Transactions on Vehicular Technology*, 72(10), 12602-122614. <https://doi.org/10.1109/TVT.2023.3275571>
- Yao, Z., & Chen, X. (2022). Efficient lane detection technique based on lightweight attention deep neural network. *Journal of Advanced Transportation*, 2022, Article 5134437. <https://doi.org/10.1155/2022/5134437>
- Yoo, S., Lee, H., Myeong, H., Yun, S., Park, H., Cho, J., & Kim, D. H. (2020, June 14-19). *End-to-end lane marker detection via row-wise classification*. [Paper presentation]. IEEE/CVF Conference on Computer Vision and Pattern Recognition Workshops (CVPRW), Seattle, USA. <https://doi.org/10.1109/cvprw50498.2020.00511>
- Zang, J., Zhou, W., Zhang, G., & Duan, Z. (2018, November 12-15). *Traffic lane detection using fully convolutional neural network*. [Paper presentation]. Asia-Pacific Signal and Information Processing Association Annual Summit and Conference (APSIPA ASC), Honolulu, Hawaii. <https://doi.org/10.23919/APSIPA.2018.8659684>



## The Macrobenthos Diversity and Dominance in Johor Straits, Malaysia

Mohd Sophian Mohd Kasihmuiddin and Zaidi Che Cob\*

Department of Earth Sciences and Environment, Universiti Kebangsaan Malaysia, 43600 Bangi, Selangor, Malaysia

### ABSTRACT

Johor Strait has received massive anthropogenic traffic in recent years, causing environmental alteration and inevitably harming macrobenthos on the seafloor. A comprehensive assessment was done in several key locations within the strait to identify macrobenthic inhabitants and possible driving factors attributing to differences in macrobenthic assemblages in these areas. Sediments were acquired using Ponar Grab in 13 key locations within the Johor Straits. Seven hundred thirty macrobenthic individuals and 46 known taxa were identified in sediments of 13 locations in the strait. Annelids *Prionospio* ( $n=295$ ), *Minuspio* ( $n=95$ ) and *Mediomastus* ( $n=82$ ) were concentrated in the central zone. Molluscs dominated the Merambong Shoals area (*Arcualuta*,  $n=66$ ), and amphipods dominated waters off Santi River (*Leucothoe*,  $n=26$ ; *Gammarus*,  $n=11$ ; *Cymadusa*,  $n=9$ ). PERMANOVA analyses ( $p<0.05$ ) showed significant differences in benthic taxa composition in all locations overall. BIOENV analyses ( $r=0.76$ ,  $p<0.05$ ) highlighted water acidity, chlorophyll-*a*, silts and total organic carbon as the main influences toward benthic assemblages throughout the study area. PCA graph indicated higher organic carbon and silts in the central area, implying favourable conditions for Sedentarian polychaetes to thrive. The east and west ends of the strait exhibited higher readings of water acidity and chlorophyll-*a*, which may directly contribute to a higher diversity of benthic communities in the areas. Lower oxygen levels in two locations in the central area (J3=2.97 mg/L, J4: 2.63 mg/L) exhibited Sedentaria polychaete-dominated region, but zero benthic organisms

in another part of the central area (J5-J9, 2.97–0.99 mg/L). This study showcased the effectiveness of environmental monitoring using macrobenthos as an indicating subject.

### ARTICLE INFO

#### Article history:

Received: 15 April 2023

Accepted: 18 December 2023

Published: 22 July 2024

DOI: <https://doi.org/10.47836/pjst.32.3.20>

#### E-mail addresses:

sophianmkmaidin@gmail.com (Mohd Sophian Mohd Kasihmuiddin)

zdcce@gmail.com (Zaidi Che Cob)

\*Corresponding author

**Keywords:** Biomonitoring, coastal environment, Johor Straits, macrobenthos, Malaysia-Singapore Causeway, Pengerang Integrated Complex, polychaete

## INTRODUCTION

The Johor (or Tebrau) Straits connect Malaysia, Singapore, and Indonesia, and the Malaccan Straits link to the South China Sea. Due to this, the waterway has served critically as a major economic hub zone as well as a political buffer zone between nations, especially Malaysia and Singapore, for years. On the strait the strait is connected to various rivers and large patches of seagrass at the west and east ends of the strait (Wan-Lotfi et al., 2013; Hossain et al., 2019). At the central part of the strait, a causeway bridges Malaysia and Singapore, which has led to economic growth between the nations for decades since the 1910s (Koh et al., 1991). Due to its strategic location, the waterway was subjected to intensive coastal and urban development between Malaysia and Singapore. It includes the reclamation of Forest City and Pengerang Integrated Complex, in which the projects were intended to accommodate the urban population and increase job employment, respectively (Rahman, 2017; Rezayee et al., 2020).

Unfortunately, concerns have risen over anthropogenic activities' effect on the strait's environmental side, particularly on the lifeforms inhabiting the seafloor. These lifeforms, collectively termed benthic communities, are generally small (~1 m), have limited mobility, and completely rely on the sediment and water surrounding the benthic group (Smith, 1964; Castro & Huber, 2019). Certain groups of benthic organisms (i.e., holothuroids and decapods) are unable to function well or even live in environments that have been altered, such as waters with a lower oxygen level and a higher concentration of heavy metals in the sediment and are, therefore very sensitive to environmental changes in the seafloor ecosystem. Due to these factors, benthic groups, especially macrobenthos, are often used as bioindicators in environmental studies, in which the presence and/or absence of certain groups of benthic taxa are to be associated with the current state of the seafloor ecosystem, ultimately assessing the effect of nearby anthropogenic activities on the environment.

Some studies made in Southeast Asian waters showcased the effectiveness of utilizing macrobenthos as an indicator to assess the extent of environmental damage done in the coastal area. In Port Blair, Andaman Island, records showed the dominance of *Capitella* and *Armandia* polychaetes on the seafloor off the three main ports of Blair. The study highlighted higher organic carbon, hydrocarbons, and heavy metals in sediment as major influences toward lower diversity in the area, regardless of dry and wet seasons. Sediments with such content were identified as favourable toward smaller-sized polychaetes but otherwise to other taxa, leading to the dominance of the former but otherwise of the latter. Malaysia's coastal and port areas showed similar findings to those in Port Blair. Sediments in Port Klang, especially near Southpoint and the Klang River, were inhabited by predominantly Capitellid, Cirratulid, and Spionid polychaetes (Sany et al., 2015; Kasihmuddin & Cob, 2021). In the north of Peninsular Malaysia, the coastal areas of Penang Island experienced major reclamation projects over time (Gholizadeh, 2015). As a result, smaller-sized

polychaetes and gastropods dominate the sediments rather than larger ones. Similar to cases in Blair and Klang, fluxes of reclaimed sediment allowed smaller-sized organisms to thrive there but otherwise for larger ones. All these studies highlighted similar findings, where constant fluxes of organic enrichment in sediment have disallowed larger-sized benthic taxa to thrive. It reduces potential foraging areas due to the smothering of sediments while at the same time providing more opportunities for deposit-feeding and easily reproductive taxa, namely Capitellid, Cirratulid, and Spionid polychaetes, to thrive in the areas (Faulwetter et al., 2014; Kasihmuddin & Cob, 2021).

Benthic studies in the Johor Straits focused on the central and both ends of the strait. Studies in the west and east of the straits were more inclined towards seagrass regions, namely the Pulai River, Merambong Shoals, Adang Cape, and Santi River (Wan-Lotfi et al., 2013; Guan, Ghaffar et al., 2014; Guan, Min et al., 2014; Mahadi et al., 2014; Woo et al., 2014; Kassim et al., 2015). Many of these studies solely focus on specific taxa, such as polychaetes (Guan, Ghaffar et al., 2014) and holothuroids (Mahadi et al., 2014). Studies that focus on multiple taxa groups (Guan, Min et al., 2014; Wan-Lotfi et al., 2013) did not fully explain how environmental parameters in the surrounding area influence benthic group distribution overall, as these studies were conducted solely to update the latest distribution benthic data in the region. Moreover, these studies were conducted when coastal development activities had just begun (Rahman, 2017), so records were outdated in this current period. It can be seen in the highly abundant holothuroids and copepods in Merambong and Pulai, respectively (Mahadi et al., 2014; Woo et al., 2014), which may not truly reflect the current state of the area, partly due to the presence of the massive, reclaimed island of Forest City. In the central zone, benthic studies were limited to only one taxon group. Azelee et al. (2014) and Saili and Mohamed (2021) focused on the effect of decreasing oxygen levels in water on green mussels (*Perna viridis*). In Pasir Gudang Industrial Zone, Mahat et al. (2018) and Zawawi (2019) too focused on biomass, weight, and length of green mussels and flower crabs (*Portunus pelagis*) and related their findings to heavy metal concentration in sediment. Eventually, researchers would link these findings with the extent of environmental damage in the central zone due to the immense anthropogenic volume (Koh et al., 1991; Shahbazi et al., 2010; Maznah et al., 2012; Nordin & Ali, 2013; Maznah et al., 2016; Yap et al., 2019; Kong et al., 2020). Though several taxa, such as green mussels and flower crabs, can be considered good bioindicators for environmental monitoring, it would be more effective if other taxa groups were also considered. A lower percentage of a certain taxa group can otherwise indicate a more impactful message about the effect of environmental alteration and hence should be considered altogether within environmental monitoring studies (Huang et al., 2012; Jennings et al., 2012; Equbal et al., 2017).

As more coastal development is on the rise, namely the Forest City, Pengerang Integrated Complex, and tidal barrage in the Johor River, there are concerns that environmental parameters will be altered permanently, leading to the potential destruction of lifeforms in the seafloor ecosystem (Rahman, 2017; Rezayee et al., 2020). As such, it would be pertinent that the latest yet comprehensive benthic assessment be done in several key locations of the Johor Straits, whereby dominance and differences in taxa could help address the underlying environmental disturbance in the region. The assessment must be done with the ever-increasing anthropogenic affluence in the Strait overall. Henceforth, this study aims to assess macrobenthic communities inhabiting the seafloor of the Johor Straits and identify potential environmental factors that influence the differences in taxonomic composition and dominance of certain benthic groups in some areas.

**METHODOLOGY**

The sampling session was done in April 2021, during the southwest monsoon. Sediment samples were collected in thirteen locations in the Johor Strait (Figure 1), of which two were selected at the west end (J1 and J2), seven at the central zone (J3 to J9, Figure 2), and four at the east end (J10 to J13). Triplicates of sediment were obtained in each sampling location using Ponar Grab with 0.023 m<sup>2</sup> scoop size and distributed for taxa assessment and sediment quality analysis. Sediments subjected to taxa assessment were first filtered through a 0.5-mm sieve and treated with a 10% formalin solution before packaging, while sediment samples subjected to sediment analysis were directly packaged without filtration or formalin treatment. The multiparameter YSI Pro Plus and fluorometer were lowered to seafloor level in each sampling location to record water quality, particularly water depth, temperature, conductivity, salinity, turbidity, dissolved oxygen, and chlorophyll-*a* (fluorometer only).



Figure 1. Sampling locations

Table 1

*Summarized sampling design for benthic assessment in Johor Straits*

Sampling Information	Description
Number of sampling locations	13
Duration of sampling	Two days (20–21 April 2021)
Type of sediment	Marine sediment
Sampling tool	Ponar Grab (0.023 m <sup>2</sup> scoop size)
Number of replicates	1. Benthic assessment: 3 2. Sediment quality assessment: 1 (divided into three replicates prior to analysis)
Sediment Treatment	1. Benthic assessment: 0.5 mm <sup>2</sup> sieve filter, followed by pure formaldehyde solution for preservation 2. Sediment assessment: No treatment

For sediment quality analysis, sediment was dried beforehand before being subjected to organic carbon analysis via the Black-Walkley method (Walkley & Black, 1934) and particle size distribution analysis via the pipette method (Indorante et al., 1990). Sediment and water qualities recorded in all sampling locations were compiled, and the data was transformed before principal component analysis (PCA) could be performed. The PCA test was used to identify which station is attributed to which parameters. Sediments subjected to taxa assessment were preserved with formalin solution and stored in double bags prior to lab analysis. In contrast, sediments subjected to sediment quality analysis were stored immediately without preservation. Water parameters were recorded using YSI multiparameters in each sampling location. In the laboratory, specimens were sorted, and their taxa were identified into genera using appropriate references (Ekman et al., 1945; Smith, 1964; Fauchald, 1977; Cutler, 1994; Rahim & Ross, 2013; Fujita & Irimura, 2015; Baharuddin et al., 2018).

The compiled taxa list for each station was assessed with biotic indices (taxa density,  $D_n$ ; taxa number,  $N$ ; individual number,  $n$ ) and ecological indices (diversity,  $H'$ ; evenness,  $J'$ ; and richness,  $D_{mn}$ ). A two-way PERMANOVA test was conducted to determine significant differences between two or more benthic assemblages within each sampling location based on polychaete dominance and locality. Lastly, a BIOENV test was performed to link a possible correlation between benthic taxa distribution in all stations with recorded sediment and water quality in Johor Straits. Biotic indices, ecological indices, PCA, and PERMANOVA tests were conducted using PAST 4.03 software, while BIOENV correlation analysis was done using PRIMER E-5.

## RESULTS

Both sediment and water quality assessments showed distinct variations. For water quality assessment (Table 2), the highest and lowest depths were recorded on the west side of the

strait, in J1 and J2, respectively. The lowest dissolved oxygen level and turbidity were recorded in J4 to J9 and J1 to J5, respectively. All stations recorded very low chlorophyll-a, except J2, J10, J11, and J12, with J10 having the highest record. For sediment quality assessment (Figure 2), organic carbon analysis indicated that all stations at the central part of the strait recorded organic carbon percentages exceeding 50%, with J9 pertaining to the highest percentage. Stations at the west and east ends of the strait showed a lower percentage of organic carbon except J13, where the station showed a similar percentage as J6 at the central part of the strait. In terms of particle size distribution (Figure 3), the percentage of silt was highest in J1, J3, J6, and J10, while the percentage of sand was highest in J2, J7, J8, J11, J12, and J13. The clay percentage was low throughout the stations. PCA analysis (Figure 4) showed that J2, J10, J11, and J12 were closely attributed to chlorophyll-a, turbidity, and sand particles, while J4, J5, J8, and J9 were closely attributed to temperature and total organic carbon. Lastly, J1 and J10 were attributed to silt particles, depth, water pH, and dissolved oxygen.

Table 2

List of water parameters recorded in every sampling location in Johor Strait. D: Depth (m), T: Temperature (°C), CD: Conductivity; SL: Salinity (ppt); TB: Turbidity (NTU), DO: Dissolved Oxygen (mg/L), pH: Water Acidity and Chl-a: Chlorophyll-a (mg/L)

	D	T	CD	SL	TB	DO	pH	Chl-a
J1	23.60	28.03	55417.00	34.41	14.60	6.71	7.73	0.15
J2	7.40	28.38	55376.00	34.13	119.00	6.30	7.68	3.62
J3	10.00	28.84	52098.00	31.57	168.00	2.97	7.28	0.70
J4	8.00	28.81	50097.00	30.78	107.00	2.63	7.25	0.15
J5	12.00	28.79	51910.00	31.5	11.70	2.85	7.22	0.17
J6	16.00	28.82	52073.00	31.55	11.60	3.05	7.14	0.12
J7	15.00	28.02	52627.00	32.5	104.00	0.99	7.07	0.18
J8	11.00	28.45	52656.00	32.21	104.00	1.20	7.10	0.20
J9	9.00	28.57	52505.00	32.00	13.80	2.19	7.18	0.19
J10	15.00	28.19	53978.00	33.3	120.00	5.61	7.48	7.81
J11	10.50	28.35	54022.00	33.22	121.00	6.11	7.50	2.97
J12	10.00	27.93	54612.00	33.93	140.00	5.90	7.54	3.26
J13	7.70	27.87	54907.00	34.18	113.00	6.35	7.55	0.51

Out of 13 sampling locations, only eight locations recorded the presence of macrobenthic specimens. A total of 730 macrobenthic individuals from 46 known taxa were sorted and identified. The highest specimen count was observed in J4 sediment ( $n = 35$ ), followed by J3 ( $n = 150$ ). Sedentaria polychaetes, particularly from families Capitellidae (*Mediomastus*),

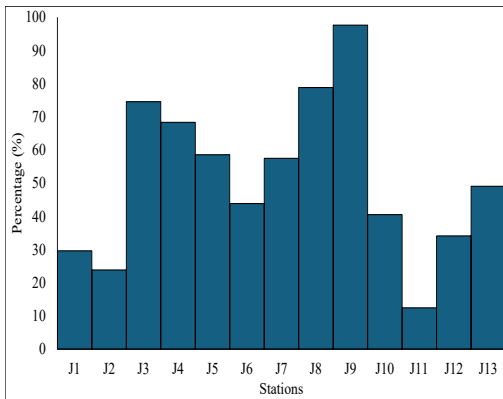


Figure 2. Percentages of organic carbon inside sediments found on the Malaysian side of the Johor Straits

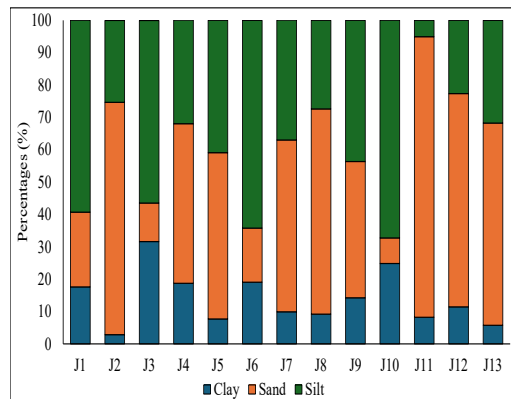


Figure 3. Particle size distribution sediments obtained from all sampling locations in the Johor Straits

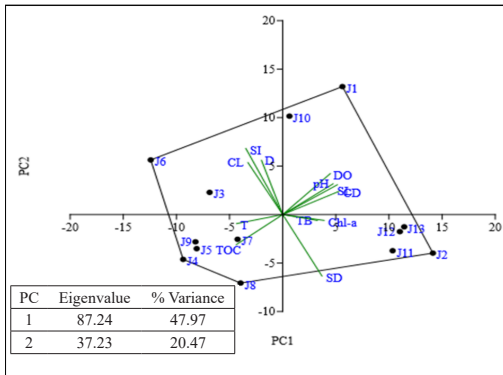


Figure 4. PCA graph on determining the relationship between sampling locations and their related environmental parameters

Cirratulidae (Cirriformia), and Spionidae (*Minuspio* and *Prionospio*), were the highest contributors to the larger abundance in both stations but also observed in other stations such as J1 and J13. Arthropods were highest at the east end of the strait, particularly in J10–J12. Arthropods in this study were mostly peracarids (amphipod, tanaid, mysid). For molluscs, more bivalve individual counts were observed in this study than in gastropods. Gastropods were found only at the westernmost end (J1) and strait’s east (J10 to J13), while a higher

individual count of *Arcualuta* bivalves was found to be extremely abundant in this station. This study’s remaining three phylum groups, brachiopod, echinoderm, and sipunculid, were considered minor phylum groups due to their lower taxa count. For sipunculid, many *Nephasoma* individuals were found in J2 but fewer in J1 and J12, and two individuals of *Themiste* were found only in J1. Echinoderms consisted of one individual of *Holothuria* sea cucumber and six individuals of *Ophiothrix* brittle star, found only in J3, J11, and J12. Lastly, one individual of Brachiopod, namely *Lingula*, was found in sediments from J12.

Overall, J1, J3, and J4 showed higher taxa numbers as well as individual counts than other stations (Table 4). While J1 recorded the highest taxa number ( $N = 17$ ), J4 contained the highest individual counts ( $n = 325$ ). The macrobenthic assemblage from the west end to the central part (J1 to J4) showed increasing taxa and individual counts. However, it

Table 3

Taxa composition of macrobenthos found in all eight sampling locations. Stations J5 to J9 were excluded from the list due to a lack of macrobenthic specimens in the sediment

	J1	J2	J3	J4	J10	J11	J12	J13
<b>Phylum Brachiopoda</b>								
Class Lingulata								
Order Lingulida								
Family Lingulidae								
<i>Lingula</i>	-	-	-	-	-	-	1	-
<b>Phylum Annelida</b>								
Class Polychaeta								
Subclass Errantia								
Order Amphinomida								
Family Amphinomidae								
<i>Eurythoe</i>	-	-	-	1	-	-	-	-
Order Eunicida								
Family Lumbrineridae								
<i>Lumbrineris</i>	1	-	-	-	-	-	-	-
Family Onuphidae								
<i>Diopatra</i>	-	-	1	-	-	-	-	-
Order Phyllodocida								
Family Glyceridae								
<i>Glycera</i>	-	-	1	2	-	2	-	-
Family Goniadidae								
<i>Goniada</i>	1	-	7	3	1	-	-	-
Family Hesionidae								
<i>Leocrates</i>	-	-	5	1	-	-	-	-
<i>Syllidia</i>	-	-	-	-	-	-	1	1
Family Nephtyidae								
<i>Micronephthys</i>	3	-	6	5	4	1	1	1
Family Phyllodocidae								
<i>Phyllodoce</i>	-	-	-	-	-	1	-	2
Family Pilargidae								
<i>Sigambra</i>	3	-	-	-	-	-	-	-
Subclass Sedentaria								
Family Chaetopteridae								
<i>Mesochaetopterus</i>	-	-	-	-	-	1	-	1
Order Canalipalpita								
Family Ampharetidae								
<i>Ampharete</i>	-	1	-	-	-	-	-	-

Table 3 (Continue)

	J1	J2	J3	J4	J10	J11	J12	J13
Family Cirratulidae								
<i>Cirriformia</i>	-	-	12	11	-	-	-	-
Family Sternaspidae								
<i>Sternaspis</i>	3	-	-	-	-	-	-	2
Family Spionidae								
<i>Minuspio</i>	3	-	33	59	-	-	-	-
<i>Prionospio</i>	8	-	69	218	-	-	-	-
Family Pectinariidae								
<i>Pectinaria</i>	-	-	-	1	-	-	-	-
Family Poecilochaetidae								
<i>Poecilochaetus</i>	1	-	-	1	-	-	1	1
Order Scolecida								
Family Capitellidae								
<i>Arenicola</i>	-	3	-	-	-	-	-	-
<i>Mediomastus</i>	18	-	35	23	-	2	3	1
Family Maldanidae								
<i>Euchymene</i>	-	-	-	-	-	-	-	1
Family Paraonidae								
<i>Paraonides</i>	1	-	1	-	-	-	-	-
Family Opheliidae								
<i>Ophelia</i>	-	-	-	-	-	1	-	-
<b>Phylum Arthropoda</b>								
Class Malacostraca								
Subclass Eumalacostraca								
Superorder Eucarida								
Order Decapoda								
Family Diogenidae								
<i>Diogenes</i>	1	-	-	-	-	-	-	-
Superorder Peracarida								
Order Amphipoda								
Family Ampeliscidae								
<i>Byblis</i>	-	1	3	-	-	-	-	-
Family Amphitoidae								
<i>Cymadusa</i>	-	-	1	-	-	-	7	2
Family Caprellidae								
<i>Caprella</i>	-	-	2	-	-	-	-	1
Family Gammaridae								
<i>Gammarus</i>	1	-	-	-	1	4	2	4

Table 3 (Continue)

	J1	J2	J3	J4	J10	J11	J12	J13
Family Leuchotoidae								
<i>Leucothoe</i>	-	-	-	-	1	15	5	5
Family Liljeborgiidae								
<i>Listriella</i>	-	1	-	-	-	-	-	-
Family Maeridae								
<i>Ceradocus</i>	-	-	1	-	-	-	-	-
Order Mysida								
Family Mysidae								
<i>Acanthomysis</i>	2	1	-	-	-	-	-	-
Order Tanaidacea								
Family Tanaididae								
<i>Tanais</i>	2	-	-	-	-	-	-	-
<b>Phylum Echinodermata</b>								
Class Holothuroidea								
Order Aspidochirotida								
Family Cucumariidae								
<i>Holothuria</i>	-	-	1	-	-	-	-	-
Kelas Ophiuroidea								
Order Ophiurida								
Family Amphiuridae								
<i>Ophiothrix</i>	-	-	-	-	-	1	5	-
<b>Phylum Mollusca</b>								
Class Bivalvia								
Subclass Autobranchia								
Order Myida								
Family Corbulidae								
<i>Corbula</i>	-	-	-	-	-	-	-	2
Order Mytilida								
Family Mytilidae								
<i>Modiolous</i>	-	66	-	-	-	-	-	-
Class Gastropoda								
Order Caenogastropoda								
Family Cerithiidae								
<i>Cerithium</i>	-	-	-	-	1	-	-	-
<i>Bittium</i>	1	-	-	-	-	-	-	-
<i>Rhinoclavis</i>	-	-	-	-	-	-	1	-
Family Nassariidae								
<i>Nassarius</i>	-	-	-	-	-	-	2	-

Table 3 (Continue)

	J1	J2	J3	J4	J10	J11	J12	J13
Order Vetigastropoda								
Family Trochidae								
<i>Gibbula</i>	-	-	-	-	-	-	-	1
Kelas Cephalopoda								
Order Octopoda								
Family Octopodidae								
<i>Histoctopus</i>	-	1	-	-	-	-	-	-
<b>Phylum Sipuncula</b>								
Class Sipunculidea								
Order Golfingiida								
Family Golfingiidae								
<i>Nephasoma</i>	1	-	10	-	-	-	1	-
<i>Themiste</i>	2	-	-	-	-	-	-	-



Figure 5. Compilation of taxa specimens found in sampling stations throughout Johor Straits. **Annelid:** (a) *Minuspio*, (b) *Mediomastus*, (c) *Pilargis*; **Mollusk:** (d) *Arcualuta*; (e) *Bittium*; **Brachopoda:** (f) *Lingula*; **Echinoderm:** (g) *Ophiothrix*, (h) *Holothuria*; **Arthropod:** (i) *Diogenes*, (j) *Acanthomysis*, (k) *Gammarus*; **Sipuncula:** (l) *Nephasoma*

abruptly reduced to zero when reaching J5 until J9, located at the central part. On the other hand, macrobenthic assemblages at the east end (J11 to J13) have almost similar taxa and individual counts compared to the east end and central part of the strait. J10 has the fewest taxa and individual numbers of macrobenthos compared to others. In terms of ecological indices, a higher diversity and richness index was seen in macrobenthic assemblages in J1, J12, and J13; a higher evenness index was seen in J10, J11, and J12. Oppositely, J2 showed the lowest diversity index, while J4 showcased the lowest value in the evenness and richness index.

Table 4

Compiled list of biotic and ecological indices in macrobenthic communities throughout the straits. St: Sampling locations; N: Taxa number; n: individual number; De: Taxa density; H': Shannon-Wiener diversity index; J': Pielou's evenness index; D<sub>mn</sub>: Menhinick's richness index

St	N	n	De	H'	J'	D <sub>mn</sub>
J1	7.67 ± 4.51	17.33 ± 10.41	753.62 ± 452.54	1.66 ± 0.79	0.81 ± 0.14	1.90 ± 0.98
J2	3.67 ± 2.08	24.67 ± 24.01	1072.46 ± 1043.78	0.73 ± 0.88	0.67 ± 0.28	1.07 ± 1.04
J3	10.33 ± 1.53	62.67 ± 18.15	2724.64 ± 789.02	1.77 ± 0.06	0.58 ± 0.11	1.31 ± 0.02
J4	7.00 ± 2.00	108.33 ± 53.00	4170.14 ± 2304.48	1.03 ± 0.29	0.41 ± 0.02	0.72 ± 0.30
J10	2.00 ± 1.00	2.67 ± 0.58	115.94 ± 25.10	0.60 ± 0.56	1.00 ± 0.00	1.24 ± 0.60
J11	4.00 ± 1.73	9.33 ± 5.51	405.80 ± 239.46	1.10 ± 0.17	0.81 ± 0.18	1.35 ± 0.30
J12	5.67 ± 0.58	10.00 ± 4.58	192.31 ± 88.13	1.59 ± 0.04	0.87 ± 0.07	1.86 ± 0.27
J13	6.00 ± 3.00	8.33 ± 6.81	160.26 ± 130.90	1.63 ± 0.48	0.94 ± 0.10	2.14 ± 0.37

The two-way PERMANOVA test for polychaete dominance indicated a significant difference between sampling locations but not for localities ( $p < 0.05$ ). However, when paired together (polychaete dominance and locality), a two-way PERMANOVA showed a significant difference between sampling locations ( $p < 0.05$ ). Lastly, BIOENV analysis (Table 4) indicated water pH, chlorophyll-a (Chl-a), silt (Si), and total organic carbon (TOC) parameters as the main environmental parameters that influence macrobenthic taxa distribution throughout sampling locations in Johor Straits ( $r = 0.76, p < 0.05$ ).

Table 5

List of parameters with strongest correlation towards macrobenthic assemblages in Johor Straits ( $p < 0.05$ )

Number of Variables	Correlation value (r)	Parameter
4	0.76	pH, Chl-a, Si, TOC
3	0.76	pH, Chl-a, Si
4	0.71	DO, pH, Chl-a, Si
4	0.71	TB, pH, Chl-a, Si, TOC
5	0.71	CD, pH, Chl-a, Si, TOC

## DISCUSSION

### Relationships Between Environmental Parameters and Macrobenthic Assemblage in the Strait

Results from the PERMANOVA analysis showed significant differences between sampling stations in terms of locality and polychaete dominance. This analysis indicated that such differences occurred due to differences in environmental parameters throughout the strait. BIOENV identified pH level, chlorophyll-*a*, silt, and organic carbon as the main driving factors for macrobenthic distribution across the straits. Organic carbon and silt contents in sediment influence polychaetes, particularly those from Subclass Sedentaria (Cho et al., 2013; Faulwetter et al., 2014). Sedentaria polychaetes are generally smaller-sized and thrive more efficiently within sediment with higher percentages of smaller-sized sediment (Dai et al., 2015; Bolam et al., 2016; Rosli et al., 2018). This group is often associated with bioaccumulation activities (Dai et al., 2015), which heightens the sedimentation rate in the area (Kristensen et al., 2012; Abessa et al., 2019). These were seen in J3 and J4, where both stations showed a higher abundance of Sedentaria polychaetes and consequently recorded a higher percentage of organic carbon and silt in the sediments.

Higher chlorophyll-*a* levels in the column water suggested a larger presence of phytoplankton in the surroundings (Deininger et al., 2017; Asha et al., 2020). Phytoplankton is an important element within the benthic ecosystem as part of the food web (Braeckman et al., 2015; Leoni, 2016). A higher presence of arthropods, particularly peracarids, is common in ecosystems with a higher phytoplankton count (Mercer et al., 2016; Zhao et al., 2019). In this study, chl-*a* record was found higher in sampling locations near Merambong Shoals (J2), Kim River (J10), Belungkor River (J11), and Santi River (J12). These locations were all seagrass biotopes, which such biotopes are commonly known to contain higher nutrient affluent due to intensive photosynthesis and nitrogen cycling activities taking place within seagrass areas (Duarte, 1995; Setiabudi et al., 2016; Asha et al., 2020).

This study also identified water acidity as the main parameter affecting macrobenthic distribution. The optimum pH in a normal benthic ecosystem is 7.50 and above (Hinga, 2002). pH levels above 7.50 are ideal for phytoplankton to perform photosynthesis (Egerton et al., 2014; Scholz, 2014). Conversely, a lower pH value could potentially harm benthic organisms, especially arthropods and molluscs (Rosenberg et al., 1991; Tripole et al., 2008). These negative effects included exoskeleton corrosion within arthropods and molluscs as well as denaturation of certain enzymes inside these macro-benthos, causing these macrobenthos to be unable to perform their life processes normally (Hale et al., 2011). Lower pH in seafloor biotopes strongly relates to the dissolved oxygen parameter. Although dissolved oxygen was not listed as a main parameter in BIOENV analysis, there was a noticeable observation of a higher number of Sedentaria polychaetes, particularly from the families Capitellidae, Cirratulidae, and Spionidae, but otherwise for other benthic

groups inside sediment with a lower oxygen level (Huang et al., 2012; Martinez-Garcia et al., 2013; Bolam et al., 2016). It was seen in J3 and J4, where the macrobenthic community in J3 has a limited number of taxa other than *Sedentaria* polychaetes, while J4 is fully dominated by polychaetes only.

The dissolved oxygen levels in J3 and J4 were lower than other stations and hence identified as hypoxic zones. Meanwhile, sediments from stations J5 to J9 did not contain any macrobenthic taxa in other parts of the central zone. Dissolved oxygen in these stations was even lower than in J3 and J4, with dissolved oxygen in J7 considered the lowest and approaching anoxic level. The absence of even these three polychaete families (Capitellidae, Cirratulidae, and Spionidae) in these locations suggested that even though these groups can live in sediments with lower oxygen levels, there is still a range of acceptable oxygen levels in the sediment required for these groups to live normally. Therefore, this parameter should also be regarded as the most important parameter differentiating sampling locations with macrobenthic communities dominated by polychaetes or otherwise and sampling locations without macrobenthos, as stated in the PERMANOVA analysis result.

### **Overview of Macrobenthic Assemblage Within Johor Strait**

Starting on the west end, J1 and J2 had low organic carbon percentages. Both stations were located within seagrass biotopes, spanning from Piai Cape to Merambong Island (Kassim et al., 2015; Hossain et al., 2019). Macrobenthic communities in J1 were more varied than in J2, comprising more polychaetes than other taxa groups. Taxa found in this study were mostly common on the seafloor with higher depth and turbidity and further off the coast, such as annelids *Lumbrineris* and *Sigambra*, arthropods *Diogenes* and *Tanais* and molluscs *Bittium* (Dong et al., 2018; Shafie et al., 2021; Sivadas et al., 2021). Smaller-sized annelids were found in greater abundance in this region. *Goniada*, *Micronephthys*, *Minuspio*, *Prionospio* and *Mediomastus* polychaetes were commonly known to inhabit sediments with higher percentages of silt and clay in which smaller particles of sediment enabled these taxa to propagate easily (Kristensen et al., 2012; Faulwetter et al., 2014) just as reflected in BIOENV analysis. J2 was surrounded by multiple seagrass biotopes, namely Pulai Estuary, Merambong Shoals and Adang Cape, where seagrass patches are in higher volume.

However, the seagrass patches might be lower than previously recorded by Woo et al. (2014) and Hossain et al. (2019), largely caused by dredged sediments from still ongoing Forest City projects (Rahman, 2017). Molluscs dominated the macrobenthic community in J2. *Arcualuta* mussels were highly abundant there and have previously been recorded in similar abundance at the Pulai River estuary, Merambong Shoals and Adang Cape (Guan, Min et al., 2014; Kassim et al., 2015; Mukhtar et al., 2019; Wong & Sigwart, 2019). This taxon is very common in seagrass meadows, where water depths are lower enough for

seagrass to absorb sunlight in a better position. The mussel's dominance is highly attributed to lower silt and clay particles, higher chlorophyll-*a*, dissolved oxygen and pH in water, as stated in the PCA graph toward Station J2 and BIOENV correlative analysis. The mussels prefer larger sediment particles to safely attach to sediments without sinking into smaller-sized silts and clays (Khongpuang, 2011). The genus is a filter feeder, foraging food particles consisting of marine litter from upwelling to survive. The mussels are generally smaller, lack predators, are able to spawn as many as hundreds of larvae into the waters at once and have a faster growth rate from larva to adult (Otero et al., 2013; Watson et al., 2021).

Favourable sediment and water conditions and suitable physiological aspects enable the mussels to thrive easily in the seagrass area. *Ampharete* and *Arenicola* polychaete *Listriella* amphipod, *Acanthomysis* mysid and *Histoctopus* octopus are common in mangrove and seagrass biotopes and usually higher in ecosystems with lesser anthropogenic influence (Jennings et al., 2012; Reise, 2012; Egerton et al., 2014; Samper-Villareal et al., 2016; Equbal et al., 2017; Bang et al., 2018; Jombodin et al., 2021; Asha et al., 2020; Sordo & Lana, 2020). Lesser polychaetes were noticed in this region, which can be attributed to a lower percentage of organic carbon in the sediment (Cho et al., 2013). Sediments in seagrass biotopes often contain a lower percentage of organic carbon due to continuous absorption by seagrasses in the region (Samper-Villareal et al., 2016).

Annelids are a major phyla group in the central region, particularly in J3 and J4. However, annelids' full domination was seen only in J4. Taxa composition in J3 was similar to that in J1, in which the station recorded the presence of arthropods and sipunculids, albeit in a smaller percentage than annelids. Arthropods (mainly amphipods) and sipunculids are common in estuaries, even with heavy anthropogenic interference, such as the Skudai River. Taxa composition in this area was almost similar to those in the Garaguacu estuary in Brazil (Gusmao et al., 2016), Swarnamukhi in India (Pandey et al., 2021) and the closest one which was Langat estuary in the state of Selangor (Azrina et al., 2006). *Minuspio* and *Prionospio* polychaetes were the most abundant annelids found in this study.

Most taxa individuals were in these two stations, with J4 retaining the highest individual count. While J3 was located near the estuary of the Skudai River, J4 was closer to a massive dredging area. J4's ecosystem was marked with distinct variations of particle size distribution and an even higher organic carbon percentage than other stations, even J3. *Minuspio* and *Prionospio* are both capable of not only surviving in environments with deprived oxygen levels but can even reproduce faster in sediments with higher organic matter (Huang et al., 2012; Cho et al., 2013; Bolam et al., 2016; Dauvin, 2018). These genera are known to be very small in size (<1 mm) and capable of reproducing at a very fast rate (Faulwetter et al., 2014). Spionid polychaetes are deposit feeders and traverse easily between smaller silt particles for both foraging and protection from larger-sized predators such as Errantian polychaetes and decapods (Cho et al., 2013).

Greater availability of silt particles enables the polychaetes to thrive better, along with increasing organic enrichment in sediment due to dredging areas nearby (Dauvin et al., 2017). Decreasing oxygen levels in water renders most benthic taxa unable to inhabit the region, hence allowing these taxa to grow numerically even faster and unhindered. The dominance of Spionid polychaetes in heavily enriched sediments but poorer oxygen levels was highly documented, as seen in Algerian, Andaman and Klang ports (Dauvin et al., 2017; Equbal et al., 2017; Kasihmuddin & Cob, 2021). The three ports' records highlighted very small percentages of Errantian polychaetes and molluscs but higher individual counts of Spionidae polychaetes. Due to the positive growth shown by Spionidae polychaetes toward increasing bioaccumulation and lowering oxygen levels in sediments, these taxa are well-suited to be utilized as bioindicators to assess the extent of organic pollution occurring in seafloor biotopes (Borja & Tunberg, 2011; Kristensen et al., 2012; Cho et al., 2013; Marin et al., 2015; Dauvin, 2018; Jorissen et al., 2018).

Sampling locations from J5 to J9 are all considered dead zones. Similar to J4, both sediments of J5 and J6 originated near the same dredging zone, recorded a higher percentage of organic carbon and lower oxygen levels, but did not contain any macrobenthos. The dredging zone encompassed from J4 to J6 and has previously recorded higher concentrations of harmful algal bloom and heavy metals (Koh et al., 1991; Egerton et al., 2014; Syaizwan et al., 2015; Curren et al., 2019; Yap et al., 2020; Hii et al., 2021). J4 was furthest from the dredging zone but closest to the Skudai River estuary. Due to its proximity to the estuary, water mixing is still possible, and the macrobenthic community could still receive nutrients and oxygen from rivers (Egerton et al., 2014). Hence, J4 can still be considered a safer zone for macrobenthos to thrive due to the area's connection to the river, albeit lower oxygen levels and higher organic carbon may restrict distribution to all but Sedentaria polychaetes in the area (Selck et al., 2011; Villnäs et al., 2012; Faulwetter et al., 2014; Ganesh et al., 2014; Dauvin, 2018), as observed in taxa composition for J4. Stations J5 and J6 were closest to the Causeway, where water current and mixing rate were noticeably lower.

The effect of these intrusions was more obvious in J7, J8 and J9, which were situated on the eastern side of the Causeway. Oxygen levels in this area were very low, with J7 almost reaching an anoxic level (0 mg/L). According to a report by Koh et al. (1991), water quality in the inner Johor Strait has declined ever since the Causeway was opened to the public in 1911. In addition to the Causeway itself, increasing dredging, settlement building, factories, and mariculture activities nearby the Causeway have led to a decrease in water pH and oxygen levels in sediment. Sediment and water quality in this area worsened, as records of faecal matters (Nordin & Ali, 2013), heavy metals (Yap et al., 2019) and hydrocarbon (Shahbazi et al., 2010) were found to be even higher than previously recorded in older environmental reports prepared by Koh et al. (1991) in the 90's. All these inevitably led to an uninhabitable seafloor ecosystem, unsuitable to even Sedentaria polychaetes themselves,

which are supposedly able to adapt even in seafloor ecosystems with extremely lower percentages of oxygen levels (Dauvin et al., 2017).

At the east end, the last four stations (J10-J13) showed varied sediment and water quality records and consequently varied macrobenthic composition. J10 has the lowest depth but retained the highest chlorophyll-*a* and organic carbon percentage, yet retained the lowest macrobenthic specimen yield in this study. This station's sediment was obtained near Kim River's estuary, where the notoriously abundant number of factories around it had been associated with water pollution cases that led to local populaces' toxic poisoning (Kamaruzzaman et al., 2010; Yap et al., 2019; Kong et al., 2020). The constant release of toxic materials from inland may cause the area unsuitable for macrobenthos to thrive despite higher chlorophyll-*a* and organic carbon in water and sediment, respectively. J11 and J12 were located near the Belungkor and Santi River estuaries. Seagrass meadow coverage was present in both locations but lower (Amri et al., 2005; Wan-Lotfi et al., 2013; Hossain et al., 2019).

Amphipods, namely *Cymadusa*, *Gammarus*, and *Leucothoe*, were found highly abundant here, similar to previous findings by Wan-Lotfi et al. (2013) in regions with higher seagrass patches. However, the study was done only in the Santi River estuary. Amphipods are common in river estuaries, especially with higher chlorophyll-*a* and small-sized sediment particles (White, 2015; Podlensinska & Drabowska, 2019; Shafie et al., 2021). Lower organic carbon percentages in both stations made these locations suitable for echinoderms (*Ophiothrix*) and brachiopods (*Lingula*). Lesser anthropogenic activities, coupled with higher chlorophyll-*a* in water and lower organic carbon in sediment, allow many phyla groups to thrive in these areas more easily than in the central region. J13's sediment was obtained off Pengelih Cape, Johor. It was also located close to a reclamation site off Pengerang Cape. The reclamation is still underway, intending to construct a petroleum processing plant (Brelsford, 2016). Sediment samples from this location retained a higher percentage of organic carbon, similar to those in J3 and J4, reflecting the extent of dredging activities in the area.

However, varied macrobenthic phyla taxa can still be found inside sediment samples. Amphipods were found highly abundant in this station, but so were Sedentaria polychaetes, such as *Euchymene* and *Poecilochaetus*, which are more common in less disturbed seafloor ecosystems (Idris & Arshad, 2013; Magalhães & Bailey-Brock, 2014). Dissolved oxygen was still high in this location despite the higher percentage of organic carbon and silt particles. The presence of amphipods and Sedentaria polychaetes other than Capitellidae, Cirratulidae, and Spionidae indicated that J13 are still habitable to macrobenthos despite increasing reclamation activities that led to increasing organic carbon and smaller-sized sediment particles in the area. However, as the reclamation project is still ongoing, there is a possibility that the accumulation of organic carbon and silt in the sediment may cause

a lowering of water pH and oxygen level, and this could cause the area to end up with the same fate as in J4, where the area becomes unsuitable for most macrobenthic groups but Sedentaria polychaetes to thrive, or even worse, the oxygen level went so low that not even Sedentaria polychaetes can live in the sediment. Therefore, long-term surveillance must be done in the area to assess the extent of damage wrought by Pengerang development towards the macrobenthic community on the seafloor.

## CONCLUSION

Unlike previous studies, this study covers the larger scope of the area, focusing on the east, central and west sides of the strait, taking into account localities as major driving forces besides environmental factors behind the distribution of macrobenthos in Johor Straits overall. Macrobenthos was found in most locations in the strait and considerably varied thanks to spatial variations of environmental parameters. PCA and BIOENV analyses both revealed higher water acidity, oxygen level, and chlorophyll-*a* were driving factors for myriads of macrobenthos, especially amphipods, bivalves (particularly Asian Date Mussels), and Errantian polychaetes, in the west and east side of the strait, where anthropogenic traffic was noticeably lower compared to the central region. In the central region, however, major urban areas and the Causeway, Capitellid, Cirratulid, and Spionid polychaetes dominated the seafloor habitat, especially in areas close to dredging zones. Higher levels of organic carbon and silt sediment particles but lower oxygen levels at the central region render the ecosystem unsuitable for all but these three taxa. These polychaete's dominance, however, does not guarantee continuous survival in the region should the oxygen level in water decrease further, as they are too unable to thrive in extremely low oxygen levels in waters, as observed in sediments from other parts of the central region. These polychaetes' resilience in ecologically stressed ecosystems showcased their suitability as bioindicator species to assess the extent of environmental disturbance in any given marine ecosystem, especially in coastal areas and ports, where the level of anthropogenic activities is higher.

This study reached two concerning conclusions about the marine ecosystems in Johor Straits. The dominance of three Sedentarian polychaetes in the Central Zone implies that the anthropogenic activities in the region have gone too far. Increasing land reclamation, uncontrolled domestic release to the sea, and the effectiveness of the Causeway as a geographical barrier that permanently altered the water current since the 1990s may have led to total environmental destruction in the area, hence making the seafloor inhabitable to most lifeforms except Capitellid, Cirratulid, and Spionid polychaetes. The diversity of macrobenthic communities on the west and east ends may not last long due to multiple land projects underway nearby. The enlargement of Forest City, the construction of a tidal barrage off the Johor River, the enlargement of ports off Belungkor Cape, and the

development of the Pengerang Integrated Complex could potentially transform the current seafloor ecosystem at the west and east ends into those of the central region. Thus, it is imperative that proper planning be made to prevent the destruction of marine habitats or at least mitigate the extent of degradation in the area. This study showed the effectiveness of utilizing macrobenthos to address key environmental issues in marine environments. It could be a useful reference for future benthic studies in the Johor Straits or Malaysian waters.

## ACKNOWLEDGMENT

The authors acknowledge the Department of Chemistry, Universiti Kebangsaan Malaysia (UKM) for water and sediment parameter analysis.

## REFERENCES

- Abessa, D. M. S., Rachid, B. R. F., Zaroni, L. P., Gasparro, M. R., Pinto, Y. A., Bicego, M. C., Hortellan, M. A., Sarkis, J. E. S., Muniz, P., Moreira, L. B., & Sousa, E. C. P. M. (2019). Natural factors and chemical contamination control the structure of macrobenthic communities in the Santos Estuarine System (SP, Brazil). *Community Ecology*, 20(2), 121–137. <https://doi.org/10.1556/168.2019.20.2.3>
- Amri, A. Y., Ooi, L. S. J., Phang, S. M., Azhar, H. H., Rahman, R. F., & Rosmadi, F. (2005). *Dugongs in Peril: The Conservation and Protection of Dugongs in Johor, Malaysia*. Universiti Malaya Maritime Research Centre.
- Asha, P. S., Diwakar, K., Sivanesh, H., Mini, K. G., & Kripa, V. (2020). Physicochemical characteristics and benthic faunal constituents of a few seagrass and mangrove habitats of Tuticorin coast, gulf of Mannar. *Journal of the Marine Biological Association of India*, 62(2), 31–39. <https://doi.org/10.6024/jmbai.2020.62.2.2130-04>
- Azelee, I. W., Ismail, R., Ali, R., & Bakar, W. A. W. A. (2014). Chelation technique for the removal of heavy metals (As, Pb, Cd and Ni) from green mussel, *Perna viridis*. *Indian Journal of Marine Sciences*, 43(3), 372–376.
- Azrina, M. Z., Yap, C. K., Ismail, A. R., Ismail, A., & Tan, S. G. (2006). Anthropogenic impacts on the distribution and biodiversity of benthic macroinvertebrates and water quality of the Langat River, Peninsular Malaysia. *Ecotoxicology and Environmental Safety*, 64(3), 337–347. <https://doi.org/10.1016/j.ecoenv.2005.04.003>
- Baharuddin, N., Basri, N. B., & Syawal, N. H. (2018). Marine gastropods (Gastropoda; Mollusca) diversity and distribution on intertidal rocky shores of Terengganu, Peninsular Malaysia. *Aquaculture, Aquarium, Conservation & Legislation*, 11(4), 1144–1154.
- Bang, C., Dagan, T., Deines, P., Dubilier, N., Duschl, W. J., Fraune, S., Hentschel, U., Hirt, H., Hülter, N., Lachnit, T., Picazo, D., Pita, L., Pogoreutz, C., Rädcker, N., Saad, M. M., Schmitz, R. A., Schulenburg, H., Voelstra, C. R., Weiland-Bräuer, N., & Bosch, T. C. G. (2018). Metaorganisms in extreme environments: Do microbes play a role in organismal adaptation? *Zoology*, 127, 1–19. <https://doi.org/10.1016/j.zool.2018.02.004>
- Bolam, S. G., McIlwaine, P. S. O., & Garcia, C. (2016). Application of biological traits to further our understanding of the impacts of dredged material disposal on benthic assemblages. *Marine Pollution Bulletin*, 105(1), 180–192. <https://doi.org/10.1016/j.marpolbul.2016.02.031>

- Borja, A., & Tunberg, B. G. (2011). Assessing benthic health in stressed subtropical estuaries, Eastern Florida, USA using AMBI and M-AMBI. *Ecological Indicators*, *11*(2), 295–303. <https://doi.org/10.1016/j.ecolind.2010.05.007>
- Braeckman, U., Provoost, P., Sabbe, K., Soetaert, K., Middelburg, J. J., Vincx, M., & Vanaverbeke, J. (2015). Temporal dynamics in a shallow coastal benthic food web: Insights from fatty acid biomarkers and their stable isotopes. *Marine Environmental Research*, *108*, 55–68. <https://doi.org/10.1016/j.marenvres.2015.04.010>
- Brelsford, R. (2016). *Petronas lets Contracts for Pengerang Complex*. Oil & Gas Journal. <https://www.ogj.com/refining-processing/article/17250167/petronas-lets-contracts-for-pengerang-complex>
- Castro, P., & Huber, M. (2019). *Marine Biology* (11th ed.). Mc-Graw Hill.
- Cho, Y. S., Lee, W. C., Kim, J. B., Hong, S. J., Kim, H. C., & Kim, C. S. (2013). Establishment of environmental assessment using sediment total organic carbon and macrobenthic polychaete community in shellfish farms. *Journal of the Korean Society of Marine Environment and Safety*, *19*(5), 430–438. <https://doi.org/10.7837/kosomes.2013.19.5.430>
- Curren, E., Yoshida, T., Kuwahara, V. S., & Leong, S. C. Y. (2019). Rapid profiling of tropical marine cyanobacterial communities. *Regional Studies in Marine Science*, *25*, Article 100485. <https://doi.org/10.1016/j.rsma.2018.100485>
- Cutler, E. B. (1994). *The sipuncula: Their systematics, biology and evolution*. Comstock Publishing Associates.
- Dai, L., Banta, G. T., Selck, H., & Forbes, V. E. (2015). Influence of copper oxide nanoparticle form and shape on toxicity and bioaccumulation in the deposit feeder, *Capitella teleta*. *Marine Environmental Research*, *111*, 99–106. <https://doi.org/10.1016/j.marenvres.2015.06.010>
- Dauvin, J. C. (2018). Twenty years of application of Polychaete/Amphipod ratios to assess diverse human pressures in estuarine and coastal marine environments: A review. *Ecological Indicators*, *95*, 427–435. <https://doi.org/10.1016/j.ecolind.2018.07.049>
- Dauvin, J. C., Bakalem, A., Baffreau, A., & Grimes, S. (2017). Benthic ecological status of algerian harbours. *Marine Pollution Bulletin*, *125*(1–2), 378–388. <https://doi.org/10.1016/j.marpolbul.2017.09.049>
- Deininger, A., Faithfull, C. L., Karlsson, J., Klaus, M., & Bergström, A. K. (2017). Pelagic food web response to whole lake N fertilization. *Limnology and Oceanography*, *62*(4), 1498–1511. <https://doi.org/10.1002/lno.10513>
- Dong, Y., Liao, M., Meng, X., & Somero, G. N. (2018). Structural flexibility and protein adaptation to temperature: Molecular dynamics analysis of malate dehydrogenases of marine molluscs. *Proceedings of the National Academy of Sciences*, *115*(6), 1274–1279. <https://doi.org/10.1073/pnas.1718910115>
- Duarte, C. M. (1995). Submerged aquatic vegetation in relation to different nutrient regimes. *Ophelia*, *41*(1), 87–112. <https://doi.org/10.1080/00785236.1995.10422039>
- Egerton, T., Morse, R., Marshall, H., & Mulholland, M. (2014). Emergence of algal blooms: The effects of short-term variability in water quality on phytoplankton abundance, diversity, and community composition in a Tidal Estuary. *Microorganisms*, *2*(1), 33–57. <https://doi.org/10.3390/microorganisms2010033>
- Ekman, V. W., Sverdrup, H. U., Johnson, M. W., & Fleming, R. H. (1945). The oceans, their physics, chemistry and general biology. *Geografiska Annaler*, *27*, Article 388. <https://doi.org/10.2307/520072>

- Eqbal, J., Thiruchitrambalam, G., Lakra, R. K., Savurirajan, M., & Satyam, K. (2017). Assessing the ecological quality of the Port Blair coast (South Andaman, India) using different suites of benthic biotic indices. *Journal of the Marine Biological Association of the United Kingdom*, 97(5), 1007–1021. <https://doi.org/10.1017/s0025315417000753>
- Fauchald, K. (1977). *The polychaete worms: Definitions and keys to the orders, families and genera*. Natural History Museum of Los Angeles County.
- Faulwetter, S., Markantonatou, V., Pavlouidi, C., Papageorgiou, N., Keklikoglou, K., Chatzinikolaou, E., Pafilis, E., Chatzigeorgiou, G., Vasileiadou, K., Dailianis, T., Fanini, L., Koulouri, P., & Arvanitidis, C. (2014). Polytraits: A database on biological traits of marine polychaetes. *Biodiversity Data Journal*, 2, Article e1024. <https://doi.org/10.3897/bdj.2.e1024>
- Fujita, T., & Irimura, S. (2015). Preliminary list of ophiuroids (Echinodermata: Ophiuroidea) collected from the Johor Straits, Singapore. *Raffles Bulletin of Zoology*, 31, 264–272.
- Ganesh, T., Rakesh, M., Raman, A. V., Nanduri, S., Moore, S., & Rajanna, B. (2014). Macrobenthos response to sewage pollution in a tropical inshore area. *Environmental Monitoring and Assessment*, 186(6), 3553–3566. <https://doi.org/10.1007/s10661-014-3638-4>
- Gholizadeh, M. (2015). *Macrobenthic community and its relations with environmental factors in coastal waters of Penang*. [Doctoral dissertation]. USM Publication.
- Guan, W. S., Ghaffar, M. A., Ali, M. M., & Cob, Z. C. (2014). The Polychaeta (Annelida) communities of the Merambong and Tanjung Adang Shoals, Malaysia, and its relationship with the environmental variables. *Malayan Nature Journal*, 66(1&2), 146-158.
- Guan, W. S., Min, L. D., Ghaffar, M. A., Ali, M. M., & Cob, Z. C. (2014). Macrobenthos composition, distribution and abundance within Sungai Pulai estuary, Johor, Malaysia. In *AIP Conference Proceedings* (Vol. 1614, No. 1, pp. 591-596). American Institute of Physics. <https://doi.org/10.1063/1.4895269>
- Gusmao, J. B., Brauko, K. M., Eriksson, B. K., & Lana, P. C. (2016). Functional diversity of macrobenthic assemblages decreases in response to sewage discharges. *Ecological Indicators*, 66, 65–75. <https://doi.org/10.1016/j.ecolind.2016.01.003>
- Hale, R., Calosi, P., McNeill, L., Mieszkowska, N., & Widdicombe, S. (2011). Predicted levels of future ocean acidification and temperature rise could alter community structure and biodiversity in marine benthic communities. *Oikos*, 120(5), 661–674. <https://doi.org/10.1111/j.1600-0706.2010.19469.x>
- Harah, M., Sidik, J., Hazma, W., & Nordiah, B. (2014). Seaweed community of the Merambong Shoal, Sungai Pulai estuary, Johore. *Malayan Nature Journal*, 66(1&2), 132–148.
- Hii, K. S., Mohd-Din, M., Luo, Z., Tan, S. N., Lim, Z. F., Lee, L. K., Leong, S. C. Y., Teng, S. T., Gu, H., Cao, X., Lim, P. T., & Leaw, C. P. (2021). Diverse harmful microalgal community assemblages in the Johor Strait and the environmental effects on its community dynamics. *Harmful Algae*, 107, Article 102077. <https://doi.org/10.1016/j.hal.2021.102077>
- Hinga, K. (2002). Effects of pH on coastal marine phytoplankton. *Marine Ecology Progress Series*, 238, 281–300. <https://doi.org/10.3354/meps238281>
- Hossain, M. S., Hashim, M., Bujang, J. S., Zakaria, M. H., & Muslim, A. M. (2019). Assessment of the impact of coastal reclamation activities on seagrass meadows in Sungai Pulai Estuary, Malaysia, using landsat data (1994–2017). *International Journal of Remote Sensing*, 40(9), 3571–3605. <https://doi.org/10.1080/01431161.2018.1547931>

- Huang, Y. C. A., Huang, S. C., Hsieh, H. J., Meng, P. J., & Chen, C. A. (2012). Changes in sedimentation, sediment characteristics, and benthic macrofaunal assemblages around marine cage culture under seasonal monsoon scales in a shallow-water bay in Taiwan. *Journal of Experimental Marine Biology and Ecology*, 422–423, 55–63. <https://doi.org/10.1016/j.jembe.2012.04.008>
- Idris, I., & Arshad, A. (2013). Checklist of polychaetous annelids in Malaysia with redescription of two commercially exploited species. *Asian Journal of Animal and Veterinary Advances*, 8(3), 409–436. <https://doi.org/10.3923/ajava.2013.409.436>
- Indorante, S. J., Follmer, L. R., Hammer, R. D., & Koenig, P. G. (1990). Particle-size analysis by a modified pipette procedure. *Soil Science Society America*, 54(10), 560–563. <https://doi.org/10.2136/sssaj1990.03615995005400020047x>
- Jennings, D. E., DiBattista, J. D., Stump, K. L., Hussey, N. E., Franks, B. R., Grubbs, R. D., & Gruber, S. H. (2012). Assessment of the aquatic biodiversity of a threatened coastal lagoon at Bimini, Bahamas. *Journal of Coastal Conservation*, 16(3), 405–428. <https://doi.org/10.1007/s11852-012-0211-6>
- Jombodin, T., Songkai, P., Wichachucherd, B., & Rodcharoen, E. (2021). The relationship between salinity and benthic fauna diversity and abundance at Songkhla Port, Thailand. *Journal of Coastal Research*, 37(6), 1173–1180. <https://doi.org/10.2112/jcoastres-d-21-00037.1>
- Jorissen, F., Nardelli, M. P., Almogi-Labin, A., Barras, C., Bergamin, L., Bicchi, E., El Kateb, A., Ferraro, L., McGann, M., Morigi, C., Romano, E., Sabbatini, A., Schweizer, M., & Spezzaferri, S. (2018). Developing foram-AMBI for biomonitoring in the Mediterranean: Species assignments to ecological categories. *Marine Micropaleontology*, 140, 33–45. <https://doi.org/10.1016/j.marmicro.2017.12.006>
- Kamaruzzaman, B. Y., Sitiwaznah, A., Shahbudin, S., Jalal, K. C. A., & Ong, M. C. (2010). The temporal variation of organic carbon during the pre-monsoon and post-monsoon seasons in Pahang River-Estuary, Pahang, Malaysia. *Oriental Journal of Chemistry*, 26(4), 1309–1313.
- Kasihmuddin, M. S., & Cob, Z. C. (2021). Distribution of benthic macroinvertebrates in seafloor northward of Pulau Indah, Klang. *Pertanika Journal of Science and Technology*, 29(1), 641–662. <https://doi.org/10.47836/pjst.29.1.34>
- Kassim, Z., Yunus, K., Jalal, K. C. A., Jaafar, I. N., Nordin, N. S., Ahmad, W. M. A. W., Ismail, A., & John, A. B. (2015). Spatial distribution trend of plankton in Sungai Pulai Estuary, the straits of Johor, Malaysia. *Sains Malaysiana*, 44(9), 1257–1262. <https://doi.org/10.17576/jsm-2015-4409-06>
- Khongpuang, S. (2011). *Spatial modelling for optimisation of bivalve culture: A case study for Green Mussel (Perna viridis) and Blood Cockle (Anadara granosa) culture in Pattani Bay, Thailand* [PhD thesis]. University of Stirling, United Kingdom. <https://www.proquest.com/docview/2239331770?pq-origsite=gscholar&fromopenview=true&sourcetype=Dissertations%20&%20Theses>
- Koh, H. L., Lim, P. E., & Midun, Z. (1991). Management and control of pollution in Inner Johore Strait. *Environmental Monitoring and Assessment*, 19(1–3), 349–359. <https://doi.org/10.1007/bf00401324>
- Kong, C. Y., Rosimah, N., Sharifinia, M., Peng, T. S. H., Yap, C. W., Hideo, O., Saupi, I. M., & Saleem, M. (2020). Higher bioavailability and contamination of copper in the Eastern Part of Johore Causeway: Will the pattern remain the same beyond 2020? *Journal of Biomedical Research & Environmental Sciences*, 1(4), 114–121.
- Kristensen, E., Penha-Lopes, G., Delefosse, M., Valdemarsen, T., Quintana, C., & Banta, G. (2012). What is bioturbation? The need for a precise definition for fauna in aquatic sciences. *Marine Ecology Progress Series*, 446, 285–302. <https://doi.org/10.3354/meps09506>

- Leoni, B. (2016). Zooplankton predators and prey: Body size and stable isotope to investigate the pelagic food web in a deep lake (Lake Iseo, Northern Italy). *Journal of Limnology*, 76(1), 85–93. <https://doi.org/10.4081/jlimnol.2016.1490>
- Magalhães, W. F., & Bailey-Brock, J. H. (2014). Polychaete assemblages associated with the invasive green alga *Avrainvillea amadelpha* and surrounding bare sediment patches in Hawaii. *Memoirs of Museum Victoria*, 71, 161–168. <https://doi.org/10.24199/j.mmv.2014.71.13>
- Mahadi, M., S. Sazlina, Aileen, T. S. H., & Zulfigar, Y. (2014). Benthic harpacticoid copepod assemblages in Merambong shoal, Johor. *Malayan Nature Journal*, 66(1&2), 14–53.
- Mahat, N. A., Mukhtar, N. K., Ismail, R., Razak, F. I. A., Wahab, R. A., & Keyon, A. S. A. (2018). Toxic metals in *Perna viridis* mussel and surface seawater in Pasir Gudang coastal area, Malaysia, and its health implications. *Environmental Science and Pollution Research*, 25(30), 30224–30235. <https://doi.org/10.1007/s11356-018-3033-8>
- Marin, A., Lloret, J., Velasco, J., Bello, C., Lillebø, A.I., Sousa, A.I., Soares, A.M.V.M., Tuchkovenko, Y., Warzocha, Z., Kornijow, R., Gormiscz, S., Drgas, A., Szymanek, L., & Margonski, P. (2015). Lagoons response using key bio-indicators and implications on ecological status (WFD). In: Lillebø, A. I., Stålnacke, P. & Gooch, G. D. (Eds.), *Coastal Lagoons in Europe* (p 167-178). IWA Publishing. <https://doi.org/10.2166/9781780406299>
- Martinez-Garcia, E., Sanchez-Jerez, P., Aguado-Giménez, F., Ávila, P., Guerrero, A., Sánchez-Lizaso, J. L., Fernandez-Gonzalez, V., González, N., Gairin, J. I., Carballeira, C., García-García, B., Carreras, J., Macías, J. C., Carballeira, A., & Collado, C. (2013). A meta-analysis approach to the effects of fish farming on soft-bottom polychaeta assemblages in temperate regions. *Marine Pollution Bulletin*, 69(1–2), 165–171. <https://doi.org/10.1016/j.marpolbul.2013.01.032>
- Maznah, I., Noor Baharim, H., & Ziba, K. (2012). Influence of river flow on oxygen depletion in inner Johor Straits. In J. M. Hidyat (Ed.), *International Conference on Water Resources* (pp. 1-11). Faculty of Civil Engineering Water Research Alliance and Department Irrigation and Drainage.
- Maznah, I., Noor Baharim, H., & Ziba, K. (2016). Estimating dissolved oxygen depletion in inner Western Johor Strait, Malaysia using a three dimensional water quality model. *Malaysian Journal of Civil Engineering*, 251(3). 240–251. <https://doi.org/10.11113/mjce.v28.16011>
- Mercer, N., Kaller, M. D., & Stout, M. J. (2016). Diversity of arthropods in farmed wetlands in the gulf of Mexico coastal plain and effects of detrital subsidies. *Journal of Freshwater Ecology*, 32(1), 163–178. <https://doi.org/10.1080/02705060.2016.1253623>
- Mukhtar, A., Mohamat-Yusuff, F., Zulkifli, S., Harino, H., Ismail, A., & Inoue, K. (2019). Concentration of organotin and booster biocides in sediments of seagrass area from Sungai Pulai Estuary, South of Johor, Malaysia. *Environments*, 6(2), Article 26. <https://doi.org/10.3390/environments6020026>
- Nordin, N., & Ali, M. M. (2013). Distribution of fecal sterols in surface sediment of Sungai Tebrau, Johor. *AIP Conference Proceedings*, 1571(2013). 460–465. <https://doi.org/10.1063/1.4858698>
- Otero, M., Cebrian, E., Francour, P., Galil, B., & Savini, D. (2013). *Monitoring marine invasive species in Mediterranean marine protected areas (MPAs): A strategy and practical guide for managers*. IUCN Centre for Mediterranean Cooperation.
- Pandey, V., Venkatnarayanan, S., Kumar, P. S., Ratnam, K., Jha, D. K., Rajaguru, S., & Dharani, G. (2021). Assessment of ecological health of Swarnamukhi River Estuary, Southeast coast of India, through AMBI indices and multivariate tools. *Marine Pollution Bulletin*, 164, Article 112031. <https://doi.org/10.1016/j.marpolbul.2021.112031>

- Podlesińska, W., & Dąbrowska, H. (2019). Amphipods in estuarine and marine quality assessment: A review. *Oceanologia*, *61*(2), 179–196. <https://doi.org/10.1016/j.oceano.2018.09.002>
- Rahim, A. A., & Ross, O. (2013). Shallow water marine *Gammaridean amphipods* of Pulau Tioman, Malaysia, with the description of a new species. *ZooKeys*, *335*, 1–31. <https://doi.org/10.3897/zookeys.335.5567>
- Rahman, S. (2017). *The Socio-Cultural Impact of Forest City*. ISEAS Yusof Ishak Institute.
- Reise, K. (2012). *Tidal flat ecology: An experimental approach to species interactions*. Springer-Verlag.
- Rezayee, M., Ling, G. H. T., Ibrahim, R., & Sadat, W. (2020). Inclusive regional development: A case study of Pengerang Region in Johor Malaysia. *International Journal of Academic Research in Business and Social Sciences*, *10*(6), 329–345. <https://doi.org/10.6007/ijarbss/v10-i6/7290>
- Rosenberg, R., Hellman, B., & Johansson, B. (1991). Hypoxic tolerance of marine benthic fauna. *Marine Ecology Progress Series*, *79*, 127–131. <https://doi.org/10.3354/meps079127>
- Rosli, N. R., Yahya, N., Idris, I., & Bachok, Z. (2018). Polychaetous annelid community structure in relation to soft bottom sediment characteristics in continental shelf of the Southern South China Sea. *Journal of Sustainability Science and Management*, *10*(1), 37–45.
- Saili, N. A. B., & Mohamed, C. A. R. (2021). Natural radioactivity of <sup>210</sup>Pb in mussels at the semi-enclosed water of the Johor Strait, Malaysia through statistical approach. *Malaysian Journal of Analytical Sciences*, *25*(1), 166–183.
- Samper-Villarreal, J., Lovelock, C. E., Saunders, M. I., Roelfsema, C., & Mumby, P. J. (2016). Organic carbon in seagrass sediments is influenced by seagrass canopy complexity, turbidity, wave height, and water depth. *Limnology and Oceanography*, *61*(3), 938–952. <https://doi.org/10.1002/lno.10262>
- Sany, S. B. T., Hashim, R., Salleh, A., Rezayi, M., & Safari, O. (2015). Ecological quality assessment based on macrobenthic assemblages indices along West Port, Malaysia Coast. *Environmental Earth Sciences*, *74*(2), 1331–1341. <https://doi.org/10.1007/s12665-015-4122-3>
- Scholz, B. (2014). Effects of varying pH on the growth and physiology of five marine microphytobenthic diatoms isolated from the Solthörn Tidal Flat (Southern North Sea, Germany). *Phycologia*, *53*(3), 252–264. <https://doi.org/10.2216/13-240.1>
- Selck, H., Drouillard, K., Eisenreich, K., Koelmans, A. A., Palmqvist, A., Ruus, A., Salvito, D., Schultz, I., Stewart, R., Weisbrod, A., van den Brink, N. W., & van den Heuvel-Greve, M. (2011). Explaining differences between bioaccumulation measurements in laboratory and field data through use of a probabilistic modeling approach. *Integrated Environmental Assessment and Management*, *8*(1), 42–63. <https://doi.org/10.1002/ieam.217>
- Setiabudi, G. I., Bengen, D. G., Effendi, H., & Radjasa, O. K. (2016). The community structure of phytoplankton in seagrass ecosystem and its relationship with environmental characteristics. *Biosaintifika: Journal of Biology & Biology Education*, *8*(3), Article 257. <https://doi.org/10.15294/biosaintifika.v8i3.6549>
- Shafie, B. B., Man, A., Ali, N. F., & Rahim, A. A. (2021). Macrobenthos diversity along the exclusive economic zone of east coast peninsular Malaysia. *Journal of Environmental Biology*, *42*(3), 817–823. [https://doi.org/10.22438/jeb/42/3\(si\)/jeb-13](https://doi.org/10.22438/jeb/42/3(si)/jeb-13)
- Shahbazi, A., Zakaria, M. P., Yap, C. K., Tan, S. G., Surif, S., Mohamed, C. A. R., Sakari, M., Bakhtiari, A. R., Bahry, P. S., Chandru, K., & Mirsadeghi, S. A. (2010). Use of different tissues of *Perna viridis* as biomonitors of polycyclic aromatic hydrocarbons (PAHs) in the coastal waters of peninsular Malaysia. *Environmental Forensics*, *11*(3), 248–263. <https://doi.org/10.1080/15275920903558513>

- Sivadas, S. K., Gupta, G. V. M., Kumar, S., & Ingole, B. S. (2021). Trait-based and taxonomic macrofauna community patterns in the upwelling ecosystem of the Southeastern Arabian Sea. *Marine Environmental Research*, 170, Article 105431. <https://doi.org/10.1016/j.marenvres.2021.105431>
- Smith, R. I. (1964). *Keys to marine invertebrates of the Woods Hole Region: A manual for the identification of the more common marine invertebrates*. Marine Biological Laboratory.
- Sordo, L., & Lana, P. (2020). Temporal variations of *Halodule wrightii* meadows and associated fauna near their southern distribution limit in the Southwestern Atlantic. *Botanica Marina*, 63(3), 215–228. <https://doi.org/10.1515/bot-2018-0106>.
- Syaizwan, Z., Ferdaus, M. Y., Ahmad, I., & Asnor, A. S. (2015). Status of heavy metals in surface sediments of the western part of the johor straits using a sediment quality guideline. *World Journal of Fish and Marine Sciences*, 7(3), 214–220.
- Tripole, S., Vallania, E. A., & del Carmen Corigliano, M. (2008). Benthic macroinvertebrate tolerance to water acidity in the grande river sub-basin (San Luis, Argentina). *Limnetica*, 27(1), 11–28.
- Villnäs, A., Norkko, J., Lukkari, K., Hewitt, J., & Norkko, A. (2012). Consequences of increasing hypoxic disturbance on benthic communities and ecosystem functioning. *PLoS ONE*, 7(10), Article e44920. <https://doi.org/10.1371/journal.pone.0044920>.
- Walkley, A., & Black, I. A. (1934). An examination of the Degtjareff Method for determining soil organic matter, and a proposed modification of the chromic acid titration method. *Soil Science*, 37(1), 29–38. <https://doi.org/10.1097/00010694-193401000-00003>
- Wan-Lotfi, W. M., Mazlan, A. G., Ramlan, O., Zaidi, C. C., & Abdullah, S. (2013). Spatial distribution pattern of macrobenthos in East Johor Straits. In M. C. A. Rahim, K. S. Fathul, M. A. Masni, & A. Norhayati (Eds.), *Malaysia Marine Ecosystem: The Studies of Johor Darul Takzim East Coast* (pp. 23–30). Faculty of Science and Technology, National University of Malaysia.
- Watson, G. J., Dyos, J., Barfield, P., Stebbing, P., & Dey, K. G. (2021). Evidence for self-sustaining populations of *Arcuatula senhousia* in the UK and a review of this species' potential impacts within Europe. *Scientific Reports*, 11(1), Article 9678.
- White, K. N. (2015). A checklist of *Amphipoda* (Crustacea) collected from the mudflats of Pulau Ubin, Singapore. *Raffles Bulletin of Zoology*, 31, 139–142.
- Wong, N. L. W. S., & Sigwart, J. D. (2019). Natural history clues to the evolution of bivalved gastropods (Mollusca: Gastropoda: Sacoglossa: Juliidae). *Marine Biodiversity*, 49(4), 1997–2007. <https://doi.org/10.1007/s12526-019-00960-0>
- Woo, S. P., Teh, C. P., Norhanis, M. R., Nithiyaa, N., Amelia-Ng, P. F., Zulfigar, Y., & Tan, S. H. (2014). Sea cucumber species of the merambong shoal with notes on the distribution and habitat of the dominant species. *Malayan Nature Journal*, 66(1&2), 139–145.
- Yap, C. K., Peng, S. H. T., & Leow, C. S. (2019). Contamination in Pasir Gudang area, Peninsular Malaysia: What can we learn from Kim-Kim River chemical waste contamination? *Journal of Humanities and Education Development*, 1(2), 82–87. <https://doi.org/10.22161/jhed.1.2.4>
- Yap, C., Nulit, R., Sharifinia, M., Tony Peng, S., Yap, C., Okamura, H., Ismail, M., & Saleem, M. (2020). Higher bioavailability and contamination of copper in the eastern part of Johore Causeway: Will the pattern remain the same beyond 2020? *Journal of Biomedical Research Environmental Sciences*, 1(4), 114–121. <https://doi.org/10.37871/jels1128>

- Zawawi, A. (2019). *Concentration of heavy metal in water, sediment and aquatic life at straits of Johor*. [Doctoral dissertation] University Teknologi Malaysia. <http://eprints.utm.my/92834/1/MohdAsadiAbdullahMSKA2019.pdf>
- Zhao, N., Zhang, G., Zhang, S., Bai, Y., Ali, S., & Zhang, J. (2019). Temporal-spatial distribution of chlorophyll-a and impacts of environmental factors in the Bohai Sea and Yellow Sea. *IEEE Access*, 7, 160947–160960. <https://doi.org/10.1109/access.2019.2950833>

## Electric Transmission Tower Corrosion Assessment Using Analytic Hierarchy Process and Health Index

Aina Shazwana Mohd Izhar<sup>1</sup>, Nor Hazwani Nor Khalid<sup>1,2\*</sup>, Fathoni Usman<sup>1,2</sup>, Mohd Supian Abu Bakar<sup>2</sup>, Nur Fadilah Adriyanshah<sup>1</sup> and Hakim Zahari<sup>3</sup>

<sup>1</sup>Civil Engineering Department, College of Engineering, Universiti Tenaga Nasional, Kajang 43000, Malaysia

<sup>2</sup>Institute of Energy Infrastructure (IEI), College of Engineering, Universiti Tenaga Nasional, Kajang 43000, Malaysia

<sup>3</sup>Asset Profiling & Rehabilitation, Grid Division, Tenaga Nasional Berhad, 50470 Kuala Lumpur, Malaysia

### ABSTRACT

A transmission tower is one of the components in power infrastructure supporting overhead power lines (OHL). Electrical components, structural, and environmental factors are classified as the primary concern as they can cause catastrophic failure in transmission lines. Transmission towers are in various environments, such as coastal and industrial areas, with different atmospheric corrosion levels due to various corrosive pollutants. For maintenance planning, it is essential to consider the effects of corrosion on towers by physical evaluation influenced by atmospheric corrosion. The physical evaluation of each element uses a scoring or rating method ranging from one to five. The Analytic Hierarchy Process (AHP) and Health Index (HI) are used to evaluate the overall condition of the towers. The study discovered that soil corrosivity in coastal areas is high, and atmospheric corrosion is due to chloride content. Although the pollutants in those areas are high and corrosive, the physical evaluation found that most industrial, coastal, and road towers are in good condition at a rating of 4 and 5. The HI result is the dominance of 71% to 85%, which indicates that the towers are in good health.

*Keywords:* Analytical hierarchy process, corrosion assessment, energy, health index, transmission tower

### ARTICLE INFO

#### Article history:

Received: 05 May 2023

Accepted: 18 December 2023

Published: 22 July 2024

DOI: <https://doi.org/10.47836/pjst.32.4.21>

#### E-mail addresses:

Aina.shazwana@uniten.edu.my (Aina Shazwana Mohd Izhar)

Hazwani@uniten.edu.my (Nor Hazwani Nor Khalid)

Fathoni@uniten.edu.my (Fathoni Usman)

mohdsupian7779@gmail.com (Mohd Supian Abu Bakar)

Nur.Fadilah@uniten.edu.my (Nur Fadilah Adriyanshah)

hakimz@tnb.com.my (Hakim Zahari)

\* Corresponding author

### INTRODUCTION

A transmission tower is one of the components in power infrastructure that supports overhead power lines (OHL). Tenaga Nasional Berhad (TNB) owns more than 723,134 km of power lines to provide electricity for Peninsular Malaysia

([https://www.tnb.com.my/assets/annual\\_report/TNB\\_IAR\\_2021.pdf](https://www.tnb.com.my/assets/annual_report/TNB_IAR_2021.pdf)). Malaysia Energy Commission 2018 annual report stated that the largest electricity consumer is from the industrial sector, which consumes around 46% of electricity, followed by the commercial sector at 30.8%. The residential sector at 20.5% ([https://www.st.gov.my/ms/contents/files/download/99/Performance\\_Statistical\\_Information\\_on\\_the\\_Malaysian\\_Electricity\\_Supply\\_Industry\\_20181.pdf](https://www.st.gov.my/ms/contents/files/download/99/Performance_Statistical_Information_on_the_Malaysian_Electricity_Supply_Industry_20181.pdf)). A study by Hashim et al. (2019) found that electricity supply interruptions are mainly due to conductor issues, about 40%, and environmental factors, about 31%. Another factor was due to structural failures with 17% and disturbances by the third party with 12%.

In order to avoid disruption to the transmission tower system, assessment and evaluation of the transmission tower condition are essential because it will deteriorate over time due to many factors, one of which is corrosion. The identification process can be done by assessing the current condition of the tower. One way to determine the condition of transmission towers is by evaluating their physical condition, including visual and corrosion assessment. Cardenas et al. (2019), Tsimberg et al. (2014), Velásquez and Lara (2018) and Wuller and Pharmatrisanti (2012) mentioned in their research that the physical evaluation is based on the common condition of the components through visual inspection and non-destructive tests using simple tools and equipment.

However, a physical evaluation is insufficient to fulfil the required conditions for the transmission tower. Moreover, the environmental effect is essential, as environmental changes significantly influence atmospheric corrosion. In their research, Usman and Khalid (2021) mentioned condition assessment studies that consider environmental elements using atmospheric corrosion levels. The effect of corrosion on the integrity of the tower structure is necessary for the maintenance plan to identify the service level of the tower.

The reason for considering atmospheric corrosion conditions is that based on studies by Krishnasamy et al. (2020) and Usman et al. (2021) stated that transmission towers in coastal areas are influenced by marine salt particles such as chloride ( $\text{Cl}^-$ ). Additionally, Corvo et al. (2008) mentioned that coastal areas are prominent for high corrosion rates. On the other hand, Usman and Rediansyah (2008) found that industrial areas emit high concentrations of sulphates ( $\text{SO}_4$ ) while nearby roads increase the emission of nitrogen dioxides ( $\text{NO}_2$ ) through vehicle combustion. Based on a study by Arroyave and Morcillo (1995), the highest corrosive effects in atmospheric corrosion are chloride ( $\text{Cl}^-$ ) and Sulphates ( $\text{SO}_4$ ), while nitrogen oxides ( $\text{NO}_2$ ) increase depending on the amount of the fuel combustions, mainly from the vehicles.

A study by Usman and Rediansyah (2008) classified atmospheric areas into six categories: urban, rural, island, highlands, industrial, and coastal. However, this study considers the area by the distance from industrial, coastal, and road areas, considering the vehicle's exhaust emission to the transmission towers due to the corrosive pollutant agents emitted in those areas. The condition assessment of the elements in this study allows the

energy infrastructure authorities to study and compare to determine the reliability and the remaining life of a transmission tower (Van-Der-Wal et al., 2004).

This study, therefore, attempts to highlight the assessment of transmission towers by applying physical evaluation methods and considering the influence of atmospheric corrosion on the deterioration of transmission towers. It is also recommended to plan for mitigation and adapting strategies. Based on the European Environment Agency (<https://www.eea.europa.eu/publications/adaptation-in-energy-system>), the long-term services of transmission towers can be improved by implementing the possible consequences of climate changes, such as the severity of extreme weather conditions, changes in temperature patterns, rising sea levels, as well as applying climate-resilient measures, such as considering temperature differentials, and corrosion damage control.

## METHODOLOGY

The Peninsular of Malaysia is located at a latitude of 4°0'0" N and a longitude of 102°30'0"E. The country has an equatorial climate characterised by hot and humid weather throughout the year. Southwest and northeast monsoons play a significant role in determining climate variability. Southwest monsoons occur between April and September, while northeast monsoons occur between October and March. The weather during the southwest monsoon is drier, and there is less rainfall than during the northeast monsoon (Kwan et al., 2013; Tang, 2019).

In Peninsular Malaysia, the most industrialised areas are primarily located in the western region, in the states of Selangor and Johor. Malaysia's heavy industries, such as electronics, textiles, and chemicals, are primarily concentrated in Selangor. Johor is another major industrial centre in Peninsular Malaysia, known for its port, electric and electronics, oil and gas, and shipbuilding industries (Frost & Sullivan, 2018). Meanwhile, the state of Penang strongly focuses on high-tech industries, such as semiconductors, medical devices, and aerospace (<https://www.oecd.org/education/imhe/47505889.pdf>). This study collected data onsite for condition assessment across the north, south, east, and west. Figure 1 shows 434 tower locations in different transmission lines collected.

### Condition Assessment of Transmission Tower

The structure of lattice transmission towers is divided into three main parts: overhead line, body, and base (Zhang et al., 2019). The data collected in this study are only on the base of the transmission towers, as shown in Figure 2. A rating method is used to systematically evaluate and quantify the extent of corrosion on the towers and provide a clear and standardised assessment of the tower's condition. The assessment involves mainly non-destructive tests and visual evaluation. The test equipment is obtained from the Universiti Tenaga Nasional Geology laboratory (UNITEN).

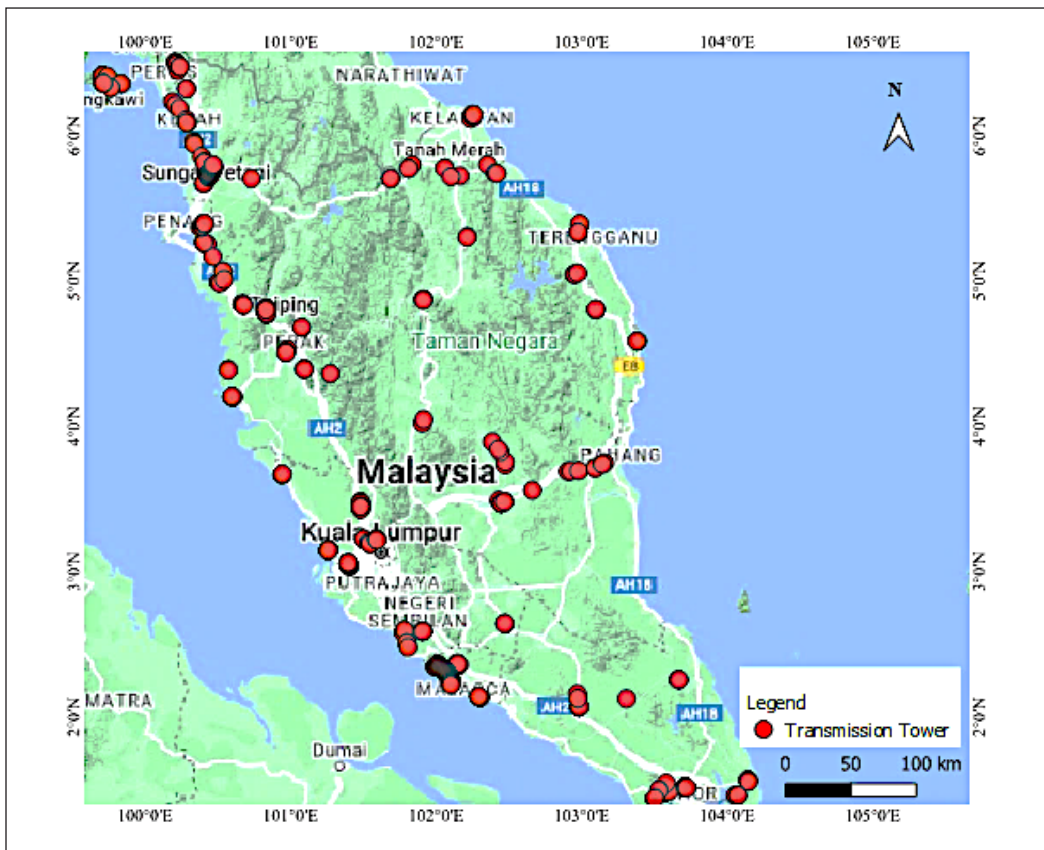


Figure 1. Study area in Peninsular Malaysia

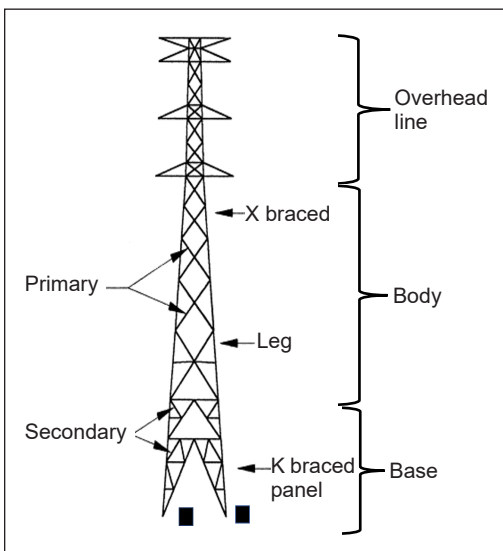


Figure 2. Design of transmission tower

Referring to the condition assessment of the transmission tower by Zhang et al. (2014), the condition of critical items considered are the structural member, foundation, and environmental condition. Therefore, the assessment criteria shown in Table 1 are based on the three elements. The assessment implies a rating system from one to five to classify the failure probability as very low, low, medium, high, and very high, which is also applied in a study by Chitpong et al. (2016). Depending on the atmospheric environment, the structural members, especially steel, are highly prone to corrosion, which can

lead to structural failure. Thus, most steel members are coated and galvanised to increase sustainability.

**Structural Member**

The structural member is the main component of the transmission tower, which is crucial to giving a proper assessment for maintenance purposes. Based on visual observation, galvanised coating thickness and corrosion condition are the assessment methods involved.

**Galvanised Thickness.** Galvanised coating thickness is conducted using equipment (Elcometer) to measure the thickness of the zinc layer (Ricci et al., 2018). Rodger et al. (2017) studied galvanised steel’s corrosion and measured the galvanised thickness using the Elcometer gauge. It is a universally used

coating thickness gauge since it provides precise, consistent measurements and fast data processing to calculate an average coating thickness. The measured value in the micron meter is represented in a rating between one and five (Table 2).

**Corrosion Condition.** Corrosion assessment based on visual inspection often requires checking the metal’s surface for corrosion symptoms such as rust, pitting, and discolouration. The inspection is interpreted in a rating of zero and seven, as in Table 3. The condition reference of visual assessment is as in Figure 3. In a previous study by Usman and Khalid (2021), a similar method was used to determine the corrosion condition of steel members, which was done by using ratings from 1 to 5.

Table 1  
*Assessment criteria for each element*

Element	Assessment Criteria
Structural member	<ul style="list-style-type: none"> <li>Galvanised thickness</li> <li>Corrosion condition</li> </ul>
Foundation	<ul style="list-style-type: none"> <li>Foundation condition</li> <li>Soil resistivity</li> </ul>
Environment	<ul style="list-style-type: none"> <li>Atmospheric corrosion level</li> </ul>

Table 2  
*Rating of galvanised coating thickness (Usman & Khalid, 2021)*

Description	Value	Rating
The thickness of the galvanised coating is adequate.	>80	5
Thin	80–60	4
Moderately Thin	60–50	3
Very Thin.	50–40	2
The layer of galvanised coating is very thin. Monitoring is necessary against corrosion.	<40	1

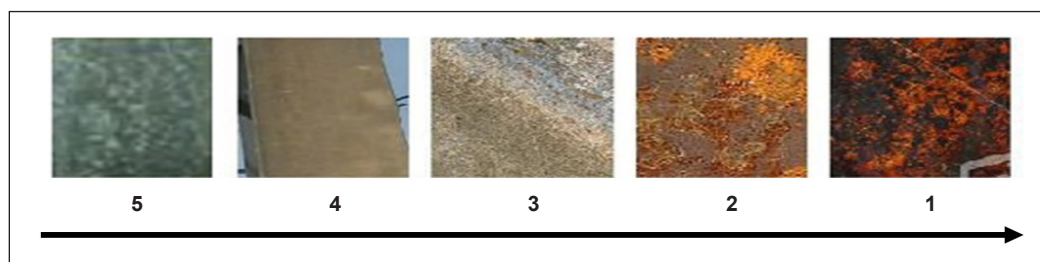


Figure 3. Visual assessment for corrosion rating (Usman & Khalid, 2021)

Table 3  
*Rating of corrosion assessment (Usman & Khalid, 2021)*

Description	Rating
Like new, galvanised layers are intact with no or little rust.	5
Good condition, galvanised layer intact with powdery rust.	4
Minimum adequacy. Most of the galvanised layers are corroded, and steel is exposed with a layer of rust	3
It is not functioning as designed, and steel members are lost due to rust.	2
Potentially hazardous: loss of steel section	1

**Foundation**

The foundation is the base component of transmission towers supporting the concrete pole to the ground. The soil condition and concrete pole placement determine the form and depth of foundations. Jyothi and Mahesh (2017) discovered that the tower legs are set in concrete, which generally provides good protection to the steel. It is found that cracks in concrete could cause water and deposited salt to immerse into the concrete, creating corrosion and decreasing the reliability of the foundation leg.

**Foundation Condition.** Besides visual observation on the concrete foundation, the rebound hammer and ultrasonic pulse velocity (UPV) test are included as non-destructive testing. Rebound hammer tests provide an instant indication of compressive strength on concrete. It is similar to a study by Krishnasamy et al. (2020), where the rebound hammer test performs the transmission line against corrosion. The test involves striking a spring-loaded hammer against the concrete’s surface and measuring the hammer’s average rebound number, which is directly related to the compressive strength of the concrete. The estimated average value of the rebound hammer test is represented in a rating between one and five, as shown in Table 4. High rebound numbers imply that the concrete has a high compressive strength to withstand heavy loads and impact.

UPV test is used to inspect concrete quality and cracks within the concrete by emitting electronic waves through the concrete. The procedure involves sending an ultrasonic pulse through the concrete and measuring the time it takes for the pulse to travel through the material and return to the surface. The test is used to determine the density and uniformity of the concrete. The measured value of UPV in km/sec is represented in a rating between one and five (Table 5). The study of UPV by Usman and Khalid (2021) revealed that concrete is of good quality

Table 4  
*Rating of rebound hammer test (Usman & Khalid, 2021)*

Concrete quality	Value	Rating
A very good hard layer	> 40	5
Good layer	30–40	4
Fair	20–30	3
Poor Concrete	< 20	2
Delaminated	0	1

with low porosity, void content, and crack density, making it strong, durable, and resistant to damage from weathering. UPV was also used to assess the condition of the transmission tower foundation.

Table 5  
*Rating of UPV (Usman & Khalid, 2021)*

Concrete Quality	Value	Rating
Very good	> 4.0	5
Good, but maybe porous	3.5–4.0	4
Poor	3.0–3.5	3
Very poor	2.5–3.0	2
Very poor and low	2.0–2.5	1

**Soil Resistivity.** Soil condition is necessary as the influence of soil resistivity is crucial in constructing transmission towers. Waters (1952) states that soil resistivity and corrosion are closely related. Soil resistivity depends on the geographical type, such as a riverbank or a mountainous area, water content, soil texture, and more. It is found that soils with a high moisture content have a lower resistivity, which is about 1.5 Ohm-m, whereas soils with a low moisture content have a higher resistivity, reaching up to 10,000 Ohm-m. Moreover, corrosion is more likely to occur in soils with lower resistivity (Sing et al., 2013).

Table 6  
*Rating of soil resistivity (Usman & Khalid, 2021)*

Corrosivity	Value	Rating
Essentially noncorrosive	>20,000	5
Mildly Corrosive	10,000–20,000	4
Moderately corrosive	5,000–10,000	3
Corrosive	3,000–5,000	2
Highly corrosive	1,000–3,000	1

The soil resistivity testing method uses the Wenner Probe method with four electrodes. Sing et al. (2013) conduct soil resistivity tests using the Wenner probe method, the most common and convenient method for determining soil resistivity. Soil assessment is conducted near or under the towers to test the resistivity of the soil. Hence, the measured value of soil resistivity in ohm-cm is represented in a rating between one and five, as shown in Table 6. A higher rating of soil resistivity indicates good soil condition.

### **Environment**

The environmental factor involved in this assessment is the atmospheric corrosion level, which is presented using a corrosion hazard map. Figure 4 illustrates the corrosion hazard

level developed by Adriyanshah et al. (2022). The corrosion hazard map is obtained from 17 weather stations owned by the Meteorological Department of Malaysia (MET). The data are climate and wet deposition, which consist of temperature, humidity, rainfall, sulphates, nitrates, and chloride. The map is represented in five levels: (1) level one indicates the lowest corrosivity environment, (2) level two indicates the low corrosivity environment, (3) level three indicates the medium, (4) level four indicates the high and (5) level five indicates the highest corrosivity environment.

The corrosion hazard level is considered due to the interaction between the metal surface and its environment. Metal surfaces interact with gases, liquids, and other elements that make up the atmosphere, resulting in atmospheric corrosion (Syed, 2006). According to a study by Fathoni et al. (2013), water (in the form of rain, humidity, and dew), oxygen, and sulphur dioxide are the main contributors to atmospheric corrosion, which can result in the production of rust and other types of corrosion on metal surfaces. Temperature, acidity, and pollution are additional causes of air corrosion.

The atmospheric area is determined by the distance to the main pollutants emitted in industrial settings, such as dust particles, SO<sub>4</sub>, NO<sub>3</sub>, and carbon emissions. Industrial

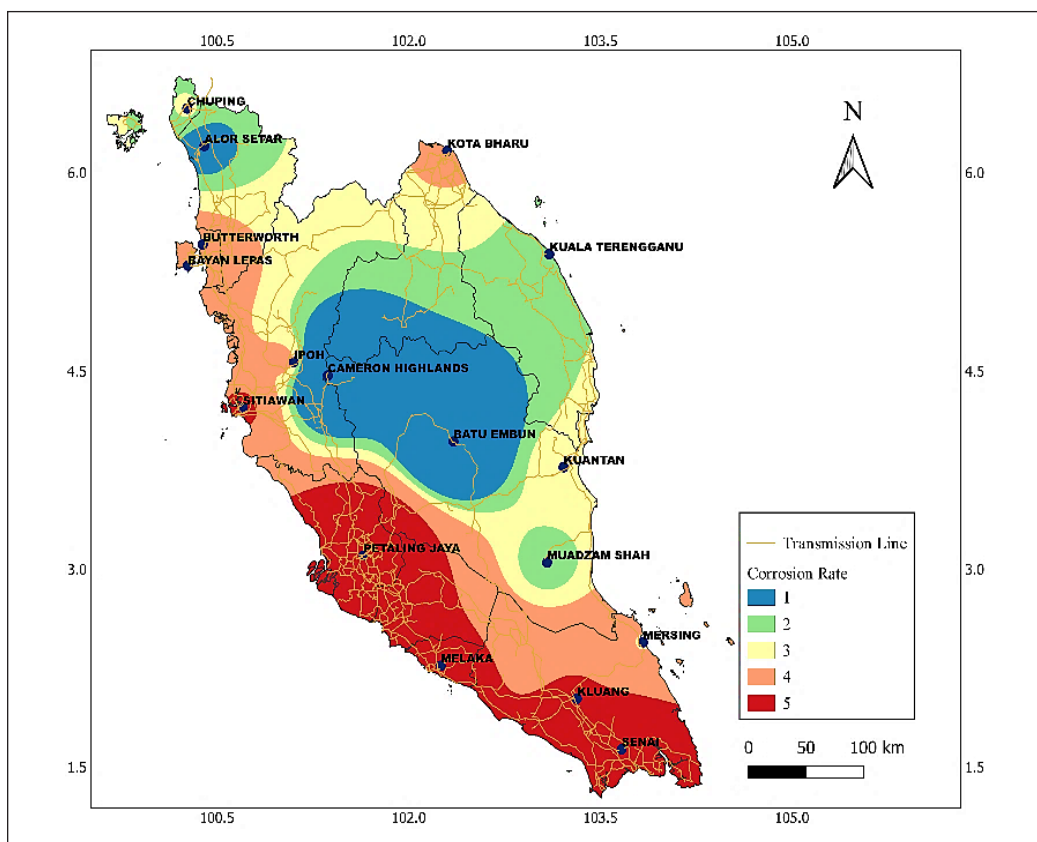


Figure 4. Corrosion hazard map (Adriyanshah et al., 2022)

pollution is mainly sourced from factories, power plants, and transportation. At the same time, coastal areas are known for their high chloride concentrations and salt aerosols in the air and moisture, which can contribute to atmospheric corrosion (Feliu et al., 1999). On the other hand, the distance from roads is influenced by vehicle combustion. The increased exhaust combustion from vehicles, which causes NO<sub>2</sub>, NO<sub>3</sub>, and particulate matter emissions, speeds up corrosion (Kumar et al., 2020).

Thus, this study also includes the environmental element to identify the condition rating of the transmission towers according to three areas: (1) coastal, (2) industrial, and (3) distance from the road because of the atmospheric corrosion decreasing the galvanised coating thickness, and finally lead to corrosion.

## Analysis Method

### *Analytical Hierarchy Process (AHP)*

AHP is a decision-making technique that determines the importance of priority in performance evaluation (Daneshmand et al., 2011; Tanaka et al., 2010; Triantaphyllou & Mann, 1995). Unlike Multicriteria Decision Making (MCDM), AHP is more likely applicable for complex decisions in various measures and comparisons, which are much more complicated to compute (Beynon, 2002; Lin & Yang, 1996; Saaty, 1977). The process of determining the weightage using AHP is determined by a pair-wise comparison of each assessment criterion against one another. The comparison is made by referring to the importance scale in Table 7 (Rajesh & Malliga, 2013; Saaty, 2008, 1977). The scale of numbers between one and nine shows the dominance of one criterion over another. Scale one is considered equally important, while scale nine is characterised as one criterion contributing higher importance to another.

Table 7  
*Importance scale (Rajesh & Malliga, 2013)*

Scale	Definition	Explanation
1	Equally important	Two criteria contribute equally to the subject
3	Moderately important	Slightly favour one criterion over another
5	Strongly important	Strongly favour one criterion over another
7	Very strongly important	One criterion is favoured very strongly over another
9	Extremely important	The evidence favouring one criterion over another is the highest

*Note.* 2,4,6,8 can be used as intermediate favours

### *Health Index (HI)*

To evaluate the overall health condition of transmission towers, researchers frequently apply the health index (HI) (Manninen et al., 2021; Naranpanawe et al., 2020). According to research by Hjartarson et al. (2003), HI is a helpful way to assess the overall condition

of a complex asset because transmission towers are frequently evaluated based on their components or characteristics. The weighting of each criterion is acquired from AHP, and the scoring or rating from the condition assessment is needed to calculate the HI value. Additionally, it is essential to note that the weightage values dictate the precision of the HI value (Irfan & Handika, 2019). The formula used to determine the overall HI is given in Equation 1, where R is the rating score,  $R_{max}$  is the rating score, and W is the weighted average of each criterion.

$$\%HI = \frac{\sum(R \times W)}{\sum(R_{Max} \times W)} \times 100 \tag{1}$$

The overall condition of the transmission tower is determined from the known HI (%), as shown in Table 8. The HI (%) value is classified from “very good” to “very poor”. In addition, the elements included in AHP and HI are from structural members and foundations of the transmission tower. The environmental element is not involved in the corrosion analysis of transmission towers, as it is used to classify the transmission tower into different atmospheric areas, coastal and industrial, and the distance from the road.

Table 8  
Health index value (Haema & Phadungthin, 2012)

Condition	Requirement	HI (%)	HI Score	Colour code
Very good	Normal maintenance	86–100	5	Blue
Good	Normal maintenance	71–85	4	Green
Fair	Increase diagnostic testing	51–70	3	Yellow
Poor	Plan to replace or rebuild, considering the risk	31–50	2	Orange
Very Poor	Immediately assess risk	0–30	1	Red

## RESULTS AND DISCUSSION

### Condition Rating of Transmission Tower

The result of the condition rating is analysed according to three different atmospheric areas: coastal area, industrial area, and distance from road. Figure 5 shows the condition rating in the coastal area. Focusing on the maximum number of towers for each assessment criterion from Table 1, the maximum number for soil resistivity and corrosion hazard levels fall under rating 1, foundation condition and galvanised thickness are at rating 5, while corrosion condition is at rating 4. The soil in the coastal area appears corrosive, and the atmospheric corrosion is high because chloride is the major pollutant in the coastal area (Pongsaksawad et al., 2021).

The condition rating for the industrial area is as in Figure 6. For soil resistivity, foundation condition, and galvanised thickness, the maximum number falls under rating 5. In contrast, the corrosion conditions were rated at rating 4, and the corrosion hazard level

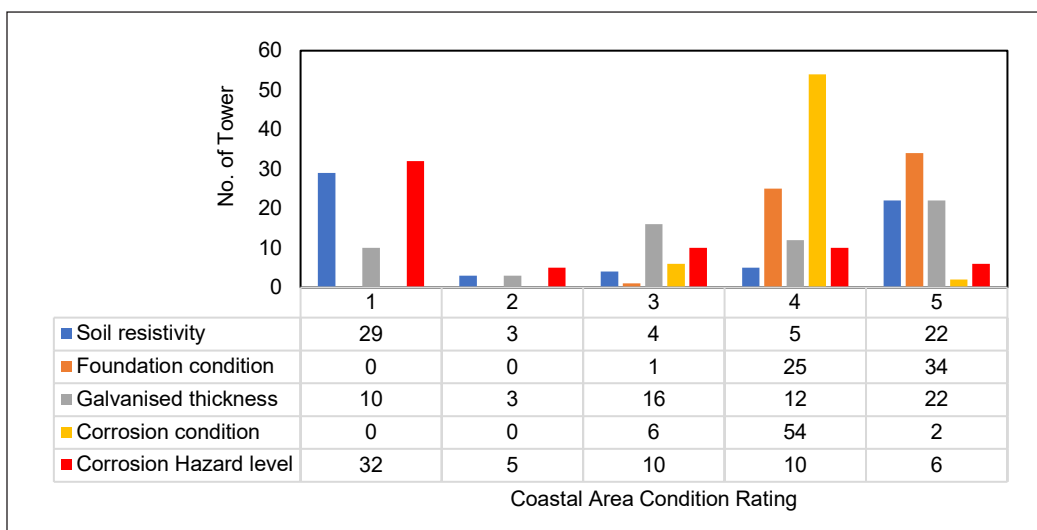


Figure 5. Condition rating in the coastal area

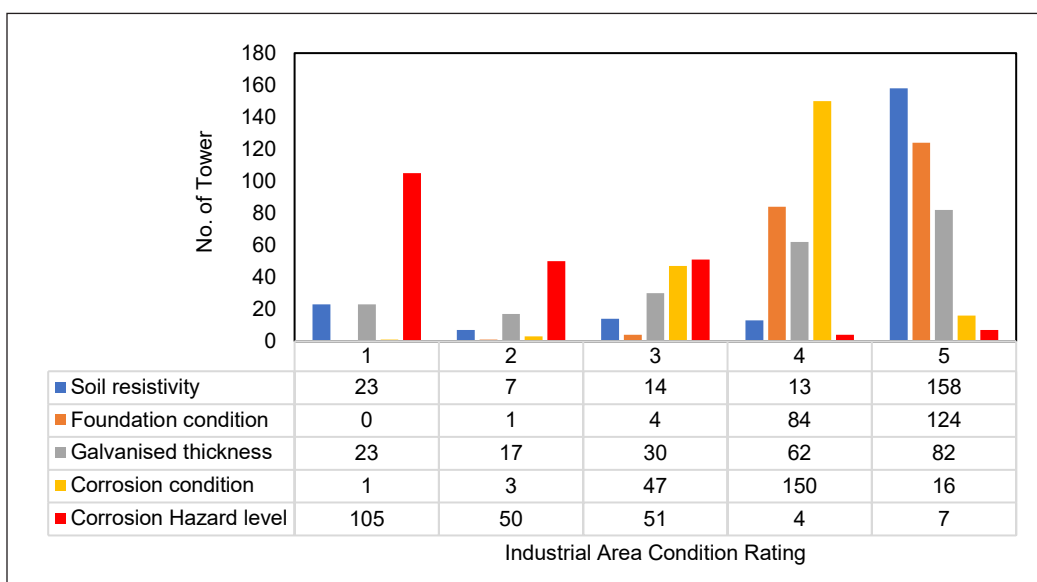


Figure 6. Condition rating in an industrial area

at rating 1. The corrosion hazard level at level 1 might be due to the pollutants emitted from the industrial sectors, such as sulphur dioxide and nitrogen dioxide. Figure 7 shows the road areas or areas with the domination of vehicle combustion, where the resulting pattern is near the industrial area result.

However, the atmospheric corrosion level recorded in the three environments is in rating 1, where the atmospheric corrosion is relatively high. The reason for this is the high presence of pollutants in the air. Industrial activities such as manufacturing, power

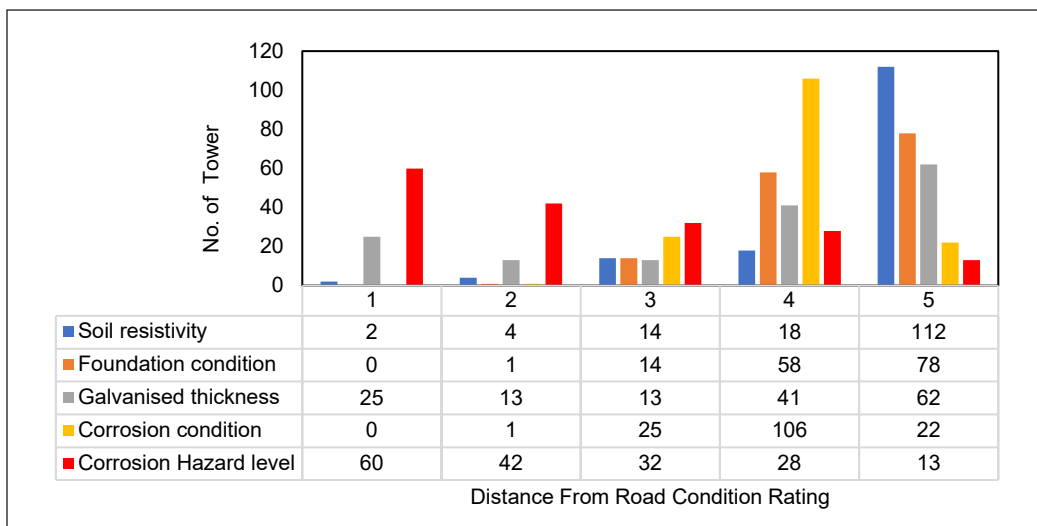


Figure 7. Condition rating in the distance from the road

generation, and chemical processing can release various corrosive compounds into the air, including acids, bases, and factory emissions. The salt spray, humidity, and temperature fluctuations in coastal areas also contribute to corrosion. The atmospheric sea salt particle itself accelerates the corrosion of steel and can cause damage to metal surfaces and structures (Wang et al., 2022). On the other hand, pollutants emitted in road areas are influenced by vehicle exhaust, which harms human health and the environment.

As a result of the findings, it is reasonable to conclude that atmospheric corrosion is significantly high due to pollution in the area. Most transmission tower contributions in the coastal, industrial, and road areas are at ratings 4 and 5, which indicates that the criteria are in good condition. This occurrence could be due to the excellent management of the maintenance schedule.

## Health Index of Transmission Tower

### *Towards Corrosion Hazard Level*

The importance and priority of each assessment criterion are compared using a scale of one to nine to obtain the weightage of the assessment criteria (Table 7). Applying Equation 1, HI is calculated by including the weightage of each assessment criterion and the condition rating. The weightage of each element is used to determine the consistency ratio (CR), where the CR must be lower than 10% (Huang et al., 2018; Saaty, 2008). The weightage of each element is 9.5% (soil resistivity), 18.6% (foundation condition), 51.0% (galvanised thickness), and 20.9% (corrosion condition). Based on the weightage, the CR obtained is 2%.

The criteria with the highest importance among assessment criteria are galvanised thickness, followed by corrosion condition. Both criteria have the same element, a structural

member that is the most vulnerable to atmospheric corrosion as it is made of steel. The thickness of galvanised coating plays an important role because steel degradation is most likely to accelerate as the protection breaks down, as stated in research by Eyre-Walker et al. (2014). Soil resistivity has the lowest weightage as the importance is the lowest. The consideration is made because the air’s corrosion rate spreads faster than in the soil due to the presence of dissolved oxygen, which can inhibit the corrosion process.

Figure 8 illustrates the correlation between HI scores and corrosion hazard levels of transmission towers, along with the corresponding number of towers at each hazard level. Among 434 towers assessed, 106 are classified in level one, dominated by a HI at a score of 5. Even though the HI indicates good condition, the atmospheric area around those 106 towers is highly corrosive, marked as level 1 in corrosion hazard level. Therefore, an increase in the deterioration rate of the towers is expected because heavy industries, coastal industries, and more conquer the atmospheric area on level 1. Most towers at corrosion hazard between level 1 to level 3 give HI score of 3 to 5.

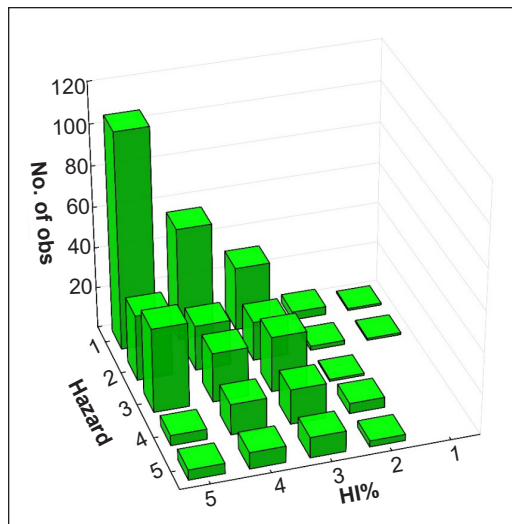


Figure 8. Corrosion hazard level by HI% score of transmission tower (x: Health Index, y: Corrosion Hazard Level, z: Number of towers)

**Towards Atmospheric Area**

Based on the graph in Figure 9, among 434 towers in this study, 143 towers close to industrial, 28 close to coastal, and 76 close to roads are 71% to 85%, indicating good

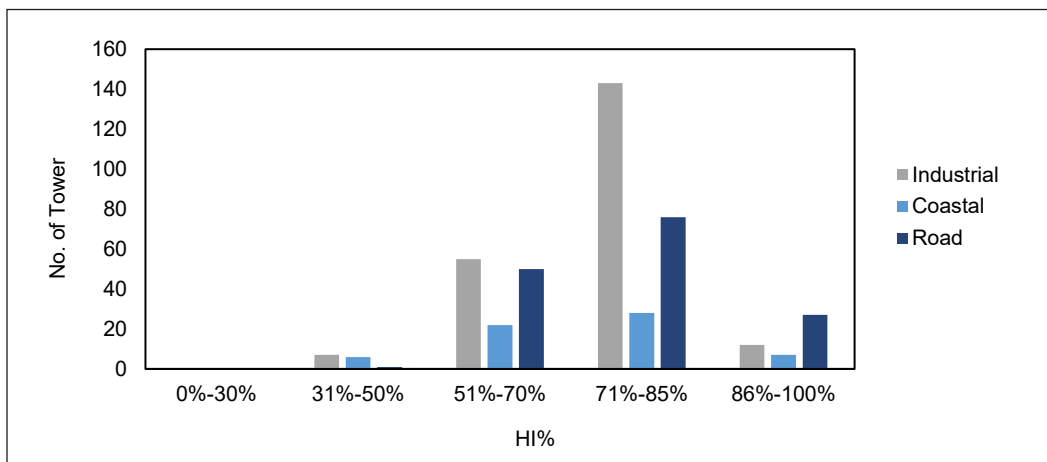


Figure 9. HI% in different environmental distances

condition and requiring regular maintenance. There are only seven towers close to the industrial sector, six towers close to the coastal sector, and one close to roads with HI between 31% to 50%, meaning poor conditions and a need to consider risk assessment. No towers are falling between 0% to 30% (very poor condition). Another possible reason is that the galvanised coating may have been suitable for the environment, as in research by Soufeiani et al. (2020) on suitable galvanised coatings for different types of corrosion. Regarding analysis, this might be due to the excellent maintenance done by the Energy Commission. The tower might have been considering corrosion prevention in the area with a higher corrosion rate.

### *Towards the Current Service Life of Transmission Towers*

A bag plot represents the relationship between towers and age to the HI (Figure 10). The colour of the bag plot is darker from the centre and lighter towards the outer, indicating a higher to lower distribution of towers. In a previous study by Haema and Phadungthin (2012), the health index for overall towers indicated that most are in good condition, between 50% and 70%.

The darker colour is between HI 58% to 88%, with service life between 10 to 45 years and 50% of 434 towers (Figure 10). In addition, there are towers between HI 68% to 88% with service life between 50 to 60 years, generally in good condition due to excellent maintenance routine. Only two out of 434 towers are in HI, between 30% and 40%, which is considered in bad condition. Further investigation into the tower discovered that the

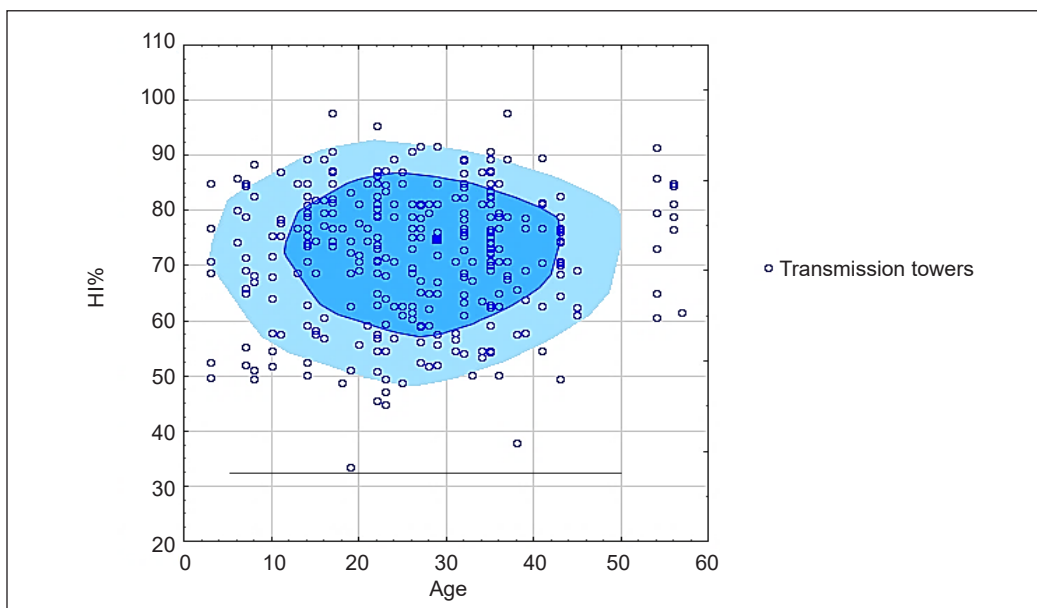


Figure 10. Distribution of transmission towers age and HI (Dark blue: high number of towers, Light blue: low number of towers, Outer range: least number of towers)

towers are in an industrial area, one in the northern part and another in the southern part of Peninsula Malaysia. This situation could be classified as unusual since most of the towers around the area have scored 40% and above. A detailed risk assessment is suggested at both towers immediately to prevent structural failure.

Based on the HI, the HI for 434 transmission towers is illustrated in Figure 11. The map is represented in five colour codes where the HI for red colour is ranging from 0% to 30%, orange colour ranging from 31% to 50%, yellow colour ranging from 51% to 70%, green colour ranging from 71% to 85%, and blue colour ranging from 86% to 100%. As seen in the map, among the 434 transmission towers are yellow, green, and blue, as indicated in Table 8. The map illustrated that most towers are in good condition and only need normal maintenance.

## CONCLUSION

This study discovered that the condition of transmission towers in three different atmospheric areas is mainly at ratings 4 and 5, which indicates good condition. However, the corrosion hazard levels recorded at rating 1 signify that those three areas have a very high corrosion level. Analysis of HI in three different atmospheric areas shows that most of the tower has HI of 71%–85%. Furthermore, the number of towers is the highest between 10 to 45 years, with HI 68% to 88%. Meanwhile, a few towers at 50 to 60 years have an HI of 60%–90%, which is good health. From 434 towers, only two falls in HI of 30% to 40%, where both towers are 19 and 39 years old. Implementing HI in transmission towers assessment ensures the safety and reliability of transmission towers. Besides providing valuable information on structural health, the authorities can take practical measures to prevent disastrous failure.

## ACKNOWLEDGEMENTS

The authors thank the Ministry of Higher Education (MOHE), Malaysia, for the research fund through the Fundamental Research Grant Scheme (FRGS), FRGS/1/2020/TK0/UNITEN/03/3. The acknowledgement is also extended to Universiti Tenaga Nasional, Malaysia, in supporting the journey of this paper to the readers.

## REFERENCES

- Adriyanshah, N. F., Khalid, N. H. N., Usman, F., Izhar, A. S. M., Jawas, J. A., & Jalal, W. N. W. (2022). Development of corrosion hazard map in peninsular Malaysia using inverse distance weighting (IDW) interpolation. In M. Awang, L. Ling & S. S. Emamian (Eds.), *Advances in Civil Engineering Materials* (pp. 225-233). Springer. [https://doi.org/10.1007/978-981-16-8667-2\\_24](https://doi.org/10.1007/978-981-16-8667-2_24)
- Arroyave, C., & Morcillo, M. (1995). The effect of nitrogen corrosion oxides in atmospheric. *Corrosion Science*, 37(2), 293–305. [https://doi.org/10.1016/0010-938X\(94\)00136-T](https://doi.org/10.1016/0010-938X(94)00136-T)

- Beynon, M. (2002). DS / AHP method : A mathematical analysis, including an understanding of uncertainty. *European Journal of Operational Research*, 140(1), 148–164. [https://doi.org/10.1016/S0377-2217\(01\)00230-2](https://doi.org/10.1016/S0377-2217(01)00230-2)
- Cardenas, L. A., Alvarez, D. L., Garcia, S. R., & Herrera, F. A. (2019, December 4-6). *Overhead lines assessment using health index*. [Paper presentation]. FISE-IEEE/CIGRE Conference - Living the energy Transition (FISE/CIGRE), Medellin, Colombi. <https://doi.org/10.1109/FISECIGRE48012.2019.8984959>
- Chitpong, J., Suwanasri, C., & Suwanasri, T. (2016, June 28 - July 1). *Evaluation criteria for condition and importance assessment of high voltage transmission line*. [Paper presentation]. 13th International Conference on Electrical Engineering/Electronics, Computer, Telecommunications and Information Technology (ECTI-CON), Chiang Mai, Thailand. <https://doi.org/10.1109/ECTICon.2016.7561237>
- Corvo, F., Perez, T., Dzib, L. R., Martin, Y., Castañeda, A., Gonzalez, E., & Perez, J. (2008). Outdoor-indoor corrosion of metals in tropical coastal atmospheres. *Corrosion Science*, 50(1), 220–230. <https://doi.org/10.1016/j.corsci.2007.06.011>
- Daneshmand, S. V., Heydari, H., & Shakeri, S. (2011). Multicriteria optimal winding scheme in HTS transformers by analytical hierarchy process. *IEEE Transactions on Applied Superconductivity*, 21(1), 2–12. <https://doi.org/10.1109/TASC.2010.2089051>
- Eyre-Walker, R., Howarth, G., Ahmed, R., & Lewin, J. (2014, November 27-28). *Application of advanced condition assessment and asset management techniques on steel tower overhead line electricity networks*. [Paper presentation]. Asset Management Conference, London, United Kingdom. <https://doi.org/10.1049/cp.2014.1047>
- Fathoni, U., Zakaria, C. M., & Rohayu, C. O. (2013). Development of corrosion risk map for Peninsular Malaysia using climatic and air pollution data. *IOP Conference Series: Earth and Environmental Science*, 16(1), Article 012088. <https://doi.org/10.1088/1755-1315/16/1/012088>
- Feliu, S., Morcillo, M., & Chico, B. (1999). Effect of distance from sea on atmospheric corrosion rate. *Corrosion*, 55(9), 883–891. <https://doi.org/10.5006/1.3284045>
- Frost & Sullivan. (2021, August 19). Rising demand for energy efficiency and sustainability boosts the southeast asian integrated facilities management market. <https://www.frost.com/news/press-releases/rising-demand-for-energy-efficiency-and-sustainability-boosts-the-southeast-asian-integrated-facilities-management-market/>
- Haema, J., & Phadungthin, R. (2012, September 18-20). *Condition assessment of the health index for power transformer*. [Paper presentation] Power Engineering and Automation Conference, Wuhan, China. <https://doi.org/10.1109/PEAM.2012.6612413>
- Hashim, R., Usman, F., & Baharuddin, I. N. Z. (2019). Determining health index of transmission line asset using condition-based method. *Resources*, 8(2), 80. <https://doi.org/10.3390/resources8020080>
- Hjartarson, T., Jesus, B., Hughes, D. T., & Godfrey, R. M. (2003, September 7-12). *Development of health indices for asset condition assessment*. [Paper presentation]. IEEE PES Transmission and Distribution Conference and Exposition (IEEE Cat. No.03CH37495), Dallas, USA. <https://doi.org/10.1109/TDC.2003.1335332>

- Huang, R., An, L., Zhang, R., Wu, J., & Liang, Y. (2018). Research on condition assessment method of transmission tower under the action of strong wind. *IOP Conference Series: Materials Science and Engineering*, 322(7), Article 072054. <https://doi.org/10.1088/1757-899X/322/7/072054>
- Irfan, J., & Handika, P. (2019, October 10-11). *Comprehensive calculation of overhead transmission line health index*. [Paper presentation]. 11th International Conference on Information Technology and Electrical Engineering (ICITEE), Pattaya, Thailand. <https://doi.org/10.1109/ICITEED.2019.8929988>
- Jyothi, B., & Mahesh, S. (2017). Design transmission tower and its foundation. *International Journal of Scientific Engineering and Technology Research*, 6(6), 1008–1014.
- Krishnasamy, R., Shyamala, G., Johnson, S. C., Sabarinathan, K., Sakthivel, S. M., & Rajesh, K. (2020). Performance management of transmission line tower foundations against corrosion by non destructive testing. *International Journal of Engineering and Advanced Technology*, 9(3), 443–447. <https://doi.org/10.35940/ijeat.c4731.029320>
- Kumar, V., Sharma, N., Tiwari, S. K., & Kango, S. (2020). Atmospheric corrosion of materials and their effects on mechanical properties: A brief review. *Materials Today: Proceedings*, 44, 4677–4681. <https://doi.org/10.1016/j.matpr.2020.10.939>
- Kwan, M. S., Tangang, F. T., & Juneng, L. (2013). Projected changes of future climate extremes in Malaysia. *Sains Malaysiana*, 42(8), 1051–1058.
- Lin, Z. C., & Yang, C. B. (1996). Evaluation of machine selection by the AHP method. *Journal of Material Processing Energy*, 57(3–4), 253–258. [https://doi.org/10.1016/0924-0136\(95\)02076-4](https://doi.org/10.1016/0924-0136(95)02076-4)
- Manninen, H., Ramlal, C. J., Singh, A., Rocke, S., Kilter, J., & Landsberg, M. (2021). Toward automatic condition assessment of high-voltage transmission infrastructure using deep learning techniques. *International Journal of Electrical Power and Energy Systems*, 128, Article 106726. <https://doi.org/10.1016/j.ijepes.2020.106726>
- Naranpanawe, L., Ma, H., Saha, T. K., Lee, C., & Ghosal, A. (2020). A practical health index for overhead conductors : Experience from Australian distribution networks. *IEEE Access*, 8, 218863–218873. <https://doi.org/10.1109/ACCESS.2020.3042486>
- Pongsaksawad, W., Klomjit, P., Khamsuk, P., Sorachot, S., Pålsson, N. S., & Viyanit, E. (2021). Chloride distribution model and corrosion map of structural steels for tropical climate in Thailand. *Science of the Total Environment*, 787, Article 147465. <https://doi.org/10.1016/j.scitotenv.2021.147465>
- Rajesh, G., & Malliga, P. (2013). Supplier selection based on AHP QFD methodology. *Procedia Engineering*, 64, 1283–1292. <https://doi.org/10.1016/j.proeng.2013.09.209>
- Ricci, G., Bertella, R., Prato, S., & Zippo, M. (2018, October 3-5). *A.R.I.E.L: A structural integrity condition based method for renewal assessment of pylons in overhead transmission lines*. [Paper presentation]. AEIT International Annual Conference, Bari, Italy.
- Rodger, J., Bartlett, S., & Atrens, A. (2017). Corrosion of the galvanising of galvanised-Steel electricity transmission towers. *Materials and Corrosion*, 68(8), 902–910. <https://doi.org/10.1002/maco.201609351>
- Saaty, T. L. (2008). Decision making with the analytic hierarchy process. *International Journal of Services Sciences*, 1(1), 83–98. <https://doi.org/10.1504/IJSSCI.2008.017590>

- Saaty, T. L. (1977). A scaling method for priorities in hierarchical structures. *Journal of Mathematical Psychology*, 15(3), 234–281. [https://doi.org/10.1016/0022-2496\(77\)90033-5](https://doi.org/10.1016/0022-2496(77)90033-5)
- Sing, L. K., Yahaya, N., Othman, S. R., Fariza, S. N., & Noor, N. M. (2013). The relationship between soil resistivity and corrosion growth in tropical region. *Journal of Corrosion Science and Engineering*, 16, 1–11.
- Soufeiani, L., Foliente, G., Nguyen, K. T. Q., & Nicolas, R. S. (2020). Corrosion protection of steel elements in façade systems – A review. *Journal of Building Engineering*, 32, Article 101759. <https://doi.org/10.1016/j.job.2020.101759>
- Syed, S. (2006). Atmospheric corrosion of materials. *Emirates Journal for Engineering Research*, 11(1), 1–24.
- Tanaka, H., Tsukao, S., Yamashita, D., Niimura, T., & Yokoyama, R. (2010). Multiple criteria assessment of substation conditions by pair-wise comparison of analytical hierarchy process. *IEEE Transactions on Power Delivery*, 25(4), 3017–3023. <https://doi.org/10.1109/TPWRD.2010.2048437>
- Tang, K. H. D. (2019). Climate change in Malaysia: Trends, contributors, impacts, mitigation and adaptations. *Science of the Total Environment*, 650, 1858–1871. <https://doi.org/10.1016/j.scitotenv.2018.09.316>
- Triantaphyllou, E., & Mann, S. H. (1995). Using the analytic hierarchy process for decision making in engineering applications: Some challenges. *International Journal of Industrial Engineering: Applications and Practice*, 2(1), 35–44.
- Tsimberg, Y., Lotho, K., Dimnik, C., Wrathall, N., & Mogilevsky, A. (2014, April 14-17). *Determining transmission line conductor condition and remaining life*. [Paper presentation]. IEEE PES T&D Conference and Exposition, Chicago, USA. <https://doi.org/10.1109/tdc.2014.6863242>
- Usman, F., Khalid, N. H. N., Omar, R. C., & Jawas, M. J. A. (2021). Atmospheric corrosion map for service life prediction of lattice steel tower using air pollution data and meteorological data. *AIP Conference Proceedings*, 2339(1), Article 020189. <https://doi.org/10.1063/5.0044393>
- Usman, F., & Khalid, N. H. N. (2021). Predicting remaining life of lattice steel transmission tower based on condition assessment and corrosion hazard data. *E3S Web of Conferences*, 325, Article 01011. <https://doi.org/10.1051/e3sconf/202132501011>
- Usman, F., & Resdiansyah, M. (2008, June 16-20). *Service life prediction of building components*. International Conference on Construction and Building Technology (ICCBT), Kuala Lumpur, Malaysia
- Van-Der-Wal, A., Ross, A. A. H. J., & Kema, T. D. C. (2004). *Condition assessment of overhead lines* (Report No. B2-204). CIGRE. <https://www.e-cigre.org/publications/detail/b2-204-2004-condition-assessment-of-overhead-lines.html>
- Velásquez, R. M. A., & Lara, J. V. M. (2018, September 19-21). *Methodology for overhead line conductor remaining life aging infrastructure and asset management*. [Paper presentation]. IEEE PES Transmission & Distribution Conference and Exhibition - Latin America (T&D-LA), Lima, Peru. <https://doi.org/10.1109/TDC-LA.2018.8511752>
- Wang, J., Liu, P., Ren, K., Wang, X., & Xu, S. (2022). Corrosion of steel materials in four environmental conditions. *Journal of Physics: Conference Series*, 2390, Article 012002. <https://doi.org/10.1088/1742-6596/2390/1/012002>

- Waters, F. O. (1952). Soil resistivity measurements for corrosion control. *Corrosion- National Association of Corrosion Engineers*, 8(12), 407–409. <https://doi.org/10.5006/0010-9312-8.12.407>
- Wuller, A. I., & Pharmatrisanti, A. (2012, September 23-27). *Transmission line assessment*. [Paper presentation]. IEEE International Conference on Condition Monitoring and Diagnosis, Bali Indonesia. <https://doi.org/10.1109/CMD.2012.6416418>
- Zhang, D., Li, W., & Xiong, X. (2014). Overhead line preventive maintenance strategy based on condition monitoring and system reliability assessment. *IEEE Transactions on Power Systems*, 29(4), 1839–1846. <https://doi.org/10.1109/TPWRS.2013.2295379>
- Zhang, T., Liu, L., Wiliem, A., Connor, S., Ilich, Z., Van Der Draai, E., & Lovell, B. (2019, December 2-4). *Deep corrosion assessment for electrical transmission towers*. [Paper presentation]. Digital Image Computing: Techniques and Applications (DICTA), Perth, Australia. <https://doi.org/10.1109/DICTA47822.2019.8945905>



## Simulating Spanning Tree Protocols in a Cable-based Tsunameter System with an Arbitrary Number of Ocean Bottom Units

Mohammad Hamdani\*, Anak Agung Ngurah Ananda Kusuma, Dedy Irawan, Tahar Agastani and Xerandy

*Research Center for Telecommunications, National Research and Innovation Agency, KST BJ Habibie, Tangerang Selatan, Banten 15314, Indonesia*

### ABSTRACT

As a country with the fourth largest population in the world prone to tsunami disasters, Indonesia needs a reliable, timely early warning system to mitigate the impact of disasters. Indonesia cable-based tsunameter (INA-CBT) is an undersea tsunami detection system comprising undersea pressure sensors and a shore station connected by underwater fiber optics designed to provide early warning to the threatened area. Since this system performs a critical role in disaster mitigation, the system must be resilient to link failure and deliver timely warning information. This system is still in its early implementation and still on a small scale. Network-wise, it uses a proprietary Layer 2 (L2) communication protocol. Extending such a network to a larger scale and assessing the system's performance may introduce challenges due to high costs and offer less flexibility. This paper aims to address those challenges and presents a scalable simulation framework of the INA-CBT system by using L2 open protocols such as spanning tree protocol (STP) and rapid spanning tree protocol (RSTP). The framework is conducted in OMNET++ simulator. The experiment shows that the downtime duration using STP and RSTP is still below the allowed value. RSTP shows a faster failover time than STP, but RSTP downtime duration fluctuates

compared to a steady one of STP. The experiments also demonstrated that the variation of downtime is affected by two aspects: the number of ocean bottom units (OBUs) in the network and the position of their blocked port.

### ARTICLE INFO

#### Article history:

Received: 10 May 2023

Accepted: 17 January 2024

Published: 25 July 2024

DOI: <https://doi.org/10.47836/pjst.32.4.22>

#### E-mail addresses:

[moha049@brin.go.id](mailto:moha049@brin.go.id) (Mohammad Hamdani)

[anak001@brin.go.id](mailto:anak001@brin.go.id) (Anak Agung Ngurah Ananda Kusuma)

[dedy012@brin.go.id](mailto:dedy012@brin.go.id) (Dedy Irawan)

[taha001@brin.go.id](mailto:taha001@brin.go.id) (Tahar Agastani)

[xera001@brin.go.id](mailto:xera001@brin.go.id) (Xerandy)

\* Corresponding author

**Keywords:** Failover time, INA-CBT, network reliability, OMNET++, spanning tree protocols

## INTRODUCTION

A reliable and timely early warning system is essential in a nation's disaster management system to mitigate the adverse impacts of natural disasters. Japan, for example, has established its national marine science and technology agency, the Japan Agency for Marine-Earth Science and Technology (JAMSTEC), to promote ocean research and activities to better understand the ocean and earth. JAMSTEC also encourages post-disaster evaluation and research to manage, reduce, and mitigate disaster risks (Mikada et al., 2003). National Oceanic and Atmospheric Administration (NOAA) is a United States agency that deals with global ocean, atmospheric, and climate research and monitoring, which especially holds a crucial role during the nation's disaster season (Domenikiotis et al., 2003). Indonesia, a nation that is prone to tsunami hazards due to its unique location's geology characteristics, has developed a national early tsunami warning system called the Indonesia Tsunami Early Warning System (INA-TEWS), which was strongly motivated by devastating experience after being struck by an unprecedented tsunami in December 2004. One major component of INA-TEWS infrastructure is an underwater cable-based tsunami detection system, which is referred to as INA-CBT. This system monitors sea conditions for possible tsunami occurrence, especially following a strong ocean-epicenter earthquake event (Privadi et al., 2021).

The INA-CBT system architecture is a series of sensors connected by fiber optic cables stretched on the seafloor, linking the sensors to the shore landing station (LS). The observed sea points have the potential to detect earth cracks based on previous research (Widiyantoro et al., 2020). Those sensors are accelerometers, pressure sensors, and thermos sensors. They actively monitor and collect underwater conditions data for earthquakes, sea levels, and potential tsunamis. These data are sent to LS and then to the data center for consolidation and further processing. This results in intense data transfer between sensors and servers in the data center.

Incoming and outgoing data traffic across the sensors are only managed at L2 layer switching due to the complexity of using various devices. Because each sensor is embedded in an OBU with limited space and dimension, the devices must be efficient and have a small dimension to avoid overheating from their electronic components.

The switching process must be made fast during normal data transmission events, and quick self-recovery must be performed upon failure due to a link loss incident; this might change the switching path. According to the tsunami detection algorithm implemented in existing INA-CBT systems (Iqbal et al., 2021), the maximum downtime for such application is set at most six minutes to prevent failure of the tsunami detection system in detecting anomalies or incidents that might have occurred.

INA-CBT infrastructures were deployed in two different locations: Labuan Bajo (Purwoadi et al., 2023) and Rokatenda (Iqbal et al., 2021). Both implement ring topologies

with a proprietary, single-brand dependency ring protocol. These topologies are still feasible for both infrastructures since only a limited number of OBUs were observed, less than three units. At this configuration, the distance between the farthest sensor and the LS can still be accommodated by using an optical signal, even at the expense of using extra optical fiber lines. Exercising the system performance while incorporating proprietary protocol is still manageable at this scale. However, design challenges come into play when the network size of the system increases. Simple star topology may not be able to facilitate a larger number of OBUs, and multi-hop optical links are required. The ring topology must also be augmented on a larger scale and have more complex configurations. A proprietary L2 protocol with more complex configurations may limit design flexibility and compound performance assessment efforts. Furthermore, using proprietary L2 protocols may incur high implementation costs for larger systems.

A simulation framework is needed to address the issues above and evaluate the network performance at a scale. Hamdani et al. (2023) discussed that our study of the existing system proved that open protocols, i.e., STP and RSTP, could perform well under a stringent downtime requirement. The simulation demonstrated that the system suffered from downtime as long as 50 s by using RSTP, while it took only 22 s downtime before recovering by using RSTP. These results were far below the six minutes of maximum downtime allowed by the INA-CBT tsunami detection algorithm (Iqbal et al., 2021). This result also opened an opportunity for STP and RSTP protocol as a potential substitution for existing INA-CBT networks (Hamdani et al., 2023), even though they were still operated on a simple topology, namely one LS and two OBUs.

The future development of INA-CBT requires more OBUs to reach longer distances and better data accuracy from more sensors. The data communication will be even more complex, so extensive testing is needed before implementation. Our contribution to this paper is to test with a simulator the INA-CBT designs with a single LS and an arbitrary number of OBUs. Several simulations were carried out to measure the downtime that may occur in every possible incident and to assess whether the downtime is still within the timeframe required by the INA-CBT system.

## **MATERIALS AND METHODS**

### **Related Work**

STP is a link management protocol that creates logical connections between L2 nodes. The spanning tree protocol was first proposed in 1985 by Digital Equipment Company (DEC) (Perlman, 1985). In 1990, the Institute of Electrical and Electronics Engineers (IEEE) published the first standard for the protocol as IEEE 802.1D based on an algorithm designed by Perlman (2000). IEEE 802.1D standard, known as STP, has been widely utilized to eliminate traffic loops that might trigger broadcast storms in a network. In 2001, the IEEE

improved the STP protocol, namely RSTP, by releasing the IEEE 802.1w standard, followed by developing multiple spanning tree protocol (MSTP), entitled the IEEE 802.1s standard. RSTP and MSTP are two newer spanning tree protocols, where the improvement is in the speed of convergence and the capacity to handle multiple spanning trees with virtual local area networks (VLANs), respectively.

All STP models will prevent network loops by blocking one of the ports. The blocking port is chosen based on the device's lowest bridge ID, where the bridge ID is calculated from the bridge priority, the system ID extension/VLAN, and the bridge's MAC address. The formula for a bridge ID is in Equations 1 and 2:

$$bridgeID(8Bytes) = bridgepriority(2Bytes) + MACAddress(6Bytes) \quad [1]$$

$$bridgeID(8Bytes) = bridgepriority(4bits) + systemID\ extension/VLAN\ (12bits) + MACAddress(6Bytes) \quad [2]$$

The device with the lowest bridge ID will be elected as a root bridge, a reference point for all interconnected switches in a spanning tree topology. As shown in Figure 1, Switch1 (SW1) is elected as a root bridge because its MAC address is the lowest one, and bridge priorities are the same with the default value (32768) in all switches. Note that the election can be manipulated by setting a lower bridge priority value than the default on the desired switch. All ports that forward traffic and not facing the root bridge are denoted as designated ports (DP), while the ports that face a root bridge are denoted as root ports (RP). Ports that cannot forward traffic are denoted as blocked ports (BP).

A spanning tree can be used for redundancy and loop avoidance in a submarine communication system (Premod et al., 2013). Spanning trees can also improve redundancy in undersea sonar communication systems. In addition, the failover times of the three suggested redundancy approaches, namely STP, RSTP, and link aggregation (LAG), were compared, respectively. Similarly, in industrial network redundancy, as demonstrated by Gunnar's research, the utilization of the RSTP is prevalent, particularly in ring topologies (Prytz, 2007). The redundancy selection is determined based on the system's needs. For example, if the system serves a critical role and needs to be responsive, it is necessary to consider protocol with the fastest failover.

The application of spanning trees is also applied in network planning (Wang et al.,

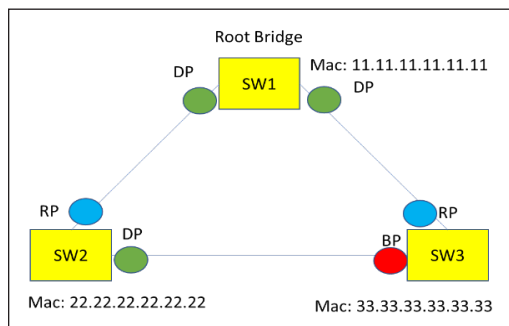


Figure 1. Spanning tree port assignment

2021). It formulated integer linear programming (ILP) to optimize the design of an optical network. The ILP method could achieve an optimal design with lower latency without network loops. Network design does not always consider Layer 2 communication between nodes. It can use Layer 3 instead, but in some cases, it requires Layer 2 communication due to data switching speed or the limited environment of the system.

In the context of improving network resiliency, the study by Marchese and Mongelli (2012) revealed that the spanning tree protocol has been the most cost-effective scheme among other L2 protocols needed to increase the resiliency of a network against link failures, especially in a ring topology. Spanning trees also build a resilient power grid topology (Kaiser & Witthaut, 2021). While using the spanning tree algorithm, calculations for link failures are conducted to analyze the topological structure to avoid the spread of link failures. It is proven that the spanning tree-based algorithm can increase the resilience of the network being built.

In general, spanning trees have been widely used to build network resilience because they are simple and easy to implement. Moreover, switch devices spanning three features are easy to find on the market. In the context of INA-CBT, in addition to network resilience among sensors and the LS, one must ensure sensor data reach the read-down station (RDS) within acceptable latencies constrained on the allocated bandwidth (Kusuma et al., 2022).

The STP algorithm is also widely used in advanced networks, such as virtual private networks (VPN) and software-defined networks (SDN). The work of Kolarov et al. (2004) discussed traffic engineering design for networks that support global open ethernet (GOE) architecture (Iwata et al., 2004), which was designed for VPN over optical network infrastructure. While the existing extensions of STP, such as RSTP and MSTP, use link metrics that are inversely proportional to link capacity, this work took the current link load into account and formulated a function to calculate the link cost. This scheme is applied in various topologies under different scenarios. Kolarov et al. (2004) observed significant improvement in network load balancing by having link cost as a function of the link load.

While STP protocol and its variants are utilized vastly in terrestrial wired and wireless networks, their application in underwater wireless networks may be arguably insignificant since this type of network in real practice is infrequent and mostly implemented wirelessly. This condition is probably due to the harsh water environment and being developed for a few specific purposes. Nevertheless, some works studied the application of the protocol in underwater networks.

Zhang et al. (2008) investigated the effectiveness of the spanning tree protocol in increasing the performance of underwater 3-D geographic routing in a wireless underwater sensor network. They explained that most spanning tree algorithms operate on a centralized and top-down approach, which results in poor routing performance for such networks. Therefore, they devised a spanning tree algorithm that used a bottom-up fashion with the

traffic load in mind called a traffic-aware routing tree. Concerning the context of this paper, it is a potential improvement applicable to our CBT network and worth further investigation.

Rather than directly implementing the current spanning tree protocol, Mupparapu et al. (2005) took the core idea of the spanning tree algorithm. It developed a novel routing scheme for underwater mobile ad hoc networks called AUSNET and COFSNET. This algorithm was developed based on dynamic source routing (Johnson & Maltz, 1996). This scheme used a spanning tree algorithm to compute the shortest path to the destination to reduce overhead in the route discovery process.

### Proposed Design and Method

This work proposed a CBT infrastructure with a single LS and multiple OBUs (Figure 2). These OBUs are arranged in series and installed on a straight line of sub-marine optical fiber. Although the OBUs are placed in such a way, they are logically connected in a ring fashion, and a spanning tree protocol runs on top of this topology. The ring topology is fairly efficient when operating under limited available transmission media (optical fiber) by long-distance, single-ended LS.

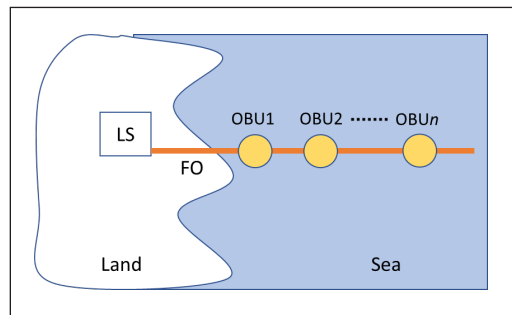


Figure 2. INA-CBT topology with a single landing station (LS)

As shown in Figure 2, the submarine-grade fiber optic cable extends from the LS onshore towards the sea. At a pre-determined distance interval, one or more OBUs are installed and linked to the optical fiber, in which the number of OBUs varies depending on needs, marked with OBU1, OBU2, and OBUn. The distance is not necessarily to be even. Each OBU has sensors to detect sea conditions and predict possible tsunamis, especially following sea-originated strong earthquake events.

Typically, a submarine fiber optic connects two communication endpoints separated by the sea. However, in a single LS INA-CBT configuration, the cable is only terminated at one side of the communication endpoint, the LS. Since LS also provides power to the OBUs, the electrical power is supplied from one source at the LS. So, the problem of breaking one of the connections is crucial because it can cause a loss of communication to a more distant OBU point.

This paper proposes a ring topology design such that the linkage from LS to OBUs forms a loop. This design can increase the robustness of the network in case of connection loss at one of the OBUs or fiber optic cores that connect between OBUs.

As depicted in Figure 3, data communication is designed to be connected sequentially from LS to OBU1, OBU2, OBU3, and OBUn. Each node represents a switch, which then

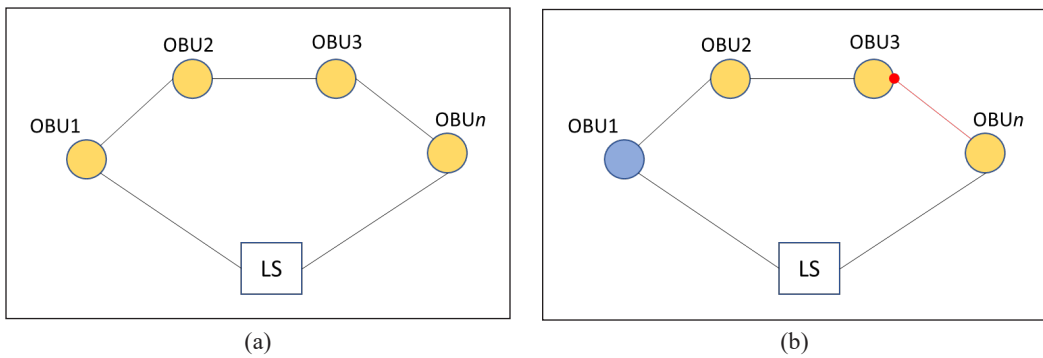


Figure 3. (a) Ring topology of INA-CBT before spanning tree being formed; and (b) Ring topology of INA-CBT after spanning tree has formed

forms an L2 loop. However, STP will avoid that by blocking one of the interconnection ports between two nodes in a ring topology. The blocked port that occurs can be located anywhere between two nodes in the network, depending on the position of the root bridge.

LS is the data destination transit center of all connected OBUs; hence, the root bridge must be at OBU1, and the active path (AP) will be OBU1 to LS. This condition can be done by configuring the OBU1 switch to become the root bridge using the bridge priority parameter with the smallest value. So, the blocked port will be among the last OBUs, and the OBU, which is at the end of the sequence (after the blocked port), will use a different path as an AP. If there is a communication loss on one of the links other than the blocked link, OBU will change its data route to the backup path (BP) depending on the location of the loss. The last block port will change its state to forward so that it can forward data, and the network loop will not happen since one of the links on the network has been broken.

In this work, ten OBUs are used as the maximum number of units and arranged in series. This arrangement considers the optical transmission capability for long-haul communications. The number of OBUs analyzed in this work starts from three since it extends the previous work (Hamdani et al., 2023), which used two OBUs in a series.

Each topology with a different composition of the number of OBU also has different characteristics. While the root bridge is set to OBU1 (since it is the nearest OBU with LS), the placement of the blocked port depends on the total number of nodes (LS is included on the total number of nodes) on the ring topology (odd or even). If the total number of nodes is even, it is obvious that the blocked port is in a certain OBU. For example, Figure 4(a) shows 6 nodes (5 OBUs and 1 LS) with the blocked port in OBU4. From the root bridge (OBU1) point of view, it counts the number of links in each tree (left or right) side. Then, a particular port that becomes a blocked state depends on the bridge ID calculated as Equation 1. If the bridge ID to the left tree is lower than the right one, the blocked port will face the right tree (OBU4 facing OBU5).

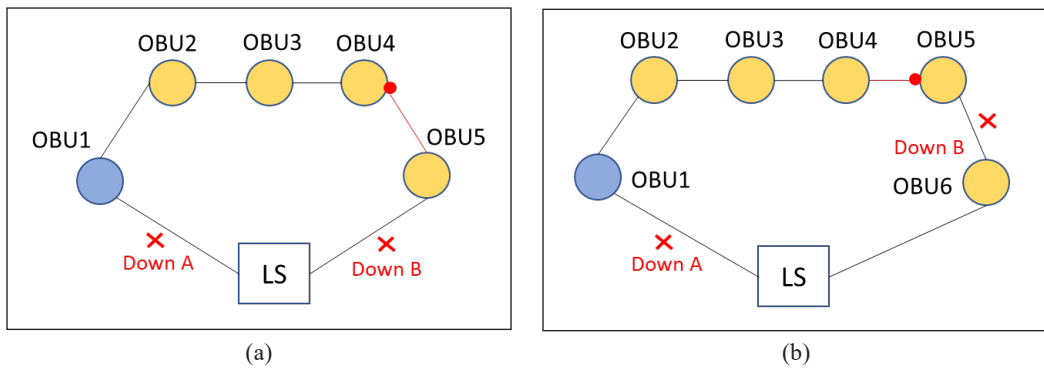


Figure 4. (a) Ring topology with single LS and five OBUs; and (b) Ring topology with single LS and six OBUs

If the number of nodes is odd, the blocked port will be between two OBUs, as shown in Figure 4(b), since the root bridge will balance all links connected from each tree side. Figure 4(b) shows 7 nodes (6 OBUs and 1 LS) where the blocked port is either in OBU4 or OBU5. Then, the calculation of bridge ID starts to determine which port will be assigned a blocked state. In this example, the port of OBU5 facing OBU4 is elected as a blocked port.

The down simulation is carried out on two links: the closest link between the root bridge to LS (down A) and the closest link to the blocked link to LS in the opposite direction (down B). This simulation is considered the worst incident that may occur during downtime. For example, when the nearest link is broken between the root bridge to the LS, the event being explored is when this broken link causes a major impact on the spanning tree topology. While the nearest link breaks between the blocked link to the LS in the opposite direction from the AP root bridge, the event being explored is the incident that causes an impact on any communication and the duration of the downtime.

Downtime measurement is performed on two events: failover and failback. Failover is downtime that occurs during down incidents until data traffic returns to normal. On the other hand, failback is downtime after the previous down incident has been recovered. It is known that the spanning tree checks its topology so that if there is a change, there will be downtime consequences under certain conditions. In the simulation, failover occurs at 100 seconds and failback at 300 seconds.

This simulation also compares using two spanning tree protocols, STP and RSTP. The two protocols are commonly used, and it is easy to get hardware devices supporting these protocols. Thus, simulation results will be an appropriate reference for real implementation. The method used is that each OBU performs a probing ping to the LS every second, with different time intervals, to avoid collisions. Downtime observations are made at each OBU when failover and failback occur from each down simulation. Furthermore, the downtime impact is compared to when the network uses STP or RSTP.

### Simulation

A simulation is needed to test the availability level based on a scenario where communication is lost on one of the links. Simulation can be done using software completely or by building a testbed system that represents the system being built (Babu & Kumar, 2022). Both simulation techniques have their advantages and disadvantages. For example, a simulation using software completely has advantages in the ease of changing parameters and values of a component, the scalability for testing various scenarios and designs, and the cost to implement. However, the drawback is that the user cannot experience hands-on in configuring physical devices. On the contrary, using testbeds offers hands-on experience with the real system. The drawbacks of the testbed system are that it is difficult to modify parameters and values as desired, the implementation cost is expensive, and its impact needs to be more scalable.

This work used Omnet++ 6.0 with the INET 4.4 framework to simulate a full software simulation. Omnet++ is a discrete event network simulator commonly used in academics because many network component parameters can be set and even developed for experimental needs (Varga, 2010). Omnet++ is easy to install on Windows and Linux platforms and has a friendly graphical user interface (GUI). The INET4.4 framework is a collection of features and functions that can be used in ethernet-based network simulations (Steinbach et al., 2011) so that users can easily create scenarios using various available protocols, such as Transmission Control Protocol (TCP) and User Datagram Protocol (UDP), even with varied traffic loads. In this simulation, the INET4.4 framework was used because it is in accordance with the INA-CBT communication scenarios, where each sensor inside the OBU communicates using TCP to LS. The available modules in the framework can represent all simulation components and the modules utilized in this simulation are shown in Table 1.

The first step in using the Omnet++ simulator is to build a network topology with the NED file, which functions to define all the components used in the simulation and create the topology (Figure 5). The next step is creating an INI file that defines simulation parameters, such as IP addresses, traffic applications, data transmission time intervals, downtime scenarios, and the simulation workflow (Algorithm 1).

Table 1  
*Modules that are used in the simulation*

Module	Objective
StandardHost	To represent the sensor inside the OBU for sending traffic data
EtherSwitch	To represent the switch inside the OBU for creating interconnection
Scenario Manager	To define the scenario, i.e., disconnection and re-connection link
L2NetworkConfigurator	To create a layer two topology with a spanning tree protocol
Ipv4NetworkConfigurator	To configure IPv4 and static routing

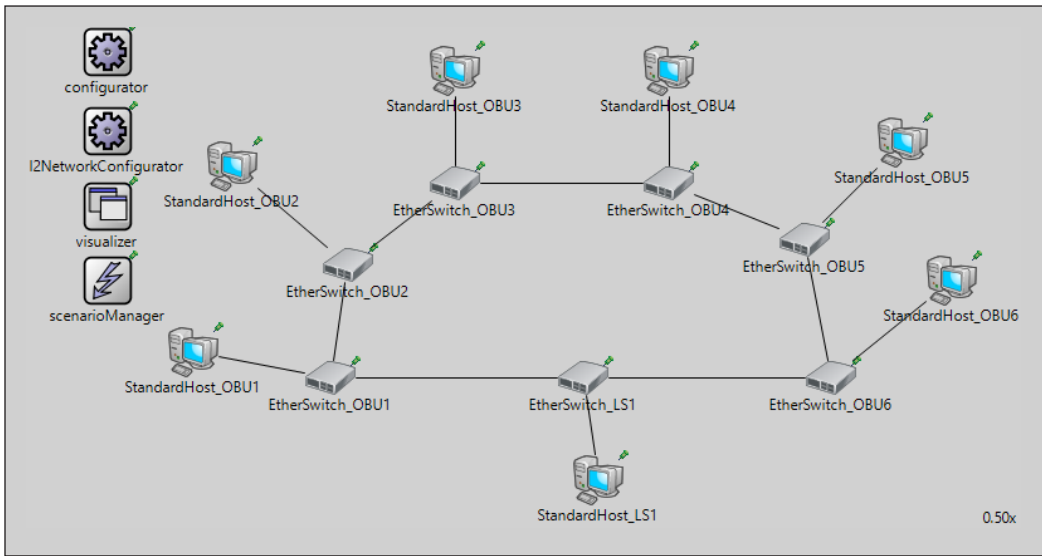


Figure 5. Simulation topology on Omnet++

## Algorithm 1

### INA-CBT Spanning Tree Simulation

- 
- 1  $S_n$   $\leftarrow$  switch of  $n$  node (for LS or OBU $n$ )
  - 2  $H_n$   $\leftarrow$  host of  $n$  node (for LS or OBU $n$ )
  - 3  $con_n$   $\leftarrow$  down connection of  $n$  (for A and B scenarios)
  - 4  $i_n$   $\leftarrow$  interval of a ping probe
  - 5  $tf$   $\leftarrow$  time failure (100 s)
  - 6  $tb$   $\leftarrow$  time failback (300 s)
  - 7 **Input:**
  - 8     set topology based on  $S_n$
  - 9     set ip\_address on each host
  - 10    set link between  $S_{LS}$  to  $S_{OBU1}$  to be the main\_path
  - 11    set protocol STP or RSTP on switches
  - 12 **Process:**
  - 13    set bridge\_priority  $S_{OBU1}$  to the lowest value (4096)
  - 14    set bridge\_priority  $S_{LS}$  to the second\_lowest (8192)
  - 15    **Loop**
  - 16       probe ping from all  $H_{OBU_n}$  to  $H_{LS}$  with  $i_n$
  - 17       **If** time meet to  $tf$
  - 18           scenario down  $con_n$  starts
  - 19           some  $H_{OBU}$  will be down

```

20          wait time to recover the success of sending a ping
21      Else time meet to tb
22          scenario recover con_n starts
23          some H_OBU will be down
24          wait time to recover the success of sending a ping
25      End loop if the spanning tree has been stable
26  Output:
27      Downtime

```

---

## RESULTS

A downtime was measured based on the ping probe made by each OBU to LS, and if it does not get a reply until a certain time, it is set as a timeout. Furthermore, downtime was tested using several criteria: failover and failback scenarios, the use of STP and RSTP, and simulated downtime on links A and B.

Since measurements were taken for each OBU, and several OBUs have the same downtime pattern, we summarize the OBU categories into nearest, middle, and farthest. The nearest OBU is closest to the down point (link A or link B); for example, down on link A (in all topologies), the nearest OBU is OBU1. The farthest is the OBU that is the farthest from the down point and the closest to the blocked link from the spanning tree calculation; for example, down on link A in a topology with six OBUs, the farthest OBU is OBU5. Meanwhile, the middle is a measurable OBU between the nearest and farthest, with the worst downtime value among them, regardless of the odd or even number of OBUs involved.

### Link Down at A

From the down simulation on link A, failover and failback using STP have the same pattern starting from four OBUs. Figures 6 and 7 show that the maximum downtime is 121 s at the nearest OBU and middle OBU. Whereas for three OBUs, the downtime on failback was 31 s faster than the downtime on failover.

Using RSTP, the downtime for the same scenario (link A down) is shorter than that of STP. In the failover simulation, the downtime values fluctuate for the nearest OBU and middle OBU (Figure 8), with a higher value for an odd number of OBUs, with a difference of 2 s longer between the nearest and middle. At the farthest OBU, the downtime values are steady at 16 s.

Figure 9 shows the failback downtime results of link A down with RSTP. The result shows that the nearest OBU's downtime values are steady at 1 s, the farthest OBU's downtime values surge starting from five OBUs and then steady at 27 s, and the middle OBU's downtime values tend to be linear with an increase in the number of OBUs.

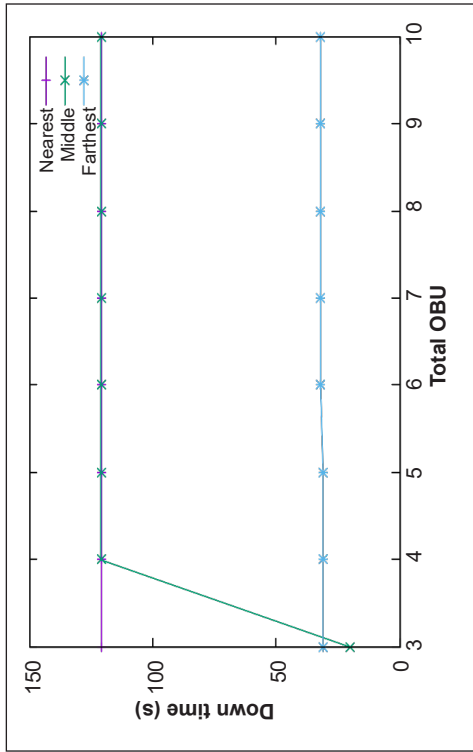


Figure 7. Failback downtime of link A down, using STP

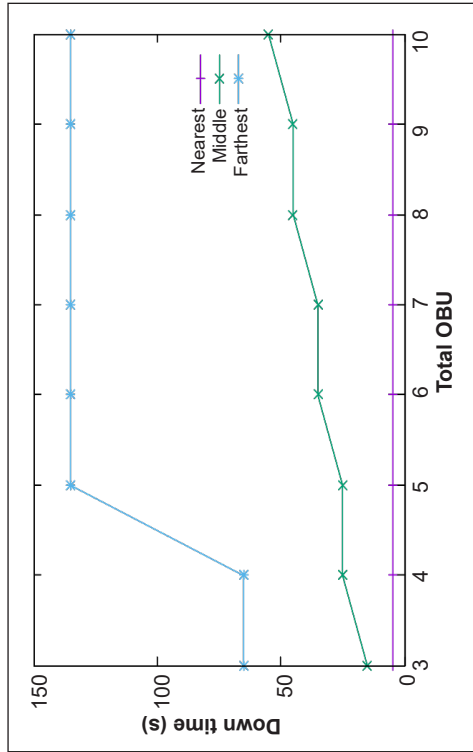


Figure 9. Failback downtime of link A down, using RSTP

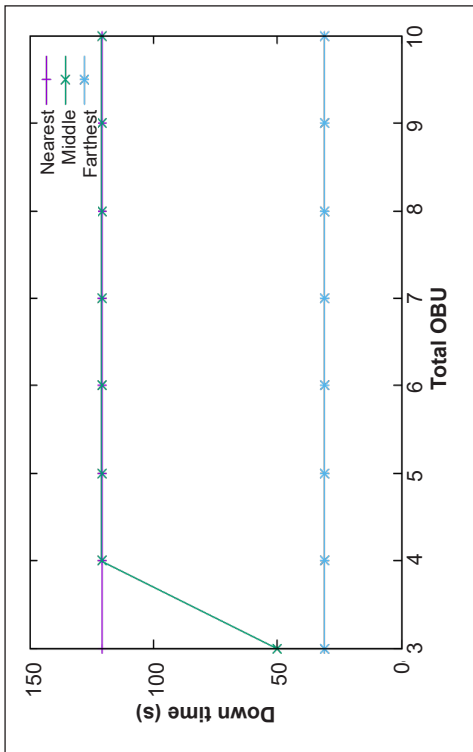


Figure 6. Failover downtime of link A down, using STP

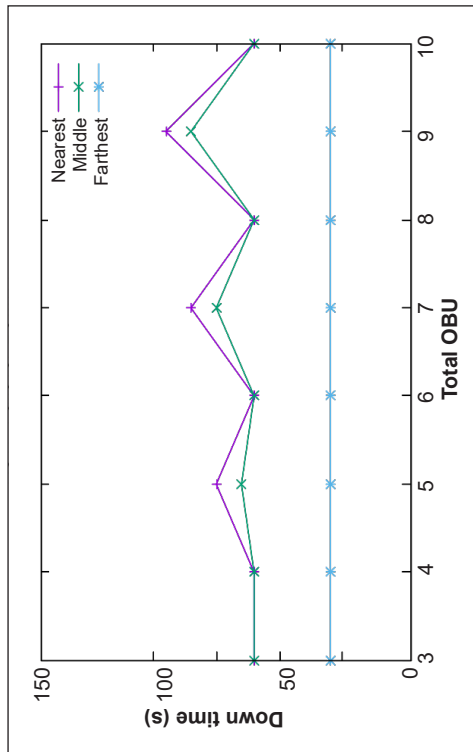


Figure 8. Failover downtime of link A down, using RSTP

### Link Down at B

The results in the link B down scenario are only the nearest category at STP and RSTP. In this scenario, the one affected is only the OBU with an AP on the link, and it does not impact the path of the root bridge. As a result, the failover downtime on STP is around the 90 s longer than on RSTP. The downtime values on RSTP fluctuate, and the ones with the odd number of OBUs are relatively longer than those of the even number of OBUs (Figure 10). In the failback event, the comparison between the nearest STP and RSTP is relatively static, with a 90 s gap between them (Figure 11).

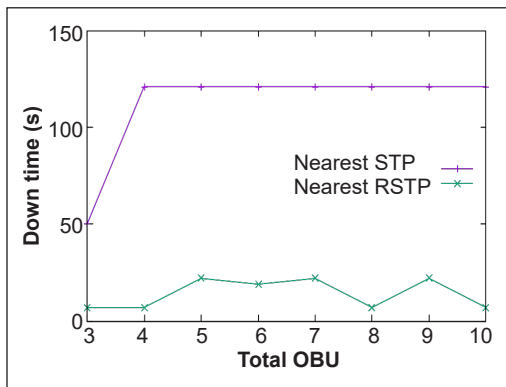


Figure 10. Failover downtime of link B down, comparing STP and RSTP

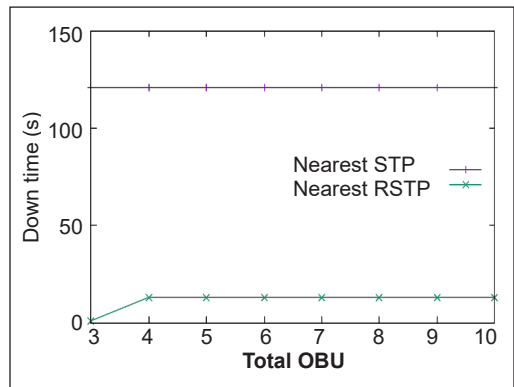


Figure 11. Failback downtime of link B down, comparing STP and RSTP

### DISCUSSION

STP behavior patterns for both downtime scenarios are mostly the same. This condition is because STP uses a delay timer to determine changes to the state of the spanning tree rather than changing it immediately once the trigger comes. In RSTP, the blocked port status can change instantly when the topology change notification (TCN) is obtained from the incident point so that data traffic can be streamed immediately. So, RSTP’s downtime is always lower than that of STPs.

RSTP has an interesting and different downtime pattern from STP, where its values fluctuate with the number of nodes, especially in failover scenarios due to the difference in distance from the incident point to nodes that have blocked ports in topologies that have an even or odd number of OBUs. When an incident occurs, the affected node will convey TCN to all nodes until it reaches the node with a blocked port and turns it into a forward state.

As shown in Figure 8, there is an interesting pattern where RSTP gives different downtime on odd and even OBUs. On odd OBUs, it shows higher downtime rather than that of even OBUs. It should be noted that the spanning tree configures all nodes inside the tree, including LS. The higher downtime in odd OBUs’ situations is due to the farther distance needed to send a TC message from the failure point to the blocked port.

The reason above has been tested by taking the different positions of the blocked port in even OBUs [eight OBUs (Figure 12)]. In the default condition, the spanning tree will calculate bridge IDs to place the blocked port on OBU6 facing OBU5 since OBU5 has a lower bridge ID (by MAC address). Then, the downtime that occurs during link A failover is 22 s. When manually changing the bridge priority value on OBU5 to be higher than the default value (32768), the blocked port changes to OBU5 facing OBU6, and the downtime that occurs with the same scenario is 27 s.

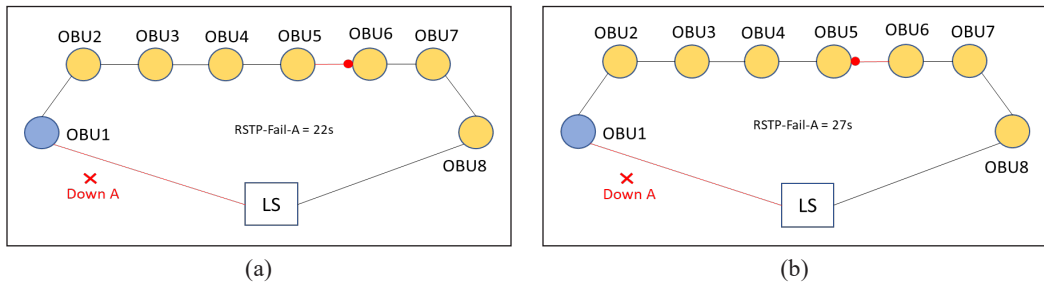


Figure 12. (a) Topology while OBU6 has a lower bridge ID as default; and (b) Topology while OBU5 has a lower bridge ID as manually configured

## CONCLUSION

This paper has presented a further assessment of using STP and RSTP for INA-CBT OBU to LS communication segment using simulation. The proposed model is scaled up successfully until ten OBUs with a ring topology. The experimental results show that the convergence time values in failover and failback scenarios are still below the system requirement of INA-CBT. As expected, RSTP shows a faster convergence time than STP, but one should be aware of the possible RSTP downtime fluctuations depending on the number of OBUs deployed. Further investigation is needed to assess the system’s dynamic behavior in scenarios with more complex topologies.

## ACKNOWLEDGEMENTS

The authors thank the National Research and Innovation Agency (BRIN), Indonesia, for supporting this research project.

## REFERENCES

- Babu, S., & Kumar, P. A. R. (2022). A comprehensive survey on simulators, emulators, and testbeds for VANETs. *International Journal of Communication Systems*, 35(8), Article e5123. <https://doi.org/https://doi.org/10.1002/dac.5123>
- Domenikiotis, C., Loukas, A., & Dalezios, N. R. (2003). The use of NOAA/AVHRR satellite data for monitoring and assessment of forest fires and floods. *Natural Hazards and Earth System Sciences*, 3(1/2), 115–128. <https://doi.org/10.5194/nhess-3-115-2003>

- Hamdani, M., Irawan, D., Kusuma, A. A. N. A., Agastani, T., & Iqbal, M. (2023). Preliminary assessment of using spanning tree open protocols in INA-CBT communication system. In P. H. Khotimah (Ed.), *The 2022 International Conference on Computer, Control, Informatics and its Applications* (pp. 6–10). Association for Computing Machinery (ACM). <https://doi.org/10.1145/3575882.3575884>
- Iqbal, M., Suwandi, B., Diana, M., Dewi, M. F., Herminawan, F. W., Giyana, R. F., Anggraeni, S. P., Firdaus, M. Y., Wibawa, Y. P., Palokoto, T. B., Utama, R. P., Marianto, F. A., Hamidah, M., Rahardjo, S., Purnomo, E., & Yogantara, W. W. (2021, November 8-9). *Performance analysis of Indonesia cable based tsunameter (INA-CBT) rokatenda ring topology*. [Paper presentation]. IEEE Ocean Engineering Technology and Innovation Conference: Ocean Observation, Technology and Innovation in Support of Ocean Decade of Science (OETIC), Jakarta, Indonesia. <https://doi.org/10.1109/OETIC53770.2021.9733745>
- Iwata, A., Hidaka, Y., Umayabashi, M., Enomoto, N., Arutaki, A., Takagi, K., Cavendish, D., & Izmailov, R. (2004). Global open Ethernet architecture for a cost-effective scalable VPN solution. *IEICE Transactions on Communications*, 87(1), 142–151.
- Johnson, D. B., & Maltz, D. A. (1996). Dynamic source routing in ad hoc wireless networks. In T. Imielinski, & H. F. Korth (Eds.), *Mobile Computing* (pp.153–181). Springer [https://doi.org/10.1007/978-0-585-29603-6\\_5](https://doi.org/10.1007/978-0-585-29603-6_5)
- Kaiser, F., & Witthaut, D. (2021). Topological theory of resilience and failure spreading in flow networks. *Physical Review Research*, 3(2), Article 23161. <https://doi.org/10.1103/PhysRevResearch.3.023161>
- Kolarov, A., Sengupta, B., & Iwata, A. (2004, November 29 – December 3). *Design of multiple reverse spanning trees in next generation of Ethernet-VPNs*. [Paper presentation]. IEEE Global Telecommunications Conference, Dallas, USA. <https://doi.org/10.1109/GLOCOM.2004.1378212>
- Kusuma, A. A. N. A., Agastani, T., Nugroho, T., Anggraeni, S. P., & Hartawan, A. R. (2022, December 6-7). *Estimating MQTT performance in a virtual testbed of INA-CBT communication sub-system*. [Paper presentation]. International Conference on Radar, Antenna, Microwave, Electronics, and Telecommunications (ICRAMET), Bandung, Indonesia. <https://doi.org/10.1109/ICRAMET56917.2022.9991213>
- Marchese, M., & Mongelli, M. (2012). Simple protocol enhancements of rapid spanning tree protocol over ring topologies. *Computer Networks*, 56(4), 1131–1151. <https://doi.org/10.1016/j.comnet.2011.10.008>
- Mikada, H., Hirata, K., Matsumoto, H., Kawaguchi, K., Watanabe, T., Otsuka, R., & Morita, S. (2003, June 25-27). *Scientific results from underwater earthquake monitoring using cabled observatories*. [Paper presentation]. International Conference Physics and Control. Proceedings (Cat. No.03EX708), Tokyo, Japan. <https://doi.org/10.1109/SSC.2003.1224100>
- Mupparapu, S. S., Bartos, R., & Haag, M. (2005, August 21-24). *Performance evaluation of ad hoc protocols for underwater networks*. [Paper presentation]. Fourteenth International Symposium on Unmanned Untethered Submersible Technology (UUST'05), Durham, USA.
- Perlman, R. (1985). An algorithm for distributed computation of a spanningtree in an extended LAN. *ACM SIGCOMM Computer Communication Review*, 15(4), 44–53. <https://doi.org/10.1145/318951.319004>
- Perlman, R. (2000). *Interconnections: Bridges, Routers, Switches, and Internetworking Protocols*. Addison Wesley.

- Premod, D. M., Kumar, K. S. A., Joseph, K. S., Kumar, B. K. P., Miny, G., & Sheno, V. S. (2013, October 23-25). *Network design for submarine sonar systems*. [Paper presentation]. Ocean Electronics (SYMPOL), Kochi, India. <https://doi.org/10.1109/SYMPOL.2013.6701937>
- Privadi, A., Damara, D. R., Widati, P. L., & Triputra, F. R. (2021, November 8-9). *Indonesia's cable based tsunameter (CBT) system as an earthquake disaster mitigation system in East Nusa Tenggara*. [Paper presentation]. IEEE Ocean Engineering Technology and Innovation Conference: Ocean Observation, Technology and Innovation in Support of Ocean Decade of Science (OETIC), Jakarta, Indonesia. <https://doi.org/10.1109/OETIC53770.2021.9733734>
- Prytz, G. (2007, September 25-28). *Network recovery time measurements of RSTP in an ethernet ring topology*. [Paper presentation]. IEEE Conference on Emerging Technologies and Factory Automation (EFTA), Patras, Greece. <https://doi.org/10.1109/EFTA.2007.4416924>
- Purwoadi, M. A., Anantasena, Y., Pandoe, W. W., Widodo, J., & Sakya, A. E. (2023, March 6-9). *Introduction to Indonesian cable-based subsea tsunameter*. [Paper presentation]. IEEE Underwater Technology (UT), Tokyo, Japan. <https://doi.org/10.1109/UT49729.2023.10103368>
- Steinbach, T., Kenfack, H. D., Korf, F., & Schmidt, T. C. (2011, March 21-25). *An extension of the OMNeT++ INET framework for simulating real-time ethernet with high accuracy*. [Paper presentation]. Proceedings of the 4th International ICST Conference on Simulation Tools and Techniques, Barcelona, Spain.
- Varga, A. (2010). OMNeT++. In K. Wehrle, M. Gunes & J. Gross (Eds.) *Modeling and Tools for Network Simulation* (pp. 35–59). Springer. [https://doi.org/10.1007/978-3-642-12331-3\\_3](https://doi.org/10.1007/978-3-642-12331-3_3)
- Wang, T., Wang, X., Wang, Z., Guo, C., Moran, B., & Zukerman, M. (2021). Optimal tree topology for a submarine cable network with constrained internodal latency. *Journal of Lightwave Technology*, 39(9), 2673–2683. <https://doi.org/10.1109/JLT.2021.3057171>
- Widiyantoro, S., Gunawan, E., Muhari, A., Rawlinson, N., Mori, J., Hanifa, N. R., Susilo, S., Supendi, P., Shiddiqi, H. A., Nugraha, A. D., & Putra, H. E. (2020). Implications for megathrust earthquakes and tsunamis from seismic gaps south of Java Indonesia. *Scientific Reports*, 10(1), Article 15274. <https://doi.org/10.1038/s41598-020-72142-z>
- Zhang, L., Kim, T. H., Liu, C., Sun, M. T., & Lim, A. (2008, December 15-18). *Traffic-aware routing tree for underwater 3-D geographic routing*. [Paper presentation]. International Conference on Intelligent Sensors, Sensor Networks and Information Processing, Sydney, Australia. <https://doi.org/10.1109/ISSNIP.2008.4762036>

## Optimum Parameters for Extraction of *Cinnamomum verum* Leaves Towards $\alpha$ -Glucosidase Inhibition

Leong Yao Shen<sup>1</sup>, Norhayati Muhammad<sup>1\*</sup>, Hariz Haikal Nasuha<sup>2</sup>, Mohd Fadzelly Abu Bakar<sup>1</sup>, Norazlin Abdullah<sup>1</sup> and Nur Fazira Abdul Rahim<sup>1</sup>

<sup>1</sup>Department of Technology and Natural Resources, Faculty of Applied Sciences and Technology, Universiti Tun Hussein Onn Malaysia, 84600 Muar, Johor, Malaysia

<sup>2</sup>Nasuha Herbs and Spice Farm, Jalan Muar, 84500 Muar, Johor, Malaysia

### ABSTRACT

*Cinnamomum verum* (kayu manis) is an herb that possesses antidiabetic properties and has been used for the treatment of diabetes traditionally. However, there is insufficient scientific data to provide optimum extraction parameters for *C. verum* leaves for antidiabetic activities. This research aims to determine the optimum extraction parameters of *C. verum* leaves towards  $\alpha$ -glucosidase inhibition and evaluate the correlation between  $\alpha$ -glucosidase inhibition, total phenolic content and DPPH radical scavenging activity. The *C. verum* was extracted with water through an infusion method under different temperatures (60.0°C, 77.5°C, 95.0°C) and extraction time lengths (10 minutes, 20 minutes, 30 minutes). The optimization process was designed using Design Expert software, which applied the Response Surface Method (RSM) and Central Composite Design (CCD). The analyses conducted were antidiabetic property ( $\alpha$ -glucosidase inhibition assay), total phenolic content (TPC) (Folin-Ciocalteu colorimetric method) and antioxidant property (2,2-diphenyl-1-picrylhydrazyl, DPPH radical scavenging activity). Results showed that the obtained optimum extraction parameters for *C. verum* leaves (81.10°C, 19.54 minutes) exhibited  $\alpha$ -glucosidase inhibition (87.30±0.67%), total phenolic content (0.12±0.00 mg GAE/g) and DPPH radical scavenging activity (51.25±0.48%). The

$\alpha$ -glucosidase inhibition positively correlates with DPPH radical scavenging activity and total phenolic content. These findings have provided a positive relationship between extraction temperature and extraction time length on antidiabetic properties of *C. verum* leaf extract.

**Keywords:** Antidiabetic, *Cinnamomum verum*, extraction parameter, infusion, Response Surface Method (RSM)

### ARTICLE INFO

#### Article history:

Received: 10 May 2023

Accepted: 18 January 2024

Published: 25 July 2024

DOI: <https://doi.org/10.47836/pjst.32.4.23>

#### E-mail addresses:

gw220024@student.uthm.edu.my (Leong Yao Shen)

norhayatim@uthm.edu.my (Norhayati Muhammad)

writetohariz@gmail.com (Hariz Haikal Nasuha)

fadzelly@uthm.edu.my (Mohd Fadzelly Abu Bakar)

norazlinh@uthm.edu.my (Norazlin Abdullah)

fazirahim23@gmail.com (Nur Fazira Abdul Rahim)

\* Corresponding author

## INTRODUCTION

Globally, diabetes is a significant healthcare burden. According to projections made by the International Diabetes Federation (IDF), 536.6 million individuals worldwide will have diabetes in 2021 (whether diagnosed or not). By 2045, that figure will have increased by 46% to 783.2 million (Ogurtsova et al., 2022). In Malaysia, diabetes cases also showed a drastic increase (15.77%), particularly in the prevalence of type 2 diabetes, which showed 14.39% (Akhtar et al., 2022). Three types of diabetes can be categorized: Type 1, Type 2, and gestational diabetes. Type 1 diabetes is an autoimmune disease caused by insufficient insulin production from  $\beta$ -cells. In contrast, the cause of type 2 diabetes is endocrine and metabolic disorders that lead to  $\beta$ -cell dysfunction in the pancreas and insulin resistance. For gestational diabetes, it can be caused by abnormal carbohydrate intolerance during pregnancy and eventually lead to maternal and fetal morbidity (Singab et al., 2014). There are several types of analyses for determining antidiabetic properties, and one of the methods is through  $\alpha$ -glucosidase inhibition assay (Lee et al., 2019).

*Cinnamomum verum*, locally known as “kayu manis,” is a Malaysian herb with antidiabetic properties (Pathak & Sharma, 2021; Singh et al., 2020). *C. verum* is an evergreen tree dispersed throughout tropical and temperate nations like Malaysia, Sri Lanka, and India. It also contributes about 70% of bark production worldwide (Fachriyah et al., 2018). *C. verum* is a traditional folk herb used in several treatments, such as antidiarrheal and anti-flatulent, and as a spice for culinary use. It also possesses antioxidant properties and phenolic content that can be used in pharmaceuticals (Tatipamula et al., 2021). *C. verum* has anti-inflammatory, antibacterial, and anticancer properties (Pathak & Sharma, 2021).

Extraction is a process of separating potential phytochemical compounds from herbal plants. The plant components will solubilize through the extraction process to obtain the crude extract that contains phytochemical contents (Nguyen et al., 2019). There are several types of extraction methods, such as infusion, decoction, maceration, and others. This study used an infusion method to extract the *C. verum* leaves. It is a process that extracts chemical compounds from plant materials in a solvent such as water, oil or alcohol by allowing the materials to remain suspended in the solvent over a certain period and is usually conducted at a temperature range of 60°C to 90°C (Katarzyna et al., 2019). A previous study reported that infusion extracts thermo-labile compounds under different extraction temperatures and extraction time lengths (Carmen et al., 2022). Both extraction parameters can affect the solubility and diffusion of *C. verum* and affect the efficiency of extraction (Nguyen et al., 2019; Singab et al., 2014).

In this study, the optimization process was crucial in evaluating the optimum parameters or conditions for a certain process, and one of the common tools in the optimization process is response surface methodology (RSM). RSM combines modeling strategies, optimization techniques, design, and analysis experiments that utilize experimental data

to improve processes (Jakub & Agnieszka, 2021). This research aims to determine the optimum extraction parameters of *C. verum* leaves on  $\alpha$ -glucosidase inhibition through Design Expert software by applying RSM and central composite design (CCD). Besides that, the correlation between  $\alpha$ -glucosidase inhibition, total phenolic content and DPPH radical scavenging activity was also evaluated.

## MATERIALS AND METHODS

### Chemicals and Reagents

The chemicals used were p-nitrophenyl-D-glucopyranoside (pNPG),  $\alpha$ -glucosidase, quercetin, Folin-Ciocalteu reagent, gallic acid monohydrate, sodium carbonate that are from Sigma-Aldrich, United States. Meanwhile, 2,2-diphenyl-1-picrylhydrazyl (DPPH) is from Calbiochem, Germany, whereas methanol is from Fisher Scientific, United States.

### Preparation of Plant Materials

*Cinnamomum verum* leaves were collected from Nasuha Herbs & Spice Farm, Muar, Johor, Malaysia, in August 2021 and authenticated by Associate Professor Dr. Alona Cuevas Linatoc, a botanist from Universiti Tun Hussein Onn Malaysia (UTHM) with the voucher specimen number (NYM-02-20).

### Sample Extraction

The *C. verum* leaves were cleaned and dried by drying oven (UN160, Memmert, Cyprus), under temperature of 60°C until the moisture content of dried leaves reached lower than 10% when tested with a moisture analyzer (MS-70, A&D Weighing, United Kingdom). It was grounded into powder form using a blender (MX-V310KSL, Panasonic, Malaysia) and stored in a desiccator at room temperature (27°C–30°C) to retain its moisture. The dried powder was weighed at about 10 g, and it was added with 2 L of distilled water through an infusion method at different extraction temperatures (60.0°C, 77.5°C, 95.0°C) and extraction time lengths (10 minutes, 20 minutes, 30 minutes). The filter paper (Nice) with a size of 24 cm diameter was used to filter the extract, and it was stored in a chiller (4°C) for further analysis.

### Experimental Design

In this study, the Design Expert software (version 6.0.4, USA) produced 11 experimental runs through Response Surface Methodology (RSM) coupled with Central Composite Design (CCD) to determine the optimum extraction parameters for achieving maximum  $\alpha$ -glucosidase inhibition of *C. verum* leaves as shown in Table 1. The independent variables were the extraction temperature ( $X_1$ ) and extraction time length ( $X_2$ ), while the dependent

variables were  $\alpha$ -glucosidase inhibition assay ( $Y_1$ ), total phenolic content ( $Y_2$ ) and DPPH activity ( $Y_3$ ).

**Antidiabetic Property ( $\alpha$ -Glucosidase Inhibition Assay)**

The antidiabetic property of extracts was determined through  $\alpha$ -glucosidase inhibition assay with slight modifications (Lee et al., 2019). The *C. verum* leaf extract was prepared in a concentration of 0.05 mL/mL, and quercetin was used as the positive control at different concentrations (0.01 M, 0.001 M, 0.0001 M, 0.00001 M, and 0.000001 M). The  $\alpha$ -glucosidase enzyme (0.01 U/mL) and *p*-nitrophenyl-D-glucopyranoside (pNPG) substrate were prepared in 1 mM phosphate buffer (pH 6.8). In each cuvette, the sample (20  $\mu$ L) was added with 20  $\mu$ L of  $\alpha$ -glucosidase and 75  $\mu$ L of phosphate buffer; the solution was preincubated at 25.0°C for 10 minutes. After preincubation, pNPG (50  $\mu$ L) was added into the solution and re-incubated at 25°C for 5 minutes. The absorbance of the mixture was determined by using a UV-Vis-spectrophotometer (T60, PG Instruments, UK) at a wavelength of 405 nm. Sodium carbonate (0.2 M) was used to terminate the reaction. The higher inhibitory rate indicates the solution has a higher potential to inhibit the  $\alpha$ -glucosidase, and the inhibition rate was calculated using Equation 1:

$$Inhibition (\%) = \frac{A_{control} - A_{sample}}{A_{control}} \times 100 \tag{1}$$

Where,  $A_{control}$ : absorbance of control solution; and  $A_{sample}$ : absorbance of sample solution.

**Total Phenolic Content (TPC)**

As in a previous study, the total phenolic content (TPC) was analyzed using the Folin-Ciocalteu colorimetric method with minor modifications (Ainsworth & Gillespie, 2007). The standard solutions were prepared using gallic acid monohydrate at different concentrations, which are 0 mg/mL, 20 mg/mL, 40 mg/mL, 60 mg/mL, 80 mg/mL, and 100 mg/mL through serial dilution. Then, gallic acid solution (0.5 mL) was inserted for each concentration into a test tube filled with Folin-Ciocalteu reagent (1 mL) and distilled water (9 mL). About 0.5 mL of 7.5% sodium carbonate solution was added to the mixture and was stored in a dark place for 2 hours (Ainsworth & Gillespie, 2007; Kunyanga et

Table 1  
*Design layout for optimization process by using RSM*

Run order	Extraction temperature, $X_1$ (°C)	Extraction time length, $X_2$ (min)
1	60.0	20
2	60.0	10
3	77.5	10
4	95.0	20
5	95.0	30
6	95.0	10
7 <sup>a</sup>	77.5	20
8 <sup>a</sup>	77.5	20
9 <sup>a</sup>	77.5	20
10	77.5	30
11	60.0	30

Notes. (a) center point

al., 2012). These standard solutions were inserted into the UV-Vis-spectrophotometer to measure the absorbance at a wavelength of 725 nm, and the results were recorded using a standard calibration curve (Bisceglie et al., 2014). The *C. verum* leaf extract was treated with the same method as standard, and the TPC value of the leaf extract was calculated using Equation 2, and it was expressed as gallic acid equivalent (mg GAE/g):

$$TPC = C \times \frac{V}{m} \quad [2]$$

Where, C: Concentration of gallic acid from the calibration curve; V: volume of the extract used; and m: mass of the extract used.

### Antioxidant Activity (DPPH Radical Scavenging Activity)

The 2,2-diphenyl-1-picrylhydrazyl (DPPH) radical scavenging activity was carried out to test the antioxidant activity of the *C. verum* leaves (Vinci et al., 2022). The concentration of *C. verum* leaf extract used was 0.05 mL/mL. Then, the sample was pipetted into 2 mL of DPPH solution (prepared by dissolving DPPH in methanol) in a test tube and wrapped with aluminum foil. The test tubes of all samples were vortexed and placed in a dark place for 30 minutes. The incubation length was 30 minutes, and the *C. verum* leaf extract's absorbance was measured using a UV-Vis-spectrophotometer at a wavelength of 517 nm (Irda, 2015). The percentage of inhibition of DPPH radical scavenging activity was calculated based on the value of absorbance through the following Equation 3:

$$\text{Antioxidant Activity (\%)} = \frac{A_{\text{control}} - A_{\text{sample}}}{A_{\text{control}}} \times 100 \quad [3]$$

Where,  $A_{\text{control}}$ : absorbance of control solution; and  $A_{\text{sample}}$ : absorbance of sample solution.

### Statistical Analysis

Each studied analysis was done in triplicates for each run. The mean for the triplicate value of  $\alpha$ -glucosidase inhibition, TPC and DPPH radical scavenging activity was measured and analyzed to determine the extracts that possess the highest potential in  $\alpha$ -glucosidase inhibition. The statistical analysis and the result of analysis of variance (ANOVA) were carried out by using Design Expert 6.0.4® (State Ease, Inc) and SPSS® (IBM, 1.0.0.1406, United Kingdom) software, and it shows a significant difference when  $p < 0.05$  (Giovanni et al., 2020).

## RESULTS AND DISCUSSION

### Model Fitting

Model fitting is important in showing the mathematical model of RSM for optimization of extraction parameters of *C. verum* leaves on different analyses studied. Table 2 shows the

polynomial equation generated through Design Expert software to fit all the independent variables and their responding dependent variables. The positive sign indicates a synergistic effect for each equation, whereas the negative sign represents an antagonistic effect (Jakub & Agnieszka, 2021; Rahim et al., 2022).

Table 2  
Polynomial equations of *Cinnamomum verum* leaves extract

Responses	Equations
$\alpha$ -Glucosidase inhibition, $Y_1$	$Y_1 = 86.63 + 5.25 X_1 - 1.69 X_2 - 6.54 X_1^2 - 3.36 X_2^2 - 2.72 X_1 X_2$
Total phenolic content, $Y_2$	$Y_2 = 0.10 + 0.01X_1 + 5.03 e^{-003}X_2$
DPPH radical scavenging activity, $Y_3$	$Y_3 = 50.53 + 8.02 X_1 + 7.81 X_2 - 13.48 X_1^2 - 10.53 X_2^2 - 2.58 X_1 X_2$

Notes. ( $X_1$ ) extraction temperature ( $^{\circ}C$ ), ( $X_2$ ) extraction time length (minutes)

Table 3 shows the ANOVA for the  $p$ -value and F-value for *C. verum* leaf extract for all analyses. Table 3 presented that the  $p$ -values for the model of all analyses were less than 0.05. Meanwhile, the F-values achieved were greater than 1 for  $\alpha$ -glucosidase inhibition (220.94), TPC (15.42) and DPPH radical scavenging activity (1266.93). All analyses are significant as the  $p$ -value is less than 0.05 and the F-value is greater than 1 (Eleni, 2010). Besides that,  $p$ -values for the lack of fit on all analyses obtained were larger than 0.05, which indicates insignificant, and this signifies that the data was fitted to the model obtained (Duarte et al., 2021).

Table 3  
ANOVA for *Cinnamomum verum* leaf extract

Responses	ANOVA					
	Sum of squares	DF	Mean square	F-value	$p$ -value	Lack of fit
$\alpha$ -Glucosidase inhibition	391.1900	5	78.2400	220.9400	<0.0001	0.5503
TPC	0.0008	2	0.0004	15.4200	0.0018	0.0665
DPPH radical scavenging activity	1783.1300	5	356.6300	1266.9300	<0.0001	0.5965

Notes. Degree of freedom (DF), total phenolic content (TPC)

### Optimization of Extraction Parameters

Table 4 shows the results of different analyses on the influence of extraction temperature and extraction time length of *C. verum*. It shows that the percentage of  $\alpha$ -glucosidase inhibition has a higher value in run orders 4, 6, 7, 8 and 9, which are  $85.81 \pm 0.98\%$ ,  $86.34 \pm 0.49\%$ ,  $86.34 \pm 0.49\%$ ,  $86.13 \pm 0.49\%$  and  $86.45 \pm 1.33\%$ , respectively, with no significant difference among each other. The extraction conditions for these run orders were at  $77.5^{\circ}C$  and  $95.0^{\circ}C$ , and extraction time lengths of 20 and 30 minutes. The results

revealed that this range of extraction temperature and extraction time length show a high  $\alpha$ -glucosidase inhibition activity, which is similar to the previous study that reported the effect of high extraction temperature (98°C) and extraction time length (20 and 30 minutes) give a high  $\alpha$ -glucosidase inhibition of *Cinnamomum burmannii* (Ervina et al., 2019). Whereas the run orders 2 (70.86±0.32%) and 11 (72.57±0.74%) showed the lowest percentage of  $\alpha$ -glucosidase inhibition. It may be because the phenolic compounds present in the *Cinnamomum* species extracts might be degraded at low extraction temperature and extraction time length in a short period, and this may contribute to a lower potential of  $\alpha$ -glucosidase inhibition. One of the phenolic compounds contributing to the antidiabetic activity is coumarin, which exists in *C. verum* leaf extract (Goyal et al., 2018). It is supported by the previous study by Matsumura et al. (2000) that stated the coumarin was diffused out from leaves as the temperature of water increased and bound with  $\alpha$ -glucosidase active site to inhibit  $\alpha$ -glucosidase in the process of glucose production and eventually reduce blood glucose level. However, as the duration of extraction time length increased, it shows the  $\alpha$ -glucosidase inhibition percentage reduced, which may be influenced by the presence of phenolic compounds in *C. verum* leaves extract has been denatured as the extracts immersed in high temperature of water for a long period (Antony & Farid, 2022).

Table 4  
The effect of extraction temperature and extraction time length for all analyses

Sample / Run order	Extraction parameters		Analyses		
	Extraction temperature, X <sub>1</sub> (°C)	Extraction time length, X <sub>2</sub> (minutes)	Antidiabetic $\alpha$ -Glucosidase inhibition, Y <sub>1</sub> (%)	TPC, Y <sub>2</sub> (mg GAE/g)	Antioxidant activity DPPH radical scavenging activity, Y <sub>3</sub> (%)
1	60.0°C	20	74.39±2.42 <sup>dc</sup>	0.0912±0.00 <sup>f</sup>	29.33±0.36 <sup>gh</sup>
2	60.0°C	10	70.86±0.32 <sup>c</sup>	0.0910±0.00 <sup>f</sup>	7.98±0.46 <sup>i</sup>
3	77.5°C	10	84.63±1.78 <sup>ab</sup>	0.0914±0.00 <sup>c</sup>	31.99±0.13 <sup>f</sup>
4	95.0°C	20	85.81±0.98 <sup>a</sup>	0.0950±0.00 <sup>a</sup>	44.46±0.16 <sup>d</sup>
5	95.0°C	30	77.16±0.49 <sup>c</sup>	0.1061±0.00 <sup>a</sup>	40.05±0.20 <sup>e</sup>
6	95.0°C	10	86.34±0.49 <sup>a</sup>	0.1083±0.00 <sup>d</sup>	29.62±0.28 <sup>g</sup>
7	77.5°C	20	86.13±0.49 <sup>a</sup>	0.1101±0.00 <sup>cd</sup>	51.25±0.48 <sup>a</sup>
8	77.5°C	20	86.45±1.33 <sup>a</sup>	0.1151±0.00 <sup>cb</sup>	50.51±0.29 <sup>ab</sup>
9	77.5°C	20	87.30±0.67 <sup>a</sup>	0.1054±0.00 <sup>b</sup>	50.14±0.19 <sup>b</sup>
10	77.5°C	30	81.96±0.81 <sup>b</sup>	0.1149±0.00 <sup>a</sup>	47.69±0.11 <sup>c</sup>
11	60.0°C	30	72.57±0.74 <sup>dc</sup>	0.1156±0.00 <sup>f</sup>	28.72±0.06 <sup>h</sup>

Notes. a-h Means different letters at each column indicate significant differences ( $p < 0.05$ ), value is presented as mean  $\pm$  SD (n=3), total phenolic content (TPC)

In addition, it shows that the TPC values for run orders 4, 5 and 10 are similar, which are 0.0950±0.00 mg GAE/g, 0.106±0.00 mg GAE/g and 0.1149±0.00 mg GAE/g, respectively, as there are no significant different ( $p < 0.05$ ). The high TPC values can be obtained at

temperatures of 77.5°C and 95.0°C with an extraction time of 30 minutes. It indicates that the TPC values increased as the temperature increased. A previous study has shown a similar result with the extract of *Matricaria chamomilla* that was prepared by infusion method at extraction temperatures of 80.0°C and 100.0°C for 10 minutes displayed an increase of TPC values as the extraction temperature increased (Sotiropoulou et al., 2020). The extraction time length in this previous study is only 10 minutes, which may be due to the extraction temperature being slightly higher than in this study, which could degrade the compounds present in the plants when the duration of extraction is longer (Romero et al., 2020). Whereas run orders 1, 2 and 11 showed the lowest phenolic content with no significant difference ( $p>0.05$ ) at the condition of 60.0°C, 10 min; 60.0°C, 20 min, and 60.0°C, 30 min, respectively because at medium temperature (60.0°C), the cell wall of plants broke down in slower rate to allow the diffusion of phenolic compounds into the surrounding solution. However, the phenolic compound was increased with extraction time length because this provides sufficient time for the phenolic compound to diffuse out from the leaves (Nguyen et al., 2019). High TPC indicates a high potential for antidiabetic, as proven in the previous study where the phenolic compounds of *Origanum majorana* leaves can show significant hypoglycemic effect and  $\alpha$ -glucosidase inhibitory activity in rat intestines (Tatipamula et al., 2021).

Moreover, the antioxidant of *C. verum* leaf extracts is determined by DPPH radical scavenging activity. Run orders 7 and 8 have a high antioxidant ability, with the percentage of inhibition obtained at 51.25±0.48% and 50.51±0.29% with no significant difference ( $p>0.05$ ). It might be because of the presence of polyphenols in the extract of these run orders that could contribute to inhibiting the DPPH radicals by providing hydrogen atoms and turning them into colorless compounds (Alaraa et al., 2018; Kodagoda et al., 2023). Based on a previous study shows that the extract of *Garcinia forbesii* can reduce serum glucose levels, and it also possesses a strong radical scavenging activity; this indicates that the remedy with stronger antioxidation activity may also come along with high antidiabetic potential (Wairata et al., 2021).

### Mixture Proportion Optimization

Figures 1, 2, and 3 show the response surface plot of *C. verum* for the interaction effect between the extraction temperature and extraction time length on different analyses. Figure 1 shows the response surface plot on the percentage inhibition of  $\alpha$ -glucosidase assay. It shows that when the water temperature was at 95.0°C and the extraction time length was 10 minutes, it exhibited a high value of  $\alpha$ -glucosidase inhibition, between 88.30% and 83.84%. Whereas, when the *C. verum* leaves were soaked in the water at 60.0°C and extraction time length of 10 minutes, they showed a lower value of  $\alpha$ -glucosidase inhibition, which is 70.45%. It displays a trend that the percentage of  $\alpha$ -glucosidase inhibition will

increase as the temperature increases. However, the high temperature will also reduce the  $\alpha$ -glucosidase inhibition activity due to the loss of phenolic compounds (Matsumura et al., 2000). Doctor et al. (2020) supported this by showing that the phenolic compounds might partially degrade after being heated to 200.0°C for 60 minutes.

Figure 2 shows the response surface plot on the total phenolic content (TPC) assay. It shows a high value of TPC was achieved when the extraction condition was at 95.0°C of extraction temperature and 30 minutes of extraction length, which is 0.12 mg GAE/g. It is comparable to the previous study, where the TPC increased because the cell wall can be easily broken down under high temperatures, and prolonged extraction time length can provide sufficient time to break down cellulose to release phenolic compounds (Kunyanga et al., 2012).

Figure 3 shows the response surface plot on DPPH radical scavenging activity. The result showed that a high percentage of DPPH radical scavenging activity (52.00%) can be obtained at 95°C with an extraction time of 30 minutes. This result showed that the DPPH radical scavenging activity could be increased as the temperature increases but decreased when extracted at a longer extraction time. The longer extraction time

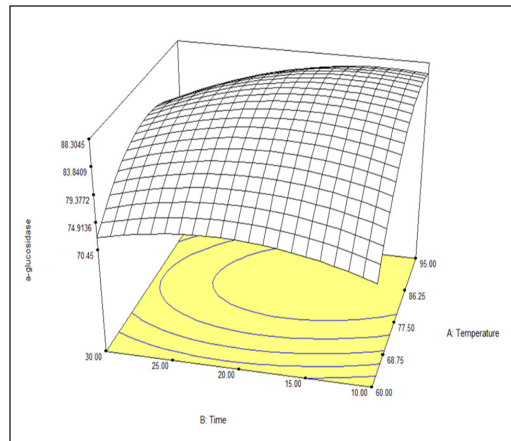


Figure 1. Response surface plot of *C. verum* leaves extract showing the effect of extraction temperature and extraction time length on  $\alpha$ -glucosidase inhibition percentage

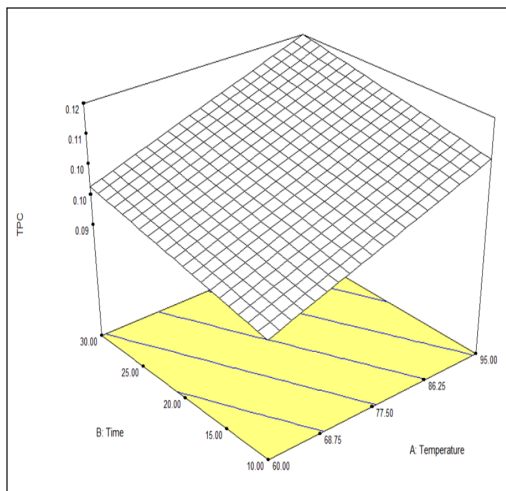


Figure 2. Response surface plot of *C. verum* leaves extract showing the effect of extraction temperature and extraction time length on total phenolic content

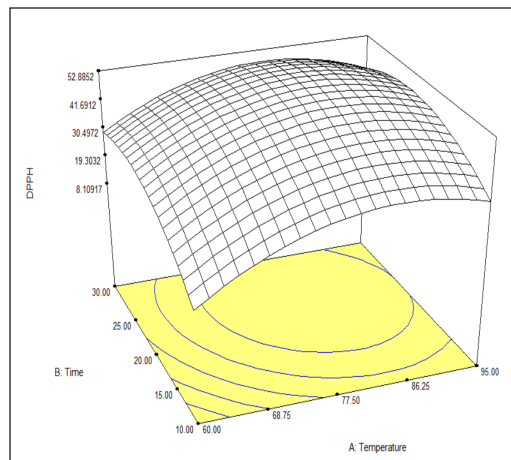


Figure 3. Response surface plot of *C. verum* leaves extract showing the effect of extraction temperature and extraction time length on DPPH radical scavenging activity

length might cause polyphenol degradation and, indeed, affect the antioxidant ability of the *C. verum* leaves (Antony & Farid, 2022). Phenolic compounds have redox characteristics that provide antioxidant activity as the hydroxyl group in plant extracts facilitates the scavenging of free radicals by the plant (Aryal et al., 2019). Hence, it can be concluded that TPC and DPPH radical scavenging activity are responsible for assessing antioxidant activity. Besides, DPPH radical scavenging activity has been widely used as it demonstrates a shorter time for analysis globally (Baliyan et al., 2022).

### Validation of the Model

Table 5 shows the validation values at an optimum *C. verum* leaves extract extraction condition. By using statistical software, the optimum extraction condition was found by maximizing the desirability responses, which are near to 1. The optimum extraction condition obtained was at an extraction temperature of 81.10°C with an extraction time of 19.5 minutes. At this condition, the  $\alpha$ -glucosidase inhibition was 83.51%, TPC values achieved was 0.12 mg GAE/g, and DPPH radical scavenging activity was 49.21%. The model’s validity was evaluated by the percentage of error achieved from the experimental and predicted values generated from Design Expert software. The error percentage should be below 5% to be considered valid and reliable as it showed a high confidence level (95%) with the true value of coverage probability (Liu et al., 2018). Table 5 shows that the validation value of all conducted analyses is below 5%, indicating a low percentage of error, and the results are reliable.

Table 5  
Experimental data of validation values at optimum extraction condition of *Cinnamomum verum* leaves extract

Responses	Predicted value	Experimental value	Percentage of error (%)
$\alpha$ -Glucosidase inhibition (%)	87.30	83.51	4.34
TPC (mg GAE/g)	0.11	0.12	2.00
DPPH radical scavenging activity (%)	51.27	49.21	4.01

Notes. Total phenolic content (TPC)

### Correlation Analysis

The correlation analysis was conducted among different analyses:  $\alpha$ -glucosidase inhibition activity, total phenolic content (TPC) and DPPH activity, as presented in Table 6. It showed that  $\alpha$ -glucosidase inhibition positively correlates with the TPC (0.63) and DPPH radical scavenging activity (0.76). It has been proven in previous studies that phenolic compounds possess high antioxidant activity along with high antidiabetic potential (Dias et al., 2020; Tatipamula et al., 2021). It indicates that  $\alpha$ -glucosidase inhibition increases as TPC and DPPH activity increases. Similar outcomes have appeared for the correlation of TPC and DPPH activity with other analyses. It is portrayed in Table 4 for run orders

Table 6  
Correlation analysis between analyses

Analyses		Pearson correlation	Significant different ( <i>p</i> -value)
$\alpha$ -Glucosidase inhibition	TPC	0.63	0.0438
$\alpha$ -Glucosidase inhibition	DPPH radical scavenging activity	0.74	0.0481
TPC	DPPH radical scavenging activity	0.76	0.0189

Notes. Total phenolic content (TPC)

7 and 8 for the TPC and antioxidant activity, whereas the antioxidant activity increases with increased extraction temperature and time.

## CONCLUSION

In a nutshell, we can deduce that the optimum extraction condition obtained was at an extraction temperature of 81.10°C with an extraction time length of 19.5 minutes exhibiting  $\alpha$ -glucosidase inhibition, 87.30%, TPC, 0.11 mg GAE/g and DPPH radical scavenging activity, 51.27%. Besides that, the correlation analysis showed that the  $\alpha$ -glucosidase inhibition positively correlates with the TPC and DPPH radical scavenging activity. Therefore, these findings can benefit the herbal industry as the optimum extraction parameters achieved can be a guideline for developing herbal products, particularly on products involving *C. verum* leaf extract.

## ACKNOWLEDGEMENTS

This research is supported by the Ministry of Higher Education (MOHE), Malaysia, through the Fundamental Research Grant Scheme (FRGS/1/2021/WAB13/UTHM/03/1) Vote No. K385, partially funded by University Tun Hussein Onn Malaysia (UTHM) under Postgraduate Research Grant Scheme (GPPS) Code Q227, and Nasuha Herbs and Spice Farm for supplying raw plant materials.

## REFERENCES

- Alaraa, O., Hamid, N., & Azharic, N. (2018). *Vernonia cinerea* leaves as the source of phenolic compounds, antioxidants, and anti-diabetic activity using microwave-assisted extraction technique. *Industrial Crops & Products*, 122(1), 533–544. <https://doi.org/10.1016/j.indcrop.2018.06.034>
- Akhtar, S., Nasir, J. A., Ali, A., Asghar, M., Majeed, R., & Sarwar, A. (2022). Prevalence of type-2 diabetes and prediabetes in Malaysia: A systematic review and meta-analysis. *PloS One*, 17(1), Article e0263139. <https://doi.org/10.1371/journal.pone.0263139>
- Ainsworth, E. A., & Gillespie, K. M. (2007). Estimation of total phenolic content and other oxidation substrates in plant tissues using Folin-Ciocalteu reagent. *Journal of Nature Protocols*, 2(4), 875–877. <https://doi.org/10.1038/nprot.2007.102>

- Antony, A., & Farid, M. (2022). Effect of temperatures on polyphenols during extraction. *Applied Sciences*, 12(4), Article 2107. <https://doi.org/10.3390/app12042107>
- Aryal, S., Baniya, M. K., Danekhu, K., Kunwar, P., Gurung, R., & Koirala, N. (2019). Total phenolic content, flavonoid content and antioxidant potential of wild vegetables from Western Nepal. *Plants*, 8(4), Article 96. <https://doi.org/10.3390/plants8040096>.
- Baliyan, S., Mukherjee, R., Priyadarshini, A., Vibhuti, A., Gupta, A., Pandey, R. P., & Chang, C. M. (2022). Determination of antioxidants by DPPH radical scavenging activity and quantitative phytochemical analysis of *Ficus religiosa*. *Molecules*, 27(4), Article 1326. <https://doi.org/10.3390/molecules27041326>
- Bisceglie, F., Pinelli, S., & Goldoni, M. (2014). Cinnamaldehyde and cumin aldehyde thiosemicarbazones and their copper and nickel complexes: a study to understand their biological activity. *Inorganic Biochemistry*, 140(1), 111–125. <https://doi.org/10.1016/i.jinorgbio.2014.07.014>
- Carmen, S. M., Benjamin, F. A., Vicente, S. S., Julissa, S. B., Lisette A. F., Alejandra, A. D., & Maria, E. Z. (2022). Antioxidant and antimicrobial capacity of *Maytenus boaria* leaves recovery by infusion and solvent extraction. *Electronic Journal of Biotechnology*, 56, 47–53. <https://doi.org/10.1016/j.ejbt.2022.02.002>
- Duarte, A. W., Bonugli-Santos, R. S. Duarte, A. L., & Gomes, E. (2021). Statistical experimental design applied to extracellular lipase production by the marine Antarctic yeast *Leucosporidium*. *Biocatalysis and Agriculture Biotechnology*, 32, 102-110. <https://doi.org/10.1016/j.bcab.2021.101954>
- Doctor, N., Parker, G., Vang, K., Smith, M., Berkant, K., & Yang, Y. (2020). Stability and extraction of vanillin and coumarin under subcritical water conditions. *Molecules*, 25(5), Article 1061. <https://doi.org/10.3390/molecules25051061>
- Dias, C., Fonseca, A. M., Amaro, A. L., Boas, A., Oliveira, A., & Santos, S. A. (2020). Natural-based antioxidant extracts as potential mitigators of fruit browning. *Antioxidants*, 9(8), Article 715. <https://doi.org/10.3390/antiox9080715>
- Ervina, M., Lie, H. S., Diva, J., Caroline, Tewfik, S., & Tewfik, I. (2019). Optimization of water extract of *Cinnamomum burmannii* bark to ascertain its in vitro antidiabetic and antioxidant activities. *Biocatalysis and Agricultural Biotechnology*, 19, Article 101152. <https://doi.org/10.1016/j.bcab.2019.101152>
- Fachriyah, E., Ariestiani, B., & Khikmah, L. (2018). Antidiabetic activity from cinnamaldehyde encapsulated by nanochitosan. *Conference on Materials Science and Engineering*, 349(1), 25–31. <https://doi.org/10.1088/1757-899X/349/1/012048>
- Goyal, M., Kaur, H., Bhandari, M., Rizvanov, A. A., Khaiboullina, S. F., & Baranwal, M. (2018). Antioxidant and immune effects of water soluble polysaccharides isolated from *Cinnamomum verum* bark. *Bio Nano Science*, 8(3), 935–940. <https://doi.org/10.1007/s12668-018-0542-3>
- Jakub, R., & Agnieszka, D. (2021). Application of response surface methodology (RSM) for the optimization of chromium (III) synergistic extraction by supported liquid membrane. *Membranes*, 11(11), Article 854. <https://doi.org/10.3390/membranes11110854>
- Kunyanga, C. N., Imungi J. K., & Okoth, M. W. (2012). Total phenolic content, antioxidant and antidiabetic properties of methanolic extract of raw and traditionally processed Kenyan indigenous food ingredients. *Journal of Food Science and Technology*, 45(2), 269–276. <https://doi.org/10.1016/j.lwt.2011.08.006>

- Katarzyna, J., Karolina, J., Patrycja, K., Mateysz, B., & Izabela, G. (2019). Mineral composition and antioxidant potential in the common poppy (*Papaver rhoeas*) petal infusions. *Biological Trace Element Research*, *199*, 371–381. <https://doi.org/10.1007/s12011-020-02134-7>
- Kodagoda, Y. K., Jayasinghe, C. V., & Dharmadasa, R. M. (2023). In vitro antioxidant and antidiabetic potential of five spiral ginger (*Costus speciosus* (J. Koeing sm) populations available in Sri Lanka. *Journal of Agriculture and Food Research*, *12*, Article 100553. <https://doi.org/10.1016/j.jafr.2023.100553>
- Lee, Y. R., Lee, S. H., Jang, G. Y., Lee, Y. J., Kim, M. Y., Kim, Y. B., Lee, J., & Jeong, H. S. (2019). Antioxidative and antidiabetic effects of germinated rough rice extract in 3T3-L1 adipocytes and C57BLKS/J-db/db mice. *Food & Nutrition Research*, *63*, 1-10. <https://doi.org/10.29219/fnr.v63.3603>
- Liu, L., Zhao, Y., Chang, D., Xie, J., Ma, Z., Sun, Q., & Yin, H. (2018). Prediction of short-term pv power output and uncertainty analysis. *Applied Energy*, *228*, 700–711. <https://doi.org/10.1016/j.apenergy.2018.06.112>
- Matsumura, T., Kasai, M., & Hayashi, T. (2000). a-glucosidase inhibitors from Paraguayan natural medicine Nangapiry, the leaves of *Eugenia uniflora*. *Journal of Pharmaceutical Biology*, *38*(4), 302–307. [https://doi.org/10.1076/1388-0209\(200009\)3841-AFT302](https://doi.org/10.1076/1388-0209(200009)3841-AFT302)
- Nguyen, Q. V., Tran, T. H., Pham, T. N., Thuoc, D. V., Cao, V. D., & Boo, K. H. (2019). Inhibitory effects of *Bidens pilosa* plant extracts on the growth of the bloom-forming alga *Microcystis aeruginosa*. *Water, Air & Soil Pollution*, *230*(24), 1-16. <https://doi.org/10.1007/s11270-019-4077-1>
- Ogurtsova, K., Guariguata, L., Barengo, N. C., Ruiz, P. L. D., Sacre, J. W., Karuranga, S., & Magliano, D. J. (2022). IDF diabetes Atlas: Global estimates of undiagnosed diabetes in adults for 2021. *Diabetes Research and Clinical Practice*, *183*, Article 109118. <https://doi.org/10.1016/j.diabres.2021.109118>
- Pathak, R., & Sharma, H. (2021). A review on medicinal uses of *Cinnamomum verum* (Cinnamon). *Journal of Drug Delivery and Therapeutics*, *11*(6-S), 161–166. <https://doi.org/10.22270/jddt.v11i6-S.5145>
- Rahim, N. F. A., Muhammad, N., & Abdullah, N. (2022). Optimum extraction condition of *Anacardium occidentale* on antiuro lithiatic activities (*in-vitro*). *Sains Malaysiana*, *51*(4), 1099–1109. <http://doi.org/10.17576/jsm-2022-5104-12>
- Romero, E. F., Chavez-Quintana, S. G., & Siche, R. (2020). The kinetics of total phenolic content and monomeric flavan-3-ols during the roasting process of *Criollo cocoa*. *Antioxidants*, *9*(2), Article 146. <https://doi.org/10.3390/antiox9020146>
- Singab, A. N., Youssef, F. S., & Ashour, M. L. (2014). Medicinal plants with potential antidiabetic activity and their assessment. *Medicinal and Aromatic Plants*, *3*(151), 2167–0412. <http://dx.doi.org/10.4172/2167-0412.1000151>
- Singh, N., Rao, A. S., Nandal, A., Kumar, S., Yadav, S. S., Ganaie, S. A., & Narasimhan, B. (2020). Phytochemical and pharmacological review of *Cinnamomum verum* J. persl-a versatile spice used in food and nutrition. *Food Chemistry*, *338*, Article 127773. <https://doi.org/10.1016/j.foodchem.2020.127773>
- Sotiropoulou, N. S., Megremi, S. F., & Tarantilis, P. (2020). Evaluation of antioxidant activity, toxicity, and phenolic profile of aqueous extracts of chamomile (*Matricaria chamomilla* L.) and sage (*Salvia officinalis* L.) prepared at different temperatures. *Applied Sciences*, *10*(7), Article 2270. <https://doi.org/10.3390/app10072270>

- Tatipamula, V. B., & Kukavica, B. (2021). Phenolic compounds as antidiabetic, anti-inflammatory, and anticancer agents and improvement of their bioavailability by liposomes. *Cell Biochemistry & Function*, 39(8), 926–944. <https://doi.org/10.1002/cbf.3667>
- Vinci, G., D'Ascenzo, F., Maddaloni, L., Antonia, S., & Tiradritti, M. (2022). The influence of green and black tea infusion parameters on total polyphenol content and antioxidant activity by ABTS and DPPH assays. *Beverages*, 8(2), Article 18. <https://doi.org/10.3390/beverages8020018>
- Wairata, J., Fadlan, A., Purnomo, A. S., Taher, M., & Ersam, T. (2022). Total phenolic and flavonoid contents, antioxidant, antidiabetic and antiplasmodial activities of *Garcinia forbesii* king: A correlation study. *Arabian Journal of Chemistry*, 15(2), Article 103541. <https://doi.org/10.1016/j.arabjc.2021.103541>

## Deflection Performance of Particleboards and Their Potential as Built-in Materials

Noor Azrieda Abd. Rashid\*, Hashim W Samsi, Nur Hanina Izzati Khairol Mokhtar, Yanti Abdul Kadir, Khairul Masseat, Siti Zaliha Ali and Muhammad Taufiq Tajuddin

*Forest Product Division, Forest Research Institute Malaysia, 52109 Kepong, Selangor Darul Ehsan, Malaysia*

### ABSTRACT

Particleboard is a commonly used material in the construction of furniture. It is an engineered wood product made from wood particles, such as wood chips, sawmill shavings, or sawdust, combined with a resin binder and compressed into sheets. The advantages of using this material are its uniformity, stability, and affordable price. Some performance must be tested to ensure its quality and strength properties so that it can be used as a built-in material. This study evaluated deflection performance based on the different thicknesses and sizes. The objective of this study was to determine the deflection properties over time. The deflection capabilities of particleboard with 16, 18 and 25 mm thicknesses and sizes of 400 × 384, 560 × 350, 760 × 330, 800 × 380 and 910 × 390 mm were investigated in three weeks. Remarkably, the particleboard with a 25 mm thickness exhibited markedly diminished deflection two to three times lower than that of 18 mm and 16 mm thickness, thereby showcasing its superior strength when subjected to various loads. Conversely, utilizing longer spans resulted in noteworthy deflection increments, implying that extended spans tend to manifest increased deflection as time progresses. These observations indicate that a thicker and shorter particleboard is well-suited for use as a building

material, given its lower deflection over time. In conclusion, this study elucidates the intricate relationship between particleboard characteristics and deflection behavior, providing valuable guidance for selecting suitable particleboards based on load requirements and structural considerations.

**Keywords:** Deflection, particleboard panels, size, strength, thickness, time

### ARTICLE INFO

#### Article history:

Received: 25 October 2023

Accepted: 02 January 2024

Published: 22 July 2024

DOI: <https://doi.org/10.47836/pjst.32.4.24>

#### E-mail addresses:

[azrieda@frim.gov.my](mailto:azrieda@frim.gov.my) (Noor Azrieda Abd. Rashid)

[hashimws@frim.gov.my](mailto:hashimws@frim.gov.my) (Hashim W Samsi)

[nurhanina@frim.gov.my](mailto:nurhanina@frim.gov.my) (Nur Hanina Izzati Khairol Mokhtar)

[yanti@frim.gov.my](mailto:yanti@frim.gov.my) (Yanti Abdul Kadir)

[khairulm@frim.gov.my](mailto:khairulm@frim.gov.my) (Khairul Masseat)

[sitizalehaali@frim.gov.my](mailto:sitizalehaali@frim.gov.my) (Siti Zaliha Ali)

[muhdtaufiq@frim.gov.my](mailto:muhdtaufiq@frim.gov.my) (Muhammad Taufiq Tajuddin)

\* Corresponding author

## INTRODUCTION

Exploration of enhancing material strength has led to a growing demand for composite materials in the construction sector. Composite panels revolutionize construction materials by merging multiple substances into a high-performance unit. These panels outshine individual materials in physical and mechanical properties (Jim, 2015; Masuelli, 2013). Material selection is the cornerstone of their design, focusing on unique qualities such as strength, weight, durability, insulation, and resistance to moisture and fire. By layering these materials, composite panels are precision-engineered to fulfill specific performance demands across various applications (Papadopoulos, 2020; Patnaik et al., 2020).

Common materials in composite panels encompass aluminum, fiberglass, carbon fiber, foam, plywood, and plastics. Wood composites, which encompass materials like chipboard, plywood, particleboard, blockboard, high-pressure laminate (HPL), medium-density fiberboard (MDF), and high-density fiberboards (HDF), are typically produced using synthetic adhesives known for their excellent waterproof and strong bonding qualities (Aliu et al., 2019). These composite panels can be customized for traits like rigidity or flexibility, making them invaluable across construction, transportation, aerospace, marine, and manufacturing industries. For instance, composite panels such as particleboard, blockboard, HPL and MDF are nowadays common materials for furniture due to their strength and durability. Notably, particleboard is a versatile and cost-effective example, crafted from waste wood materials such as wood chips, sawmill shavings, offcuts, and sawdust. It eventually makes it an ideal raw material for mass-producing panel-based furniture (Grzegorzewska et al., 2020; Malaysian Panel-Products Manufacturers' Association, 2023; Wu & Vlosky, 2000).

In the context of composite boards, two critical factors, "creep" and "deflection," are pivotal for assessing their strength and durability. Creep refers to the gradual deformation of a material over time under a sustained load or stress (Betten, 2008). In the context of particleboard, creep can result in permanent deformation, ultimately compromising the board's structural integrity. The extent of creep is influenced by a multitude of factors, including the magnitude of the applied load (Jeya & Bouzid, 2018), temperature conditions (Ayrilmis et al., 2009), and the intrinsic properties of the material (Georgiopoulou et al., 2015). Conversely, deflection is a critical parameter in understanding how a particleboard or any composite board behaves when subjected to external loads. It is the extent to which the board bends or flexes under the influence of applied forces. This property is instrumental in determining the board's structural integrity and suitability for specific applications (Rackham et al., 2009).

Particleboard deflection hinges on key factors. Firstly, load distribution is paramount, with uniformity reducing deflection, while uneven loads induce excess deflection and structural issues. The second factor is span length or the gap between supports, notably

impacts deflection, with longer spans prone to more deflection due to reduced support. Material stiffness is also vital, as stiffer materials decrease deflection, bolstering structural integrity. The next key factor is adequate edge support, essential in shelving or cabinetry applications. Lastly, environmental factors, like moisture and temperature fluctuations, can influence deflection, potentially weakening adhesives and affecting dimensional stability (Rackham et al., 2009; Tankut, 2009).

Furthermore, deflection testing is a standard procedure used to assess a panel's ability to withstand mechanical stress and deformation, providing valuable data for engineering and design purposes in various industries. Generally, the composite panel is subjected to incremental loading during the test until the desired load level or failure occurs. Deflection measurements are collected at predetermined locations on the panel's surface. This data allows engineers to evaluate the panel's stiffness, strength, and overall structural performance. The setup and apparatus for deflection testing can vary based on standards, test methods, and available equipment (Hardiyatmo, 2011; Sharaf et al., 2020; Zhao et al., 2021).

Manufacturers must implement strategies to improve their performance and durability to make composite panels suitable for use as a built-in material or in furniture construction (Fan & Schodek, 2007). It involves carefully choosing materials stiff and resistant to deformation over time. They also need to design their products to minimize bending or sagging when bearing typical loads (Jivkov et al., 2010; Liu et al., 2016). Installing these panels correctly according to the manufacturer's guidelines is crucial to prevent excessive forces or stress that could weaken their structural integrity. Additionally, in a technical bulletin by the Composite Panel Association (2022), the most important factors in designing a shelf system are shelf thickness and the distance between supports. The thicker the shelf and the closer the supports, the stronger the shelf will be and the less it will exhibit deflection.

Therefore, this study aimed to determine the impact of various thicknesses and dimensions on the deflection performance of a specific composite panel, specifically particleboard, over three-week. All particleboards of different thicknesses and sizes were subjected to three levels of loading, categorized as light, medium, and heavy, to ensure consistent results. The deflection tests were conducted following established procedures and standards (BS 4875-7, 2006; BS EN 16122, 2012; BS EN 16121, 2013) to assess the overall performance of the tested particleboard.

## **MATERIALS AND METHODS**

### **Materials**

Particleboard with 16 mm, 18 mm, and 25 mm thicknesses was manufactured and supplied by the composite panels industries in Peninsular Malaysia. A digital dial gauge and digital

caliper were purchased from Mitutoyo (Kanagawa, Japan), shelf support pin nails were obtained from common Malaysia’s supplier and measuring tape was purchased from Stanley (Maryland, USA).

### Specimen Preparation and Setup

A total of 18 particleboard samples were categorically distributed into three groups based on thickness: 16 mm, 18 mm, and 25 mm. Each sample’s length and width were meticulously measured and labeled (Figure 1a), resulting in six replicates per thickness category. The classification of each particleboard is shown in Table 1. Subsequently, all specimens were methodically supported by four shelf support pin nails, each with a width of 14.80 mm (Figure 1b). These pins were precisely centered on two parallel edges, maintaining a consistent spacing of 230 mm between them (Figure 1c). This meticulous setup and labeling procedure ensured uniformity and accuracy in the experimental process.

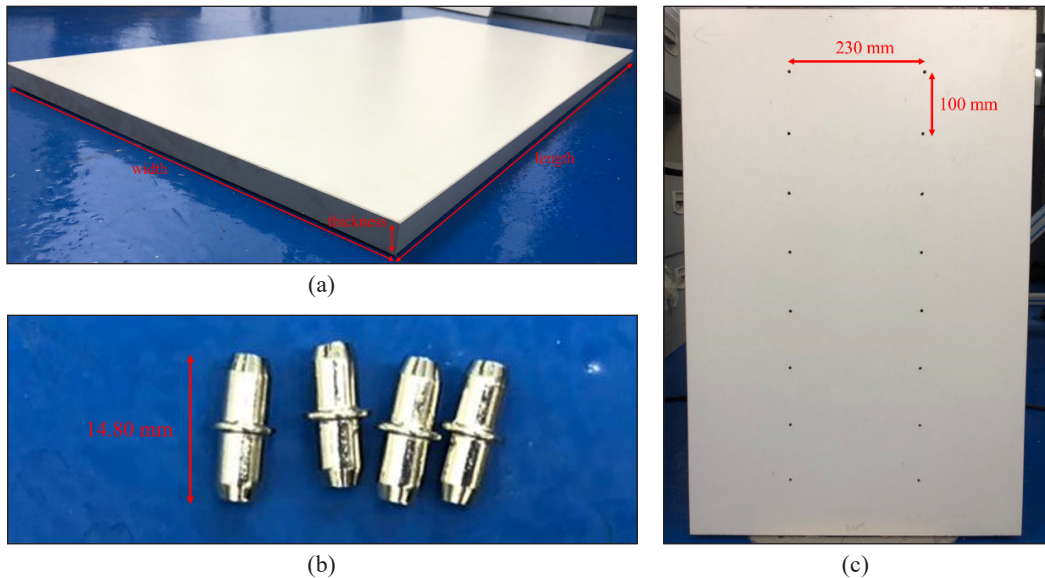


Figure 1. (a) Measurement of length, width and thickness of a particleboard; (b) shelf support pin nails; and (c) spacing between shelf supports on two parallel edges of the support board

Table 1  
Classification of particleboard tested based on different sizes and thicknesses

Label	Size (length × width), mm	Thickness, mm		
A	400 × 384	16	18	25
B	560 × 350	16	18	25
C	760 × 330	16	18	25
D	800 × 380	16	18	25
E	910 × 390	16	18	25

**Load Determination**

The load applied to the samples was calculated using a specific formula: the product of the sample’s area and a loading factor. This calculation was determined based on the standards, BS EN 16121 (2013), level 1–2 and BS 4875-7 (2006), level 5, where each loading factor was duplicated. For example, replicates 1 and 2 were subjected to a loading factor of 1.5, while replicates 3 and 4 had a loading factor of 2 applied. Replicates 5 and 6 were tested with a loading factor of 2.5. A summary of the load determination is shown in Table 2. Figure 2 shows the types of loads applied to the sample, which were 100 g, 500 g, 1 kg, 2 kg, 5 kg and 10 kg, respectively. This approach ensured a systematic and controlled variation in the applied loads across the experimental replicates.



Figure 2. Types of loads applied for deflection test of a particleboard

Table 2  
Summary of load determination according to loading factor for each particleboard

Label	Size (length × width), mm	Thickness, mm	Loading Factor/ Replicates						Total number of particleboards tested for each size
			1.5		2.0		2.5		
A	400 × 384	16	1	2	3	4	5	6	18
B	560 × 350	18	1	2	3	4	5	6	18
C	760 × 330	25	1	2	3	4	5	6	18
D	800 × 380		1	2	3	4	5	6	18
E	910 × 390		1	2	3	4	5	6	18
Overall									90

**Deflection Testing**

Deflection testing of the particleboard was performed at the FRIM Furniture Testing Laboratory (FTL) according to BS EN 16122 (2012), clause 6.1.4. The arrangement of all panels utilized a set of supporting boards (Figure 3a). Prior to subjecting the samples to load, an initial reading was taken using a dial gauge (Figure 3b) with an accuracy of ±0.01 mm to establish a baseline measurement. The deflection of the particleboard was measured at a point 10 mm from the front edge where the deflection is greatest. The loads were uniformly distributed onto the samples after determining the loading conditions. Subsequently, deflection readings were recorded immediately after the load

was applied. This deflection testing protocol was systematically conducted over three weeks, with readings documented at regular intervals of 24 hours.

### Statistical Analysis

Statistical analyses were performed using GraphPad Prism version 8.0.2. All data are presented as mean  $\pm$  SD. The means were compared using two-way analysis of variance (ANOVA) followed by Tukey's post-hoc test. Differences were considered statistically significant at  $p < 0.05$ .

## RESULTS AND DISCUSSION

### Deflection of Particleboard

The effects of three different particleboard thicknesses, 16 mm, 18 mm and 25 mm, on the deflection ( $\delta$ ) of the particleboards at varying sizes were investigated. Determination of the deflection performance over three weeks was carried out under constant load conditions. The sizes (length  $\times$  width) in mm tested were 400  $\times$  384 (A), 560  $\times$  350 (B), 760  $\times$  330 (C), 800  $\times$  380 (D), and 910  $\times$  390 (E).

#### *Particleboard of 16 mm in Thickness*

Overall, low deflection performances ( $\delta < 0.9$  mm) were observed for A and B compared to other sizes (Figure 4). This indicates that the loads applied to A and B had a lesser impact on the bending characteristics of the particleboard than on the other sizes. This phenomenon can be attributed to using a shorter span, leading to the lowest achievable maximum deflection, as indicated in prior research (D'Antino & Pisani, 2021). Conversely, the highest deflection value was recorded at the longest span, E, with a mean deflection measurement of  $\delta = 11.45$  mm. The deflection exhibited a peak on day 2 following the application of the loads, with a continuous increment observed until it reached a plateau after approximately one week.

During the testing of span C, the total deflection at the end of the week increased approximately 7 to 9 times in comparison to that of spans A and B. Similarly, span D also exhibited a notable increase in total deflection, ranging from approximately 4 to 8 times

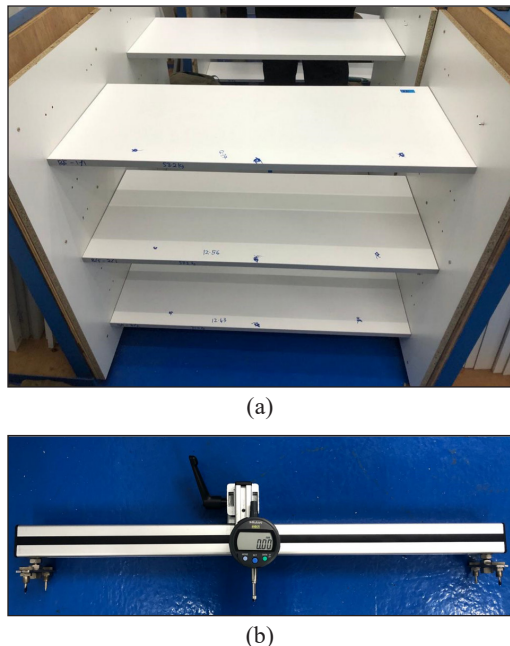


Figure 3. (a) Arrangement of panels on a set of supporting boards; and (b) a digital dial gauge used for deflection measurement

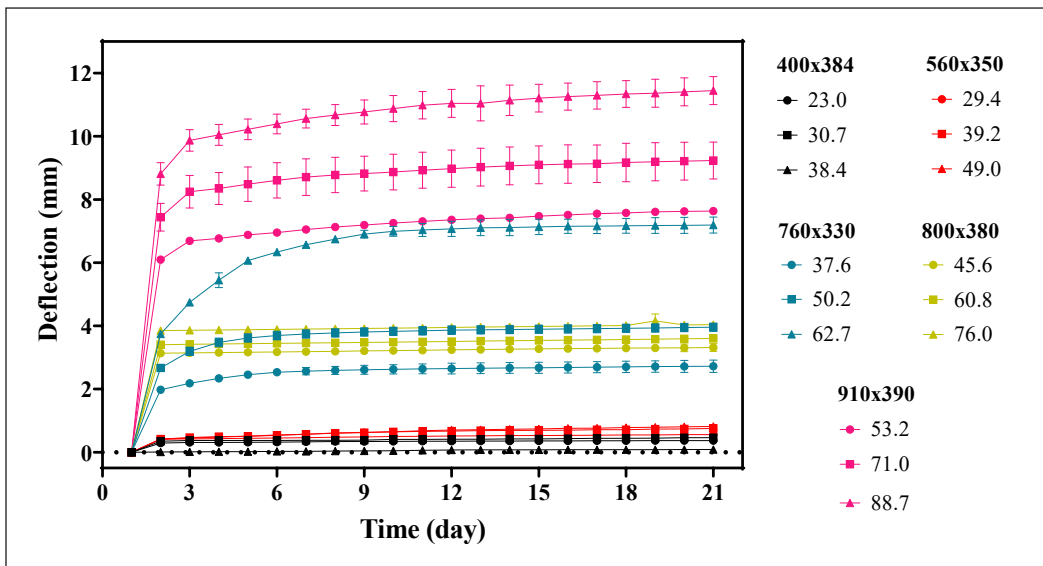


Figure 4. Performance of 16 mm-particleboard under loading with a factor of 1.5, 2 and 2.5 as denoted by “●”, “■” and “▲” shape

to that of spans A and B. This result revealed that spans C and D have similar deflective capabilities, especially in bearing loads weighing 45.6 kg to 60.8 kg.

Furthermore, the increase in the extent of this deflection corresponded directly to the loading factor employed for load determination. Specifically, the greatest deflection was observed when a loading factor 2.5 was applied across all span sizes, followed by loading factors of 2 and 1.5, in decreasing order of deflection magnitude. These findings underscore the significant influence of load weight on the overall performance of the particleboard and highlight the distinct effects of different particleboard sizes on deflection behavior.

### Particleboard of 18 mm in Thickness

When particleboards with a thickness of 18 mm were used, the same deflection pattern was observed (Figure 5). The highest deflection was consistently noted at the longest span, E, followed by D, C, B and A, for all load applied. In direct comparison to the 16 mm particleboard, it is noteworthy that the total deflection value for 18 mm thickness exhibited a reduction of 27%, with a recorded mean value of  $\delta = 9.04$  mm at span E. This reduction in the deflection strongly indicates that the increased thickness of the particleboard confers greater structural strength, thereby diminishing its susceptibility to deflection under load.

Additionally, the disparity in the overall deflection performance of span C was narrower for the 18 mm particleboard compared to the 16 mm variant, exhibiting a 29% to 59% reduction across all applied loads. Conversely, span D displayed heightened deflection with 18 mm thickness compared to the 16 mm thickness. Increasing board thickness should

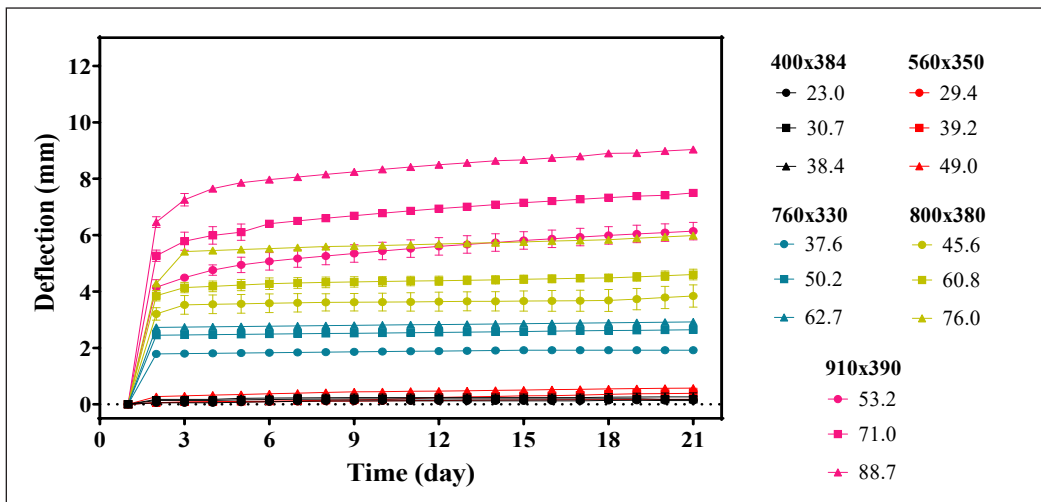


Figure 5. Performance of 18 mm-particleboard under loading with a factor of 1.5, 2 and 2.5 as denoted by “●”, “■” and “▲” shape

theoretically lead to decreased deflection due to the additional layers or plies, thereby enhancing its structural integrity (Composite Panel Association, 2022). Nevertheless, the results for span D deviate from this expectation, potentially due to imbalances in the panel structure, including aspects such as panel density or internal bond. Despite these observations, it remains evident that longer spans manifest greater deflection compared to shorter spans.

### Particleboard of 25 mm in Thickness

When examining particleboard with a thickness of 25 mm, a consistent deflection performance pattern was observed with that of the 16 mm and 18 mm variants, with the longest span, E, exhibiting the highest deflection ( $E > D > C > B > A$ ). However, a notable distinction for this particular thickness was the mean total deflection value, recorded at  $\delta = 3.93$  mm, occurring at span E under a loading factor 2.5 (Figure 6). It is worth emphasizing that this value represented a significant reduction, approximately two to three times lower when compared to the respective values observed for 18 mm and 16 mm thicknesses. This outcome again highlights the substantial influence that particleboard thickness exerts on the deflection performance of the panel.

Furthermore, in contrast to spans A and B, both spans C and D demonstrated an enhancement in deflection performance ranging from approximately 4 to 11 times, corroborating previous findings that longer spans tend to exhibit amplified deflection. It is worth noting that all tests were conducted in accordance with the prescribed standards (BS 4875-7, 2006; BS EN 16122, 2012; BS EN 16121, 2013), ensuring the reliability of the results and their potential for replication in future studies.

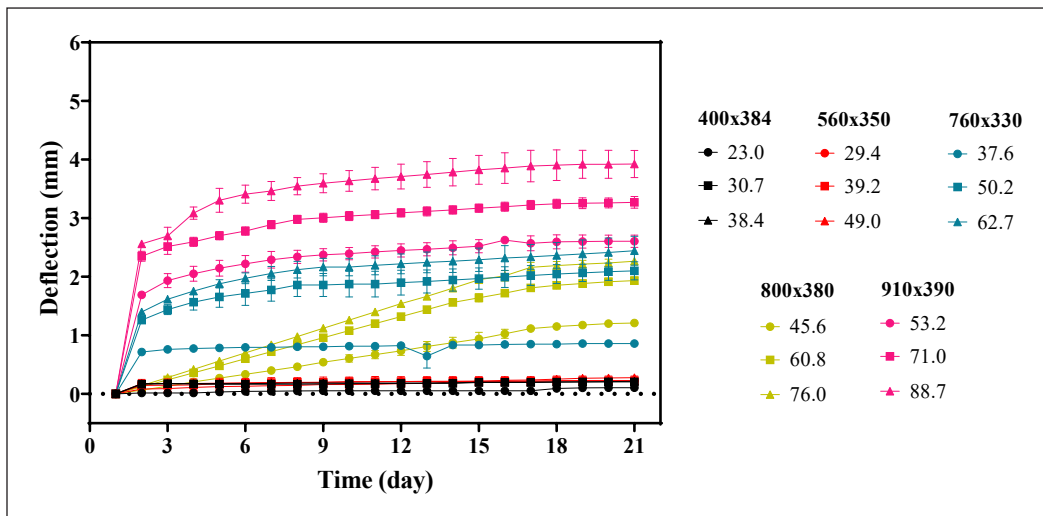


Figure 6. Performance of 25 mm-particleboard under loading with a factor of 1.5, 2 and 2.5 as denoted by “●”, “■” and “▲” shape

### Comparison Between All Thicknesses Tested

A comprehensive statistical analysis was performed to assess the significance of particleboard thickness and size and derive meaningful conclusions differences. The graphical representation of our findings exhibited a general trend of increasing deflection readings across all spans. Notably, a deviation from this trend was observed when thicker particleboard was employed (Figure 7). Upon closer examination, the analysis indicated no statistically significant differences in deflection performance among all thicknesses for spans A and B. It suggests that, at these specific spans, particleboard thickness had a relatively minor impact on deflection behavior. Furthermore, it is worth noting that loads ranging from 23 to 49 kg could be applied to both spans over three weeks without causing substantial deflection. It indicates that spans A and B, measuring  $400 \times 384$  and  $560 \times 350$ , respectively, demonstrated an equivalent strength and load capacity of up to 49 kg. Consequently, there is potential for material reduction in the furniture design at these specific sizes.

In contrast, it is important to highlight that the disparities in thickness exhibited statistically significant effects for spans C, D, and E. To illustrate, span C displayed marked differences in deflection performance when comparing the 16 mm thickness with 18 mm and 25 mm thicknesses across all applied loads. Similarly, span D revealed a statistically significant divergence in deflection when comparing the 25 mm thickness with the 16 mm and 18 mm variants, particularly under a load of 45.6 kg. Furthermore, it is noteworthy that, in the case of spans other than C and D, statistically significant differences emerged across all thicknesses for all loads applied to the specimens. This finding implies that thicker

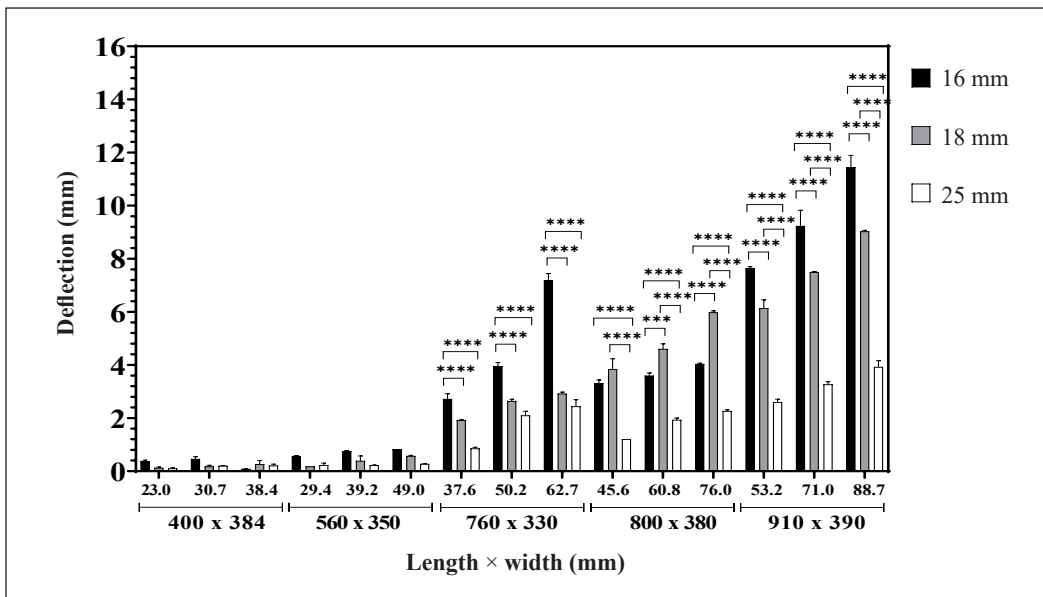


Figure 7. Comparison between particleboard thickness and sizes

particleboard demonstrates reduced deflection readings, while extended spans contribute to an increase in deflection readings over time.

According to Mirski et al. (2019), the thickness of particleboard predominantly correlates with two critical material properties: the modulus of rigidity and the tensile strength perpendicular to the board plane. Generally, when thickness increases, the modulus of rigidity tends to decrease, while the modulus of elasticity tends to increase. In the study of panel deflection, a uniform load was applied across the entire surface to simulate balanced stress, mimicking domestic use. Uneven loading on a shelf can result in exaggerated moments, potentially leading to rupture. The Composite Panel Association (1998) stated that the load, shelf span, and panel thickness influence the extent of shelf deflection. Moreover, the structural design of the panel's shelf is directly related to its maximum load-bearing capacity. This relationship underscores the importance of considering not only board thickness but also the geometric aspects of the material when assessing its mechanical properties and structural behavior.

## CONCLUSION

This study provides a practical exploration of how different particleboard thicknesses and sizes perform in terms of deflection over three weeks. Notably, the 25 mm-thick particleboards substantially reduced deflection, showcasing its superior strength under various applied loads. Conversely, longer spans revealed a notable increase in deflection performance, suggesting that particleboards spanning extended distances tend to exhibit

greater deflection over time. However, amidst this lies an opportunity for material optimization in furniture design at dimensions of  $400 \times 384$  and  $560 \times 350$ , as both sizes demonstrated comparable strength and a common load capacity. This research sheds light on the intricate relationship between particleboard thickness, span size, and deflection behavior over an extended duration. These findings offer valuable insights for the judicious selection of particleboard, especially in domestic storage applications, considering the requisite load-bearing capacities and structural considerations.

## ACKNOWLEDGEMENTS

This research was made possible by the generous support of the Twelfth Malaysia Plan (RMK 12) grant. The authors thank FRIM's Furniture Testing Laboratory (FTL), Malaysia, for providing the necessary infrastructure and facilities to conduct this research. Additionally, the authors appreciate the participants and volunteers who generously contributed their time and effort to make this study possible.

## REFERENCES

- Aliu, A. O., Daramola, A. S., & Fakuyi, F. F. (2019). Comparative analysis of deflective capability and breaking points of wood composites. *The International Journal of Engineering and Science*, 8(7), 25–27. <https://doi.org/10.9790/1813-0807012527>
- Ayrlimis, N., Laufenberg, T. L., & Winandy, J. E. (2009). Dimensional stability and creep behavior of heat-treated exterior medium density fiberboard. *European Journal of Wood and Wood Products*, 67(3), 287–295. <https://doi.org/10.1007/s00107-009-0311-7>
- Betten, J. (2008). *Creep Mechanics* (3rd ed.). Springer.
- BS 4875-7:2006. (2006). *Strength and stability of furniture: Domestic and contract storage furniture-Performance requirements*. British Standard.
- BS EN 16121:2013. (2013). *Non-Ddmestic storage furniture. requirements for safety, strength, durability and dtability*. British Standard
- BS EN 16122:2012. (2012). *Domestic and non-domestic storage furniture–Test methods for the determination of strength, durability and stability*. British Standard.
- Composite Panel Association. (1998). *Particleboard and MDF for shelving*. Composite Panel Association. [https://tafisa.ca/sites/default/files/documents/CPA\\_TB\\_Shelving.pdf](https://tafisa.ca/sites/default/files/documents/CPA_TB_Shelving.pdf)
- Composite Panel Association. (2022). *Particleboard and MDF for shelving*. Composite Panel Association. <https://www.compositepanel.org/wp-content/uploads/Technical-Bulletin-Particleboard-MDF-for-Shelving.pdf>
- D'antino, T., & Pisani, M. A. (2021). A proposal to improve the effectiveness of the deflection control method provided by eurocodes for concrete, timber, and composite slabs. *Materials*, 14(24), Article 7627. <https://doi.org/10.3390/ma14247627>

- Fan, J., & Schodek, D. (2007, September 16-19). *Personalized furniture within the condition of mass production*. [Paper presentation]. Proceedings of the 9th International Conference on Ubiquitous Computing Ubicomp, Innsbruck, Austria.
- Georgiopoulos, P., Kontou, E., & Christopoulos, A. (2015). Short-term creep behavior of a biodegradable polymer reinforced with wood-fibers. *Composites Part B: Engineering*, 80, 134-144. <https://doi.org/10.1016/j.compositesb.2015.05.046>
- Grzegorzewska, E., Burawska-Kupniewska, I., & Boruszewski, P. (2020). Economic profitability of particleboards production with a diversified raw material structure. *Maderas: Ciencia & Tecnologia*, 22(4), 537–548. <https://doi.org/10.4067/S0718-221X2020005000412>
- Hardiyatmo, H. C. (2011). Method to analyze the deflection of the nailed slab system. *International Journal of Civil & Environmental Engineering*, 11(4), 22–28.
- Jeya, R. P. K., & Bouzid, A. H. (2018). Compression creep and thermal ratcheting behavior of high-density polyethylene (HDPE). *Polymers*, 10(2), Article 156. <https://doi.org/10.3390/polym10020156>
- Jim, W. (2015). *The science and technology of composite materials - Curious*. Australian Academy of Science. <https://www.science.org.au/curious/technology-future/composite-materials>
- Jivkov, V., Yordanov, Y., & Marinova, A. (2010). Improving by reinforcement the deflection of shelves made of particleboard and MDF. In A. Teischinger, C. Marius, M. Dunky, D. Harper, G. Jungmeier, H. Militz, M. Musso, A. Petutschnigg, A. Pizzi, S. Wieland & T. M. Young (Eds.), *Processing Technologies for the Forest and Biobased Products Industries* (pp. 205–207). Deutsche Nationalbibliothek.
- Liu, Y., Shi, S., & Sheng, L. (2016). Deflection design of joinery melamine shelf in cabinet furniture. In P. F. Viger (Ed.), *Proceedings of the 2016 3rd International Conference on Mechatronics and Information Technology* (pp. 781–785). Atlantis Press. <https://doi.org/10.2991/icmit-16.2016.141>
- Malaysian Panel-Products Manufacturers' Association. (2023). *Particleboard*. Malaysian Panel-Products Manufacturers' Association. <http://mpma.com.my/particleboard-3158-182346/>
- Masuelli, M. A. (2013). Introduction of fibre-reinforced polymers – Polymers and composites: Concepts, properties and processes. In *Fiber Reinforced Polymers - The Technology Applied for Concrete Repair* (Chapter 1). IntechOpen. <https://doi.org/10.5772/54629>
- Mirski, R., Derkowski, A., Dziurka, D., Dukarska, D., & Czarnecki, R. (2019). Effects of a chipboard structure on its physical and mechanical properties. *Materials*, 12(22), Article 3777. <https://doi.org/10.3390/ma12223777>
- Papadopoulos, A. N. (2020). Advances in wood composites. *Polymers*, 12(1), Article 48. <https://doi.org/10.3390/polym12010048>
- Patnaik, P. K., Swain, P. T. R., Mishra, S. K., Purohit, A., & Biswas, S. (2020). Composite material selection for structural applications based on AHP-MOORA approach. *Materials Today: Proceedings* 33(8), 5659-5663. <https://doi.org/10.1016/j.matpr.2020.04.063>
- Rackham, J. W., Couchman, G. H., & Hicks, S. J. (2009). *Composite slabs and beams using steel decking: Good practice for design and construction*. Steel Construction Institute.

- Sharaf, H. K., Ishak, M. R., Sapuan, S. M., Yidris, N., & Fattahi, A. (2020). Experimental and numerical investigation of the mechanical behavior of full-scale wooden cross arm in the transmission towers in terms of load-deflection test. *Journal of Materials Research and Technology*, 9(4), 7937–7946. <https://doi.org/10.1016/j.jmrt.2020.04.069>
- Tankut, N. (2009). Effect of various factors on the rigidity of furniture cases. *African Journal of Biotechnology*, 8(20), 5265–5270. <https://doi.org/10.5897/AJB2009.000-9446>
- Wu, Q., & Vlosky, R. P. (2000). Panel products: A perspective from furniture and cabinet manufacturers in the Southern United States. *Forest Products Journal*, 50(9), 45–50.
- Zhao, X., Huang, Y., Fu, H., Wang, Y., Wang, Z., & Sayed, U. (2021). Deflection test and modal analysis of lightweight timber floors. *Journal of Bioresources and Bioproducts*, 6(3), 266–278. <https://doi.org/10.1016/j.jobab.2021.03.004>



## Energy Audit on Two 22-TPH Coal-fired Boilers of a Pineapple Processing Plant

Jay Nelson Corbita<sup>1,2\*</sup>, Leonel Pabilona<sup>1</sup> and Eliseo Villanueva<sup>1</sup>

<sup>1</sup>Mechanical Engineering Department, University of Science and Technology of Southern Philippines – Cagayan de Oro Campus, CM Recto Avenue, Lapasan, Cagayan de Oro City, 9000, Philippines

<sup>2</sup>Del Monte Philippines, Inc., Bugo, Cagayan de Oro City, 9000, Philippines

### ABSTRACT

The price of coal used by a pineapple processing plant has increased from 3.90 Php/kg in 2018 to 8.60 Php/kg in 2022, thus increasing steam generation costs. This study conducted an energy audit on the two 22-TPH coal-fired boilers of the pineapple processing plant to determine boiler efficiency, quantify sources of heat loss, identify energy conservation measures, and calculate energy and coal savings. The coal-fired boilers investigated were fluidized bed combustion boilers with a reverse osmosis feedwater system. The boiler efficiency was calculated using an indirect method, considering energy losses from sensible heat in refuse and blowdown water. Of the three performance tests conducted, the average boiler efficiency is at 80.655%. The top five sources of heat loss were dry flue gas, hydrogen in coal, moisture in coal, surface radiation and convection, and boiler blowdown. These sources account for 18.322% of the energy input. The identified energy conservation measures include the installation of an automatic oxygen trim control, the installation of an economizer, the installation of a caustic injection system, and the insulation of uninsulated surfaces. These measures have a total potential energy savings of 52,494,974 MJ/yr and coal savings of 2,594,579 kg/yr. While a caustic injection system is not yet installed, setting blowdown TDS to 2,090 ppm can reduce energy consumption by 1,656,496 MJ/yr and coal consumption by 81,873 kg/yr. Using coal with lower hydrogen and moisture content can

also reduce energy loss by 6,096,810 MJ/yr per 0.5% reduction in hydrogen content and 6,816,813 MJ/yr per 5% reduction in moisture content.

**Keywords:** Boiler performance test, energy audit, fluidized bed coal-fired boiler, indirect method efficiency, reverse osmosis

### ARTICLE INFO

#### Article history:

Received: 04 November 2023

Accepted: 06 February 2024

Published: 22 July 2024

DOI: <https://doi.org/10.47836/pjst.32.4.25>

#### E-mail addresses:

[jaycorbitanelson@yahoo.com](mailto:jaycorbitanelson@yahoo.com) (Jay Nelson Corbita)

[leonel.pabilona@ustp.edu.ph](mailto:leonel.pabilona@ustp.edu.ph) (Leonel Pabilona)

[ep\\_villanueva@yahoo.com](mailto:ep_villanueva@yahoo.com) (Eliseo Villanueva)

\* Corresponding author

## INTRODUCTION

Steam is primarily used in the canning operations of a pineapple processing plant for the thermal processing of its products. Two 22-TPH coal-fired boilers generate steam, with two oil-fired boilers as backup. But the price of coal has been increasing for the past few years. For the coal used by the pineapple processing plant, the price has increased from Php 3.90 per kg last January 2018 to Php 8.60 per kg in January 2022. Its increase in coal prices results in higher operating costs. In this study, an energy audit was conducted on the coal-fired boilers of the pineapple processing plant to determine energy conservation measures. The boilers audited in this study were fluidized bed combustion boilers. Due to process constraints, the steam system involved in this study does not have a condensate recovery system. Less than a year before the study was conducted, reverse osmosis equipment was installed in series with the existing water softeners to reduce boiler blowdown loss.

Several industries conducted energy audits to increase the operating efficiency of steam systems. These energy audits are conducted to identify energy conservation measures that could reduce the energy input or increase the energy output of a steam system. Varying methodologies are used in conducting energy audits. According to Kumar et al. (2018), an energy audit can range from a simple walk-through audit to a more detailed, comprehensive one. In addition to varying methodologies, energy audits can be applied to varying system types. For steam-generating unit audits, applications can be performed on varying boiler types.

Dagleish and Grobler (2008) conducted a five-day walk-through audit to identify energy conservation opportunities for a pineapple processing facility. Conducting a walk-through energy audit is relatively simple. However, since it only relies on available data during the walk-through, it cannot accurately quantify the different sources of energy loss in the system. A more detailed comprehensive audit for coal-fired boilers was performed by Joshi et al. (2021), Sahai and Kumar (2017), Bora and Nakkeeran (2014), Kumar et al. (2018), Namdev et al. (2016), Gupta et al. (2011). In their studies, the sources of energy losses were quantified, and the indirect method boiler efficiency was determined. In calculating the indirect method boiler efficiency, the sources of energy loss considered by Joshi et al. (2021), Sahai and Kumar (2017), Bora and Nakkeeran (2014), and Kumar et al. (2018) were loss due to dry flue gas, loss due to evaporation of water formed from hydrogen in fuel, loss due to evaporation of moisture in fuel, loss due to moisture present in air, loss due to partial conversion of carbon to CO, loss due to radiation losses, and loss due to unburnt carbon. In addition to these seven sources of energy loss, Namdev et al. (2016) considered the loss from the sensible heat in fly and bottom ash, while Gupta et al. (2011) also considered both losses from the sensible heat in fly and bottom ash and loss due to boiler blowdown.

In addition to the varying methodologies used in energy audits, energy audits were also conducted in varying boiler types. Joshi et al. (2021) performed an energy audit on two 18

TPH traveling grate boilers and one 12 TPH fluidized bed combustion boiler. Sahai and Kumar (2017) determined the efficiency of a 100 TPH fluidized bed combustion boiler. Bora and Nakkeeran (2014) conducted a performance test on a coal-fired stoker boiler, while Kumar et al. (2018) conducted an energy audit on the pulverized coal boiler of a thermal power plant in India. Namdev et al. (2016) also conducted an energy audit on a pulverized coal boiler. Gupta et al. (2011) conducted an efficiency test for a coal-fired stoker boiler of a pulp and paper mill.

Previously conducted detailed energy audits on coal-fired boilers were able to determine the top contributors to the energy loss. Energy conservation measures were determined to increase boiler efficiency based on this information and the operating parameters recorded. In the study of Joshi et al. (2021), the oxygen level in the flue gas of the 12 TPH boiler and Thermax 18 TPH boiler could still be reduced to optimal values. In addition, the discharge flue gas temperature of the Thermax 18 TPH boiler was relatively high. The thermography survey also indicated regions with damaged or absent insulation. With these, the recommendations of Joshi et al. (2021) included reducing the excess air supplied, installing a secondary economizer, and repairing damaged insulation. In the study of Sahai and Kumar (2017), the three sources with the highest heat loss were consistently dry flue gas, hydrogen in fuel, and moisture in fuel. Recommendations from the study included controlling the excess air, preheating the combustion air, and proper fuel selection. According to Bora and Nakkeeran (2014), the source of energy loss with the highest contribution is heat in dry flue gas at 11.36%. With this, boiler efficiency improvements include recovering heat from the exhaust gases and improving the burner controls that manage the fuel-to-air ratio. In the energy audit conducted by Namdev et al. (2016), energy conservation measures identified include maintaining coal particle size within 70 to 74 microns to reduce the 6.1442% unburned carbon loss, continuous monitoring of excess air to reduce the 4.5993% dry flue gas loss, using of primary air from pre-heater to reduce the 1.7918% loss due to moisture of coal, and replacing old insulation to reduce the 1.0014% radiation losses. In the study of Gupta et al. (2011), the highest source of heat loss was combustibles in refuse, which resulted in a percentage loss of 6.03%. One of the recommendations to reduce heat loss from this source was to conduct a sieve analysis of coal once every shift to correct oversized coal fed to the boiler. Regular sampling of the ash for unburnt carbon analysis was also recommended. The second highest source of heat loss was dry flue gas, which resulted in a 5.93% percentage loss. Excess air was at 75%, which could be lowered to 40%–50%. Installation of an oxygen trim control was recommended. Without the oxygen trim control, flue gas analysis was recommended to be conducted every 2 hours to correct the excess air based on the reading. Other energy conservation measures identified were the repair of soot blowers, installation of automatic blowdown control, and proper insulation of boiler surfaces and fittings.

From the above studies, an energy audit determining the indirect method boiler efficiency could effectively identify major contributors to boiler energy loss. Energy conservation measures can be identified from the quantified losses, and energy savings from these measures can then be quantified. Looking at the methodology used by previous studies, only the study of Namdev et al. (2016) and Gupta et al. (2011) considered loss due to sensible heat in the refuse. In addition, only the study of Gupta et al. (2011) considered loss due to blowdown water. Bora and Nakkeeran (2014) indicate that most standards used in calculating boiler efficiency, including IS8753, ASME PTC 4.1, and BS845, do not include loss due to blowdown water in the efficiency calculations. However, for applications with zero to low condensate recovery percentage, like the steam system involved in this study, loss due to blowdown significantly affects the boiler efficiency. In this study, an energy audit that determines the indirect method of boiler efficiency was conducted. In determining the indirect method boiler efficiency, both the losses due to sensible heat in the refuse and due to blowdown water were considered. These losses were accounted for in the study of Gupta et al. (2011). However, in that study, the boiler investigated was stoker-fired. In this study, the boiler that will be investigated is a fluidized bed combustion boiler. Thus, this study's novelty is considering loss due to sensible heat in refuse and loss due to blowdown water in determining the indirect method efficiency of fluidized bed combustion boilers.

This study aims to conduct an energy audit on the two 22-TPH fluidized bed combustion coal-fired boilers of a pineapple processing plant to quantify the sources of energy loss and determine the indirect method boiler efficiency. Energy conservation measures were identified from the quantified sources of energy loss, and the potential energy and coal savings from the identified energy conservation measures were calculated in MJ/year and kg/year, respectively. According to Peña (2011), fluidized bed technology has higher combustion efficiency compared to grate boilers. It asserts the significance of conducting a study that performs a detailed energy audit on fluidized bed boilers. Specifically, the fluidized bed boilers investigated have a reverse osmosis feedwater system. From the study of Kocabas and Savas (2021), installing a reverse osmosis system for the boiler feedwater was one of the improvement suggestions to reduce blowdown loss. It asserts the significance of investigating the efficiency of a steam-generating unit that uses reverse osmosis equipment in its feedwater system. Aside from being used to improve the efficiency of the fluidized bed boilers investigated, the results of this study can also be used as a reference in conducting a detailed energy audit for other fluidized bed boilers. The energy conservation measures identified can be applied to fluidized bed boilers with similar operating conditions, especially those used in industrial steam systems with zero to low condensate recovery due to process constraints. In addition, the results of this study could be used as a reference on the degree of heat loss due to blowdown water on steam-generating units with zero to low condensate recovery if a reverse osmosis feedwater system is used.

## MATERIALS AND METHODS

### Performance Test

Performance tests were conducted to determine the boiler efficiency and quantify the sources of energy loss. The sources of energy loss considered in this study are unburned carbon in refuse, heat in the dry flue gas, moisture in coal, moisture from burning of hydrogen in coal, moisture from air supplied, formation of carbon monoxide, sensible heat in refuse, surface radiation and convection, and boiler blowdown. Since the operating parameters of the two 22-TPH coal-fired boilers are the same, the performance tests were only conducted on one boiler—for this study, coal-fired boiler 2. The results of the performance tests and the identified energy conservation measures, including the quantified energy conserved per year for each measure, were treated as applicable to coal-fired boilers 1 and 2. The performance tests were performed at three trials, each for 4 hours. Table 1 presents the data collected for each performance test, the frequency of data collection and the instrument or method used to collect the data. The ultimate analysis of the coal used was conducted by a testing laboratory based on ASTM D4239-18e1 (Method A), ASTM D5373-16, and ASTM D3176-15 (by difference). In determining the heat loss due to surface radiation and convection, the steam generating system was divided into sections and measurement points for each section were pre-determined. The uninsulated surfaces of the steam generating system were also determined prior to the performance test and were considered separate sections from the insulated portions. The equipment manual and as-built drawings determined data on surface areas and fan efficiencies needed to complete the calculations.

Table 1  
*Performance test data collection plan*

<b>Data</b>	<b>Frequency</b>	<b>Instrument / Method</b>
Feedwater temperature	Every 15 minutes	Nutech Engineers RTD
Total dissolved solids (TDS)	Every 15 minutes	Myron L Company DS meter
Total feedwater supplied	Every Hour	Rosemount flow transmitter integrated with FactoryTalk View Site Edition Version 10
Steam pressure	Every 15 minutes	Baumer pressure gauge
Total coal input	Every Hour	Rotary feeder integrated with FactoryTalk View Site Edition Version 10
Heating value of coal	Start, Middle, End	CAL3K-A oxygen bomb calorimeter
The total mass of refuse	Every Hour	Adam CPWplus-150 weighing scale
Temperature of refuse	Every Hour	FLUKE TiS60+ thermal imager
Proximate analysis	Start, Middle, End	Navas Instruments TGA-2000A
Flue gas temperature	Every 15 minutes	Nutech Engineers RTD
Flue gas analysis	Every 15 minutes	ecom J2KN pro portable emission analyzer
Air supply DBT and RH	Every 15 minutes	Extech Instruments EN300 environmental meter
Power consumption of fans	Every Hour	FLUKE-435-II three-phase power quality analyzer

The performance tests were conducted during the operation of the pineapple processing plant. Thus, the steam load of the boiler during the tests depended on the facility's operation. The tests were conducted after the meal break of the canning operations to minimize load fluctuation during the test period.

### Calculation of Heat Losses and Boiler Efficiency

The calculation procedures in the Steam Generating Units Power Test Codes of The American Society of Mechanical Engineers (1965) were used to determine the heat loss due to unburned carbon in refuse, heat in the dry flue gas, moisture in coal, moisture from burning of hydrogen in coal, moisture from air supplied, formation of carbon monoxide, and sensible heat in refuse. The Fired Steam Generators Performance Test Codes of The American Society of Mechanical Engineers (2009) calculation procedures were used to determine the heat loss due to surface radiation and convection. The heat loss due to unburned carbon in the refuse per kg of coal burned  $L_1$  was obtained using Equation 1 from the kg of carbon in the refuse per kg of coal burned  $C_{\text{refuse}}$ .

$$L_1 = C_{\text{refuse}} \times 33,820 \quad [1]$$

The heat loss due to heat in the dry flue gas per kg of coal burned  $L_2$  was obtained using Equation 2 from the mass of dry flue gas per kg of coal  $m_{\text{dry}}$ , mean specific heat of the dry flue gas  $c_{p(\text{dry})}$ , and the difference between the discharge flue gas temperature  $T_f$  and air supply dry bulb temperature  $T_a$ .

$$L_2 = m_{\text{dry}} \times c_{p(\text{dry})} \times (T_f - T_a) \quad [2]$$

The heat loss due to moisture in coal per kg of coal burned  $L_3$  was calculated through Equation 3 using the percent moisture in coal  $m_{w(\text{coal})}$  from the coal proximate analysis, enthalpy of the water vapor in flue gas  $h_{w(\text{flue})}$ , and enthalpy of saturated liquid at ambient conditions  $h_{\text{amb}(\text{liq})}$ .

$$L_3 = m_{w(\text{coal})} \times (h_{w(\text{flue})} - h_{\text{amb}(\text{liq})}) \quad [3]$$

The heat loss due to moisture from burning of hydrogen in coal per kg of coal burned  $L_4$  and the heat loss due to moisture from air supplied per kg of coal burned  $L_5$  were calculated using the percent hydrogen in coal  $H$ , kg of moisture per kg of dry air supplied  $m_{w(a)}$ , and kg of dry air supplied per kg of coal  $m_a$ . Equations 4 and 5 are used to calculate  $L_4$  and  $L_5$ , respectively.  $h_{\text{amb}(\text{vap})}$  is the enthalpy of saturated vapor in ambient conditions.

$$L_4 = 8.936 \times H \times (h_{w(\text{flue})} - h_{\text{amb}(\text{liq})}) \quad [4]$$

$$L_5 = m_{w(a)} \times m_a \times (h_{w(\text{flue})} - h_{\text{amb}(\text{vap})}) \quad [5]$$

The heat loss due to the formation of carbon monoxide per kg of coal burned  $L_6$  was determined through Equation 6 using the percent carbon monoxide in the flue gas CO, percent carbon dioxide in the flue gas  $CO_2$ , and the kg carbon burned per kg of coal  $C_b$ .

$$L_6 = \frac{CO}{CO_2 + CO} \times 23,516 \times C_b \quad [6]$$

The heat loss due to sensible heat in refuse per kg of coal burned  $L_7$  was calculated through Equation 7 using the specific heat of refuse  $c_{\text{refuse}(A)}$ , kg of refuse collected per kg of coal burned  $Ref_A$  and the difference between the refuse temperature  $T_{\text{refuse}(A)}$  and ambient temperature  $T_a$ .

$$L_7 = \sum_{\text{All Collection Points}} c_{\text{refuse}(A)} \times (T_{\text{refuse}(A)} - T_a) \times Ref_A \quad [7]$$

The heat loss due to surface radiation and convection per kg of coal burned  $L_8$  was obtained through Equation 9 using the total heat transfer rate from all surfaces  $\dot{Q}_{\text{surf}}$  and the average coal firing rate  $\dot{m}_{\text{coal}}$ .  $\dot{Q}_{\text{surf}}$  is the sum of all heat transfer rates from a surface  $\dot{Q}_{\text{surf}(S)}$ , calculated using Equation 8.  $H_{c(S)}$  is the convection heat transfer coefficient,  $H_{r(S)}$  is the radiation heat transfer coefficient,  $A_s$  is the surface area,  $T_s$  is the surface temperature, and  $T_{s(a)}$  is the average ambient air temperature within 2ft-5ft from the surface.

$$\dot{Q}_{\text{surf}(S)} = \frac{0.293}{1000} (H_{c(S)} + H_{r(S)}) A_s (T_s - T_{s(a)}) \quad [8]$$

$$L_8 = \frac{\dot{Q}_{\text{surf}}}{\dot{m}_{\text{coal}}} \quad [9]$$

The heat loss due to blowdown per kg of coal burned  $L_9$  was calculated through Equation 10 using the total mass of blowdown discharged  $m_{\text{tot}(BD)}$ , total mass of coal supplied  $m_{\text{tot}(coal)}$ , and the difference between the blowdown enthalpy  $h_{BD}$  and feedwater enthalpy  $h_{FW}$ .

$$L_9 = \frac{m_{\text{tot}(BD)} \times (h_{BD} - h_{FW})}{m_{\text{tot}(coal)}} \quad [10]$$

After obtaining  $L_1$  to  $L_9$ , the percent heat loss  $L_{1(\%)}$  to  $L_{9(\%)}$ , which quantifies the portion of the heat input lost due to the corresponding source of heat loss, was then obtained using Equation 11.  $HHV_{\text{coal}}$  is the higher heating value of the coal used, and  $B$  is the energy from heat credits per kg of coal burned.

$$L_{n(\%)} = \frac{L_n}{HHV_{\text{coal}} + B} \times 100\% \quad [11]$$

The indirect method boiler efficiency  $\eta_{\text{Boiler}}$  was then calculated using Equation 12 from  $L_{1(\%)}$  to  $L_{9(\%)}$ .

$$\eta_{\text{Boiler}} = 100\% - L_1(\%) - L_2(\%) - L_3(\%) - L_4(\%) - L_5(\%) - L_6(\%) - L_7(\%) - L_8(\%) - L_9(\%) \quad [12]$$

The boiler efficiency, percent heat losses, and significant operating parameters were determined for each trial. The average boiler efficiency, average percent heat losses, and average operating parameters were then calculated. These average values were used to identify steam energy conservation measures and quantify the potential energy and coal savings from the identified measures. This study did not conduct further experiments to determine actual energy and coal savings from the identified conservation measures.

## RESULTS AND DISCUSSION

### Boiler Efficiency and Heat Losses

The average boiler efficiency obtained from the three performance tests was 80.655%. The total heat loss is at 19.345%. Figure 1 presents the percentage contribution of each source to the total heat loss. The % heat loss quantifies the portion of the total energy input lost due to the corresponding source. The % total loss quantifies the portion of the total heat loss due to the corresponding source.

The highest percentage loss is due to the heat in the dry flue gas. It consumes 10.266% of the energy input and 53.071% of the total heat loss. From Equation 2, this source of heat loss increases as the mass of dry flue gas per kg of coal and flue gas discharge temperature increase. Since the mass of dry flue gas per kg of coal increases as the amount of air supplied per kg of coal increases, an increase in the excess air supplied to the boilers increases the heat loss due to heat in the dry flue gas.

The heat loss due to moisture from burning hydrogen in coal is 3.337%, 17.25% of the total heat loss. The heat loss due to moisture in coal is at 3.126%, which is 16.161% of the total heat loss. From Equations 3 and 4, these heat losses are directly proportional to the percent hydrogen in coal and the percent moisture in coal.

The fourth major contributor to the reduction in the efficiency of the steam-generating unit is the heat loss from surface radiation and convection. This source reduces efficiency by 0.892%, 4.613% of the total heat loss. From Equation 8, the heat loss from this source is significantly increased by an increase in the surface temperature.

After the heat loss from surface radiation and convection, boiler blowdown water is the source with the next highest heat loss. The heat loss from this source accounts for 0.701% of the energy input, which is 3.624% of the total heat loss. From Equation 10, the heat loss due to the blowdown is dependent on the total mass of the blowdown discharged. According to Harrell (2004), the mass of the blowdown discharged is proportional to the ratio between the feedwater TDS and the blowdown water TDS.

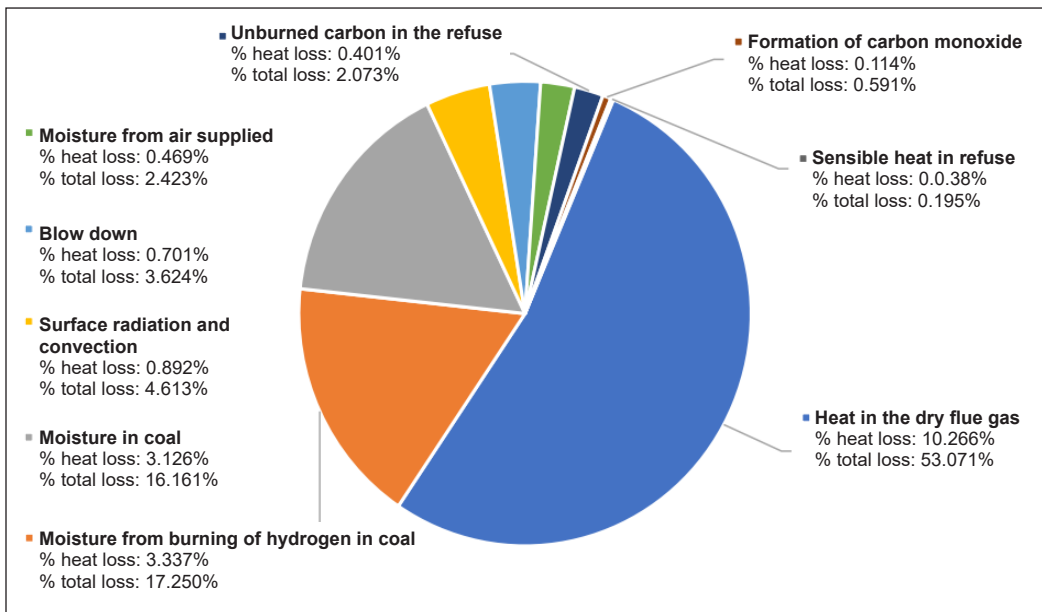


Figure 1. Percentage contribution of sources of heat loss

The heat loss due to moisture from the air supplied reduces the steam generating efficiency by 0.469%, which is 2.423% of the total heat loss. From Equation 5, the heat loss due to moisture from air supplied increases as the kg of moisture per kg of dry air supplied increases. The amount of moisture per kg of dry air supplied depends on the dry bulb temperature and relative humidity of the air supplied. In addition, heat loss due to moisture from the air supplied also increases as the air supplied per kg of coal increases. Thus, heat loss due to moisture increases as the excess air supplied to the boilers increases.

The heat loss due to unburned carbon in the refuse is 0.401%, 2.073% of the total heat loss. The heat loss due to the formation of carbon monoxide is 0.114%, which is 0.591% of the total heat loss. From equations 1 and 6, the heat loss due to these sources is calculated from the amount of carbon in the refuse per kg of coal burned and the percent carbon monoxide in the flue gas analysis. The source with the lowest heat loss is the sensible heat in refuse. The heat loss due to sensible heat in refuse is at 0.038%, which is 0.195% of the total heat loss.

Table 2 presents the identified operating parameters which significantly affect the sources of heat loss. Table 2 also gives the average values of these parameters during the three performance tests conducted.

### Comparison of Results with Other Studies

Table 3 compares this study's results to previous studies using indirect method boiler efficiency. From the table, the source with the highest heat loss is heat in the dry flue

gas, except for the study of Namdev et al. (2016) and Gupta et al. (2011). UNIDO (2016) asserts that energy loss from dry flue gas almost always accounts for the highest energy loss in steam generation. Both in the study of Namdev et al. (2016) and Gupta et al. (2011), the factor identified that significantly affected the high loss due to unburned carbon is the size of the coal fed to the boiler. Table 3 also shows that the energy loss due to unburned carbon is less on fluidized bed boilers compared to the other types of boilers. Peña (2011) asserts that fluidized bed technology has higher combustion efficiency compared to grate boilers.

Comparing the results of this study with the fluidized bed boilers investigated by Joshi et al. (2021) and Sahai and Kumar (2017), for all three fluidized bed boilers, the three sources with the highest contribution

to the energy loss are the heat in the dry flue gas, moisture from burning hydrogen in coal, and moisture in coal. Looking at the heat loss due to the dry flue gas, the percent loss from this source obtained in this study was less than both boilers investigated by Joshi et al. (2021) and Sahai and Kumar (2017). The excess air of the boilers investigated in this study is significantly less at 89.92% compared to the excess air of the boiler investigated by Joshi et al. (2021) at 208.82%. For the boiler investigated by Sahai and Kumar (2017), the excess air was lower at an average of 41.48%, but the flue gas discharge temperature was higher at an average of 173.8°C. The higher heating value of the coal was significantly less at 13,464.11 kJ/kg versus the coal used in this study at 20,139.26 kJ/kg.

From Equation 11, the percent heat loss increases as the higher heating value decreases, resulting in a high percent heat loss due to heat in the dry flue gas in the study of Sahai and Kumar (2017). Looking at the heat loss due to moisture from burning hydrogen in coal, the percent loss from this source obtained in this study was also less than the boilers investigated by Joshi et al. (2021) and Sahai and Kumar (2017). It could be explained by the lower hydrogen content of the coal used in this study at 2.82%, compared to the hydrogen content of the coal used by Joshi et al. (2021) at 3.28% and Sahai and Kumar (2017) at 5.24%. Looking at the heat loss due to moisture in coal, the percent loss obtained

Table 2  
*Average values of significant operating parameters*

Parameter	Unit	Average
Flue gas discharge temperature	°C	169.4313
Flue gas % oxygen	%	9.4908
Excess air percentage	%	89.915
Coal % hydrogen	%	2.8183
Coal % moisture	%	23.593
Average temperature of insulated surfaces	°F	118.72
The average temperature of uninsulated surfaces	°F	247.25
TDS of feedwater	ppm	81.2941
TDS of blowdown water	ppm	1610.784
Feedwater temperature	°C	94.09
Steam pressure	kg/cm <sup>2</sup>	10.7530
Ambient dry bulb temperature	°C	33.2049
Ambient relative humidity	%	76.1657
kg of carbon in the refuse per kg of coal burned	kg/kg	0.00241
Flue gas % carbon monoxide	%	0.0158

Table 3  
 Comparison with other studies which used indirect method boiler efficiency

	Boiler Type	L <sub>1</sub> (%)	L <sub>2</sub> (%)	L <sub>3</sub> (%)	L <sub>4</sub> (%)	L <sub>5</sub> (%)	L <sub>6</sub> (%)	L <sub>7</sub> (%)	L <sub>8</sub> (%)	L <sub>9</sub> (%)	η <sub>Boiler</sub>
This Study	Fluidized Bed	0.401	10.266	3.126	3.337	0.469	0.114	0.038	0.892	0.701	80.655
Joshi et al., 2021 (12 TPH Thermax)	Fluidized Bed	0.710	11.820	1.770	4.200	0.930	1.110	-	0.650	-	78.820
Sahai & Kumar, 2017	Fluidized Bed	1.848	12.932	2.000	9.424	0.637	0.293	-	0.321	-	72.456
Joshi et al., 2021 (18 TPH Thermax)	Traveling Grate	2.700	8.300	2.330	3.750	0.380	0.790	-	1.260	-	80.480
Joshi et al., 2021 (18 TPH ISGEC)	Traveling Grate	2.510	5.880	1.230	4.350	0.270	0.360	-	1.010	-	84.310
Bora & Nakkeeran, 2014	Stoker Fired	3.060	11.360	2.530	5.390	0.360	0.040	-	0.430	-	76.830
Gupta et al., 2011	Stoker Fired	6.030	5.930	1.140	3.770	0.255	0.079	0.410	0.700	0.700	80.980
Kumar et al., 2018	Pulverized Coal	3.610	6.873	3.410	5.250	0.280	1.420	-	0.397	-	77.720
Namdev et al., 2016	Pulverized Coal	6.144	4.599	1.792	2.875	0.116	0.271	0.469	1.001	-	82.730

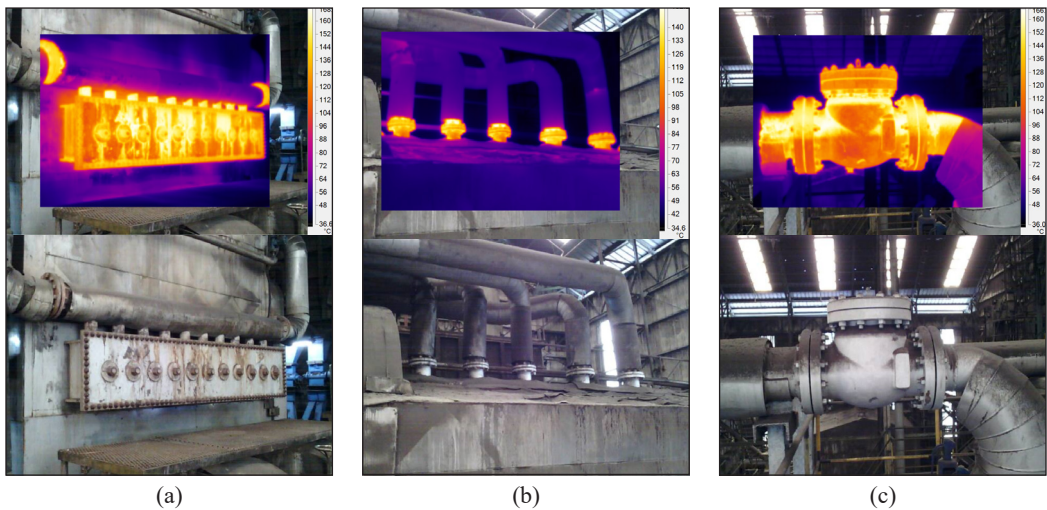


Figure 2. Thermal image of sample uninsulated surfaces: (a) Uninsulated inbed header at the riser side; (b) uninsulated row of flanges; and (c) uninsulated check valve

in this study was higher than both boilers investigated by Joshi et al. (2021) and Sahai and Kumar (2017). This source of heat loss is highly dependent on the moisture content of the coal. It is asserted by the significantly higher moisture content of the fuel used in this study at 23.593% compared to the moisture content of the coal used in the study by Sahai and Kumar (2017) at 9.88%. Comparing the efficiencies of the three fluidized bed boilers, the efficiency of the boiler audited in this study is higher than that of the other two. It could be explained by the significantly higher excess air in the study of Joshi et al. (2021) and the significantly lower heating value of the coal in the study of Sahai and Kumar (2017). The hydrogen content of the coal used in the studies of Joshi et al. (2021) and Sahai and Kumar (2017) was also higher than the coal used in the boiler investigated in this study.

### Significant Operating Parameters

Heat in the dry flue gas was the source with the highest heat loss per kg of coal burned. The operating parameters obtained in the performance tests showed that the average excess air supplied to the boiler was 89.915%. It is significantly higher than the recommended excess air for fluidized bed boilers, according to Agrawal and Dubey (2016), which is 20%–25%. As a result, the oxygen percentage in the flue gas is also significantly high at an average value of 9.49% vs the standard value of 4%–4.5%. This deviation from the standard excess air and percent oxygen values was also observed by Joshi et al. (2021), Bora and Nakkeeran (2014), and Gupta et al. (2011) in the steam-generating units they investigated. In addition, the average temperature of the discharged flue gas was 169.43°C, which is higher than the ideal temperature of 148.89°C for coal-fired boilers, according to the Advanced Manufacturing Office (2012) of the U.S. Department of Energy. High flue

gas temperature was also recorded in the steam-generating units investigated by Joshi et al. (2021) and Bora and Nakkeeran (2014).

The second and third sources with the highest percent loss are the moisture from burning hydrogen in coal and the moisture in coal, respectively. From the performance test results, the average percent hydrogen of the coal supplied is 2.8183%, and the average percent moisture is 23.593%. Similar results were obtained in the fluidized bed boilers that Joshi et al. (2021) and Sahai and Kumar (2017) investigated. Following the heat loss due to heat in the dry flue gas, moisture from burning hydrogen in coal was the second highest source of heat loss. Moisture in coal, on the other hand, was the third-highest source of heat loss.

Heat loss from surface radiation and convection accounts for 4.613% of the total heat loss. From the conducted energy audit, 33.495m<sup>2</sup> of the steam generating unit's surface is uninsulated. From the performance tests, these uninsulated surfaces incur heat loss at an average rate of 32.64kW, contributing to 28.6% of the heat loss from surface radiation and convection. The surface temperature on these uninsulated surfaces reaches 140.78°C to 335.18°C. Figure 2 shows thermal images of sample uninsulated surfaces. Uninsulated boiler surfaces were also observed in the units that Joshi et al. (2021) and Gupta et al. (2011) investigated.

Heat loss from boiler blowdown water accounts for 3.624% of the total heat loss. Less than a year before the performance tests were conducted, a reverse osmosis system was installed in series with the existing water softeners to further treat the boiler feedwater. Before the reverse osmosis system was installed, the water softeners solely performed feedwater treatment, and the TDS output of these softeners was 280 ppm. The boiler water TDS was maintained at 2,500 ppm to prevent rapid scale build-up. Since the reverse osmosis system can reduce the feedwater TDS to 30 ppm, the supplier recommended setting the boiler water TDS so that a maximum of 50 cycles of concentration (COC) is used. It ensures that the maximum silica concentration is not exceeded in the boiler. It explains the low TDS of the blowdown during the performance tests at an average of 1,610.784 ppm. However, during the reverse osmosis system's operation, the feedwater's pH decreased to 5, versus the minimum pH requirement of 8.5. With this, reverse osmosis water was mixed with soft water not treated by the reverse osmosis system to satisfy the minimum pH requirement, resulting in the increase of the feedwater TDS from the system capacity of 30 ppm to an average of 81.2941 ppm in the performance tests. With the parameters obtained, the actual cycle of concentration is only at 19.81 COC. At this cycle of concentration, both the boiler silica and TDS are below the maximum concentration, indicating excessive boiler blowdown. Excessive blowdown was also highlighted in the study of Gupta et al. (2011).

The heat loss due to moisture from the air supply accounts for 2.423% of the total heat loss. The same with the heat loss due to heat in the dry flue gas, the heat loss due to moisture from the air supplied increases as the excess air supplied to the steam generating

unit increases. From the results of Joshi et al. (2021), heat loss due to moisture from the air supplied was 0.27% for the boiler with the lowest excess air percentage and 0.93% for the boiler with the highest excess air percentage.

The heat loss due to unburned carbon in the refuse and the formation of carbon monoxide is related to the steam-generating unit's combustion efficiency. The heat loss due to unburned carbon in the refuse and the heat loss due to the formation of carbon monoxide accounts for 2.073% and 0.591% of the total heat loss, respectively. The significantly low heat loss from these sources asserts Peña (2011) and Agrawal and Dubey (2016) that fluidized bed boilers have high combustion efficiency.

### Energy Conservation Measures

An automatic oxygen trim control can be installed to control the excess air supplied and reduce the heat loss from heat in the dry flue gas. Joshi et al. (2021) and Gupta et al. (2011) also recommended this in their studies. An oxygen sensor installed at the flue gas duct will control the opening of the forced draft fan dampers to ensure that excess air supplied to the boiler is within 20%–25%. Reducing the excess air from the current average of 89.915% to an average of 22.5% reduces heat loss due to heat in the dry flue gas from 2,075.848 kJ/kg to 1,356.586 kJ/kg. In addition, it reduces heat loss due to moisture from air supplied from 94.8 kJ/kg to 61.326 kJ/kg. These reductions in heat loss per kg of coal translate to a 3.72% increase in boiler efficiency. With an average annual coal consumption of 41,360,043.33 kg, the oxygen trim control has a potential energy savings of 36,895,557.88 MJ/year, translating to a potential reduction in coal consumption of 1,823,573.56 kg/year.

The other factor contributing to the high heat loss due to heat in the dry flue gas is the high temperature of the discharged flue gas. An economizer can be installed after the dust collector, using excess heat to preheat the feedwater. Joshi et al. (2021) and Bora and Nakkeeran (2014) also identified this heat recovery system in their studies. Reducing the flue gas temperature from the current average of 169.43°C to 148.89°C reduces the heat loss from the current 2,075.85 kJ/kg to 1,763.083 kJ/kg. It translates to a 1.55% increase in boiler efficiency. It has a potential energy savings of 15,735,698.41 MJ/year, translating to a potential reduction in coal consumption of 777,741.42 kg/year.

Suppose both the automatic oxygen trim control and economizer are installed. In that case, the excess air will be reduced to an average of 22.5%, and the flue gas discharge temperature will be reduced to 148.89°C. These can potentially reduce boiler heat loss by 966.655 kJ/kg, translating to a 4.78% increase in boiler efficiency. These installations have a potential energy savings of 46,794,288.01 MJ/year, which translates to a potential reduction in coal consumption of 2,312,821.15 kg/year.

Heat loss is due to moisture from burning hydrogen in coal, and moisture in coal is dependent on the properties of the coal supplied. Thus, the heat loss from these sources can

only be reduced by changing the coal supply. For every 0.5% reduction in the hydrogen content of the coal supply, heat loss is reduced by 119.775 kJ/kg. It translates to a potential energy savings of 6,096,809.76MJ/year and a potential reduction in coal consumption of 301,336.58 kg/year. For every 5% reduction in the moisture content of the coal supply, heat loss is reduced by 134.036 kJ/kg. This potential is 6,816,812.51MJ/year in energy savings and 336,922.92 kg/year in coal consumption. The importance of the properties of the coal supplied to the boilers was asserted by the comparison of the results of this study with the results of Joshi et al. (2021) and Sahai and Kumar (2017). Percent loss due to hydrogen in coal in this study was lesser since the hydrogen content of the coal used was also lesser, and the percent heat loss due to moisture in coal in this study was higher compared to that of Sahai and Kumar (2017) since the moisture content of the coal used was also significantly higher.

The fourth source with the highest heat loss is surface radiation and convection. If uninsulated surfaces were insulated, the surface temperature would be reduced. This reduction in surface temperature reduces the heat loss due to the uninsulated surfaces from 32.64 kW to 7.257 kW. It will reduce the heat loss due to surface radiation and convection by 40.138 kJ/kg, translating to a 0.20% increase in boiler efficiency. This potential is 2,053,057.45 MJ/year in energy savings and 101,472.96 kg/year in coal consumption. Joshi et al. (2021) and Gupta et al. (2011) identified the same findings and recommendations in their studies.

To decrease the heat loss due to blowdown, the blowdown water TDS can be increased to 2,090 ppm. This TDS setting ensures the boiler does not exceed the maximum silica concentration. Setting the blowdown water TDS to 2,090 ppm increases the cycles of concentration to 25.71 COC, which would then reduce the total blowdown discharged by 22.85%. Heat loss due to blowdown will reduce from 141.745 kJ/kg to 109.376 kJ/kg, translating to a 0.16% increase in boiler efficiency. It has a potential energy savings of 1,656,496.30 MJ/year, which translates to a potential reduction in coal consumption of 81,872.81 kg/year. This energy conservation measure does not require investment since only the setting of the blowdown water TDS will be adjusted.

To fully utilize the capacity of the reverse osmosis system to reduce feedwater TDS to 30 ppm, a caustic injection system can be installed to increase the feedwater pH from 5 to 8.5 minimum requirement. To ensure that the boiler's maximum silica concentration is not exceeded, the blowdown water TDS will then be set to 1,500 ppm. It increases the cycles of concentration to 50 COC, which would reduce the total blowdown discharged by 60.33%. Heat loss due to blowdown will reduce from 141.745 kJ/kg to 56.239 kJ/kg, translating to a 0.42% increase in boiler efficiency. It has a potential energy savings of 4,361,534.33 MJ/year, which translates to a potential reduction in coal consumption of 215,570.09kg/year. The blowdown water TDS should be set to 1,500 ppm in this identified

energy conservation measure. It means that the previous energy conservation measure of setting the blowdown water TDS to 2,090 ppm can be implemented while a caustic injection system has not yet been installed.

Figures 3 and 4 summarize the identified energy conservation measures, the heat loss reduction from these conservation measures, and the corresponding energy and coal savings. Installing an automatic oxygen trim control, economizer, caustic injection system,

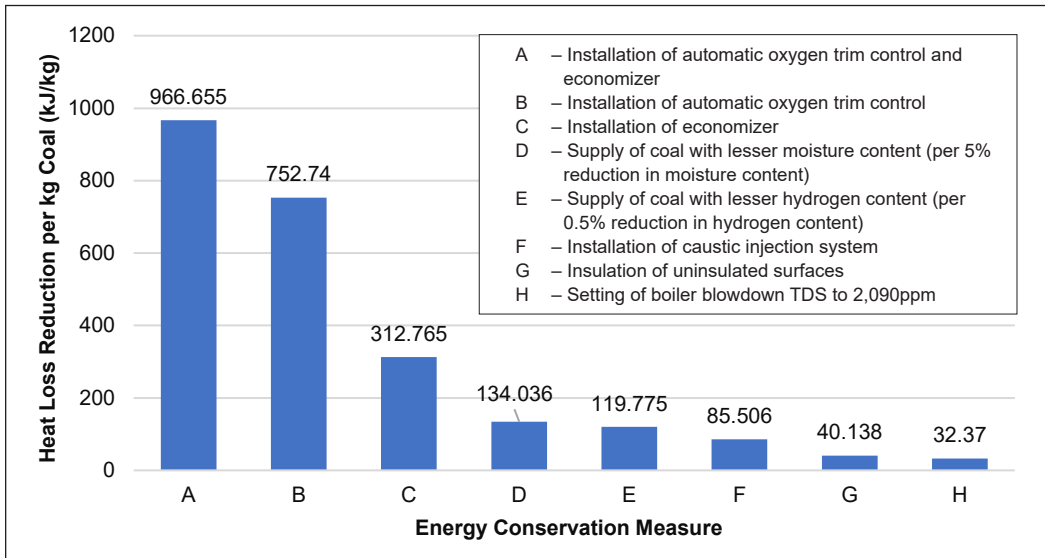


Figure 3. Heat loss reduction of identified energy conservation measures

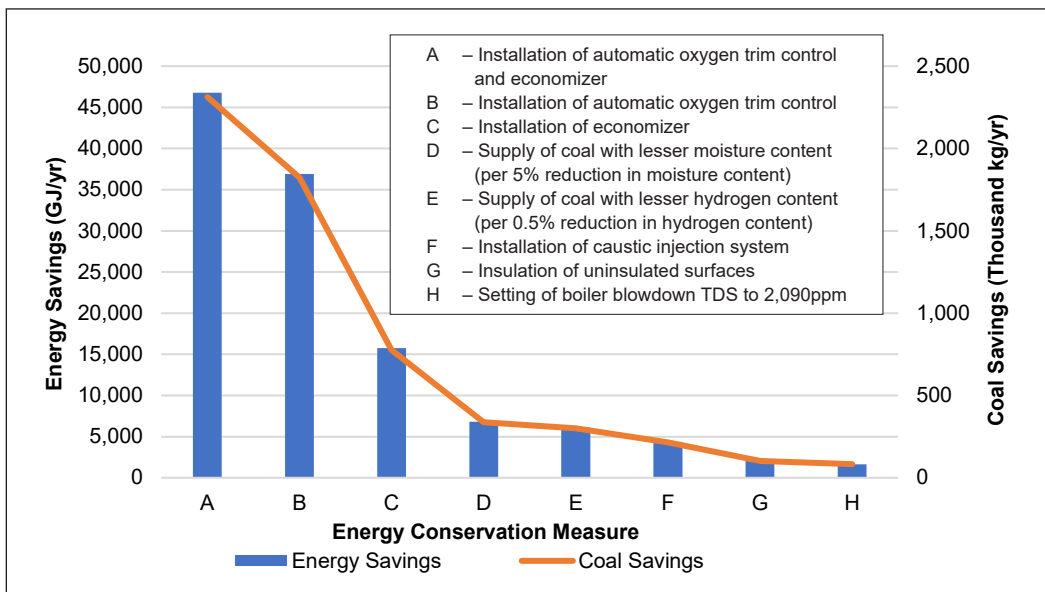


Figure 4. Energy and coal savings of identified energy conservation measures

and insulating uninsulated surfaces can reduce heat loss by 1,092.299 kJ/kg and increase boiler efficiency by 5.4%. It equals a total potential energy savings of 52,494,973.74 MJ/yr and coal savings of 2,594,579.18 kg/yr. Using coal supply with lesser hydrogen content results in a reduction in heat loss by 119.775 kJ/kg per 0.5% reduction in hydrogen content, while using coal supply with lesser moisture content results in a reduction in heat loss by 134.036 kJ/kg per 5% reduction in moisture content.

## **CONCLUSION AND RECOMMENDATIONS**

From the performance tests, the average efficiency of the 22-TPH coal-fired boilers is 80.655%. The top five sources of heat loss are heat in the dry flue gas, moisture from burning hydrogen in coal, moisture in coal, surface radiation and convection, and boiler blowdown. These sources account for 18.322% of the energy input to the boilers.

The identified energy conservation measures include the installation of an automatic oxygen trim control, the installation of an economizer, the installation of a caustic injection system, and the insulation of uninsulated surfaces. These measures have a total potential energy savings of 52,494,974 MJ/yr and coal savings of 2,594,579 kg/yr. While a caustic injection system is not yet installed, setting blowdown TDS to 2,090ppm can reduce energy consumption by 1,656,496 MJ/yr and coal consumption by 81,873 kg/yr. Using coal with lower hydrogen and moisture content can also reduce energy loss. For each 0.5% reduction in hydrogen content, heat loss and coal consumption are reduced by 6,096,810 MJ/year and 301,337 kg/year, respectively. For each 5% reduction in moisture content, heat loss and coal consumption are reduced by 6,816,813 MJ/year and 336,923 kg/year, respectively.

Further study on the effect of decreasing the excess air on combustion efficiency can be conducted, and factors affecting the combustion efficiency can be further analyzed. With these, the ideal setting of the boiler operating parameters can then be determined to optimize combustion efficiency at the ideal excess air supply. In addition, fuel switching can also be investigated to consider alternate fuels. Energy analysis can then be conducted to determine efficiency and emission performance using identified alternate fuels (Arromdee & Kuprianov, 2021; Campoli et al., 2021; Channapattana et al., 2023; Shi et al., 2020; Srinidhi et al., 2019).

## **ACKNOWLEDGEMENTS**

The authors thank the Mechanical Engineering Department of the University of Science and Technology of Southern Philippines for their recommendations in conducting this study and Del Monte Philippines, Inc. Bugo Cannery for supporting the execution of the performance tests.

## REFERENCES

- Advanced Manufacturing Office. (2012). *Use Feedwater Economizers for Waste Heat Recovery*. U.S. Department of Energy. [https://www.energy.gov/sites/prod/files/2014/05/f16/steam3\\_recovery.pdf](https://www.energy.gov/sites/prod/files/2014/05/f16/steam3_recovery.pdf)
- Agrawal, T., & Dubey, S. K. (2016). Fluidized Bed Combustion (FBC) in coal based thermal power plants. *International Journal of Advance Research in Science and Engineering*, 5(3), 299-308.
- Arromdee, P., & Kuprianov, V. I. (2021). Experimental study and empirical modeling of CO and NO behaviors in a fluidized-bed combustor firing pelletized biomass fuels. *Biomass Conversion and Biorefinery*, 11(5), 1507-1520. <https://doi.org/10.1007/s13399-019-00542-x>
- Bora, M. K., & Nakkeeran, S. (2014). Performance analysis from the efficiency estimation of coal fired boiler. *International Journal of Advanced Research*, 2(5), 561-574.
- Campli, S., Acharya, M., Channapattana, S. V., Pawar, A. A., Gawali, S. V., & Hole, J. (2021). The effect of nickel oxide nano-additives in *Azadirachta indica* biodiesel-diesel blend on engine performance and emission characteristics by varying compression ratio. *Environmental Progress & Sustainable Energy*, 40(2), Article e13514. <https://doi.org/10.1002/ep.13514>
- Channapattana, S. V., Campli, S., Madhusudhan, A., Notla, S., Arkerimath, R., & Tripathi, M. K. (2023). Energy analysis of DI-CI engine with nickel oxide nanoparticle added azadirachta indica biofuel at different static injection timing based on exergy. *Energy*, 267, Article 126622. <https://doi.org/10.1016/j.energy.2023.126622>
- Dalgleish, A. Z., & Grobler, L. J. (2008). Energy conservation opportunities at a pineapple processing facility. *Energy Engineering*, 105(1), 6-23. <https://doi.org/10.1080/01998590809509363>
- Gupta, R. D., Ghai, S., & Jain, A. (2011). Energy efficiency improvement strategies for industrial boilers: a case study. *Journal of Engineering and Technology*, 1(1), 52-56.
- Harrell, G. (2004). Boiler blowdown energy recovery. *Energy Engineering*, 101(5), 32-42. <https://doi.org/10.1080/01998590409509277>
- Joshi, P. M., Shinde, S., & Chaudhary, K. (2021). A case study on assessment performance and energy efficient recommendations for industrial boiler. *International Journal of Research and Review*, 8(4), 61-69. <https://doi.org/10.52403/ijrr.20210410>
- Kocabas, C., & Savas, A. F. (2021). Reducing energy losses of steam boilers caused by blowdown with using the FMEA method. *Smart Science*, 9(2), 70-79.
- Kumar, A., Sharma, S., & Gangacharyulu, D. (2018). Energy audit of coal fired thermal power plant. *International Journal of Engineering Research & Technology*, 7(7), 1-9.
- Namdev, A. K., Tiwari, A. C., Shukla, M. G. K., & India, B. J. (2016). Energy audit of a boiler and waste heat recovery system in thermal power plant. *International Journal of Engineering Research and General Science*, 4(6), 133-142.
- Peña, J. A. (2011, November 16-17). Bubbling fluidized bed. When to use this technology. In *Industrial Fluidization South Africa, Southern African Institute of Mining and Metallurgy* (pp. 57-66). Johannesburg, South Africa.

- Sahai, A., & Kumar, S. (2017). To calculate and improvement in the efficiency of FBC boiler. *International Research Journal of Engineering and Technology*, 4(9), 244-260.
- Shi, Y., Liu, Q., Shao, Y., & Zhong, W. (2020). Energy and exergy analysis of oxy-fuel combustion based on circulating fluidized bed power plant firing coal, lignite and biomass. *Fuel*, 269, Article 117424. <https://doi.org/10.1016/j.fuel.2020.117424>
- Srinidhi, C., Madhusudhan, A., & Channapattana, S. V. (2019). Effect of NiO nanoparticles on performance and emission characteristics at various injection timings using biodiesel-diesel blends. *Fuel*, 235, 185-193. <https://doi.org/10.1016/j.fuel.2018.07.067>
- The American Society of Mechanical Engineers. (1965). *Steam Generating Units Power Test Codes* (ASME PTC 4.1). The American Society of Mechanical Engineers
- The American Society of Mechanical Engineers. (2009). *Fired Steam Generators Performance Test Codes* (ASME PTC 4-2008). The American Society of Mechanical Engineers
- UNIDO. (2016). *Manual for Industrial Steam Systems Assessment and Optimization*. United Nations Industrial Development Organization. <https://www.unido.org/sites/default/files/2017-11/SSO-Manual-Print-FINAL-20161109-One-Page-V2.pdf>



**REFEREES FOR THE PERTANIKA  
JOURNAL OF SCIENCE & TECHNOLOGY**

**Vol. 32 (4) Jul. 2024**

The Editorial Board of the Pertanika Journal of Science and Technology wishes to thank the following:

Abdul Samad Shibghatullah  
*(UCSI, Malaysia)*

Helena Sovová  
*(ICPF, Czech Republic)*

Abhigyan Nath  
*(PtJNMMC, India)*

Inderdeep Singh  
*(IITR, India)*

Acaroglu Mustafa  
*(Selçuk University, Turkey)*

José Alfredo Hernández Pérez  
*(UAEM, Mexico)*

Ahmad Khusairi Azemi  
*(USM, Malaysia)*

Khanh Le Nguyen Quoc  
*(TMU, Taiwan)*

Aizat Alias  
*(UMP, Malaysia)*

Kishore Debnath  
*(IITR, India)*

Ali Abd Almisreb  
*(IUS, Bosnia and Herzegovina)*

Mahadimenakbar Mohd.  
Dawood  
*(UMS, Malaysia)*

Ali Omran Al-Sulttani  
*(UOB, Iraq)*

Mohamed Abd Rahman  
*(IIUM, Malaysia)*

Alper Savasci  
*(Abdullah Gul Universitesi, Turkey)*

Mohd Hendra Hairi  
*(UTeM, Malaysia)*

An Liqiang  
*(NCEPU, China)*

Mohd Shahrime Mohd Asaari  
*(USM, Malaysia)*

Belinda Chiew Meng Chong  
*(UiTM, Malaysia)*

Mohd Yuhazri Yaakob  
*(UTeM, Malaysia)*

Binson Abraham  
*(Saintgits College of Engineering, India)*

Murat Tolga Ozkan  
*(Gazi University, Turkey)*

Edi Syams Zainudin  
*(UPM, Malaysia)*

Muthu Krishnan  
*(KIT, India)*

Goutam Khankari  
*(DVC, India)*

Ng Chuck Chuan  
*(XMU, Malaysia)*

Haider Hadi Jasim  
*(University of Basrah, Iraq)*

Norashikin Mohd Fauzi  
*(UMK, Malaysia)*

Norhaizan Mohd Esa  
(UPM, Malaysia)

Shafkat Kibria  
(Leading University, Bangladesh)

Nur Azida Che Lah  
(UniKL, Malaysia)

Shailendra Singh  
(ITBHU, India)

Nurul Huda Ahmad Ishak  
(UMT, Malaysia)

Shamsul Aizam Zulkifli  
(UTHM, Malaysia)

Ong Meng Chuan  
(UMT, Malaysia)

Shefa Abdulrahman Dawood  
(University of Mosul, Iraq)

Pavol Bozek  
(STU, Slovakia)

Solley Joseph  
(Christ University, India)

Prashanth Gurunath Shivakumar  
(USC, USA)

Srinidhi Campli  
(JSPMRSCOE, India)

Rohana Hassan  
(UiTM, Malaysia)

Teh Jiashen  
(USM, Malaysia)

Rusdianto Roestam  
(President University, Indonesia)

Wan Nor Shuhadah Wan Nik  
(UNISZA, Malaysia)

Sergio Souto Maior Tavares  
(UFF, Brazil)

Yap Chee Kong  
(UPM, Malaysia)

Seyed Mojib Zahraee  
(RMIT, Australia)

Yudong Zhang  
(University of Leicester, UK)

---

DVC – Damodar Valley Corporation  
ICPF – Institute of Chemical Process Fundamentals  
IITR – Indian Institute of Technology Roorkee  
ITBHU – Indian Institute of Technology (Banaras Hindu University)  
IUS – International University of Sarajevo  
JSPMRSCOE – JSPM'S Rajarshi Shahu College of Engineering  
KIT – Kalaingarunani Institute of Technology  
NCEPU – North China Electric Power University  
PUJNMMC – Pt. Jawahar Lal Nehru Memorial Medical College  
RMIT – Royal Melbourne Institute of Technology  
STU – Slovak University of Technology  
TMU – Taipei Medical University  
UAEM – Universidad Autónoma del Estado de Morelos  
UFF – Universidade Federal Fluminense

UiTM – Universiti Teknologi MARA  
UMK – Universiti Malaysia Kelantan  
UMP – Universiti Malaysia Pahang  
UMS – Universiti Malaysia Sabah  
UMT – Universiti Malaysia Terengganu  
UniKL – University Kuala Lumpur  
UniZA – Universiti Sultan Zainal Abidin  
UOB – University of Baghdad  
UPM – Universiti Putra Malaysia  
USC – University of Southern California  
USM – Universiti Sains Malaysia  
UTeM – Universiti Teknikal Malaysia Melaka  
UTHM – Universiti Tun Hussein Onn Malaysia  
XMU – Xiamen University

---

While every effort has been made to include a complete list of referees for the period stated above, however if any name(s) have been omitted unintentionally or spelt incorrectly, please notify the Chief Executive Editor, *Pertanika* Journals at [executive\\_editor.pertanika@upm.edu.my](mailto:executive_editor.pertanika@upm.edu.my)

Any inclusion or exclusion of name(s) on this page does not commit the *Pertanika* Editorial Office, nor the UPM Press or the university to provide any liability for whatsoever reason.



Determining Process Variability Using Fuzzy Triangular Distribution in Dynamic Value Stream Mapping <i>Thulasi Manoharan, Faieza Abdul Aziz, Zulkiffle Leman and Siti Azfanizam Ahmad</i>	1765
<i>Review Article</i>	
The Importance of Vegetation Landscape in Firefly Habitats <i>Nurhafizul Abu Seri and Azimah Abd Rahman</i>	1789
Vision-Based Multi-Stages Lane Detection Algorithm <i>Fayez Saeed Faizi and Ahmed Khorsheed Al-sulaifanie</i>	1811
The Macrobenthos Diversity and Dominance in Johor Straits, Malaysia <i>Mohd Sophian Mohd Kasihmuddin and Zaidi Che Cob</i>	1829
Electric Transmission Tower Corrosion Assessment Using Analytic Hierarchy Process and Health Index <i>Aina Shazwana Mohd Izhar, Nor Hazwani Nor Khalid, Fathoni Usman, Mohd Supian Abu Bakar, Nur Fadilah Adriyanshah and Hakim Zahari</i>	1855
Simulating Spanning Tree Protocols in a Cable-based Tsunameter System with an Arbitrary Number of Ocean Bottom Units <i>Mohammad Hamdani, Anak Agung Ngurah Ananda Kusuma, Dedy Irawan, Tahar Agastani and Xerandy</i>	1875
Optimum Parameters for Extraction of Cinnamomum verum Leaves Towards $\alpha$ -Glucosidase Inhibition <i>Leong Yao Shen, Norhayati Muhammad, Hariz Haikal Nasuha, Mohd Fadzelly Abu Bakar, Norazlin Abdullah and Nur Fazira Abdul Rahim</i>	1891
Deflection Performance of Particleboards and Their Potential as Built-in Materials <i>Noor Azrieda Abd. Rashid, Hashim W Samsi, Nur Hanina Izzati Khairol Mokhtar, Yanti Abdul Kadir, Khairul Maseat, Siti Zaliha Ali and Muhammad Taufiq Tajuddin</i>	1905
Energy Audit on Two 22-TPH Coal-fired Boilers of a Pineapple Processing Plant <i>Jay Nelson Corbita, Leonel Pabilona and Eliseo Villanueva</i>	1919

<i>Review Article</i>	
Computer Vision—The Frontier of Modern Environmental Diagnostics: A Review	1591
<i>Anna Sergejevna Olkova and Evgeniya Vladimirovna Tovstik</i>	
A Deep Learning-based Classification Model for Arabic News Tweets Using Bidirectional Long Short-Term Memory Networks	1609
<i>Chin-Teng Lin, Mohammed Thanoon and Sami Karali</i>	
Borderline-DEMNET: A Workflow for Detecting Alzheimer’s and Dementia Stage by Solving Class Imbalance Problem	1629
<i>Neetha Papanna Umalakshmi, Simran Sathyanarayana, Pushpa Chicktotlikere Nagappa, Thriveni Javarappa and Venugopal Kuppanna Rajuk</i>	
Novel Reactive Power Control Strategy for Mitigating Voltage Rise in the Malaysian Low Voltage Distribution Network with High PV Penetration	1651
<i>Mustafa Abo Alwez, Jasronita Jasni, Raghad Wahab, Mohd Amran Mohd.Radzi and Norhafiz Azis</i>	
<i>Review Article</i>	
Processing Plants Damage Mechanisms and On-Stream Inspection Using Phased Array Corrosion Mapping—A Systematic Review	1665
<i>Jan Lean Tai, Mohamed Thariq Hameed Sultan and Farah Syazwani Shahar</i>	
Effects of Unavailability of Conventional Energy Units on Power Generation System Adequacy	1687
<i>Athraa Ali Kadhem and Noor Izzri Abdul Wahab</i>	
Single Deformation Occurrence During Testing of Kenaf Composite Through Momentum Trapping Modification on Split Hopkinson Pressure Bar	1707
<i>Muhammad Fauzinizam Razali, Sareh Aiman Hilmi Abu Seman, Mohd Syakirin Rusdi and Siti Nuha Majiddah Abdul Aziz</i>	
Application of Fuzzy Analytic Network Process in Selection of Bio- composite Filament for Fused Deposition Modeling Process	1721
<i>Hazliza Aida Che Hamid, Mastura Mohammad Taha, Syahibudil Ikhwan Abdul Kudus, Noryani Muhammad, Mohd Adrinata Shaharuzaman, Loh Yueh Feng and Ahmad Ilyas Rushdan</i>	
Optimizing Bagged Trees in an Ensemble Classifier for Improved Prediction of Diabetes Prevalence in Women	1753
<i>Jose Candia Jr., Airish Mae Adonis and Jessica Perlas</i>	

Foreword <i>Mohd Sapuan Salit</i>	i
Evaluation of Glutathione S-transferases Expression as Biomarkers by Heavy Metals in <i>Geloina expansa</i> from Sepang Besar River, Selangor, Malaysia <i>Sarini Ahmad Wakid, Nor Azwady Abd Aziz, Zazali Alias, Muskhazli Mustafa, Wan Mohd Syazwan and Syaizwan Zahmir Zulkifli</i>	1439
Blood CO Status Classification Using UV-VIS Spectroscopy and PSO-optimized 1D-CNN Model <i>Audrey Huong, Kim Gaik Tay, Kok Beng Gan and Xavier Ngu</i>	1461
Effects of Different Throttle Opening and Air Intake Lengths on the Volumetric Efficiency of SI Engine Using 1D Simulation Method <i>Mohamad Firzan Ahmad Harazi, Abdul Aziz Hairuddin, Azizan As'arry and Siti Ujila Masuri</i>	1481
Experiment and Analysis of a Hybrid Composite Post-tension Plate Girder <i>Sahib Al Mustawfi, Nor Azizi Safiee, Nabilah Abu Bakar, Izian Abd Karim and Noor Azline Mohd Nasir</i>	1501
Conversion Factor Estimation of Stacked Eucalypt Timber Using Supervised Image Classification with Artificial Neural Networks <i>Vinicius Andrade de Barros, Carlos Pedro Boechat Soares, Gilson Fernandes da Silva, Gianmarco Goycochea Casas and Helio Garcia Leite</i>	1527
Low Resource Malay Dialect Automatic Speech Recognition Modeling Using Transfer Learning from a Standard Malay Model <i>Tien-Ping Tan, Lei Qin, Sarah Flora Samson Juan and Jasmina Yen Min Khaw</i>	1545
The Green Energy Effect on an HCCI Engine from Used Cooking Oil-based Biodiesel from Malaysia <i>Muntasser Abdulabbas Mossa, Abdul Aziz Hairuddin, Nuraini Abdul Aziz and Hasyuzariza Muhamad Tobib</i>	1565



**Pertanika Editorial Office, Journal Division,**  
Putra Science Park,  
1st Floor, IDEA Tower II,  
UPM-MTDC Center,  
Universiti Putra Malaysia,  
43400 UPM Serdang,  
Selangor Darul Ehsan  
Malaysia

<http://www.pertanika.upm.edu.my>  
Email: [executive\\_editor.pertanika@upm.edu.my](mailto:executive_editor.pertanika@upm.edu.my)  
Tel. No.: +603- 9769 1622

**PENERBIT**  
**UPM**  
UNIVERSITI PUTRA MALAYSIA  
**PRESS**

<http://www.penerbit.upm.edu.my>  
Email: [penerbit@upm.edu.my](mailto:penerbit@upm.edu.my)  
Tel. No.: +603- 9769 8851

